Development and Validation of Numerical Tools to Implement Climate Sensitive Design and Control for Ground Source Heat Pumps with Horizontal Collectors

AUTHOR:

MICHAEL GREENE

A THESIS SUBMITTED FOR THE DEGREE OF DOCTOR OF PHILOSOPHY

DEPARTMENT OF MECHANICAL AND INDUSTRIAL ENGINEERING,

GALWAY-MAYO INSTITUTE OF TECHNOLOGY,

GALWAY, IRELAND

SUPERVISOR:

DR. JOHN LOHAN

Development and Validation of Numerical Tools to Implement Climate Sensitive Design and Control for Ground Source Heat Pumps with Horizontal Collectors

Author: Michael Greene

Abstract

At the outset of the 21st century, growth in the Sustainable Energy Technologies (SETs) market is driven by the need to secure energy supply, limit the environmental impact of fossil fuels and to generate economic growth. By 2020, the Irish government targets SETs to deliver 12% (0.65Mtoe) of annual thermal energy consumption. The Ground Source Heat Pump utilising a horizontal collector ($GSHP_{HC}$) is one of the most popular thermal SETs in Ireland, accounting for 61% of all heat pump installations as of 2010. $GSHP_{HC}$ thermal output is relatively constant and controllable compared to wind and solar technologies. However, the Coefficient of Performance (COP) which dictates the cost effectiveness of $GSHP_{HC}$, is sensitive to a broad transient system which includes the building, heat distribution system, collector design, ground type, climate and operational control. The combined influence of the latter four elements has received limited attention to date and therefore provided the focus for this *HP-IRL/H* study.

The *HP-IRL/H* study was motivated by the Irish heat pump industry's needs and identified knowledge deficits in the literature. Using a multi-disciplinary *thermo-environmental* analysis methodology, this study aimed to demonstrate the potential $GSHP_{HC}$ performance gain from a novel and holistic *Climate Sensitive Design and Control* (*CSDC*) approach in a *Cool Marine* climate, through the following experimental and numerical objectives: (i) conduct a literature review to identify all $GSHP_{HC}$ design, control and environmental parameters; (ii) construct a fully functional experimental facility; (iii) characterise ground temperature response to seasonal, diurnal and weather fluctuations as well as quantifying ground heat transfer processes and properties; (iv) characterise the sensitivity of $GSHP_{HC}$'s COP to collector design, climate and operational control; (v) develop a transient $GSHP_{HC}$ numerical simulation method incorporating the aforementioned characteristics; and (vi) demonstrate and quantify the potential performance gains from *CSDC* using the numerical simulation method.

The *thermo-environmental* analysis methodology necessitated a literature review across five distinct disciplines of climatology, soil physics, heat transfer, fluids and thermodynamics. Uniquely, the key literature from these five disciplines is presented across the first 7 chapters of this thesis for the first time, with a uniform nomenclature throughout.

In the most comprehensive study to date, a full-scale testing facility comprising a 15kW heat pump and 430m^2 horizontal collector, serving a 1,125m^2 commercial building, delivered over

50 million experimental data points from 130 climate, ground, collector, heat pump and building sensors between 2007 and 2010. This data has allowed accurate measurement and analytical characterisation of the ground's thermal energy resource and properties, in addition to the $GSHP_{HC}$'s thermodynamic, thermal and hydraulic performance. Findings indicate an annual average ground temperature of 11.72ºC, with seasonal and diurnal mean-to-peak amplitudes of 6.7 and 1.92K respectively, while average ground thermal diffusivity and conductivity were shown to be 1.05 x 10^{-6} m^2/s and 2.6W/mK respectively. The $GSHP_{HC}$'s COP dropped by 1.67% per 1K reduction in source temperature, thermal drawdown in the source was shown to be proportional to heat extraction rate, while heat pump COP was reduced by 8 to 13% when all circulating and standby power was considered.

A suite of 11 analytical equations and 5 numerical models have been compiled. The simple, yet effective numerical approaches maintained high accuracy while uniquely catering for all the *HP-IRL/H* collector dynamics including: closely positioned *parallel, in-line* pipes with thermal interference; hourly weather influence at the surface; multiple surface covers and ground layers; thermally coupled collector and heat pump performance transience; as well as new *CSDC split-level collector* designs and novel control strategies. The ground response to heat extraction model (NL-4) had an average error of ±0.25K over 2 months of continuous heat extraction, while the coupled collector and heat pump model (NL-5) simulated source return temperature with an average error of ±0.13K over 6 hours for both cyclic and continuous operation.

A preliminary numerical test demonstrated the potential of the *CSDC* approach by simulating the thermal performance of alternative collector designs and control strategies. The deployment of *split-level collectors* at -0.5 and -1.75m utilising *collector temperature feedback control*, produced a 4.6% COP advantage over 2 months compared to the high performing *HP-IRL/H* collector, by taking advantage of reduced volumetric heat extraction and using intelligent feedback control to capture the positive elements of both the diurnal and seasonal ground thermal energy resources. Additional modifications including a southerly incline with a *split-level collector* can result in average COP increases of 6.5 to 7.9% over 3 months. Further developments, particularly on using the next generation of improved models to simulate intelligent control of inclined, *split-level collectors* coupled with thermal storage, could boost SPF by up to 10% in *Cool Marine* regions and further justify the *CSDC* approach.

Declaration

The substance of this thesis is the original work of the author and due reference and acknowledgment has been made, when necessary, to the work of others. No part of this thesis has already been accepted for any degree and is not been concurrently submitted in candidature for any other award.

Signed:_____ Date:_____

Michael Greene (Candidate)

Signed:_____ Date:_____

Dr. John Lohan (Supervisor)

Statement of Confidentiality

The material contained in this thesis may not be used, sold, assigned or disclosed to any other person, organisation or corporation without the expressed permission of each of the following:

Author: Michael Greene

michael.h.greene@gmail.com

Galway-Mayo Institute of Technology Contact: John Lohan

john.lohan@gmit.ie

Dedication

To my mother and father

Acknowledgments

I would like to take this opportunity to acknowledge all those who made this project possible.

Firstly, I would like to offer my thanks and appreciation to my supervisor, Dr. John Lohan. Without John's advice and encouragement, this task would not have been possible.

I would like to acknowledge the support and contribution of the Galway-Mayo Institute of Technology (GMIT), the School of Engineering and Gerard McMichael, the Research Office, as well as George McCourt and everyone at the *IiBC*. Many thanks.

I would like to thank Paul Sikora and *Dunstar Ltd.*, Enterprise Ireland and the Department of Education and Science for the financial support which made this project possible.

Thank you to the Buildings and Estates Office for allowing us to dig nine holes in the ground, thanks to Brian Gilmore electrician, technicians Ray Clarke and Mark Deegan and everyone who helped dig holes and install sensors.

Thanks to all the post graduates and researchers at GMIT for the support and the good memories. To everyone who passed through the PF1 office; in particular Laurentiu, Niall, Andrew and Fran; the TESSA team; everyone who's been through the Kevin Fitzgerald office; and all the GMedTech lads and ladies.

To NUIG and GMIT friends, the band, the soccer lads, the tag-rugby group, the hurling lads and friends at home in Clare, thank you for the fun and distraction.

To my parents and all my family, thank you for your support, love and encouragement.

Finally, a special thanks to my darling girlfriend Flori for her love, support and companionship; also thanks for fixing my computer over and over 'I'll build you a heat pump if the furnace breaks'.

PUBLISHED WORK

The following publications resulted from this project:

Greene, M., Lohan, J., Burke, N., Dimache, L. and Clarke R., 2010. An Efficient Numerical Method for Simulation of Long-term Operation of Horizontal Ground Heat Exchangers with Parallel Shallow Pipes. *Renewable Energy Beyond 2020*, Trondheim, Norway, June 7th – 8th.

Burke, N., **Greene, M.** and Lohan, J., 2008. Experimental Characterisation of Both Air and Ground Source Heat Pump Technologies in the Irish Maritime Climate. *The Challenge of Sustainability Conference*, Dundalk IT, Ireland, June 20th.

Greene, M., Burke, N., Lohan, J. and Clarke, R., 2008. Ground Temperature and Moisture Content Surrounding Horizontal Heat Pump Collectors in a Maritime Climate Region. *9th International Energy Agency – Heat Pump Conference*, Zürich, Switzerland, May 20th – 22nd.

Burke, N., **Greene, M.**, Lohan, J. and Clarke, R., 2008. Heat Pump Performance Sensitivity to Horizontal and Vertical Collector Configurations in a Maritime Climate Region. *9th International Energy Agency – Heat Pump Conference*, Zürich, Switzerland, May 20th – 22nd.

Greene, M., Burke, N., Lohan, J. and Clarke, R., 2007. Ground Temperature Gradients Surrounding Horizontal Heat Pump Collectors in a Maritime Climate Region. *WIT Transactions on Ecology and the Environment*, 1, pp.309-319

Lohan, J., Burke, N., and **Greene, M.**, 2006. Climate Variables that Influence the Thermal Performance of Horizontal Collector Ground Source Heat Pumps. *8th Biennial ASME Conference on Engineering Systems Design and Analysis*, Torino, Italy, July 4th – 7th.

Lohan, J., **Greene, M.**, and Burke, N., 2006. The Development of a Ground Source Heat Pump Characterisation Facility for the Irish Maritime Climate. *Renewable Energy in Maritime Island Climates (REMIC2)*, Dublin Institute of Technology, Dublin, Ireland, April 26th – 28th, pp. 119-124.

TABLE OF CONTENTS

TABLE OF FIGURES

TABLE OF TABLES

NOMENCLATURE

Abbreviation	Name
ANN	Artificial Neural Networks
ASHP	Air Source Heat Pump
B	Brine (GHE fluid – approximately 70% water and 30% ethylene glycol)
BES	Building Energy Simulation
Cfb	Maritime climate classification
CSDC	Climate Sensitive Design and Control
DAQ	Data Acquisition
EET	Energy Efficient Technologies
EFD	Explicit Finite Difference
ESRI	Economic and Social Research Institute
FDM	Finite Difference Method
FEM	Finite Element Method
FP	Field Point
GHE	Ground Heat Exchanger
GSHP	Ground Source Heat Pump
$GSHP_{HC}$	Ground Source Heat Pump with Horizontal Collector
$GSHP_{VC}$	Ground Source Heat Pump with Vertical Collector
$GSHP_{WS}$	Ground Water Source Heat Pump
GTD	Ground Temperature Distribution
HC	Horizontal Collector
HDPE	High Density Polyethylene
HGHE	Horizontal Ground Heat Exchanger
HP-IRL	Heat Pump Study in Ireland's Maritime Climate
HP-IRL/A	ASHP specialisation of the HP-IRL study
HP-IRL/H	HC specialisation of the HP-IRL study
HP-IRL/V	VC specialisation of the HP-IRL study
HSET-IRL	Hybrid Sustainable Energy Technology Study in Ireland's Maritime Climate
HVAC	Heating Ventilation and Air Conditioning
IFD	Implicit Finite Difference
IiBC	Innovation in Business Centre (site of experimental test facility)
$LCCO_2$	Life Cycle CO_2 Analysis
LPG	Liquid Petroleum Gas
PSD	Particle Size Distribution
RET	Renewable Energy Technology
RTD	Resistive Thermal Device (temperature sensor)
SET	Sustainable Energy Technology
SOL-IRL	Solar Thermal Study in Ireland's Maritime Climate

SPF	Seasonal Performance Factor
TDR	Time Domain Reflectometer (moisture sensor)
VBHE	Vertical Borehole Heat Exchanger
VC	Vertical Collector
VFD	Variable frequency drive
W	Water (as commonly used for hydronic space heating fluid)
WSHP	Water Source Heat Pump

Symbol	**Name**	**Unit**
A	Mean to peak amplitude	K
A	Area	m^2
C	Volumetric heat capacity	J/m^3K
COP	Coefficient of Performance	-
D	Diameter	m
D	Duty	%
DC	Diffusion coefficient	-
E	Evaporation	kg/m^2
E"	Evaporation flux density	m^3/m^2s
Fo	Fourier number	-
G	Ground heat transfer	J/m^2
H	Sensible heat transfer	J/m^2
H_f	Pipe head loss (major)	m
H_m	Pipe head loss (minor)	m
J"	Water flux density	m^3/m^2s
K	Hydraulic conductivity	m/s
K	Minor loss coefficient	-
L	Length	m
L_f	Specific latent heat of fusion of water	J/kg
L_t	Total length of one parallel, in-line pipe	m
L_v	Specific latent heat of vaporisation	J/kg
M	Moisture content	m^3/m^3
N	Number of pipes on collector manifold	-
Nu	Nusselt number	-
P	Pressure	Pa
PATV	Peak annual temperature variation	K
PDTV	Peak diurnal temperature variation	K
PE	Potential energy	J
Pr	Prandtl number	-
PS	Spacing between in-line collector pipes	m
Q	Thermal energy	J
Q"	Total energy flux	J/m^2
R	Thermal resistance	K/W

R^2	Goodness of fit value	-
Re	Reynolds number	-
RH	Relative humidity	%
R_n	Net radiation	J/m^2
T	Temperature	ºC
TS	Trench spacing	m
U	Combined heat transfer coefficient	W/m^2K
V	Volume	m^3
$\dot{V}$	Volumetric flow rate	m^3/s
W_T	Trench size (width)	m
Z	Vertical dimension (below the surface is negative)	m
Z	Gravimetric potential	m
Z_{prec}	Precipitation level	m
a	Albedo	-
b	Constant of moisture release	-
c	Specific heat capacity	J/kgK
c_p	Constant pressure specific heat capacity	J/kgK
d	Day of the year	day
f	Friction factor	-
h	Convection coefficient	W/m^2K
h	Specific enthalpy	kJ/kg
hr	Hour of the day	h
k	Thermal conductivity	W/mK
m	Mass	kg
$\dot{m}$	Mass flow rate	kg/s
$\dot{m}$"	Mass flux	kg/m^2s
p	Porosity	-
q	Heat transfer rate	W_{th}
q'	Heat transfer rate per meter	W/m
q"	Heat flux density	W/m^2
r	Radius	m
r	Resistance coefficient	s/m
s	Specific entropy	kJ/kgK
t	Time	s
u	Velocity	m/s
w	Rate of electrical energy consumption	W
Δ	Change (difference between two values)	
ΔT_{hp}	Temperature lift achieved by heat pump	K
$\Delta T_{s,r/\infty}$	Thermal drawdown in source return temperature	K
Θ	Angle of incidence	º
Φ	Ground water potential	m

Ω	Latitude	º
α	Thermal diffusivity	m^2/s
$\acute{\alpha}$	Altitude above horizon	º
β	Slope of surface (North facing angle for Northern Hemisphere)	º
$\beta_{\Delta L}$	Local heat transfer ratio	-
γ	Azimuth from North (orientation)	º
δ	Angle of declination	º
ε	Emissivity	-
η	Thermal efficiency	-
θ	Volumetric content	m^3/m^3
λ	Phase	º
ν	Kinematic viscosity	m^2/s
ξ	Weighting factor	-
ρ	Density	kg/m^3
σ	Stephan-Boltzmann constant	W/m^2K^4
φ	Calculation factor for fluid in pipe	-
ψ	Matric potential	m
ψ_e	Air entry potential	m
ω	Angular velocity	rad/s

Subscripts	**Name**
Carnot	Carnot
D	Diffuse
F	Collector fluid (water glycol mix)
G	Ground heat transfer
H	Sensible heat transfer
HC	Horizontal collector
LB	Lower boundary
L_t	Total length of pipe
LvE	Latent heat transfer
LW	Longwave
LWI	Longwave incoming
LWO	Longwave outgoing
N	Number of pipes
P	Pump
P	Profile
R	Reflected radiation
R_n	Net radiation
S	Solar (short wave)
a	Air
ag	Air in ground volume
av	Average

b	Brine
bulk	Bulk
c	Compressor
coil	Coil
cond	Condensing
cond	Conduction
conv	Convection
cool	Cooling
cos	Cosine
cov	Covered
c-s	Clear-sky
d	Daily (also Daily Average)
dry	Oven dried ground
eg	Ethylene glycol
ent	Entering
evap	Evaporating
exit	Exiting
exp	Experimental
f	Flowing from heat pump
g	Ground
gas	Gas
h	Hourly (also Hourly Average)
heat	Heating
hp	Heat pump
i	The i^{th} component or state
ice	Ice
in	Inner
lag	Lagging
lam	Laminar
lin	Linear
liq	Liquid
m	Monthly (also Monthly Average)
max	Maximum
min	Minimum
n	Net
o	Outer
orb	Orbit
p	Pipe
p-g	Pipe ground interface
prec	Precipitation
r	Returning to heat pump
rad	Radial
real	Real
r-o	Run-out pipe

room	Room
rot	Rotation
s	Heat source for heat pump
sat	Saturated
set	Set-point
sg	Solids in ground volume
sim	Simulated
sk	Heat sink for heat pump
st	Stored
stb	Standby
sun	Sun
sur	Ground surface
t	Total
ter	Terrestrial
th	Thermal
true	True
turb	Turbulent
vap	Vapour
w	Water
wg	Water in ground volume
wi	Water infiltration
wind	Wind
wp	Water percolation
y	Annual (also Annual Average)
∞	Farfield

Superscripts	**Name**
p	Previous time step
↑	Extending upward
↓	Extending downward

Ref Number	**Name**
AL-#	Analytical model number #
HC#	Horizontal collector test period number #
$H_{P\#,\ Zm}$	Heat flux sensor in profile number # positioned at Zm
$M_{P\#,\ Zm}$	Moisture content measurement in profile number # positioned at Zm
NL-#	Numerical model number #
P#	Experimental profile number #
$S_{P\#,\ Zm}$	Soil sample taken from profile number # at Zm
$T_{P\#,\ Zm}$	Temperature measurement in profile # positioned at Zm

CHAPTER 1

INTRODUCTION

1. INTRODUCTION

While this project is concerned with the operation of Ground Source Heat Pumps (GSHPs) with horizontal collectors, this chapter presents the broader economic and environmental context which motivated and shaped the study. At the outset of the 21st century, growth in the Sustainable Energy Technologies (SETs) market is driven by the need to secure energy supply, limit the environmental impact associated with over-reliance on fossil fuels and in some countries such as Ireland, to generate economic growth. Therefore, the motives, incentives and drivers for GSHP focused research in Ireland are reviewed within the following six sections:

- Sustainable Energy
- Ground Source Heat Pumps
- Overview of GSHP Research
- Summary of Motivations, Aim and Objectives
- Project Overview
- Thesis Layout

1.1 SUSTAINABLE ENERGY

Sustainable energy can be defined as energy sources that are not expected to be depleted in a time frame relevant to the human race and therefore contribute to the sustainability of all species (Lund, 2010). Such energy sources include *renewable energy* such as sunlight, wind, rain, waves, tides and geothermal heat – that are naturally replenished within a time span of a few years (Lund, 2010). A *sustainable energy strategy* typically seeks to deliver the following three technological changes (Lund, 2007):

- Energy savings on the demand side (through moderate and efficient use)
- Efficiency improvements in the production of energy
- Replacement of fossil fuels by various sources of *renewable energy*

Sustainable energy strategy is used by Lund (2007) as an umbrella term for moderate and efficient use of non-renewable resources such as fossil fuels with an increased fraction of renewable sources such as solar, wind and geothermal energy. Additionally, Renewable Energy Technologies (RETs) are typically considered to be a subset of SET, as shown in Figure 1-1. Figure 1-1 also shows that Energy Efficient Technologies (EET) such as Heat Recovery Ventilation (HRV) and Phase Change Materials (PCMs) can be considered a subset

of SET. It will be seen in the next section that GSHP is an efficient thermal energy provider and is also partially or entirely an RET depending on the means of electricity production.

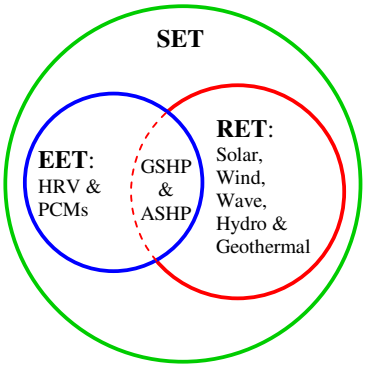

Figure 1-1: RET and EET as subsets of SET, GSHP is always an EET and is either partially or entirely an RET depending on the means of electricity production

Reflecting recent predictions that peak oil production will occur between 2010 (Groppe, 2005) and 2020 (Koppelaar, 2005; Deffeyes, 2002), increased evidence of CO_2 induced climate change (IPCC, 2007) and the need to create SET based industries (Kammen *et al.*, 2004), it is no surprise that the annual SET investment globally increased fourfold between 2004 and 2008 to reach $120billion/annum in 2008 (REN21, 2009). Across the European Union (EU) the SET market has been further boosted by EU commitments to the United Nations Framework Convention on Climate Change (UNFCCC) under the Kyoto Protocol and government incentives to boost uptake of sustainable technologies. In fact, growth in both investment and uptake of SET internationally has been viewed as almost 'crisis proof' during the recent global recession (REN21, 2009).

1.1.1 Energy in Ireland

Recent data shows that Ireland imported 89% of all energy used in 2008, 81% of which was derived directly from oil and gas (Howley *et al.*, 2009). Annual energy usage is spread almost equally across transport (5.5 Mtoe), thermal energy production (5.4 Mtoe) and electricity production (5 Mtoe) (Howley *et al.*, 2009). Ireland's contribution to the EU's Kyoto Protocol commitment has limited growth in green house gas emissions between 2008 and 2012 to 13% above the 1990 levels (DEHLG, 2007). The EU aims for much greater reductions by 2020 and Ireland's contribution is likely to require a reduction below 1990 emission levels (DEHLG, 2007). According to the Economic and Social Research Institute (ESRI), the Irish economy contracted by 3% and 7.3% in 2008 and 2009 respectively. As a result, reduction in energy

imports and increased exports of SET knowledge and products is seen by many as the key to stimulating the economy and generating employment (HLGGE, 2009).

1.1.2 Irish Energy Policy

Reflecting the concerns outlined in Sub-section 1.1.1, the Irish Government has introduced a range of *green policies* to promote the uptake in SET and stimulate the 'green economy' as follows:

- 2002 – Sustainable Energy Authority of Ireland (SEAI) founded
- 2006 – ReHeat: Incentives for SET in commercial/industrial/agriculture sectors
- 2006 – Greener Homes Scheme: Incentives for SET in residential sector
- 2007 – Dwelling Energy Assessment Procedure (DEAP) introduced
- 2007 – White Paper: 'The Energy Policy Framework 2007-2020' (DCMNR, 2007)
- 2007 – Irish National Climate Change Strategy 2007-2012 (DEHLG, 2007)
- 2007 – Part L of the Building Energy Regulations upgraded (DEHLG, 2007)
- 2007 – Initial planning permission exemptions for SET (DEHLG, 2007)
- 2008 – Increased planning permission exemptions for SET (DEHLG, 2008)
- 2009 – 'Green Economy' in Ireland policy launched (HLGGE, 2009)
- 2010 – SEAI Strategic Plan 2010-2015 published (SEAI, 2010)
- 2010 – National Renewable Energy Action Plan (NREAP) (DCENR, 2010)
- 2011 – Part L of the Building Energy Regulations upgraded (DEHLG, 2010)

The proposed NREAP targets the delivery of 16% of overall energy from *renewable* sources by 2020. This ambitious target is to be achieved by delivering 40% of electricity and 12% of thermal energy (0.65 Mtoe) from *renewable* sources, with 10% of transport running on electricity (DCENR, 2010). While the country is on target to meet the electrical requirement, with 14.4% renewable in 2009 (Dennehy *et al.*, 2010), '*for historical, geographical and demographical reasons, renewable heat poses a significant challenge for Ireland*' (DCENR, 2010). Renewable heat has slowly risen from 3.5% in 2005 to 4.3% by the end of 2010 (DCENR, 2010). The heat pump is one technology that could make a significant contribution to the 12% thermal energy target, as it can be used to supply heat to residential, commercial and industrial sectors by extracting *renewable* heat embodied in nearby air, water or ground reservoirs. Heat pumps and in particular ground source heat pumps, have received considerable government support between 2002 and 2010 through *green policies* such as the 2006 Greener Homes Scheme.

1.2 GROUND SOURCE HEAT PUMPS

A heat pump is a device which transfers heat from a lower temperature medium (heat source) to a higher temperature medium (heat sink) (Cengel & Boles, 2002). A heat pump system comprises a *vapour-compression* unit coupled with two heat reservoirs, one reservoir acting as the heat source and the other as the heat sink. Typically, the building acts as the sink in winter (for heating) and then the source in summer (for cooling), with the ground, water or air playing the opposite role during each season. A GSHP is coupled directly or indirectly with the ground or ground water, while an Air Source Heat Pump (ASHP) uses the air outside. With GSHP, the heat pump device is ground-coupled because the ground is a *'low-grade solar energy storage medium'* (Mei, 1987) with a '*large volume available'* (VDI-4640, 2004). The ground also offers a *'suitable temperature level*' (VDI-4640, 2004) or *'less severe temperatures* [than air]*'* (Garimella, 2003) and *'relatively uniform temperatures* [compared to air]*'* (Lund *et al.*, 2003). While many heat pumps can provide both heating and cooling to a building, the primary use of GSHP in Ireland is for heating during late autumn, winter and much of spring.

1.2.1 Coefficient of Performance

By using a heat pump, 'low grade' solar and geothermal heat which is abundant and *renewable* in the ground, water or air can be 'upgraded' to a useful space heating temperature; this 'upgrading' requires the input of some work typically provided by an electrical compressor. The ratio of useful heating delivered by a heat pump to the electrical input required to run a heat pump is known as the Coefficient of Performance (COP). For a typical heat pump the COP can range from 2 to 6 (200 to 600%) in heating mode (Sanner *et al.*, 2003). Part L of the Irish building regulations requires that all heat pumps operate at a COP greater than 2.5 (DEHLG, 2008). COP is inversely proportional to the temperature difference between the heat source and sink, known as 'temperature lift' (ΔT_{hp}) [K]. As a rule of thumb, the COP increases by 2 to 2.5% for every 1K reduction in temperature lift (Cengel & Boles, 2002; Warnelof & Kronstrom, 2005; Burke *et al.*, 2008). The ratio of total GSHP useful heat output [kWh_{th}] to total electrical consumption [kWh] over a heating season is known as Seasonal Performance Factor (SPF). SPF typically ranges from 3 to 3.8 for a properly installed GSHP, but is directly influenced by the local climate (Sanner *et al.*, 2003).

A steady increase of 2.5% per annum has been reported in the average COP published for operational GSHPs between 1976 and 2000 (Lazzarin, 2007), currently the average COPs reported lie between 3.3 (Lazzarin, 2007) and 3.4 (Gupta & Irving, 2008). While COP

increase is limited by the laws of thermodynamics, average GSHP COPs of between 3.5 and 4.3 for 2020 have been projected (Burke, 2010). COP and SPF are discussed in greater technical detail in the subsequent chapters.

1.2.2 Environmental Potential

SEAI encourages the use of GSHP in Ireland, quoting CO_2 emissions reductions of up to 40% compared to oil for heating a 180m^2 residential property (SEAI, 2006). In the United Kingdom (UK), installation of GSHP can achieve a 40 to 60% reduction in heating related CO_2 emissions compared to oil (Lund *et al.*, 2003; EST, 2007; Gupta & Irving, 2008) and 15% reduction compared to gas (Gupta & Irving, 2008). In Whitehorse, Canada, where the majority of national power comes from hydro-electric plants, an 85% CO_2 reduction can be achieved by switching from oil to GSHP (Caneta-Research, 2003). On average '*reductions in* [primary] *energy consumption of 30 to 70% in the heating mode and 20 to 50% in the cooling mode can be obtained'* in Canada (Retscreen, 2005). In Japan, it is estimated that using large-scale GSHP for district heating and cooling can result in an 85% reduction in CO_2 emissions for a 1km^2 area of high-rise buildings in Nishi-Shinjuku, Tokyo (Genchi *et al.*, 2002). The average CO_2 emissions resulting from electricity production in Ireland has reduced by 2% per annum between 1990 and 2008 (Howley *et al.*, 2009). With targets of 40% renewable electricity production (DCENR, 2010) and a conservative projected average COP of 3.75 by 2020, emissions savings achieved by GSHP as compared with oil fired boilers can increase from 42% to 64%, as summarised in Table 1-1. Table 1-1 data has been derived from various Irish Government reports (SEAI, 2008; Howley *et al.*, 2009; DCENR, 2010). In addition, GSHP-output is not subject to the short-term fluctuations in supply which are difficult to predict for other SETs, giving GSHP the practical advantages over solar and wind energy of 'controllability', 'reliability' and 'predictability'.

Table 1-1: Current (2010) and projected (2020) CO_2 emissions reduction that may accrue from replacing oil and gas based heating systems with GSHPs in Ireland

	2010	**2020**
Electricity from renewable sources (implied low to zero CO_2 emissions) [%]	14	40
Emissions for electricity production [kgCO_2/kWh]	0.57	0.4
Average reported GSHP COP [-]	3.3	3.75
Emissions for space heating [kgCO_2/kWh$_{th}$]	0.17	0.1
Emissions savings compared to oil at 0.272 kgCO_2/kWh$_{th}$ and 90% efficiency [%]	42	64
Emissions savings compared to mains gas at 0.203 kgCO_2/kWh$_{th}$ and 90% efficiency [%]	23	52

1.2.3 Ground Coupling

There are two common methods used to achieve the ground-coupling of a GSHP; these are the Horizontal Ground Heat Exchanger (HGHE) and the Vertical Borehole Heat Exchanger (VBHE), shown in Figures 1-2(a) and (b) respectively (Lund *et al.*, 2003). These are also known as Horizontal and Vertical Collectors (HC and VC) and the combination of heat pump and collector type is referred to in this thesis as $GSHP_{HC}$ and $GSHP_{VC}$ respectively. Horizontal collectors consist of a heat exchange fluid circulated through long plastic pipes, typically 35 to 60 m long per kW of heating or cooling capacity and buried horizontally in shallow (1 to 2 m deep) pits or trenches (Retscreen, 2005; Florides & Kalogirou, 2007). Vertical collectors consist of a heat exchange fluid being circulated through vertically aligned U-bend plastic pipes placed in deep (45 to 150 m) boreholes (Retscreen, 2005).

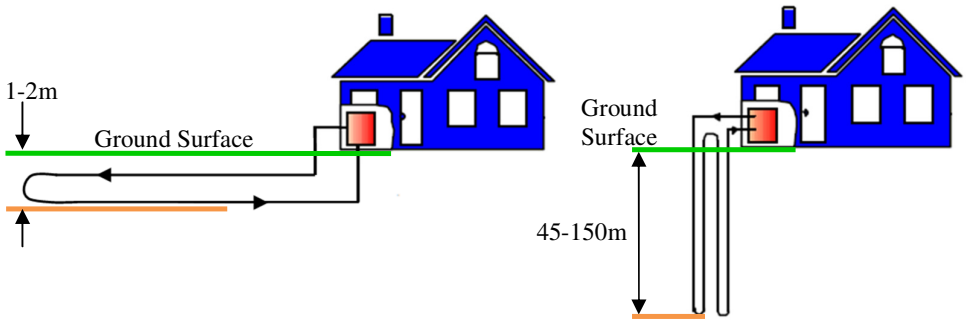

(a) Horizontal Collector (HC) **(b) Vertical Collector (VC)**

Figure 1-2: The two basic configurations of GSHP ground collectors (Lund *et al.* 2003)

As depicted in Figure 1-3, the horizontal collector is the most common installation type in Ireland with 61% of all installations, followed by the vertical collector at 22% (Burke, 2010). While $GSHP_{HC}$ are the most common, being less expensive to install than $GSHP_{VC}$ and perceived as cheaper to run than *ASHP*, there is a lack of independent heat pump performance data and detailed collector design information in Ireland. The SEAI recommends that 'a*ll heat pump systems are at their most efficient when the source temperature is* [kept] *as high as possible, the heat distribution temperature is* [kept] *as low as possible and pressure losses in air and water systems are* [kept] *to a minimum*' (SEAI, 2008). This statement, while entirely true, provides a designer or installer with little advice on how these desirable conditions can be achieved and maintained.

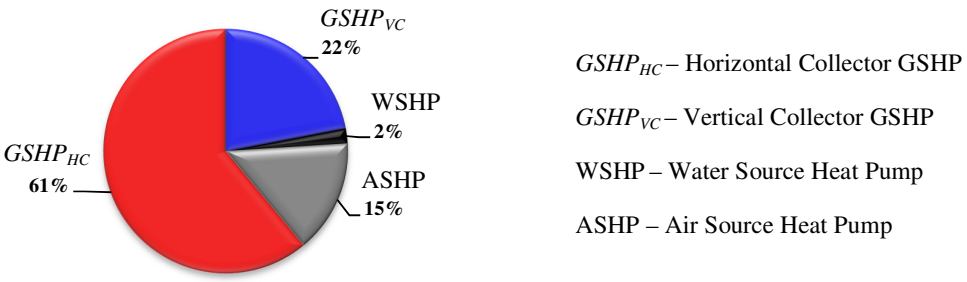

Figure 1-3: Composition of the Irish heat pump market by heat source type (Burke, 2010)

1.2.4 Design Variables

Due to its dominant position in the Irish market, this thesis focuses on characterising and boosting the performance of $GSHP_{HC}$. There are many aspects to $GSHP_{HC}$ design and operational control, referred to as the $GSHP_{HC}$ *design variables,* these are discussed in greater technical detail in Chapter 2 and include the following:

- *Maximum heat demand* and *annual heat requirement* of the built environment
- *Heat distribution system* in the built environment
- Heat pump type – *capacity, extraction, delivery* and COP/SPF
- *Collector flow configuration*
- *Collector pipe routing*
- *Thermo-hydraulic collector dimensioning*
- *Pipe layout and burial*
- *Backfill material*
- *Surface cover*
- *Operational control*

Gupta & Irving (2008) recognised that one of '*the most significant* [barriers to $GSHP_{HC}$ uptake] *is the lack of independently-verified, accurate tools for their sizing*' (Gupta & Irving, 2008). Design recommendations are available from the SEAI (SEAI, 2006) and the UK's Energy Savings Trust (EST, 2007), along with continental guidelines from Germany (VDI-4640, 2004; Sanner, 2008), Canada (Retscreen, 2005) and others summarised by Sanner (2008) and Burke (2010). There are also standards such as the British Standards BS EN15450:2007 and BS EN15316-4-2 which appear to be in a state of flux (Gupta & Irving, 2008). A list of design guides is presented in Table 2-11 and standards are included in Appendix A. There are numerous basic guides that all seek to deliver horizontal collectors that avoid harsh continental climate winters. Additionally, collectors are typically only buried

under grass covered sites with collectors under car parks, driveways, roads and even beneath the building itself not commonly utilised. There is an absence of design guides for milder climates that may offer a performance advantage with appropriate collector design and control.

1.2.5 The Market, Costs and Payback

GSHP have maintained a 10% annual increase in sales in about 30 countries between 1993 and 2003 (Lund *et al.*, 2003). Worldwide it is estimated that GSHP accounted for 30 GWth of installed *capacity* with use of geothermal heat reaching an estimated 15 GWth by the end of 2008 (REN21, 2009). In Ireland, the Greener Homes Scheme, introduced in 2006, has accelerated the uptake in GSHP; according to SEAI's Statistical Support Unit, over 6060 heat pump grant aid applications were approved between 2006 and March 2010. SEAI encourages the use of GSHP in Ireland, quoting a residential heating cost reduction of up to 70% compared to oil for a 180m^2 residential property (SEAI, 2006). A similar saving is found in this study, summarised in Table 1-2, using night rate electricity to power the GSHP. The data used for Table 1-2 is derived from national and international sources (Gupta & Irving, 2008; Burke, 2010; SEAI, 2010).

Table 1-2: Comparison of GSHP, oil and gas heating capital and running costs

	$GSHP_{HC}$	$GSHP_{VC}$	Medium fuel oil	Mains Gas
System capital cost/kW$_{th}$ [€]	1300[1]	1700[1]	90-120	100-150
Fuel/power input cost/kWh [€]	0.173(0.087)[2]	0.173(0.087)[2]	0.068	0.047
Conversion efficiency [-]	3.3	3.3	0.9	0.9
Running cost per kWh$_{th}$ [Euros]	0.052(0.026)[2]	0.052(0.026)[2]	0.075	0.052
Reduction in running cost with GSHP [%]			30.6(65.3)[2]	0(47.2)[2]

[1] These values correspond to the average of Burke's (2010) findings in Ireland and the upper limit of Gupta and Irving's (2008) findings in the UK. [2] Values in brackets represent night rate prices

One drawback to $GSHP_{HC}$ and particularly $GSHP_{VC}$ is the high capital cost (Warnelof & Kronstrom, 2005; Gupta & Irving, 2008). While GSHP are seen to have lower running costs than traditional heating systems, the *payback time* (capital cost divided by annual cost reduction) is often excessive due to high capital cost and customers opt for oil or gas boilers. This is compounded by instances of over-sizing (increasing the capital cost) or under-sizing and poor installation (increasing the running cost) due to the absence of proper guidelines for $GSHP_{HC}$ *design variables*. Continued research is seen as the key to reducing payback time by: establishing proper guidelines to eliminate over and under-sizing, reducing capital costs and

running costs respectively (Sanner *et al.*, 2003); introducing intelligent design and control to increase the operational efficiency and further reduce running costs (Healy & Ugursal, 1997; Esen *et al.*, 2006) and finally, aggressive research has been proven to fast-forward the 'learning by doing' process for manufacturers and installers and bring about quicker cost reductions for energy technologies (McDonald & Schrattenholzer, 2001). This project responds to each of these calls.

1.3 OVERVIEW OF GSHP RESEARCH

Research into GSHPs began in the 1940's (Grandall, 1946; Ingersoll & Plass, 1948). However, a research bias exists as the majority of research over the last twenty five years has focused on $GSHP_{VC}$ (Bose *et al.*, 2002; Sanner *et al.*, 2003). For example, $GSHP_{VC}$ have benefited from simulation (Eskilson & Claesson, 1988; Hellstrom & Sanner, 1994; Diao *et al.*, 2004; Michopoulos & Kyriakis, 2009) and experimentation (Kavanaugh, 1984; Hepbasli *et al.*, 2003; Lim *et al.*, 2007). Bose *et al.* (2002) summarised the extensive research into $GSHP_{VC}$ particularly in North America and also recognised that by comparison, considerably less research has been conducted in the area of $GSHP_{HC}$. The oil shortage in the 1970's inspired initial $GSHP_{HC}$ research (Metz, 1979). Research continued through the 1980's (Mei, 1986) and early 1990's (Drown & Den Braven, 1992; Tarnawski & Leong, 1993; Piechowski, 1996). However, it was not until considerable SET market growth began at the beginning of the 21st century, that a significant level of research into $GSHP_{HC}$ emerged, but in continental regions such as Sweden (Warnelof & Kronstrom, 2005) and Turkey (Esen *et al.*, 2007; Demir *et al.*, 2009).

1.3.1 Recent Research

The most recent $GSHP_{HC}$ research in Europe has been conducted in Turkey, with experimental characterisation (Koyun *et al.*, 2009), Finite Difference Method (FDM) simulation (Esen *et al.*, 2007; Demir *et al.*, 2009) and applications of Artificial Neural Networks (ANN) (Esen *et al.*, 2008) all underway. Work at the University of Nottingham in the UK is focused on using the heat contained in rain water to boost GSHP performance (Doherty *et al.*, 2004; Gan *et al.*, 2007; Wu *et al.*, 2010) along with environmental and economic research at Oxford Brookes University (Gupta & Irving, 2008). Previous research in North America has delivered simulated and experimental data from the Oklahoma State University (Chiasson, 1999; Hern, 2004), the University of Idaho (Drown & Den Braven, 1992; Wibbels & Den Braven, 1994), the National Laboratories USA (Metz, 1979; Mei,

1986) and Canada (Svec, 1991; Tarnawski & Leong, 1993; Healy & Ugursal, 1997). Further research has been carried out in Australia (Piechowski, 1996) and China (Bi *et al.*, 2002). In Ireland, recent experimental work has been conducted at the Cork IT (O'Connell & Cassidy, 2003) and at the Galway-Mayo IT (Burke *et al.*, 2008; Burke, 2010). The majority of this research has emanated from *Continental* climate regions which experience extreme winter cooling, summer heating or both. For this reason horizontal collectors are purposely shielded from the negative climate influences and therefore no research with the exception of Burke (2010) has reported efforts to utilise positive climate aspects. This study sought to address this.

1.3.2 Climate

Due to proximity to the Atlantic Ocean and the associated weather patterns, Ireland experiences a maritime climate (Peel *et al.*, 2007). The maritime climate is categorised as *Cfb* in the Koppen-Geiger system (Kottek *et al.*, 2006) or *Cool Marine* in the Koeppe and De Long system (Koeppe & De Long, 1958). Ireland shares this *climate classification* with most of the UK, small parts of other European countries such as Norway, Denmark, the Netherlands and Belgium, large parts of western France, Spain and Portugal along with New Zealand, Chile and America's Pacific North West. This group represents a population of over 100 million (Burke, 2010) and will be referred to as the *Cool Marine geo-cluster*. A geo-cluster is defined as '*virtual transnational areas/markets with strong similarities'* (Poireau, 2010). As can be seen from both Table 1-3 and Figure 1-4, the *Cool Marine* climate differs greatly to others such as *Humid Continental* and *Moderate Subpolar* under which GSHP research was conducted in New York (Metz, 1979) and Ottawa (Svec, 1991) respectively. Climate classification is discussed in greater detail in Sub-section 3.1.1 and the worldwide Koeppe and De Long (1958) climate classification system is included in Appendix B. Comparison between *Cool Marine* and *Humid Continental,* or simply *Continental* climates, is frequently made throughout this thesis.

Table 1-3: Climate classifications for three regions where GSHPs are used (Koeppe & De Long, 1958)

No.	Climate Classification	Air Temperature	Precipitation	Example
1.	*Cool Marine*	Coldest month between -1.1ºC and +7.2ºC	>890 mm/y, winter maximum, no dry month	Dublin, Ireland
2.	*Humid Continental*	Coldest month under +4.4ºC, annual range more than 21.6K	>400 mm/y poleward margins, >560 mm/y equatorial margins	New York, USA
3.	*Moderate Subpolar*	One to four months under -1.1 °C, at least one month above +10 °C; not more than two months above +15.5 °C	Maximum occurs in summer	Ottawa, Canada

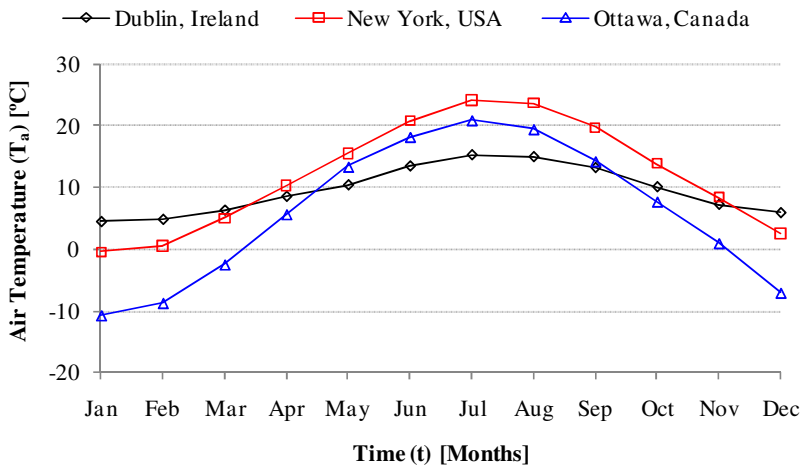

Figure 1-4: Multi-year monthly averaged air temperatures for Dublin (Cool Marine), New York (Humid Continental) and Ottawa (Moderate Subpolar) where $GSHP_{HC}$ research has been conducted (WMO, 2010)

Comparing Dublin where the annual average air temperature ($T_{a,y}$) is about 9.8ºC to New York State where $T_{a,y}$ is about 12ºC in Figure 1-4 the following observations can be made:

- The first noticeable feature is that the Irish annual air temperature (T_a) [ºC] oscillation is considerably flat compared to the other regions; $A_{a,y}$, the mean-to-peak amplitude of T_a, is just 5K in Ireland compared with 12K in New York
- The average winter minimum $T_{a,min}$ is approximately 5K cooler in New York than Dublin, meaning winter *maximum heat demand* for the same building design is higher in New York
- The average summer maximum $T_{a,\,max}$ is approximately 9K warmer in New York than Dublin, the New York summer temperatures of 24ºC necessitate considerable active cooling while this is not required in Dublin as average summer temperatures do not exceed 15ºC
- T_a in New York during January, February and December are lower than Dublin temperatures, T_a in March and November are approximately equal at both locations and during all other months T_a in New York exceeds that in Dublin
- Depending on solar gains and daily T_a maximums, the months of April and May, along with September and October are interesting in that heating may be required for Irish buildings during these months but not for buildings in New York
    - This is interesting since the temperature lift (ΔT_{hp}) between source and sink will be at its lowest at these times and the 'useful' heat delivered, since it is necessary, should contribute to a higher SPF for a well managed Irish $GSHP_{HC}$

- Due to the mild winter and spring in Ireland $GSHP_{HC}$ may benefit from collecting shallow heat near the surface which is replenished by the mild climate
- For the $GSHP_{VC}$, the absence of a summer cooling load in Dublin means no heat is rejected to the VBHE during summer, this is referred to as 'heating constrained' (Spitler & Cullen, 2008)
    - Without this recharge and the long heating season, $GSHP_{VC}$ may experience a reduction in average operating temperature over a number of years in Ireland, compared with New York or other hot summer climate regions

The latter three points are just a sample of 'climate sensitive' issues which can arise with $GSHP_{HC}$ and $GSHP_{VC}$ respectively.

The influence of the Gulf Stream generates winter ocean temperatures around Ireland and the UK that are consistently 7 to 8K higher than non-maritime regions at similar northern latitudes (Bryden & Imawaki, 2001). Consequently, mild and moist winter conditions prevail and the potential for improved $GSHP_{HC}$ performance exists in *Cool Marine* regions (Lohan *et al.*, 2006); consistently high soil moisture content has been shown to improve GSHP COP (Drown & Den Braven, 1992) by 35% over dry soil (Leong *et al.*, 1998). However, research to inform optimums for $GSHP_{HC}$ *design variables*, similar to the simulated 'sensitivity analysis' conducted in Canada (Healy & Ugursal, 1997) has not been reported for *Cool Marine* regions. Furthermore, the benefits of using ground-heat exchange in horticulture (Gauthier *et al.*, 1997), aquaculture (Tarnawski *et al.*, 2009) or passive houses (Badesku, 2007) in both winter and summer as a heating and cooling store respectively, have not been fully assessed in *Cool Marine* climate regions.

1.3.3 Research Bias

The reasons for the *research bias* towards $GSHP_{VC}$ in the literature may be related to both climate and building practices since much of the research has been conducted in the United States (US). In the US, boreholes are used to provide a heat source in winter but more importantly a means of efficiently rejecting summer heat in densely populated cities and suburbs. As a result, 46% of US installations are $GSHP_{VC}$ (Lund *et al.*, 2003) which take up very little useful space and are not subject to summer sunshine heat gains. In Ireland, the $GSHP_{HC}$ is the most common installation (O'Connell & Cassidy, 2003; Burke, 2010) mainly due to lower installation costs, the space available in one-off housing, the mild winter conditions and the absence of a heat rejection load. Additionally, GSHP in Ireland like most of Northern Europe are sized for heating loads, as opposed to the common practice in the US

where they are sized for cooling loads (Lund *et al.*, 2003). Due to the relatively comfortable summer temperatures associated with the *Cool Marine* climate, the primary use of GSHP in Ireland is for heating in late autumn, winter and through much of spring. For this reason it makes sense that future GSHP research in Ireland be tailored toward winter heating using $GSHP_{HC}$ under Irish *Cool Marine* climate parameters, rather than relying on research conducted in different climates such as *Continental*, that use $GSHP_{VC}$ predominately for summer cooling applications. In addition, Feist (2004) recognised that in the case of passive house design that '*it would be folly to directly copy details, especially those for insulation, windows and ventilation from the Central European* [*Humid Continental*] *example to other parts of the world'*. Similar logic applies for the transfer of $GSHP_{HC}$ *design variables* between climate regions (Lohan *et al.*, 2006; Burke, 2010).

1.3.4 Research Direction

Groups advocating both the use of heat pumps and further GSHP research are:

- Sustainable Energy Authority of Ireland (SEAI)
- Geothermal Association of Ireland (GAI)
- European Heat Pump Association (EHPA)
- International Energy Agency Heat Pump Centre (IEA-HPC)
- Renewable Heating and Cooling Platform (RHC Platform)
- European Renewable Energy Research Centres Agency (EUREC Agency)

European Union (EU) programmes are currently supportive of energy related research. One relevant EU work package is in the area of Energy efficient Buildings (EeB), labelled EeB.NMP.2011-4. This package supports research under a '*geo-clusters approach to support European energy efficiency goals*' (Poireau, 2010). Climate is one transnational similarity which is a key determinant in the area of thermal energy efficiency, design and control practices. As mentioned in Section 1.3.2, Ireland is a member of a virtual *Cool Marine geo-cluster* which includes several other EU member-states. Therefore, conducting research with a climate sensitive approach in a '*Cool Marine'* climate, which then serves all members of the *Cool Marine geo-cluster*, is consistent with current European Union policy for energy efficiency research.

In the area of $GSHP_{HC}$, the future direction of research may be best assessed by looking into the recent past. As far back as 1997 the move towards more intelligent and location specific design is evident. For instance, sensitivity analysis was used to establish $GSHP_{HC}$ *design*

variables for Canada (Healy & Ugursal, 1997) and the influence of climate conditions on technology choice, design and ultimately performance was characterised (Zogou & Stamatelos, 1998). In order to further this type of analysis, Bose *et al.* (2002) made a call for *'computationally efficient methods for simulating ground loop heat exchangers'* since *'little or no work has been done to model horizontal systems'*. Similar calls have been made previously in the US (Svec, 1987) and more recently in Europe (Dumont & Frere, 2005). In 2002, work done on modelling horizontal collectors was limited to radial geometry models of single pipes (Mei, 1986; Piechowski, 1996), with the exception of work on bridge decks at Oklahoma State University (Chiasson, 1999). Subsequently, models of collector pipes in a Cartesian geometry have been produced in Turkey (Esen *et al.*, 2007; Demir *et al.*, 2009) and the next generation of simulation techniques may involve ANN (Esen *et al.*, 2008). However, for the moment it seems the potential for $GSHP_{HC}$ in *Cool Marine* climates has not yet been thoroughly explored through the combined processes of experimentation, simulation, sensitivity analysis and intelligent design and operational control. This was therefore prioritised as necessary in this study for the development of higher performance, climate sensitive horizontal collectors for *Cool Marine* regions.

1.4 SUMMARY OF MOTIVATIONS, AIM AND OBJECTIVES

There is a definite expressed need for a national and European-wide increase in the use of *renewable* and *sustainable* thermal energy technologies. Heat pumps and GSHP in particular have been recognised as one such technology and have been promoted and incentivised through *green policies* due to their environmental and economic advantages. As a result, substantial market growth has occurred; in Ireland this growth is in the area of $GSHP_{HC}$. However, long payback times exist relative to the alternative fossil fuel based options. A need exists to reduce payback time through research that yields standardised $GSHP_{HC}$ *design variables* and operational guidelines for individual climates such as the *Cool Marine* climate. During 20 years of international research effort there has been considerable *research bias*, with focus mainly on $GSHP_{VC}$ in *Humid Continental* climate regions such as in the USA. Additionally, the limited $GSHP_{HC}$ research emanates from *Continental* climate regions where collector-climate interaction during harsh winters is understandably avoided.

To date, the potential $GSHP_{HC}$ SPF improvement which may result from utilising the potentially positive weather fluctuations in a *Cool Marine* climate region has not yet been fully exploited. It is therefore concluded that the aim of this research project should be to:

'*Develop and experimentally validate numerical methods suitable to demonstrate the potential performance gain from Climate Sensitive Design and Control (CSDC) for $GSHP_{HC}$ in Cool Marine regions*'

This aim is to be achieved by undertaking the following objectives:

1. $GSHP_{HC}$ literature and technology review:
   - Define the $GSHP_{HC}$ *design variables*, *environmental* (climate and ground) *conditions* and operational control parameters with the potential to influence installation costs and both operational and seasonal performance (COP and SPF)
2. Development of an experimental testing facility:
   - Review of best practice in experimentation
   - Develop facility capable of measuring:
     - The influence of climate on ground temperature
     - COP sensitivities to collector design, ground temperature and operational control
3. Characterisation of the ground thermal energy content:
   - Defining the typical ground temperature variation with depth and time
   - Investigating heat and mass transfer at the *ground-atmosphere interface* and in the underground layers
   - Investigating ground thermal and hydraulic properties
4. Investigating $GSHP_{HC}$ operation:
   - Measure $GSHP_{HC}$ performance for a variety of test periods with varying climate conditions and operational control
   - Thermodynamic system characterisation
   - Hydraulic system characterisation
   - Thermal system characterisation
5. Development of a $GSHP_{HC}$ simulation model:
   - Review of best practice in simulation
   - Develop a model capable of simultaneously simulating:
     - The influence of climate and collectors on ground temperature
     - COP sensitivities to collector design, ground temperature and operational control
6. Simulate new collector designs aimed at improving COP
   - Simulations involve limiting and offsetting cooling at the *collector-ground interface*
   - Increasing thermal energy absorbed and retained by the ground

- Alternative collector designs and control strategies that utilise positive climate influences at the surface as well as stable temperatures underground

1.5 PROJECT OVERVIEW

Based on the motivations, aim and objectives outlined, this Irish heat pump study for $GSHP_{HC}$, identified as *HP-IRL/H*, was initiated. *HP-IRL/H* was conducted as a subset of *HP-IRL* (a wider heat pump study) at the Centre for the *integration* of Sustainable Energy Technologies (C*i*SET). C*i*SET is a research centre established at the Galway-Mayo Institute of Technology (GMIT) in 2007. The goal of C*i*SET is to conduct high quality, independent research on SET that aids the integration of these technologies into a variety of applications including the built environment within the *Cool Marine* climate. C*i*SET conducts research on $GSHP_{HC}$, $GSHP_{VC}$, ASHP, solar thermal flat plate and evacuated tube collectors, solar PV, wind turbines, heat recovery and thermal storage. Performance data on each technology is gathered using the fully-functional, life-size and dedicated testing rigs displayed in Figure 1-5. Integration strategies are then tested using the measured performance trends incorporated into holistic numerical simulations.

(a) GSHP **(b) ASHP** **(c) Solar Energy** **(d) Wind**

Figure 1-5: A sample of the technologies undergoing long term experimental characterisation at CiSET

HP-IRL has run since 2007 in conjunction with a solar thermal study *SOL-IRL* (2007) and a hybrid sustainable technology study *HSET-IRL* (2007). The heat pump study is broken down into three sections on ASHP (*HP-IRL/A*), $GSHP_{HC}$ (*HP-IRL/H*) and $GSHP_{VC}$ (*HP-IRL/V*). This thesis is only concerned with the *HP-IRL/H* study. The entire *HP-IRL* study with extensive experimental data and analysis on ASHP, $GSHP_{HC}$ and $GSHP_{VC}$ is presented in Burke (2010). The *HP-IRL/H* experimental test facility is discussed in greater detail in Chapter 3, measured data and characterisation of trends are presented in Chapters 4, 5 and 6,

while simulation methods along with design and control findings are summarised in Chapters 7 and 8.

Researchers at C*i*SET are acutely aware of spatial and temporal variations in the environment, depicted in Figures 1-6(a), (b) and (c), which influence sustainable energy technologies and buildings. These are referred to as the *environmental conditions* and include the following:

- Spatial (latitude) and temporal (seasonal and diurnal) variation in terrestrial solar intensity (Figure 1-6(a))
- Spatial and temporal variations in key weather parameters such as air temperature, cloud cover, humidity, incident solar radiation, wind speed and precipitation (Figure 1-6(b))
- Site specific *micro-environments*, caused by factors such as slope and orientation, shading and sheltering, soil type, moisture content and surface cover, landscaping and ground usage (Figure 1-6(c))

Effort is made within the research to account for many of these spatial and temporal variations using models so that the methodology has applicability in other regions.

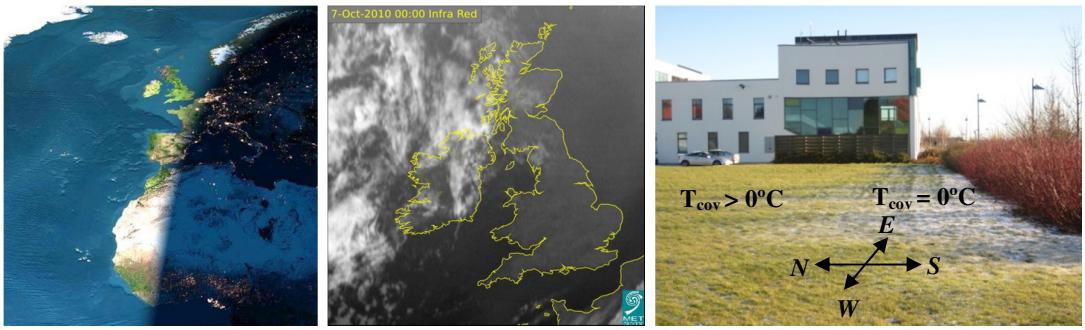

(a) Spatial, seasonal and diurnal variation in solar intensity **(b) National and regional weather patterns, with latitude, altitude and maritime influences** **(c) Microenvironments effecting solar intensity and wind speed**

Figure 1-6: Spatial and temporal variations in environmental conditions which influence the availability of thermal energy from the climate and the ground

1.6 THESIS LAYOUT

This thesis consists of nine chapters in total, including this one. Throughout the thesis cross reference is made to other chapters, sections and sub-sections. Citations within the text refer to published material listed in the 'Reference' section. Reference is also made to additional and supplementary information located in the 'Appendices'. The nine chapters are:

- **Chapter 1 – Introduction**

- **Chapter 2 – Literature and Technology Review**: presents a review of $GSHP_{HC}$ *design variables*, the current sizing, design and analysis methods, and concludes with the refined *HP-IRL/H* methodology
- **Chapter 3 – Experimental and Numerical Methods**: describes the *HP-IRL/H* experimental test facility and provides a brief introduction and catalogue of the numerical methods, details of which are given in subsequent chapters
- **Chapter 4 – Ground Thermal Energy Resources**: presents a comparison of Ground Temperature Distribution (GTD) in a variety of locations at varied latitudes and with different climate classifications, along with a Fourier-type analysis of the measured *HP-IRL/H* GTD data
- **Chapter 5 – Ground Heat Transfer**: describes the energy balance at the *ground-atmosphere interface*, the heat transfer processes in the ground, ground thermal properties and simulation methods followed by a comparison between the heat transfer in experimental ground profiles with differing surface covers and ground properties
- **Chapter 6 – $GSHP_{HC}$ Experimental Characterisation**: presents measured heat pump performance under a variety of operational characteristics, along with characterisation of $GSHP_{HC}$ thermodynamic, thermal and hydraulic performance using existing and novel analytical models
- **Chapter 7 – $GSHP_{HC}$ Numerical Simulation**: describes development of transient numerical methods for simulation of tow-way interactions between the heat pump, the collector, the ground and the climate
- **Chapter 8 – Climate Sensitive Design and Control**: presents a sample of *CSDC* designs and control strategies proposed for $GSHP_{HC}$ efficiency improvement and the simulated results
- **Chapter 9 – Conclusions and Recommendations**: Summarises the conclusions and recommendations from the foregoing eight chapters and outlines future work

In Chapter 2 a literature review is pursued to refine the scope and objectives of this research.

CHAPTER 2

LITERATURE AND TECHNOLOGY REVIEW

2. LITERATURE AND TECHNOLOGY REVIEW

The aspects of $GSHP_{HC}$ design investigated in *HP-IRL/H* and the methods used are introduced in this chapter as part of a literature and technology review. A review of over 15 publications on horizontal collectors revealed 7 distinct *design groups* that include 23 *design variables.* Additionally, 12 design guides and 12 software tools were *catalogued* and 14 recent publications aimed at improving the cost effectiveness of ground heat exchangers were also reviewed. Based on this a *Climate Sensitive Design and Control* (*CSDC*) approach to $GSHP_{HC}$ was defined and the basis of a multi-disciplinary *thermo-environmental* analysis was developed across the following six sections:

- Introduction to $GSHP_{HC}$ heating systems
- Horizontal collectors
- $GSHP_{HC}$ *design variables*
- $GSHP_{HC}$ design guides
- $GSHP_{HC}$ analyses
- *HP-IRL/H* thermo-environmental analysis

2.1 INTRODUCTION TO $GSHP_{HC}$ HEATING SYSTEMS

Based on Ireland's *Cool Marine* climate, this *HP-IRL/H* project focused on $GSHP_{HC}$ in the winter heating mode. Figure 2-1 presents a holistic view of such a $GSHP_{HC}$ heating system which includes the primary elements; the horizontal collector and the building (heat source and heat sink) plus the heat pump unit. Additionally the influence of climate, the roles of control and storage, the electricity supply and the potential to create SET hybrids based around $GSHP_{HC}$ are also included. When analysing a broad system such as the $GSHP_{HC}$ shown in Figure 2-1, Lundqvist (2010) defines the following 5 levels of analysis which can be applied:

- Level 0: Heat pump components (such as the compressor or heat exchangers)
- Level 1: The heat pump unit
- Level 2: The heat pump system including source and sink
- Level 3: The heat pump and building system including occupants (≈ *HP-IRL/H*)
- Level 4: The energy system which includes the heat pump and building and the electricity supply

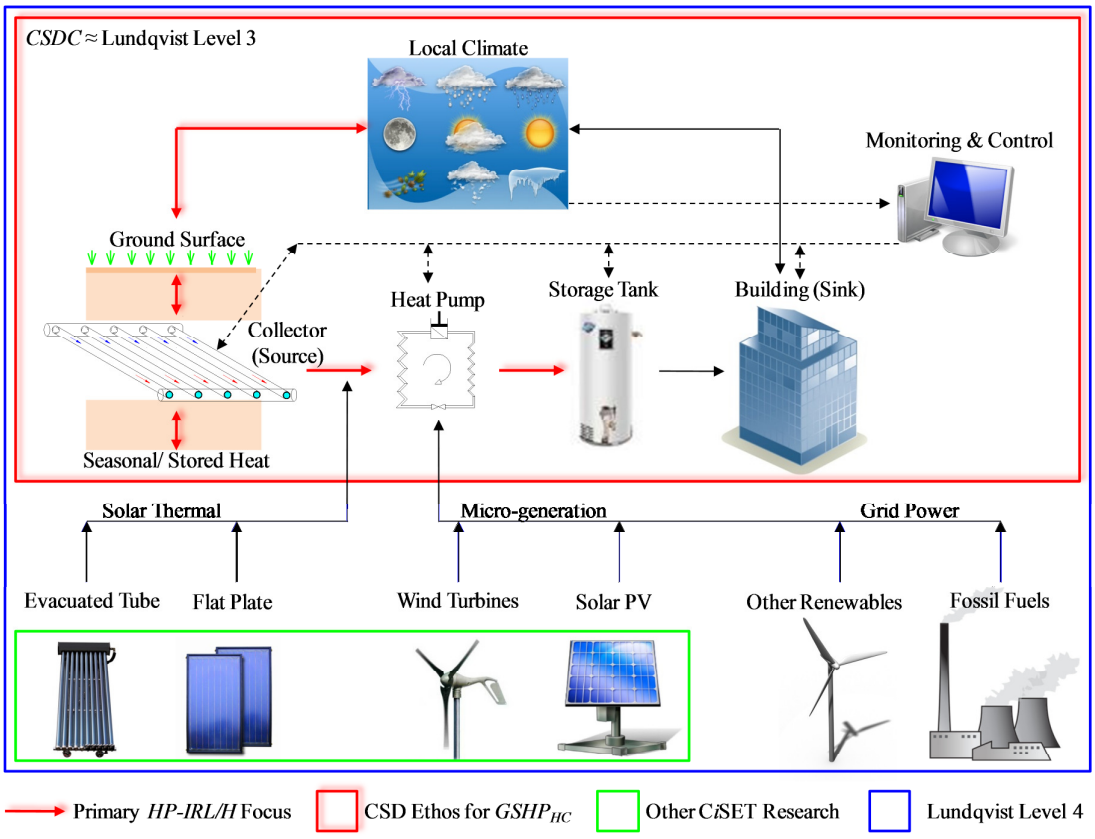

Figure 2-1: Holistic view of a $GSHP_{HC}$ system including the collector and the building (heat source and sink) and the heat pump unit, along with the climate influence, the role of control and storage, the electricity supply and the potential for SET hybrids based around $GSHP_{HC}$

The blue outline encompassing all elements in Figure 2-1 describes the extent of a Lundqvist (2010) Level 4 analysis which aims to capture all energy interactions. However, this *HP-IRL/H* project is concerned primarily with thermal energy interactions and the significant influence of climate on both the heat source (supply) and the heat sink (demand). This approach to system analysis, design and control is defined by the red outline in Figure 2-1 and has been identified as the *CSDC* approach. Interactions between all the elements within the red *CSDC* outline influence the $GSHP_{HC}$ performance and the system must be viewed in a holistic manner. However, as marked with red arrows, the primary focus of the *HP-IRL/H* project was on the simultaneous interactions between climate conditions, the ground, the horizontal collector and the heat pump which collectively, have received only limited attention to date. The primary elements within the red *CSDC* outline (collector, building and heat pump) are briefly discussed in the next three sub-sections, after which attention is placed primarily on the horizontal collector.

2.1.1 Horizontal Collector (Heat Source)

The horizontal collector, represented in Figure 2-1, has intrigued researchers over the past four decades. Experimental research has been conducted to characterise the undisturbed GTD in Poland (Popiel *et al.*, 2001) along with the sensitivity of COP to winter conditions in New York (Metz, 1981), ground type in Idaho (Drown & Den Braven, 1992), collector depth in Turkey (Inalli & Esen, 2004) and variable-duty 'thermal drawdown' in Ireland (Burke, 2010). Simulation of horizontal collectors is also possible using commercially available TRNSYS (Transient Energy Systems Simulation Tool, TESS-Inc., USA) as well as custom models presented in the literature from USA (Mei, 1986), Australia (Piechowski, 1996) and most recently from Turkey (Demir *et al.*, 2009). It has already been shown in Sub-section 1.3.3 that there is an absence of published $GSHP_{HC}$ research compared with $GSHP_{VC}$. Additionally, within this limited $GSHP_{HC}$ research there has been an absence in research, specifically on the collector component of the $GSHP_{HC}$ system and particularly in *Cool Marine* climates. Therefore the *HP-IRL/H* horizontal collector merited further investigation and further details are presented in Section 2.3 and Chapter 3.

2.1.2 Building (Heat Sink)

Heating of buildings as represented in Figure 2-1, has been under constant scrutiny for as long as heating, central heating or HVAC systems have been used, even dating to the era of the Roman Empire. Today, the extensive experimentation of the past has led to empirical data and trusted Building Energy Simulation (BES) software packages such as ENERGYPLUS, IES and TRNSYS. These can be programmed to include extensive heating system, building fabric and climate details, and are used to solve for hourly heating/cooling loads, heating/cooling efficiencies and primary energy consumption. The International Energy Agency (IEA) has been running a BES validation project called BESTEST at the National Renewable Energy Laboratory (NREL) in Golden, Colorado since 1981. BESTEST has compared predictions from a wide variety of BES packages such as CA-SIS, ENERGYPLUS and TRNSYS-TUD with experimental data and with each other (Neymark *et al.*, 2002). Simpler spreadsheet type packages are also available for domestic energy audits such as the Dwelling Energy Assessment Procedure (DEAP) in Ireland and the Standard Assessment Procedure (SAP) in the United Kingdom. It is clear that the built environment is already a specialist research area and a detailed building energy analysis was deemed beyond the scope of this *HP-IRL/H* project. However, in the context of $GSHP_{HC}$ heating systems, a brief description of the relevant building energy details are now given.

Relevant Building Energy Details

Occupants of a building typically dictate the appropriate *thermal comfort level*. This typically involves air temperatures between 22 and 27ºC and relative humidity ranging between 40 and 60% (Cengel & Boles, 2002). For the majority of buildings, this thermal comfort level is at odds with the external ambient conditions which typically vary with the seasons and heat will be lost or gained by the building in cold and warm conditions respectively. Heat is transferred to and from a building primarily by conduction through the building's envelope known as 'fabric loss/gain', along with substantial heat transfer through air leakage, known as 'ventilation loss/gain'. In order to maintain the thermal comfort level in a building, the environmental heat loss or gain must be balanced by equivalent heating or cooling, respectively. The amount of heating or cooling required depends primarily on: the size of the building, the temperature difference between the interior and exterior and also the condition of the building's envelope; the latter is often characterised using an 'effective U-value' [W/m^2K]. Additionally, there are other factors which may have significant influence on heating and cooling such as 'solar gains', 'casual gains' from occupants, the business activities undertaken and the 'base load gains' from electrical power consumed. A detailed summary of the methods and models used to quantify heat loss and gain are presented in the CIBSE Building Energy Code – Part 2 (CIBSE, 1981).

The maximum rate of heating is required when the outdoor air temperature is at its minimum; this is known as the *maximum heat demand* [kW]. The associated outdoor air temperature is referred to as the 'design temperature' and varies from location to location. In order to predict heat loss in buildings, design temperatures for different regions are often specified; these are then quoted in the GSHP literature to support GSHP capacity selection, such as -2ºC for *Cool Marine* conditions in Ireland (Burke, 2010) and -12ºC for *Continental* conditions in New York State (Metz, 1981). Since exterior temperatures vary with time of year and the weather, the *annual heat requirement* [kWh] for a building depends on the integral of the interior-exterior temperature differential over the entire heating season. This is often the sum of the daily average or maximum temperature differentials and the approach is referred to as the 'degree-days method'.

According to the International Energy Agency's Heat Pump Centre, heat pumps can be used to heat a building in either 'monovalent' or 'bivalent' form as follows:

- Monovalent heat pumps have the capacity to match 100% of the *maximum heat demand*, evaluated at the local winter design temperature, and meet 100% of the

annual heating requirement, evaluated using the local degree-days data (IEA-HPC, 2010)

- Bivalent heat pumps are sized for 20-60% of the *maximum heat demand* and meet around 50-95% of the *annual heating requirement*, in a *Continental* climate residence (IEA-HPC, 2010)
- For bivalent systems the additional capacity is provided by another means such as a fuel burning boiler

Heat that is generated by a central heating system is typically supplied to the zones of a building by circulating either warm air or warm water through a piping network with heat dissipaters in each room; this is known as a *heat distribution system*. Reflecting variation in heat dissipater design, heat distribution systems operate at different temperatures and Table 2-1 summarises the flow temperatures of various heating and cooling *distribution systems*.

Table 2-1: Typical flow temperatures for heating and cooling distribution systems (IEA-HPC, 2010)

Application		Flow temperature range [°C]
Air distribution	Air heating	30 to 50
	Under-floor (air) heating	30 to 45
Hydronic systems	Modern radiators	45 to 55
	Conventional radiators	60 to 90
	Under-floor (water) heating	30 to 35
District heating	District heating	70 to 100
	District heating – hot water/steam	100 to 180
Space cooling	Cooled air	10 to 15
	Chilled water	5 to 15
	District cooling	5 to 8

2.1.3 Heat Pump

In heating mode, the COP of the heat pump unit represented in Figure 2-1 is essentially governed by its response to changes in ground energy supply (source temperature) and building energy demand (sink temperature); this dictates the amount of electrical power consumed. This type of heat pump behaviour is measured by test-institutes such as *Arsenal Research*, Austria using the DACH standard or by other European Heat Pump Association (EHPA) approved institutes such as:

- HVAC-Stuttgart (HLK-Stuttgart), Stuttgart, Germany
- Institute of Air and Refrigeration (ILK-Dresden), Dresden, Germany
- Scientific Partner (SP), Sweden
- University of Technology Buchs (NTB), Switzerland

In order for a test-institute to award the EHPA's *European Quality Label for Heat Pumps*, they must be accredited to BS EN 17025 and be capable of testing heat pumps to BS EN 14511 (parts 1 to 4) or BS EN 255 with measurement standards compliant with BS EN 12102. Table 2-2 presents an example of the typical test-institute findings during heat pump testing. This data was generated at the *Arsenal* testing institute in Austria (Zottl, 2003) and displays the performance statistics of the 15 kW *Solterra 500* heat pump used in this study and described in Chapter 3. Heat pumps are tested in laboratory based tests at two standardised heat delivery temperatures (W for water) of 35 and 50ºC, while the source temperature (B for brine solution) is varied between +5, 0 and -5ºC.

Table 2-2: Solterra 500 heat hump performance in a standard industry datasheet, as measured by Arsenal Research, Austria (Zottl, 2003)

B/W [ºC]	Capacity (q_{sk}) [kW_{th}]	COP [-]
B5/W35	17.365	4.5
B0/W35	15.232	4
B-5/W35	13.317	3.5
B5/W50	16.584	3.1
B0/W50	14.576	2.8
B-5/W50	12.778	2.4

It can be seen from Table 2-2 that the GSHP's capacity and COP depend on both the source and sink temperatures. Lower heat distribution temperatures, discussed in Sub-section 2.1.2, produce higher COPs. For this reason, a low temperature distribution system such as under-floor heating enables a GSHP to operate with a COP that is 60% higher than conventional radiators, as shown in Table 2-3. However, since less is known about the sensitivity of source temperature to heat collector design, this *HP-IRL/H* project focused on identifying the combination of factors that could be used to maintain the highest source temperature.

Table 2-3: Variation in the COP of a GSHP with distribution system temperature (IEA-HPC, 2010)

Heat distribution system (flow/return temperature)	COP of a GSHP
Under-floor heating (30 to 35ºC)	4.0
Modern radiators (45 to 55ºC)	3.5
Conventional radiators (60 to 90ºC)	2.5

While the *Solterra 500's* thermodynamic cycle was not under investigation in this project, some brief background on the common heat pump cycle is now given for the purpose of reference in subsequent $GSHP_{HC}$ discussion and analyses.

Relevant Heat Pump Details

The *ideal vapour-compression cycle* heat pump, an idealised form of the common *vapour-compression* heat pump, is used to discuss the main components and the operating principle of the *Solterra 500* used in this study. The system, depicted in Figure 2-2, is charged with a refrigerant, such as *R407C* described in Appendix C, which then circulates in a cycle. There are four main components to the *ideal vapour-compression* heat pump as follows:

- Evaporator: a heat exchanger facilitating heat transfer between the 'source fluid' and the refrigerant in contra-flow
- Compressor: an electrical scroll or reciprocating compressor which raises the pressure and consequently the temperature of the refrigerant
- Condenser: a heat exchanger facilitating heat transfer between the refrigerant and the 'sink fluid' in contra-flow
- Expansion valve: a device which expands and lowers the refrigerant pressure

The circulation and the thermodynamic cycle are driven by a pressure differential created by the compressor and the expansion valve and can be divided into 4 processes as follows:

- Process 1 → 2: Isentropic compression of vapour in the compressor
- Process 2 → 3: Constant-pressure heat rejecting condensation in the condenser
- Process 3 → 4: Pressure drop in the expansion valve at constant enthalpy
- Process 4 → 1: Constant-pressure heat absorbing evaporation in the evaporator

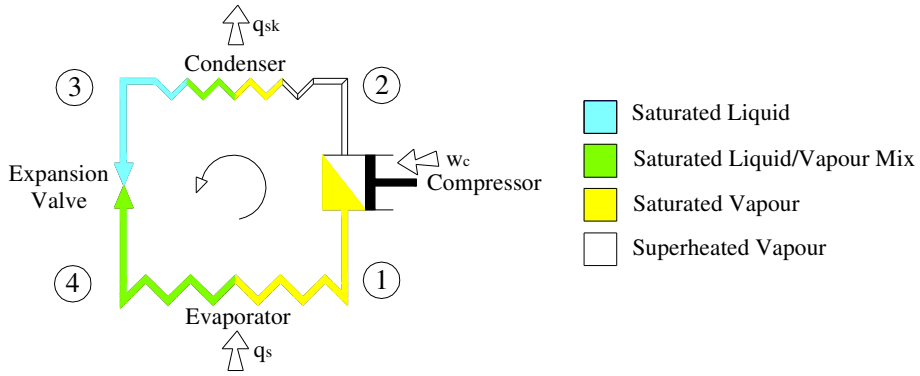

Figure 2-2: Schematic of the 4 processes in an ideal vapour-compression heat pump cycle

The T-s diagram shown in Figure 2-3(a) is used to display the relationship between temperature (T) and specific entropy (s), note the isentropic compression in Process 1 → 2. The P-*h* diagram, shown in Figure 2-3(b) is used to display the relationship between pressure

(P) and specific enthalpy (h), note the constant pressure heat absorption in Process 4 → 1, constant pressure heat rejection in Process 2 → 3 and the constant enthalpy expansion of the refrigerant in Process 3 → 4.

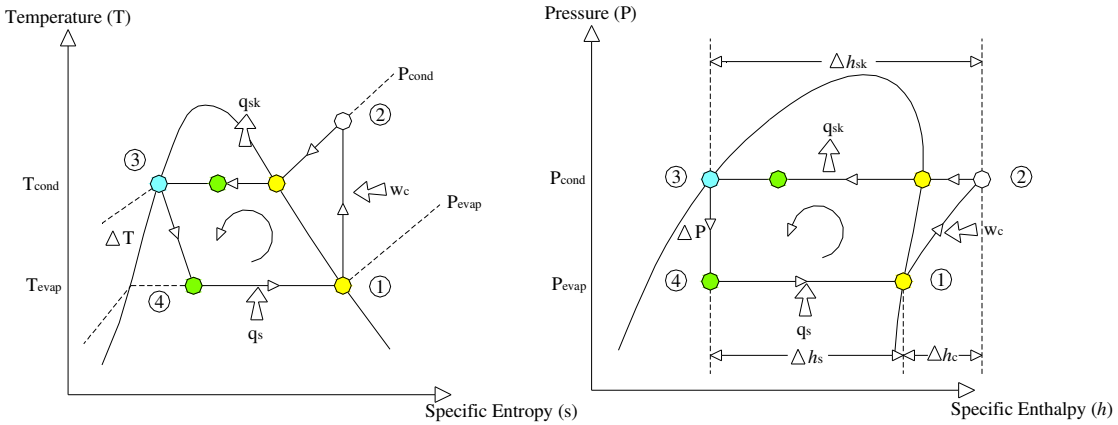

(a) Temperature – Specific Entropy (T-s) Diagram **(b) Pressure – Specific Enthalpy (P-*h*) Diagram**

Figure 2-3: The ideal vapour compression cycle described using T-s and P-*h* diagrams

The COP of the *ideal vapour-compression cycle* in both heating and cooling can be calculated using Equations 2-1 and 2-2 respectively with knowledge of the enthalpies at States 1 through 4. The 'state postulate' dictates that two independent intensive properties define a state (Cengel & Boles, 2002) as follows:

- State 1: Specific enthalpy h_1 of saturated vapour h_{vap} at P_{sat} equal to P_{evap}
- State 2: Specific enthalpy h_2 of superheated vapour at P_{cond} with entropy of State 1
- State 3: Specific enthalpy h_3 of saturated liquid h_{liq} at P_{sat} equal to P_{cond}
- State 4: Specific enthalpy h_4 of State 4 equals that of State 3

The COPs for heating and cooling are then evaluated as follows:

$$COP_{heat} = q_{sk}/w_c = \Delta h_{sk}/\Delta h_c = (h_2 - h_3)/(h_2 - h_1) \quad (2\text{-}1)$$

$$COP_{cool} = q_s/w_c = \Delta h_s/\Delta h_c = (h_1 - h_4)/(h_2 - h_1) \quad (2\text{-}2)$$

While the *vapour-compression cycle* described is highly idealised, variants of this which include real life processes such as compressor in-efficiencies and pressure drops across components have been used to further the understanding of vapour-compression and develop better heat pumps. Additionally, research has been undertaken in the areas of: cataloguing environmental problems with CFC (ozone depleting) and HFC (greenhouse gas) refrigerants

(Sand *et al.*, 1997); replacing HFCs using natural refrigerants (Lorentzen, 1995); analysing alternative CO_2 heat pump systems (Neksa, 2002); minimising refrigerant charge using mini-channel heat exchangers (Fernando *et al.*, 2004; Palm, 2007); modelling of reciprocating and scroll compressors (Duprez *et al.*, 2007); and theoretical and experimental testing of heat pumps fitted with Variable Frequency Drives (VFD) (Karlsson & Fahlen, 2007; Karlsson, 2007).

Vapour-compression heat pumping technology has been designed for many years and delivered in the form of air conditioning, refrigeration, and ASHP allowing the heat pump element of the technology to be continually improved. If improvement in $GSHP_{HC}$ is to be continued then further development on the collector element is needed (Gupta & Irving, 2008).

2.2 HORIZONTAL COLLECTORS

This *HP-IRL/H* project focused on the horizontal collector in winter mode only, while still considering the holistic view, presented in Figure 2-1, by utilising accepted information and empirical data on the built environment and heat pumps discussed in Sub-sections 2.1.2 and 2.1.3 respectively.

The source capacity, shown on the left of Figure 2-4, reflects the capacity of the collector to supply energy from the ground heat source to the heat pump. The source capacity should be designed to match the heat pump extraction over the course of the heating season.

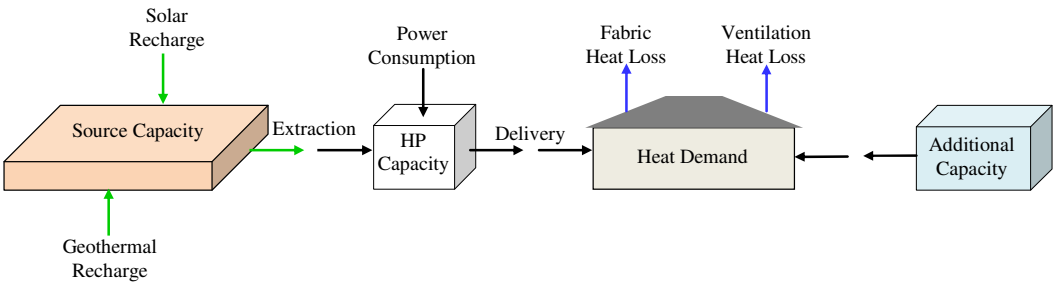

Figure 2-4: Mapping the thermal energy transfers involved in maintaining acceptable thermal comfort levels in a building using either a monovalent or bivalent GSHP heating system to match heat losses during the typical winter heating season

As summarised in Table 2-4, to size this source capacity one can start with the built environment and use the following procedure:

- Start with the building energy software or calculation methods, identified in Sub-section 2.1.2, to find the building's *maximum heat loss* and *annual heat requirement*
- Then decide on the heat pump capacity (q_{sk}) [kW] needed for either a 'monovalent' or 'bivalent' GSHP heating system, also described in Sub-section 2.1.2.
- Knowing this heat pump capacity, an appropriate heat pump make and model is then chosen which can deliver this capacity:
    - At the building's *heat distribution* temperature (T_{sk}) [ºC], discussed in Sub-section 2.1.3
    - And within the range of source temperatures (T_s) [ºC], discussed in Sub-section 2.1.3
    - Expected ground temperatures are discussed in Chapters 4 and 5
    - Bearing in mind that ground source temperature drops when a collector is run for a period of time as discussed in Chapters 6 and 7
- From the heat pump's data sheet, information specifically on the GSHP's ground extraction (q_s) [kW] should be given
    - If not, extraction (q_s) can be deduced from the heat pump capacity (q_{sk}) and COP which are given in standard data sheets
- The source capacity [kW] should then match the heat pump extraction [kW] for a correctly sized and functioning $GSHP_{HC}$
- The collector must now be designed to achieve this source capacity

Good collector design seeks to match source capacity and the heat pump extraction throughout the heating season. The source capacity typically drops during the heating season due to the falling ground temperatures and *thermal drawdown* resulting from heat extraction. The following stipulations can be placed on source capacity:

- At ground-source steady-state, the collector provides sufficient low-grade heat, above a prescribed temperature, so that the heat pump can meet the building's *maximum heat loss*
    - Ground-source steady-state is the relatively constant temperature condition of the heat source after *thermal drawdown* stabilises
- Can be used by the heat pump to meet the buildings *annual heat requirement* without falling below a predefined minimum collector design temperature

For the sizing procedure Spitler & Cullen (2008) recommend sizing for the *annual heating/cooling requirement* rather than the *maximum heat loss* particularly in regions where

heat pump operation is predominantly in winter 'heating constrained' or in summer 'cooling constrained'.

Table 2-4: Summary of GSHP and collector sizing procedure

Step	Component	Key Parameters	Climate Sensitive?	Other Sensitivities
1.	Building	Maximum heat loss, annual heat requirement	Highly	Building envelope, solar gains, casual gains and electrical gains
2.	Heat distribution system	Distribution temperature	Not directly	Heat dissipater type and thermal resistance/efficiency
3.	Heating system and heat storage	Monovalent/bivalent system; Short-term/long-term heat storage	Not directly	Percentage of maximum heat loss and annual heat requirement met by GSHP
4.	Heat pump	Influence of source and sink temperatures and mass flow rates on thermal performance	Indirectly through source and sink	Heat pump type, model and nominal capacity; Effect of cyclic operation on SPF
5.	Collector pipe network dimensioning	Thermo-hydraulic design of pipe network and circulating pumps	Not directly	Mass flow rate along with number, length and diameter of pipes
6.	Collector burial underground	Pipe depth, pipe spacing, thermal properties and moisture content	Highly	Ground area available, presence of bedrock
7.	System operational control	Day/night operation; Demand/supply driven control	Highly	Occupancy times, thermal comfort requirements

2.3 $GSHP_{HC}$ DESIGN VARIABLES

Introduced in Sub-section 1.2.3, horizontal collectors typically consist of a water and anti-freeze mixture circulated through long polyethylene pipes at an appropriate flow rate, using common water circulation pumps. Typically, the optimum flow rate is recommended by the heat pump manufacturer. As a rule of thumb, Kavanaugh & Raffery (1997) recommend 0.162 to 0.192 [m^3/h] per kW_{th} of heating capacity. Typically, the total length of pipe depends on the ground type and the pipe depth below the surface depends on winter weather conditions. As a rule of thumb, 35 to 60m of piping per kW_{th} of heating capacity is buried horizontally in shallow (1 to 2m deep) pits or trenches (Retscreen, 2005; Florides & Kalogirou, 2007). Rules of thumb are also expressed as W/m; however Spitler & Cullen (2008) strongly disagree with the use of rules of thumb particularly in heating constrained or cooling constrained large buildings. In addition to these simple guidelines, many other design and dimensioning issues identified as the *$GSHP_{HC}$ design variables* must be considered, and these are now discussed.

2.3.1 Collector Flow Configuration

A range of typical *collector flow configuration* options are shown in Figure 2-5. These usually consist of either a number of pipes connected in a *parallel array* (using both a flow and return manifold/header), as depicted in Figure 2-5(a), or one long pipe (sometimes several pipes connected together) in a *series array*, as depicted in Figure 2-5(b).

(a) Typical parallel array

(b) Typical series array **(c) HP-IRL/H co-located manifolds** **(d) Reverse-return headers**

Figure 2-5: Horizontal collector flow configuration and pipe routing options

Typically, one long pipe in a *series array* returns the fluid at a temperature close to the ground's farfield temperature. However, splitting this long pipe into a number of shorter *parallel array* pipes allows for a higher overall collector flow rate. This produces higher source capacity with lower head loss, albeit with a return temperature typically lower than that of the *series array*. Within the literature, there appears to be a lack of attention paid to the thermal and hydraulic characteristics that differentiate these two *collector flow configurations*. These characteristics are discussed in greater detail in Sub-section 6.3.3.

2.3.2 Collector Pipe Routing

In *parallel arrays*, the flow and return manifolds can be *co-located* for convenience, as is the case for the *HP-IRL/H* manifolds shown in Figure 2-5(c). The collector pipes are then *looped pipes,* as shown in Figure 2-5(d) (Retscreen, 2005), as opposed to the *straight pipes* shown in Figure 2-5(b). The 'reverse return', as depicted in Figure 2-5(d), is also recommended to balance pressure loss and insure equal flow rates in the pipes (Retscreen, 2005). However, this is not essential when short supply legs with negligible head loss are employed, such as those in Figure 2-5(c). For the *parallel array* a set of *run-out* pipes (GLD2010, 2010) are typically used to route the fluid between the heat pump and the manifolds. In *series arrays*, *manifolds* and *run-outs* are not always necessary and the *series pipe* is sometimes routed from the

evaporator exit back to the evaporator entrance. Additionally, *serpentine pipes* shown in Figure 2-5(b), are often used since the full length of the *series pipe* is typically confined to a limited plot of ground.

2.3.3 Collector Pipe Dimensions

The *collector pipe dimensions* also referred to as '*characteristic dimensions'* (Paepe & Janssens, 2003), are summarised in Table 2-5. From the perspective of source return temperature during $GSHP_{HC}$ *operation,* many of the ground and climate parameters influence the dimensioning of a collector (Aittomaki & Toivanen, 1999), most notably the soil's thermal conductivity (k_g) [W/mK]. The required length (L_t) [m] of collector pipes is inversely proportional to ground thermal conductivity. Alternatively, from a thermo-hydraulic perspective, pipe head loss (H_f) [m] and heat transfer effectiveness (NTU) depend on collector dimensioning alone and can be considered independent of ground and climate parameters (Paepe & Janssens, 2003). Figure 2-6 displays the influence of mass flow rate ($\dot{m}_s$) [kg/s] on key performance parameters.

Table 2-5: Summary of the collector pipe dimensions

No.	Variable/Parameter/Decision	Symbol	Units
1.	Inner diameter	D_{in}	[m]
2.	Outer diameter	D_o	[m]
3.	Length	L_t	[m]
4.	Number of pipes	N	[-]
5.	Source flow rate	$\dot{V}_S$	[m^3/s]

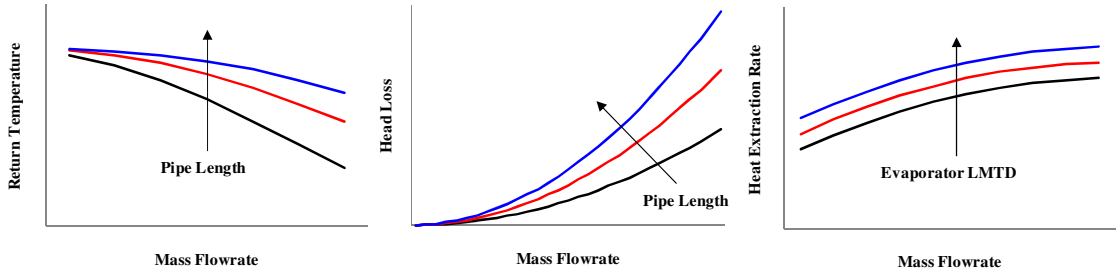

(a) Collector performance **(b) Collector head loss** **(c) Evaporator extraction**

Figure 2-6: Thermo-hydraulic collector design

As displayed in Figure 2-6(a), the temperature difference between fluid at a pipe's exit and pipe wall temperature ($T_{F,Lt} - T_p$) [K] decays exponentially with the ratio of length (L) [m] to

mass flow rate ($\dot{m}_s$) [kg/s] (Incorpera & DeWitt, 2002; Paepe & Janssens, 2003). Increasing the pipe internal diameter (D_{in}) [m] reduces the convection coefficient (h) [W/mK] for mass flow rate ($\dot{m}_s$) [kg/s].

As displayed in Figure 2-6(b), the pressure drop for a fluid flowing in a pipe (ΔP) [kPa] increases linearly with the ratio of length to internal diameter (L/D_{in}) and with the second power of velocity (u) [m/s] (White, 1999; Paepe & Janssens, 2003). Increasing D_{in} has a duel positive influence of reducing both velocity and (L/D_{in}) for flow rate ($\dot{m}_s$).

Since COP increases with source return temperature ($T_{s,r}$) by 2 to 2.5% per Kelvin (Cengel & Boles, 2002; Warnelof & Kronstrom, 2005; Burke *et al.*, 2008) and power consumption increases with pressure loss in the system, the initial reaction is then to choose a pipe of recommended length (35 to 60m/kW_{th}) with a low mass flow rate.

However, there is one more constraint to be adhered to and this is the heat pump extraction (q_s) [kW]. A low fluid velocity through the evaporator will generate a higher temperature drop in the evaporator (ΔT_{evap}) [K] in order to meet the heat pumps source-side heat extraction rate (q_s). Additionally, as shown in Figure 2-6(c), the heat transfer coefficient and hence the heat extraction rate in the evaporator (q_s) increases with mass flow rate. The influences of collector pipe dimensions are assessed in Chapter 6.

2.3.4 Pipe Layout and Burial

Two options exist for *pipe layout* and these are the *in-line* or the *slinky* type *pipe layout.* Figure 2-7(a) displays a typical *in-line pipe layout*, where pipes are laid approximately parallel with centre to centre pipe spacing (PS) [m]. Figure 2-7(b) shows the typical *slinky pipe layout* where pipes are laid in coils of diameter (D_{coil}) [m]. *Slinky* coils can be buried as single or double coils as shown in Figure 2-7(c) and are typically used when collector area is limited (Retscreen, 2005). Simulations have shown that *in-line* pipes absorb more heat per meter of pipe while *slinky* pipes absorb more heat per meter of trench (Wu *et al.*, 2010). Both the *in-line* and *slinky* pipes can be buried in a set of parallel trenches or in a single large pit as shown in Figures 2-6(a) and (b); in either case the centre to centre distance between *in-line* or *slinky* pipes effects the thermal performance of the collector particularly during long duration *duty cycles*. Typically, collector thermal performance improves with the available area (A_{HC}) (Healy & Ugursal, 1997), however increased collector area and excavation of this area increases capital cost (Healy & Ugursal, 1997).

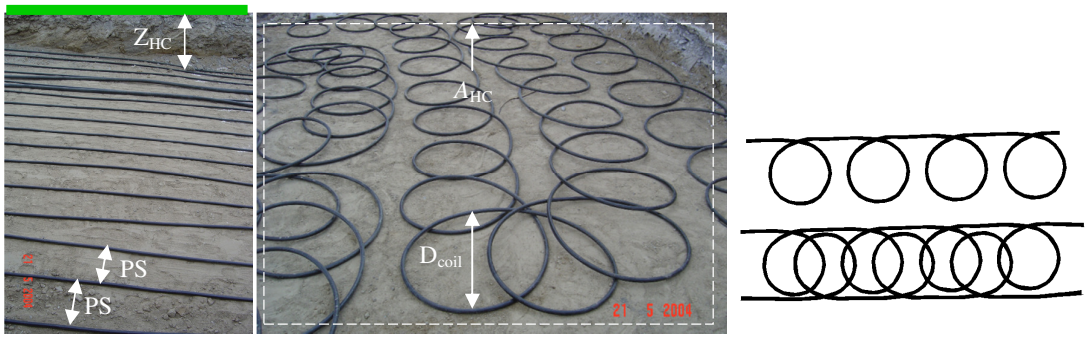

(a) In-line pipe layout **(b) Slinky pipe layout** **(c) Single and double slinky coils**

Figure 2-7: Options for collector pipe layout and burial

The *in-line* and *slinky* pipes are placed at a depth Z_{HC} below the ground surface. The collector depth depends on many factors such as the climate extremes experienced at the surface, the cost of digging trenches or pits and the proximity of bedrock. In terms of climate extremes an optimum depth exists where sufficient protection is present in winter without sacrificing recharge in summer. It has been shown that heat pump COP decreases sharply as the collector depth is reduced to less than 0.38m in the *Moderate Sub-polar* climate of Halifax, Canada (Healy & Ugursal, 1997). However, Burke (2010) presents evidence that shallower collectors positioned less than 0.5m deep can operate successfully in the Irish *Cool Marine* climate particularly in spring. The key decisions to be made during collector burial are summarised in Table 2-6.

Table 2-6: Summary of the key decisions to be made during the collector pipe layout and burial process

No.	Variable	Symbol	Units
1.	Total collector area	A_{HC}	[m^2]
2.	Slinky coil diameter	D_{coil}	[-]
3.	In-line pipe spacing	PS	[m]
4.	Collector depth	Z_{HC}	[m]

Additionally, *'stacked'* (Retscreen, 2005) or *'double-layer'*(Tarnawski *et al.*, 2009) collectors can be deployed, as shown in Figure 2-8(c) the two levels are typically connected in series and are used when space is limited (Tarnawski *et al.*, 2009). Another concept called the *split-level collector* (Burke, 2010) involves two *parallel array* collectors operating in parallel or alternately.

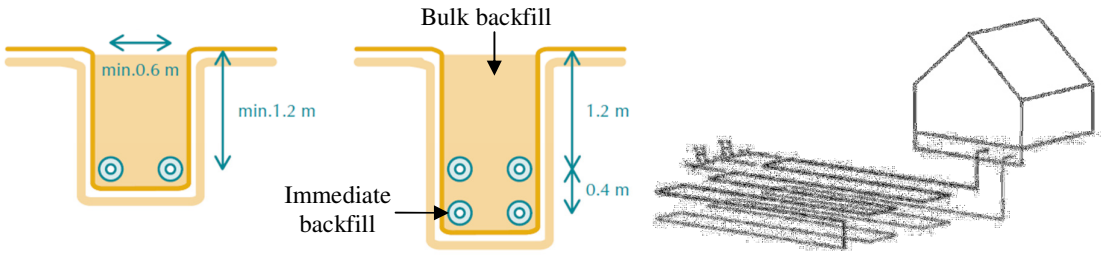

(a) Single **(b) Stacked (Retscreen, 2005)** **(c) Double-layer (Tarnawski *et. al.* 2009)**

Figure 2-8: Conventional and unconventional collectors

Using ground temperature analysis it has been shown that *split-level collectors* at 0.3 and 0.9m, under brick and grass respectively, activated by ground temperature feedback control, can raise the SPF by 8.1% from 2.98 to 3.22 when compared to a single collector at 0.9m depth (Burke, 2010). Simulations of *split-level collectors* at a variety of Z_{HC} are presented in Chapter 8.

2.3.5 Backfill Material

Claesson and Dunand (1983) recognised that about 50% of the heat extracted by collector pipes is drawn from within five pipe diameters of the collector pipe. Therefore, thermal performance of the collector depends strongly on the *backfill material* that surrounds it (Mei, 1987); in particular the soil texture and moisture content (Leong *et al.*, 1998). The *backfill material* can be broken into the following two parts as shown in Figure 2-8(b):

- *Immediate backfill*: around the collector pipes
- *Bulk backfill*: the remainder of the ground volume

The thermal properties of the ground can be estimated using soil texture classification by taking soil samples (Salomone & Marlowe, 1989). As summarised in Table 2-7, the primary properties of interest are thermal conductivity, specific heat capacity and density of the ground solids along with the porosity of the ground and the moisture content of the pores (Drown & Den Braven, 1992; Leong *et al.*, 1998).

Table 2-7: Summary of the primary backfill properties

No.	Variable	Symbol	Units
1.	Ground specific heat capacity	(c_g)	[W/m^2K]
2.	Ground thermal conductivity	(k_g)	[W/mK]
3.	Ground porosity	(p_g)	[m^3/m^3]
4.	Ground density	(ρ_g)	[kg/m^3]
5.	Moisture content	(θ_{wg})	[m^3/m^3]

From the perspective of cost and convenience it is common for an *immediate backfill* such as sand to be brought in but quite uncommon for the *bulk backfill* to be imported into the collector site; the existing material is usually returned into the pit or trenches. The role of *backfill material* is assessed in Chapters 4, 5 and 6.

2.3.6 Surface Cover

For horizontal collector systems, the main thermal recharge is provided by solar radiation on the surface (Florides & Kalogirou, 2007). The *surface cover* and the landscaping therefore play an important role. These aspects are typically governed by the client who should be informed of the performance implications of various surface cover options by the designer/installer. As summarised in Table 2-8, the primary properties of the surface that influence solar recharge are the shortwave albedo, longwave emissivity, porosity, natural moisture content and thermal diffusivity. The slope and orientation of the surface cover also asserts an influence on the underground temperature (Safanda, 1999; Bennie *et al.*, 2008). The influence of surface cover is assessed in Chapter 5.

Table 2-8: Summary of the primary surface cover properties that impact on the grounds capacity to be recharged by incident solar radiation (for bare ground cov→sur)

No.	Variable	Symbol	Units
1.	Surface cover albedo	(a_{cov})	[-]
2.	Surface cover Porosity	(p_{cov})	[m^3/m^3]
3.	Surface cover diffusivity	(α_{cov})	[m^2/s]
4.	Surface slope	(β_{cov})	[°]
5.	Surface cover emissivity	(ε_{cov})	[-]
6.	Surface cover moisture content	(θ_{cov})	[m^3/m^3]
7.	Surface orientation	(γ_{cov})	[°]

2.3.7 $GSHP_{HC}$ Operational Control

For either the monovalent or bivalent GSHP the operational control can vary as follows:

- Heat demand driven usage:
  - The GSHP system is automatically activated according to occupancy schedules with thermostatic control
  - The GSHP system is manually activated according to the occupants preferences with thermostatic control
- Electrical supply driven usage:
  - The GSHP system is automatically/manually activated according to the best value electrical power which is typically night-rate electricity

- Heat delivered outside of demand (off-demand) can be stored in an insulated water tank or in the concrete floor

However, Burke (2010) proposes a novel strategy identified as *source-side management*:

- Source supply driven usage:
  - Ideally, the GSHP system is automatically activated at times when the ground energy content around the collector is at a local optimum
  - Heat delivered off-demand is stored in an insulated water tank, a phase-change tank or in the concrete floor
  - With *split-level collectors*, the selection of optimum heat source is extended to two distinct ground levels potentially offering superior energy content as well as increased volume

Simulations of the aforementioned *split-level collectors* using a novel *collector-temperature feedback control* strategy are presented in Section 8.2.4.

2.3.8 Summary of $GSHP_{HC}$ Design Variables

Table 2-9 presents a summary of the principle parameters in ground heat exchangers, as summarised by VDI-4640 (2004) from the current 'conservative' design perspective.

Table 2-9: Principle parameters in ground heat exchangers (VDI-4640, 2004)

Pre-specified (inflexible) parameters	Freely selectable (flexible) parameters
Location/weather	Flow rate
Thermal properties of the ground	Pipe length
Backfilling material	Pipe diameter
Water content of the ground	Pipe material
Ground stratification	Installation depth
Useable ground area	Distance from grid pipes or nearby buildings
Ground water temperature and level	
Building heating/cooling load	

However, this *HP-IRL/H* project proposes an 'alternative' design approach for all SET based on a *CSDC* approach. Table 2-10 presents a summary of the *$GSHP_{HC}$ design groups* according to the *CSDC* approach. *CSDC* focuses on embracing individual climate parameters at a proposed SET site to inform the finer points of the final SET design with the aim of achieving more affordable solutions that offer better performance and lower environmental impact. *CSDC* also includes an integrated systems approach to SET deployment which includes close examination of the SET design and control strategies along with the building's

heating/cooling profile, central heating/cooling system and Building Energy Management Systems (BMS). Integration technologies based on enhanced system feedback, monitoring and control of system components, monitoring of real-time and predicted weather patterns and the use of extra thermal storage are potentially key components, along with the deployment of hybrid SET systems. While more difficult to construct and execute, these solutions offer the potential to increase the usability of the available renewable energy, increase the renewable energy fraction and reduce energy costs.

Table 2-10: Design groups according to the CSDC ethos

Inflexible	Freely flexible	Potentially flexible
Location/weather	Collector flow configuration	Building heat demand and annual requirement
Useable ground area	Collector pipe routing	Heat distribution system
Ground water	Collector pipe dimensions	Building energy management system
Utility costs	Collector pipe layout and burial	Bulk ground backfill
Material costs	Immediate collector backfill	Water content of the ground
	Operational control strategy	Surface slope and orientation and cover type

2.4 $GSHP_{HC}$ DESIGN GUIDES

Table 2-11 presents a summary of the various guides that exist for collector design and dimensioning (Burke, 2010).

Table 2-11: Collector sizing guides, adapted from Burke (2010)

Author (Year)	Location	Minimum return temperature ($T_{s,r,min}$) [ºC]	Ground temperature drawdown ($\Delta T_{s,r/\infty}$) [K]	Annual extraction flux ($Q''_{s,y}$) [kWh/m^{2}a]	Collector thermal characteristics [W/m^2] or [m/kW]	Collector depth $\lvert Z_{HC} \rvert$ [m]	Pipe Spacing (PS) [m]	Trench size (W_T) [m]	Trench spacing (TS) [m]
Kavanaugh & Rafferty (1997)	USA	-	-	-	-	≥1.5m	0.3 to 0.6m	-	-
IGSHPA (1997)	USA	-4ºC	-	-	-	1.5m	≥0.6m	-	-
VDI-4640 (2001)	Germany	-	-12K (base) -18K (peak)	50 to 70kWh/m^{2}a	8 to 40W/m^2	1.2 to 1.5m	0.3 to 0.8m	-	-
Hepbasli A. (2004)	Turkey	-	-	-	Local experience	1.2 to 3.0m	0.3m	0.9 to 1.8m	3.7 to 4.6m
*BRE (2004)	UK	-	-	-	-	1 to 1.5m	-	-	
EHPA (2005)	Europe	-	-	-	-	0.9 to 1.5m	-	-	-
Retscreen (2005)	Canada	-6ºC	-	-	33 to 55m/kW	1.2 to 2.0m	-	0.15 to 0.6m	1.5 to 4.0m
ASHRAE (2003)	USA	-	-	-	20W/m^2 minimum	≥1.2m	≥0.6m	-	-
EN 15450 (2007)	Europe	-	-12K	50 to 70kWh/m^{2}a	8 to 40W/m^2	-	-	-	-
*Rawlings *et. al.*(2007)	UK	-5ºC	-	-	-	1 to 2m	0.3m	-	3m
Brown R. (2009)	BSRIA UK	-	-	-	8 to 40W/m^2 (depending on soil type)	≥1.5m	≥0.8m	-	-

* Note: Identifies design guides published in *Cool Marine* climate regions

Figure 2-9 presents one example of these dimensioning guides, the VDI-4640 nonogram, adapted from SIA-Documentation D0136. The nonogram is used for 4-step sizing as follows:

1. Define the 'Heating power in kW' (1 to 20kW) to match either part or all of the building's *maximum heat demand* (this is equivalent to the heat pump capacity)
2. Identify the nominal COP of the proposed heat pump unit (2.5 to 3.5) and read off 'Evaporation power in kW' (1 to 15kW) (this is equivalent to the source capacity)
3. Specify the ground type which predominates at the proposed site (type 1 to 4)
4. The nonogram now allows the following key collector dimensions to be defined:
   - Collector area in m^2
   - Collector pipe length in m

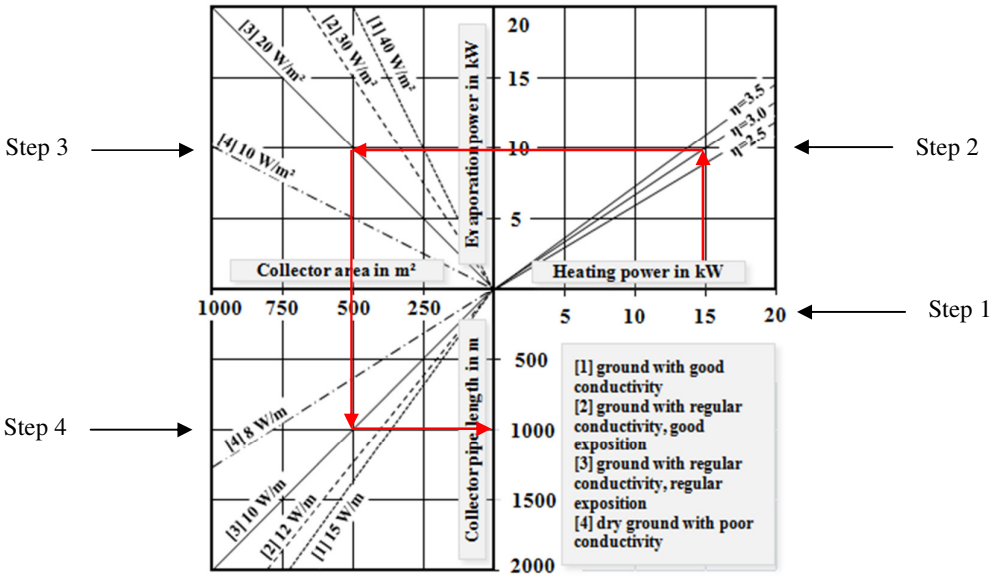

Figure 2-9: The VDI 4640 nonogram for horizontal collector sizing from SIA-Documentation D0136

The following can be assumed:

- An optimum evaporator (collector) flow rate for efficient heat pump performance is often recommended or set by the heat pump manufacturer/installer
- The pipe or pipes can be buried with depth and spacing according to Table 2-11
- Existing *backfill material* and *surface cover* can be employed

In addition to the design guides listed in Table 2-11, a number of design and sizing software packages listed in Table 2-12 also exist.

Table 2-12: Software packages available for heat pump collector design, adapted and supplemented from Burke (2010)

Software	Cost	$GSHP_{VC}$	$GSHP_{HC}$	Basis of Calculation Method	Country of Origin
CLGS	$500 (€350)	✓	✓	IGSHPA *et al.* (1997)	USA
ECA	$395 (€280)	✓	✓	ASHRAE (2003 - 2006)	USA
Earth Energy Designer	-	✓	×	(Eskilson, 1987)	Sweden
EnergyPlus	Free	✓	×	Not available	USA
GchpCalc	$300 (€210)	✓	×	Kavanaugh and Rafferty (1997)	USA
GeoStar	NA	NA	NA	Not available	China
G-HEADS	-	✓	✓	Tarnawski and Leong (1990,1991 and 1993)	Canada
GLD2010 *Residential*	$800 (€560)	✓	✓	Kavanaugh and Rafferty (1997) & Eskilson (2000)	USA
GLD2010 *Complete*	$4250 (€2975)	✓	✓	Not available	USA
$GLHE_{PRO}$	$525 (€370)	✓	×	Eskilson (2000)	USA/Sweden
GROCS	-	✓	✓	Metz (1985)	USA
GS2000™	Free	✓	×	Not available	USA & Canada
RETScreen®	Free	✓	✓	IGSHPA *et al.* (1997)	USA & Canada
TRNSYS	Component cost	✓	✓	Mei (1986)	USA

These software packages often reference climate values for their specific region of origin (Burke, 2010) and these software tools, as can be seen in Table 2-12, originate predominantly in *Continental* climate regions in USA and *Moderate Sub-polar* regions in Canada. There appears to be no design software originating in a *Cool Marine* climate region. These software tools are intended for use by designers of GSHP for residential and commercial buildings, however they are not intended for academic investigation of climate, design and control sensitivities and therefore were not utilised in this *HP-IRL/H* study.

2.5 $GSHP_{HC}$ ANALYSES

To build on and supplement the dimensioning guides and software tools presented, a number of $GSHP_{HC}$ analyses have also been presented. These analyses are motivated by differing rationale and involve a variety of $GSHP_{HC}$ *design variables,* with differing objectives and analysis methods.

2.5.1 Life Cycle CO_2 Analysis

The relationship between the CO_2 emissions reduction achieved during heat pump operation and the CO_2 emissions during production and installation of the $GSHP_{HC}$ requires a Life Cycle Analysis such as the Life Cycle CO_2 ($LCCO_2$) analysis completed for Canada (Caneta-Research, 2003) and Japan (Genchi *et al.*, 2002). Both studies showed very positive CO_2 reductions for GSHP over the full lifecycle of the system. A CO_2 payback time in the region of 1.7 years is quoted for switching from ASHP to GSHP in district heating and cooling system in Tokyo (Genchi *et al.*, 2002). For individual systems in smaller buildings in Canada,

it is stated that GSHP has the lowest CO_2 emissions over a twenty year lifetime when compared to ASHP, electric heating and natural gas (Caneta-Research, 2003). Since conditions such as electricity production, $GSHP_{HC}$ installation methods and the COP of an ASHP all differ in Ireland; a similar $LCCO_2$ type analysis for $GSHP_{HC}$ in Ireland is justified, but was considered outside the scope of this project.

2.5.2 Techno-economic Analysis

A techno-economic analysis comparing the cost of installation with typical performance and running costs has already been published for *ASHP,* $GSHP_{HC}$ and $GSHP_{VC}$ in Ireland as part of the *HP-IRL* project (Burke, 2010) and for $GSHP_{HC}$ in Turkey (Esen *et al.*, 2006). Following a survey of 30 Irish heat pump suppliers (18 responses) between May and July 2009, it was concluded that the average cost per kW of heat pump capacity was €1,221 and €1,673 for $GSHP_{HC}$ and $GSHP_{VC}$, respectively (Burke, 2010). Additionally, experimental testing of *HP-IRL* systems between 2007 and 2009 showed that the average SPFs for the $GSHP_{HC}$ *and* $GSHP_{VC}$ were 2.90 and 2.95, respectively (Burke, 2010). In Turkey, the $GSHP_{HC}$ was compared to conventional heating systems such as electric resistance, medium fuel oil, Liquid Petroleum Gas (LPG), coal, oil and natural gas using the *annualised life cycle cost method.* It was shown that $GSHP_{HC}$ offers a more cost effective alternative when compared to all the conventional heating systems with the exception of natural gas (Esen *et al.*, 2006).

2.5.3 Thermo-hydraulic Analysis

The relationship between the fluid's nominal head loss and temperature-rise in the ground piping for variable collector dimensions requires a 'thermo-hydraulic' analysis. According to a Belgian study, this type of problem is independent of climate and the 'specific pressure loss' can be used to define the optimum heat exchanger (Paepe & Janssens, 2003). According to a Canadian study, an air velocity (u_a) of 4 m/s, found using 'sensitivity analysis', is close to optimum for earth-air heat exchange in ducts (Gauthier *et al.*, 1997). In both the Belgian and Canadian analyses, the focus was on direct earth-air heat exchange, however the analysis techniques of 'specific pressure loss' and 'sensitivity analysis' respectively are equally applicable to $GSHP_{HC}$ design.

2.5.4 Other Analyses

While Paepe & Janssens (2003) concluded that the thermo-hydraulic analysis of a Ground Heat Exchanger (GHE) is independent of climate, there are many other aspects of $GSHP_{HC}$ design which are highly climate sensitive. A sensitivity analysis using simulation has been completed to establish suitable ranges for $GSHP_{HC}$ *design variables* for the *Moderate Subpolar* climate in Halifax, Canada (Healy & Ugursal, 1997). In addition, parametric studies have been completed on the subject of backfill materials (Mei, 1987) and optimum GHE depth for ground-air temperature differential (Stevens, 2004). In the *Semiarid Continental* climate of Turkey an experimental facility consisting of two $GSHP_{HC}$ in the series configuration, buried at 1 and 2m depths respectively, has produced a series of five analyses from different disciplines as follows:

- 2004 – Experimental thermal analysis (Inalli & Esen, 2004)
- 2006 – Techno-economic analysis (Esen *et al.*, 2006)
- 2007(a) – Energy-exergy analysis (Esen *et al.*, 2007)
- 2007(b) – Finite difference numerical analysis (Esen *et al.*, 2007)
- 2008 – ANN analysis (Esen *et al.*, 2008)

2.5.5 Analyses Summary

Table 2-13 presents a summary of the published analyses and findings on the $GSHP_{HC}$ *design groups* and individual *design variables* identified in this chapter. This table includes 15 publications between 1994 and 2010 from 6 different *climate classifications* ranging from *Moderate Subpolar* to *Dry summer Subtropical* and including 3 studies which are partially or entirely based on *Cool Marine* regions. Based on the absence of quality literature or calls within the existing literature in Table 2-13, the following 5 $GSHP_{HC}$ *design groups* were identified for further investigation:

- *Collector flow configuration*
- *Collector dimensions*
- *Pipe layout and burial*
- *Surface cover*
- *Operational control*

Investigations and discussions on *collector flow configuration* and *collector dimensions* are presented in Sub-section 6.3.3. Simulations of *surface cover* are presented in Section 8.1, while simulations of *split-level collectors*, a form of *pipe layout and burial*, with a variety of operational control strategies are presented in Section 8.2.

Table 2-13: Summary of published analyses and findings for the $GSHP_{HC}$ design groups

Design group	Variable/Parameter	Author (Year)	Climate	Findings
GSHP	Heat pump capacity (q_{sk}) [kW]	Healy & Ugursal (1997) Nova Scotia	*Moderate Subpolar*	Simulated capacities of 6.8 to 9.7kW in bivalent system; opted for 9.7kW to reduce energy costs for secondary system of lower η
		Spitler & Cullen (2008) Duluth & Houston	*Humid Continental* & *Humid Subtropical*	In this commercial heat pump study two cities were used as case studies; Duluth was 'heating constrained' Houston was 'cooling constrained' in both cases sizing for the *maximum heat loss/gain* alone caused operational problems
Collector flow configuration	Configuration (parallel vs. series)	-	-	The question of parallel vs. series has received limited attention; surprisingly, testing of the series option seems to dominate in the literature ***This question therefore merits investigation***
Collector pipe routing	Pipe routing (looped/straight/serpentine)	-	-	The question of pipe routing has received limited attention; however it has limited influence on performance
Collector dimensions	Source flow rate ($\dot{V}_s$) [m]	Kavanaugh & Rafferty (1997) USA	N/A	As a 'rule of thumb' flowrates of between 0.162 and 0.192 m^3/h is recommended per kW_{th} of heat pump capacity
		Gauthier et al. (1997) Quebec		Ground-to-air heat exchange study Parametric study yielded an optimum air velocity of 4m/s
		Healy & Ugursal (1997)	N/A	Conducted simulations at flowrates of between 0.32 and 0.69l/s; conclude increased heat exchange and pumping power consumption occurred at higher flow rates
		Hepbasli et al. (2003) Turkey	N/A	Pumping energy should be 6 to 7% of total energy consumption
	Number of pipes (N) [-]	Paepe & Janssens (2003) Belgium	N/A	In this ground-to-air heat exchange study the authors deem selection of pipe number to be independent of climate and apply a thermo-hydraulic technique of 'specific pressure loss' to find optimum pipe length
	Collector pipe length (L_t) [m]	Paepe & Janssens (2003) Belgium	N/A	In this ground-to-air heat exchange study the authors deem selection of length to be independent of climate and apply a thermo-hydraulic technique of 'specific pressure loss' to find optimum pipe length
		Retscreen (2005) Canada	N/A	As a 'rule of thumb' lengths of between 35 and 60m is recommended per kW_{th} of heat pump capacity
		Spitler & Cullen (2008) Duluth & Houston	*Humid Continental* & *Humid Subtropical*	In this commercial heat pump study two cities were used as case studies; Duluth was 'heating constrained' Houston was 'cooling constrained' in both cases pipe-sizing using 'rules of thumb' (m/kW_{th}) alone caused operational problems due to the load placed on the ground source
	Material	Koyun *et al.* (2009) Turkey	N/A	Compared series collectors with common polyethylene and aluminium-finned pipes; concluded that heat transfer rate per unit mass of fluid [kJ/kg(s)] was 26% higher for finned pipes; however cost was not evaluated
	Pipe size (D_{in}) [m]	Healy & Ugursal (1997) Nova Scotia	N/A	Simulations were conducted with pipes ranging from ¾ to 1½" (19 to 38mm); results showed that systems should be sized to minimize pumping costs
		Paepe & Janssens (2003)	N/A	Recommends applying the thermo-hydraulic technique of 'specific pressure loss' to find optimum pipe diameter
				Table 2-12 continues next page

	Source fluid	Healy & Ugursal (1997) Nova Scotia	N/A	Based on price, thermal performance and minimal corrosive effects, ethylene glycol was recommended with the percentage depending on local climate conditions
		-	-	While many studies have investigated collector dimensioning and produced either rules of thumb, the precise method for dimensioning a collector is still unclear ***This question therefore merits investigation***
Pipe layout and burial	Layout (inline/slinky)	Wu *et al.* (2010) Nottingham, UK	*Cool Marine/ Cool Littoral*	When comparing *in-line* with *slinky*; simulations show that *in-line* pipes extract more heat per meter of pipe while *slinky* pipes extract more heat per meter of trench
	Burial depth (Z_{HC}) [m]	Healy & Ugursal (1997) Nova Scotia	*Moderate Subpolar*	Collector depth in simulations was varied; results show that transitioning between 1 and 0.38m COP drops from 2.7 to 2.6 and from 0.38 to 0.1m COP drops more dramatically to 2.4
		Inalli & Esen (2004) Turkey	*Semiarid Continental/ Dry Summer Subtropical*	Using collectors buried at 1 and 2m depths in the same location respective COPs of 2.66 and 2.81 were observed
		Burke (2010) Ireland	*Cool Marine*	Using observed ground temperatures and a simulated heat pump operation it was shown that split-level collectors at 0.3 and 0.9m utilized with intelligent control could achieve an 8.1% increase in SPF ***This question therefore merits investigation***
	Collector area (A_{HC}) [m]	Healy & Ugursal (1997) Nova Scotia	*Moderate Subpolar*	As expected, simulations showed an improvement in COP with increased collector area; however, the rate of COP improvement also reduces with increased collector area while land cost increases linearly, this means when land is scarce an optimum area exists
	Pipe spacing (PS)	Healy & Ugursal (1997) Nova Scotia	*Moderate Subpolar*	Using a fixed A_{HC} the pipe spacing and total pipe length buried in the pit were then negatively related; simulations indicated that a pipe spacing of 0.5m was optimal
Backfill material	Immediate backfill	Salomone & Wechsler (1984)	N/A	Results showed that increasing the fractions of medium and coarse sand in a granular mixture increases the thermal conductivity
		Mei (1987)	N/A	Simulations showed that using a special 'fluidised mixture' as immediate backfill means 47% and 23% more heat is transferred than with clay and sand respectively
		Remund (1994)	N/A	Equal amounts of sand, silt and clay had better conductivities than soils with textures dominated by one particle size
	Bulk backfill	-	-	Replacement of the existing material with a bulk backfill for both domestic and commercial GSHP collectors is an expensive task, cost is prohibitive and payback is unproven
Surface cover	Surface slope (β_{cov}), orientation (γ_{cov}) and cover type	-	-	The question of surface slope has received no attention to date ***This question therefore merits investigation***
Operational control	Climate senstive collector control	Burke (2010)	*Cool Marine*	Experimental results indicated COP gain from intelligent split-level collectors ***This question therefore merits investigation***

2.6 HP-IRL/H ANALYSIS

Despite the foregoing research, analysis and resulting design methods, a deficit still exists in knowledge of $GSHP_{HC}$ particularly in the area of collector design and sizing (Paepe & Janssens, 2003; Gupta & Irving, 2008) along with operational feedback control and source-side management (Burke, 2010); this deficit is even more pronounced in *Cool Marine* regions. Therefore, this study seeks to supplement the current knowledge using an analysis and optimisation process based on heat-transfer fundamentals. Combined elements of the progressive multi-disciplinary analysis used on $GSHP_{HC}$ in Turkey (Esen *et al.*, 2006; Esen *et al.*, 2007; Esen *et al.*, 2008) and the sensitivity analysis used on $GSHP_{HC}$ in Canada (Healy & Ugursal, 1997) were applied. With increased sensitivity to the *environmental conditions* (both soil and climate) and the local *micro-environmental conditions* the novel analysis process is referred to as *thermo-environmental analysis*. This is a multi-disciplinary analysis and draws together elements of the following disciplines:

- Solar physics and climatology
- Soil physics and geotechnical engineering
- Heat transfer and mass transfer
- Fluid mechanics and hydraulics
- Thermodynamics

Even though *thermo-environmental analysis* does not include a techno-economic analysis, consideration was still given to the capital cost of the entire $GSHP_{HC}$ installation; a design that is thermally optimised is of little use unless it can achieve a shorter payback than the standard design.

2.7 SUMMARY

This chapter described the following aspects of the *HP-IRL/H* project:

- A holistic schematic of a $GSHP_{HC}$ space heating system was used to define the scope of this project which included the following primary elements:
  - Collector (Heat Source)
  - Building (Heat Sink)
  - Heat Pump
- Along with the additional elements of:
  - Climate influence
  - Heat storage, monitoring and control

- Electricity supply
- Hybrid system options

- The *HP-IRL/H* project focused on the horizontal collector and operational control, these being key elements of the climate → ground → heat pump interaction, while still maintaining a holistic view of the system
- A review of over 15 publications revealed that horizontal collector design can involve as many as 7 *design groups* and 23 *design variables*
- The novel *CSDC* approach, which places increased emphasis on designing for the local environment, was proposed to boost performance while reducing cost and environmental impact
- A literature review was conducted of:
  - 12 design guides published in 7 different countries between 1997 and 2007
  - 12 design software tools developed in 4 countries
  - 14 recent publications on $GSHP_{HC}$ analyses involving the following methods:
    - $LCCO_2$ analysis
    - Techno-economic (Payback) analysis
    - Thermo-hydraulic analysis
    - Sensitivity analysis and multi-disciplinary analysis
- Responding to recent calls and identified gaps in the literature *HP-IRL/H* focused on a novel *thermo-environmental analysis* of the following *design groups*:
  - *Collector flow configuration*
  - *Collector dimensions*
  - *Pipe layout and burial*
  - *Surface cover*
- The CSDC approach required a novel *thermo-environmental analysis* involving a multi-disciplinary study including elements of the following disciplines:
  - Solar physics and climatology
  - Soil physics and geotechnical engineering
  - Heat transfer and mass transfer
  - Fluid mechanics and hydraulics
  - Thermodynamics

Chapter 3 outlines the *HP-IRL/H* experimental facility used to generate experimental data for both informing and validating the numerical models employed for design.

CHAPTER 3

EXPERIMENTAL AND NUMERICAL METHODS

GMIT
GALWAY-MAYO INSTITUTE OF TECHNOLOGY
INSTITIÚID TEICNEOLAÍOCHTA NA GAILLIMHE-MAIGH EO

3. EXPERIMENTAL AND NUMERICAL METHODS

A dedicated, full-scale $GSHP_{HC}$ experimental testing facility was constructed and a suite of $GSHP_{HC}$ analytical and numerical tools were compiled, to address the needs identified in Chapters 1 and 2 for $GSHP_{HC}$ research in Ireland's *Cool Marine* climate. This chapter describes the test facility and provides an introduction to the numerical methods which are developed in subsequent chapters. The design of this facility was informed by both the needs of the industry and the knowledge deficits discussed in Chapter 2, as well as previous experimental facilities cited in this chapter. This thesis is only concerned with $GSHP_{HC}$ and for this reason only this element of the wider *HP-IRL* facility is described; information on the $GSHP_{VC}$ and ASHP testing facilities can be found in Burke (2010).

In the most intensive investigation undertaken to date, the *HP-IRL/H* experimental testing consisted of monitoring the climate, ground, collector, heat pump and building for 3.5 years from 2007 to 2010. During this time, over 70,000kWh$_{th}$ of heat was delivered to the test building, while over 50 million data points were generated at 5 minute intervals using 130 sensors. The *HP-IRL/H* numerical methods consisted of 11 analytical equation groups and 5 transient numerical models. This chapter is divided into eight sections as follows:

- Experimental literature review
- *HP-IRL/H* test site
- $GSHP_{HC}$ system description
- $GSHP_{HC}$ test program
- Ground energy monitoring
- Climate monitoring
- Data Acquisition (DAQ)
- Introduction to the numerical methods

3.1 EXPERIMENTAL LITERATURE REVIEW

The purpose of this literature review was to inform the design and instrumentation of the *HP-IRL/H* experimental facility so that it complied with the best international practice and facilitated continuous monitoring of all elements of the *CSDC* approach, identified in Figure 2-1. Thirteen experimental studies, published between 1979 and 2009 in 8 countries, are presented in Table 3-1.

Table 3-1: Summary of $GSHP_{HC}$ testing facilities with specific horizontal collector testing capabilities

No.	Study (Year)	Location	Climate Classification	Research Topic	Test Size, Duration
1.	Metz. P.D. (1979)	Upton, NY, USA	*Humid Continental*	GSHP in a cold climate	House with GSHP, t > 2 yr.
2.	Drown and Den Braven (1992)	Moscow, ID, USA	*Semiarid Continental/ Cool Marine*	Effect of soil properties and cycling on GSHP	325m^2 building with GSHP, t > 1 yr.
3.	Piechowski, M. (1995)	Melbourne, Australia	*Humid Subtropical*	HGHE for cooling, heat and mass modelling	Hot water circulated in HGHE, t ≈ 1 yr.
4.	Bi, Y. *et al*. (2002)	Beijing, China	*Humid Continental*	Spiral, semi-vertical heat exchanger and model	HGHE temperature distribution, t ≈ 1 month
5.	Hern, S. (2004)	Oklahoma, USA	*Humid/Semiarid Continental*	Multiple hybrid system testing	Hybrid GSHP test-bed, t > 1 yr.
6.	Dumont and Frere (2005)	Mons, Belgium	*Cool Littoral*	Residential GSHP performance tests	2 family houses with GSHP, t = 3 yr.
7.	Warnelof *et al.* (2005)	Tranas, Sweden	*Cool Littoral/ Moderate Sub Polar*	Trial of a new compact collector	150m^2 building with GSHP, t ≈ 2 yr.
8.	Esen, H. *et al.* (2007)	Elazig, Turkey	*Semiarid Continental/ Dry Summer Subtropical*	HGHE analysis and modelling	16.24m^2 building with GSHP, t > 1 yr
9.	Gan, G. *et al.* (2007)	Nottingham, England	*Cool Marine/Cool Littoral*	Utilising rainwater heat for GSHP	Cool water circulated, rainwater HGHE, t > 1 yr.
10.	Hamada *et al.* (2007)	Sapporo, Japan	*Humid Continental*	New 'no-dig' heat exchanger	One cooling season and one heating season
11.	Karlsson and Fahlen (2007)	Boras, Sweden	*Cool Littoral/ Moderate Sub Polar*	Capacity-control through VSD	2 heat pumps, VFD, t > 1yr
12.	Demir, H. *et al.* (2008)	Istanbul, Turkey	*Semiarid Continental/ Dry Summer Subtropical*	HGHE analysis and modelling, new HGHE trials	Chilled water circulated, still in operation
13.	Pulat, E. *et al.* (2009)	Bursa, Turkey	*Semiarid Continental/ Dry Summer Subtropical*	GSHP with HGHE analysis	Chilled water circulated underground, still in operation

Note: Climates based on Koeppe and De Long (1958)

A *climate classification* from the Koeppe and De Long (1958) classification system is assigned to each experimental site for comparison. All the available design and dimensioning data for the collector experiments listed in Table 3-1 are given in Table 3-2; the most likely dimensions presented are capacity (q_{sk}), length (L_t), pipe diameter (D_{in}) and collector area (A_{HC}). The design and construction of the *HP-IRL/H* facility began in late 2005 and therefore only the first nine of the publications listed in Table 3-1 were available to the design team at

the outset. However, information from the more recent publications was also incorporated into the *HP-IRL/H* test program.

Table 3-2: Details of experiment dimensions for each experimental study listed in Table 3-1

No.	Author	Use	q_{sk} [kW]	Flow Config.	Pipe Routing	L_t [m]	D_o [mm]	Layout	A_{HC} [m^2]	PS [m]	Z_{HC} [m]	SPF
1.	Metz	Heating 104m^2	3.4	Series	Serpent	152	46	In-line	200	1 to 2	-1.2	2.2
2.	Drown & Den Braven	Heating 325m^2	-	2 pipes, config. unclear	Clusters & looped	300 &76	33	Flat vortex & unclear	32 & unclear	-	-0.75	-
3.	Piechowski	Cooling	3.6	2 series options	Straight	12 &24	25	In-line & stacked	N/A	N/A & 0.6	-1.8 & -1.2 to -1.8	-
4.	Bi *et al.*	Heating	-	Series	Clustered	-	20	3-D Spiral loop	7	0.8	-0.8 to -3	-
5.	Hern	Heating & cooling	-	Series	-	80	20	-	-	-	-	-
6.	Dumont & Frere	Heating 2 areas	7 & 9.6	-	-	250 & 377	-	-	75 & 125		-0.6	2.9 & 2.7
7.	Warnelof *et al.*	Heating 150m^2	6	9 series type modules	N/A	N/A	40	N/A	<50	0.1	-1.5 to -2	3.3
8.	Esen *et al.*	Heating 16.24m^2	4.3	2 series options	Serpentine	50 & 50	16	In-line	15	0.3	-1 & -2	2.66 & 2.81
9.	Gan *et al.*	Heating	-	1 custom rainwater		-	-		0.5	N/A	-	-
10.	Hamada *et al.*	Heating	2.9	1 no-dig		83.2	60		-	N/A	-3	-
11.	Karlsson and Fahlen	Heating	-	-		-	-		-		-	-
12.	Demir *et al.*	Heating & cooling	4 & 2.7	Parallel	Straight	40	13	In-line	800	3	-1.8	-
13.	Pulat *et al.*	Heating	0.82	Series	-	20	16		5.04	0.3	-2	2.52

3.1.1 Climate Influence

Climate classifications, briefly introduced in Sub-section 1.3.2, are used to describe the typical weather in a region and this allows regions of similar climate to be identified. Today, *climate classifications* are based on long-term records of air temperature and rainfall. The earliest work on *climate classification* was carried out by Wladamir Köppen around 1900 using plants as climate indicators; the latest revision of this system was presented by Rudolf Geiger in 1961 and is now known as the Köppen-Geiger classification. This classification is still extensively used in a variety of disciplines (Peel *et al.*, 2007) and is shown in Figure 3-1 (Koeppe & De Long, 1958). Figure 3-1 highlights that the Köppen-Geiger classification is somewhat limited and lacks the geographical resolution to differentiate climates in some areas

(Kottek *et al.*, 2006; Peel *et al.*, 2007). For instance it suggests that Northwest Europe including Ireland, Britain, France, Belgium, Holland, Denmark and Germany share the same *Cf* climate. An improvement on this system, based on rainfall and temperature records with increased resolution was published by Koeppe and De Long (1958). This map is presented in Figure 3-2 (Koeppe & De Long, 1958) and shows greater climate differentiation across Northern Europe.

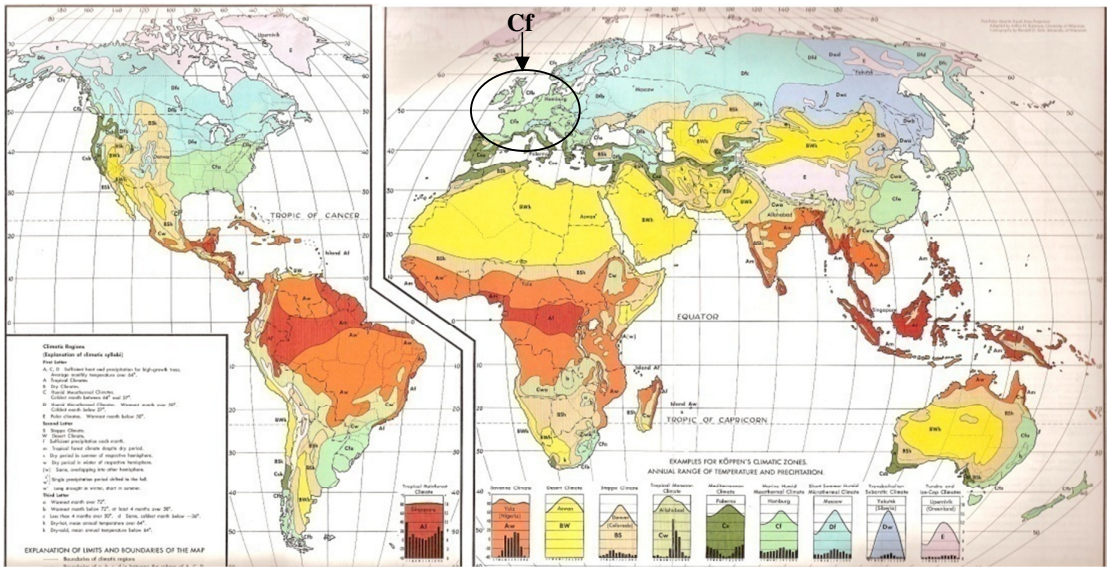

Figure 3-1: The Köppen-Geiger world climate classification map (Koeppe and De Long, 1958)

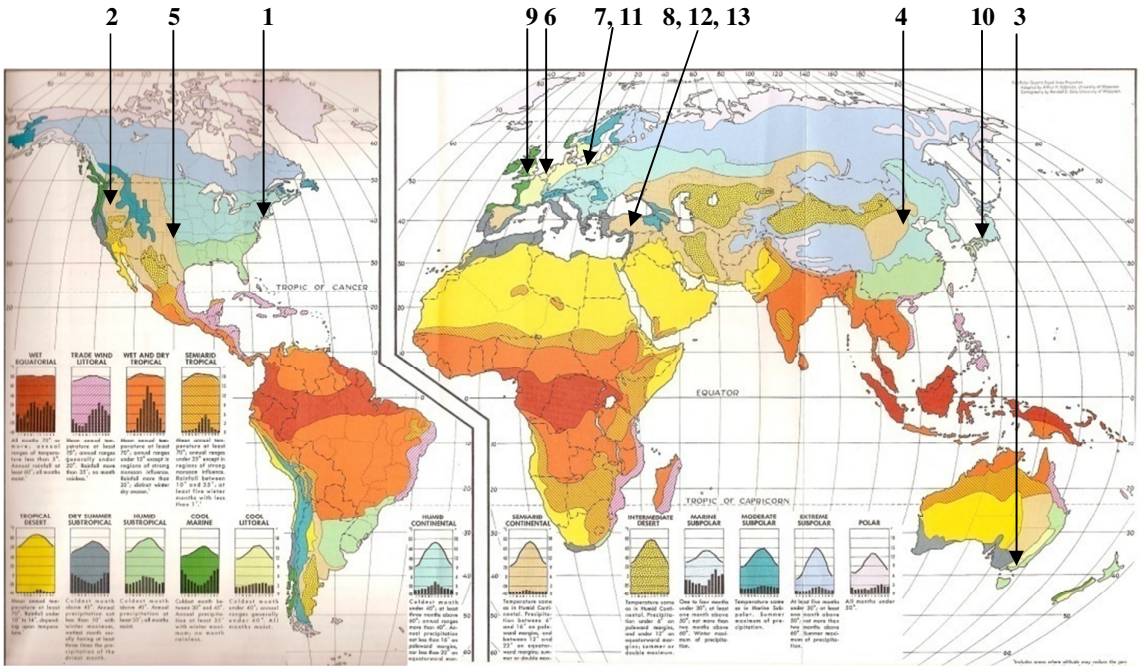

Figure 3-2: The Koeppe and De Long world climate classification map (Koeppe and De Long, 1958) with heat pump experimental facilities from Table 3-1 overlaid

The locations of the various $GSHP_{HC}$ experimental facilities from Table 3-1 are overlaid and the absence of test sites within the Cool Marine climate is noticeable. The complete Koeppe and De Long *climate classification* system is presented in Appendix B.

3.1.2 Early Continental Climate Experiments

Early experimental work on GSHP was carried out at the US National Laboratories in Brookhaven (BNL) (Metz, 1979; Metz, 1981) and Oakridge (ORNL) (Mei, 1986; Mei, 1987). At the BNL, a $GSHP_{HC}$ used to heat a 104m^2 building was monitored during winter operation (Metz, 1981). The climate in New York State is classified as *Humid Continental* with the coldest month under +4.4ºC (Koeppe & De Long, 1958); air temperature in this *'cold* [winter] *climate'* reached extremes of -24ºC during $GSHP_{HC}$ testing in 1980. The 104m^2 test building had a design heat loss of 3.4kW at the -12ºC outdoor design temperature. To satisfy this heat demand, a water-to-air heat pump unit was installed using two 76m pipes connected in a *series array* and looped in the ground. Metz (1981) used kilowatt-hour meters, running time meters, RS805 Btu-meters, Ramapo flow-meters and copper-constantan thermocouples in combination with Fluke 2240C data-logging to monitor $GSHP_{HC}$ performance for at least two years and made the following conclusions:

- During the period of November 20, 1979 to March 2, 1980 the $GSHP_{HC}$ system extracted 10.2 x 10^9 Joules of thermal energy from the ground, the average air temperature during this period was -2ºC and the system operated with an SPF of 2.2
- The minimum source return temperature observed was -4ºC and this compared favourably with the BNL's custom 'GROCS' software prediction of -7ºC

Ten years after the BNL experiment, research from an experimental test facility at the University of Idaho was published (Drown & Den Braven, 1992; Wibbels & Den Braven, 1994). Although the western border of Idaho is about 560km from the Pacific Ocean, a *Cool Marine* climate is still experienced in many of its western counties while a *Semi-arid Continental* climate predominates in eastern and central regions. At the university's test facility, a 325m^2 building was again heated with a water-to-air heat pump utilising a 300m coil buried under the buildings foundation and a 76m pipe placed in a sewer trench. Drown & Den Braven (1992) used thermocouples, thermal conductivity probes, water flow meters, differential pressure air flow meters, electrical power meters and hour-meters in combination with an analogue to digital interface and a personal computer to monitor $GSHP_{HC}$ performance, ground temperature and ground thermal conductivity for at least one year and made the following conclusion:

- Increasing the moisture content of a given soil, results in increased thermal conductivity and improved heat transfer to the horizontal ground coil

3.1.3 Cyclic Heat Pump Operation

The second publication from study No. 2 focused on the effect of cyclic operation (Wibbels & Den Braven, 1994). This type of heat pump operation occurs when the building's heat demand is a fraction of the heat pump's capacity. Capacity is relatively constant for a single speed compressor and cycling refers to the process of periodic (on/off) operation managed by the heat pump control system. Wibbels & Den Braven (1994) compared simulations of $GSHP_{HC}$ with both fixed and variable capacity heat pumps and made the following conclusions:

- The source return temperature was sensitive to the length of the modelled pipe
- Cyclic operation decreased the heat pump COP
- Higher COPs were delivered by multi-speed or variable speed heat pumps

Similarly, in a theoretical analysis it was found that introducing VFDs into single speed compressors could prevent cycling and increase COP by between 5 and 15% (Esen *et al.*, 2008). However, in an experimental investigation of two heat pumps fitted with VFDs (study No. 11 in Table 3-1), Karlsson & Fahlen (2007) found that while one heat pump delivered the theoretical COP gains, a second heat pump showed a reduction in COP; this was due to a compressor which was not VFD compatible and performed inefficiently. Finally, Karlsson & Fahlen (2007) concluded that it is difficult to translate COP gains using VFDs into SPF gains unless the entire system including the compressor, ground heat exchangers and circulating pumps are compatible.

3.1.4 Combined Heat and Moisture Transfer

In the *Humid Subtropical* climate of Melbourne, study No. 3 focused on summer heat rejection to the ground and the influence of combined heat and moisture transfer mechanisms on HGHE performance (Piechowski, 1996). While some additions of the Köeppen-Geiger classification identify Melbourne as *Cf* (analogous to *Cool Marine*) the *Humid Subtropical* label used by Koeppe and De Long (1958) is more appropriate, with the average air temperature fluctuating between 10ºC in winter and 20ºC in summer. Piechowski (1996) arranged Type-T thermocouples around the buried pipes along with Time Domain Reflectometers (TDR) for moisture content monitoring and data-loggers. Water was heated

with an electrical element and circulated underground to cool. Piechowski (1996) concluded that movement of ground water in the vapour phase was a factor in heat flow, but conduction remained the primary heat transfer mechanism for moisture contents in excess of $0.15m^3/m^3$. In terms of conduction it was found that moisture content had a substantial influence on thermal properties and drying ground diminished the heat rejection rate (Piechowski, 1996).

3.1.5 New Collector Designs

Testing of new collector designs was reported from studies No. 4, 7, 9, 10 and 13. In study No. 4, the 'spiral semi-vertical' design shown in Figure 3-3(a) was tested in China (Bi *et al.*, 2002). This collector consisted of a single pipe buried from 0.8 to 3m depth in a double spiral fashion; the concentric-spirals having diameters of 0.8m and 2.4m respectively. The temperature distribution around the concentric-spirals was measured and simulated, but few experimental results are given.

In study No. 7, a new 'compact collector', shown in Figure 3-3(b), with additional heat from a heat recovery unit was tested in Sweden (Warnelof & Kronstrom, 2005). This factory-made collector is installed in modules and is intended for use where space is limited. As a result of limited collector area in the Swedish *Cool Littoral/Moderate Sub Polar* climate, additional heat was needed to run the heat pump and this was provided by a heat recovery unit. While this combination appears to have a lot of potential, the publication does not detail the experimental results, stating that an SPF of 3.3 was maintained in a cold climate. It does however provide further evidence of the ongoing efforts being made to improve collector design and performance.

(a) Spiral semi-vertical **(b) Compact collector** **(c) No-dig method for spiral collector**

Figure 3-3: New collector designs proposed between 2002 and 2007 (Bi *et al.*, 2002; Warnelof & Kronstrom, 2005; Hamada *et al.* 2007)

In the University of Nottingham in the UK, study No. 9, an experimental rig was built to assess the potential of using thermal energy in rainwater to boost the performance of GSHP (Gan *et al.*, 2007). This experiment was carried out in the UK climate which is typically *Cool Marine*, similar to Ireland, with an area of *Cool Littoral* in the South East of England. However, this experimental study is primarily laboratory based and does not involve coupling of the ground with a full-scale GSHP and building. Results indicate that a considerable thermal energy resource exists in rainwater potentially collected from roofs, car parks and driveways and this could have a positive impact on horizontal collector performance.

At the Hokkaido University in Japan, study No. 10, another 'spiral semi-vertical' design, similar to that tested in China (Bi *et al.*, 2002), is tested. The novelty of this collector design, shown in Figure 3-3(c), is that no digging is needed (Hamada *et al.*, 2007). This 'no-dig' collector is installed with a spiral drilling rig and back-reamer resulting in lower installation costs with improved cost effectiveness for GSHP. The collector, when tested with a 2.9kW heat pump, was found to produce a '*stable temperature source'*. Additional testing focused on the relationship between the energy needed to circulate the fluid and heat transfer characteristics at a variety of flow rates. However, optimum flow rate ranges are not stated (Hamada *et al.*, 2007).

3.1.6 Recent Continental Climate Experiments

The most recent experimental research outside of *HP-IRL* has been carried out in studies No. 8, 12 and 13, all located in the *Semiarid Continental/ Dry Summer Subtropical* climate of Turkey. Study No. 8, shown in Figure 3-4 (a), involves experimental testing of two collector systems. Both comprise of a single pipe in the *series configuration*, buried in a *serpentine* style at 1m and 2m depths respectively in Elazig, Turkey (Esen *et al.*, 2007). Another collector pipe, again in *series*, of similar dimensions to that of Esen *et al.* (2007) is deployed in Bursa, Turkey with sensors and data acquisition installed (Pulat *et al.*, 2009). However, it is the *parallel*, *inline* collector pipes of study No. 12 from Istanbul, Turkey (Demir *et al.*, 2009) which is the closest match to the typical Irish design. To the author's knowledge, this facility is the only sample in the literature, other than *HP-IRL/H,* of pipes connected in the *parallel configuration* and also buried with *in-line layout*. In contrast, the spacing between the pipes (PS) is 3m which is far greater than the *HP-IRL/H* spacing (0.25 to 0.4m) and what is common in Ireland. This facility, shown in Figure 3-4(b) has been used to validate numerical simulations (Demir *et al.*, 2009) and also to test a modification to the collector using the 'finned pipe' deployed by Koyun *et al.* (2009).

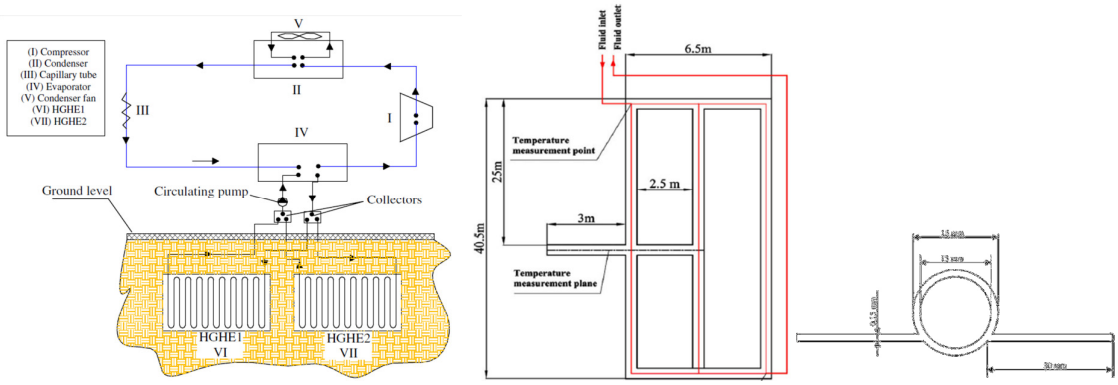

(a) Series pipes at 1 and 2m depths **(b) Parallel pipes at 3m spacing** **(c) Finned collector pipe**

Figure 3-4: Schematics of three recent experimental studies from Turkey (Esen *et al.*, 2007; Demir *et al.*, 2009; Koyun *et al.*, 2009)

The pipe shown in Figure 3-4(c) uses an aluminium fin designed to reduce localised thermal resistance and increase the rate of heat extraction from the ground. Results show that the length of collector pipe required for a given capacity is reduced by utilising the aluminium finned pipe. However, performance results and increased costs of the new installation are not quoted.

The remaining studies from Table 3-1 not discussed in detail in this section are No. 5 (Hern, 2004) and No. 6 (Dumont & Frere, 2005). Hern (2004) designed a hybrid system which included a 'ground loop' however limited details are available on this loop. The findings of Dumont and Frere (2005) are discussed in Chapter 6 when relevant.

3.1.7 Summary

Based on the cited literature, it is clear that the current best practice in experimental testing involves the installation of a dedicated network of sensors and the collection of high resolution data using a DAQ system. While the aims of the $GSHP_{HC}$ research presented here are as varied as the climates at each site, some key points can be extracted. For example, the influence of climate is seen even in the titles such as *'in a cold climate'* (Metz, 1981) and *'for mild climate'* (Pulat *et al.*, 2009). The dominant variables seen to influence the performance of a $GSHP_{HC}$ in experiments No. 1 to 13 are summarised in no particular order, as follows:

- Climate (Metz, 1981; Pulat *et al.*, 2009)
- Soil properties (Drown & Den Braven, 1992; Piechowski, 1996)
- Pipe length and design (Metz, 1981; Wibbels & Den Braven, 1994; Koyun *et al.*, 2009)

- Parallel pipes (Demir *et al.*, 2009)
- Duty and cycling (Wibbels & Den Braven, 1994; Karlsson & Fahlen, 2007)
- Combined heat and moisture movement (Piechowski, 1996)

Other aspects also investigated are:

- New collector designs and configurations (Bi *et al.*, 2002; Warnelof & Kronstrom, 2005; Hamada *et al.*, 2007; Gan *et al.*, 2007; Koyun *et al.*, 2009)
- Hybrids, alternative uses of ground loops (Hern, 2004)

As a result, the *HP-IRL/H* facility was designed to allow assessment of these variables in the Irish *Cool Marine* climate as follows:

- Testing was carried out, with full exposure to weather, over 3.5 years
- Four different surface coverings were present
- A variety of soil textures present around the collector were sampled
- Vertical measurement profiles were placed at seven different positions along the length of the in-line collector pipes and included temperature, moisture and heat flux sensors
- Ground temperatures were recorded along the collector at a variety of pipe spacings varying from 0.25 to 0.4m
- Heat pump performance was measured at duty varying between low, moderate and intense
- Two configurations, inline and slinky were deployed for testing

Additionally, over the course of the *HP-IRL/H* project the $GSHP_{HC}$ system was modified to create the potential in subsequent studies to undertake the following:

- A SOL-$GSHP_{HC}$ hybrid – where excess heat from solar thermal collectors in autumn, winter and spring is added to the source return fluid prior to entering the heat pump's evaporator
- A SOL-HC storage system – where excess heat from solar thermal collectors in summer and autumn is directed to the ground collector to boost ground temperature
- Reverse collector flow direction and isolate individual collector pipes

3.2 HP-IRL/H TEST SITE

The *HP-IRL/H* experimental investigation was conducted at the Galway-Mayo Institute of Technology (GMIT), Dublin Rd., Galway, between 2007 and 2010; construction of the testing facility began in 2004. Galway City is situated on the north eastern shore of Galway Bay, an inlet of the Atlantic Ocean on Ireland's west coast, shown in Figures 3-5(a) and (b). The test building is the Innovation in Business Centre (IiBC), shown in Figure 3-5(c), which is located at approximately 53º 16' 39''N and 9º 00' 43''W, less than 0.5km from the ocean. The IiBC building, with a floor area of 1,125m^2, serves as an incubation centre for start-up companies with office spaces to accommodate 70 people. Work carried out by start-up companies involves intensive use of computers and other electronics which consume a considerable amount of electricity. The IiBC building has been heated predominately using GSHP since 2006 with heat delivered to offices, unusually, by hydronic radiators.

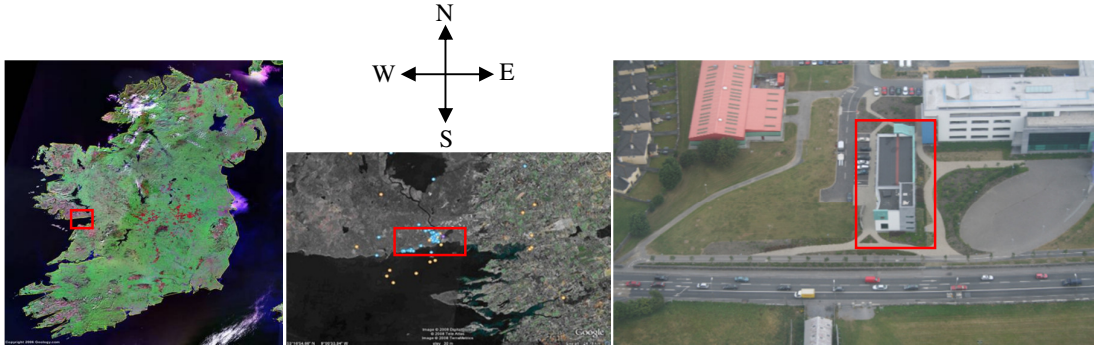

(a) Galway Bay, Ireland **(b) Galway City** **(c) IiBC Building, GMIT, Dublin Rd., Galway**

Figure 3-5: The HP-IRL/H test site location on Galway Bay, Ireland

3.2.1 IiBC Space Heating

The IiBC's *maximum heat demand* is estimated at 60kW$_{th}$ for a -2ºC outdoor *design temperature* and an internal temperature of +21ºC. This can be broken down into 40kW$_{th}$ in fabric heat losses and 20kW$_{th}$ in ventilation heat loss from air leakage (Stephens, 2003). As depicted in Figure 3-6, the IiBC heating system is bivalent. The primary-source consists of two, 30kW$_{th}$ LPG condensing boilers with a maximum distribution temperature of 80ºC, with two, 15kW$_{th}$ GSHPs offering a maximum output temperature of 50ºC, as a secondary heat source. The heat pumps utilise one HGHE or HC and one VBHE or VC identified as $GSHP_{HC}$ and $GSHP_{VC}$ respectively. Both heat pumps and both gas boilers are connected to the same storage/buffer tank as shown in Figure 3-6. The IiBC is divided into two heating zones 'East Zone' and 'West Zone' and the storage tank supplies heat to both zones via two separate

hydronic radiator *distribution systems*; these conventional radiators were in place before the GSHP was included as a secondary heating system.

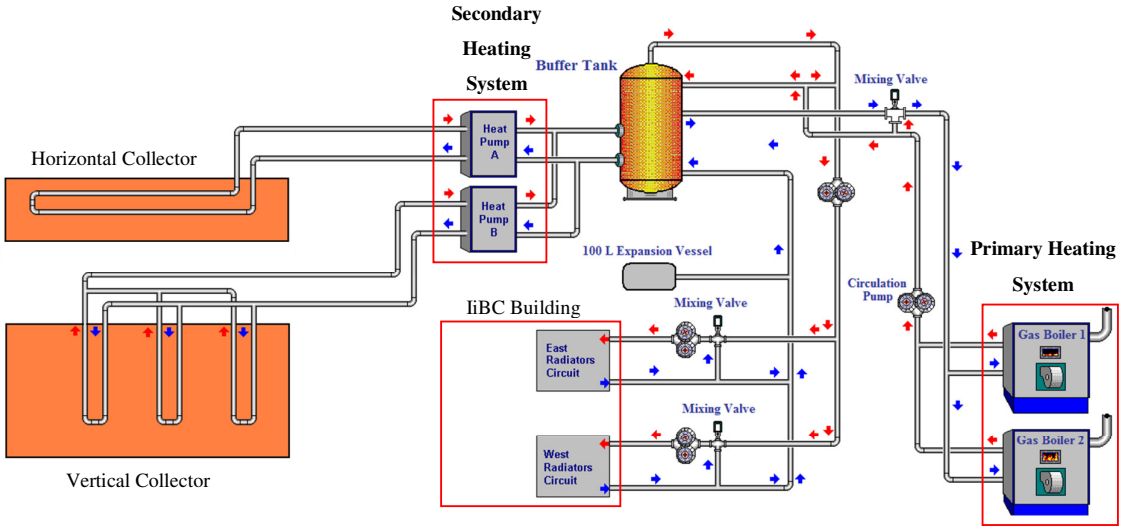

Figure 3-6: The heating system of the IiBC Building comprises of both GSHP and LPG Boilers

As discussed in Sub-section 2.1.3, conventional radiators are not ideal for GSHP and are designed for a typical flow temperature of 60 to 90ºC (IEA-HPC, 2010). The *HP-IRL/H* system is essentially a GSHP retrofit and as a result the following operational issues arose:

- The GSHPs and LPG boilers cannot be operated simultaneously unless the LPG system output is set below 50ºC
- While the two heat pumps operating in a combined master-slave configuration can deliver 30kW$_{th}$ of heat at a temperature of 50ºC, the radiators cannot dissipate more than 15-16kW$_{th}$ at this flow temperature when the internal air temperature is 20ºC

As a result, the two GSHPs only rarely operate simultaneously and the combined output of the master ($GSHP_{HC}$) and slave ($GSHP_{VC}$) has a maximum of 15-16kW$_{th}$ at -2ºC outside air temperature.

3.2.2 GSHP Contribution to Space Heating

Despite the operational issues outlined in Sub-section 3.2.1, both GSHPs have been used extensively between 2006 and 2010. As shown in Table 3-3 and Figure 3-7 GSHP was the main supplier of heat to the IiBC Building between 2007 and 2009. This was made possible since the well-insulated IiBC typically does not require 60kWth due to the combination of mild winter conditions, casual gains from the occupants, solar gains and the considerable

amount of heat generated by the computers and other electronics in the IiBC offices. In total, these make a contribution of approximately 30kW$_{th}$ to the IiBC heating requirement during working hours and as a result the GSHPs can be used to meet the remaining heat load for external air temperatures between 3 and 16ºC. Table 3-3 shows that almost 70,000kWh$_{th}$ of energy was delivered to the IiBC by *GSHP$_{HC}$* over almost 7,000 hours of operation between 2006 and 2009. A monthly breakdown in heat delivered to the IiBC, across *GSHP$_{HC}$*, *GSHP$_{VC}$* and LPG, between January 2007 and May 2009 is presented in Figure 3-7.

Table 3-3: Heat supplied and operating time for GSHP$_{HC}$ and GSHP$_{VC}$ over 3 heating seasons

Heating Season	GSHP$_{HC}$ Heat Supplied (Operating Time)	GSHP$_{VC}$ Heat Supplied (Operating Time)
2006/2007	23,348 kWh$_{th}$ (2,515 hours)	2,492 kWh$_{th}$ (109 hours)
2007/2008	23,623 kWh$_{th}$ (2,766 hours)	26,010 kWh$_{th}$ (2,458 hours)
2008/2009	22,543 kWh$_{th}$ (1,581 hours)	45,509 kWh$_{th}$ (5,582 hours)

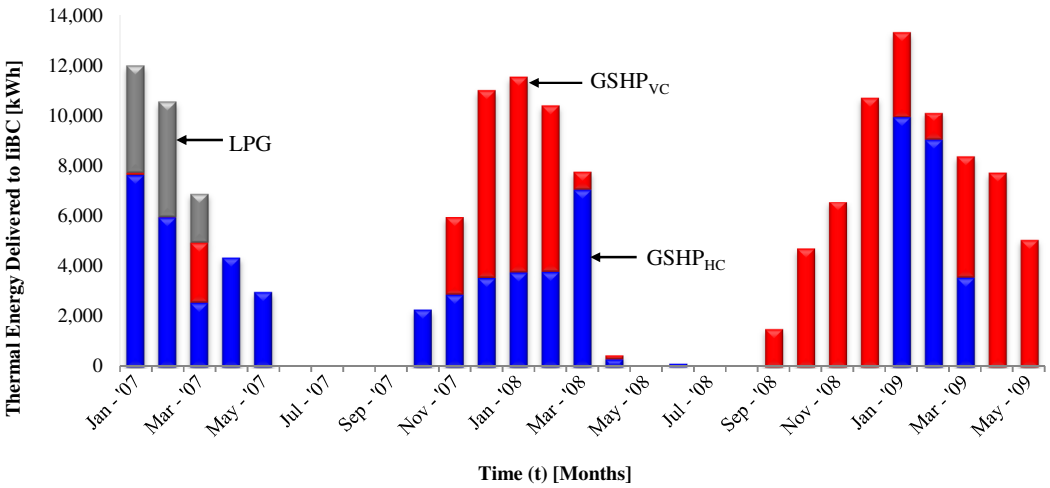

Figure 3-7: IiBC's monthly total heating supply divided by heat source: GSHP$_{HC}$, GSHP$_{VC}$ and LPG

3.3 GSHP$_{HC}$ SYSTEM DESCRIPTION

The *GSHP$_{HC}$* system used in the *HP-IRL/H* study was designed and built by an Irish company *Dunstar Ltd.* The system consists of a *Solterra 500* 15kW$_{th}$ *vapour-compression* heat pump coupled to a horizontal collector comprising a 10 x 150m long *parallel pipe, in-line* array. This section contains a description of the components of the system and the operational principle.

3.3.1 Solterra 500 Heat Pump

The *Solterra 500* heat pump, shown in Figure 3-8, was designed and manufactured in Ireland by *Geostar Engineering Ltd*. The *ideal vapour-compression cycle*, described in Sub-section 2.1.3, approximates the *Solterra 500's* cycle. The function of the *Solterra 500* within the $GSHP_{HC}$ system is displayed in Figure 3-9.

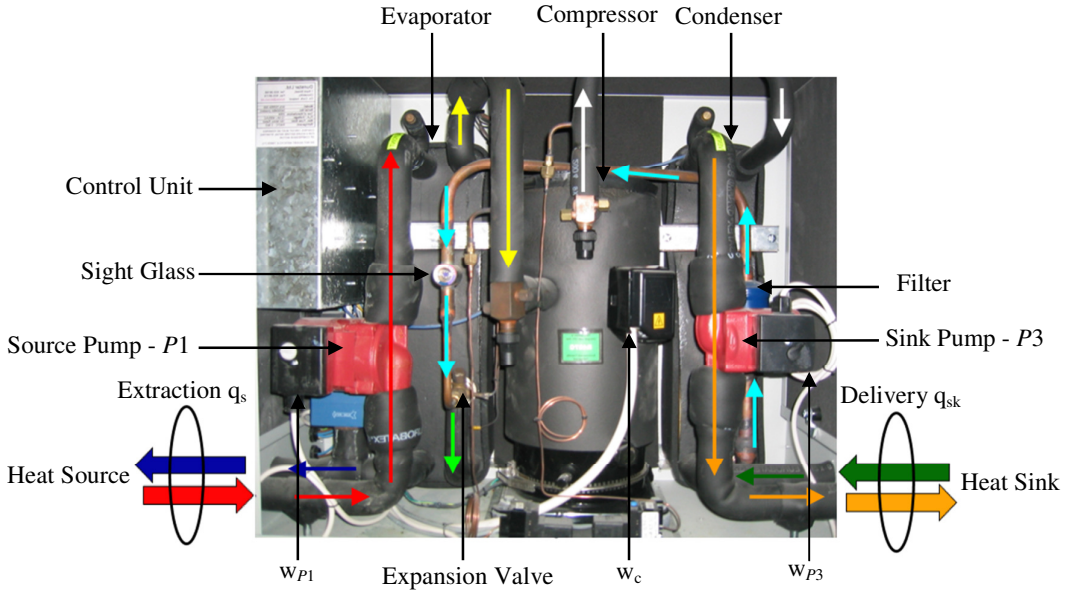

Figure 3-8: A photograph of the Solterra 500 used in HP-IRL/H including component labels with the ideal vapour-compression colour coding from Sub-section 2.1.3 overlaid

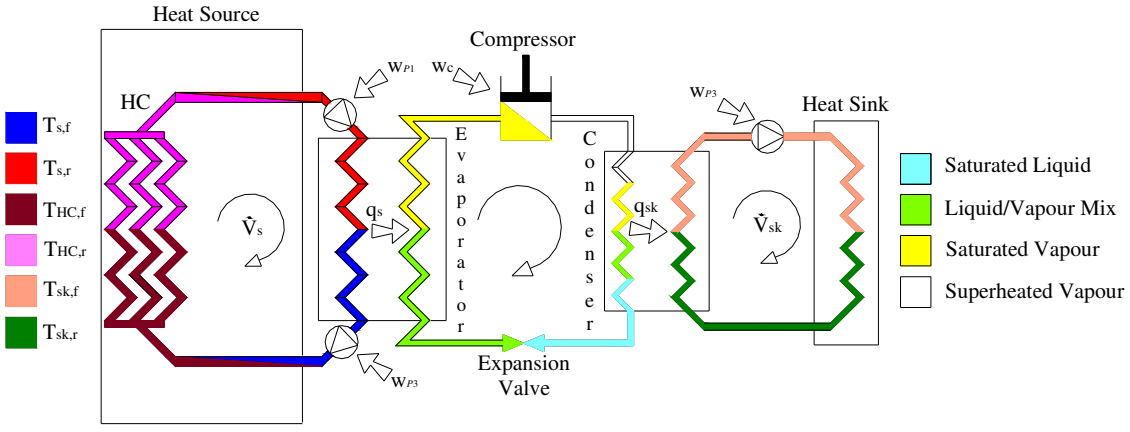

Figure 3-9: A colour coded schematic of the $GSHP_{HC}$ system with the heat source on the left and the heat sink on the right coupled by the ideal vapour-compression cycle described in Sub-section 2.1.3

The *Solterra 500* is charged with 2.3kg of *R407C,* a HFC-refrigerant, which absorbs heat (q_s) in the evaporator (*Stainless-steel plate heat exchanger*, ΔP_F = 32.45 kPa). The *R407C* is then compressed by a *Copeland* scroll compressor (*ZB 42KCE-PFJ-551*). The compressed *R407C*

rejects heat (q_{sk}) in the condenser (*Stainless-steel plate heat exchanger*) before expansion in the *Danfoss TE2* expansion valve. The performance of the *Solterra 500* was independently assessed by *Arsenal Research* in accordance with the '*D-A-C-H testing regulation for brine/water heat pumps*' (Zottl, 2003). A summary of the *Arsenal Research* findings are presented in Table 2-2, where B and W represent the source and sink fluids – brine and water respectively, ΔT_{hp} [K] represents the temperature lift, q_{sk} and q_s [kW_{th}] represent the sink heat delivery and source heat extraction rates respectively, w_c [kW] represents the compressor's power consumption, COP_{heat} [-] is the heat pumps Coefficient of Performance in heating mode and η_c [-] is the compressor's thermal efficiency.

Table 3-4: Solterra 500 vapour-compression heat hump performance generated by the independent, Arsenal Research centre, Austria (Zottl, 2003)

B/W [°C]	ΔT_{hp} [K]	q_{sk} [kW_{th}]	q_s [kW_{th}]	w_c [kW]	COP_{heat} [-]	η_c [-]	error-q [±kW_{th}]
B5/W35	30	17.365	13.884	3.871	4.5	0.899	0.147
B0/W35	35	15.232	11.729	3.844	4	0.911	0.139
B-5/W35	40	13.317	9.88	3.808	3.5	0.902	0.133
B5/W50	45	16.584	11.752	5.317	3.1	0.908	0.144
B0/W50	50	14.576	9.81	5.273	2.8	0.903	0.136
B-5/W50	55	12.778	8.008	5.24	2.4	0.910	0.13
Mean						0.9055	0.1381

However, the *Arsenal* testing was carried out under laboratory conditions over a range of standardised and stable source and sink conditions and the COP, calculated to BS EN14511, does not include the power consumed by collector circulating pumps. Therefore, the focus of *HP-IRL/H* was placed on characterising the system performance of the *Solterra 500* under *Cool Marine* climate conditions. This anchored the research in the areas of collector efficiency characterisation, collector simulation and operational control strategies. Whereas, research on the heat pump *vapour-compression cycle*, was deemed unnecessary and both beyond the scope of the research and outside the remit of *HP-IRL/H*.

3.3.2 Horizontal Collector

The horizontal collector shown in Figure 3-10 was designed and installed by *Dunstar Ltd.* in 2004. The collector consists of 10, High Density Polyethylene (HDPE) pipes, each 150m long with outer diameter of 32mm and wall thickness of 3mm, connected in *parallel configuration* to a flow manifold and looped in the ground to the return manifold.

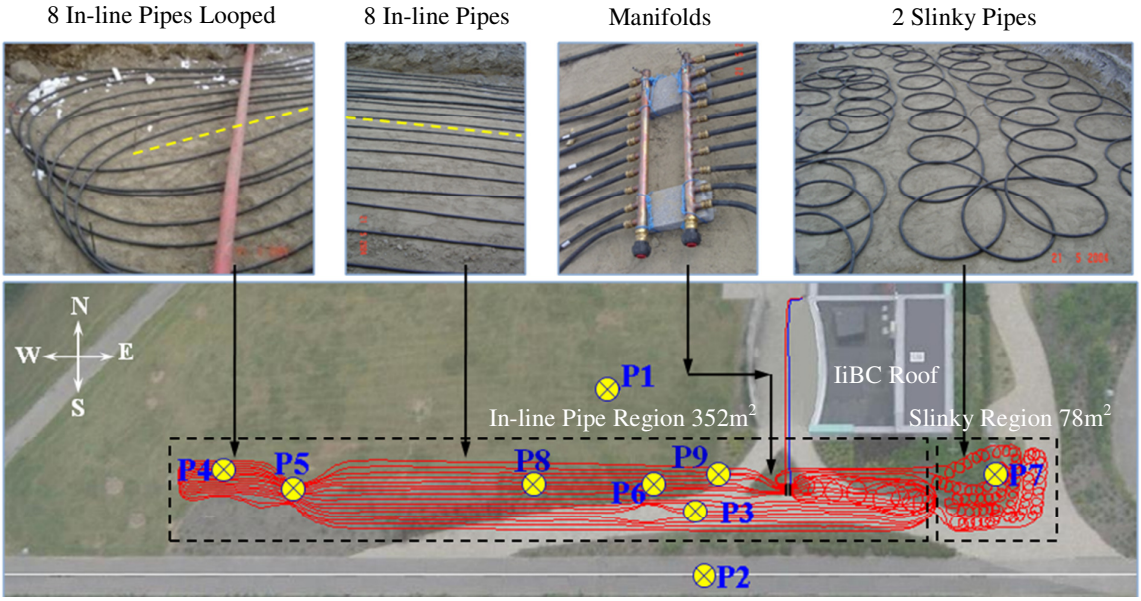

Figure 3-10: An aerial photograph of the collector site with a CAD image of the collector piping (created using a composite of collector installation photographs) and 9 vertical measurement profiles (P#) superimposed

The flow and return manifolds are co-located underground in a manhole and are coupled with the *Solterra 500* flow and return respectively by two 30m long HDPE *run-out* pipes with an outer diameter of 63mm and wall thickness of 5.8mm. The collector contains a mixture of 70% water and 30% *ethylene glycol* by weight, circulated by two *Grundfos UPS 25-80* pumps at a nominal flow rate of 70l/min through the *Solterra 500* evaporator and divided equally at the flow manifold so that each of the ten pipes carry approximately 7l/min through the ground to the return manifold.

The ten pipes are buried in the ground at approximately 0.8 to 1.35m depth, in a layer of sand 0.2 to 0.3m thick, occupying a total collector area of 430m^2. As shown in Figure 3-10, eight of the *looped pipes* are buried in the *in-line layout* while the remaining two are buried in *slinky* coils. The *in-line* pipes occupy an area of about 352m^2 with a pipe spacing ranging between 0.25m at restrictions and bends to 0.4m on the straight. The slinky coils occupy an area of about 78m^2 with coil diameters of between 0.5 and 0.75m.

The *$GSHP_{HC}$ design variables* are summarised in Table 3-5 and are listed in accordance with the *design groups* discussed in Section 2.3. The thermo-physical properties of the source fluid and collector piping are summarised in Table 3-6.

Table 3-5: Horizontal collector design summary

$GSHP_{HC}$ design group	Variable/Parameter	Symbol	Value	Units
Heat Pump	Extraction	(q_s)	8.0 – 13.9	[kW]
Collector flow configuration	Configuration	-	Parallel	-
Collector pipe routing	Pipe routing	-	Looped	-
Collector dimensions	Source flow rate	($\dot{V}_s$)	70	[l/min]
	Number of pipes	(N)	10	-
	Collector pipe length	(L_t)	150	[m]
	Material	-	1" HDPE	-
	Inner diameter	(D_{in})	0.026	[m]
	Outer diameter	(D_o)	0.032	[m]
	Source fluid	-	Water-glycol 70-30%	-
Run-out pipes	Run-out pipe length	(L_{r-o})	30	[m]
	Material	-	2" HDPE	-
	Inner diameter	(D_{in})	0.063	[m]
	Outer diameter	(D_o)	0.051	[m]
Pipe layout and burial	Layout	-	8 in-line/2 slinky	-
	Burial depth	(Z_{HC})	-0.8 to -1.35	[m]
	Collector area	(A_{HC})	430	[m^2]
	In-line area	($A_{in-line}$)	352	[m^2]
	Slinky area	(A_{slinky})	78	[m^2]
	Pipe spacing	(PS)	0.25-0.4	[m]
	Coil Diameter	(D_{coil})	0.5-0.75	[m]
Backfill material	Immediate backfill	-	Sand	-
	Bulk backfill	-	Existing material	-
Surface cover	Surface slope	(β)	0	[º]
	Orientation	(γ)	N/A	[º]
	Cover Type	-	4 types	-

Table 3-6: Horizontal collector thermo-physical properties at 0ºC and 1atm

Material/Substance	Property	Symbol	Value @ 0ºC	Units
Water	Density	(ρ_w)	1000	[kg/m^3]
	Specific Heat Capacity	($c_{p,w}$)	4210	[J/kgK]
	Conductivity	(k_w)	0.596	[W/mK]
	Kinematic Viscosity	(ν_w)	$1.788x10^{-6}$	[m^2/s]
	Prandtl Number	(Pr_w)	13.67	[-]
Ethylene Glycol	Density	(ρ_{eg})	1115	[kg/m^3]
	Specific Heat Capacity	($c_{p,eg}$)	2300	[J/kgK]
	Conductivity	(k_{eg})	0.25	[W/mK]
	Kinematic Viscosity	(ν_{eg})	$4.927x10^{-5}$	[m^2/s]
	Prandtl Number	($Pr_{,eg}$)	528	[-]
Source fluid (70/30)	Density	(ρ_f)	1059	[kg/m^3]
	Specific Heat Capacity	($c_{p,f}$)	3650	[J/kgK]
	Conductivity	(k_f)	0.47	[W/mK]
	Kinematic Viscosity	(ν_f)	$3.31x10^{-6}$	[m^2/s]
	Prandtl Number	(Pr_f)	25	[-]
HDPE-Pipe	Density	(ρ_p)	952.5	[kg/m^3]
	Specific Heat Capacity	($c_{p,p}$)	2250	[J/kgK]
	Conductivity	(k_p)	0.49	[W/mK]
	Diffusivity	(α_p)	$2.36x10^{-6}$	[m^2/s]

3.3.3 Modifications to $GSHP_{HC}$

In 2010, some modifications were made to the *Dunstar Ltd.* horizontal collector design for the purposes of research and trials to be conducted on ground heat storage. Firstly, the system was drained of the water and *ethylene glycol* mixture, while ball valves were installed on each of the ten collector pipes by *SIRUS Ltd.* This means that the number of pipes with fluid flow and the flow rate in pipes can be modified in future tests. In addition, a set of connections and by-passes with isolation valves, pictured in Figure 3-11 were installed by *ROCO Manufacturing Ltd.* on the source run-out pipes of the *Solterra 500* to allow for flow reversal in the collector. This means that the original return manifold can become the flow and the original flow manifold can become the return through correct valve manipulation, however the flow direction through the *Solterra 500* evaporator remains the same. Finally, a shell and tube heat exchanger was installed in series with the source return *run-out* from the ground before the fluid enters the heat pump. This was done to allow solar panels on the roof of the IiBC to provide a solar energy boost to the heat pump in winter and also to allow storage of excess heat underground in summer using the horizontal collector for heat rejection.

Only the flow reversal option was used for testing during this *HP-IRL/H* project. However, the other modifications offer an interesting potential to expand this facility to a hybrid *SOL-$GSHP_{HC}$* system in the future.

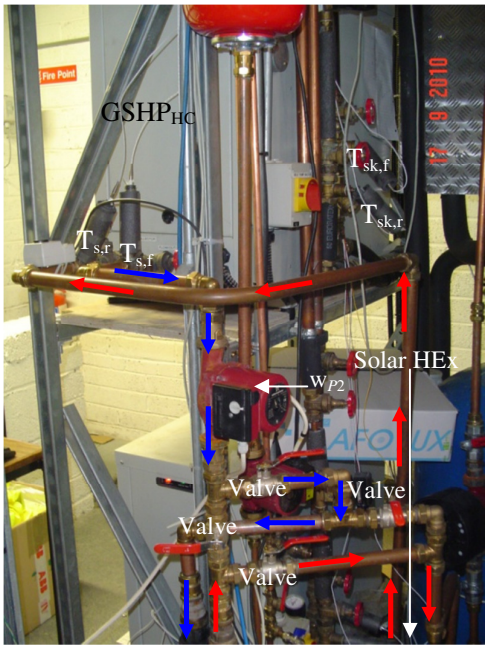

Figure 3-11: Modifications to $GSHP_{HC}$ flow and return to allow 'flow reversal' in the collector pipes and potential SOL-$GSHP_{HC}$ hybrid

3.4 $GSHP_{HC}$ TESTING

While *Arsenal Research* produced accurate performance data on the *Solterra 500*, the *HP-IRL/H* study focused on measuring the holistic $GSHP_{HC}$ system performance while operating in an actual application. This 'actual application' included supplying heat to an occupied building over a number of heating seasons while extracting heat from a typical ground source. Additionally, the resulting *HP-IRL/H* system data was required to develop and validate numerical models of the $GSHP_{HC}$ and collector area. The idealised schematic, displayed in Figure 3-12, is used to represent the combined *experimental-numerical analysis domain*.

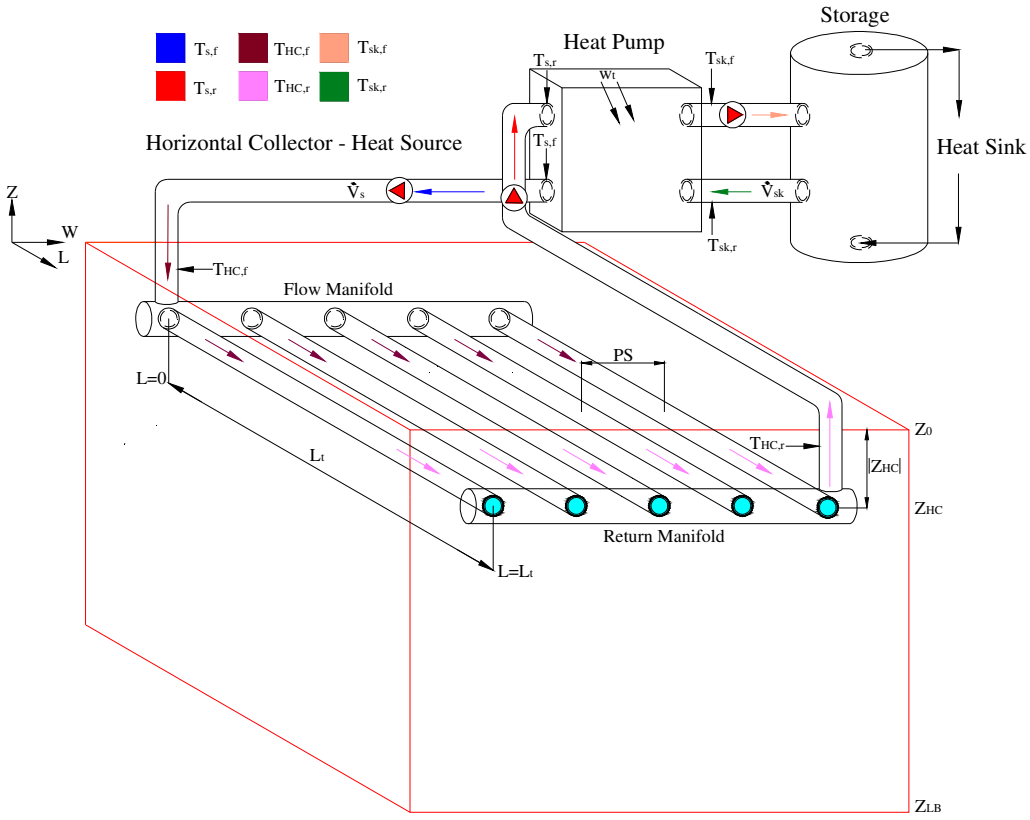

Figure 3-12: Idealised schematic of $GSHP_{HC}$ representing the experimental-numerical analysis domain with approximate locations of measurement sensors also included

For these reasons, along with those outlined in Chapter 2 and Section 3.1, the sensors listed in Table 3-7 were installed to measure the variables needed to quantify $GSHP_{HC}$ capacity (q_{sk}) [kW_{th}], extraction from the source (q_s) [kW_{th}] and COP [-]. The variables measured and approximate locations of the sensors are depicted in Figure 3-12. Data from these 9 sensors was recorded at one minute intervals between 2007 and 2010.

Table 3-7: Sensors used to monitor the performance of $GSHP_{HC}$

No.	Variable	Instrument	Model #	Units	Factory accuracy
1.	$T_{s,f}$	Omega PT100 Class B 1/10 DIN	PR-11-3-100	ºC	±0.03ºC @ 0ºC
2.	$T_{s,r}$	Omega PT100 Class B 1/10 DIN	PR-11-3-100	ºC	±0.03ºC @ 0ºC
3.	$T_{HC,f}$	Omega PT100A	P-M-A-6-100	ºC	±0.3ºC @ 0ºC
4.	$T_{HC,r}$	Omega PT100A	P-M-A-6-100	ºC	±0.3ºC @ 0ºC
5.	$T_{sk,f}$	Omega PT100 Class B 1/10 DIN	PR-11-3-100	ºC	±0.03ºC @ 0ºC
6.	$T_{sk,r}$	Omega PT100 Class B 1/10 DIN	PR-11-3-100	ºC	±0.03ºC @ 0ºC
7a.	$\dot{V}_s$	Burkett Paddle Wheel Flow Meter	8030 HT	l/min	±2% @ 1m/s
7b.	$\dot{V}_s$	Endress + Hauser Prosonic	93UA1	l/min	Calibration
8a.	$\dot{V}_{sk}$	Burkett Paddle Wheel Flow Meter	8030 HT	l/min	±2% @ 1m/s
8b.	$\dot{V}_{sk}$	Endress + Hauser Prosonic	93UA1	l/min	Calibration
9.	w_t	Vydas Power Meter	UPC	W	±0.5%

The most accurate temperature sensors afforded to *HP-IRL/H* were used to measure the temperature difference (ΔT) [K] across the heat source/evaporator ($T_{s,r} - T_{s,f}$) and the heat sink/condenser ($T_{sk,f} - T_{sk,r}$). These are the *Omega PT100 Class B 1/10 DIN* RTD sensors with an accuracy of ±(1/10)*(0.3+0.005T)ºC thereby allowing the temperature difference to be measured with an accuracy of ±2*(1/10)*(0.3+0.005T)ºC. These sensors were calibrated with the on-site DAQ system using a *Jofra (D55SE)* temperature calibrator and a deionised ice-water slurry test and details of these tests are presented in Appendix D.

In order to determine q_s or q_{sk} using Equation 3-1, the volumetric flow rate ($\dot{V}$) [m^3/s] in the source and sink circuits is required. These flow rates were measured in l/min using the *Burkett* paddle wheel flow meter *8030T* with an accuracy of ±2% @ 1m/s. Since the flow rate and temperature difference are multiplied in Equation 3-1, the accuracy of the result is sensitive to flow rate error. For this reason a second assessment of flow rate was performed using an *Endress+Hauser Prosonic* ultrasonic flow meter. This flow meter was calibrated on-site for use with copper piping and details of the ultrasonic flow meter and the calibration are given in Appendix E.

$$q = \rho c_p \dot{V} \Delta T \tag{3-1}$$

As discussed in Sub-section 3.3.2 and as shown in Figure 3-10 and Figure 3-12, two 30m long, 63mm *run-out* pipes are used to connect the heat pump to the flow and return manifolds. These pipes are installed in ducts in the building and ducts leading to, but not forming part of, the collector. While these pipes have 10mm of thermal insulation, they still have the potential to influence the amount of heat supplied to the heat pump. Accordingly, the fluid temperature is also measured at the flow and return manifolds using *Omega PT100A* RTD sensors with a

rated accuracy of ±0.3ºC. The calibration of these sensors with the DAQ is also presented in Appendix D. All temperature sensors used to measure fluid temperatures in pipes are installed using *binder points* and the protruding parts of the sensor are insulated for thermal stability, as shown in Figure 3-13.

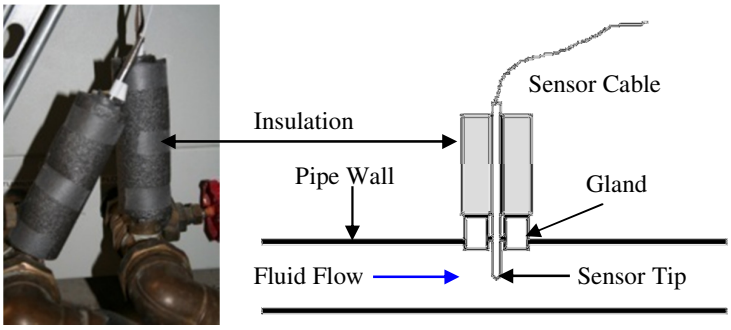

Figure 3-13: Temperature sensor installation procedure for pipes

A *Vydas* power meter, with an accuracy of ±0.5%, was installed to measure the total power supplied (w_t) [W] including: the compressor (w_c), the two pumps used to circulate fluid in the source (w_{P1} & w_{P2}), one sink pump (w_{P3}) and the standby power (w_{stb}).

Operating Principle and Experimental Monitoring Procedure

Power is supplied to the $GSHP_{HC}$ system by means of an isolator switch. The $GSHP_{HC}$ system can then be 'called' either by manually switching the system to 'hand' or automatically by the *BMS* according to a predefined schedule, provided the system has previously been switched to 'auto'.

At this point the $GSHP_{HC}$ source side (No. 1 and 2) and sink side (No. 3) circulating pumps are powered up and provided 'collector flow' is detected by the *Solterra 500* then power is supplied to the compressor after a user-defined time delay. The heat pump now operates on the *vapour-compression cycle* extracting heat from the source, upgrading this heat through consumption of electrical power in the compressor and delivering heat to the sink.

The $GSHP_{HC}$ has a user-defined, sink-side, temperature set-point (for example 35 to 50ºC) and when the sink flow temperature reaches this value the compressor shuts down while the circulation pumps remain on. The compressor will remain off for a user-defined 'off-cycle time' and then comes back on continuing the *vapour-compression cycle* until the set-point is again reached. The heat pump delivers heat to a storage tank and from this a separate circuit, the *heat distribution system*, delivers heat to the building, as shown in Figure 3-12.

The *heat distribution system* can also be 'called' either by manually switching the system to 'hand' or automatically by the *BMS* according to a predefined schedule, provided the system has previously been switched to 'auto'. The heat distribution system is divided into two zones, the East and West Zone, as shown in Figure 3-6. The piping to both zones is fitted with three-port-valves, labelled 'mixing valve' in Figure 3-6, controlled by thermostats within the East and West zones of the IiBC building. These three-port-valves operate on a sliding scale controlled by the East and West zone room temperatures. When the East and West zones reach a user-defined set-point, the *thermal comfort level*, these three-port-valves will close until heat loss from the building results in the temperature dropping below the set-point.

Therefore, the operation of the $GSHP_{HC}$ – *IiBC* heating system, from the ground-heat gained in the collector pipes through to the heat loss from the building fabric, is interdependent. During this process referred to as $GSHP_{HC}$ *operation* data is recorded at 1 minute intervals and archived. A sample of this data recorded during the 11th of November 2007 is shown in Figure 3-14. During this period the $GSHP_{HC}$ operated as follows:

- Power is supplied to the system at all times, standby power of 0.05kW is drawn
- Stagnant fluid surrounding sensors for $T_{s,f}$, $T_{s,r}$, $T_{sk,f}$ and $T_{sk,r}$ is initially [00:00 to 06:00] in thermal equilibrium with the 'plant room' which houses the *Solterra 500*
- The system in auto mode was 'called' by the BMS schedule from 06:00 to 20:00
- From 06:00 the source and sink circulation pumps are powered up bringing the fluid flowing past sensors for $T_{s,f}$ and $T_{s,r}$ along with $T_{sk,f}$ and $T_{sk,r}$ into thermal equilibrium with the ground and the storage tank, respectively
- At 06:10 the compressor is powered up and the evaporator and condenser develop a temperature difference across the source and the sink respectively
- From 06:10 until 07:40 the source is cooled and the sink is heated until the sink 'set-point' of 50ºC is achieved and the system then begins *cyclic operation* until 20:00
- Heat is extracted at a rate of 13kW and the heat pump is operational for approximately 50% of the time, this equates to an equivalent extraction rate of 6.5kW

Data was automatically archived in the one-minute format and data was also archived by the research team in an hourly averaged format. The *HP-IRL/H* COP is defined using Equation 3-2, where power consumed by the compressor (w_c), source-side pumps (w_{P1} +w_{P2}) and standby power (w_{stb}) are included. Error in COP calculation of ±4% is discussed in Appendix F.

$$COP_{heat} = [q_{sk}/(w_c + w_{P1} + w_{P2} + w_{stb})] \pm 4\% \quad (3\text{-}2)$$

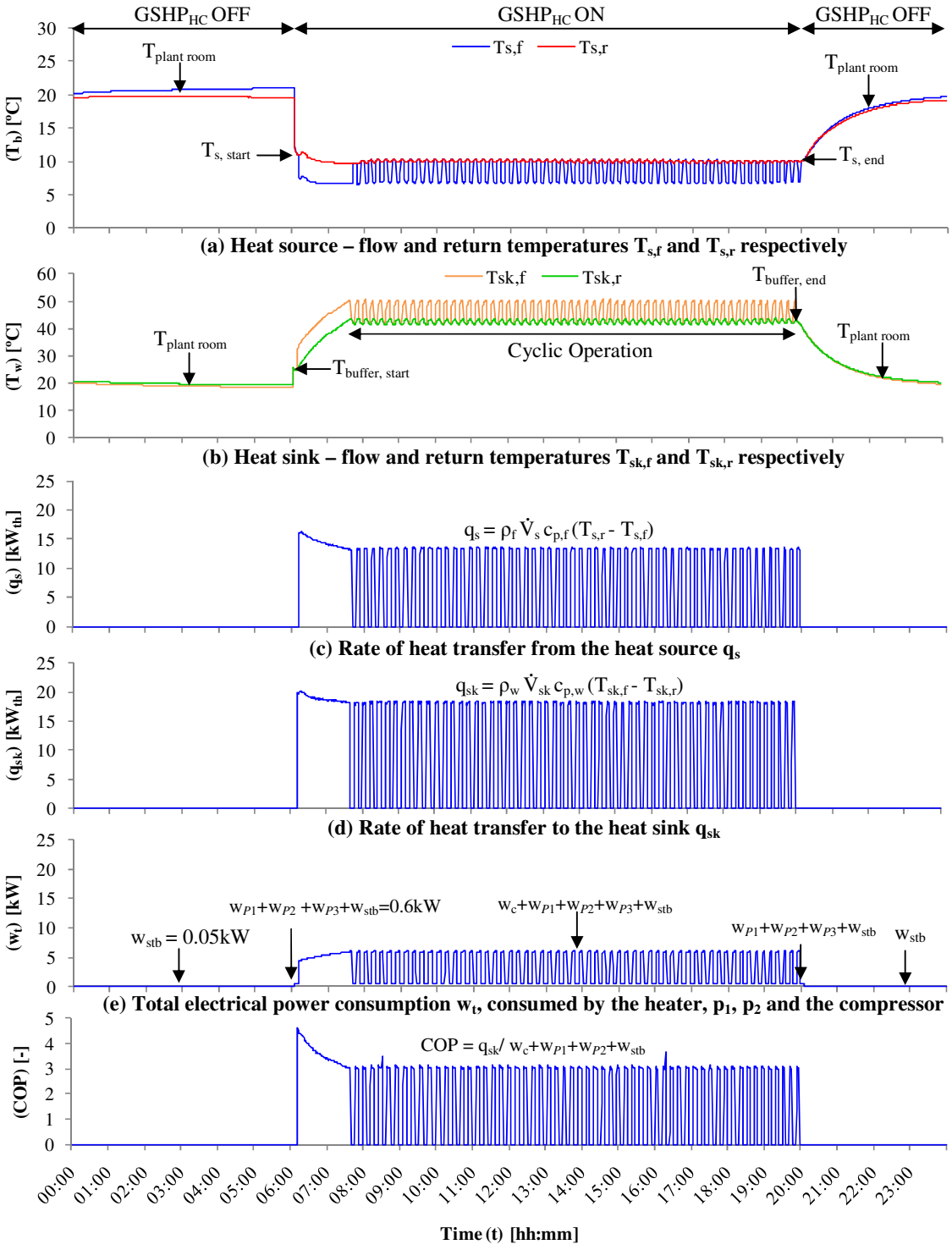

(a) Heat source – flow and return temperatures $T_{s,f}$ and $T_{s,r}$ respectively

(b) Heat sink – flow and return temperatures $T_{sk,f}$ and $T_{sk,r}$ respectively

(c) Rate of heat transfer from the heat source q_s

(d) Rate of heat transfer to the heat sink q_{sk}

(e) Total electrical power consumption w_t, consumed by the heater, p_1, p_2 and the compressor

(f) GSHP$_{HC}$ system COP including total source-side power consumption w_t

Figure 3-14: Overview of GSHP$_{HC}$ operation using data from 11/11/2007 at a 1-minute resolution

3.5 GROUND ENERGY MONITORING

Since $GSHP_{HC}$ COP is inversely proportional to the temperature lift, fluctuations in the source temperature generate COP fluctuations. For this reason, the temperature distribution in the ground surrounding the collector was of interest. Based on the literature review presented in Section 3.1 and the knowledge deficits outlined in Chapter 2, the influence of the following parameters on ground temperature were studied:

- Seasonal cycles, diurnal cycles and weather
- $GSHP_{HC}$ operation and duty cycles
- Ground surface cover, thermal properties and moisture content
- Collector pipe depth, length and spacing

In order to monitor the influence of these parameters, measurement sensors were distributed throughout the 9 vertical test profiles shown in Figure 3-15. Each test profile is identified by a Profile reference number (P#). These test profiles consisted of temperature, moisture content and heat flux sensors buried in a vertical orientation beneath the surface extending to a maximum depth of 1.8m.

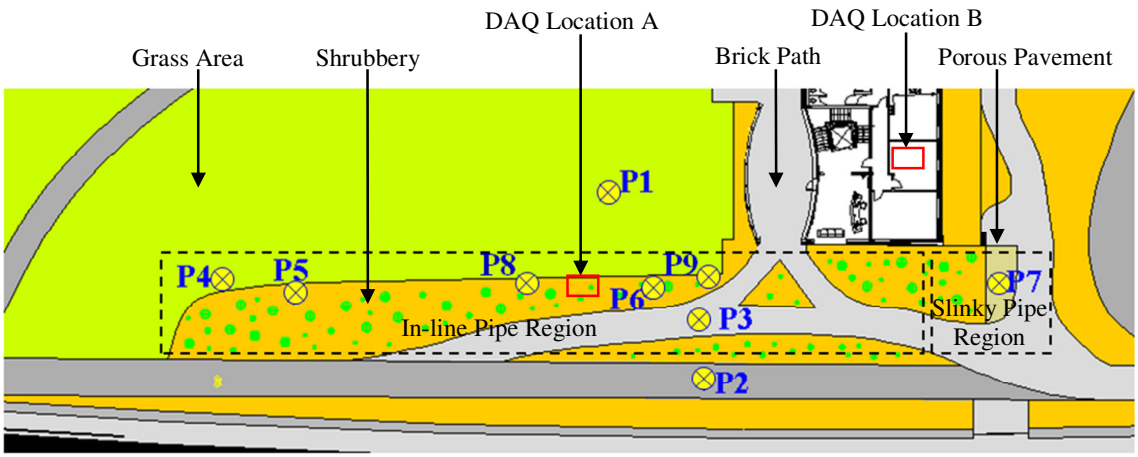

Figure 3-15: Schematic plan view of the collector area, showing both surface covers and locations of the nine experimental vertical profiles (P1 – P9)

3.5.1 Experimental Profile Positions

The positioning of these vertical profiles satisfied a number of criteria. Firstly, since the profiles were installed after the collector was buried and the surface landscaped, the profiles were placed in areas where access to the collector was possible and also where sensors cables could be routed safely to DAQ Location A as shown in Figure 3-15. Location A consists of two IP-rated stainless-steel control cabinets which were positioned within a custom made

stainless steel enclosure. The second criterion for choosing each profile position was driven by the scientific goals of the project. Profile positions were selected based on ground surface covering, distance along the collector pipe length (L), pipe spacing (PS) and in-line or slinky layout for example. Figures 3-10 and 3-15 display an aerial photograph and a plan view of the collector area with the positions of the test profiles P1 to P9 along with the DAQ Location A, relative to the surface covers and the collector beneath.

The first profile (P1), a reference profile, is located outside the collector area and at a sufficient distance not to be influenced by the collector. This profile was used to measure the undisturbed ground temperature distribution and characterise the influence of weather on the grounds thermal energy content outside the collector. The temperature distribution in P1 can also be compared with the other profiles within the collector area such as P5 to assess the level of 'thermal drawdown' caused by the collector during $GSHP_{HC}$ operation. A second reference profile (P2) was designed to measure the undisturbed temperature distribution under black asphalt, however due to problems installing sensors in the compacted gravel, P2 was decommissioned.

The remaining profiles P3 to P9 were installed at positions of interest within the collector area. Details of each experimental profile (P1 to P9) including the ground cover present, details of the collector pipes at that position and the number and type of sensors buried are summarised in Table 3-8. Temperature, moisture content and heat flux sensors are labelled T, M and H respectively and photographs of the ground cover types are displayed in Figure 3-16. A cross sectional view of experimental profiles P1, P3 and P4 are presented in Figure 3-17; P5, P6 and P7 are presented in Figure 3-18; P8 is displayed in Figures 3-19 and 3-20; and P9 is displayed in Figure 3-21.

Table 3-8: Details of experimental test profiles P1 through P9, shown in Figures 3-10 and 3-15

Ref. #	Description	Cover	L(m)	Z_{HC}(m)	PS(m)	D_{coil} (m)	T	M	H
P1	Reference Profile	Grass	N/A	N/A	N/A	N/A	8	3	0
P2	Decommissioned	Asphalt	-	-	-	-	-	-	-
P3	Gravel Profile	Brick	43	1.15	0.4	N/A	5	2	0
P4	Loop Profile	Grass	90	1.045	0.25	N/A	4	1	0
P5	Constriction	Shrubs	100	1.015	0.25	N/A	8	2	0
P6	In-line Return	Shrubs	138	1.2	0.4	N/A	7	0	0
P7	Slinky	Porous Paving	-	0.86	N/A	0.5	8	2	0
P8	Intensive	Shrub & Grass	125	1.1	0.25/0.75	N/A	14	12	8
P9	Heat Flux	Grass	145	1.35	0.25	N/A	2	0	2

(a) Grass (b) Brick (c) Porous Pavement (d) Wood Chip (e) Shrubs

Figure 3-16: Horizontal collector surface cover types

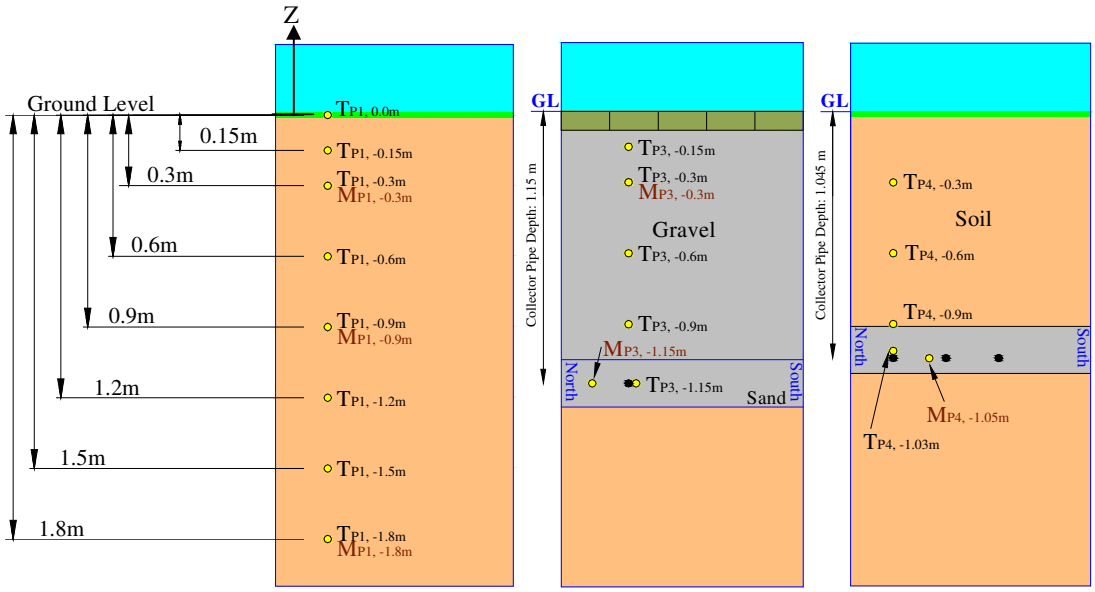

(a) P1 – Grass (b) P3 – Brick (c) P4 – Grass

Figure 3-17: Cross sectional views of profiles P1 – P3, the collector is represented by a black dot

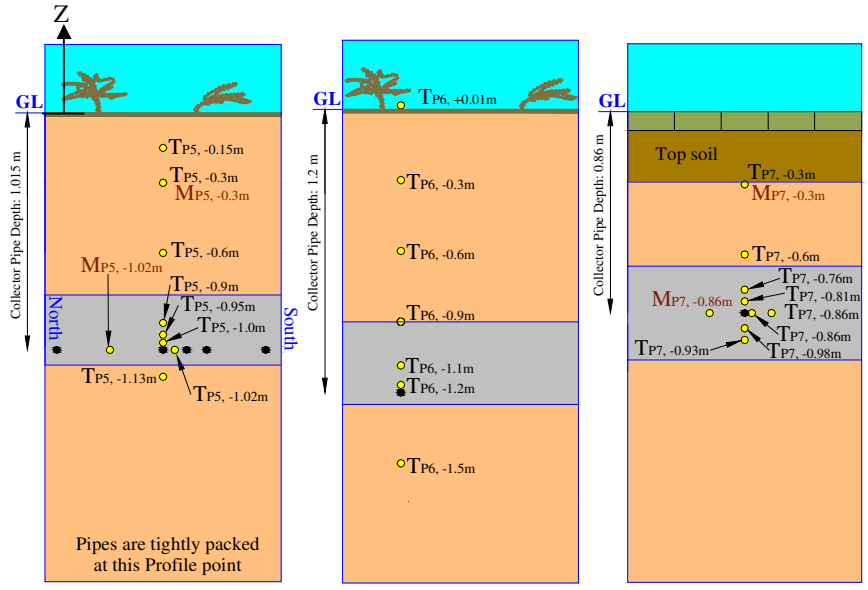

(a) P5 – Shrubs/Chips (b) P6 – Shrubs/Chips (c) P7 – Porous Pavement

Figure 3-18: Cross sectional views of profiles P5 – P7, the collector is represented by a black dot

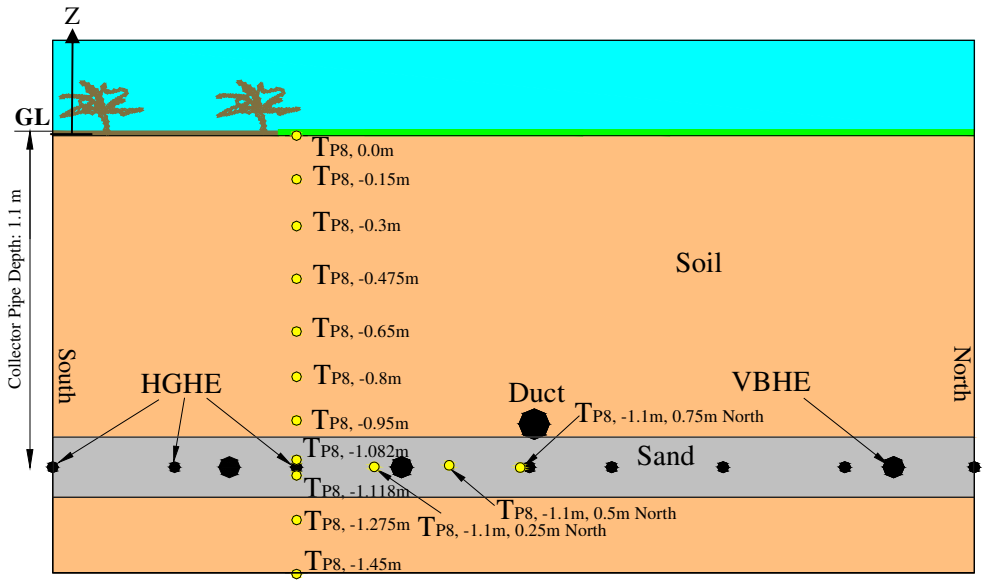

Figure 3-19: P8 intensive temperature profile under shrubs/chips and grass boarder

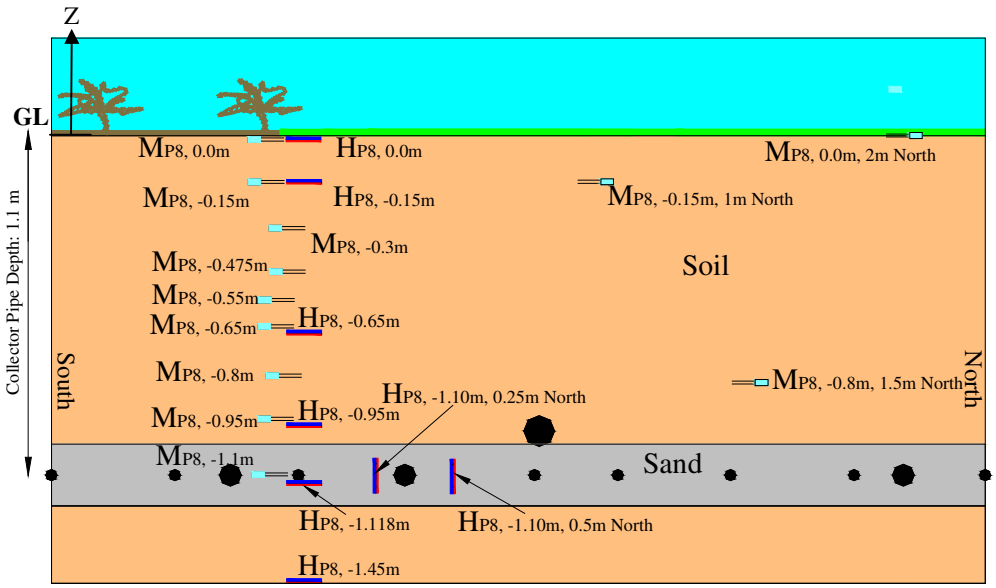

Figure 3-20: P8 intensive heat flux and moisture profile under shrub/chips and grass boarder

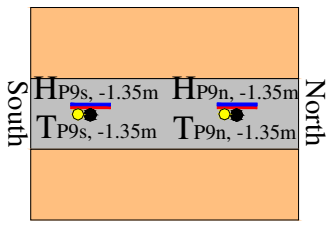

Figure 3-21: P9 heat flux and temperature sensors at the end (L=145m) or start (L=5m) of the collector pipes depending on the collector flow direction

3.5.2 Sensor Details

The sensor type and accuracies used in P1 to P9 are summarised in Table 3-9.

Table 3-9: Details of sensors buried in experimental profiles P1 to P9

Ground Variable	Sensor	Model #	Accuracy
Temperature (P1 to P7)	Sontay 4-Wire PT100 Class A	TT555/PT100A/S	±0.3ºC
Moisture Content (P1 to P7)	Campbell Scientific TDR	CS625	±2.5%
Temperature (P8 & P9)	Sontay 3-Wire PT100 Class A	TT555/E/30m/R	±0.3ºC
Moisture Content (P8 & P9)	Campbell Scientific TDR	CS616-L	±2.5%
Heat Flux (P8 & P9)	Hukseflux	HFP01	-

Details of the moisture content and heat flux sensor calibrations carried out on site are given in Appendix G. The *HFP01* heat flux sensors measure both heat flux direction and magnitude. All *HFP01* sensors are pointed in the same direction with the blue side facing upwards for vertically aligned sensors and the blue side facing south for horizontally aligned sensors, as shown in Figures 3-20 and 3-21.

3.5.3 Sensor Installation

P1 to P7 were installed in late 2006 and early 2007, while P8 and P9 were installed in September 2009. Installation of sensors in all nine profiles involved removal of the surface cover plus manual excavation of the ground beneath to avoid damaging the collector. Sensors were then installed to collector depth and below, as shown in Figures 3-22 and 3-23, with the sensor positions and the corresponding cables labelled and catalogued.

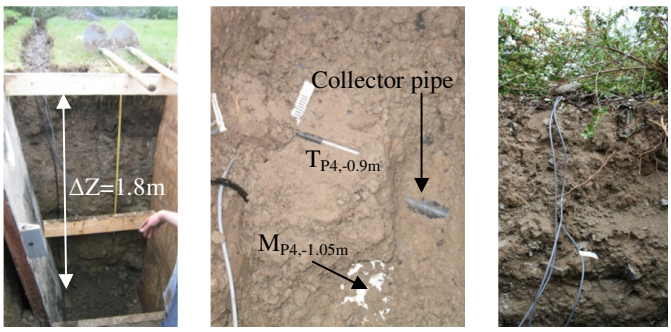

(a) P1 – 1.8m view (b) P4 – collector pipe (c) P6 – sub-surface

Figure 3-22: Manual excavations undertaken between August 2006 and March 2007 to facilitate sensor installation in P1 through P7

Numerous soil samples were taken during the excavation process for the purposes of soil analysis as shown in Figure 3-23(c). Soil was then replaced with effort made to preserve the original layering, compaction and consolidation levels.

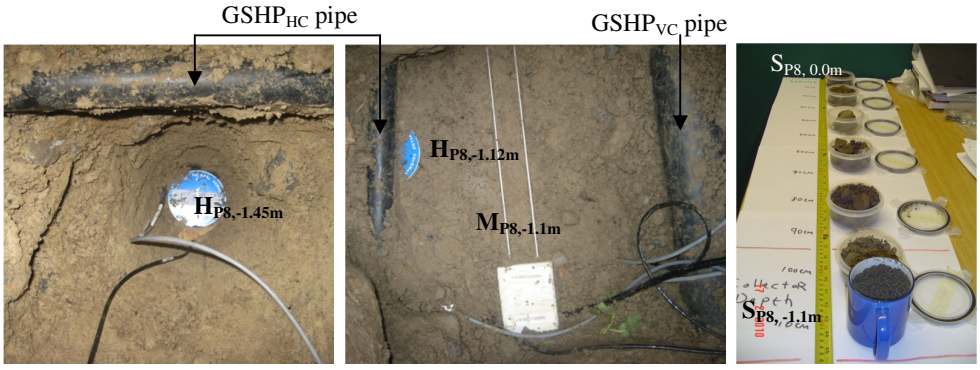

(a) P8 – Below the pipe **(b) P8 – Pipe level** **(c) P8 – Soil samples**

Figure 3-23: Sensor installation and soil sampling at P8 and P9 during September 2009

3.6 WEATHER STATION

One aspect of the *HP-IRL/H* test facility which differentiates it from the other facilities listed in Table 3-1 is the presence of an accurate, onsite weather station. This is located on the 3rd floor roof of the IiBC and pictured in Figure 3-24. Details of the weather station sensor types and accuracies are presented in Table 3-10. Calibration certificates and on-site calibration of weather station components are presented in Appendix H.

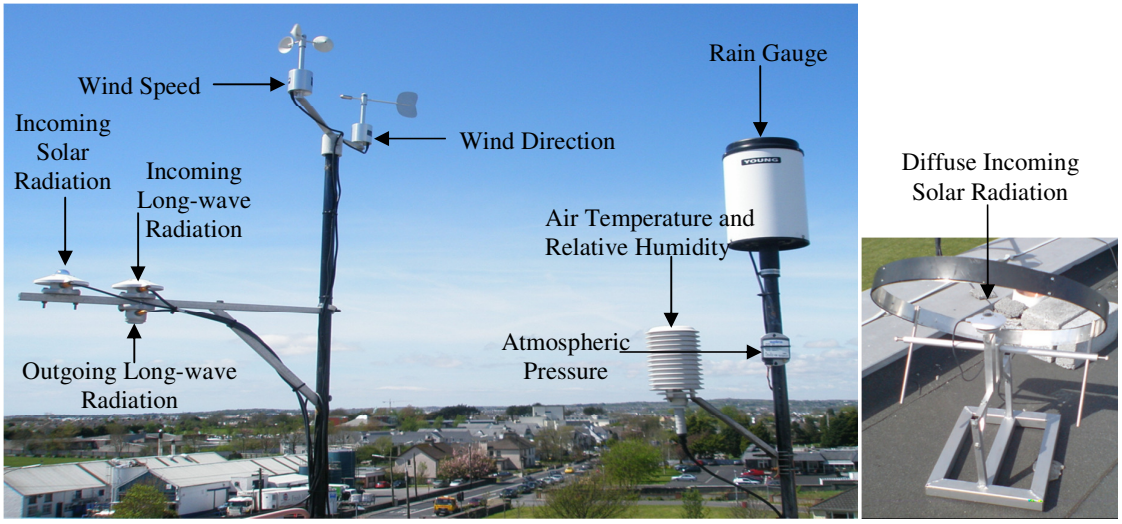

(a) Elevated weather station components on IiBC rooftop **(b) CMP3 with shadow ring**

Figure 3-24: The CiSET weather station located on the 3rd floor roof of the IiBC

Table 3-10: Details of the on-site weather station used for HP-IRL/H and other CiSET research

No.	Climate Variable	Instrument	Model	Units	Accuracy
1	Total Solar Radiation ($q"_{S,t}$)	Kipp & Zonen Pyranometer	CMP3	[W/m^2]	±10% Daily Total
2	Diffuse Radiation ($q"_{S,D}$)	Kipp & Zonen Pyranometer	CMP3	[W/m^2]	±10% Daily Total
2a	Reflected Radiation ($q"_{S,R}$)	Kipp & Zonen Pyranometer	CMP3*	[W/m^2]	±10% Daily Total
3	Incoming Long Wave ($q"_{LWI}$)	Kipp & Zonen Pyrgeometer	CGR3	[W/m^2]	±10% Daily Total
4	Outgoing Long Wave ($q"_{LWO}$)	Kipp & Zonen Pyrgeometer	CGR3	[W/m^2]	±10% Daily Total
5	Air Temperature (T_a)	Vaisala Temperature Probe	HMP45C	[ºC]	±0.35ºC @ 0ºC
6	Relative Humidity (RH)	Vaisala Humidity Probe	HMP45C	[%]	±2.5% @ 10-100%
7	Air Pressure (P_a)	Setra Barometric Sensor	278	[hPa]	±0.5hPa @ 20ºC
8	Wind Speed (u_{wind})	Vector Ins. Anemometer	A100L2	[m/s]	±0.3m/s
9	Wind Direction (λ_{wind})	Vector Ins. Potentiometer	W200P	[º]	±0.3º
10	Precipitation Levels (Z_{prec})	RM Young Tipping Bucket	52202	[mm]	±2% up to 25mm/hr
11	Precipitation Temperature (T_{prec})	Custom Device	-	[ºC]	±0.35ºC @ 0ºC

* The CMP3 sensor used to measure parameter No. 2 has also been used to measure parameters No. 2a on occasion

3.7 DATA ACQUISITION

To produce an accurate and consistent stream of data, all the sensors described in Tables 3-7, 3-9 and 3-10 were connected to a DAQ system for high resolution and automated data-logging. While the entire DAQ system for all C*i*SET research including *HP-IRL/H* was commissioned as part of a separate project (Clarke, 2009), a brief description is given in this section.

3.7.1 DAQ Locations

Since the DAQ caters for 130 sensors in a variety of locations, the two central DAQ locations, shown in Figure 3-15, were established as follows:

- Location A consists of two IP-rated stainless steel enclosures, A_1 and A_2, situated within the collector area
- Location B is on the wall of the IiBC 3rd floor plant room

All sensor cables were routed to the nearest location where a compatible DAQ module was positioned. Table 3-11 summarises the distribution of sensors attached to the *HP-IRL/H* DAQ system and the corresponding DAQ location. Since the DAQ caters for a variety of sensor outputs, three custom DAQ hardware stations were created at DAQ locations A_1, A_2 and B. All three DAQ stations were connected via *Category 5* network cables and *Linksys* network switches to a *Dell Optiplex Gx280* PC with a *Pentium IV* processor (2.8GHz). This PC was connected to GMIT's network to facilitate communication between local PC's and the three DAQ stations. The PC was powered by an Un-Interruptible Power Supply (UPS) to prevent power surges and/or power loss.

Table 3-11: Distribution of sensors attached to the HP-IRL/H data acquisition system

No.	System Component	Details of Measurement	Sensors	Location
1.	*IiBC* central heating	East & west – flow & return temperature	4	B
2.	*IiBC* room temperatures	East & west – room temperature	2	B
3.	$GSHP_{HC}$ heating system	Source & sink – flow & return temperature, flow rates and power	7	B
4.	$GSHP_{HC}$ collector	Horizontal collector – flow & return temperatures	2	A_1
5.	$GSHP_{HC}$ collector area	Ground – temperature(72), moisture(22) and heat flux(10)	104	A_1 & A_2
6.	*CiSET* weather station	Climate – variables	11	B
		Total:	130	

3.7.2 Locations A_1 and B

The DAQ stations at A_1 and B utilise *National Instruments* (NI) *Field Point* (FP) modules, the FP hardware at location B is pictured in Figure 3-25, a list of all the FP hardware used at location A_1 and B is presented in Table 3-12.

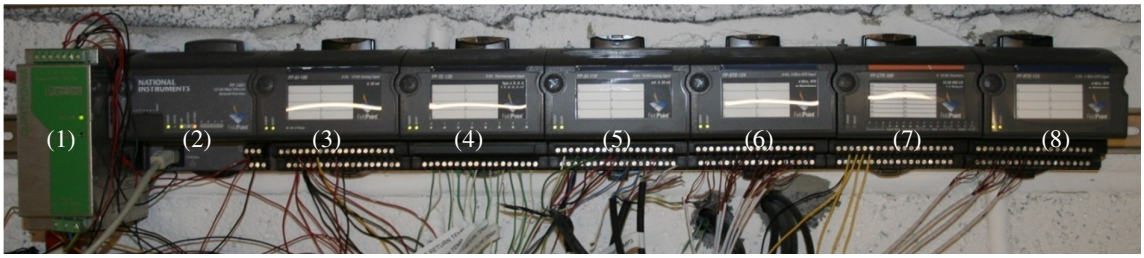

(1) PS4 (2) FP-1601 (3) FP-AI-100 (4) FP-TC-120 (5) FP-AI-100 (6) FP-RTD-124 (7) FP-CTR-500 (8) FP-RTD-124

Figure 3-25: National Instruments FP data acquisition at DAQ location B in the IiBC plant room (Figure 3-15)

An NI power supply (PS4) was used as part of the DAQ hardware to supply 24V to the modules. The power supply was run via an UPS to prevent power loss or surges. The FP-1601 control modules were assigned an IP address by GMIT's network administrator to allow communication with the modules. The setup of the FP modules was carried out through Measurement and Automation eXplorer (MAX) software. The FP modules are connected to the network and appear in the MAX software when updated. The modules can be configured to the user's requirements, with appropriate name, measurement range and scanning intervals.

Table 3-12: National Instruments Field Point modules installed for *HP-IRL/H* at locations A_1 and B

No.	Module/Item	Quantity	Function	DAQ Location
1	FP-AI-100	1	Voltage and current analogue input module	B
2	FP-AI-110	1	Voltage and current analogue input module	B
3	FP-RTD-124	2	4 wire RTD input module	B
4	FP-RTD-124	7	4 wire RTD input module	A_1
5	FP-RTD-122	2	2 &3 wire RTD input module	A_1
6	FP-CTR-500	1	Counter input module	B
7	FP-TC-120	1	Thermocouple input module	A_1
8	FP-1601	2	Network control module	A_1 & B
9	PS4	2	24V power supply to FP modules	A_1 & B
10	FP-TB-1	16	Terminal base (32 points)	A_1 & B
11	FP-TB-3	1	Terminal base (16 points)	B

3.7.3 LabVIEW

The National Instruments DAQ system was controlled and monitored using *LabVIEW 8.20*, running on the *Dell Optiplex Gx280* PC. A total of 18 *LabVIEW* Virtual Instruments (VIs) and 42 sub-VIs were created to construct and operate the *HP-IRL* DAQ system. These VIs were used to program and display the sensor outputs via the Field Point modules.

A *LabVIEW* VI comprises of a front panel and a block wiring diagram display panel. The block diagram is used for the setup and virtual wiring of each VIs configuration which allows the programming of each Field Point module, sensor logging intervals and signal manipulation. The front panel is used as the display screen for the live data. All live data is also archived with time-stamps (dd/mm/yyyy hh:mm:ss) and stored in Comma Separated Value (CSV) files.

3.7.4 Location A_2

The DAQ station at A_2 utilises *Campbell Scientific CR1000* to cater for the heat flux (*HFP01*) and moisture (*CS625* and *CS616-L*) sensors. Table 3-13 contains the details of the *Campbell Scientific* DAQ station at location A_2 pictured in Figure 3-26. The *CR1000* uses the *Loggernet* software created by *Campbell Scientific*. The setup of the hardware was performed using the *EZSetup* tool and data is collected using the *Connect* tool which communicates with the *CR1000*.

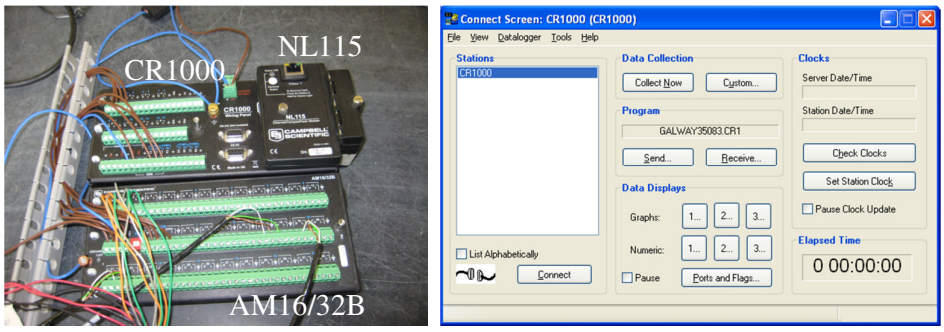

(a) CR1000, AM16/32B and NL115 **(b) Loggernet software Connect tool**

Figure 3-26: Campbell Scientific data acquisition of ground moisture and heat flux sensors at location A_2

Table 3-13: Campbell Scientific hardware installed for *HP-IRL/H*

No.	Item	Quantity	Function	Location
1	CR1000	1	Measurement and control module	A_2
2	AM16/32B	1	16/32 Channel relay multiplexer (MUX)	A_2
3	NL115	1	Ethernet interface and compact flash	A_2

3.7.5 Archiving

Measurements from all 130 sensors in Table 3-11 are recorded at specified intervals, time-stamped and stored in CSV files, such as the 'Air temperature' file shown in Figure 3-27(a). From the data in these CSV files, hourly, daily, weekly, monthly and annual averages are extracted and archived to *MS-Excel* spreadsheets in related groups such as 'weather', 'ground temperatures' and 'heat pump measurements'.

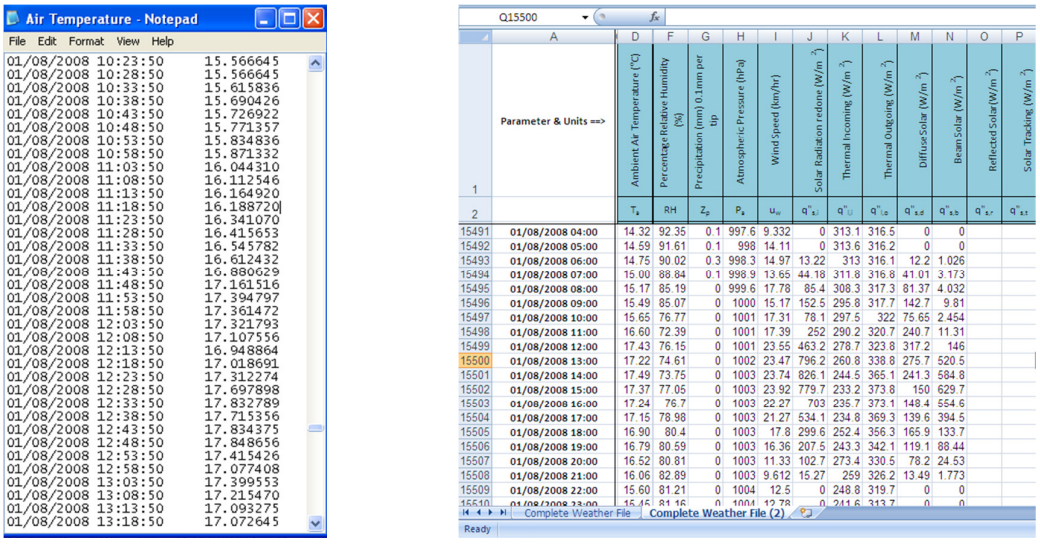

(a) Air temperature data from Labview **(b) Hourly data from 10 weather station sensors**

Figure 3-27: Archiving of time-stamped data followed by averaging/summing and saving for analysis

It was important that all averaging was consistent so that average measurements from a variety of sensors can be compared accurately in a time-series and also so that data simulated using measured boundary conditions can be compared with observed results in a time-series. Several options were available for averaging such as a backward-average (value for 12:00 includes 11:01, 11:02....12:00), a central-average (value for 12:00 includes 11:31, 11:32...12:30) and a forward-average (value for 12:00 includes 12:00, 12:01.....12:59). The latter forward-averaging method was used at all times in the *HP-IRL/H* study.

3.8 INTRODUCTION TO NUMERICAL METHODS

In addition to the experimental study described in this chapter, a complimentary numerical study was pursued. The following were the objectives of the numerical study:

- Develop and validate an accurate replica of the *HP-IRL/H* collector and heat pump system using a numerical simulation tool
  - Building confidence in the numerical simulation method
  - While also increasing confidence in the scope, resolution and accuracy of the experimental facility
- This tool can then be used to simulate new collector designs and novel feedback control strategies emanating from the *HP-IRL/H* project

For numerical simulation of a $GSHP_{HC}$ system the following four options were reviewed:

- Use of a commercial, Finite Element Method (FEM) software, such as ANSYS (ANSYS Inc., USA), to create a model of the collector ground volume
  - ANSYS is an excellent tool for creating both transient and steady-state simulations and is particularly useful for working with complex geometries
  - However, ANSYS is not intended for use in holistic SET simulations such as the $GSHP_{HC}$ – *IiBC* system
  - ANSYS is not intended for simulating responsive control of energy systems
  - The spatial and temporal changes in source fluid temperature (T_F (L,t)) as it warms in the ground pipes and cools the surrounding ground does not correspond to any of the typical ANSYS heat transfer load-conditions
  - Inclusion of the transient weather conditions in an ANSYS model is possible but not straight forward and not common practice in ANSYS simulations

- The dimensions of the $GSHP_{HC}$ system (5 x 0.5 x 150m) can be catered for in ANSYS but will result in a large number of Degrees of Freedom and this will lead to significant solution time

- Use of a commercial, component-based SET software, such as TRNSYS (TESS-Inc., USA), to create a holistic model of the collector, the heat pump and the building
  - Unlike ANSYS, TRNSYS is developed specifically for use in holistic SET simulations, such as the $GSHP_{HC}$ – *IiBC* system, by coupling individual 'off the shelf' component models of the collector, the heat pump and the building
  - However, the TRNSYS component model for the ground collector is based on a single isolated pipe in an infinite medium and this is not compatible with the *HP-IRL/H parallel, inline* collector which is sensitive to the surface conditions
- Use of a commercial design software for $GSHP_{HC}$, such as GLD2010 (Thermal Dynamics Inc., USA) or others listed in Table 2-12
  - These software are intended to be used by collector designers and installers
  - These software provide quickly simulated results on the long term thermal performance of a proposed collector size
  - However, they are not intended for academic analyses on collector design with feedback control such as the *HP-IRL/H thermo-environmental analysis* that includes diverse influences such as climate, coupled collector and heat pump performance transience, operational control desired within *CSDC*
- Develop a simulation method for $GSHP_{HC}$ as an objective of the *HP-IRL/H* project:
  - This approach has been pursued by Mei (1986) and Piechowski (1996) and recently by Esen *et al.* (2007) and Demir *et al.* (2009) but without the inclusion of coupled collector and heat pump performance transience and *collector temperature feedback control*
  - This presented a significant and time consuming research task which forms the core of Chapters 5, 6 and 7
  - However, creating specific models for *HP-IRL/H* allowed for custom/tailored simulation of the *Solterra 500* heat pump and the horizontal collector built by *Dunstar Ltd.* under the *Cool Marine* conditions of the Irish climate with high resolution
  - In addition, creating a custom model allowed for inclusion of new collector designs and crucially, elements of responsive control, which up to this point were not investigated in specific $GSHP_{HC}$ numerical studies

- This process of investigating existing methods and developing a simulation method for the *HP-IRL/H* project provided a huge learning experience and formed the basis of subsequent numerical research within the C*i*SET group

Based on assessment of the four options, a decision was made to create a customised yet generic $GSHP_{HC}$ simulation method. Due to the broad nature of a $GSHP_{HC}$ system, model development involved a range of multi-disciplinary analytical and numerical studies on elements of the climate, ground, collector and the heat pump before assembling validated component models for a system level analysis using the Finite Difference Method (FDM). Figure 3-28 extracts the *CSDC* elements of $GSHP_{HC}$ depicted in Figure 2-1 and describes both the primary numerical objective and approach within the red outline, surrounded by the secondary analytical outcomes and sub-models required within the blue outline.

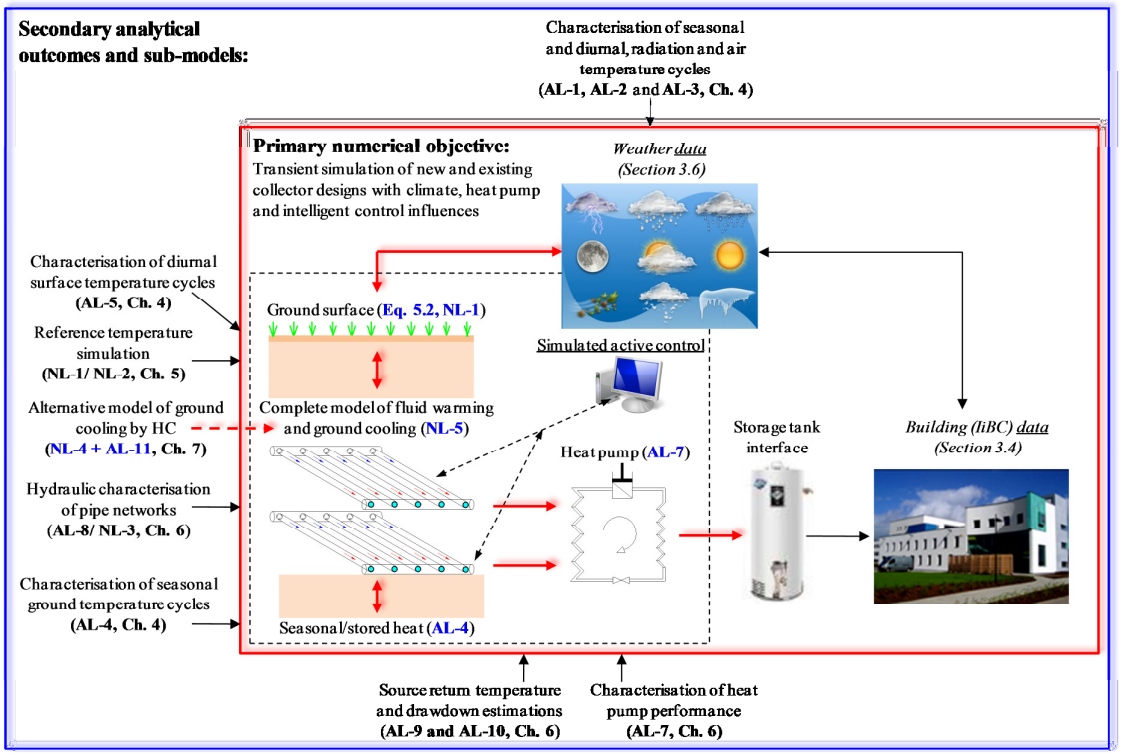

Figure 3-28: Overview of $GSHP_{HC}$ numerical study showing the primary numerical objective and approach within the red outline, surrounded by the secondary analytical outcomes and sub-models within the blue outline; analytical (AL-#) and numerical (NL-#) models are defined in Table 3-14

The models identified in Figure 3-28 and listed in Table 3-14, are of two distinct types defined as follows:

- Analytical equation groups (AL-#): a combination of basic formulae and/or empirical correlations with a specific purpose
    - These were used to investigate individual aspects of the climate, the ground, the collector and the heat pump in Chapters 4 through 6 as well as serving as sub-models in Chapter 7
- Numerical models (NL-#): step-wise simulations of transient processes, typically based in the FDM
    - These were used to simulate some or all of the $GSHP_{HC}$ system by *Dunstar Ltd.* in Chapter 7 and to test new collector designs and control in Chapter 8
    - A number of the analytical models (AL-#) were used as either sub-models or initial/boundary conditions within the step-wise numerical models (NL-#)

The choice of model depends on the objectives of the specific investigation. The development of each model in addition to its validation and trial investigations conducted are described in the subsequent chapters with details of sections and sub-sections listed in Table 3-14.

Table 3-14: Labels for analytical and numerical methods and the location of descriptions

Model No.	Description	Location
AL-1	Hourly clear-sky solar radiation intensity	Sub-section 4.2.1
AL-2	Multiyear average daily air temperature trend	Sub-section 4.2.2
AL-3	Multiyear average hourly air temperature trend	Sub-section 4.2.3
*AL-4	Multiyear average daily ground temperature variation with depth	Sub-section 4.2.4
*AL-5	Multiyear average hourly ground temperature variation with depth	Sub-section 4.2.5
AL-6	Influence of moisture content on thermal properties	Sub-section 5.3.4
*AL-7	Source and sink dependent heat pump component model	Sub-section 6.2.2
AL-8	Collector head loss curve, flow rate and pumping power	Sub-section 6.3.1
AL-9	Estimating source return temperature	Section 6.4
AL-10	Estimating steady-state thermal drawdown	Sub-section 6.5.1
*AL-11	Spatial and temporal variation in collector heat extraction rate	Section 6.6
*NL-1	One dimensional transient ground temperature simulation	Sub-section 5.4.1
NL-2	One dimensional transient ground temperature simulation with moisture and ice content (using *SHAW23* software)	Sub-section 5.4.2
NL-3	Collector head loss curve, flow rate and pumping power (using *Pipe Flow Expert* software)	Sub-section 6.3.1
NL-4	Two-dimensional GTD response to $GSHP_{HC}$	Section 7.2
NL-5	Underground fluid warming and three-dimensional ground cooling	Section 7.3

Note: * Identifies the models which are partially or entirely used as sub-models within the larger numerical models NL-4 and NL-5

The numerical study employed generic and easily implementable models for climate, heat pump and responsive control sensitivity. This allowed key dimensions of the collector to be changed including pipe spacing, length, depth, soil and surface types and most significantly

control strategies whereas many of the existing 'off the shelf' models did not allow such scope and flexibility. The analytical and numerical methods developed can be implemented in any equation-solving software from *MS-Excel* spreadsheets upward, to be used for further $GSHP_{HC}$ study, analysis and design.

Within C*i*SET, this numerical study is seen as a stepping-stone towards simulation of $GSHP_{HC}$ employing *split-level collectors* with responsive control. Limitations of these numerical methods are discussed in Sub-section 7.5.2 and potential improvements and upgrades are described in Section 9.3 as part of future work.

3.9 SUMMARY

This chapter has documented the following aspects of the *HP-IRL/H* project:

- A review was conducted of 13 $GSHP_{HC}$ experimental research facilities, constructed between 1979 and 2009, in 8 different countries, representing 7 different *climate classifications*
    - Of these studies, only one was located in a fully *Cool Marine* region and this study was conducted indoors in a laboratory eliminating the direct influence of climate
- The *IiBC*, a full-scale, functional building was used for an in depth experimental study of a $GSHP_{HC}$ system operating in an actual application and exposed to the local climate
- A commercially available $GSHP_{HC}$ system, the *Solterra 500* with a horizontal collector designed and built by *Dunstar Ltd.* in 2004, supplied over 70,000kWh_{th} of heat to the test building between 2007 and 2010
- 15 sensors were installed between 2005 and 2006 to measure the standard performance indicators of the *Solterra 500* heating system
- Over 100 sensors were installed in 9 vertical profiles (P1 to P9) between 2006 and 2009 to measure ground temperature, moisture content and heat flux
- 11 additional sensors were installed between 2005 and 2006 to measure climate variables impacting on the $GSHP_{HC}$ *– IiBC system*
- Two types of DAQ hardware located in two DAQ locations and supported by two data-logging software packages monitored, conditioned and archived the measurements generated by 130 sensors
- Over 50 million data points were generated at 5 minute intervals using the 130 sensors distributed around the *experimental-numerical analysis domain*

- 11 analytical models (AL-1 to AL-11) and 5 transient numerical models (NL-1 to NL-5) were developed or adapted for prediction or replication of measured data within the *experimental-numerical analysis domain* and these are described in the subsequent chapters where they are most relevant
- The combination of the most extensive experimental facility to date with an in depth numerical investigation provided the unique opportunity to undertake a *thermo-environmental analysis* and deliver on the objectives of the *CSDC* approach

Chapter 4 describes the first phase of the experimental-numerical *CSDC* approach which involves characterising measured climate and ground temperature fluctuations, using recognised seasonal and diurnal periodic models, in order to better understand the ground heat resource utilised by $GSHP_{HC}$.

CHAPTER 4

GROUND THERMAL ENERGY RESOURCES

GMIT
GALWAY-MAYO INSTITUTE OF TECHNOLOGY
INSTITIÚID TEICNEOLAÍOCHTA NA GAILLIMHE-MAIGH EO

4. GROUND THERMAL ENERGY RESOURCES

Using the experimental facility described in Chapter 3, the thermal energy resource embodied in the ground under *Cool Marine* conditions is characterised. The ground temperature varies with both time and depth and is therefore defined by the transient GTD. Measured data is compared with analytical models on a number of occasions and further information on these periodic models (AL-1 to AL-5) is presented in Section 4.2. Measured GTD data comes from the reference profile (P1) which, as indicated in Figure 3-10, is located outside the collector area and is independent of heat pump operation. Both this chapter and Chapter 5 deliberately exclude the impact of $GSHP_{HC}$ operation on ground temperatures and concentrate on climate and ground type issues. The purpose of this chapter is to describe the measured charging and discharging of the thermal energy in the ground's surface layer using recognised periodic models for the following reasons:

- Improve knowledge of the Irish GTD under *Cool Marine* conditions using characteristic values of periodic models
- Compare the GTD measured across a number of international locations with varying climates using these key characteristic values
- Generate initial and boundary conditions for system level models of $GSHP_{HC}$
- Establish optimum ground position, collector design and control strategies for horizontal collectors

This chapter is divided into five sections as follows:

- Ground energy definitions
- Periodic models
- Literature review
- *HP-IRL* geothermal resource
- *HP-IRL* seasonal resource
- *HP-IRL* diurnal resource

4.1 GROUND ENERGY DEFINITIONS

It is difficult to define the precise volume of ground from which $GSHP_{HC}$ absorbs thermal energy since the burial depth of horizontal collectors varies between 0.9 and 3.0m depending on the country (as shown in Table 2-11) and the impact of $GSHP_{HC}$ operation varies with heat pump duty. For the purposes of this thesis, $GSHP_{HC}$ utilise the ground's thermal energy

extending from the ground surface to a depth where variation in temperature with time of year due to the seasons is negligible. This point is identified as the *seasonal stability depth* and depends on the ground's thermal properties; for a PT100A which is an RTD temperature sensor, negligible can be defined as a temperature variation with time of year that is less than or equal to the standard uncertainty of ±0.3K. Thermal energy in this volume of ground is defined in Figure 4-1(a) as a 'mixed resource' (Rybach & Sanner, 2000) since it consists of thermal energy supplied by both geothermal and solar heat fluxes. The heat resource extending from the *seasonal stability depth* (considered to be 15m) to a nominal depth of 200m is defined in Figure 4-1(a) as the 'shallow geothermal resource' (Rybach & Sanner, 2000; Sanner *et al.*, 2003). However, in some countries such as Germany (VDI-4640, 2004) and USA all energy stored below the surface in the form of heat is referred to as geothermal energy (Rybach & Sanner, 2000).

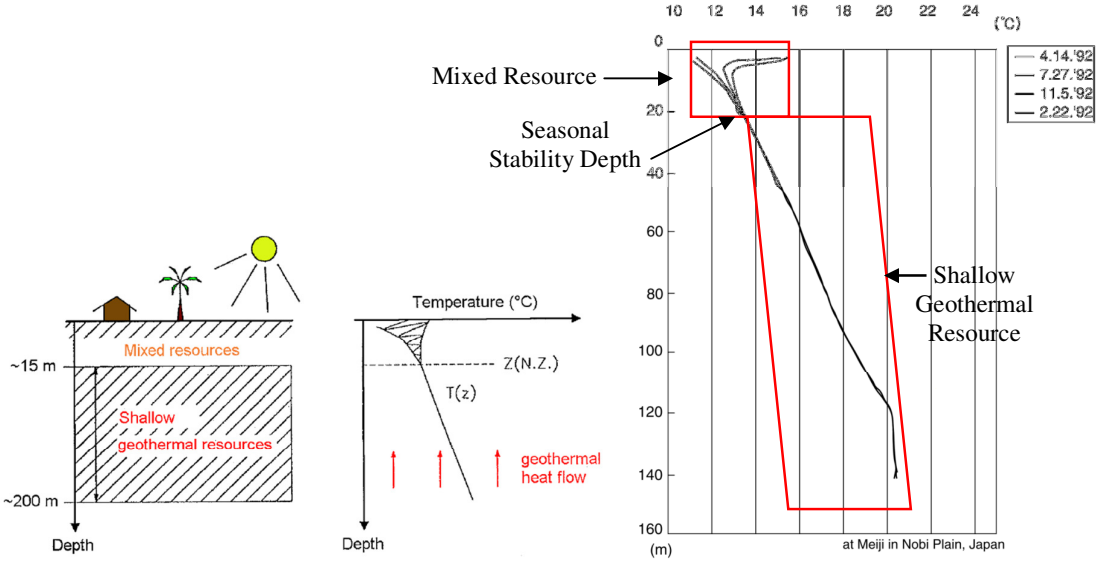

(a) Mixed and geothermal (Rybach & Sanner, 200) **(b) Resources in Japan (Takasugi *et al.* 2001)**

Figure 4-1: Definitions and measurements of ground temperature distribution

An alternative definition of ground energy uses 'temperature zones' (Popiel *et al.*, 2001) with zones as follows:

- Surface zone: extending from the surface to a depth of about 1m where ground temperature is sensitive to short term changes in weather
- Shallow zone: reaching from a depth of 1m to a depth of between 8 and 20m, depending on the ground type; this zone is sensitive to seasonal cycles in weather

- Deep zone: below about 8 to 20m where the ground temperature is constant in time and increases with depth according to the geothermal gradient

While the definitions used by Popiel *et al.* (2001) differ from those used by Ryback & Sanner (2000), the description of ground temperature distribution is essentially the same. Measurements which characterise the 'shallow' and 'deep' zones (Popiel *et al.*, 2001) also referred to as the 'mixed' and 'shallow geothermal' resource respectively (Rybach & Sanner, 2000; Sanner *et al.*, 2003) are reported from Nobi Plain, Japan and presented in Figure 4-1(b) (Takasugi *et al.*, 2001).

For the purposes of this chapter and for the remainder of this thesis, three ground thermal energy resources are defined. These are the *geothermal resource*, the *seasonal resource* and the *diurnal resource* and these are listed in Table 4-1 in this order. The *diurnal stability depth* is identified as the depth at which temperature variation with time of day due to day-night cycles is negligible; this depends on the ground's thermal properties.

Table 4-1: Ground thermal energy resource classifications with depth for *HP-IRL/H*

No.	Resource Name	Location	Influences
1	Geothermal Resource	Below the *seasonal stability depth*	Local Tectonics
2	Seasonal Resource	From the *diurnal stability depth* to the *seasonal stability depth*	Seasons
3	Diurnal Resource	From the surface to the *diurnal stability depth*	Seasons, Diurnal & Short-term Weather Influence

Additionally, the vertical dimension (Z) [m] defined for the *HP-IRL/H* project is positive above the ground's bulk surface and negative below, as shown in Figure 4-2. The *seasonal* and *diurnal resources* are directly influenced by the intensity of solar radiation cycles. Therefore, a description of these cycles using recognised periodic models is now presented.

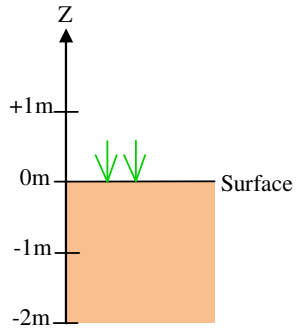

Figure 4-2: Definition of the vertical dimension Z with respect to the bulk ground surface

4.2 PERIODIC MODELS

As the Earth orbits the Sun, completing one orbit in approximately 365 days, it rotates about its own axis, completing one rotation in approximately 24 hours. However, the axis about which the Earth rotates is inclined at approximately 23.4º relative to the axis of the orbit, as shown in Appendix I. The tilt on the Earth's axis of rotation leads to a periodic (seasonal) variation in the latitude (Ω) at which the Sun's rays are normal to the Earth's surface, known as the Sun's angle of declination (δ), and this results in a variation in the Sun's altitude above the horizon ($\acute{\alpha}_{sun}$). Figures 4-3(a), (b) and (c) display variation in the Sun's altitude from wide-lens photographs taken at the *HP-IRL/H* test site around noon during winter, spring and summer respectively. This variation produces three effects which impact on the GTD, listed in order of influence as follows:

- The intensity of solar radiation on a flat surface is proportional to the cosine of the Sun's angle of incidence (Θ), which is the angle between the Sun's rays and the surface normal; in relative terms, cosΘ is low in winter, average in spring and autumn and high in summer
- The length of day changes with the seasons; in relative terms, total hours of sunshine are low in winter, average in spring and autumn and high in summer
- The thickness of the Earth's atmosphere through which the Sun's rays must travel changes with the seasons, the route through the atmosphere is thick in winter, average in spring and autumn and thin in summer

(a) Winter **(b) Spring** **(c) Summer** **(d) $\acute{\alpha}_{sun}$ and Θ definitions**

Figure 4-3: Periodic variation in the Sun's altitude above the southern-horizon at noon over 3 seasons at the HP-IRL/H site

In addition to this seasonal change in solar radiation intensity, the cycle of day to night, referred to as the diurnal cycle, means the altitude and azimuth of the sun changes with time of day and by night the sun is below the horizon. The first five analytical models used in *HP-*

IRL/H (AL-1 to AL-5) define the periodic seasonal and diurnal trends in the local environment. These trends are: the hourly clear-sky solar radiation intensity (AL-1); the multi-year average daily and hourly air temperature patterns (AL-2 and AL-3 respectively); and the multi-year average daily and hourly ground temperature variation with depth (AL-4 and AL-5 respectively).

4.2.1 Model AL-1: Hourly Clear-Sky Solar Radiation Intensity

This method allows estimation of hourly clear-sky radiation intensity on any surface given the location, slope and orientation of that surface. This is important given that nearly all SETs derive power directly or in-directly from solar energy. The method is based on the vector calculus technique for solar engineering (Sproul, 2007).

The variation in the phase of the year (λ_y) [°] with the day of the year (d) is described by Equation 4-1, where $d_{S,max}$ has a value of 172 (June 21st) equivalent to the summer solstice in the Northern hemisphere.

$$\lambda_y\,(d) = \left(d - d_{S,max}\right)\frac{360^o}{365} \tag{4-1}$$

The variation in the Sun's angle of declination (δ) [°] (the latitude at which the Sun's rays are perpendicular to the Earth's surface) with the phase of the year and hence the day of the year (d) is defined in Equation 4-2.

$$\delta\,(d) = 23.44^\circ\,\cos\lambda_y \tag{4-2}$$

The variation in the phase of the day (λ_d) [°] with the hour of the day (hr) is defined in Equation 4-3, where $hr_{S,max}$ theoretically always has a value of 12 (12:00) equivalent to noon.

$$\lambda_d(hr) = (hr - hr_{S,max})\frac{360^\circ}{24} \tag{4-3}$$

However in Galway, Ireland, which is on the western edge of the GMT time-zone and subject to daylight savings, $hr_{S,max}$ has a value of 12.5 from late October to late March and 13.5 for the remainder of the year. Interestingly, in Figure 4-3(c) the photograph of the Sun in summer was inadvertently taken at 12:30 rather than 13:30 and hence the Sun is slightly left of its noon position.

The altitude of the Sun with respect to the horizon ($\acute{\alpha}_{sun}$) [°] is found using Equation 4-4, where Ω [°] is the latitude of the site being studied.

$$\acute{\alpha}_{sun}(\Omega, d, hr) = \sin^{-1}(\cos\delta\cos\Omega\cos\lambda_d + \sin\delta\sin\Omega) \quad (4\text{-}4)$$

The Sun's azimuth with respect to North (γ_{sun}) [º] is found by first calculating γ_{cos} [º] the azimuth angle with a period of 180º using Equation 4-5.

$$\gamma_{cos}(\Omega, d, hr) = \cos^{-1}\left(\frac{\sin\delta\cos\Omega - \cos\delta\sin\Omega\cos\lambda_d}{\cos\acute{\alpha}_{sun}}\right) \quad (4\text{-}5)$$

Then the true azimuth with respect to North (for a 360º period) (γ_{sun}) [º] is found using the following logic:

$$\text{for } \lambda_d < 0 \; then \; \gamma_{sun} = \gamma_{cos} \text{ and for } \lambda_d > 0 \; then \; \gamma_{sun} = 360^o - \gamma_{cos}$$

The clear-sky, solar intensity ($q"_{c\text{-}s}$) [W/m^2] incident on a surface of slope (β) [º] and orientation/azimuth from due North (γ) [º] at a latitude (Ω) [º] is given by Equation 4-6, where $q"_{ter}$ is the terrestrial solar radiation constant (intensity of solar radiation perpendicular to a surface under clear skies at the site being studied) and Θ [º] is the Sun's angle of incidence (angle between Sun's rays and the surface normal)

$$q"_{c-s}(\Omega, d, hr, \beta, \gamma) = q"_{ter}\cos\Theta \quad (4\text{-}6)$$

The cosine of the angle of incidence ($\cos\Theta$) [-] is found using Equation 4-7, where β [º] is the slope of the surface and γ [º] is the orientation/azimuth of the surface.

$$\cos\Theta(\Omega, d, hr, \beta, \gamma) = \sin\beta\cos\acute{\alpha}_{sun}\cos(\gamma - \gamma_{sun}) + \cos\beta\sin\acute{\alpha}_{sun} \quad (4\text{-}7)$$

The value of $q"_{c\text{-}s}$ should equal zero for all surfaces (regardless of slope) until the Sun has cleared the horizon; therefore, the following condition applies to all calculations:

$$\text{for } \acute{\alpha}_{sun}(\Omega, d, hr) < 0°; \quad q"_{c-s}(\Omega, d, hr, \beta, \gamma) = 0 W/m^2$$

Due to cloud cover which is difficult to predict, this clear-sky value is an over-estimation for most locations and particularly for *Cool Marine* locations. A percentage of the hourly $q"_{c\text{-}s}$ could be calculated based on an average cloud cover value or daily cloud cover observations could be used to improve the accuracy of this method. On clear days the $q"_{c\text{-}s}$ value is correct for each hour.

4.2.2 Model AL-2: Multi-year Average Daily Air Temperature Trend

The variation in the multi-year average daily air temperature $T_{a,d}$ [ºC] with the day of the year (d) is tracked using Equation 4-8 where, $T_{a,y}$ [ºC] is the annual average air temperature, $A_{a,y}$

[K] is the mean-to-peak amplitude of the annual air temperature oscillation and ω_{orb} [º/day] is the angular velocity of Earth's orbit described by Equation 4-9 (Campbell & Norman, 1998).

$$T_{a,d}(d) = T_{a,y} + A_{a,y}\cos[\omega_{orb}(d - d_{a,max})] \quad (4\text{-}8)$$

$$\omega_{orb} = \frac{360^{o}}{365} \quad (4\text{-}9)$$

The maximum in the annual air temperature occurs after the maximum solar intensity, as shown in Equation 4-10, lagging by an amount ($d_{a,lag}$), typically around 31 days in Ireland.

$$d_{a,max} = d_{S,max} + d_{a,lag} \quad (4\text{-}10)$$

4.2.3 Model AL-3: Multi-year Average Hourly Air Temperature Trend

The variation in the multi-year average hourly air temperature $T_{a,h}$ [ºC] with both the hour of the day (hr) and day of the year (d) is tracked using Equation 4-11 where, $T_{a,d}$ (d) [ºC] is described in Equation 4-8, $A_{a,d}$ [K] is the mean-to-peak amplitude of the diurnal air temperature oscillation and ω_{rot} [º/day] is the angular velocity of Earth's rotation described by Equation 4-12 (Campbell & Norman, 1998).

$$T_{a,h}(d, hr) = T_{a,d}(d) + A_{a,d}\cos[\omega_{rot}(hr - hr_{a,max})] \quad (4\text{-}11)$$

$$\omega_{rot} = \frac{360^{o}}{24} \quad (4\text{-}12)$$

The maximum in the daily air temperature occurs after the maximum solar intensity, as shown in Equation 4-13, lagging by an amount ($hr_{a,lag}$), typically around 2 to 3 hours in Ireland.

$$hr_{a,max} = hr_{S,max} + hr_{a,lag} \quad (4\text{-}13)$$

4.2.4 Model AL-4: Multi-year Average Daily Ground Temperature Variation with Depth

The variation in average ground temperature ($T_{g,d}$) [ºC] with the day of the year (d) and the vertical dimension (Z) [m] can be described using Equation 4-14 (Incorpera & DeWitt, 2002).

$$T_{g,d}(d, Z) = T_{g,y} + \left\{A_{sur,y}\exp^{Z\sqrt{\frac{\omega_{orb}}{2\alpha_{g,d}}}}\cos[\omega_{orb}(d - d_{sur,max}) + Z\sqrt{\frac{\omega_{orb}}{2\alpha_{g,d}}}]\right\} \quad (4\text{-}14)$$

Where, Z [m] is the vertical dimension defined in Figure 4-2, this is negative below the ground surface. $T_{g,y}$ [ºC] is the average annual ground temperature (equal at all depths) and $A_{sur,y}$ [K] is the mean-to-peak amplitude of the ground surface temperature (T_{sur}) [ºC] annual oscillation. The angular velocity of Earth's orbit ω_{orb} [rad/day] is calculated using Equation 4-15; radians must be used for compatibility.

$$\omega_{orb} = \frac{2\pi}{365} \tag{4-15}$$

The ground's thermal diffusivity α_g [m^2/s] is converted to $\alpha_{g,d}$ [m^2/day] as follows:

$$\alpha_{g,d}\ [m^2/day] = 24 * 60 * 60 * (\alpha_g[m^2/s]) \tag{4-16}$$

The maximum in the annual ground surface temperature ($T_{sur,max}$) occurs after the maximum solar intensity, as shown in Equation 4-17, lagging by an amount ($d_{sur,lag}$) which is typically about 31 days in Ireland.

$$d_{sur,max} = d_{S,max} + d_{sur,lag} \tag{4-17}$$

Equation 4-14 is the most commonly quoted equation in GTD and *GSHP$_{HC}$* literature and is used to describe the lower boundary condition of any transient ground simulation.

4.2.5 Model AL-5: Multi-year Average Hourly Ground Temperature Variation with Depth

The variation in hourly ground temperature ($T_{g,h}$) [ºC] with the hour of the day (hr), the day of the year (d) and the vertical dimension (Z) [m] can be described using Equation 4-18 (Elias *et al.*, 2004).

$$T_{g,h}(d, hr, Z) = T_{g,d}(d, Z) + \left\{A_{sur,d} \exp^{Z\sqrt{\frac{\omega_{rot}}{2\alpha_{g,h}}}} \cos[\omega_{rot}(hr + hr_{sur,max}) + Z\sqrt{\frac{\omega_{rot}}{2\alpha_{g,h}}}]\right\} \tag{4-18}$$

Where, $T_{g,d}$ (d) [ºC] is described in Equation 4-14 and $A_{sur,d}$ [K] is the mean-to-peak amplitude of the ground surface temperature (T_{sur}) [ºC] diurnal oscillation. The angular velocity of the Earth's rotation ω_{rot} [rad/s] is defined using Equation 4-19; radians must be used for compatibility.

$$\omega_{rot} = \frac{2\pi}{24} \tag{4-19}$$

The ground's thermal diffusivity α_g [m^2/s] is converted to $\alpha_{g,h}$ [m^2/h] as follows:

$$\alpha_{g,h}[m^2/h] = 60 * 60 * (\alpha_g[m^2/s]) \quad (4\text{-}20)$$

The maximum in the daily ground surface temperature ($T_{sur,max}$) occurs after the maximum solar intensity, as shown in Equation 4-21, lagging by an amount (hr_{lag}) which is typically about 3 to 4 hours in Ireland.

$$hr_{g,max} = hr_{S,max} + hr_{lag} \quad (4\text{-}21)$$

4.2.6 Purpose of Periodic Models AL-1 to AL-5

While it will be shown in the subsequent sections that these idealised periodic models have good accuracy only when replicating multi-year average or multi-year maximum (for AL-1) data-sets, they are still used frequently in this chapter to:

- Improve the understanding of periodic variations in solar intensity, air temperature and ground temperatures at the *HP-IRL/H* site
- Characterise the timing and amplitude of underground temperature oscillations, with respect to surface oscillations, for different depths and thermal diffusivities

It will also be shown in Chapters 5, 6, 7 and 8 that these models can be used to:

- Provide initial-conditions in a step-wise analysis or simulation when there is no other method to evaluate the initial state of the system
- Provide boundary conditions in a ground simulation domain
- Inform the positioning and control strategy for intelligent collectors

These models can also be used to assess weather data and establish the deviation from the expected/typical/multi-year average value which is of practical use in controlling hybrid systems involving combinations of solar thermal, air-source and ground-source heat pumps.

4.3 LITERATURE REVIEW

A literature review was conducted of previous studies that explored vertical GTD and 11 of the key experimental and numerical investigations are listed in Table 4-2. The literature presented in this chapter extends beyond GSHP research and includes publications from disciplines such as agriculture and climatology where the GTD and the variables which influence it are also of interest. Climate classification and air temperature (T_a) [ºC] is of significant interest in this discussion as they impact directly on the GTD. It is striking in Table 4-2 that vertical GTD's have been reported from only one *Cool Marine* region.

Table 4-2: Experimental facilities on the vertical Ground Temperature Distribution (GTD)

No.	Study (Year)	Location	Climate Classification	Research Topic	Test Details
1.	Mihalakakou *et. al* (1996 & 1997)	Athens, Greece and Dublin, Ireland	*Dry Summer Subtropical and Cool Marine respectively*	Effect of surface cover on the heat resource for HGHE	Profiles to 1.2m depth, t = 10 yr.
2.	Safanda (1999)	Prague, Czech Republic	*Humid Continental*	Effect of surface slope and orientation on GTD over a year	Profiles to 200m depth, t= 2 yr.
3.	Van Buren *et. al.* (1999)	Ontario, Canada	*Extreme Sub Polar*	Temperature of rainwater runoff from pavements	Profiles to 0.6m, t > 0.5 yr.
4.	Asaeda and Ca (2000)	Saitama, Japan	*Humid Continental*	Effect of permeable pavement on GTD	Profiles to 0.58m depth, t ≈ 1 yr.
5.	Beltrami (2000)	Nova Scotia, Canada	*Extreme/Moderate Sub Polar*	Meteorological records in GTD	Profiles to 1m depth, t > 1 yr.
6.	Popiel *et. al.* (2001)	Poznan, Poland	*Humid Continental/Cool Littoral*	Effect of surface cover on GTD	Profiles to 7m depth, t ≈ 2 yr.
7.	Chacko and Renuka (2002)	Thiruvananthapuram, India	*Wet and Dry/Semiarid Tropical*	GTD for agricultural and climate research	Profiles to 0.5m, t = 1 yr.
8.	Qin *et. al.* (2002)	University of Negev, Israel	*Dry Summer Subtropical/ Semiarid Continental*	Complete numerical solution to surface energy balance	Profiles to 0.3m depth, t = ?
9.	Elias *et. al.* (2004)	Sao Paulo, Brazil	*Wet Equatorial, Wet and Dry Tropical*	Improvement to GTD analytical model	Limited observed results
10.	Smerdon *et. al.* (2004)	USA x 3 and Czech Republic x 1	*Variety of climates detailed in discussion*	Establishing air temperature histories using GTD	Profiles to 7.7m depth, t = 1 yr.
11.	Takebayashi (2009)	Kobe, Japan	*Humid Continental*	Effect of surface cover on urban heat island effect	IR imaging, t ≈ 2 yr.

Note: *Climate classifications* based on Koeppe and De Long (1958)

4.3.1 Characterising the Seasonal Resource

The majority of literature is concerned with experimental measurement and either analytical characterisation or numerical simulation of seasonal surface effects penetrating into the ground (Popiel *et al.*, 2001; Smerdon *et al.*, 2004; Pollack *et al.*, 2005). Figure 4-4 displays a large data-set recorded from 1993 to 2003 at four different test sites and presented in Smerdon *et al.* (2004); this data demonstrates the effects of location, climate, time of year and depth on the ground temperatures.

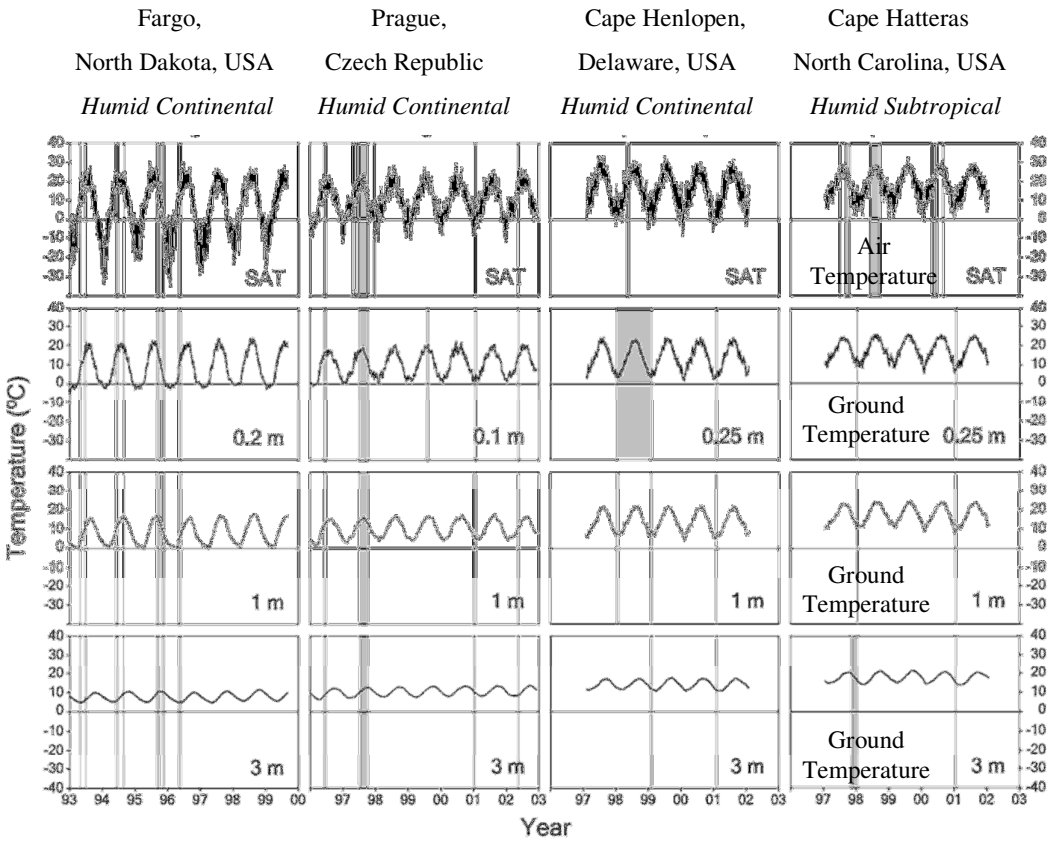

Figure 4-4: Variation in air temperature, ground temperature near the surface and ground temperature at 1 and 3m depths for 4 locations over 7 years (Smerdon *et al.*, 2004)

4.3.2 Seasonal Variation in Ground Temperature Distribution

Due to summer charging and winter discharging of the grounds thermal energy, the surface temperature (T_{sur}) oscillates in a periodic fashion with the same period as the oscillation in the Sun's angle of declination which causes the seasons, but with a phase lag. It can be seen from Equation 4-14 that the downward propagation of the surface oscillation will be exponentially attenuated and linearly phase shifted with depth (Smerdon *et al.*, 2004). The ground's thermal diffusivity can vary considerably from site to site and $d_{sur,max}$ can vary depending on latent and sensible heat storage at the *ground-atmosphere interface*. Equation 4-14 allows the annual GTD of a site to be characterised for easy comparison between sites using just four variables ($T_{g,y}$, $A_{sur,y}$, $d_{sur,max}$ and $\alpha_{g,d}$), rather than an entire data set like that presented in Figure 4-4. Similarly, Equation 4-8 can be used to reduce an air temperature data set to three variables ($T_{a,y}$, $A_{a,y}$ and $d_{a,max}$). Tests of Equation 4-14 on the dataset of Figure 4-4 predict the temperature change with depth to a high accuracy, the coefficient of determination (R^2) is said to be in a range of 0.995 and 0.999 (Smerdon *et al.*, 2004). Similar uses and accuracies of Equation 4-14 are presented for predicting seasonal variation in mean daily or weekly

temperatures (Campbell & Norman, 1998; Popiel *et al.*, 2001). However, Equation 4-14 is unable to account for diurnal cycles and unpredictable weather events.

4.3.3 Influences of Location

In order to compare the variation of GTD with location and the associated climate, Table 4-3 has been prepared using information taken from five publications (Beltrami, 2001; Popiel *et al.*, 2001; Mihalakakou, 2002; Smerdon *et al.*, 2004; Burke, 2010). Latitudes for each site are taken from the respective publication while *climate classifications* are based on location and derived using the Koeppe & De Long (1958) map in Figure 3-2. The annual average ground and air temperatures ($T_{g,y}$ and $T_{a,y}$ respectively) and the annual mean-to-peak amplitude of the T_{sur} and T_a oscillation ($A_{sur,y}$ and $A_{a,y}$ respectively) are taken from the relevant publication.

Table 4-3: Ground temperature and climate information taken from the literature for nine locations

Author (Year)	Location	Ω	Climate	$T_{a,y}$	$A_{a,y}$	$T_{g,y}$	$A_{sur,y}$
Beltrami (2000)	Nova Scotia, Canada	45º	H.C./ Moderate Sub Polar	7.4ºC	11.5K	9.4ºC	10.4K
Popiel *et. al.* (2001)	Poznan, Poland*	52º	H.C./ Cool Littoral	9.4ºC	11.6K	10.3ºC	11.1K
Mihalakakou *et. al.* (2002)	Athens, Greece*	37º	Dry Summer Subtropical	-	-	16.7ºC	12.4K
Mihalakakou *et. al.* (2002)	Dublin, Ireland*	53º	Cool Marine	-	-	9.2ºC	5.9K
Smerdon *et. al* (2004)	Cape Hatteras, North Carolina	35º	Humid Suptropical	18.1ºC	8.6K	17.1ºC	7.9K
Smerdon *et. al* (2004)	Cape Henlopen, Delaware	38º	Humid Continental	15ºC	10.8	13.5ºC	9.9K
Smerdon *et. al* (2004)	Fargo, North Dakota	46º	Humid Continental	5.8ºC	17.8K	9.1ºC	13.8K
Smerdon *et. al* (2004)	Prague, Czech Republic	50º	Humid Continental	9.9ºC	10.1K	10.3ºC	8.83K
Burke (2010)	Galway, Ireland	53º	Cool Marine	9.8ºC	5.2K	11.7ºC	6.7K

Note: * Studies in these locations involved comparison between grass covered and bare ground GTD, but only data for grass is presented

As expected, a relationship can be established between GTD and both latitude and *climate classification*. It can be seen that the $T_{g,y}$ for Cape Hatteras, Athens and Cape Henlopen, with latitudes of 35, 37 and 38º respectively, vary between 17.1, 16.7 and 13.5ºC. The $T_{g,y}$ observations for the remaining 6 sites with latitudes of between 45 and 53º vary between 9.1 and 11.7ºC. All sites studied are in the Northern Hemisphere and, as expected, the mean annual ground temperature is a function of latitude with regions closer to the Tropic of Cancer, latitude of 23.5º, receiving greater amounts of solar radiation and therefore reaching a higher steady-state $T_{g,y}$ to achieve equilibrium.

The mean-to-peak amplitude $A_{sur,y}$, which is the variation between $T_{g,y}$ and the summer maximum of multi-year average ($T_{sur,max}$) shows a closer correlation with *climate classification* than latitude. For example when comparing Poznan, Poland (52º) with Dublin, Ireland (53º), the $T_{g,y}$ varies by only 1.1K while the $A_{sur,y}$ varies by 5.2K. This difference may be attributed to the maritime influence in Ireland, where the Atlantic oceans thermal mass plus

the Gulf Stream result in less extreme variations between summer and winter temperatures. The highest $A_{sur,y}$ and $A_{a,y}$ are observed in Fargo, North Dakota. Fargo is surrounded by land for hundreds of kilometres and experiences a *Humid Continental* climate. Although Fargo is located at a latitude 6 to 7º south of Poznan and Dublin the winter minimums in T_a are 10K cooler in Fargo than Dublin or Poznan.

In addition to the $T_{g,y}$ being influenced by latitude and the $A_{sur,y}$ showing patterns of *climate classification* and maritime effects, the GTD is also affected by the type of weather at the surface both in summer and winter. Detailed analyses have been conducted into the influence of weather type on: surface temperature, downward penetration, amplitude attenuation and phase lag (Beltrami, 2001; Schmidt *et al.*, 2001; Smerdon *et al.*, 2004). It is noticeable in Table 4-3 that of the seven locations where both $T_{g,y}$ and $T_{a,y}$ are stated, the $T_{g,y}$ value exceeds $T_{a,y}$ in all but two of these since the ground surface absorbs solar radiation and then looses heat to the air above and to the ground below (Campbell & Norman, 1998); a temperature difference must exist to facilitate this process. In winter, cooler temperatures and the reduced solar intensity forces the ground to release the embodied heat. In regions with extreme winters such as Nova Scotia, ground and air temperature shown in Figure 4-5 (Beltrami, 2001), the moisture in the ground freezes and releases the latent heat of fusion, this results in a constant temperature (≈0ºC) in the surface layer over many months. This depends on the amount of moisture available for freezing and the intensity of the winter cold. Come spring, this frozen ground thaws by consuming solar energy and sensible heat which slows down the onset of spring in the ground surface layer, causing a prolonged phase lag.

The two locations where $T_{g,y}$ does not exceed $T_{a,y}$ are Cape Hatteras, North Carolina and Cape Henlopen, Delaware. The difference between the air and ground temperature relationship at the two Capes relative to the other locations is attributed to the cause of the attenuation (Smerdon *et al.*, 2004). In North Dakota for example, the attenuation is clearly dominant in winter (Smerdon *et al.*, 2004) where the release of stored summer heat and the latent heat of freezing in the ground causes the T_g to remain significantly higher than the T_a in winter. In the Capes however, winter freezing does not occur and the attenuation of the seasonal variation occurs predominantly in summer (Smerdon *et al.*, 2004) where the storage of heat underground and the evaporation of precipitated surface water cause the ground surface to remain cooler than the warm air moving in from the south. In all locations except for Galway, Ireland, $A_{a,y}$ exceeds $A_{sur,y}$ meaning the ground achieves attenuation of the multi-year average seasonal T_a oscillation. In all locations except for Galway, it can be seen that processes at the *ground-atmosphere interface* cause the mean daily T_{sur} to be cooler and warmer, relative to

the mean daily T_a in summer and winter respectively. The lack of attenuation at the surface in Ireland is investigated further in Sub-section 4.3.4.

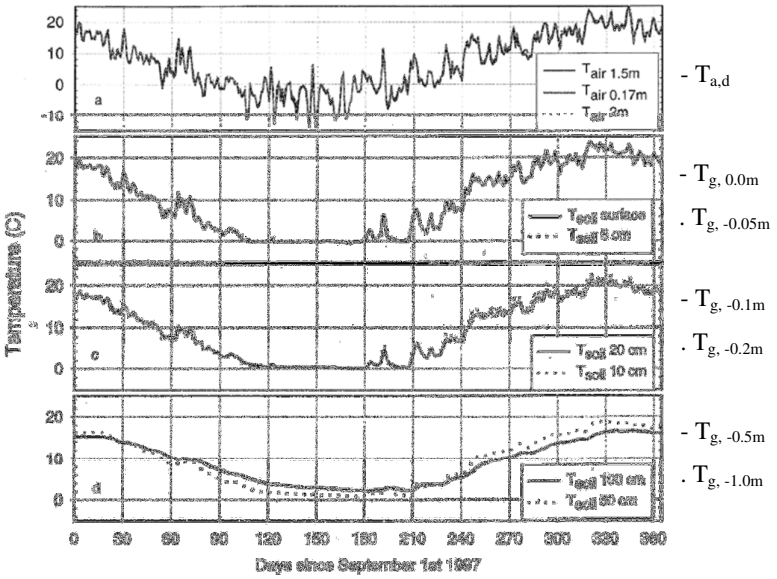

Figure 4-5: Air temperature and ground temperatures measured in Nova Scotia (Beltrami, 2001)

4.3.4 Irish Conditions

Firstly, a noticeable difference of 2.5K exists between the $T_{g,y}$ of 9.2ºC reported for Dublin on the East-coast (Mihalakakou & Lewis, 1996) and the $T_{g,y}$ of 11.7ºC reported for Galway on the West-coast (Burke, 2010). Observed multi-year average $T_{g,y}$ of 10.4, 10.2, 10.8 and 9.8ºC are reported by Met Eireann for Dublin (East), Cork (South) and Shannon (West) Airports and Claremorris (West) respectively (Met, 2010). The $T_{g,y}$ of 11.7ºC presented for Galway is 1.4K above the average of 10.3ºC from the 4 Met Eireann stations. While the Galway values are highly accurate (±0.3ºC) and based on data recorded at the *HP-IRL* site over 3 years from 8 ground sensors (Burke, 2010), annual reports show that 2009 had a warmer than average summer and 2008 had a warmer than average winter (Met, 2010).

The amplitude of the mean-to-peak surface oscillation $A_{sur,y}$ reported for Dublin is 5.9K (Mihalakakou, 2002) and for Galway 6.7K (Burke, 2010). Observed $A_{sur,y}$ of 7.6, 6.4, 7 and 6.8K are reported by Met Eireann for Dublin (East), Cork (South) and Shannon (West) Airports and Claremorris (West) respectively (Met, 2010). The $A_{sur,y}$ of 6.7K presented for Galway is 0.25K below the average of 6.95K from the 4 Met Eireann stations. Multi-year average winter T_{sur} in Ireland are either equal to T_a or slightly below at some observation

stations, as shown in Figure 4-6 for multi-year mean data from the west of Ireland (Martin & Goswami, 2005; Met, 2010).

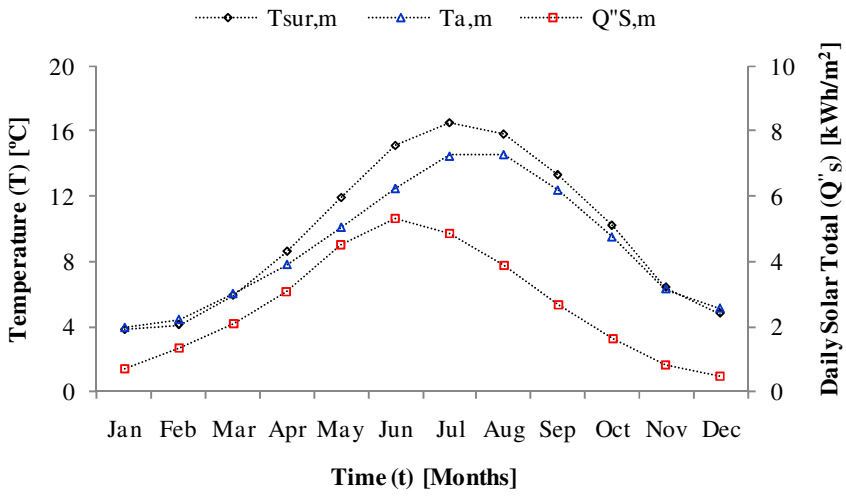

Figure 4-6: Monthly average of daily solar energy totals, air temperature and surface temperature trends in the West of Ireland, compiled from the 10 year records (Martin & Goswami, 2005; Met, 2010)

This may be due to the fact that the multi-year average winter T_a never drops below +4ºC meaning freezing of the surface layer caused by sub-zero air temperatures does not occur frequently, or for long periods of time. In summer the surface is heated by the Sun but the air above is continually replenished with cooler air from the ocean. As a result, observed multi-year mean T_{sur} are higher than multi-year mean T_a in summer, as shown in Figure 4-6. As a result $A_{sur,y}$ is greater than $A_{a,y}$.

4.3.5 Phase Lag

In the absence of ground freezing during the Irish winter, the on-set of spring is relatively early. The start of spring is February 1st in the Irish calendar and ground temperatures typically facilitate growth of flora, such as the daffodil (narcissus pseudonarcissus), from this time. It can be seen in Figure 4-6 that the T_{sur} and T_a lag behind the solar radiation oscillation by about 1 month, yielding maximums between July 21st and 24th and minimums between January 21st and 24th. This contrasts with Nova Scotia where more extreme lag caused by the freezing and thawing of the ground surface results in maximums in August and minimums in February (Beltrami, 2001). The T_{sur} in Ireland does not show a significant lag behind T_a and in some datasets T_a can be seen to lag behind the T_{sur}. By comparison, the ground surface oscillation has been reported to lag the air temperature oscillation by 8 days in Fargo, North

Dakota and 4.6 days in Cape Hatteras, North Carolina (Smerdon *et al.*, 2004), again attenuation effects of freezing and evaporation respectively along with maritime influences are the likely cause.

4.3.6 GTD Graphical Representation

As the name suggests the GTD varies in both space and time and therefore it is not straightforward to represent graphically. Three graphical techniques are typically employed and a combination of these is used in the *HP-IRL/H* project when appropriate. The first method is to present ground temperature variation with time for one depth, or for many depths, as shown in Figure 4-4. Weather patterns such as air temperature or solar radiation can be displayed above or below this data with the same timescale, as shown in Figure 4-5. An alternative method is presented in Figure 4-7(a) (Popiel *et al.*, 2001) where the amplitude attenuation with depth is evident by plotting ground temperature gradients at various times of the year. Finally, a hybrid method of these two is shown in Figure 4-7(b) (Pollack *et al.*, 2005). This method displays the variation in GTD with both depth and time simultaneously and also includes weather overlays. Burke (2010) mapped the impact of heat extraction with a ground heat collector using this technique. While it can be difficult to identify exact temperatures, temperature ranges are clearly defined using colour coding.

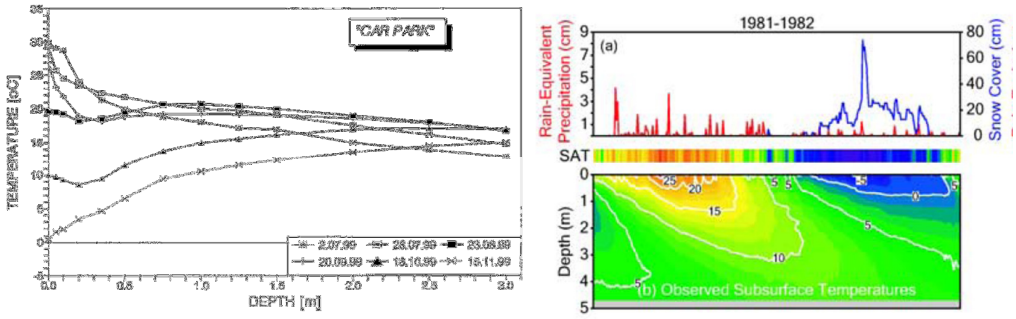

(a) Temperature variation (Z), (t) (Popiel *et al.*, 2001) (b) Temperature variation (Z, t) (Pollack *et al.*, 2005)

Figure 4-7: Graphics showing temperature variation with depth and time using two different methods

4.3.7 Summary

This literature review has presented a summary of the experimental procedures, analytical methods, key findings and graphical techniques used to assess GTD and ground thermal energy. The following observations were made:

- The research has predominately focused on assessing seasonal changes in GTD

- Equation 4-14 has been used widely to characterise and compare the effect of seasons on GTD at different locations using four variables ($T_{g,y}$, $A_{sur,y}$, $d_{sur,max}$ and $\alpha_{g,d}$)
- The mean annual ground temperature $T_{g,y}$ increases as the Tropics and the Equator are approached
- The amplitude of the annual T_{sur} oscillation $A_{sur,y}$ is closely related to the *climate classification* and is also influenced by proximity to the sea
- The mean annual ground temperature $T_{g,y}$ is higher than mean annual air temperature $T_{a,y}$ in 5 of the 7 locations studied, given that the Sun heats the Earth which in turn heats the atmosphere
- In 8 of the 9 locations studied, $A_{sur,y}$ was lower than $A_{a,y}$ showing attenuation of the seasonal air temperature oscillation by the ground
- The attenuation is caused by sensible ground heat release and storage along with latent ground water freezing and evaporation in winter and summer respectively
- In the two locations where $T_{a,y}$ exceeds $T_{g,y}$ the attenuation of the $A_{a,y}$ in the ground was predominantly in summer and no freezing took place in winter
- Galway, Ireland was the only location of 9 where $A_{sur,y}$ exceeded $A_{a,y}$
- Driven by infrequent freezing during mild winters and maritime air currents in summer, Irish multi-year average T_{sur} and T_a are typically equal in winter and T_{sur} exceeds T_a in summer
- Observed multi-year average $T_{g,y}$ and $A_{sur,y}$ in Ireland have ranges of 9.2 to 11.7ºC and 5.9 to 7.6K with averages of 10.3ºC and 6.95K, respectively
- The variation in GTD with time and depth can be graphed separately, with high resolution, or simultaneously with less resolution using colour coding of temperature ranges

As expected the GTD in Ireland differs greatly from the other locations investigated. Winter cooling is far less extreme; the onset of spring is much quicker and summer heating is also less extreme. Given the nature of $GSHP_{HC}$ these are potentially very positive attributes.

Having overviewed international research on GTD in this section, a detailed investigation of GTD at the *HP-IRL* site is presented in the next section. This is done using a form of Fourier analysis, where the primary geothermal influence and seasonal waveform are first characterised before examining the diurnal waveform and the weather influence. For this reason, the subsequent 3 sections are presented in the order of geothermal resource → seasonal resource → diurnal resource.

4.4 HP-IRL GEOTHERMAL RESOURCE

Below the *seasonal stability depth* defined in Section 4.1, ground temperature no longer varies with time as well as depth. As a result, a single variable called the *geothermal gradient,* typically defined in ºC/km or K/km, defines the heat resource. Geothermal gradients are a result of intense heat at the planet's centre caused by decaying radioactive material within the Earth's core (Pahud, 2002) and the extreme pressure caused by gravitational forces holding the planet together. Pahud (2002) states that 99% of the Earth's mass has a temperature in excess of 1000ºC while only 1% of the Earth's mass has a temperature below 100ºC and this geothermal heat can be used as follows:

- 0 to 1000m depth – heating with heat pumps
- 1000 to 3500m depth – heat without heat pumps
- 3500 to 6000m depth – hot dry rock systems for heat and power production

Ireland, like much of North Western Europe with the exception of Iceland and France, does not boast abundant high-grade hydrothermal or geothermal energy resources due to the lack of tectonic activity (Rybach & Sanner, 2000; Allen *et al.*, 2003). A report commissioned by SEAI on Ireland's geothermal resource states a measured *geothermal gradient* of 10 to 15K/km exists in the south of the island and this increases to 25 to 30K/km in the north (Goodman *et al.*, 2004). This is low in comparison to a gradient of 70K/km calculated using the data in Figure 4-1(b), reported from Nobi Plain, Japan (Takasugi *et al.*, 2001).

Measurements taken using PT100A temperature sensors attached to the outside of $GSHP_{VC}$ piping as part of *HP-IRL/V* are summarised in Table 4-4. This data shows that at a depth of 95m below the surface the average temperature is 11.37ºC (Burke, 2010). These temperatures were taken over three years as part of *HP-IRL/V*, during the summer months when the $GSHP_{VC}$ had not been used for 148 consecutive days. In comparison, temperature measurements taken at eight depths in P1, over a three year period as part of *HP-IRL/H*, indicate a mean ground temperature at all depths ($T_{P1,\ 0.0m}$ to $T_{P1,\ -1.8m}$) of 11.72ºC. While accounting for the warmer than average winter of 2008 and summer of 2009 (Met, 2010), this indicates that the *geothermal gradient* in the first 50m of ground at the *HP-IRL/H* site is relatively insignificant. Ignoring the seasonal resource, it is observed that between Z= -50 and -95m a 0.47K temperature differential exists; this is equivalent to a *geothermal gradient* of 10.44K/km, which falls within the SEAI range published for the south of Ireland (Goodman *et al.*, 2004).

Figure 4-8 presents a summary of the geothermal and seasonal resources at the *HP-IRL* site. The GTD to Z= -20m was created using AL-4 calibrated down to Z= -1.8m using data from P1. At depths greater than 20m the *geothermal gradient* was based on data from *HP-IRL/V* summarised in Table 4-4. Ground temperature gradients are presented for 4 different times of the year, to a depth of 20m. The times chosen are 1 month after the standard equinox and solstice days, the latter corresponding to peak variations in ground surface temperature.

Table 4-4: Ground temperature measurements taken from the 100m deep vertical boreholes used in the HP-IRL/V project

Year	Date	$GSHP_{VC}$ Off-time	Z= -5m	Z= -50m	Z= -95m	Accuracy
2007	Oct	148	13ºC	11.1ºC	11.5ºC	±0.3ºC @ 0 ºC
2008	Oct	148	13.8ºC	10.9ºC	11.4ºC	±0.3ºC @ 0 ºC
2009	Oct	148	13.4ºC	10.7ºC	11.2ºC	±0.3ºC @ 0 ºC
Mean		148	13.4ºC	10.9ºC	11.37ºC	±0.3ºC @ 0 ºC

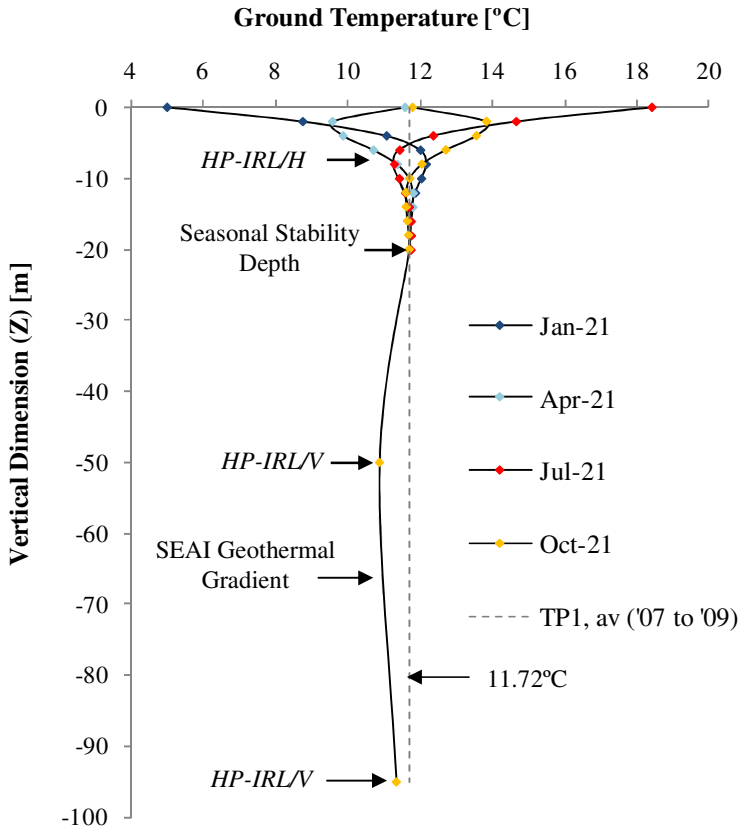

Figure 4-8: Vertical profiles of 3 year mean ground temperature to a depth of 95m on four dates throughout the year with January 21st and July 21st representing the extremes in surface temperature

4.5 HP-IRL SEASONAL RESOURCE

From the ground surface to the *seasonal stability depth*, about 8 to 20m below grade – depending on ground type, the ground is subject to charging and discharging caused by the changing seasons. However, like the environment above it, this ground-volume maintains a stable average annual temperature. In *HP-IRL/H* this is a $T_{g,y}$ of 11.72ºC ±0.3ºC compared to a $T_{a,y}$ of 9.8ºC ±0.3ºC. This difference in average temperatures allows the ground to reject the same total amount of heat to its surroundings as it receives from the sun over a year.

4.5.1 Seasonal Ground Temperature Mapping

Figure 4-9 gives a graphical introduction to the seasonal variation in ground temperature with time and depth at the *HP-IRL* site for the 366 days in 2008 using the graphical technique of colour coded temperature ranges. Figure 4-9(a) was created using daily totals ($Q"_{S,t}$) and averages of T_a and $T_{P1,\ 0.0m}$ measurements; this displays the annual phase lag in the $T_{a,d}$ and $T_{P1,\ 0.0m}$ oscillations with respect to $Q"_{S,t}$. Figure 4-9(b) shows a secondary representation of the $T_{a,d}$ data in Figure 4-9(a) using the same colour coding for temperature ranges as used in Figure 4-9(c), (d) and (e). Figure 4-9(c) was created using daily averages of observed T_g at 8 depths in P1 from $T_{P1,\ 0.0m}$ to $T_{P1,\ -1.8m}$. Figure 4-9(d) was created using the numerical simulation technique, identified as NL-1, to a depth of 8m. NL-1 uses weather data records to calculate the ground temperatures and is described in detail in Section 5.4. Finally, Figure 4-9(e) was created using $T_{g,d}$ from the analytical model AL-4, described in Section 4.2, with 0.25m space increments to a depth of 20m. The values used for equation inputs are detailed in Table 4-5. From visual inspection of Figure 4-9 the following conclusions are drawn:

- The T_{sur} ($T_{P1,\ 0.0m}$) and T_a oscillations lag the radiation intensity oscillation by about one month
- T_{sur} is in excess of T_a in summer and equal on occasions in the winter
- In winter, T_{sur} shows considerable attenuation of short-term T_a fluctuations
- While, seasonal T_{sur} changes resulting from the Earth's tilt penetrate to a depth of 16m, a major influence from this oscillation is not seen below -8 to -10m
- The linear phase shift of the ground temperature oscillation with depth can be clearly seen in Figure 4-9(d)
- The analytical method AL-4 models the seasonal pattern with decent accuracy however NL-1 can simulate the short term changes near the ground surface
- The accuracy of AL-4 and NL-1 improves with depth, due to dampening of the weather influence

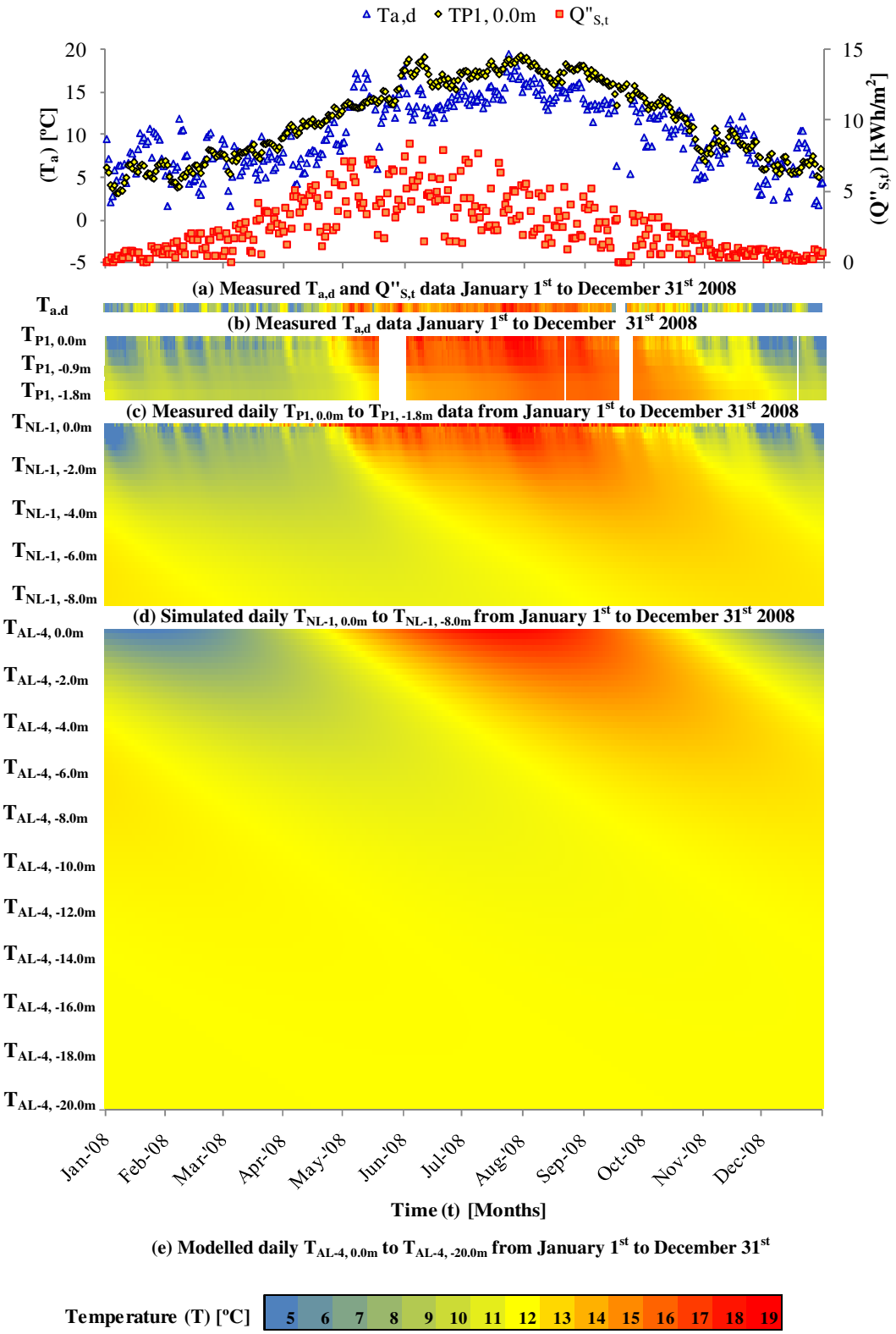

Figure 4-9: Plots of temperature variation with depth and time for observed, simulated and analytically modelled mean daily ground temperatures from January 1st to December 31st of 2008

4.5.2 Surface Energy Balance

The volume of ground from the Earth's surface to the *seasonal stability depth* is essentially a large thermal mass, facilitating an energy balance between the solar energy absorbed and the heat loss or gain to the atmosphere. Equation 4-22 describes the typical surface energy balance (Mihalakakou *et al.*, 1997; Flerchinger, 2000; Qin *et al.*, 2002). Where, the first three terms R_n, H and L_vE represent the atmospheric influences of net radiation, sensible heat transfer and latent heat transfer respectively. Summing the magnitude of these atmospheric influences produces a net deficit and surplus of surface energy in winter and summer respectively; the fourth term G, which represents heat transfer with the ground beneath the surface, balances the equation.

$$R_n + H + L_vE + G = 0 \tag{4-22}$$

This means the ground cools down in winter and heats up in summer. However, summing the atmospheric terms over the whole year creates an approximate balance, as shown in Equation 4-23. This means the net annual effect on ground temperature is zero. Average annual ground temperature ($T_{g,y}$) is equal at all depths down to the *seasonal stability depth* and is constant from year to year.

$$\sum_1^{365}(R_n + H + L_vE) \approx \sum_1^{365} G \approx 0 \tag{4-23}$$

The daily and monthly sums of the surface energy ($R_n + H + L_vE$) at the *HP-IRL/H* site during 2008 are presented in Figure 4-10 and Figure 4-11 respectively. The methods used to calculate these values are presented in detail in Section 5.1. Since the seasonal changes in ground energy are quite slow moving, they are not detected in Figure 4-10. However, in Figure 4-11 the net deficit and surplus patterns throughout the year are clearly evident. The short-term (hourly) ground surface energy balance is discussed in greater detail in Section 5.1. Over the year, monthly totals sum to +10kWh/m^2 rather than the theoretical total of zero. The positive and negative months sum to a total of +32kWh/m^2 and -22kWh/m^2 respectively, reflecting the mild winter of 2007 – 2008 (Met, 2010).

Interestingly, February shows a net positive flux while March shows a net negative flux, this is most likely caused by a milder than average February throwing the balance off temporarily. This suggests that this surplus energy available in February of 2kWh/m^2 could be extracted using $GSHP_{HC}$.

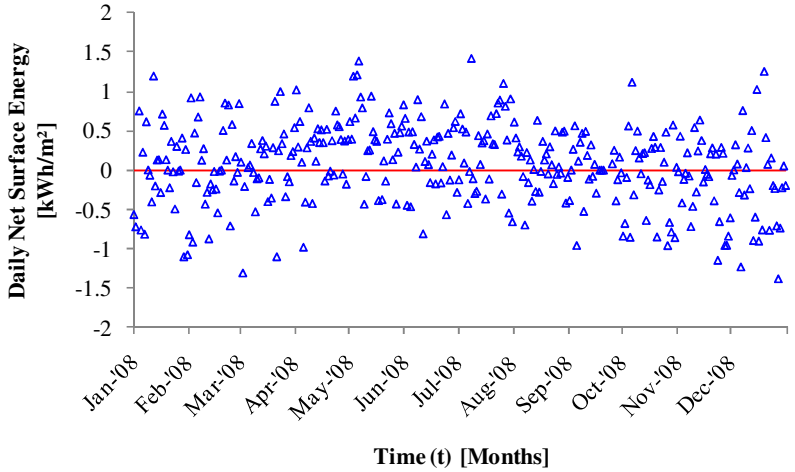

Figure 4-10: Daily net surface energy transfers at the HP-IRL/H site

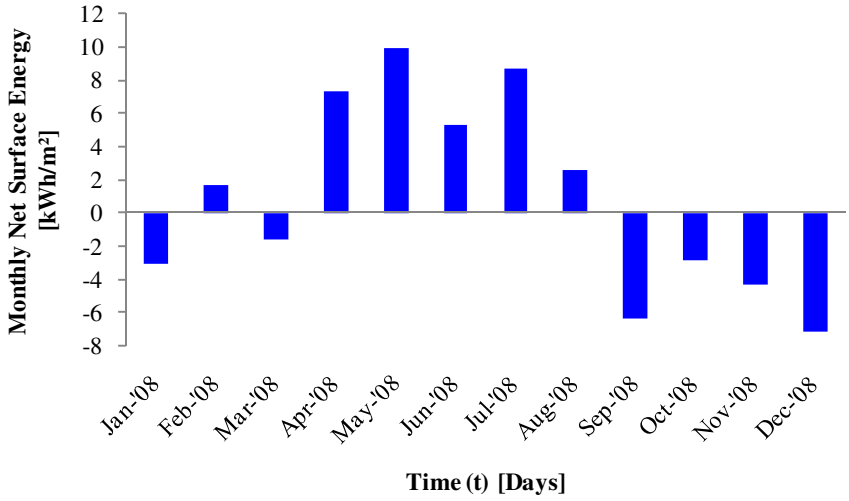

Figure 4-11: Monthly net surface energy transfers at the HP-IRL/H site

4.5.3 Seasonal Surface Oscillation and Ground Propagation

Figure 4-12(a) displays $T_{P1,\ 0.0m}$ over 3 years from January 2007 to December 2009. To the right of this, a 3 year average of these mean daily temperatures is presented. This is compared with $T_{AL\text{-}4,\ 0.0m}$ calculated using AL-4 and the input values in Table 4-5. For Table 4-5, $T_{g,y}$ was found by averaging three years worth of ground temperatures at eight different depths in P1 and $A_{sur,y}$ was established as the best fit to the three year average $T_{P1,\ 0.0m}$ oscillation. Additionally, $d_{sur,max}$ is set at 204 days which is equivalent to July 23rd meaning the phase at this time is 0 rad (Cos0 = 1) and therefore $T_{sur,d} = T_{sur,max}$ on this day which is one month after the summer solstice. The angular velocity of Earth's orbit (ω_{orb}) is found using Equation 4-15 and the daily ground diffusivity ($\alpha_{g,d}$) [m^2/d] is found using Equation 4-16, the ground

diffusivity (α_g) [m^2/s] is discussed in Sub-section 4.5.4. The R^2 evaluation of $T_{AL\text{-}4,\ 0.0m}$ at the surface is 0.8853 over three years and 0.9526 when compared with the three year average, as summarised in Table 4-6.

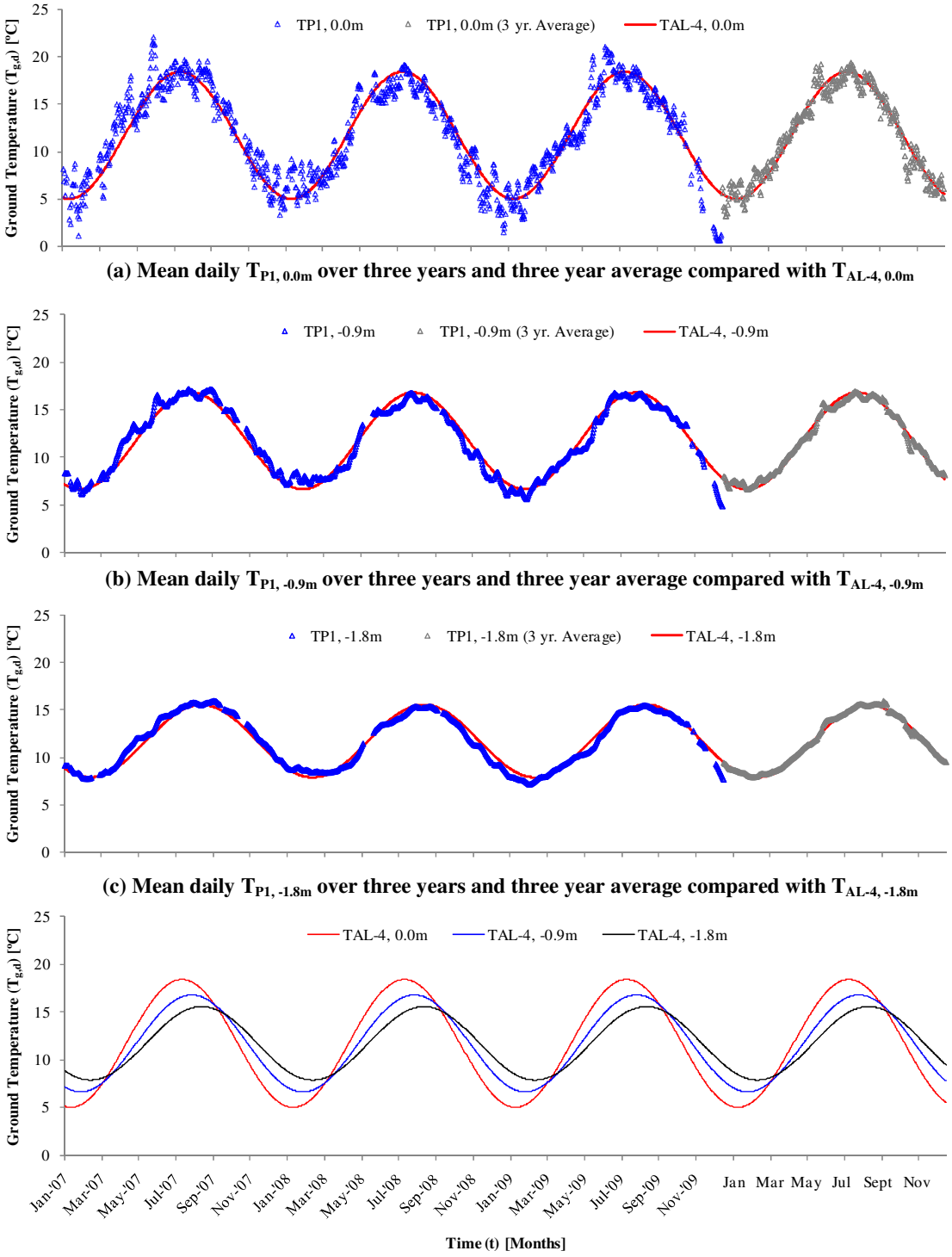

(a) Mean daily $T_{P1,\ 0.0m}$ over three years and three year average compared with $T_{AL\text{-}4,\ 0.0m}$

(b) Mean daily $T_{P1,\ -0.9m}$ over three years and three year average compared with $T_{AL\text{-}4,\ -0.9m}$

(c) Mean daily $T_{P1,\ -1.8m}$ over three years and three year average compared with $T_{AL\text{-}4,\ -1.8m}$

(d) $T_{AL\text{-}4,\ 0.0m}$, $T_{AL\text{-}4,\ -0.9m}$ and $T_{AL\text{-}4,\ -1.8m}$ plotted simultaneously

Figure 4-12: Measured and modelled ground temperatures between 2007 and 2009 and three year average ground temperatures at the ground surface, 0.9 and 1.8m depths

Table 4-5: Site specific HP-IRL/H input values used for variables in model AL-4 (Sub-section 4.2.4)

Variable	Symbol	Unit	Value
Annual Mean to Peak Amplitude	$A_{sur,y}$	[K]	6.7
Day of Maximum Temperature	$d_{sur,max}$	[day]	204
Average Annual Temperature	$T_{g,y}$	[ºC]	11.72
Angular Speed of Earth's Solar Orbit	ω_{orb}	[rad/day]	0.0172
Thermal diffusivity	$\alpha_{g,d}$	[m^2/day]	0.09072

As mentioned in Section 4.5.2, the ground acts to balance the net surface energy. The summer-surplus and winter-deficit in surface energy therefore propagate below the surface until enough energy is stored or released respectively to achieve an energy balance. Due to the time required for summer heating and winter cooling effects to penetrate into the ground, and because the successive layers of ground can store and release heat, peaks and troughs in the temperature oscillation occur later underground and the intensity of summer heating and winter cooling is reduced with depth (Campbell & Norman, 1998).

Figures 4-12(b) and (c) display $T_{P1, -0.9m}$ and $T_{P1, -1.8m}$, respectively, measured between January 2007 and December 2009 with a three year average of these measurements displayed to the right. The ground temperatures calculated with AL-4, using inputs from Table 4-5, for depths of 0.9 and 1.8m are also overlaid on Figures 4-12(b) and (c) respectively. The R^2 evaluation of AL-4 at these depths is also displayed in Table 4-6. For *HP-IRL/H*, Table 4-5 was compiled using best fit to the three year average data. The accuracy of AL-4 is therefore at its best when compared to this data, with mean R^2 of 0.978. However, the accuracy is diminished only slightly when compared with data over the three years, with mean R^2 of 0.935. As expected the accuracy of AL-4 improves with depth as shown in Table 4-6. Finally, Figure 4-12(d) highlights the amplitude attenuation and phase shift by comparing the AL-4 models of *HP-IRL/H* data at 0.0, 0.9 and 1.8m depths.

Table 4-6: Comparison of AL-4 and observed ground temperatures

		3 years				3 yr. mean			
Model	**Comparison**	**$T_{P1, 0.0m}$**	**$T_{P1, -0.9m}$**	**$T_{P1, -1.8m}$**	**Mean**	**$T_{P1, 0.0m}$**	**$T_{P1, -0.9m}$**	**$T_{P1, -1.8m}$**	**Mean**
AL-4	Linearity	1.0015	0.99976	0.9995	1.000	0.9954	0.9979	0.9971	0.997
AL-4	R^2	0.8853	0.954	0.9657	0.935	0.9526	0.9873	0.9941	0.978

4.5.4 Thermal Diffusivity

Thermal diffusivity (α_g) [m^2/s] is the ratio between the heat transfer capability of the soil known as thermal conductivity (k_g) [W/mK] and the heat storage capability of each layer known as the volumetric heat capacity (C_g) [J/m^3K]. Modelling ground surface temperature ($T_{P1,\ 0.0m}$) using analytical model AL-4 is independent of both Z and α_g (Z=0.0m) and therefore depends only on $T_{g,y}$, $A_{sur,y}$ and $d_{sur,max}$. Below the surface, the ground temperature becomes dependent on α_g and Z and also depends on the values of $T_{g,y}$, $A_{sur,y}$ and $d_{sur,max}$ used in the approximation of the surface temperature oscillation. By calibrating AL-4 using multi-year average data for a best fit to the surface oscillation $T_{P1,\ 0.0m}$ (best fit is measured using linearity and R^2 values), it follows that the best approximation of diffusivity is the value which produces a best fit for two or more underground measurement points, such as $T_{P1,\ -0.9m}$ and $T_{P1,\ -1.8m}$. For the *HP-IRL/H* site, this is a value of 1.05 x 10^{-6} m^2/s. Similar methods used to estimate the average bulk ground diffusivity are 'range and lag methods' and 'amplitudes and phase angles of the 1st and 2nd harmonics' employed by Tessy Chacko and Renuka (2002).

Figure 4-13 displays ground thermal diffusivity values presented by 7 authors from 5 distinct locations (Mei, 1987; Wibbels & Den Braven, 1994; Gauthier *et al.*, 1997; Ochsner *et al.*, 2001; Incorpera & DeWitt, 2002; Badesku, 2007; Demir *et al.*, 2009). Values quoted vary from a maximum of 1.8 x 10^{-6} m^2/s (Ochsner *et al.*, 2001) to a minimum of 1 x 10^{-7} m^2/s (Incorpera & DeWitt, 2002) with an average of 7.84 x 10^{-7} m^2/s.

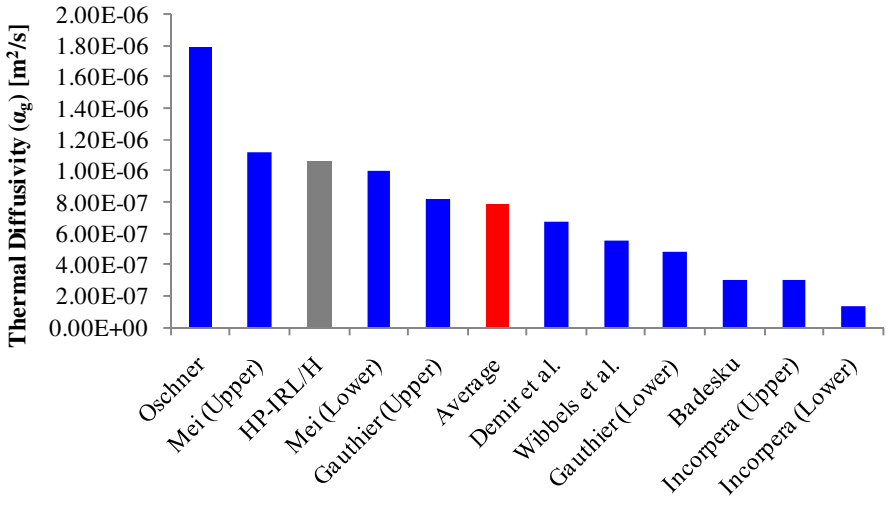

Figure 4-13: Ground/soil thermal diffusivity values/ranges quoted by seven authors

Based on the range of values quoted in the literature a *thermal diffusivity range* has been established for the purpose of subsequent comparison and discussion in this thesis. Figure 4-14 displays the linear range with a data point for each value used; the blue-dot indicates the *HP-IRL/H* value while the red-cross approximates the average value from the literature.

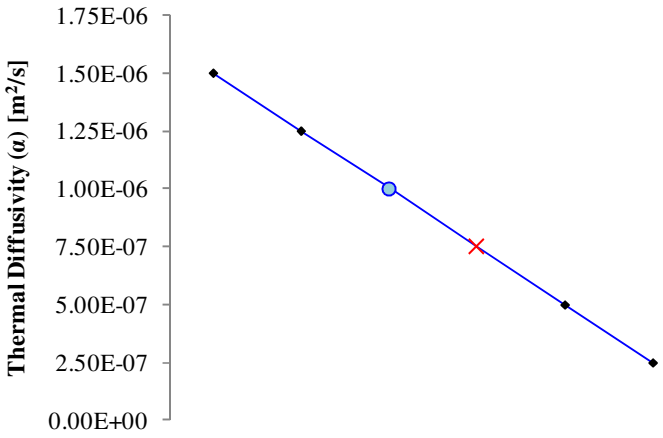

Figure 4-14: The range of reported ground thermal diffusivities used for the remainder of this thesis

4.5.5 Amplitude Dampening

The depth of penetration of the seasonal surface pattern is directly related to the ground's thermal diffusivity. The Peak Annual Temperature Variation (PATV) in $T_{g,d}$ can be calculated for any depth using Equation 4-24, where $A_{sur,y}$ [K] is the mean-to-peak amplitude of the annual T_{sur} oscillation, Z [m] is the vertical dimension (depths have negative sign), ω_{orb} [rad/d] is the rotational speed of the Earth's solar orbit defined in Equation 4-15 and the daily ground diffusivity ($\alpha_{g,d}$) [m^2/d] is found using Equation 4-16 .

$$PATV(Z) = 2A_{sur,y}\exp^{\left(Z\sqrt{\frac{\omega_{orb}}{2\alpha_{g,d}}}\right)} \quad (4\text{-}24)$$

It can be seen in Figure 4-15 that the penetration of the seasonal oscillation is greater for higher ground diffusivities, this occurs when the conduction of the ground exceeds the grounds ability to store or release heat. The average thermal diffusivity at the *HP-IRL* site has been estimated at 1.05 x $10^{-6}m^2$/s, the PATV is therefore totally dampened out by about Z= -16m, this is the *seasonal stability depth*. However, since the amplitude decays exponentially the PATV is reduced from 13.4K at Z=0m to less than 1K by Z= -10m.

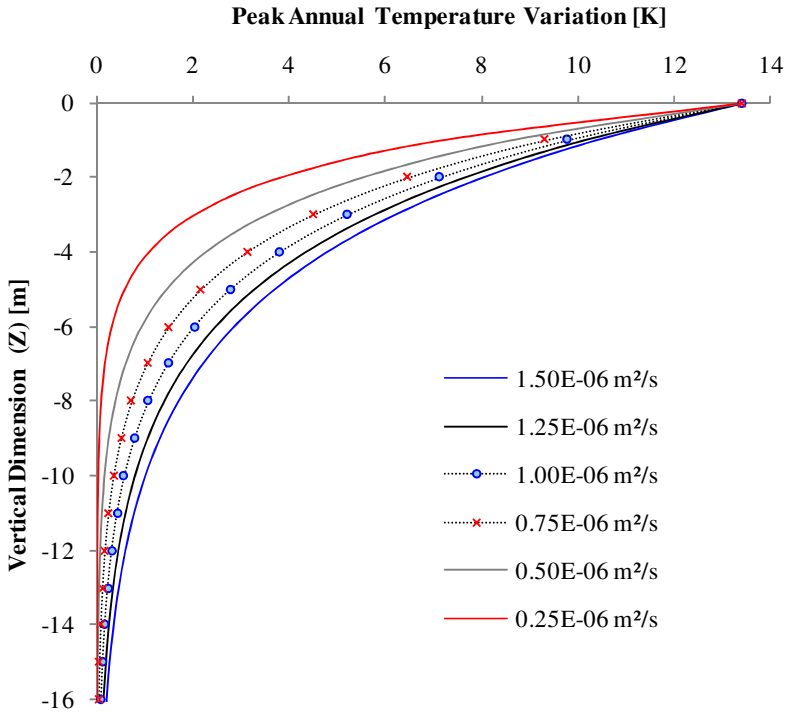

Figure 4-15: The dampening of the PATV with depth for a range of 6 ground thermal diffusivities

Based on values used to plot the line for α_g = 1.0 x 10^{-6} m^2/s in Figure 4-15, the average annual ground temperature variation from Z= 0m to Z= -16m at the *HP-IRL/H* site is 2.89K, yielding an average increase and decrease of 1.45K in summer and winter respectively. It has been shown in Figure 4-11 and discussed in Sub-section 4.5.2 that the net surplus and deficit in surface energy during the positive and negative months of 2008 were +32kWh/m^2 and -22kWh/m^2, respectively. Ignoring the milder than average winter in 2008 (Met, 2010) and assuming the surplus and deficit balance by taking the average of the 2008 values then the theoretical surplus and deficit were +27kWh/m^2 and -27kWh/m^2, respectively.

As shown in Figure 4-16, half the surplus and half the deficit cancel one another out while the remaining +13.5kWh/m^2 and -13.5kWh/m^2 heat and cool the ground above and below the average temperature $T_{g,y}$ during summer and winter respectively. Correspondingly, the following calculation estimates the amount of surplus surface energy [kWh/m^2] required to raise or lower the temperature by 1.45K in a 16m deep, vertical volume of ground with a 1m^2 cross section. The volumetric heat capacity is estimated at 2.19 x 10^6 J/m^3K, this value is discussed in Section 5.3.

$$\frac{16\text{m} * 2.19 \text{ x } 10^6 \text{J/m}^3\text{K} * 1.45\text{K}}{60\text{min} * 60\text{sec} * 1000\text{W/kW}} = 14.11\text{kWh/m}^2$$

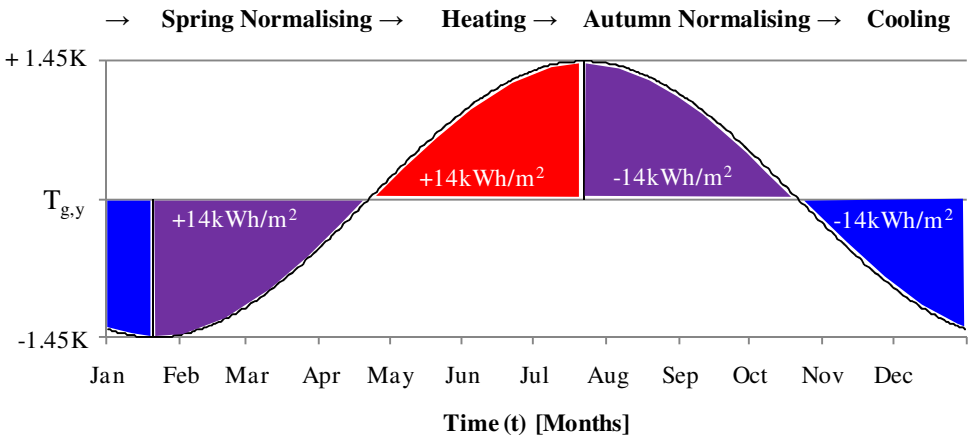

Figure 4-16: Distribution of the net surplus and deficit surface energy to ground temperature spring normalisation, summer heating, autumn normalisation and winter cooling

4.5.6 Seasonal Phase Lag

Figure 4-9(a) shows that the air and surface temperature oscillations lag behind the solar radiation oscillation by one month. In addition, the seasonal effects at the ground's surface require time to penetrate downward into the ground. Variation in seasonal phase lag with the vertical dimension (Z), defined using Equation 4-25, is shown in Figure 4-17. It can be seen that the phase lag at the *HP-IRL/H* site reaches 180 days at a depth of 10m.

$$\text{Seasonal Phase Lag } (Z) = 32 + \frac{365}{2\pi} Z \sqrt{\frac{\omega_{orb}}{2\alpha_{g,d}}} \qquad (4\text{-}25)$$

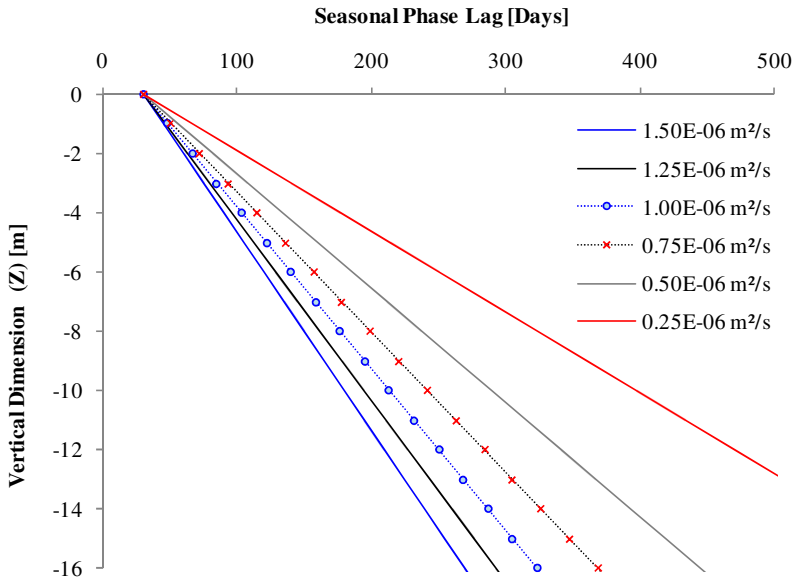

Figure 4-17: Seasonal phase lag in the ground temperature oscillation compared to the seasonal solar oscillation as a function of depth and the ground's thermal diffusivity

This means the residual of the previous summer's maximum at this point coincides with the current winter minimum at the surface. However, as was seen in Figure 4-15 the PATV has attenuated to 1K at this depth meaning the residual of the summer energy has been reduced to +0.5K.

4.6 HP-IRL/H DIURNAL RESOURCE

While the tilt in the Earth's axis of rotation as it orbits the sun produces the seasons and the change in T_{sur}, the rotation itself causes night and day and the resulting diurnal fluctuation in the T_{sur}. A surface energy balance, similar to that discussed in Sub-section 4.5.2 for the seasonal resource, applies to the diurnal resource but with a period of twenty four hours. The atmospheric terms in Equation 4-22 ($R_n + H + L_vE$) would typically (but not always) produce a net surplus and deficit in surface energy during daylight and night-time respectively. The surplus/deficit would again be balanced by heat transfer with the ground (G). This short-term energy balance is discussed in greater detail in Section 5.1.

4.6.1 Diurnal Ground Temperature Mapping

Figures 4-18 and 4-19 display the influence of diurnal cycles and weather on the GTD during a one week period in summer and winter 2008 respectively, using colour-coded temperature mapping to display temperature variation with both depth and time. The hourly solar radiation flux ($q''_{S,t}$), air temperature ($T_{a,h}$) and surface temperature ($T_{P1,\ 0.0m}$) are shown in Figures 4-18(a) and 4-19(a). Figures 4-18(b) and 4-19(b) display the observed GTD in P1 from Z= 0.0 to -1.8m. Figures 4-18(c) and 4-19(c) present the GTD from Z= 0.0 to -2m, simulated using NL-1 (described in Section 5.4), while Figures 4-18(d) and 4-19(d) contain the GTD from Z= 0.0 to -2m calculated using the analytical model AL-5. Observations from Figures 4-18 and 4-19 are:

- Impact of climate on ground temperature successfully captured by the experimental facility
- The most influential climate parameters are solar radiation in summer and air temperature (with the lack of sunshine) in winter
- Diurnal cycles (with a period of 24 hours) are driven by solar radiation cycles and penetrate to Z= -0.5 to 0.7m; whereas prolonged 4 to 5 day weather events penetrate to Z= -1.5m

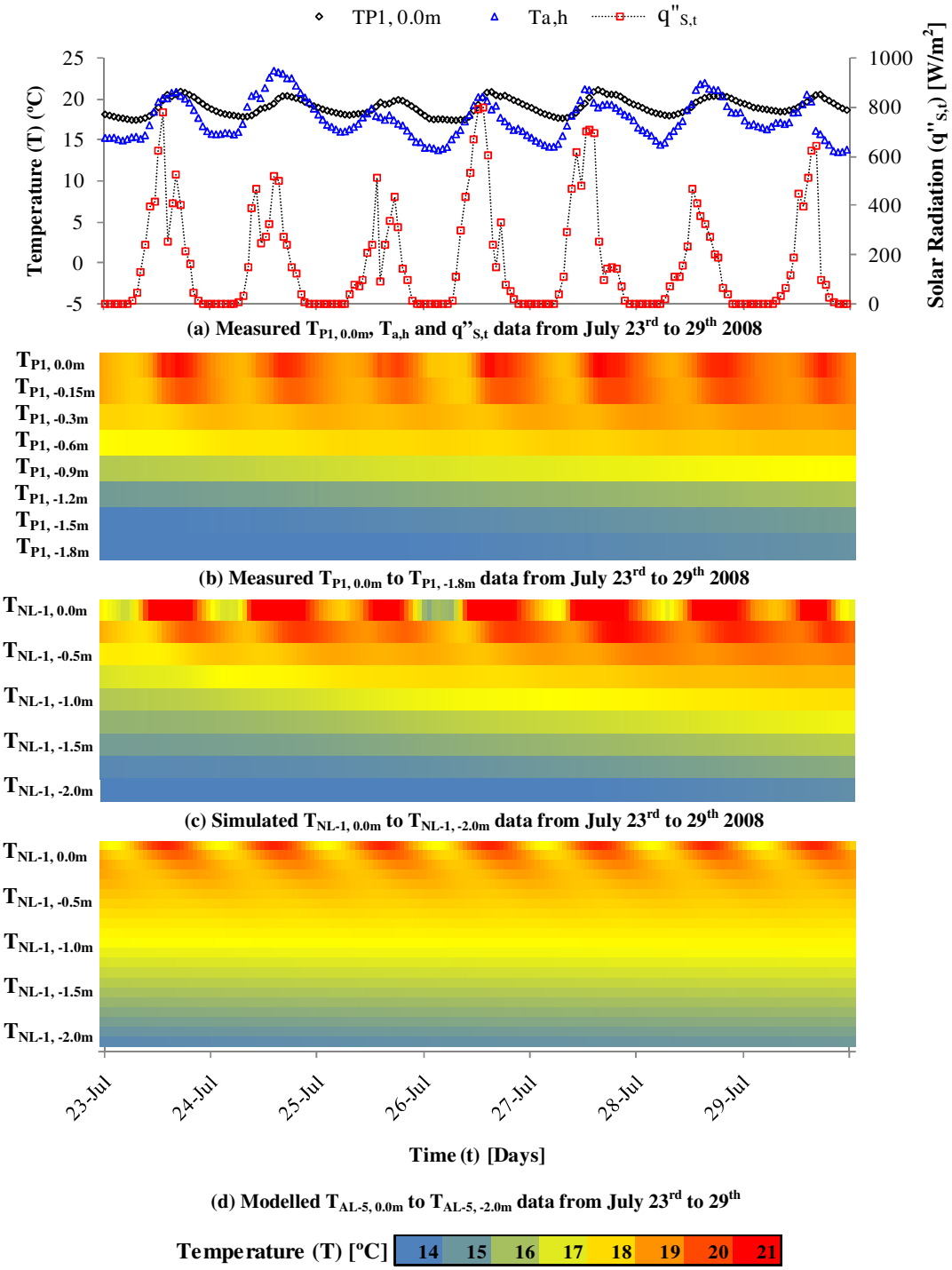

Figure 4-18: Plots of ground temperature variation with time and depth taken from measured data, a numerical simulation and an analytical model over one summer week in July 2008

- In general both the analytical (AL-4) and numerical (NL-1) methods give a good approximation of ground temperatures, R^2 accuracy is discussed in Section 5.4:
  - Analytical methods are based on multiyear averages and as expected do not include weather events but can replicate temperatures at Z= -1.0m

- Numerical methods are based on energy balance and therefore are sensitive to weather events accurately predicting temperature changes near the surface

➢ It is clear from Figure 4-19 why collectors are buried below Z= -1.0m in *Continental* regions since even a moderate *Cool Marine* cooling-event penetrates to this depth after 4 to 5 days

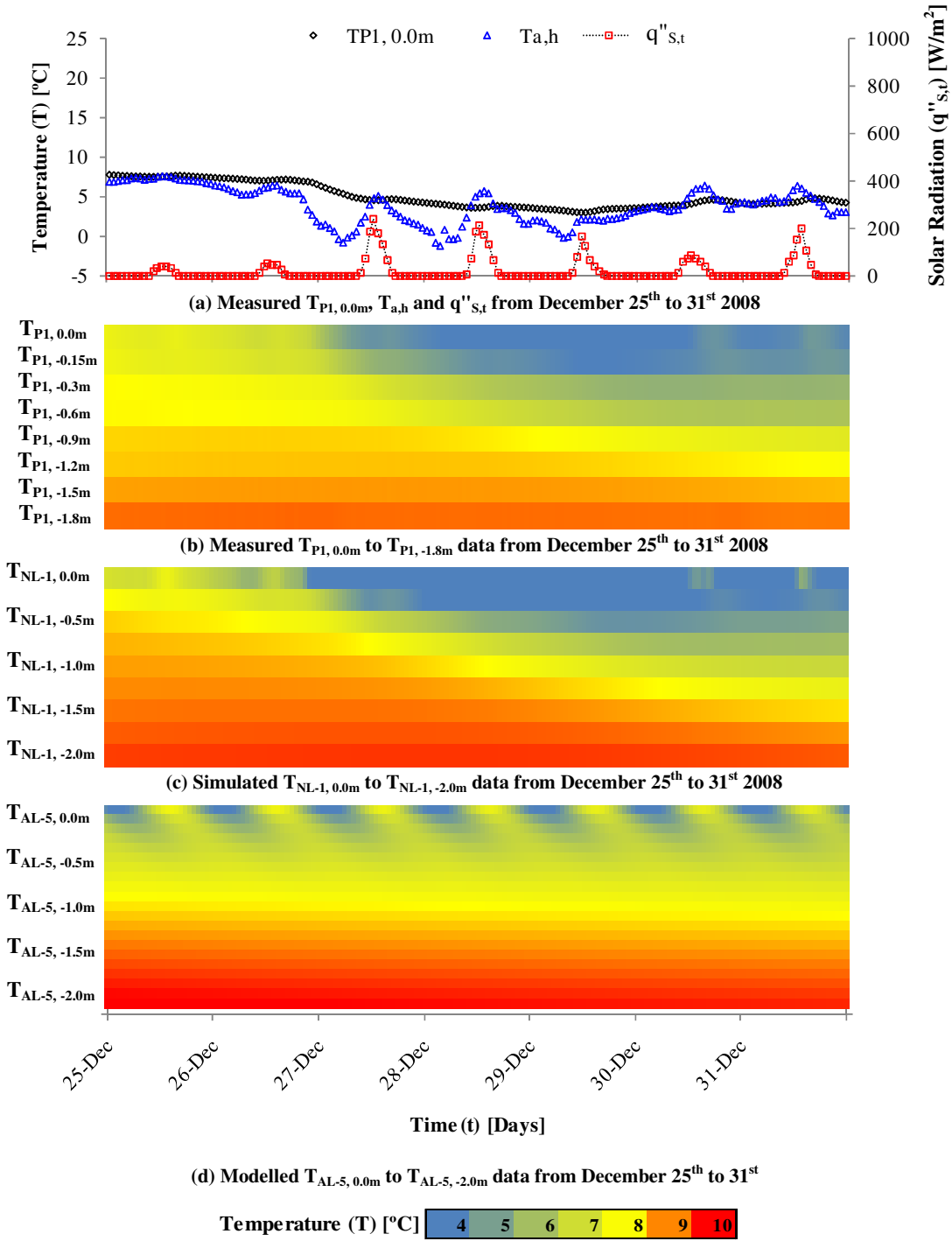

Figure 4-19: Plots of ground temperature variation with time and depth taken from measured data, a numerical simulation and an analytical model over one winter week in December 2008

4.6.2 Diurnal Surface Oscillation

As it is difficult to establish predictive accuracy from the colour coded maps in Figures 4-18 and 4-19, this section explores ground temperature predictive accuracy using standard time series plots for a sample week taken from midway through each of the four seasons.

The idealised hourly surface temperature ($T_{sur,h}$) oscillates about the daily average ($T_{sur,d}$) in accordance with Equation 4-18, lowest before dawn and highest in the afternoon. Figure 4-20 displays surface temperatures calculated using AL-5, using the inputs from Table 4-7, compared with measured $T_{P1,\ 0.0m}$ values for a one-week period during spring, summer, autumn and winter. The sources of $T_{g,y}$, $A_{sur,y}$, ω_{orb}, $\alpha_{g,d}$ and $d_{sur,max}$ were discussed in Sub-section 4.5.3 and values are presented in Table 4-5. For Table 4-7, the diurnal mean-to-peak amplitude $A_{sur,d}$ was found using three-years worth of daily mean, maximum and minimum ground surface temperatures from *HP-IRL/H*. The angular velocity of Earth' rotation ω_{rot} is calculated using Equation 4-19. The hourly thermal diffusivity $\alpha_{g,h}$ [m^2/h] is calculated using Equation 4-20 where thermal diffusivity α_g [m^2/s] is discussed in Sub-section 4.5.4. The hour of maximum surface temperature ($hr_{sur,max}$) is set as 4 hours after solar noon; however, noon at the *HP-IRL/H* site varies from 12:30 to 13:30 with daylight savings so $hr_{sur,max}$ is set to 16:30 between October and March and 17:30 for the remainder of the year.

Table 4-7: HP-IRL/H inputs for variables in AL-5

Variable	Symbol	Units	Value
Daily Mean to Peak Amplitude	$A_{sur,d}$	[K]	1.97
Hour of Maximum Temperature	$hr_{sur,max}$	[h]	16.5 – 17.5
Hourly Thermal Diffusivity	$\alpha_{g,h}$	[m^2/h]	0.00378
Angular Velocity of Earth's Rotation	ω_{rot}	[rad/h]	0.2618

Seasonal phase lag mentioned in Sub-section 4.5.6 is seen in Figures 4-20(a) and (c) with March temperatures still below average from winter cooling and September temperatures still above average from summer heating. Figure 4-20 shows that at times such as the evening of March 18th, 21st and 24th and June 20th and 23rd 2008 the analytical expression in Equation 4-18 gives a remarkable prediction of T_{sur} with very little input information. However, at other times such as the mornings of December 20th to 26th 2008 there is a 4 to 5K error in mean hourly surface temperature prediction/replication. This is to be expected, as AL-5 is based on a multi-year average waveform and these large discrepancies are associated with short or medium term weather events.

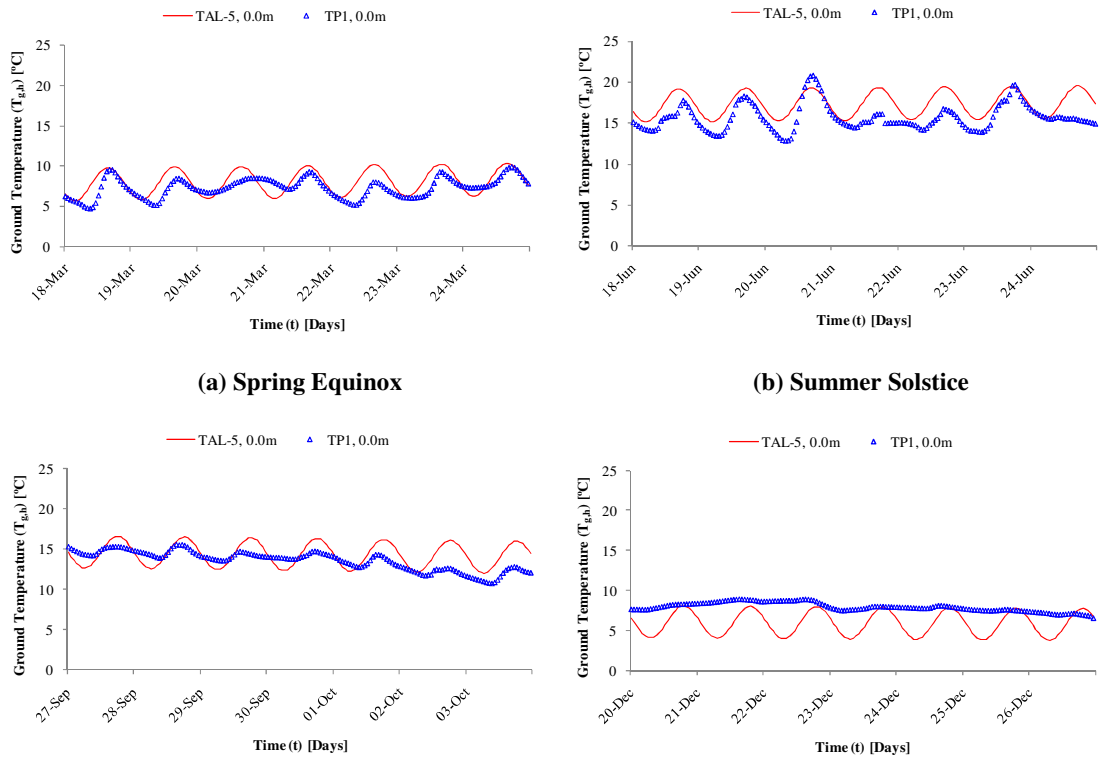

(a) Spring Equinox **(b) Summer Solstice**

(c) Autumn (DAQ outage on 21st) **(c) Winter Solstice**

Figure 4-20: Measured ($T_{P1,\ 0.0m}$) and predicted ($T_{AL\text{-}5,\ 0.0m}$) ground temperatures in P1 for each season of 2008

When comparing $T_{AL\text{-}5,\ 0.0m}$ to $T_{P1,\ 0.0m}$ over 12 months, AL-5 has an R^2 value of only 0.84, this increases to 0.89 at $T_{P1,\ -0.15m}$ and 0.95 at $T_{P1,\ -0.9m}$ (equivalent to AL-4). While AL-5 is a useful tool for understanding the timing and depth of penetration of diurnal cycles it lacks accuracy when predicting/replicating hourly surface temperatures.

4.6.3 Short Term Weather Influence

The inaccuracy of Equation 4-18 to predict hourly surface temperatures, as displayed in Figure 4-20, can be partly attributed to the seasonal variation in diurnal surface temperature amplitude ($A_{sur,d}(d)$) but is primarily due to the influence of local short term weather patterns (cold fronts, warm fronts, winds, clouds) which cannot be predicted/replicated with a basic waveform like Equation 4-18.

Seasonal variation in diurnal amplitude is due to the driving forces of diurnal amplitude, such as solar intensity, being weaker in spring and autumn than in summer for example. Attempts have been made to account for this by introducing a third oscillation, into Equation 4-18, which describes the variation in the daily amplitude through the year (Elias *et al.*, 2004).

However, the best way to account for this seasonal variance and, more significantly, the short term weather fluxes is to carry out a transient hourly surface energy balance. The primary variables in the balance are net solar and long-wave radiation, air temperature, wind speed and relative humidity. A finite difference energy balance technique, identified as NL-1, was created as part of *HP-IRL/H* and allows for the simulation of hourly ground temperatures at any depth. NL-1 is presented in Section 5.4 along with a combined heat and moisture model of P1 created in the *SHAW23* simulation environment and identified as NL-2.

4.6.4 Ground Propagation

Due to the time lag and the heat storage in successive ground layers, discussed for the seasonal resource in Sub-section 4.5.3, tracking the diurnal oscillation as it propagates underground involves a dampened oscillation. It is necessary to sum together two dampened oscillations, one seasonal and one diurnal. Some authors state that one dampened wave can describe ground penetration of the diurnal oscillation in the same way as the seasonal oscillation (Campbell & Norman, 1998). However, one dampened oscillation is typically not sufficient since $T_{g,d}$ oscillates about $T_{g,y}$ which is equal at all depths, while the $T_{g,h}$ oscillates about ($T_{g,d}$(d,Z)) which varies with both time and depth. Equation 4-18, which sums the idealised $T_{g,d}$ and $T_{g,h}$ oscillations, can describe the diurnal propagation as displayed in Figure 4-21. The R^2 accuracy of AL-5 is discussed in greater detail in Sub-section 5.4.3 where AL-5, NL-1 and NL-2 are compared. The amplitude dampening and phase shift in the diurnal oscillation between 0.0 and -0.15m is clearly evident in Figures 4-21(a) and (b); the predictive accuracy also improves with depth.

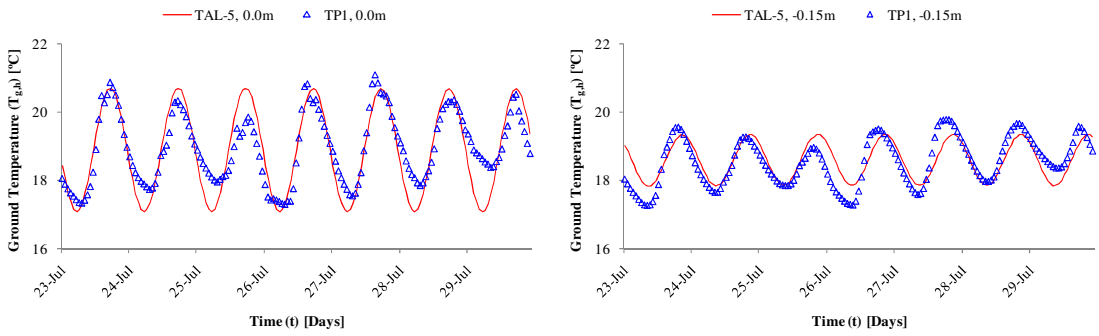

(a) $T_{AL\text{-}5,\ 0.0m}$ compared with $T_{P1,\ 0.0m}$ **(b) $T_{AL\text{-}5,\ -0.15m}$ compared with $T_{P1,\ -0.15m}$**

Figure 4-21: Measured and predicted hourly surface ($T_{P1,\ 0.0m}$) and ground temperatures ($T_{P1,\ -0.15m}$) for reference profile P1 during one week in July, 2008

4.6.5 Amplitude Dampening

Like the seasonal oscillation, the depth of penetration of the diurnal oscillation is directly related to the grounds heat transfer to heat storage ratio, the thermal diffusivity (α_g) [m^2/s]. The Peak Diurnal Temperature Variation (PDTV) in $T_{g,h}$ can be calculated using Equation 4-26, where $A_{sur,d}$ [K] is the mean-to-peak amplitude of the daily T_{sur} oscillation, Z [m] is the vertical dimension, ω_{rot} [rad/h] is the angular velocity of the Earth's rotation and $\alpha_{g,h}$ [m^2/h] is the hourly thermal diffusivity defined in Table 4-7.

$$PDTV(Z) = 2A_{sur,d}\exp^{\left(Z\sqrt{\frac{\omega_{rot}}{2\alpha_{g,h}}}\right)} \quad (4\text{-}26)$$

It can be noted from Figure 4-22 that the depth of penetration of the diurnal oscillation increases with diffusivity where the heat transfer rate supersedes the heat storage. For *HP-IRL/H*, with a diffusivity of approximately 1.05 x $10^{-6}m^2/s$, the PDTV is eliminated by Z= -1m this is the *diurnal stability depth*. Since the PDTV undergoes exponential decay it is reduced from 4K at Z= 0.0m to less than 0.5K at Z= -0.3m.

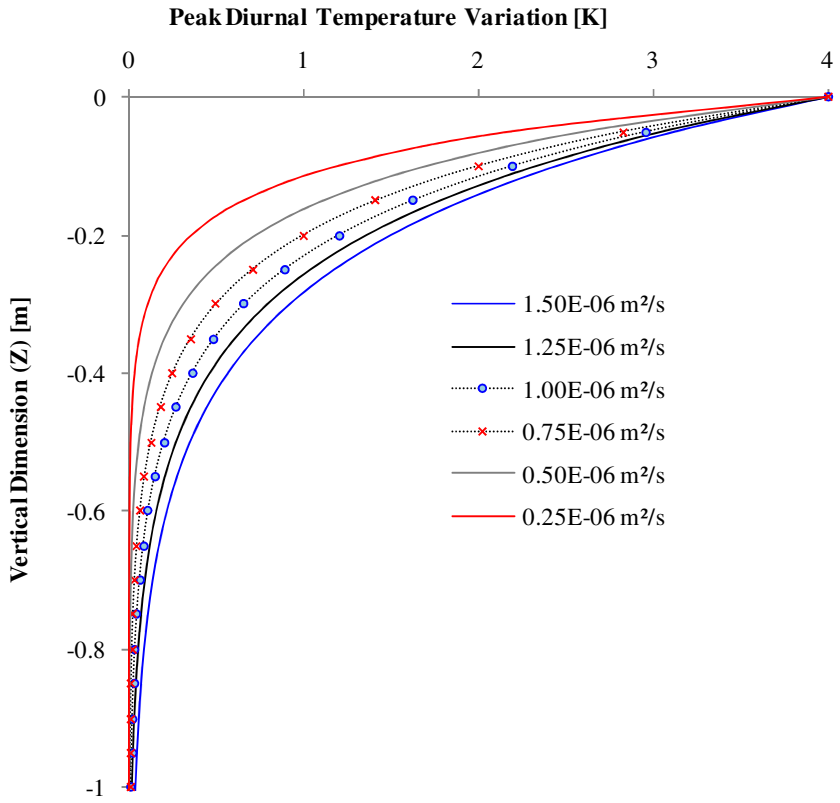

Figure 4-22: The reduction of the peak daily surface temperature variation with depth for a range of 4 thermal diffusivities

4.6.6 Diurnal Phase Lag

In the same way as the annual surface temperature oscillation lags the radiation totals in Figure 4-9, so too the diurnal ground temperature oscillation lags the hourly radiation intensity. Figure 4-23 and Figure 4-24 display measured and modelled variations in solar radiation, air temperature and surface temperature for a day in both March and June of 2008 respectively. It can be seen on both days that air temperature lags solar radiation by 2 to 3 hours (2 hours in AL-3) while ground temperature lags solar radiation by 3 to 4 hours (4 hours in AL-5). It can also be seen that daylight savings shifts all three oscillations by one hour.

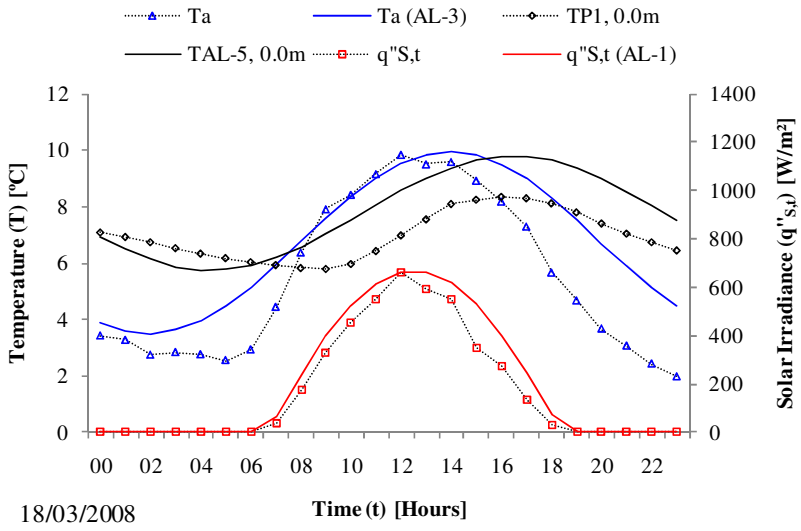

Figure 4-23: Data and models of radiation, air temperature and surface temperature during March 2008 displaying the diurnal time lag at the surface

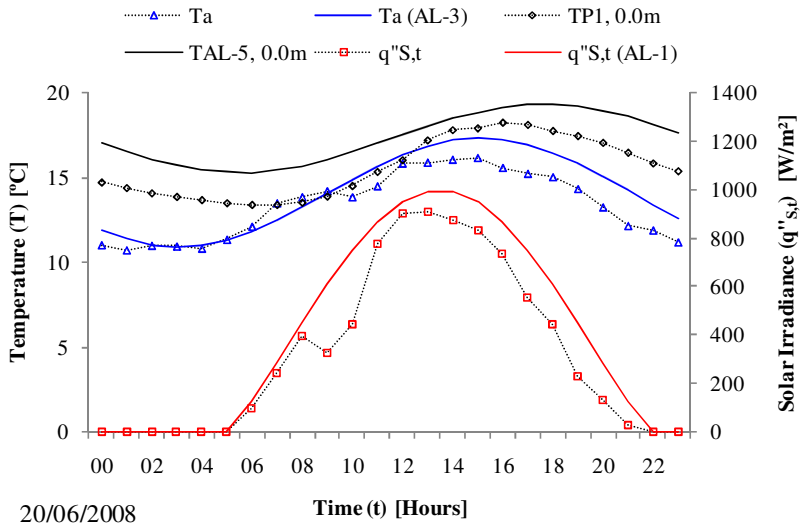

Figure 4-24: Data and models of radiation, air temperature and surface temperature during June 2008 displaying the diurnal time lag at the surface

In addition, the diurnal influences at the ground's surface require time to penetrate downward into the ground. This phase lag is accounted for with a linear phase lag term in Equation 4-18 and is presented in Equation 4-27, where Z [m] is the vertical dimension, ω_{rot} [rad/h] is the angular velocity of the Earth's rotation and $\alpha_{g,h}$ [m^2/h] is the hourly thermal diffusivity defined in Table 4-7.

$$\text{Diurnal Phase Lag } (Z) = 4 + \frac{24}{2\pi} Z \sqrt{\frac{\omega_{rot}}{2\alpha_{g,h}}} \quad (4\text{-}27)$$

Figure 4-25 displays the phase lag in the diurnal oscillation with depth. It can be seen that at the *HP-IRL/H* site the phase lag is equivalent to 12 hours at Z= -0.4m. This means the oscillations maximum at this point corresponds to the minimum at the surface. However Figure 4-22 shows that the PDTV has reduced to approximately 0.25K at this depth, meaning the residual of the noon energy from the previous day has been reduced to +0.125K.

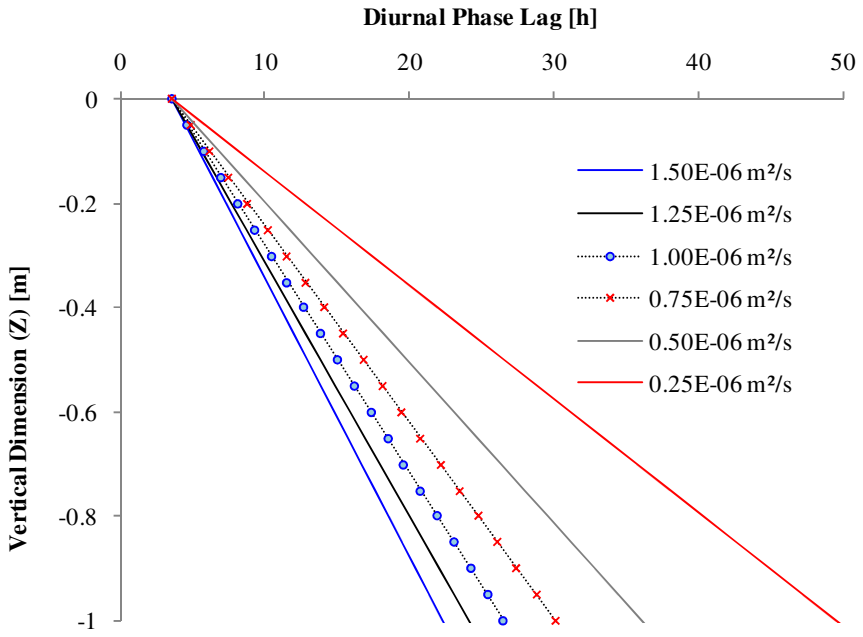

Figure 4-25: Diurnal phase shift in ground temperature oscillations compared to the diurnal solar radiation oscillation

4.7 SUMMARY

This chapter presented an analysis of the ground temperature distribution, which varies with both time and depth, and makes the following contributions to the objectives of the *HP-IRL/H* project:

- The *seasonal* (≈ -8 to -15m) and *diurnal* (≈ -0.5 to -1.5m) *stability depths* which depend on ground-type were established, along with the vertical dimension (Z), in order to define 3 ground heat resources:
  - *Geothermal resource* – below the *seasonal stability depth*
  - *Seasonal resource* – between the *diurnal* and *seasonal stability depths*
  - *Diurnal resource* – between the surface and the *diurnal stability depth*
- 5 simple periodic models, identified as analytical methods AL-1 to AL-5, were developed in order to describe the timing and amplitude of periodic variations in:
  - Daily and hourly solar radiation intensity
  - Daily and hourly air temperature
  - Daily and hourly ground temperature variation with depth
- A review was conducted of 11 ground temperature studies, from 11 countries with 9 different climate classifications between 1996 and 2009
  - Based on 5 of the 11 studies, the air and ground temperature records from 9 sites at 9 different latitudes with 7 different climate classifications were compared using models AL-2 and AL-4 to summarise air and ground temperature variation, the findings are summarised in detail in Sub-section 4.3.7
- The *geothermal gradient* at the *HP-IRL/H* site was examined using 3 years worth of ground temperature measurements between Z= 0 and -95m, results showed that:
  - At depths greater than -50m, the expected *geothermal gradient* of 10.44K/km exists
  - Between the surface and -50m, the *geothermal gradient* appears insignificant, however it may be masked by above average surface temperatures in 2008 and 2009
- The experimental facility successfully measured the influence of the seasonal and diurnal cycles, as well as the short term weather events, which impact on *HP-IRL/H* ground temperatures
- The average ground temperature over 3 years between Z= 0 and -1.8m was found to be 11.72ºC ±0.3ºC while the average air temperature was 9.8ºC ±0.3ºC during the same period
- The mean-to-peak amplitude in the ground and air temperature seasonal oscillations were found to be 6.7 and 5.2K respectively
- The maximum surface temperatures at *HP-IRL/H* site occur on July 23rd this is 32 days after the summer solstice

- The average thermal diffusivity value between Z= 0 and -1.8m was found to be 1.05 x 10^{-6} m^2/s
- The *seasonal stability depth* at the *HP-IRL/H* site was found to be at Z= -16m
- The average seasonal temperature variation in this 16m volume was 2.9K
    - The summer heating and winter cooling of 1.45K and -1.45K correspond to a surface energy surplus and deficit of +14.11kWh/m^2 and -14.11kWh/m^2 respectively
    - An additional surplus and deficit of 14.11kWh/m^2 and -14.11kWh/m^2 cancel each other out in the spring and autumn normalisation phases
    - Interactions at the surface produce a surplus and deficit of +32 kWh/m^2 and -22 kWh/m^2 during two 6 month in 2008
- Model AL-4 was calibrated to replicate 3 year average ground temperatures with an accuracy of R^2 = 0.978 for all depths between Z= 0.0 and -1.8m and could then predict daily ground temperatures with an accuracy of R^2= 0.935 for all depths between Z =0 and -1.8m over three years
- The mean-to-peak amplitude of the diurnal surface temperature oscillation was found to be 1.97K
- The maximum surface temperature occurred 3 to 4 hours after solar noon, values of 16:30 and 17:30 were established for normal and daylight savings times respectively
- The *diurnal stability depth* was established at Z= -1m
- The R^2 accuracies of AL-5 when used to predict $T_{P1,\ 0.0m}$ and $T_{P1,\ -0.15m}$ were 0.84 and 0.89 respectively, further information on hourly temperatures is presented in Section 5.4.3
- These findings on the *seasonal* and *diurnal resource* oscillations can be used in *CSDC* for design and intelligent control of *split-level collectors* which utilize positive elements of both resources in order to achieve COP gain for $GSHP_{HC}$

Chapter 5 continues this investigation of ground thermal energy resources by investigating ground heat transfer processes, thermal properties and methods to maximise solar energy absorbed and retained by the ground surface layer.

CHAPTER 5

GROUND HEAT TRANSFER

GMIT
GALWAY-MAYO INSTITUTE OF TECHNOLOGY
INSTITIÚID TEICNEOLAÍOCHTA NA GAILLIMHE-MAIGH EO

5. GROUND HEAT TRANSFER

While the solar-driven *seasonal* and *diurnal resources* at the *HP-IRL/H* site were characterised using temperature mapping and analytical methods in Chapter 4, subsequent characterisation and simulation of interactions between the $GSHP_{HC}$ and the ground in Chapters 6 and 7, require a more in depth understanding of ground heat transfer and thermal properties. Therefore, this chapter investigates the transient heat-transfer processes at the *ground-atmosphere interface*, heat movement in the underground layers and thermal properties. In all over 20 publications on ground heat transfer were reviewed. Thermal properties of the ground were measured and compared with common correlations. Two types of 1-D simulations representing ground heat transfer were conducted in order to test methods which can be adapted to simulate $GSHP_{HC}$ and climate interaction with the ground in Chapter 7. This chapter is divided into five sections:

- *Ground-atmosphere interface*
- Underground heat transfer
- Thermal and hydraulic properties
- Ground temperature simulation
- Influence of surface cover

5.1 GROUND-ATMOSPHERE INTERFACE

Since the transfer processes which influence both the *seasonal* and *diurnal* ground thermal energy resources, defined in Chapter 4, occur at the *ground-atmosphere interface*, a theoretical review of these processes relevant to the *HP-IRL/H* site is presented.

5.1.1 Literature Review

Eight of the relevant studies, undertaken between 1993 and 2009 which describe thermal energy transfer at the *ground-atmosphere interface* are presented in Table 5-1. These studies were undertaken to investigate diverse aspects ranging from the impact of freeze/thaw processes (Engelmark & Svensson, 1993) to the effect of permeable and non-permeable pavements on ground temperature (Asaeda & Thanh Ca, 2000). These studies represent findings from 9 countries and 6 *climate classifications* with only one author reporting from the Irish *Cool Marine* climate (Mihalakakou, 2002). The methods and findings of these authors and others are discussed in detail throughout the subsequent text.

Table 5-1: Literature review on heat transfer at the ground-atmosphere interface

No.	Study (Year)	Location	Typical Climate Classification	Research Topic
1.	Engelmark and Svensson (1993)	Canada	*Moderate Sub-polar*	Numerical modelling of freezing and thawing in soil
2.	Šafanda (1999)	Czech Republic	*Humid Continental*	Surface temperature as a function of slope angle and orientation
3.	Asaeda and Ca (2000)	Japan	*Humid Continental*	Permeable pavement during hot summer weather
4.	Popiel et. al. (2001)	Poznan, Poland	*Humid Continental/Cool Littoral*	Effects of surface cover
5.	Mihalakakou (2002)	Athens, Greece and Dublin, Ireland	*Dry Summer Subtropical* and *Cool Marine* respectively	Estimating soil surface temperature
6.	Qin *et. al.* (2002)	Isreal and Sweden	*Dry Summer Subtropical/Semiarid Continental* and *Cool Littoral* respectively	Complete surface energy balance
7.	Palyvos (2008)	Greece	*Dry Summer Subtropical*	Convection heat transfer in urban environments
8.	Saito and Šimůnek (2009)	Japan and USA	*Humid Continental*	Effect of meteorological models on surface energy balance simulations

Note: *Climate classifications* based on Koeppe and De Long (1958)

5.1.2 Ground-Atmosphere Interface Energy Balance

The *ground-atmosphere interface* can be either the bulk ground surface (for bare ground) or the exposed surface of a covering material (for grass/shrub covered ground). For the purposes of clarity, the following definitions have been implemented:

- Surface cover temperature (T_{cov}) [ºC]: refers to the temperature of the non-bulk (standing or diffuse) ground cover material such as grass or shrubs (at $Z > 0$m)
- Ground surface temperature (T_{sur}) [ºC]: refers to the surface temperature of the first bulk ground layer such as soil, gravel, brick, concrete or asphalt (at $Z = 0$m)
- Ground temperature (T_g) [ºC]: refers to the temperature of the bulk ground layers beneath the surface (at $Z < 0$m)
- GTD: as defined in Chapter 4, refers to the spatial and temporal variation of the ground temperature (T_g) in all the bulk ground layers

A thermal energy balance is the most common way to define heat transfer at the *ground-atmosphere interface*. A schematic of the key thermal energy transfers at this interface is shown in Figure 5-1.

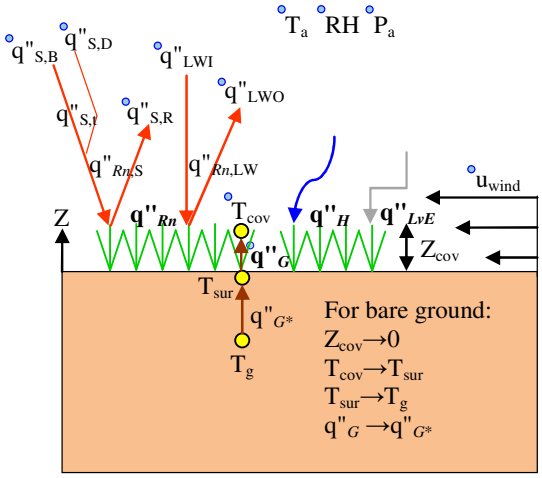

Figure 5-1: Schematic of the thermal energy transfers occurring at the ground-atmosphere interface for covered (Z_{cov}) and bare ($Z_{cov}\rightarrow 0$) ground surfaces; the blue dots identify the parameters measured at the *HP-IRL/H* site

The standard expression for the energy balance, introduced in Equation 4-22, is now re-written using heat flux terms and expressed in Equation 5-1 without a storage term (Mihalakakou *et al.*, 1997; Flerchinger, 2000; Qin *et al.*, 2002; Mihalakakou, 2002).

$$q"_{R_n} + q"_H + q"_{L_vE} + q"_G = 0 \tag{5-1}$$

When an energy storage term is included, the energy balance is then expressed using Equation 5-2, where ΔZ [m] is the thickness of the *ground-atmosphere interface* layer of density (ρ) [kg/m^3] and specific heat capacity (c) [J/kgK].

$$\rho c \Delta Z \frac{dT}{dt} = q"_{R_n} + q"_H + q"_{L_vE} + q"_G \tag{5-2}$$

The grouped terms on the left represent the rate of change in heat storage [W/m^2] and the terms on the right represent the net radiation flux ($q"_{Rn}$) [W/m^2], sensible heat flux ($q"_H$) [W/m^2], evaporation heat flux ($q"_{LvE}$) [W/m^2] and ground heat flux ($q"_G$) [W/m^2] respectively.

This expression or similar has been used in *Dry Summer Subtropical* and *Cool Marine* regions (Mihalakakou *et al.*, 1997; Mihalakakou, 2002), *Dry Summer Subtropical* and *Semi-arid Continental* regions (Qin *et al.*, 2002) and *Moderate Sub-polar* regions (Hermansson, 2004) to predict *ground-atmosphere interface* temperature. It has also been used in combination with precipitation analysis to predict ground temperature, moisture content and ice content in a Simultaneous Heat and Water model (*SHAW23*), which is suitable for the majority of *climate classifications* (Flerchinger, 2000).

The first term in Equation 5-2 is $q"_{Rn}$ [W/m^2] which represents net thermal radiation heat flux. As shown in Figure 5-1, this is the sum of the net solar (short-wave) ($q"_{Rn,S}$) and net long-

wave ($q''_{Rn,LW}$) thermal radiation fluxes at the *ground-atmosphere interface* as presented in Equation 5-3 (Saito & Simunek, 2009).

$$q''_{R_n} = q''_{R_n,S} + q''_{R_n,LW} = (1 - a)q''_{S,t} + (\varepsilon_{cov}\varepsilon_a\sigma T_a^4 - \varepsilon_{cov}\sigma T_{cov}^4) \text{ (bare ground, } T_{cov} \rightarrow T_{sur}) \quad (5\text{-}3)$$

Thermal radiation occupies a wavelength range from 0.1 to 100μm in the spectrum of electromagnetic radiation and represents radiation emitted from an object because of its temperature (Incorpera & DeWitt, 2002). This range can be sub-divided into the visible (0.4 to 0.7μm) and infrared (0.75 to 100μm) ranges.

The short-wave or solar incoming heat flux ($q''_{S,t}$) [W/m^2] is the sum of all shortwave radiation coming from the Sun to the *ground-atmosphere interface*. The Sun is often approximated as a blackbody at 6000K; solar radiation has a wavelength between 0.29 and 4.0μm with 45% in the visible spectrum and 55% in the near-infrared spectrum (Campbell & Norman, 1998). The $q''_{S,t}$ reaches the ground as either beam ($q''_{S,B}$) [W/m^2] or diffuse ($q''_{S,D}$) [W/m^2] radiation. Beam radiation is received directly from the Sun through relatively clear skies, while diffuse radiation is shortwave solar radiation which has been disrupted by media in the Earth's atmosphere, such as clouds.

The intensity of the beam radiation ($q''_{S,B}$) at the *ground-atmosphere interface* is proportional to the cosine of the sun's angle of incidence (Θ) [º]. The angle Θ (the angle between the Sun's rays and a surface normal) depends on the sites latitude (Ω) [º], slope (β) [º] and orientation (γ) [º] along with the day of the year (d) and hour of the day (hr). The influence of Ω, β, γ, d and hr can be accounted for using vector analysis (Sproul, 2007); the Sproul method is incorporated within model AL-1 in Sub-section 4.2.1. However, cloud cover also influences $q''_{S,B}$ and this parameter depends on the changing local weather patterns, the prediction of which is beyond the scope of *HP-IRL/H*.

For this reason the variation in total $q''_{S,t}$ is measured at the *HP-IRL/H* site using the *Kipp and Zonen CMP3* pyranometer described in Section 3.6. The diffuse component ($q''_{S,D}$) is also measured using the *CMP3* pyranometer fitted with a 'shadow ring' (shown in Figure 3-24(b)) to remove the beam component ($q''_{S,B}$) which can then be calculated ($q''_{S,B} = q''_{S,t} - q''_{S,D}$). The *ground-atmosphere interface* reflects some of this incident radiation ($q''_{S,R}$) [W/m^2] and the ratio of reflected radiation to incident radiation ($q''_{S,R}$ / $q''_{S,t}$) is known as albedo (a) [-]. Therefore, (1 - a) $q''_{S,t}$ is the net of the shortwave radiation ($q''_{Rn,S}$) that is absorbed by the ground surface as quantified in Equation 5-3.

The net longwave radiation heat flux ($q''_{Rn,LW}$) [W/m^2] is thermal radiation between 4.0 and 100μm (typically peaking at 10μm) (Campbell & Norman, 1998) and is found by subtracting the outgoing longwave radiation flux (q''_{LWO}) [W/m^2] from the incoming longwave radiation flux (q''_{LWI}) [W/m^2]. The outgoing longwave radiation results from the *ground-atmosphere interface* radiating heat to the atmosphere and is therefore related by the *Stephan-Boltzmann Law* to the fourth power of T_{cov} [K] multiplied by the surface emissivity (ε_{cov}) [-] and the Stephan-Boltzmann constant (σ) [5.6697 x 10^{-8} W/m^{2}K^4] as shown in Equation 5-3. The incoming longwave radiation results from the atmosphere radiating heat to the *ground-atmosphere interface* and is therefore related to the fourth power of the atmosphere's temperature T_a [K] by the atmosphere's emissivity (ε_a) [-] and the Stephan-Boltzmann constant (σ), as shown in Equation 5-3. Since the *ground-atmosphere interface* in turn reflects some (1 - ε_{cov}) of this radiation the absorbed incoming component is represented by $\varepsilon_{cov}\varepsilon_a\sigma T_a^4$ in Equation 5-3. The emissivity of the atmosphere (ε_a) can be related to the air temperature (T_a) [K] and relative humidity (RH) [%] of the atmosphere (Golaka & Exell, 2004; Saito & Simunek, 2009). Both the incoming and outgoing longwave radiation components q''_{LWI} and q''_{LWO} respectively are measured at the *HP-IRL* site using *Kipp and Zonen CGR3* pyrgeometers as described in Section 3.6.

The second term in Equation 5-2 is the sensible heat flux (q''_H) [W/m^2] at the *ground-atmosphere interface*. This sensible heat transfer occurs through the combined processes of conduction and advection (bulk fluid motion) in the air above the *ground-atmosphere interface* (Incorpera & DeWitt, 2002). This heat transfer results from a temperature difference ($T_a - T_{cov}$) [K] between the air and the *ground-atmosphere interface* and therefore can be related to this temperature difference using *Newton's Law* in Equation 5-4. The local convection heat transfer coefficient (h) [W/m^{2}K] represents a combination of the conduction and advection heat transfer effects. The local convection coefficient is a function of the wind speed (u_{wind}) [m/s] above the *ground-atmosphere interface* and many empirical correlations have been formulated to quantify this parameter (Palyvos, 2008).

$$q''_H = h(T_a - T_{cov}) \quad \text{(for bare ground } T_{cov} \rightarrow T_{sur}) \tag{5-4}$$

The third term in Equation 5-2 is the latent heat flux (q''_{LvE}) [W/m^2] at the *ground-atmosphere interface*. This heat transfer occurs through the processes of ground moisture evaporating or transpiring at the *ground-atmosphere interface*. Firstly, the moisture evaporation flux (E") [m^3/m^{2}s] is quantified, this may include both bulk surface evaporation flux (E''_{sur}) [m^3/m^{2}s] and plant transpiration flux (E''_{plant}) [m^3/m^{2}s], and then multiplied by the density of water (ρ_w) [kg/m^3] and the specific latent heat of vaporisation of water (L_v) [2257 kJ/kg] in Equation 5-5.

$$q''_{L_vE} = L_v \rho_w (E''_{sur} + E''_{plant}) \quad (5\text{-}5)$$

The rate of evaporation depends on a number of factors such as ground moisture content (θ_{wg}) [W/m^{2}k] , relative humidity (RH) [%], interface type and temperature difference (T_a-T_{cov}). Demir *et al.* (2009) states that Equation 5-6 can be used to describe the latent heat flux, however values for the coefficients f, h_a, a, r_a and b are not clearly defined by Demir *et al.* (2009).

$$q''_{L_vE} = 0.0168 f h_a [(aT_{cov} + b) - r_a(aT_a + b)] \text{ (for bare ground } T_{cov} \rightarrow T_{sur}) \quad (5\text{-}6)$$

Evaporation is discussed again in model NL-1, Sub-section 5.4.1, and detailed information from many sources is compiled in the Simultaneous Heat and Water *SHAW23* technical documentation presented by Flerchinger (2000).

The final term in Equation 5-2 is the ground heat flux (q''_G) [W/m^2]. This heat transfer results from a temperature difference between the ground surface and the surface cover ($T_{sur} - T_{cov}$) and is therefore proportional to the temperature gradient across the first interface layer expressed using *Fourier's Law* in Equation 5-7.

$$q''_G = -k_g \frac{\partial T}{\partial z} = -k_g \frac{(T_{sur} - T_{cov})}{(Z_{sur} - Z_{cov})} \text{ (for bare ground } T_{sur} \rightarrow T_g,\ T_{cov} \rightarrow T_{sur},\ Z_{sur} \rightarrow Z_g \ \&\ Z_{cov} \rightarrow Z_{sur}) \quad (5\text{-}7)$$

Surface covers (such as grass) and ground surface materials (such as soil) are porous and contain moisture. When conditions are present for freezing ($T_{cov} \approx 0$ºC), the specific latent heat of fusion of water (L_f) [333.7 kJ/kg] must be extracted from this moisture at constant temperature ($T_{cov} \approx 0$ºC) before the temperature T_{cov} begins to drop below 0ºC (for bare ground $T_{cov} \rightarrow T_{sur}$). Freezing is discussed in Sub-section 5.2.4 and detailed information is presented in the Simultaneous Heat and Water *SHAW23* technical documentation (Flerchinger, 2000). The four terms in Equation 5-2 account for the significant heat transfer processes at the *ground-atmosphere interface.* However, some additional processes such as precipitation heat flux (q''_{prec}) [W/m^2] can be included to improve accuracy (Demir *et al.*, 2009). Figure 5-2(a) shows the incoming solar radiation ($q''_{S,t}$) measured on a flat surface at *HP-IRL/H* and the ground heat flux (q''_G) measured at the grass-soil interface in Profile 8 for a two day period in June, 2010. Figure 5-2(b) displays the air (T_a) surface cover (T_{cov}) and ground surface (T_{sur}) temperatures which are T_a, $T_{P6,\ +0.01m}$ and $T_{P1,\ 0.0m}$ respectively measured during the same two-day period. Figure 5-2(c) displays the temperature differences (T_a - T_{cov}) and (T_{sur} - T_{cov}). Figure 5-2(a) shows that approximately 10% of the incident solar radiation was conducted into the ground. Typically, between 25 and 30% of the incident radiation is

reflected meaning the remaining 60 to 65% is transferred away from the surface through sensible heat flux, longwave radiation and evaporative heat flux.

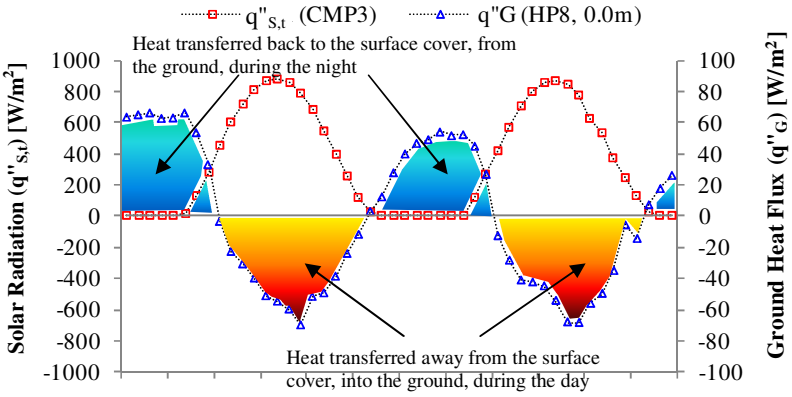

(a) Measured solar incoming radiation and heat flux at the grass-soil interface in P8

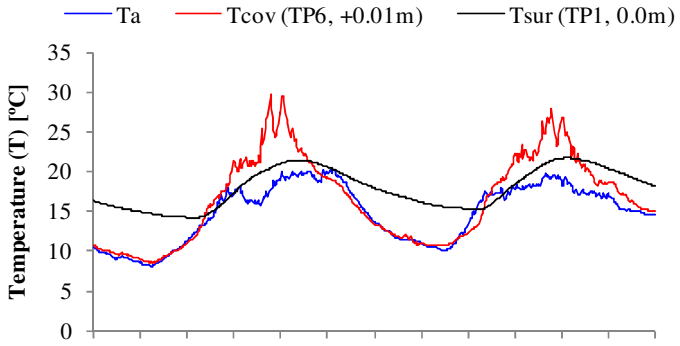

(b) Measured air, surface cover and ground surface temperature

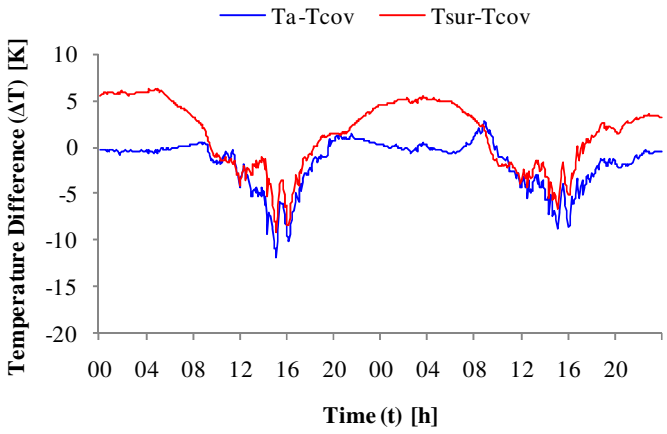

(c) Measured temperature difference between the surface cover and the air and ground

Figure 5-2: Measured data from P1, P6 and P8 at the HP-IRL/H site from 20th to 21st June 2010

5.2 UNDERGROUND HEAT TRANSFER

Since the operation of horizontal collectors for $GSHP_{HC}$ depends on heat transfer in the ground, the following theoretical investigation of these processes at the *HP-IRL/H* site was undertaken.

5.2.1 Literature Review

Numerous studies have been reported in the area of underground heat transfer, primarily on the subject of simultaneous heat and moisture transfer. A summary of 5 related studies from 5 countries is presented in Table 5-2 and the findings are discussed in detail throughout the subsequent text.

Table 5-2: Literature review on underground heat transfer

No.	Study (Year)	Location	Climate	Research Topic
1.	De Vries (1958)	-	-	Simultaneous transfer of heat and moisture in porous media
2.	Thomas *et al.* (1995)	Cardiff, Wales	*Cool Marine*	Modelling 2-D heat and moisture transfer including gravity effects
3.	Piechowski (1995)	Melbourne, Australia	*Humid Subtropical*	Heat and moisture transfer around a cooling mode HGHE in Polar Coordinates
4.	Flerchinger (2000)	Idaho, USA	*Cool Marine/Semiarid Continental*	Simultaneous heat and water software
5.	Mendes *et al.* (2002)	Brazil	*Wet Equatorial/Wet and Dry Tropical*	Mathematical method to solve the coupled ground heat and mass equations

5.2.2 One-Dimensional Heat Diffusion in the Ground

Considering an area of ground with a relatively uniform *ground-atmosphere interface*; consisting of a bare surface or surface cover of reasonably consistent albedo, emissivity, slope and orientation; the temperature of the ground beneath is considered to vary only with depth and time. Assuming the ground or at least distinct layers of the ground can be treated as a homogenous solid with reasonably uniform thermal properties, then the 1-D heat diffusion equation displayed in Equation 5-8 equates the rate of change in temperature (T) [ºC] with time (t) [s] to the second derivative of temperature with respect to the vertical dimension (Z) [m] (Incorpera & DeWitt, 2002).

$$C_g \frac{\partial T}{\partial t} = \frac{\partial}{\partial Z}\left[k_g \frac{\partial T}{\partial Z}\right] \quad (5\text{-}8)$$

Where, C_g [J/m^{3}K] is the volumetric heat capacity, equivalent to density ρ_g [kg/m^3] multiplied by specific heat capacity c_g [J/kgK], and k_g [W/mK] represents the thermal conductivity of the ground. For a simplified case when k_g is constant, Equation 5-8 is often re-written using the ground's thermal diffusivity ($\alpha_g = k_g/C_g$) [m^2/s]. Applying the aforementioned simplification to Profile 1 for example, where the thermal diffusivity is 1.05 x 10^{-6} m^2/s, then Equation 5-8 can be re-written for say $T_{P1,\,-0.15m}$ using Equation 5-9.

$$\frac{\partial T_{P1,-0.15m}}{\partial t} = \alpha_g \frac{[(T_{P1,-0.3m} - T_{P1,-0.15m})/0.15] - [(T_{P1,-0.15m} - T_{P1,0.0m})/0.15]}{0.15} \quad (5\text{-}9)$$

For 3-D conduction around collector pipes, coordinates shown in Figure 5-3, the 3-D heat diffusion equation shown in Equation 5-10 can be used to include the width (W) and length (L) dimensions as well as the vertical dimension (Z) (Incorpera & DeWitt, 2002), although ground heat transfer along the L dimension is typically quite weak.

$$C_g \frac{\partial T}{\partial t} = \frac{\partial}{\partial W}\left[k_g \frac{\partial T}{\partial W}\right] + \frac{\partial}{\partial Z}\left[k_g \frac{\partial T}{\partial Z}\right] + \frac{\partial}{\partial L}\left[k_g \frac{\partial T}{\partial L}\right] \quad (5\text{-}10)$$

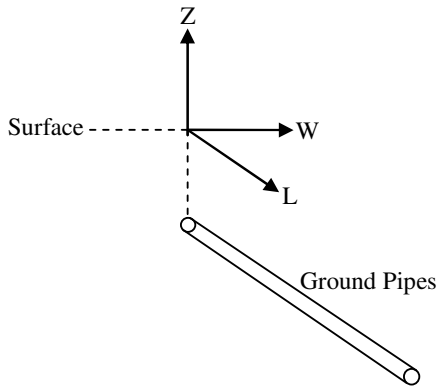

Figure 5-3: Coordinate system for ground heat, moisture or GSHP$_{HC}$ differential equations

5.2.3 Groundwater

This project sought to investigate *GSHP$_{HC}$* operation using a *thermo-environmental analysis* and therefore it was necessary to also review the impact of groundwater on *GSHP$_{HC}$*. Therefore, while the heat conduction equation described in Equation 5-8 can be used to describe 1-D heat conduction for a homogenous solid with uniform properties, the ground in reality is a porous medium. A selected ground volume (V_g) [m^3] consists of a variety of solid particles (V_{sg}) [m^3], water (V_{wg}) [m^3] and air (V_{ag}) [m^3] as described in Equation 5-11.

$$V_g = V_{sg} + V_{wg} + V_{ag} \quad (5\text{-}11)$$

Dividing by the total V_g gives the volumetric content (θ) of each constituent in m^3/m^3 which sums to one unit as described in Equation 5-12. The units m^3/m^3 are included for these fractions as a reminder that they were derived from volume only, and do not apply directly to mass.

$$1 = \theta_{sg} + \theta_{wg} + \theta_{ag} = \theta_{sg} + p \tag{5-12}$$

The sum of the volumetric water (θ_{wg}) [m^3/m^3] and air content (θ_{ag}) [m^3/m^3] equals the porosity (p) [m^3/m^3] which is the volume of voids in the selected ground volume. The porosity is constant, a function of particle size, shape and compaction, while the volumetric water and air content are inversely proportional (also referred to as negatively related). The density of dried ground can be described as dry bulk density (ρ_{bulk}) [kg/m^3] which includes pores or particle density (ρ_{sg}) [kg/m^3] without pores, the relationship between these is summarised in Equation 5-13.

$$\frac{\rho_{bulk}}{\rho_{sg}} = \frac{m_{dry}/V_g}{m_{dry}/V_{sg}} = \frac{V_{sg}}{V_g} = \theta_{sg} \tag{5-13}$$

The volumetric water content can include water as ice (θ_{ice}) [m^3/m^3], liquid water (θ_{liq}) [m^3/m^3] or water vapour (θ_{vap}) [m^3/m^3] as follows:

$$\theta_{wg} = \theta_{ice} + \theta_{liq} + \theta_{vap} \tag{5-14}$$

The ground is divided into two regions identified as ‘unsaturated’ and ‘saturated’ (Marshall *et al.*, 1996) shown in Figure 5-4 and described as follows:

- The unsaturated ground water above the ‘water table’ is layered from the surface down as follows:
  - Soil moisture
  - Intermediate vadose water
  - Capillary water
- The saturated ground water below the ‘water table’ is often referred to as:
  - Phreatic water

The unsaturated ground water zone may be saturated at times, given sufficient precipitation, however it is not saturated at all times like the ground below the water table. Given extremely dry or wet weather, the depth of the water table may vary.

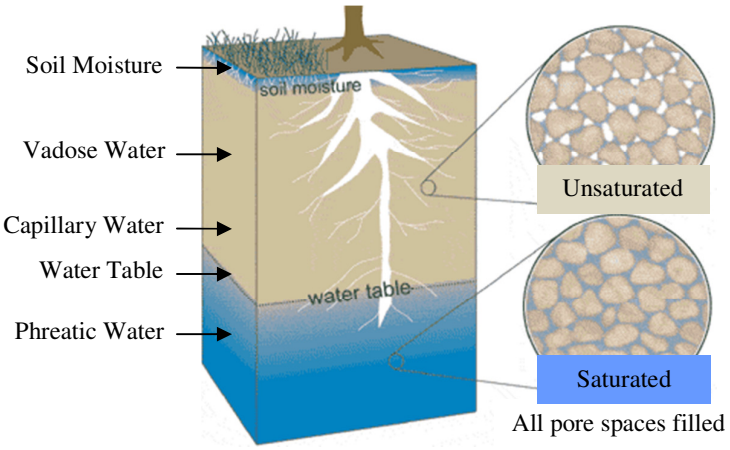

Figure 5-4: Groundwater in unsaturated and saturated ground (Vision Learning, 2010)

5.2.3.1 Seasonal Ground Moisture Content Mapping

Figure 5-5 presents a 10 month graph showing the variation in mean daily soil moisture content ($\theta_{wg,d}$) with depth and time in P8 with the corresponding daily weather data streams of total solar energy flux $Q''_{S,t}$, air temperature $T_{a,d}$, relative humidity (RH_d) and precipitation levels ($Z_{prec,d}$) overlaid.

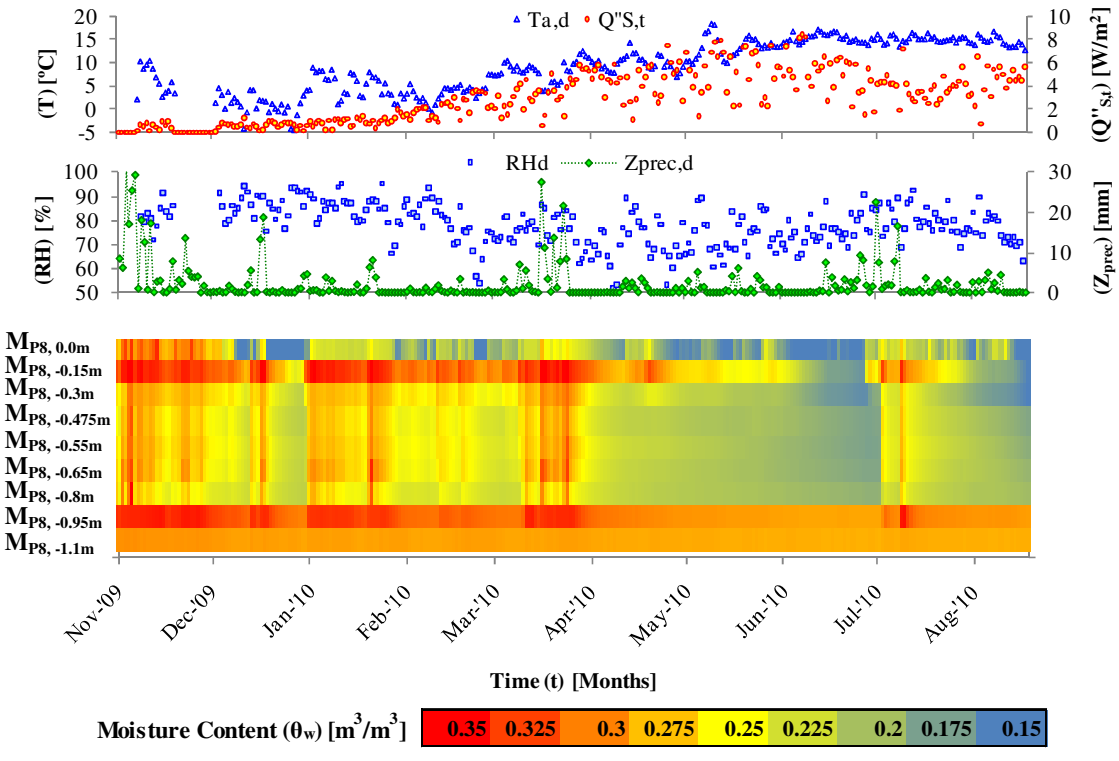

Figure 5-5: Variation in ground moisture content to a depth of 1.1m in profile 8 at the HP-IRL/H site between November 2009 and August 2010

It is noticeable that considerable drying takes place at the surface during the summer months; 2010 produced a relatively dry summer by Irish standards as the maritime nature of Ireland's weather often results in wet summers. During the winter months it can be seen that soil moisture content at *HP-IRL/H* collector depth (Z= -0.8 to -1.35m) is consistently above $0.25m^3/m^3$. $M_{P8,\ -1.1m}$ measures a continuous value of $0.3m^3/m^3$, reacting to neither drying nor wetting in the layers above, suggesting a near saturated layer or localised water table above a consolidated layer. The moisture content at 0.0m was $0.35m^3/m^3$ when measured in November 2009 after a 2 week period of above average rainfall. The moisture content at 0.0m was $0.15m^3/m^3$ when measured in mid-June after a 2 week summer dry period. The layers from Z= 0.0 to -0.8m react to rain events within one day indicating good porosity.

5.2.3.2 Ground-atmosphere Interface Water Balance

In the same way as the atmosphere influences ground temperature, the atmosphere also influences ground water at the *ground-atmosphere interface*. Equation 5-15 describes a water flow balance with a storage term for the *ground-atmosphere interface* layer of thickness ΔZ [m] (Campbell & Norman, 1998). Equation 5-15 is written in a form analogous to the energy balance in Equation 5-2.

$$\Delta Z \frac{d\theta_{wg}}{dt} = J''_{wi} - J''_{wp} - E''_{sur} - E''_{plant} \tag{5-15}$$

The grouped terms on the left represent the rate of change in water stored per square meter of land area [m^3/m^2s] with thickness ΔZ [m]. The terms on the right are the infiltration water flux (J''_{wi}) [m^3/m^2s], ground water percolation flux (J''_{wp}) [m^3/m^2s], evaporation flux from the soil surface (E''_{sur}) [m^3/m^2s], and plant transpiration water flux (E''_{plant}) [m^3/m^2s]. The latter terms in Equation 5-15 have negative signs because the flux occurs primarily in that 'single' direction, whereas signs in Equation 5-2 are positive as the flux direction varies with time. The water flux units [m^3/m^2s] can be reduced to [m/s], known as 'Darcy flow', however this does not translate to the ground water velocity (u_{wg}) [m/s] since water can only travel through the porous fraction (p) of the ground, u_{wg} is defined as J''_{wg}/p.

The infiltration flux (J''_{wi}) depends on a number of factors such as precipitation levels (Z_{prec}), snowmelt, run-off (on slopes) and ponding. Both the surface evaporation flux (E''_{sur}) and plant transpiration (E''_{plant}) are dependent on *ground-atmosphere interface* factors as discussed in Sub-section 5.1.2. *Darcy's Law* shown in Equation 5-16 is typically used to evaluate ground water flux J''_{wg} [m/s] in terms of hydraulic conductivity (K) [m/s] and total water potential (Φ)

[m] gradient (dΦ/dZ) [-] (Marshall *et al.*, 1996; Campbell & Norman, 1998; Flerchinger, 2000).

$$J''_{wg} = -K(\theta_{wg})\frac{d\Phi(\theta_{wg})}{dZ} \quad (5\text{-}16)$$

Darcy's law is expressed in Equation 5-16 in a form that is analogous to *Fourier's Law* used in Equation 5-7, where water potential (Φ) is analogous to temperature (T). The hydraulic conductivity, analogous to k_g, is expressed as $K(\theta_{wg})$ due to its strong dependency on moisture content in unsaturated soil. Equation 5-17 is a simple expression commonly used to relate the hydraulic conductivity to the saturated hydraulic conductivity (K_{sat}) [m/s], the saturation ratio (θ_{wg}/θ_{sat}) and the exponent of moisture release (b) [-] (Piechowski, 1996; Campbell & Norman, 1998; Flerchinger, 2000).

$$K(\theta_{wg}) = K_{sat}\left(\frac{\theta_{wg}}{\theta_{sat}}\right)^{(2b+3)} \quad (5\text{-}17)$$

Total water potential (Φ) [m], expressed as meters of head, is a measure of the potential energy (PE = mgZ) [J] per unit weight (PE/mg) [m] required to move water from a reference pure-water pool (at a reference height Z_0) to the point in question. Total potential can include components due to matrix (ψ) [m], gravimetric (Z) [m], solute, pressure and humidity potentials (Marshall *et al.*, 1996; Campbell & Norman, 1998). For basic ground water movement in the vertical Z-dimension, total potential consists of matric and gravitational potential ($\Phi = \psi + Z$) [m].

Matric potential (ψ) [m] is caused by cohesion/absorption in clays only and capillarity/surface tension in the pores between clays, silts and sands. Matric potential is an attractive potential and is a function of moisture content, it is therefore always either negative for unsaturated soil or zero when soil is at or near saturation. Gravitational potential (Z) [m] is measured relative to the reference height (Z_0) [m] and is therefore positive above and negative below this reference point; Z_0 in the *HP-IRL/H* project is equal to the bulk ground surface (Z= 0m).

Equation 5-18 is a simple method commonly used to estimate matric potential (ψ) [m], as a function of moisture content, based on the saturation ratio (θ_{wg}/θ_{sat}), the air entry potential (ψ_e) [m] and the exponent of moisture release (b) (Piechowski, 1996; Campbell & Norman, 1998; Flerchinger, 2000). The values of K_{sat}, θ_{sat}, b and ψ_e depend on soil type, known as texture, this is discussed in Sub-section 0 and values for a range of soil textures are presented in Table 5-6.

$$\psi(\theta_{wg}) = \psi_e\left(\frac{\theta_{wg}}{\theta_{sat}}\right)^{-b} \quad (5\text{-}18)$$

5.2.3.3 One-Dimensional Water Diffusion in the Ground

Derived for a total potential ($\Phi = \psi + Z$) [m], Equation 5-19 equates the rate of change in moisture content (θ_{wg}) [m^3/m^3] with time (t) [s] to the second derivative of matric potential (ψ) [m] plus the first derivative of hydraulic conductivity (K) [m/s] with respect to the vertical dimension (Z) [m] (Marshall *et al.*, 1996). Equation 5-19 is approximately analogous to Equation 5-8 used for heat diffusion.

$$\frac{\partial \theta_{wg}}{\partial t} = \frac{\partial}{\partial Z}\left[K\frac{\partial \Phi}{\partial Z}\right] = \frac{\partial}{\partial Z}\left[K\left(\theta_{wg}\right)\left(\frac{\partial \psi(\theta_{wg})}{\partial Z} + 1\right)\right] \quad (5\text{-}19)$$

5.2.3.4 Groundwater Freezing

The moisture contained in soil pores at the *ground-atmosphere interface* can freeze as mentioned in Sub-section 5.1.2 and this process can extend through the ground. Equation 5-20 presents a revised version of Equation 5-8 that includes the latent heat lost/gained at a point during an increase/decrease in ice content (θ_{ice}) (Engelmark & Svensson, 1993; Endrizzi *et al.*, 2008), where L_f [333.7 kJ/kg] is the specific latent heat of fusion of water and ρ_{ice} [kg/m^3] is the density of the increasing/decreasing ice.

$$C_g\left(\theta_{ice}, \theta_{liq}\right)\frac{\partial T}{\partial t} - L_f \rho_{ice}\frac{\partial \theta_{ice}}{\partial t} = \frac{\partial}{\partial Z}\left(k_g\left(\theta_{ice}, \theta_{liq}\right)\frac{\partial T}{\partial Z}\right) \quad (5\text{-}20)$$

Similarly, Equation 5-21 presents a revised version of Equation 5-19 which includes an ice content term (Engelmark & Svensson, 1993), where ρ_l [kg/m^3] is liquid water density.

$$\frac{\partial \theta_{liq}}{\partial t} + \frac{\rho_{ice}}{\rho_{liq}}\frac{\partial \theta_{ice}}{\partial t} = \frac{\partial}{\partial Z}\left[K(\theta_{wg})\left(\frac{\partial \psi(\theta_{wg})}{\partial Z} + 1\right)\right] \quad (5\text{-}21)$$

Also, the local thermal properties of the ground are influenced by the local moisture content (θ_{wg}) and more specifically by the fractions of ice (θ_{ice}) and liquid water (θ_{liq}) present.

5.2.4 Coupled Heat and Water Transport in the Ground

It can be seen in Sub-sections 5.1.2 and 5.2.3.2 that the evaporation water flux (E''_{sur}) [m^3/m^2s] and transpiration water flux (E''_{plant}) [m^3/m^2s] at the *ground-atmosphere interface* are common features in both the energy and the mass balance, described in Equations 5-2 and 5-15 respectively. In fact, all heat and mass transfer processes in soil can be viewed as coupled and to develop an elegant solution these processes may be considered simultaneously. The total heat transfer in a porous medium, such as soil, can be viewed as conduction

combined with water movement in both the vapour and liquid states while at the same time temperature gradients can drive mass transfer (De Vries, 1958; Thomas & Li, 1995; Piechowski, 1996; Cahill & Parlange, 1998; Flerchinger, 2000; Deru & Kirkpatrick, 2001). The components of this simultaneous process can be described as follows:

- Heat is transferred along temperature gradients in the stagnant ground solids, liquids and vapours through conduction in the normal way (see Equation 5-8)
- Liquid moisture is transferred along water potential gradients in the ground pores through normal isothermal moisture transfer (see Equation 5-19)
- Heat is therefore transferred by the isothermal moisture transfer through heat advection
- Moisture is also transferred along a temperature gradient through the processes of evaporation in warm pores, diffusion (along vapour pressure gradients) and condensation in cooler pores
- Heat is therefore intrinsically transferred by this evaporation-condensation process
- Local thermal properties in a ground volume are dependent on the local moisture content (possibly in three phases) which is transient
- Energy balance at the *ground-atmosphere interface* influences the temperature and moisture distribution
- Mass balance at the *ground-atmosphere interface* also influences the temperature and moisture distribution
- Freezing of moisture influences the moisture transfer (moisture becomes locked in ice), the latent thermal energy processes (freezing/thawing) and the thermal properties
- Finally, during extreme changes from dry soil to wet soil a phenomenon known as the 'heat of wetting' occurs

Given the complexity of the situation, human reasoning or short analytical formula are not sufficient to simultaneously analyse or quantify the interactions. Therefore, the only solution is to write equations (in many cases differential equations) for the variation in temperature (T) [º], moisture content θ_{wg} [m^3/m^3] and the associated water potential (ψ) [m], ice content (θ_{ice}) [m^3/m^3] and also the variation in properties: hydraulic conductivity (K) [m/s], ground thermal conductivity (k_g) [W/mK] and volumetric heat capacity (C_g) [J/kgK] and then solve these equations simultaneously at each time-step (De Vries, 1958; Thomas & Li, 1995; Piechowski, 1996; Cahill & Parlange, 1998; Flerchinger, 2000; Deru & Kirkpatrick, 2001).

These equations have been assembled by many authors in a variety of forms (De Vries, 1958; Thomas & Li, 1995; Piechowski, 1996; Cahill & Parlange, 1998; Flerchinger, 2000; Deru &

Kirkpatrick, 2001). Currently, researchers seek more efficient mathematical solutions to these cumbersome equations (Liu, 1991; Mendes *et al.*, 2002). The equations assembled by Flerchinger (2000) at the United States Department of Agriculture (USDA) were developed into the Simultaneous Heat and Water (*SHAW23*) software which is used in this *HP-IRL/H* project and therefore these equations are described briefly in Sub-sections 5.2.4.1 and 5.2.4.2.

5.2.4.1 One-Dimensional Coupled Heat-Transport Process

The governing equation for 1-D heat transport processes in the ground is presented in Equation 5-22 (Flerchinger, 2000); this is a progression of Equation 5-20 for heat diffusion with freezing (Engelmark & Svensson, 1993; Endrizzi *et al.*, 2008) which represents a progression of Equation 5-8 for heat diffusion (Incorpera & DeWitt, 2002).

$$C_g(\theta_{ice}, \theta_{liq})\frac{\partial T}{\partial t} - \rho_{ice}L_f\frac{\partial \theta_{ice}}{\partial t} = \frac{\partial}{\partial Z}\left[k_g(\theta_{ice}, \theta_{liq})\frac{\partial T}{\partial Z}\right] - \rho_{liq}c_{p,w}\frac{\partial J''_{liq}T}{\partial Z} - L_v\left(\frac{\partial J''_{vap}}{\partial Z} + \frac{\partial \rho_{vap}}{\partial t}\right) \quad (5\text{-}22)$$

The grouped terms in [W/m^3] represent, from left to right respectively: the sensible heat term for change in stored energy due to a temperature increase/decrease, latent heat term for change in stored energy due to an ice content increase/decrease, net heat diffusion into a layer through conduction, net heat diffusion into a layer due to water advection and net latent heat evaporation within the soil layer (Flerchinger, 2000).

Where, C_g [J/m^{3}K] and T [ºC] are the volumetric heat capacity and temperature of the soil respectively, ρ_{ice} [kg/m^3] is the density of ice, L_f [J/kg] is the specific latent heat of fusion, θ_{ice} [m^3/m^3] is the volumetric ice content, k_g [W/mK] is the soil thermal conductivity, ρ_{liq} [kg/m^3] is the density of liquid water, $c_{p,w}$ [J/kgK] is the specific heat capacity of water, J''_{liq} [m/s] is the liquid water flux, L_v [J/kg] is the specific latent heat of vaporisation of water, J''_{vap} [kg/m^{2}s] is the water vapour flux and ρ_{vap} is the vapour density [kg/m^3] within the soil.

The variations in C_g and k_g with θ_{ice} and θ_{liq} are described in Sub-section 5.3.4 and calculation of J''_{liq} is described in Sub-section 5.2.3.2. The total vapour flux J''_{vap} consists of two fluxes $J''_{vap,\Phi}$ and $J''_{vap,T}$ due to a water potential gradient and a temperature gradient respectively, as described in Flerchinger (2000).

5.2.4.2 One-Dimensional Coupled Water-Transport Process

The governing equation for 1-D water transport processes in the ground is presented in Equation 5-23 (Flerchinger, 2000); this is a progression of Equation 5-21 for moisture

diffusion with freezing (Engelmark & Svensson, 1993) which represents a progression of Equation 5-19 for moisture diffusion (Marshall *et al.*, 1996).

$$\frac{\partial \theta_{liq}}{\partial t} + \frac{\rho_{ice}}{\rho_{liq}} \frac{\partial \theta_{ice}}{\partial t} = \frac{\partial}{\partial Z}\left[K(\theta_{wg})\left(\frac{\partial \psi(\theta_{wg})}{\partial Z} + 1\right)\right] + \frac{1}{\rho_{liq}} \frac{\partial J''_{vap}}{\partial Z} \quad (5\text{-}23)$$

The grouped terms in [m^3/m^3s] represent, from left to right respectively: the change in volumetric liquid content, the change in volumetric ice content, net liquid flux into a layer and net vapour flux into a layer (Flerchinger, 2000).

Where, θ_{liq} [m^3/m^3] is the volumetric water content, ρ_{ice} [kg/m^3] is the density if ice, ρ_{liq} [kg/m^3] is the density of water, θ_{ice} [m^3/m^3] is the volumetric ice content, K [m/s] is the hydraulic conductivity, ψ [m] is the water potential and J''_{vap} [kg/m^2s] is the net vapour flux into a layer. The variations in K and ψ with moisture content are defined in Section 5.2.3.2. The total vapour flux J''_{vap} consists of two fluxes $J''_{vap,\Phi}$ and $J''_{vap,T}$ due to a water potential gradient and a temperature gradient respectively, as described in Flerchinger (2000).

One of the most obvious examples of coupled heat and mass transfer is at the ground surface (Marshall *et al.*, 1996). Warming of the surface during the day creates a vapour pressure gradient which causes water vapour to move upward into the plants/atmosphere and also downward into cooler soil layers ($J''_{vap,T}$). At night when the surface layer cools considerably, the water vapour returns from the layers below (Marshall *et al.*, 1996). This can be seen in the *HP-IRL/H* data shown in Figure 5-6, where the incident sunshine during the daylight hours creates a periodic pattern in the surface layer's moisture content in Profile 8.

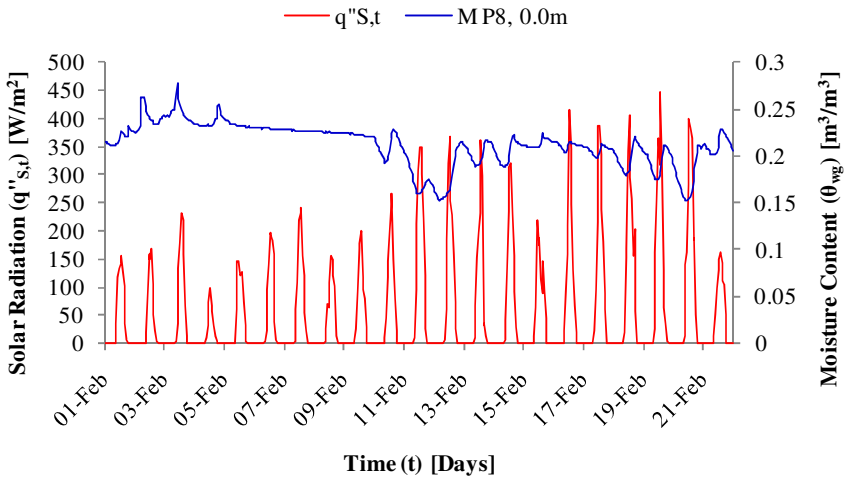

Figure 5-6: Cyclic water migration in and out of the surface layer during night and day respectively

The importance of coupled heat and mass transfer analysis to $GSHP_{HC}$ has been questioned over the years. It has been applied to heat rejection HGHE in dry Australian summer (Piechowski, 1996) and $GSHP_{HC}$ collectors in the cold Canadian winter (Tarnawski & Leong, 1993; Healy & Ugursal, 1997; Leong *et al.*, 1998). However, Gauthier *et al.* (1997) concluded that moisture gradients accounted for less than 0.1% of the total heat transfer in soil, a finding supported by the work of Puri (1986). Simulations of $GSHP_{HC}$ at ORNL, USA (Mei, 1986), Quebec, Canada (Gauthier *et al.*, 1997) and Turkey (Esen *et al.*, 2007; Demir *et al.*, 2009) were conducted using pure conduction with good predictive accuracy reported.

Therefore, due to the inconsistencies within the literature, the magnitude of coupled heat and mass transfer at the mild and moist *HP-IRL/H* site is experimentally investigated in Section 7.1.6.

5.3 THERMAL AND HYDRAULIC PROPERTIES

While ground temperature describes the thermodynamic 'quality' of the ground thermal energy resource, ground thermal properties must also be known in order to define the 'quantity' of energy available (thermal energy content) and the ease or 'efficiency' with which it can be extracted.

Ground thermal properties are key determinants in the performance of a horizontal or vertical collector but can vary considerably from site to site. Ground thermal properties are difficult to quantify 'in situ' and the loss of structure in a ground sample, during removal, can influence the validity of the results. Additionally, the presence of groundwater can influence both the thermal properties of the ground and the types of heat transfer processes in the ground. Therefore, the moisture influence and hydraulic properties are also of interest. This section presents a theoretical and experimental investigation of ground properties at the *HP-IRL/H* site and aims to quantify the average in-situ density, specific heat capacity and thermal conductivity of the *HP-IRL/H* site for use in numerical simulations in Chapters 7 and 8.

5.3.1 Literature Review

Table 5-3 presents a review of 8 studies on the subject of ground thermal properties relevant to $GSHP_{HC}$ from 4 countries, published between 1984 and 2004. *Climate classification* has been replaced with soil/ground type which is commonly referred to as 'texture'. Methods and findings from the publications listed in Table 5-3 are discussed in detail in the subsequent text.

Table 5-3: Ground thermal properties literature review

No.	Study (Year)	Location	Soil/Ground Type	Research Topic	Methods
1	Salomone and Wechsler (1984)	Maryland, USA	Coarse sand, medium sand, silt and silty clay	Thermal properties and soil type	Thermal needle
2	Mei (1987)	Tennessee, USA	Clay, sand and fluidized mixture	HGHE performance and backfill material	Numerical Simulation
3	Remund and Schulte (1991)	South Dakota, USA	Sharpsburg silty clay	HGHE performance and moisture	Numerical Simulation
4	Remund (1994)	South Dakota, USA	Clay, sand, clay loam, silt loam, silty clay loam, sandy loam	Thermal Performance Evaluation	Physical Testing and Analysis
5	Leong *et. al* (1998)	Canada & Finland	Sand, silty loam and silty clay	HGHE performance and soil type/moisture	Numerical Simulation
6	Ochsner *et. al.* (2001)	Iowa, USA	Sandy loam, clay loam, silty loam and silty clay	Thermal properties and soil moisture	Thermo-TDR and analytical models
7	Côté and Konrad (2004)	Sainte-Foy Canada	Dolostone, limestone, sandstone etc.	Thermal conductivity of base course materials	Thermal conductivity rig
8	O'Connell and Cassidy (2004)	Cork, Ireland	Irish sandy loam	Pipe-ground thermal contact resistance	Guarded Hot Plate Test Rig and Analytical Model

5.3.2 Soil Texture

Typically, the soil texture, plasticity and cohesiveness form the basis for standardised soil classification systems (Salomone & Wechsler, 1984). Soil texture describes the mixture of particle sizes which make up a soil sample and is also defined as the Particle Size Distribution (PSD). Soil particle sizes can be classified as follows:

- Course-grained including:
  - Gravels
  - Sands
- Fine-grained including:
  - Silts
  - Clays

Soil texture or PSD can be established by passing a soil sample through a series of calibrated sieves. The particle size-limit system used by the International Society of Soil Science (ISSS), the United States Department of Agriculture (USDA), the Massachusetts Institute of Technology (MIT) and the British Standards Institute (BSI) are displayed in Figure 5-7

(Marshall *et al.*, 1996). Based on results from the PSD analysis, soil classifications can be defined using Figure 5-8(a).

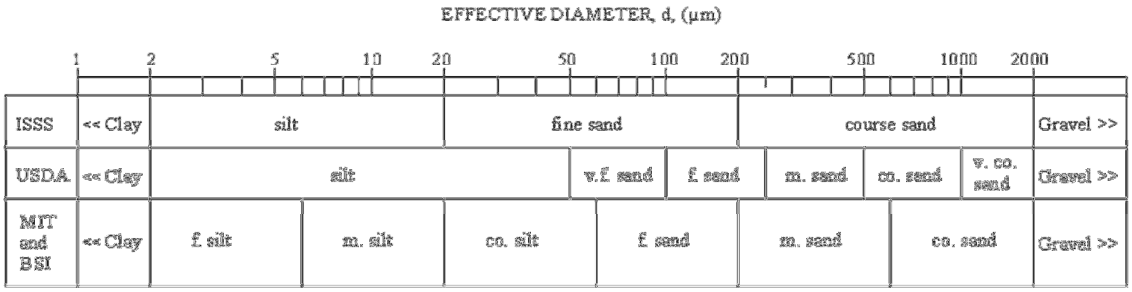

Figure 5-7: Particle size-limit system used by ISSS, USDA and MIT (Marshall *et al.* 1996) (f = fine, m= medium, co= course, v= very)

Clays (the smallest particles) are both plastic and cohesive, while gravels, sands and silts are non-plastic and non-cohesive (Salomone & Wechsler, 1984). Significant texture information can be gained from a soil sample by: measuring the mass of a saturated and an oven-dried undisturbed sample (yielding the porosity), passing a dry sample through a 75μm sieve (separating the course-grains and fine-grains by volume) and examining a moistened sample between ones fingers for plasticity and cohesion using standardised methods (Marshall *et al.*, 1996). These methods and others have been applied to the ground/soil samples shown in Figure 5-8(b) which were taken at 6 different depths down to the collector depth in experimental profile P8 at the *HP-IRL/H* site. The findings of this process are presented in Table 5-4, where sand is the dominant particle size between Z= -0.05 and -1.05m.

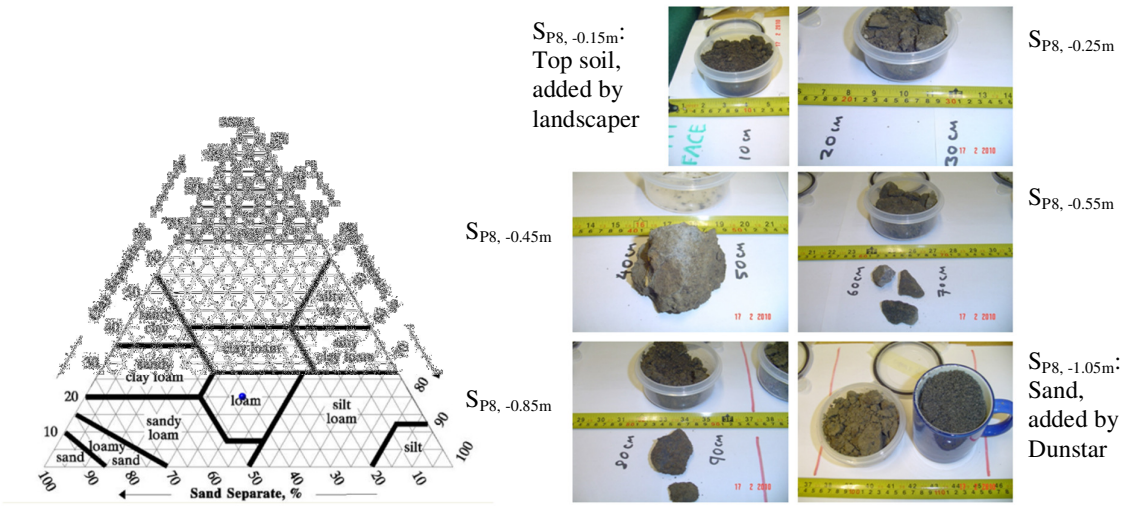

(a) Soil texture classification **(b) Soil samples from P8 in the HP-IRL/H site**

Figure 5-8: Texture classification and soil sampling at P8 during September 2009

Table 5-4: Soil sample textures from P8 within the collector area at the HP-IRL/H site

Name	Z Range	Texture	Clay	Silt	Sand	Other
$S_{P8, -0.05m}$	0 to -0.1m	Sod/ Roots	-	-	-	Organics
$S_{P8, -0.15m}$	-0.1 to -0.2m	Peat/ Top Soil	0.1	0.1	0.1	Organics
$S_{P8, -0.25m}$	-0.2 to -0.3m	Sandy clay loam with some gravel	0.3	0.1	0.55	Gravel
-	-	-	-	-	-	-
$S_{P8, -0.45m}$	-0.4 to -0.5m	Sandy loam with cement traces	0.05	0.25	0.7	Waste cement
$S_{P8, -0.55m}$	-0.5 to -0.6m	Sandy loam with gravel	0.05	0.25	0.6	Gravel
-	-	-	-	-	-	-
-	-	-	-	-	-	-
$S_{P8, -0.85m}$	-0.7 to -1.0m	Sandy clay loam with gravel	0.3	0.1	0.5	Gravel
-	-	-	-	-	-	-
$S_{P8, -1.05m}$	-1.0 to -1.1m	Sandy loam (fines migrated into sand)	0.1	0.25	0.65	0

5.3.3 Influence of Soil Texture on Thermal and Hydraulic Properties

One of the key determinants of ground thermal properties is texture (Salomone & Wechsler, 1984; Remund, 1994; VDI-4640, 2004). Table 5-5 presents typical variation in ground properties, k_g, ρ_g, C_g and α_g with texture (VDI-4640, 2004).

Table 5-5: Thermal properties of soils as a function of soil texture and moisture (VDI-4640, 2004)

Soil texture	(k_g)	Typical (k_g)	(ρ_g)	(C_g)	(α_g)
	[W/mK]	[W/mK]	[kg/m^3]	[MJ/m^{3}K]	[m^2/s]
Gravel, dry	0.4-0.5	(0.4)	1500-1800	1.4-1.6	0.27 x 10^{-6}
Gravel, saturated	Approx. 1.8	(1.8)	Approx. 2200	Approx. 2.2	0.75 x 10^{-6}
Sand, dry	0.3-0.8	(0.4)	1160-1700	1.3-1.6	0.28 x 10^{-6}
Sand, saturated	1.7-5.0	(2.4)	1600-2200	2.2-2.9	0.94 x 10^{-6}
Clay or silt, dry	0.4-1.0	(0.5)	930-1300	1.5-1.6	0.32 x 10^{-6}
Clay or silt, saturated	0.9-2.3	(1.7)	1200-1700	1.6-3.4	0.68 x 10^{-6}
Peat	0.2-0.7	(0.4)	N/A	0.5-3.8	0.19 x 10^{-6}

Similarly, hydraulic properties vary with texture (Piechowski, 1996; Campbell & Norman, 1998; Saxton & Rawls, 2006). Table 5-6 presents the hydraulic properties θ_{sat}, ψ_e, K_{sat}, b and ρ_{bulk}, which were discussed in Sub-section 5.2.3, as a function of soil texture (Piechowski, 1996).

Salomone & Wechsler (1984) state that increasing the fraction of medium and coarse sand increases heat conduction, while Remund (1994) concludes that equal fractions of sand, silt and clay exhibit the optimum conduction properties. In terms of water infiltration, it can be seen from Table 5-1 that a high fraction of sand increases the saturated hydraulic conductivity (K_{sat}) which increases moisture movement.

Table 5-6: Hydraulic properties of soils as a function of soil texture (Piechowski, 1996)

Soil texture	Clay	Silt	Sand	(θ_{sat})	(ψ_e)	(K_{sat})	(b)	(ρ_{bulk})
	[-]	[-]	[-]	[m^3/m^3]	[m]	[m/s]	[-]	[kg/m^3]
Sand	0.0-0.1	0.0-0.15	0.85-1.0	0.395	-0.035	1.76×10^{-4}	4.05	1480-1785
Loamy sand	0.0-0.15	0.0-0.3	0.7-0.9	0.41	-0.0178	1.56×10^{-4}	4.38	1410-1775
Sandy loam	0.0-0.2	0.0-0.5	0.4-0.8	0.435	-0.0718	0.35×10^{-4}	4.9	1290-1760
Loam	0.07-0.27	0.28-0.5	0.23-0.52	0.451	-0.146	0.07×10^{-4}	5.39	1270-1695
Silt loam	0.0-0.27	0.5-0.88	0.0-0.5	0.485	-0.566	0.07×10^{-4}	5.3	1230-1550
Silt	0.0-0.12	0.8-1.0	0.0-0.2	-	-	-	-	1120-1600
Sandy clay loam	0.2-0.35	0.0-0.28	0.45-0.8	0.420	-0.0863	0.6×10^{-5}	7.12	1405-1725
Clay loam	0.27-0.4	0.15-0.53	0.2-0.45	0.476	-0.361	0.25×10^{-5}	8.52	1270-1560
Silty clay loam	0.27-0.4	0.4-0.73	0.0-0.2	0.477	-0.146	0.17×10^{-5}	7.75	1260-1565
Sandy clay	0.35-0.45	0.0-0.2	0.45-0.65	0.426	-0.0616	0.22×10^{-5}	10.4	1395-1710
Silty clay	0.4-0.6	0.4-0.6	0.0-0.2	0.492	-0.174	0.1×10^{-5}	10.4	1200-1545
Clay	0.4-1.0	0.0-0.4	0.0-0.45	0.482	-0.186	0.13×10^{-5}	11.4	1265-1535

5.3.4 Influence of Moisture Content on Thermal and Hydraulic Properties

Thermal conductivity and heat capacity of all soils increase with water content (De Vries, 1958; Drown & Den Braven, 1992; Remund, 1994; Piechowski, 1996; Flerchinger, 2000; Deru & Kirkpatrick, 2001). Figure 5-9(a) displays the influence of moisture content, temperature and vapour diffusion on thermal conductivity (Deru & Kirkpatrick, 2001), while Figure 5-9(b) shows the influence of moisture content only (Ochsner *et al.*, 2001). Salomone & Wechsler (1984) defined a 'critical moisture content' which Piechowski (1996) identified at about $0.15 m^3/m^3$. Below this critical moisture content, vapour flow begins to exceed liquid flow and drying occurs around HGHE rejecting heat in summer resulting in a 'thermal instability' condition (Salomone & Wechsler, 1984) which has a significant negative impact on the HGHE's heat rejection rate in summer.

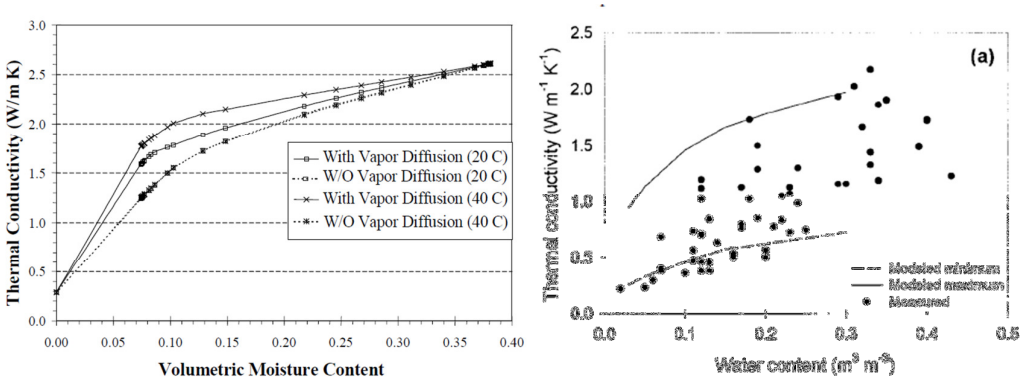

(a) Deru & Kirkpatrick (2001) **(b) Ochsner *et al.* (2001)**

Figure 5-9: Influence of moisture content on ground's thermal conductivity

The variation in thermal conductivity (k_g) [W/mK] with solids fraction (v_s) [m^3/m^3], liquid water content (θ_{liq}) [m^3/m^3], ice content (θ_{ice}) [m^3/m^3], air content (θ_{ag}) [m^3/m^3] and any other constituents can be estimated using Equations 5-24 (Piechowski, 1996; Campbell & Norman, 1998; Deru & Kirkpatrick, 2001; Ochsner *et al.*, 2001), where k_i [W/mK] is the thermal conductivity of the i^{th} constituent, θ_i [m^3/m^3] is the volumetric content of the i^{th} constituent and ξ_i [-] is the ratio of the temperature gradient in the i^{th} constituent to the temperature gradient in the medium. The ξ_i ratio is typically defined using shape factors (g_1, g_2 and g_3) described in Ochsner *et al.* (2001) and summarised in Appendix J.

$$k(\theta_{sg}, \theta_{liq}, \theta_{ice}, \theta_{ag} \ldots . n) = \frac{\sum_{i=1}^{n} k_i \theta_i \xi_i}{\sum_{i=1}^{n} \theta_i \delta_i} \quad (5\text{-}24)$$

The variation in volumetric heat capacity (C_g) [J/m^3K] with moisture content (θ_{wg}) [m^3/m^3] can be estimated using Equations 5-25 (Piechowski, 1996; Campbell & Norman, 1998; Deru & Kirkpatrick, 2001; Ochsner *et al.*, 2001), where ρ_{bulk} [kg/m^3] is the soil bulk density (described in Sub-section 5.2.3), $c_{p,sg}$ [J/kgK] is the specific heat capacity of soil solids, while ρ_{wg} [kg/m^3] and $c_{p,wg}$ [J/kgK] are the density and specific heat capacity of liquid water respectively.

$$C_g(\theta_{wg}) = \rho_{bulk} c_{p,sg} + \rho_{wg} c_{p,wg} \theta_{wg} \quad (5\text{-}25)$$

The thermal diffusivity (α_g) [m^2/s] as a function of moisture content (θ_{wg}) [m^3/m^3] is then the ratio of conductivity ($k_g(\theta_{wg})$) to volumetric heat capacity ($C_g(\theta_{wg})$). The combination of Equation 5-24 and 5-25 are identified as Model AL-6 and will be referenced subsequently in this thesis. Figure 5-10 was created using AL-6 for a 'sandy loam' soil with bulk density of $1550kg/m^3$, saturated moisture content of $0.4m^3/m^3$, thermal conductivity of solids of 5W/mK and g_1 value of 0.1. Additional information is presented in Appendix J.

As expected, the thermal conductivity decreases rapidly when moisture content drops below the critical value of 0.1 to $0.15m^3/m^3$. Above the critical moisture content, thermal conductivity continues to increase with moisture content, but at a more moderate rate. The volumetric heat capacity increases at a constant rate and therefore the thermal diffusivity peaks at 0.1 to $0.15m^3/m^3$. At the saturation moisture content, $0.4m^3/m^3$ for sandy loam, thermal conductivity and heat capacity are at a maximum while thermal diffusivity has a value of approximately 9.5×10^{-7} m^2/s which is equivalent to diffusivity at a moisture content $0.05m^3/m^3$. For a moisture content of 0.25 to $0.3m^3/m^3$, which is the moisture content range observed in Figure 5-5 for the *HP-IRL/H* site during winter, k_g, C_g and α_g have values in the range of 2.3 to 2.5W/mK, 2.1 to $2.4MJ/m^3K$ and 1.125 to 1.06×10^{-6} m^2/s respectively.

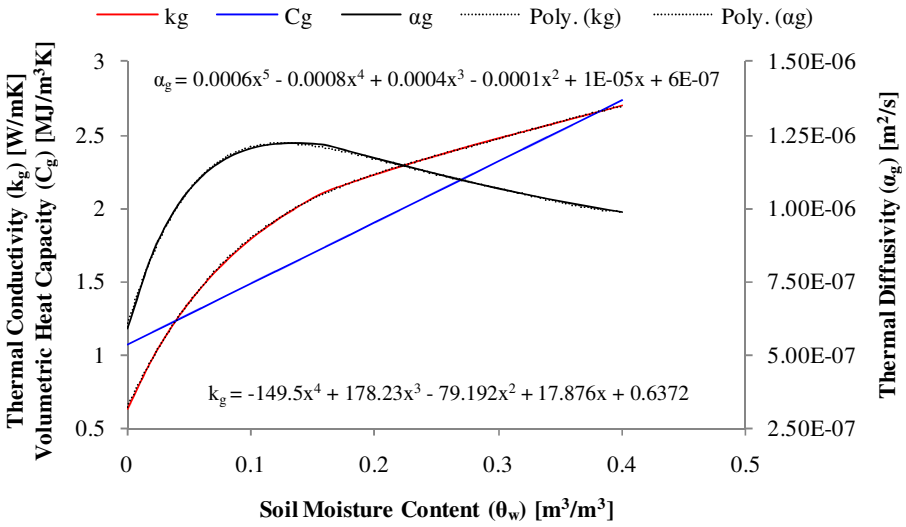

Figure 5-10: Variation of thermal properties with moisture content, calculated using AL-6, for a loamy sand with a bulk density of 1550kg/m^3, saturated moisture content of 0.4m^3/m^3, thermal conductivity of solids of 5W/mK and g_1 value of 0.1

The conductivity and diffusivity trends shown in Figure 5-10 can be written in terms of moisture content (θ_{wg}) alone using Equations 5-26 and 5-27 respectively. These trends will be utilized in Chapter 7.

$$k_g(\theta_{wg}) = -149.5\theta_{wg}^{\ 4} - 178.23\theta_{wg}^{\ 3} - 79.192\theta_{wg}^{\ 2} + 17.876\theta_{wg} + 0.6372 \quad (5\text{-}26)$$

$$\alpha_g(\theta_{wg}) = 0.0006\theta_{wg}^{\ 5} - 0.0008\theta_{wg}^{\ 4} + 0.0004\theta_{wg}^{\ 3} - 0.0001\theta_{wg}^{\ 2} - 1x10^{-5}\theta_{wg} + 6x10^{-7} \quad (5\text{-}27)$$

Common, empirical expressions for variation in hydraulic conductivity (K) [m/s] and matric potential (ψ) [m] with moisture content (θ_{wg}) [m^3/m^3] are presented in Equations 5-17 and 5-18 respectively; these require empirical inputs of K_{sat}, θ_{sat}, b and ψ_e which depend on soil texture as shown in Table 5-6. Figures 5-11(a) and (b) display the variation in Log K and Log ($-\psi$) with θ_{wg} calculated using Equation 5-17 and 5-18 respectively, with inputs (K_{sat}, θ_{sat}, b and ψ_e) for sand and clay from Piechowski (1996) and Campbell & Norman (1998). In addition, more complex expressions have also been suggested for this purpose along with measured data (De Vries, 1958; Thomas & Li, 1995; Marshall *et al.*, 1996; Deru & Kirkpatrick, 2001). Figures 5-12(a) and (b) display best fits to measured hydraulic conductivity and matric potential variation with θ_{wg} respectively for both loamy sand and Yolo light clay, which are at opposite ends of the soil texture range. The sand and clay have saturation moisture contents of approximately 0.4 and 0.5m^3/m^3 respectively, which is in agreement with Table 5-6. The relative flatness of the matric potential curve for sand between

moisture contents of 0.1 and 0.4m^3/m^3, when compared with the clay curve, indicates that moisture drains more rapidly from sand (Deru & Kirkpatrick, 2001).

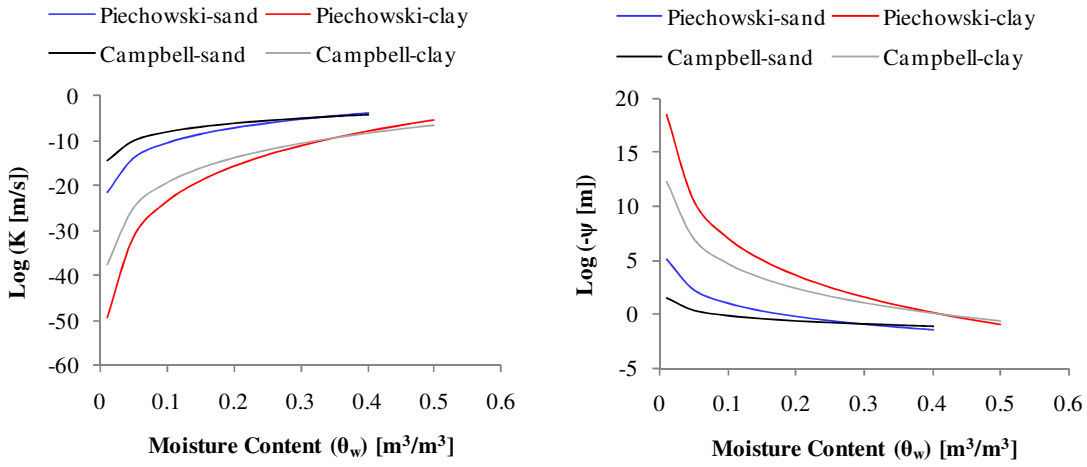

(a) Hydraulic Conductivity from Equation 5-17 **(b) Matric Potential from Equation 5-18**

Figure 5-11: Influence of moisture content on hydraulic properties calculated using K_{sat}, θ_{sat}, b and ψ_e and from Piechowski (1996) and Campbell & Norman (1998)

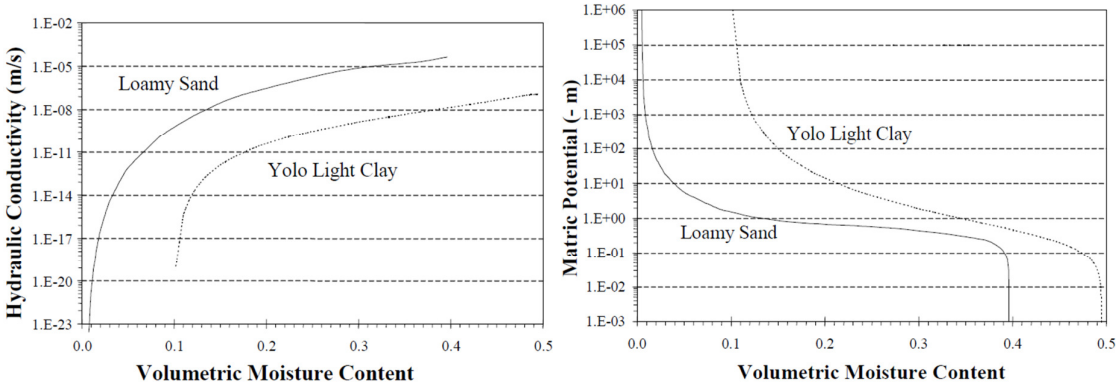

(a) Log of K with moisture content **(b) Log of -ψ with moisture content**

Figure 5-12: Variation in soil hydraulic properties with moisture content (Deru & Kirkpartick, 2001)

5.3.5 HP-IRL/H Thermal Conductivity Measurement

A wide range of ground thermal conductivity values are quoted in the literature. Figure 5-13 displays ground thermal conductivity values presented by nine authors internationally (Mei, 1987; Wibbels & Den Braven, 1994; Gauthier *et al.*, 1997; Deru & Kirkpatrick, 2001; Ochsner *et al.*, 2001; Incorpera & DeWitt, 2002; Badesku, 2007; Demir *et al.*, 2009; Pulat *et al.*, 2009). Values quoted range from a maximum of 3.72W/mK (Ochsner *et al.*, 2001) to a minimum of 0.52W/mK (Incorpera & DeWitt, 2002) with an average of 1.834W/mK.

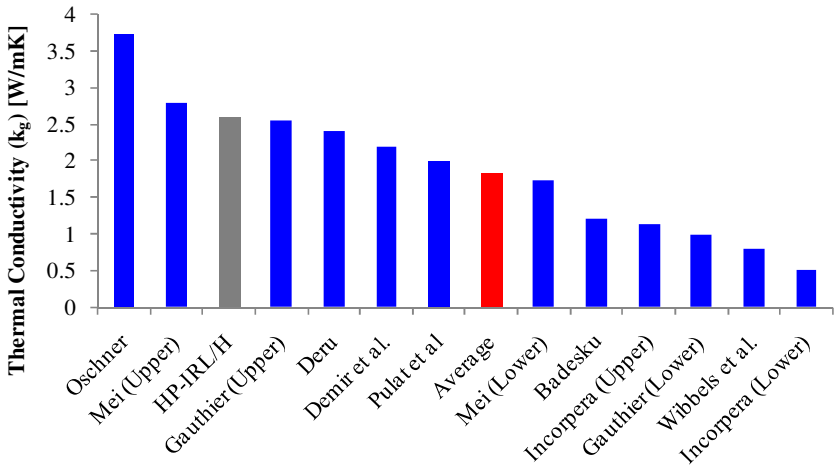

Figure 5-13: Soil thermal conductivity values reported in the literature

While Figure 5-10 displays the variation in thermal conductivity with moisture content from a commonly used model and Figure 5-13 displays thermal conductivity values quoted in the literature, it was also possible to experimentally measure ground thermal conductivity using the *HP-IRL/H* test facility described in Chapter 3 and a method trialled in Appendix G. The test method, identified as 'Undisturbed Heat Flux', involved simultaneous measurement of the ground heat flux (q") [W/m^2], the ground temperature gradient (dT/dZ) [K/m] and ground moisture content (θ_{wg}) [m^3/m^3] at a depth of 0.65m in P8 between December 2009 and January 2010; the horizontal collector had not been used since April 2009. The experimental profile used and a sample of the measured data are shown in Figures 5-14(a) and (b) respectively.

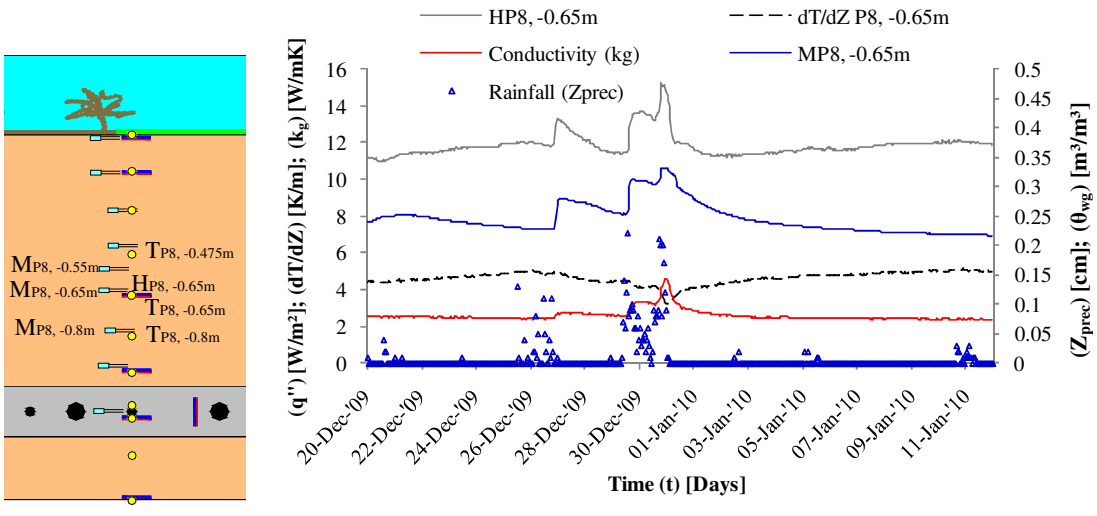

(a) P8 cross section **(b) Measured heat flux, temperature gradient, rainfall, moisture and conductivity**

Figure 5-14: In-situ measurement of the variation in ground thermal conductivity with moisture content from 20/12/2009 to 11/01/2010

The conductivity (k) [W/mK] can be calculated using a variation of *Fourier's law* as follows:

$$k = \left| q'' / \frac{\Delta T}{\Delta Z} \right| \tag{5-28}$$

Equation 5-28 can be implemented using data from two temperature sensors ($T_{P8,\ -0.475m}$ and $T_{P8,\ -0.8m}$) and one heat flux sensor ($H_{P8,\ -0.65m}$) as expressed in Equation 5-29. This was done during a period of a relatively stable and undisturbed thermal gradient across the key heat flux sensor, $H_{P8,\ -0.65m}$.

$$k = \left| H_{P8,-0.65m} / \left(\frac{T_{P8,-0.475m} - T_{P8,-0.8m}}{-0.475-(-0.8)} \right) \right| \tag{5-29}$$

As well as producing minimum, average and maximum ground conductivity values of 2.3, 2.6 and 4.1W/mK, this method was also sensitive to the influence of rainfall and hence ground moisture content on thermal conductivity. It can be seen in Figure 5-14(b) that heavy rainfall between the 26th of December and the 1st of January resulted in a 44% increase in the soil moisture content from 0.231 to 0.332m^3/m^3 which resulted in a 64% increase in thermal conductivity from 2.5 to 4.1W/mK. Figure 5-15 compares the measured and modelled (AL-6) variation in thermal conductivity with moisture content at P8. It can be seen that while model AL-6 gives a decent estimate of thermal conductivity between 0.2 and 0.25m^3/m^3, the measured thermal conductivity increases sharply with moisture content between 0.25 and 0.35m^3/m^3. Reasons for this sharp increase require further investigation potentially in an extensive laboratory-based experiment using soil from the *HP-IRL/H* site.

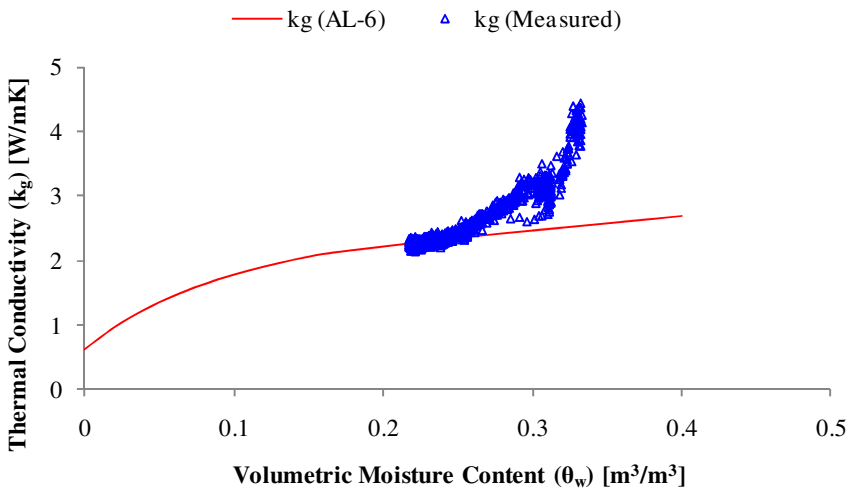

Figure 5-15: Measured and modelled (AL-6) variation in thermal conductivity with moisture content, measured data was recorded in P8 at one hour intervals between December 2009 and January 2010

5.3.6 Summary of HP-IRL/H Mean Properties

The mean ground thermal diffusivity (α_g) was defined as 1.05 x 10^{-6} m^2/s in Section 4.5.3 using a best fit to Equation 4-14. Therefore, mean volumetric heat capacity (C_g) [J/m^3K] is found as follows:

$$C_g = k_g/\alpha_g = 2.6/1.05 \times 10^{-6} = 2.48 \times 10^6 \, J/m^3K \quad (5\text{-}30)$$

Dry bulk density (ρ_{bulk}) [kg/m^3] was measured by removing a bulk sample from the ground, oven drying and sealing the sample in plastic (without disturbing the sample structure) before placing it in a specific gravity rig (*ELE Buoyancy Balance System).* This yielded a dry bulk density of 1337kg/m^3. The variation in ground density (ρ_g) [kg/m^3] with ground moisture content (θ_{wg}) is defined using Equation 5-31, where θ_{wg} in P8 was seen to vary between 0.15 and 0.35m^3/m^3, as shown in Figure 5-5.

$$\rho_g = \theta_{sg}\rho_{sg} + \theta_{wg}\rho_w = \rho_{bulk} + \theta_{wg}\rho_w = 1337 + \theta_{wg}998 \approx 1487 \rightarrow 1686 \quad (5\text{-}31)$$

Mean specific heat capacity ($c_{p,g}$) [J/kgK] was then found to be 1563.2 J/kgK by dividing volumetric heat capacity (C_g = 2.48 x 10^6 J/m^3K) by the density (ρ_g = 1586.5 kg/m^3) which was evaluated at the average moisture content (θ_{wg} = 0.25m^3/m^3). Table 5-7 compares the mean *HP-IRL/H* properties with the average of values quoted by 9 authors internationally (Mei, 1987; Wibbels & Den Braven, 1994; Gauthier *et al.*, 1997; Deru & Kirkpatrick, 2001; Ochsner *et al.*, 2001; Incorpera & DeWitt, 2002; Badesku, 2007; Demir *et al.*, 2009; Pulat *et al.*, 2009). The *HP-IRL/H* thermal diffusivity corresponds to the upper limit of the literature range, which is to be expected, since the thermal conductivity also corresponds to the upper limit. It was seen in Sub-section 5.3.2 that sand was the dominant particle size during the PSD sampling of P8. Salomone & Wechsler (1984) found that increased medium and coarse sand fractions can increase thermal conductivity; similarly Table 5-5 shows that saturated sand has the highest thermal conductivity range of all textures. Finally, Table 5-6 and Figure 5-12 indicate that sandy soils have higher hydraulic conductivity and lower matric potential than soils with high silt or clay fractions which increases water movement. The volumetric heat capacity and specific heat capacity measured at the *HP-IRL/H* site are well within the range from the literature. These properties are used for simulations in Chapters 7 and 8.

Table 5-7: Comparison of average reported values with mean HP-IRL/H values

Property	Symbol	Units	Literature Mean	Standard Deviation	*HP-IRL/H*
Thermal Diffusivity	(α_g)	[m^2/s]	6.9 x 10^{-7}	4.1 x 10^{-7}	1.05 x 10^{-6}
Thermal Conductivity	(k_g)	[W/mK]	1.694	0.91013	2.6
Volumetric Heat Capacity	(C_g)	[J/m^3K]	2.50 x 10^6	8.13 x 10^5	2.48 x 10^6
Density	(ρ_g)	[kg/m^3]	1760.2	220.035	1586.5
Specific Heat Capacity	($c_{p,g}$)	[J/kgK]	1455.33	571.984	1563.2

5.4 GROUND TEMPERATURE SIMULATION

Two methods were used in *HP-IRL/H* to simulate hourly changes in vertical ground temperature profiles using measured weather parameters. The first, identified as NL-1, involves ground conduction only and was created as part of the *HP-IRL/H* project, while the second, identified as NL-2, calculates the coupled heat and mass transfer in the ground using the *SHAW23* software tool.

While many complex ground temperature and water models/software are in existence, these are mainly 1-D models such as *SHAW23* used in the area of agriculture research and are incapable of incorporating the 2-D or 3-D influence of a horizontal collector. Therefore, it was necessary to develop a customised, albeit simplified, 1-D numerical simulation method (NL-1) which could be easily adapted to 2-D and quasi-3-D collector simulations in collector models NL-4 and NL-5 respectively. Since the application of NL-4 and NL-5 was to predict and compare the performance of different horizontal collector designs, the complex ground water functions of agricultural models, such as *SHAW23*, were dropped in favour of robustness and ease of implementation.

5.4.1 Model NL-1: One-Dimensional Transient Ground Temperature Simulation

In order to examine the simulation potential of the surface energy balance (Equation 5-2) combined with the heat diffusion equation (Equation 5-8) and to assess the accuracy and usefulness of this combination for subsequent $GSHP_{HC}$ simulation, a ground temperature simulation model, NL-1, was created. The following is a summary of the method employed:

- 1-D transient model – $T_g(Z,t)$
- Explicit Finite Difference (EFD) approximation of Equation 5-8
- *Ground-atmosphere interface* energy balance using Equation 5-2
- Deep ground condition and initial conditions using Equation 4-14
- Pure conduction heat transfer in the ground
- Implemented in spreadsheet format in *MS-Excel*
- *Visual Basic macros* were used to sort and prepare weather input files
- Vertical depth increment of 0.25m
    - Temperatures at intermediate depths can be interpolated
- Time increments of 60 minutes

The model geometry and a sample of the resulting spreadsheets are shown in Figures 5-16(a) and (b) respectively. The temperatures T_{cov}, T_{sur} and T_g defined in Sub-section 5.1.2 have

been assigned numerical nodes at the *ground-atmosphere interface*, for a bare ground surface $T_{cov} \rightarrow T_{sur}$ and $T_{sur} \rightarrow T_g$. Below the surface the ground has been divided into layers of thickness ΔZ each with a temperature T_Z and the lower boundary temperature is defined as T_{LB} at Z_{LB}.

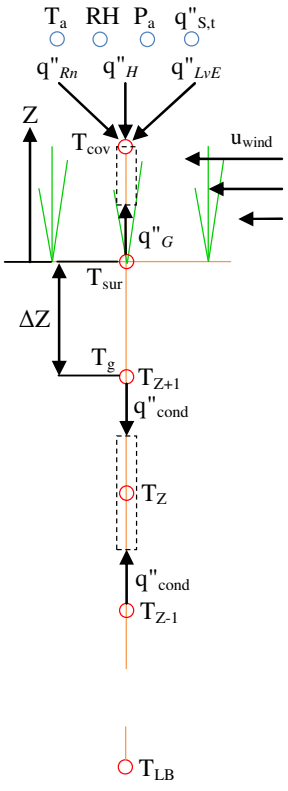

(a) NL-1 nodal Geometry

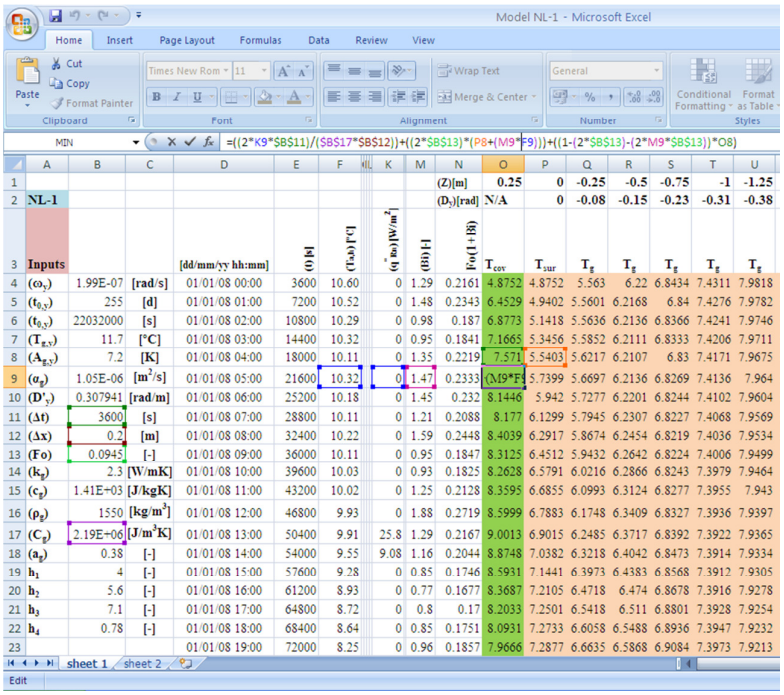

(b) Spreadsheet with nodal T equations interconnected in Z and t

Figure 5-16: NL-1 numerical simulation technique

5.4.1.1 Heat Transfer with the Finite Difference Method

Finite Difference Method (FDM) is one of a number of numerical methods which allow a differential equation such as Equation 5-8 or 5-19, describing a parameter which varies in both time and space, to be represented as a collection of algebraic equations with initial and boundary conditions. These can then be solved using a computer. Finite Element Method (FEM) and Finite Volume are other methods, with FEM being extremely useful for complex geometries. Given the simple geometry of this 1-D heat transfer problem then Equation 5-32, an Explicit Finite Difference (EFD) equation, is suitable to solve Equation 5-8 (Incorpera & DeWitt, 2002).

$$T_Z = Fo\left(T_{Z+1}^p + T_{Z-1}^p\right) + (1 - 2Fo)T_Z^p \qquad (5\text{-}32)$$

Where T_Z (ºC) represents the temperature of the node (ground layer) of interest in the current time-step (t), T_Z^p represents the temperature of this node in a previous time-step (p= t - Δt) and T_{Z+1}^p and T_{Z-1}^p represent the temperatures of the layers above and below respectively in the previous time-step. Therefore, as expected the current temperature of a soil layer depends on the previous temperature of that layer and the layers around it. The Fourier number Fo [-] is a calculation coefficient which combines the soils thermal properties and the temporal and spatial dimensions of the model as follows:

$$Fo = \frac{\alpha \Delta t}{(\Delta Z)^2} \leq SC \tag{5-33}$$

For EFD the Fourier number must satisfy certain Stability Criteria (SC) to insure model stability. For stability, the T_Z^p coefficient must be greater than zero, for this simple 1-D node Fo must not exceed 0.5. The Fo stability criteria are stated in the subsequent models involving more complex nodes. Since the thermal properties and density of the surface cover can differ greatly from the underlying ground and because the ground layers may exhibit varying properties, the Fourier number can be varied with depth for improved accuracy. Variations of this FDM are used in 1-D, 2-D and a quasi-3-D form in all of the subsequent models involving the ground and the *GSHP$_{HC}$*. The key node in a 1-D ground temperature simulation is the ground-atmosphere interface and the energy balance used for this node now described.

5.4.1.2 Surface Energy Balance

The surface energy balance is based directly on Equation 5-2. When constructing FD energy balance equations, the convention is to consider all heat transfer into the node of interest as positive and then write the energy balance equations accordingly, as expressed in Equation 5-34. The storage term represents a surface layer which is half the thickness (ΔZ/2) of the underground layers (ΔZ) as shown in Figure 5-16(a).

$$\rho_g c_g \frac{\Delta Z}{2} \frac{(T_{cov} - T_{cov}^p)}{\Delta t} = (q''_{R_n} + q''_{L_vE}) + h\left(T_a - T_{cov}^p\right) + k_g \left(\frac{T_{sur}^p - T_{cov}^p}{\Delta Z}\right) \tag{5-34}$$

This can be re-written in terms of the surface node in the current time-step as Equation 5-35, where all symbols have been previously defined.

$$T_{cov} = \frac{2(q''_{R_n} + q''_{L_vE})\Delta t}{\rho_g c_g \Delta Z} + \frac{2h\Delta t}{\rho_g c_g \Delta Z}\left(T_a - T_{cov}^p\right) + \frac{2\alpha \Delta t}{\Delta Z^2}\left(T_{sur}^p - T_{cov}^p\right) + T_{cov}^p \tag{5-35}$$

Using the Fourier number (Fo) [-] (Equation 5-33) and the Biot number (Bi) [-] (Equation 5-37), then Equation 5-35 can be re-written as Equation 5-36.

$$T_{cov} = \frac{2(q''_{Rn}+q''_{LvE})\Delta t}{\rho_g c_g \Delta Z} + 2Fo\left(T^p_{sur} + BiT_a\right) + (1 - 2Fo - 2BiFo)T^p_{cov} \quad (5\text{-}36)$$

$$Bi = \frac{h\Delta Z}{k} \quad (5\text{-}37)$$

For stability, the coefficient of T^p_{cov}, which is (1-2Fo-2BiFo) must not drop below zero. Therefore, the stability criterion for the surface node is:

$$Fo(1 + Bi) \leq \frac{1}{2} \quad (5\text{-}38)$$

The net radiation (q''_{Rn}) can be written using Equation 5-3, where the long-wave radiation from the surface (q''_{LWO}) can be evaluated as a function of T^p_{cov}. For a sloped surface of angle (β) [°] and orientation (γ) [°], the solar radiation $q''_{s,t}$ measured on a flat surface (β=0°) at every hour can be modified using Equation 5-39. The hourly cosine of the Sun's angle of incidence cosΘ (Ω,β,γ,d,hr) can be found using model AL-1, described in Sub-section 4.2.1.

$$q''_{s,t}(\beta,\gamma) = q''_{s,D} + [\cos\Theta(\beta,\gamma)\frac{q''_{s,t(\beta=0)}}{\cos\theta_{(\beta=0)}}] \quad (5\text{-}39)$$

The atmospheric emissivity (ε_a) [-] can be calculated using Equation 5-40 (Saito & Simunek, 2009).

$$\varepsilon_a = 0.179P^{1/7}_{a,vap}\exp(\frac{350}{T_a}) \quad \text{with } P_{a,vap} \text{ in hPa} \quad (5\text{-}40)$$

Where, the atmospheric water-vapour pressure ($P_{a,vap}$) [hPa] can be calculated using Equation 5-41 and 5-42 (Golaka & Exell, 2004).

$$P_{a,vap} = 0.01(RH)P_{a,sat} \quad [hPa] \quad (5\text{-}41)$$

$$P_{a,sat} = 6.112\exp\left(\frac{17.67T_a}{T_a+243.5}\right) \quad [hPa] \quad (5\text{-}42)$$

The convection coefficient (h) [W/m^{2}K] in Equation 5-37 is calculated using the correlations in Equations 5-43 and 5-44 (Palyvos, 2008), which depend on wind speed (u_{wind}) [m/s].

$$h = 3.95u_{wind} + 5.8 \ (u_{wind} \leq 5m/s) \quad (5\text{-}43)$$

$$h = 7.1(u_{wind})^{0.78} + 5.36\exp^{-0.6u_{wind}} \ (u_{wind} > 5m/s) \quad (5\text{-}44)$$

The evaporative heat flux q''_{LvE} can be defined using Equation 5-45 (Qin *et al.*, 2002), where L_v [2257kJ/kg] is the latent heat of vaporisation, $P_{a,vap}$ and $P_{sur,vap}$ [kPa] are the air and surface vapour pressures, P_a [kPa] is the atmospheric air pressure and r_a and r_{sur} [s/m] are the air and surface evaporation resistance coefficients described in Qin *et al.* (2002).

$$q''_{L_vE} = \frac{0.622L_v(P_{a,vap}-P_{sur,vap})}{(P_a(r_a+r_{sur}))} \quad (5\text{-}45)$$

Surface freezing is not considered in this NL-1 model since it is not common at the *HP-IRL/H* site, the surface layer was only below 0.3ºC for 0.7% of the 3.5 year *HP-IRL/H* project, however soil freezing is included in model NL-2.

A precipitation heat flux can be included using Equation 5-46 (Demir *et al.*, 2009).

$$q''_{prec} = \dot{m}''_{prec} c_{p,w} (T_a - T_{cov}^{p}) \quad (5\text{-}46)$$

Where the precipitation mass flux ($\dot{m}''_{prec}$) [kg/m^{2}s] is found as follows:

$$\dot{m}''_{prec} = [\rho_w (Z_{prec}/1000)]/3600 \quad Z_{prec} \text{ is recorded in mm/h} \quad (5\text{-}47)$$

As a lower boundary condition for the NL-1 simulation, model AL-4 which is described in Section 4.2.4 can be applied to calculate ground temperatures below a 2m depth where changes follow a seasonal pattern and are not influenced by short term fluctuations.

5.4.2 Model NL-2: One-Dimensional Transient Ground Temperature Simulation with Moisture and Ice Content

In order to examine the *SHAW23* software which combines the surface energy and water balance (Equation 5-2 and 5-15) with the coupled heat and mass transfer processes (Equation 5-22 and 5-23) and to assess its accuracy and usefulness, a ground simulation model, NL-2, was completed. NL-2 is a complete environmental model of the *HP-IRL/H* site using the *Simultaneous Heat and Water SHAW23* software tool developed by the *US Department of Agriculture (USDA)* (Flerchinger, 2000). The following is a summary of the method employed:

- 1-D transient model – $T_g(Z,t)$
- Implicit Finite Difference (IFD) approximations of Equations 5-22 and 5-23
- *Ground-atmosphere interface* energy balance using Equation 5-2
- *Ground-atmosphere interface* water balance using method equivalent to Equation 5-15
- Hydraulic properties at a node are a function of moisture content using Equation 5-17 and 5-18
- Thermal properties are a function of moisture content using Equation 5-24 and 5-25
- Texture dependent inputs for hydraulic and thermal property sub-routines were taken from Table 5-6 based on the texture analysis of the *HP-IRL/H* site in Table 5-4
- Deep ground and initial conditions require T and θ_{wg} data or analytical (AL-4) input
- Coupled heat and mass transfer in the ground

- *SHAW23* completes an iterative solution using Newton Raphson method in *Fortran*
- *Visual Basic macros* were used to sort and prepare weather input files
- Vertical depth increment of 0.15 to 0.3m
- Time increment of 60 minutes

SHAW23 solves the coupled heat and water transport problem, Equations 5-22 and 5-23 respectively, using IFD and an iterative procedure at each time-step. This involves first solving Equation 5-22 with IFD (Sol-1-T) and then solving Equation 5-23 with IFD (Sol-1-θ) using the results of Sol-1-T. Equation 5-22 is then solved again (Sol-2-T) using the results of Sol-1-θ and the deviation from the first solution (Sol-1-T – Sol-2-T) is evaluated. This process is repeated until convergence of solutions for both equations is achieved for each time-step.

The model geometry, along with a sample of the output results matrix (T, θ_{liq}, θ_{ice} and ψ) after each time-step, is presented in Figure 5-17. *SHAW23* has the facility to include vegetation ground cover such as grass, shrubs or trees; T_{cov} is therefore identified as the vegetation node (T_{plant}) [ºC]. A complete description of the software can be found in the *SHAW23 Technical Documentation* (Flerchinger, 2000).

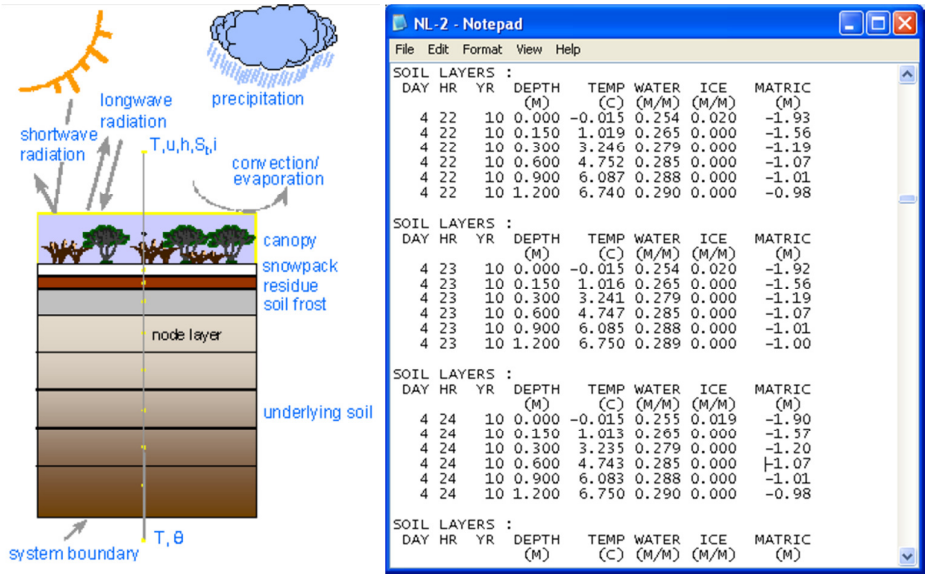

(a) SHAW23 nodal Geometry **(b) Matrices of T, θ_{liq}, θ_{ice} and ψ output after each time-step**

Figure 5-17: NL-2 numerical simulation technique using SHAW23 software

5.4.3 Ground Temperature Prediction Comparative Study

The analytical model AL-5 (Section 4.2.5) and the numerical models NL-1 and NL-2 were compared with hourly *HP-IRL/H* ground temperatures measured during 2008. The nodal geometries of AL-5, NL-1 and NL-2 are shown alongside the experimental profiles P1, P3

and P6 in Figure 5-18. For comparison, $T_{P6,\ +0.01m}$ is used as the surface cover node (T_{cov}), while $T_{P1,\ 0.0m}$ is used as the bulk surface node (T_{sur}) and $T_{P1,\ -0.15m}$ to $T_{P1,\ -1.8m}$ are used as the ground temperature (T_g) nodes. Temperatures for depths not corresponding to an exact node or sensor are calculated through interpolation between the closest points; over short distances, interpolation introduces minimal error.

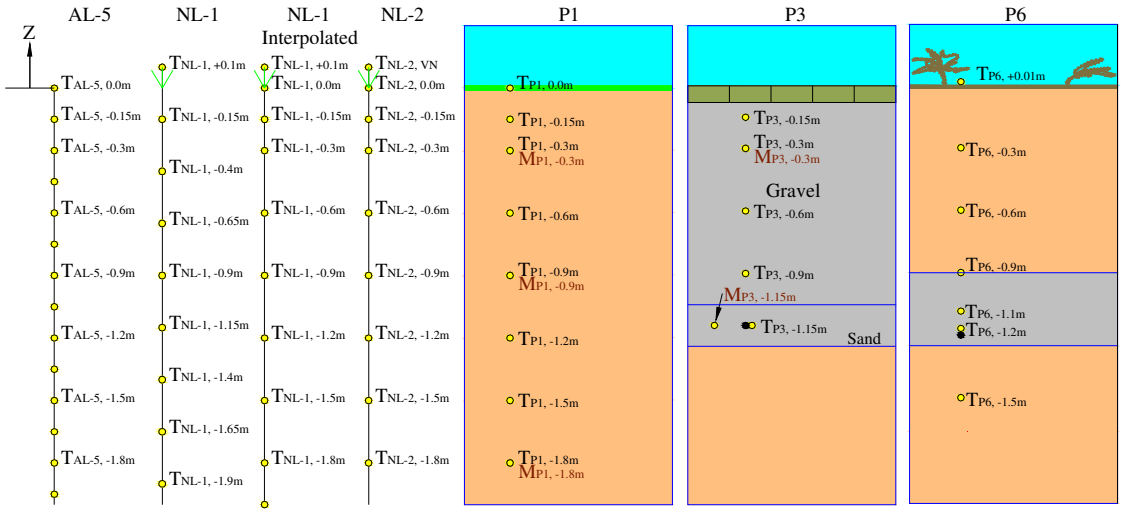

(a) Model and simulation nodes **(b) Vertical experimental profiles P1, P3 and P6**

Figure 5-18: Schematics of temperature nodes in models and sensors in the experimental profiles

The R^2 value is frequently used to evaluate model or simulation results. R^2 becomes 1 in the absence of error and 0 if there is no relationship between measured and estimated values (Kim *et al.*, 2007). The R^2 formula is presented in Equation 5-48 (Kim *et al.*, 2007), where X_i and Y_i represent the i^{th} value of the simulated and observed temperatures respectively.

$$R^2 = \left[\frac{n(\sum_{i=1}^{n} X_i Y_i) - (\sum_{i=1}^{n} X_i)(\sum_{i=1}^{n} Y_i)}{\sqrt{\left[n\sum_{i=1}^{n} X_i^2 - (\sum_{i=1}^{n} X_i)^2\right]\left[n\sum_{i=1}^{n} Y_i^2 - (\sum_{i=1}^{n} Y_i)^2\right]}}\right]^2 \quad (5\text{-}48)$$

The simulated temperature data is also plotted against observed data to check for linearity. Table 5-8 presents the results of the comparative study. Unsurprisingly, AL-5 which involves a waveform moving about multiyear average values has good linearity, however since short term weather fluctuations are not incorporated the R^2 values are the poorest of the three. NL-1 also has good linearity and much improved R^2 values, due to energy balance with hourly weather data. NL-2 has R^2 values similar to NL-1 but lacks some linearity at the bulk ground surface (T_{sur}). This may be due to error at the T_{plant} (T_{cov}) and T_{sur} interface. However, NL-2

was the only method of the three which accurately predicted ground surface frost ($T_{sur} \approx 0$ºC) in January 2010, as shown in Figure 5-19.

Table 5-8: Comparison of simulated and observed ground temperatures for three methods

Model	Comparison	T_{cov} ($T_{P6, +0.01m}$)	T_{sur} ($T_{P1, 0.0m}$)	T_g ($T_{P1, -0.15m}$)
AL-5	Linearity	N/A	1.0207	1.0317
AL-5	R^2	N/A	0.8412	0.8995
NL-1	Linearity	1.0864	1.0091	0.9728
NL-1	R^2	0.8551	0.9026	0.972
NL-2	Linearity	1.0235	0.8959	0.909
NL-2	R^2	0.7913	0.9375	0.9685

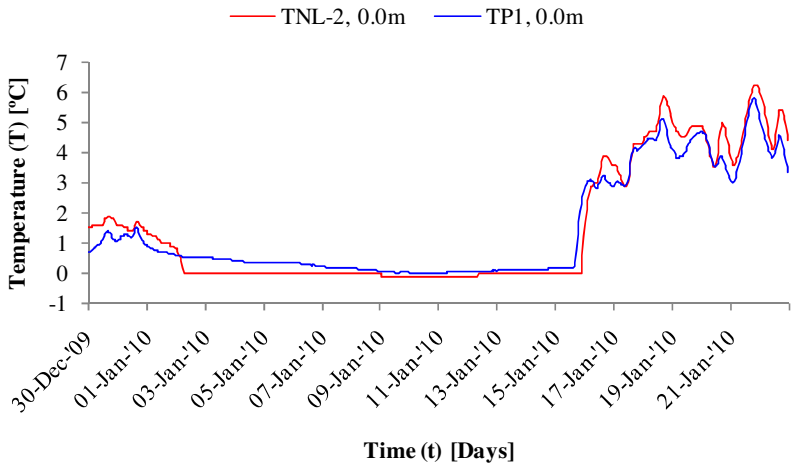

Figure 5-19: Comparison of NL-2 with measured ground surface temperatures ($T_{P1, 0.0m}$) during sub-0ºC ambient air temperatures

Mapping of daily ground temperature variation with both time and depth is displayed in Figure 5-20 for measured temperatures ($T_{P1, 0.0m}$ to $T_{P1, -1.8m}$) and the simulated temperatures ($T_{NL-1, +0.1m}$ to $T_{NL-1, -1.8m}$) and ($T_{NL-2, VN}$ to $T_{NL-2, -1.8m}$) between January 1st and December 31st 2008. The air temperature (T_a) and daily solar totals ($Q''_{S,t}$) for each day are displayed above these plots. Finally, the temperature differences (ΔT) between the simulated and observed values ($T_{NL-1} - T_{P1}$ and $T_{NL-2} - T_{P1}$) are displayed below the temperature maps.

The observations from these temperature maps and the supporting date are:

- NL-1 and NL-2 can both predict the seasonal trends in ground temperature using weather data inputs
- NL-1 has an average error of -0.2K at all depths over one year
- NL-2 has an average error of -0.5K at all depths over one year

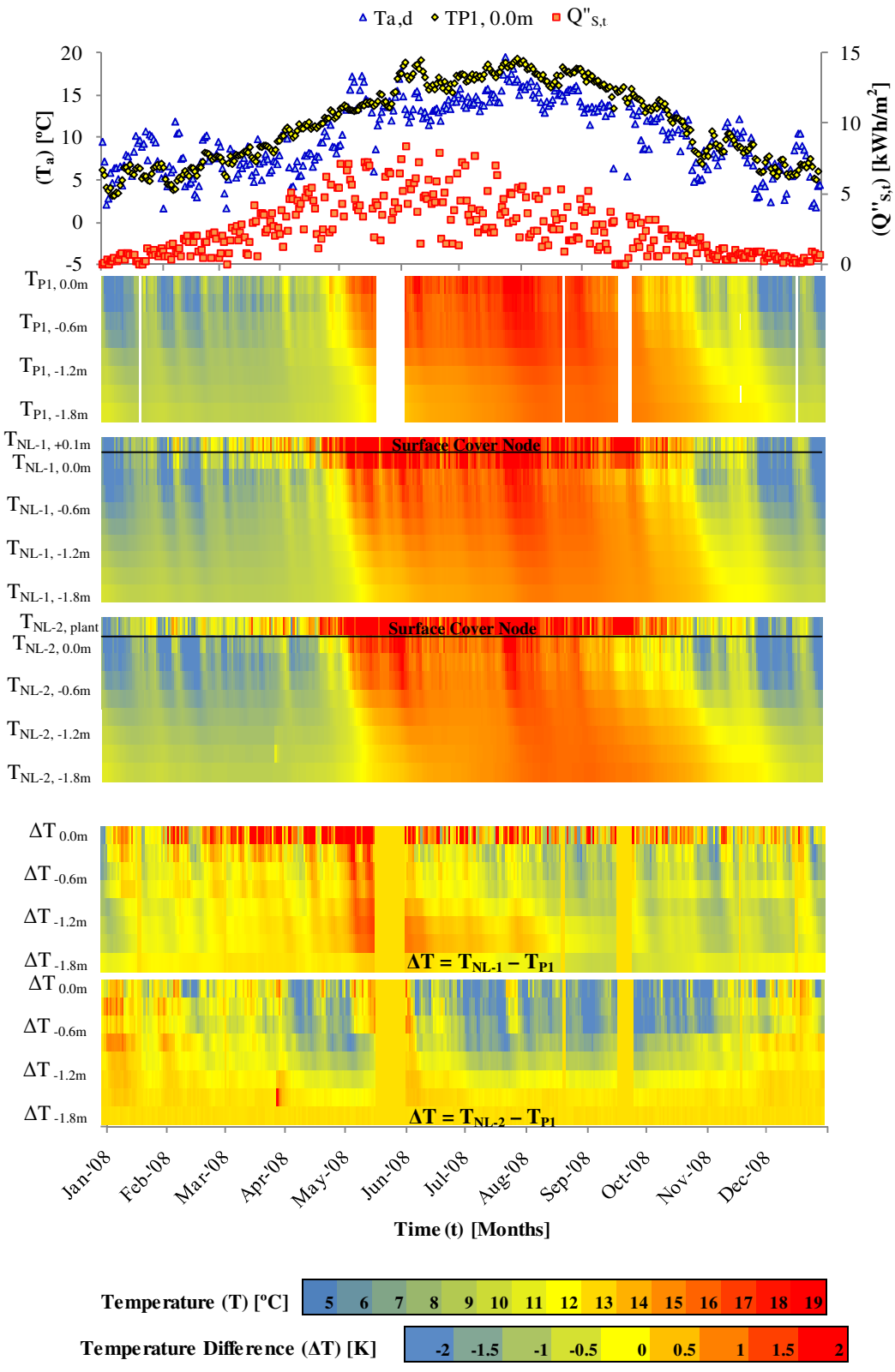

Figure 5-20: Comparison of simulated ground temperatures with measured values

- NL-1 has an R^2 value of 0.9026 at Z= 0.0m and R^2 improves with depth

- NL-2 has an R^2 value of 0.9375 at Z= 0.0m and R^2 improves with depth
- NL-1 tends to over-estimate ground temperature by 2K at the start of May 2008, this is possibly due to under-estimating the evaporation
    - Many evaporation correlations exist however due to the number of variables involved no single-coefficient law equivalent to *Newton's law* exists
- NL-2 tends to under-estimate ground temperature by -2K between April and November 2008, this is possibly due to over-estimating the evaporation
- NL-1 is a more straightforward method, it is faster to code, requires less inputs and is faster to run
- NL-2 is a more complete method but requires more complex inputs and solution

The comparison of NL-1 and NL-2 under *Cool Marine* conditions indicates that NL-1 has equivalent or better accuracy than NL-2 and is suitable to be used in $GSHP_{HC}$ simulation. Further investigation of NL-1's predictive accuracy over hourly and daily time periods is presented in Section 7.4.1 along with NL-1 parametric studies.

5.5 INFLUENCE OF SURFACE COVER

Given that the *ground-atmosphere interface* is the environment's plane of influence on ground temperature distribution, it is surprising that the effect of surface cover type, slope and orientation have seen only limited research. It has been reported that bare ground surfaces such as gravel, pavement and asphalt reach temperatures significantly higher than ground surfaces beneath a grass cover in summer, however in winter with the weakened solar intensity this effect in not as profound (Mihalakakou & Lewis, 1996; Popiel *et al.*, 2001; Takebayashi & Moriyama, 2009). Figure 5-21(b) show summer surface temperatures for bare soil which are 8 to 10ºC higher than those under grass by in Athens, Greece. However, temperatures shown in Figure 5-21(a) are quite similar in Dublin, Ireland (Mihalakakou, 2002). Winter surface temperatures in Dublin are almost identical under both grass and bare soil; however in Athens the bare soil temperature is still slightly higher.

The differences between the two sites is due mainly to the abundance of sunshine in Athens (37ºN) compared with Dublin (53ºN). The effect of surface cover penetrates downward affecting the GTD. Popiel *et al.* (2001) reported that the temperature of the ground 1m below a 'bare' car park was about 4ºC higher than that recorded 1m beneath a grass covered surface during summer months however in winter the temperature distributions were almost the same. The temperature differences reported by both Popiel *et al.* (2001) and Mihalakakou (2002) are

likely to be caused by the lower albedo of darker bare surfaces, the lack of shading and insulation provided by grass or shrub cover and the absence of moisture in brick or pavement which would remove heat as it evaporates and also increase the volumetric heat capacity.

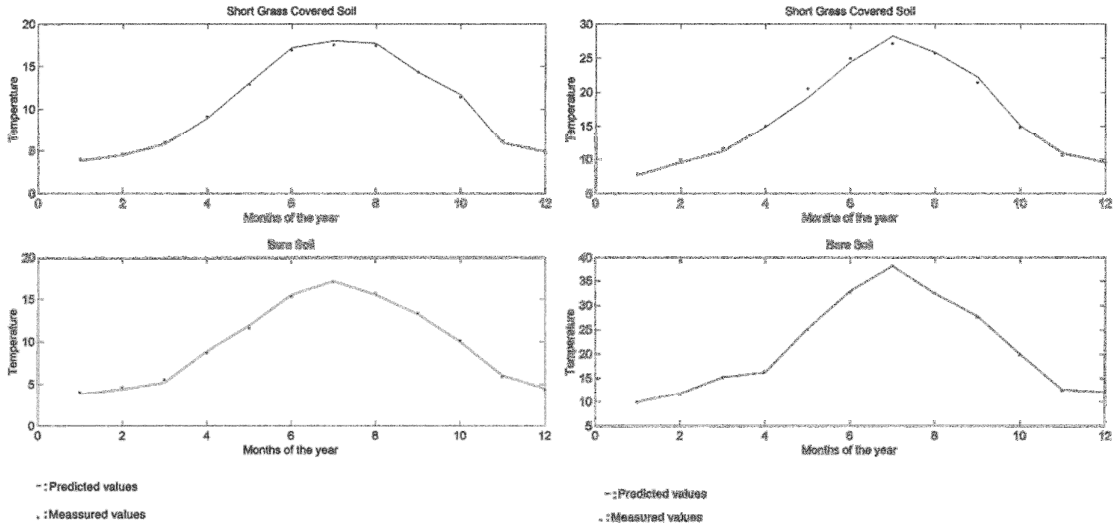

(a) Dublin, Ireland **(b) Athens, Greece**

Figure 5-21: Predicted and measured values for grass covered soil (top) and bare soil (bottom) in Dublin, Ireland (left) and Athens, Greece (right) (Mihalakakou, 2002)

Studies have experimentally characterised the negative results of this heating on urban areas and water systems (Van Buren *et al.*, 2000) and experimentally tested ways to mitigate this heating, mainly by introducing more grass into the surface of urban areas (Asaeda & Thanh Ca, 2000; Takebayashi & Moriyama, 2009). However, few methods have been proposed to take advantage of this effect, one example proposed is the asphalt solar collector for summer water heating (Loomans *et al.*, 2003). It was a goal of the *HP-IRL/H* project to investigate if these positive effects could be harnessed to deliver higher $GSHP_{HC}$ SPFs.

5.5.1 HP-IRL/H Surface Temperature Comparative Study

Using the ground temperature data recorded in *HP-IRL/H*, a comparison is made between the observed temperatures in profiles P1, P3 and P6, shown in Figure 5-18, with grass cover, bare brick and shrub cover respectively. Similar comparisons have been made in Dublin/Athens (Mihalakakou & Lewis, 1996), in Saitama, Japan (Asaeda & Thanh Ca, 2000) and in Poznan, Poland (Popiel *et al.*, 2001).

5.5.1.1 Surface Thermal Properties and Surface Cover

A comparison between the ground temperature under grass cover at $T_{P1, -0.15m}$ and bare brick at $T_{P3, -0.15m}$ in the *HP-IRL/H* site is displayed in Figure 5-22. When compared with the grass covered soil in profile P1, observed ground temperature at 0.15m depth in the bare brick profile P3 is significantly higher (≈ +7 to +8K) during summer and marginally lower (≈ -1 to -2K) during winter. Hence brick surface covers would suit summer hot water applications, but should be avoided for winter space-heating applications.

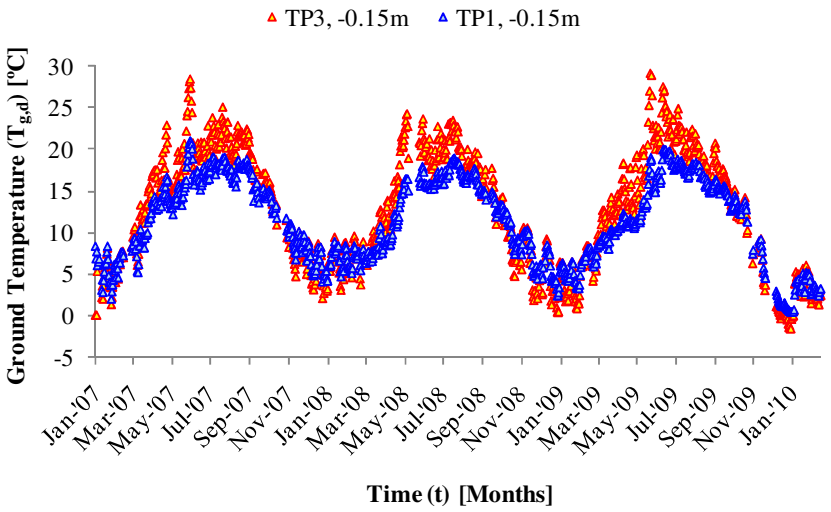

Figure 5-22: Comparison of daily averaged ground temperatures at a depth of 0.15m under grass (P1) and brick (P3) within the HP-IRL/H site

The variation in surface temperature between the P1 and P3 can be attributed to the following reasons:

- The albedo (a) [-] defines the ratio of reflected to incident solar radiation; the albedo of grass is typically taken as 0.23 while the albedo of brick is typically quoted as 0.05 to 0.1, therefore brick absorbs more solar radiation
- Emissivity (ε) [-] defines the ratio between the longwave thermal radiation emitted by a solid such as brick (ε≈0.96) or grass (ε≈0.96) and a black body (ε=1) at a temperature T [K]; since the emissivity of grass and brick are quite similar, a similar amount of heat is radiated by the two surfaces
- Diffusivity (α) [m^2/s] defined in Sub-section 4.5.3 is the ratio of thermal conductivity to volumetric heat capacity and defines how quickly the temperature of a solid reacts to changes in the temperature of its surroundings; by its nature grass would have a

lower conductivity and therefore both summer and winter temperatures under the grass cover show less extreme variation than under the brick. This insulating effect is also shown in Figure 5-23 during a cold weather period in 2009 when $T_{P3, -0.15m}$ shows sub-0ºC temperatures while $T_{P1, -0.15m}$ shows temperatures above 0ºC

- The volumetric moisture content θ_{wg}, of surface cover has a significant influence on the ground temperature due to the processes of evaporation and freezing which result in less extreme temperatures in summer and winter respectively; P1 which has a soil bulk surface and contains about 10 to 30% moisture by volume compared to P3 which has a brick bulk surface and contains less than 2.5% moisture by volume

5.5.1.2 Freezing and Thawing

The influence of moisture on both the sensible and latent heat capacity of the ground in both summer and winter is shown in Figure 5-22. This influence during winter, the time when $GHSP_{HC}$ is used, is shown at higher resolution over a 1 month period in Figure 5-23.

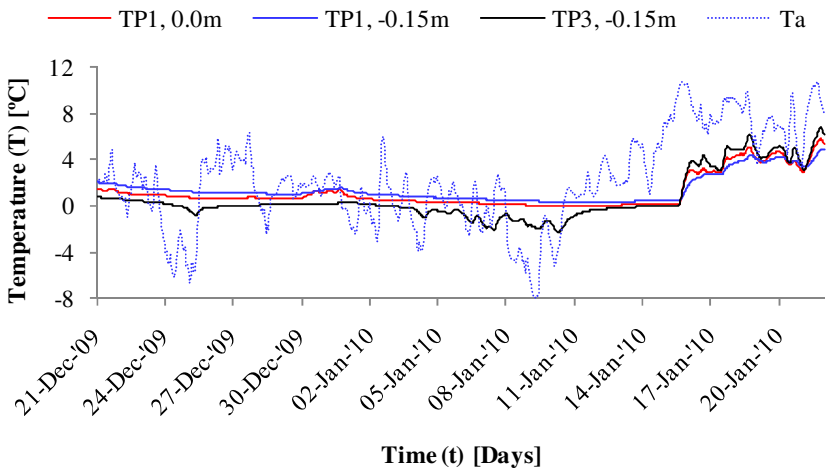

Figure 5-23: Surface insulation and moisture content effects during a cold weather period in 2009-2010

During the cold period between the 21st of December and the 16th of January, where air temperature is consistently below 0ºC at night and drops as low as -8ºC, the ground temperature at a depth of 0.15m in P1 remains at between 0.5 and 1ºC while the ground temperature in P3 drops below 0ºC and reaches a minimum of -2ºC. During this period the temperature in P1 at the bulk surface hovers just above 0ºC indicating that freezing of surface and surface cover moisture was taking place. The latent heat of water available to this

freezing process insured that the cold atmospheric conditions were unable to penetrate to a depth of 0.15m in P1, whereas this latent heat was not available at the *ground-atmosphere interface* in P3. Consequently, it is shown in Figure 5-23 that P3 heats up more rapidly than the frozen P1 when air temperatures begin to rise.

Soil freezing in Ireland typically occurs for short time periods and is confined to the first 5cm of surface cover plus ground surface. Table 5-9 presents the number of hours where the temperature was less than +0.3ºC at the *HP-IRL/H* facility over 3.64 years (31,872 hours), using recorded values of T_a, $T_{P1,\ 0.0m}$, $T_{P1,\ -0.15m}$ and $T_{P5,\ -1.0m}$. The temperature of +0.3ºC was chosen for the following two reasons:

- It allows for sensor error, sensors were tested at 0ºC and found to be within ±0.3ºC
- It would be invalid to check for freezing at temperature less than 0ºC since freezing occurs at a constant temperature of 0ºC and it is impractical to test for temperatures that are exactly 0.0ºC

Table 5-9: Quantifying the number of hours that temperatures in the HP-IRL/H site were below +0.3ºC between 2007 and 2010

Parameter	Sensor	Hours with T< +0.3ºC	% of 31,872 hour data-set
Air temperature	T_a	536	1.68%
Surface Cover	$T_{P6,\ +0.01m}$	520	1.63%
Bulk surface	$T_{P1,\ 0.0m}$	224	0.70%
Bulk ground	$T_{P1,\ -0.15m}$	0	0%
Collector *'constriction profile'*	$T_{P5,\ -1.0m}$	0	0%

Over the 3.64 years of the *HP-IRL/H* project, the air temperature (T_a), surface cover temperature ($T_{P6,\ +0.01m}$), surface temperature ($T_{P1,\ 0.0m}$) and ground temperature ($T_{P1,\ -0.15m}$) were less than 0.3ºC for 1.68%, 1.63%, 0.7% and 0% of that time. More importantly, the temperature at the *collector-ground interface* ($T_{P5,\ -1.0m}$) was below 0.3ºC for 0% of the *HP-IRL/H* test program. This data indicates that no significant freezing is caused by either surface cooling or collector heat extraction within the *HP-IRL/H* collector volume; some slight freezing is detected at the ground surface but only for 0.7% of the 3.64 year test program. Therefore, it can be concluded that soil freezing algorithms in collector models are not necessary for simulations under Irish *Cool Marine* conditions.

5.5.1.3 Shading and Insulation

Figure 5-24 displays the *HP-IRL/H* collector area where the surface covers discussed in Sub-section 3.5.1 are shown. This photograph was taken at the beginning of December 2010 during a two week period of cold days and sub-zero Celsius nights. The purpose of this photograph was to examine the influence of shading from shrubs on ground temperature when the sun is at a low noon altitude in winter time. Figure 5-25 displays measured data from the cold period in question. The hypothesis was that shading caused by shrubs to the south would result in lower ground temperatures at $T_{P8,\ 0.0m}$ than $T_{P1,\ 0.0m}$. The results, shown in Figure 5-25, indicate only a slight variation with $T_{P8,\ 0.0m}$ less than $T_{P1,\ 0.0m}$ by a maximum of -1.7K.

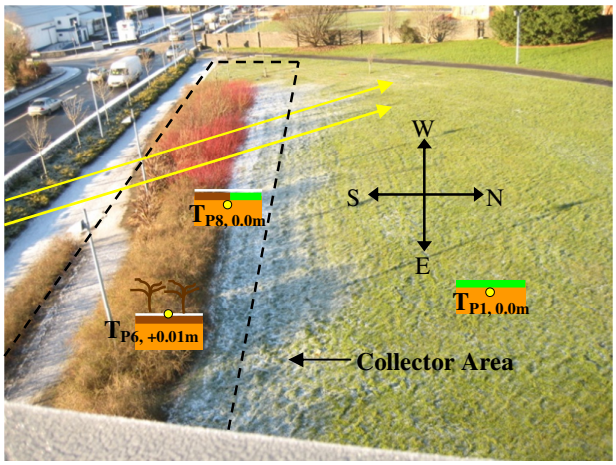

Figure 5-24: The HP-IRL/H collector area photographed at 11:30am on December 8th 2010 during a period of 14 cold days and sub-zero nights; November 26th to December 10th 2010

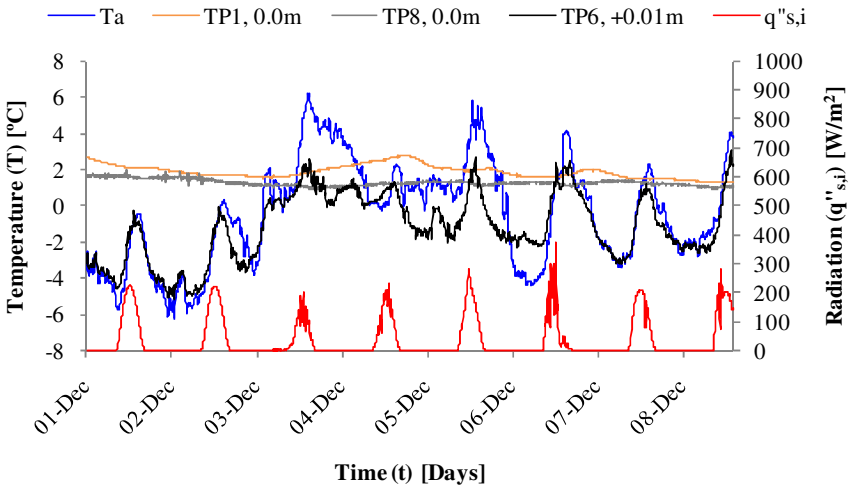

Figure 5-25: A study of shading and insulating effects during a cold weather period in 2010

However, the results also show the insulating influence of a moisture laden vegetative cover. In P6, the surface sensor $T_{P6, -0.01m}$ was buried at Z=+0.01m protruding above the soil surface and grass; it can be seen that $T_{P6, +0.01m}$ follows the T_a extremes. However, in P1 and P8 the sensors $T_{P1, 0.0m}$ and $T_{P8, 0.0m}$ respectively were buried at the bulk ground surface but below the grass and roots. This layer provides insulation from the cold surface conditions and also latent heat in the form of freezing moisture, as a result $T_{P1, 0.0m}$ and $T_{P8, 0.0m}$ record a minimum of 1 to 1.5ºC during this period compared to a minimum of -5ºC at $T_{P6, 0.01m}$.

These findings indicate that a moist vegetative surface cover acts as insulation with a built in phase change mechanism during cold winter periods and protects the ground beneath from excessive cooling in winter. Conversely, it is shown in Sub-section 5.5.1.1 that brick reacts more positively to sunshine in spring. Simulations undertaken by Burke (2010) indicate that twin collectors buried under both grass and asphalt for use in different seasons produce an 8% SPF improvement.

5.5.1.4 Slope and Orientation

The amount of solar radiation absorbed by a surface is influenced by slope and orientation as well as albedo. The effects of surface slope and orientation on incident radiation intensity are well understood and documented (Allen *et al.*, 2006; Sproul, 2007). The theoretical basis is presented in AL-1 (Section 4.2.1) and the impact on soil temperature has been assessed using NL-1 and NL-2 and results are presented in Section 8.1. Measured and modelled findings, reflecting the influence of slope and orientation on surface temperature have been published in the Czech Republic (Safanda, 1999), South Korea (Kang *et al.*, 2000) and the UK (Bennie *et al.*, 2008).

It has been shown that the southerly sloping surface of mountains in the Czech Republic can have an average surface temperature that is between 0.6 and 2ºC higher than that of flat surfaces and northerly slopes (Safanda, 1999). This temperature difference is due to the southerly slopes having a superior angle of incidence with the Sun's rays and has been used to advantage for centuries in growing grapes for example. Increased surface temperatures have been measured on South-Westerly slopes due to the combination of a superior angle of incidence at a time of day when air temperature is at its diurnal maximum (Bennie *et al.*, 2008).

As well as receiving more radiation on average than a flat surface the 'signature' of the annual radiation wave is also changed, as demonstrated in Figure 5-26 (Allen *et al.*, 2006). The

annual oscillation in Figure 5-26(b) appears as the first harmonic of the oscillation in Figure 5-26(a) with two peaks in spring and autumn respectively. Measurements indicate that during spring and autumn both the daily average $T_{g,d}$ (ºC) and the diurnal amplitude $A_{g,d}$ [K] were largest on South facing slopes (Kang *et al.*, 2000). This solar signature can be achieved for any surface such as a solar panel or indeed the ground surface of a shallow $GSHP_{HC}$ collector.

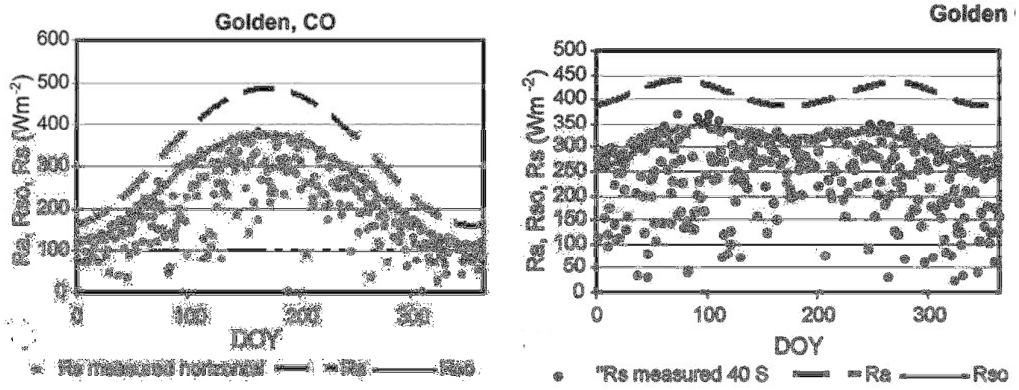

(a) Solar intensity on a flat surface **(b) Solar intensity on a southerly slope (40º)**

Figure 5-26: Measured, predicted terrestrial and predicted surface solar radiation for a flat surface and a south facing surface at a 40º incline at Golden, Colorado

The potential to improve the performance of a south facing solar collector in winter by tilting it forward to improve the Sun's angle of incidence has been well documented (Gunerhan & Hepbasli, 2007), as have the benefits of solar tracking (Poulek & Libra, 1998). However a similar study for improving $GSHP_{HC}$ performance by burying pipes on a south facing slope has not been published. The reason for this may be that in most countries the collector pipes are buried at 1.5 to 2m depth or more to avoid the extreme surface cooling. Additionally, the presence of snow on the surface, common in *Continental* winters, reflects the Sun's rays in winter.

However, in Ireland, the mild *Cool Marine* winters mean that pipes are buried at 0.8 to 1m and typically only light snow is present for no more than a couple of days per year. Modelled results predict that pipes can be buried even closer to the surface (0.5m depth) for improved $GSHP_{HC}$ performance in spring time (Burke, 2010). Therefore, the potential of a southerly sloping shallow collector pipe array for late autumn or spring use will be investigated numerically in Chapter 8.

5.6 SUMMARY

The chapter presents analysis of the transient heat transfer processes influencing the ground temperature distribution in the seasonal and diurnal resources and makes the following contributions to the *HP-IRL/H* project:

- The ground temperature analysis was divided into the following distinct parts for the purpose of discussion:
  - Energy exchange at the *ground-atmosphere interface*
  - Heat transfer in the underground layers

Ground-atmosphere interface

- A review was conducted of 8 studies on the *ground-atmosphere interface* from 9 countries published between 1993 and 2009
- Three key temperatures, T_{cov}, T_{sur} and T_g, were established at the *ground-atmosphere interface*
- Four key heat transfer processes, q''_{Rn}, q''_{H}, q''_{LvE} and q''_{G}, were identified at the *ground-atmosphere interface* and quantified using the recognised equations supported with data from the *HP-IRL/H* facility

Underground heat-transfer

- A review was conducted of 5 key studies on underground heat transfer from 5 countries published between 1958 and 2002
- Based on these 5 studies, other relevant books and articles and supported by *HP-IRL/H* data a review was presented on:
  - Underground heat diffusion
  - Ground water and its diffusion
  - Freezing of ground water
  - Coupled heat and water transfer combined with ice formation

Thermal and hydraulic properties

- A review was conducted of 8 $GSHP_{HC}$ studies on ground thermal properties from 4 countries published between 1984 and 2004
- Based on these 8 studies, other relevant books and articles and supported by *HP-IRL/H* data a review was presented on:
  - Soil texture
  - Influence of texture on thermal and hydraulic properties
  - Influence of moisture content on thermal and hydraulic properties

- A summary of the mean ground properties α_g, k_g, C_g, ρ_g and c_g at the *HP-IRL/H* site is presented
- All required inputs for simulating the *HP-IRL/H* collector are now quantified

Ground temperature simulation

- A 1-D ground temperature simulation model, identified as NL-1, was developed as part of *HP-IRL/H*
- A 1-D ground temperature, moisture and ice content simulation model, identified as NL-2, was completed using the *SHAW23* software tool
- An hourly ground temperature prediction comparative study found that:
  - AL-5 (described in Section 4.2.5) has an R^2 of 0.8412 at 0.0m
  - NL-1 has an R^2 of 0.9026 at 0.0m with an average annual error of -0.2K at all depths, NL-1 is easily adapted for use with $GSHP_{HC}$ collector pipes
  - NL-2 has an R^2 of 0.9375 at 0.0m with an average annual error of -0.5K at all depths, *SHAW23* models all ground heat transfer processes but is not suitable for collector simulation
- Comparison of NL-1 and NL-2 under *Cool Marine* conditions indicates that NL-1 has equivalent or better accuracy than NL-2 and is suitable to be used in $GSHP_{HC}$ simulation

Influence of surface cover

- Using experimental data from the *HP-IRL/H* facility and the literature, the influence of the following were assessed
  - Surface type and properties
  - Moisture freezing/thawing
  - Shading/insulation
  - Slope and orientation
- Temperatures under brick (P3) are higher (≈ +7 to +8K) in summer and lower (≈ -1 to -2K) during winter, when compared to temperatures under grass (P1)
- No significant freezing is caused by either surface cooling or collector heat extraction within the *HP-IRL/H* collector volume
  - Soil freezing algorithms are typically not necessary for *Cool Marine* conditions
- Shading from shrubs to the south can reduce surface temperature by -1.7K
- Moisture laden vegetation at the surface protects the ground from winter freezing

With ground thermal energy and heat transfer now characterised, Chapter 6 presents $GSHP_{HC}$ thermodynamic, thermal and hydraulic performance data with analytical characterisation.

CHAPTER 6

$GSHP_{HC}$ EXPERIMENTAL CHARACTERISATION

GMIT
GALWAY-MAYO INSTITUTE OF TECHNOLOGY
INSTITIÚID TEICNEOLAÍOCHTA NA GAILLIMHE-MAIGH EO

6. $GSHP_{HC}$ EXPERIMENTAL CHARACTERISATION

Using data from the experimental facility described in Chapter 3, the operation and performance of $GSHP_{HC}$ were characterised using simple analytical models presented in this chapter. This work was undertaken to: further the knowledge of $GSHP_{HC}$ system performance operating under *Cool Marine* conditions, derive the sub-models such as AL-7 for numerical simulations in Chapters 7 and identify experimental datasets for validating simulations in Chapter 7. This chapter is divided into the following six sections:

- *HP-IRL/H* test program (2007 – 2010)
- *Solterra 500* thermodynamic characterisation
- $GSHP_{HC}$ hydraulic and thermal characterisation
- Estimating collector return temperature
- Thermal drawdown
- Spatial and temporal variation in collector heat extraction rate

Unlike Chapters 2, 3, 4, 5 and 7, this chapter does not include a literature review. A comprehensive literature review on 13 experimental characterisation facilities in 7 *climate classifications* and their related methods and findings was presented in Section 3.1.

6.1 HP-IRL/H TEST PROGRAM (2007-2010)

This section presents a summary of the *HP-IRL/H* test program which spanned 3.5 years, between 2007 and 2010. Over the course of the 1328 day test program the $GSHP_{HC}$ operated for 303 days and delivered 72,514 kWh of energy. The $GSHP_{HC}$ operating principle and the experimental monitoring procedure are described in Section 3.4. For the purposes of clarity the following terms are defined:

- Heat pump capacity: the maximum rate at which the heat pump delivers heat
- Delivery: the rate at which the heat pump actually delivers heat
- Demand: the rate at which the building requires heat
- Duty: the percentage time the heat pump operates; this depends on the capacity/demand ratio as well as heating schedules
- Source capacity: the rate at which the ground can supply heat
- Extraction: the rate at which heat is extracted from the heat source; this depends on the duty and also on the temperature lift which the heat pump must achieve

- Drawdown: the temperature difference between the source return temperature and the source far-field temperature; this depends on collector design and duty

Due to the transient and cyclic nature of heating system operation and the length of the *HP-IRL/H* test program, the terms above can define representative rates, such as kWh$_{th}$/day, as well as average and instantaneous rates (kW$_{th}$), both are used in the subsequent discussions.

6.1.1 Test Rationale

The goals of the holistic, climate sensitive test program were to examine *GSHP$_{HC}$* performance during varied weather conditions and *IiBC* heat demand, in addition to generating substantial experimental data for the validation of analytical and numerical models. As a result, performance was measured during tests spanning 1 to 69 days; tests were conducted in autumn, winter and spring over 3.5 years, with heat pump duty levels varying between 10 and 100%. As indicated in Figure 6-1, testing was predominantly conducted during the following four periods:

- January to May, 2007
- October, 2007 to May, 2008
- January to May, 2009
- February, 2010

The horizontal collector was operated and monitored for 10 individual test periods, identified in Figure 6-1 as "HC#". The total heat extracted ($Q_{s,d}$) [kWh$_{th}$] each day is identified for HC1 through HC10. The details of each test period (HC#) are presented in Table 6-1.

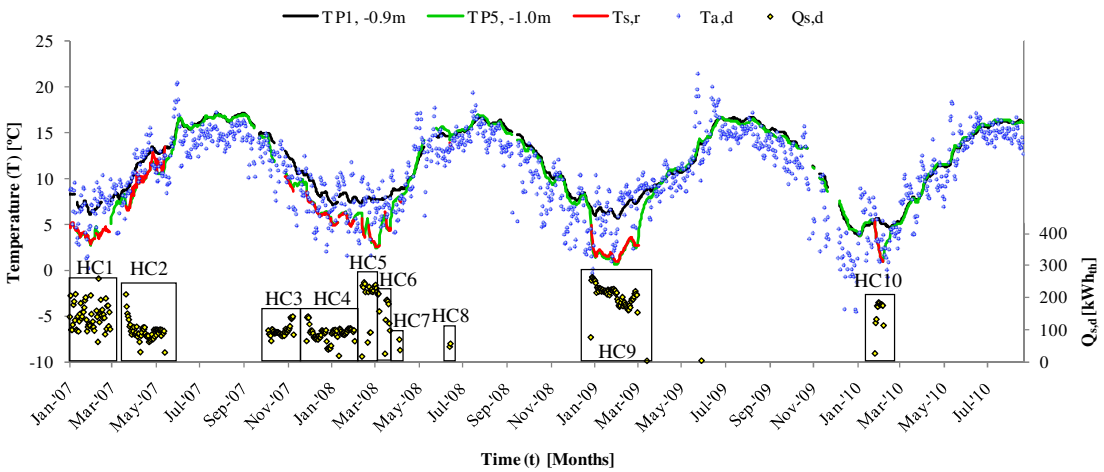

Figure 6-1: Thermal history of the *HP-IRL/H* project from January 2007 to August 2010, displaying the reference and collector profile temperature, the daily heat extracted and the source return temperature.

Table 6-1: Overview of HP-IRL/H test program between January 2007 and February 2010; adapted and supplemented from Burke (2010)

Test Period	Dates	Demand	Term	Duration	Application	Description
HC1	01/01/07 to 10/03/07	Moderate	Long	69 days	Domestic/Commercial	First IiBC heating season observational period with moderate thermal extraction rates.
HC2	31/03/07 to 24/05/07	Low	Long	55 days	Domestic	Prolonged steady state low level thermal extraction, indicative of autumn/spring time domestic dwelling utilisation.
HC3	08/11/07 to 19/11/07	Moderate	Medium	11 days	Domestic	Fixed daily extract and recovery periods, indicative of domestic dwelling utilisation.
HC4	07/12/07 to 12/02/08	Low	Long	68 days	Domestic	Comparative heat pump operation period with the $GSHP_{HC}$ and $GSHP_{VC}$ in simultaneous operation.
HC5	22/02/08 to 27/02/08	Intensive	Short	6 days	Domestic/Commercial	Steady-state thermal extraction and subsequent recovery period, indicative of extreme utilisation.
HC6	01/03/08 to 17/03/08	Intensive	Medium	16 days	Domestic/Commercial	Steady-state thermal extraction and subsequent recovery period, indicative of extreme utilisation.
HC7	14/04/08 to 15/04/08	Low	Short	24 hours	Domestic	Recording localised collector profile thermal extraction and recovery temperature gradients.
HC8	23/06/08 to 24/06/08	Moderate	Short	15 hours	Domestic	Recording localised collector profile thermal extraction and recovery temperature gradients.
HC9	05/01/09 to 11/03/09	Intensive	Long	66 days	Commercial	Prolonged steady-state intensive thermal extraction, indicative of peak winter utilisation (commercial application).
HC10	05/02/10 to 17/02/10	Intensive	Medium	13 days	Domestic	Examining the influence of flow rate reduction and flow reversal

The duty was dictated by the *IiBC* building heat demand which was influenced by ambient air temperature (T_a) [ºC], solar intensity ($q''_{s,t}$) [W/m^2], wind speed (u_{wind}) [m/s] and heating schedules defined by the Building Energy Management System (BMS). For the purpose of analysis and discussion and for consistency with both *HP-IRL/V* and *HP-IRL/A* (Burke, 2010) duty was categorised as follows:

- Low demand: 10 to 40% (5 warmer months – from May through September, allowing for domestic hot water demand in summer)
- Moderate demand: 40 to 70% (4 moderate months – October, November, March and April)
- Intensive demand: 70 to 100% (3 cooler months – December, January and February)

The test period duration is characterised as follows:

- Short-term: Period of less than one week
- Medium-term: Periods between one week and one month
- Long-term: Periods longer than one month

The daily extraction $Q_{s,d}$ [kWh_{th}] is the sum of the hourly heat extracted $Q_{s,h}$ [kWh_{th}] which is equivalent to the integral of the average hourly extraction rate ($q_{s,h}$) [kW_{th}], as shown in Equation 6-1.

$$Q_{s,d} = \sum_0^{23} Q_{s,h} = \int_0^{23} q_{s,h} \tag{6-1}$$

Due to the fixed capacity of heat pumps such as the *Solterra 500*, the *$GSHP_{HC}$* can be off for part of an hour when building demand is less than heat pump capacity. Once $T_{sk,f}$ reaches the set-point temperature ($T_{sk,set}$) the heat pump will shut off and remain off for a user-defined interval as described in Section 3.4.

For consistency with *HP-IRL/V* and *HP-IRL/A* (Burke, 2010) and for the purposes of the analytical characterisation presented in this chapter (where Δt is typically in hours), $q_{s,h}$ equals the hourly duty (D_{hp}) [%] multiplied by the current extraction rate (q_s) [kW] as shown in Equation 6-2. The hourly duty depends on the building demand which is a function of outdoor air temperature (T_a), solar intensity ($q''_{s,t}$), wind speed (u_{wind}) and the BMS on/off schedule ($\begin{bmatrix}1\\0\end{bmatrix}$). The extraction rate depends on the source return ($T_{s,r}$) and sink flow ($T_{sk,f}$) temperatures which are transient; this is discussed in greater detail in Sub-section 6.2.2.

$$q_{s,h} = D_{hp}\left(T_a, q''_{s,i}, u_w, \begin{bmatrix}1\\0\end{bmatrix}\right) q_s(T_{s,r}, T_{sk,f}) \tag{6-2}$$

Therefore, a heat pump extracting heat from the source at a rate of 10kW for 30 minutes in each hour (D_{hp}=0.5) is considered to have an equivalent influence on the source as a heat pump extracting at 5kW for the entire hour (D_{hp}=1). Transient simulation is conducted in Chapter 7 with a Δt of both 12 minutes and 1 minute which allows the instantaneous q_s values to be used.

The ground temperature drawdown ($\Delta T_{s,r/\infty}$) [K], displayed in Equation 6-3, is the difference between the source return temperature ($T_{s,r}$) [ºC] and the farfield ground temperature ($T_{g,\infty}$) [ºC] at collector depth (Burke, 2010; VDI-4640, 2004); $T_{P1,\ -0.9m}$ is taken as the appropriate farfield temperature in the *HP-IRL/H* project.

$$\Delta T_{s,r/\infty} = T_{s,r} - T_{g,\infty} = T_{s,r} - T_{P1,-0.9m} \tag{6-3}$$

Some of the expected initial observations from Figure 6-1 were:

- The reference temperature ($T_{P1,\ -0.9m}$) oscillates with the seasons as characterised in Chapter 4 and simulated in Chapter 5
- Comparing HC1 and HC2 in Figure 6-1 highlights that the *IiBC* demand and hence the daily heat extraction ($Q_{s,d}$) is a function of the mean daily ambient air temperature ($T_{a,d}$) [ºC]
- The drawdown, cooling of the heat source ($T_{s,r}$ - $T_{P1,\ 0.0m}$), is a function of the heat extracted ($Q_{s,d}$); again a comparison of HC1 and HC2 in Figure 6-1 demonstrates this effect

Table 6-2 summarises the results recorded, including COP, within each of the 10 test periods. The energy extracted by the collector over all 10 test periods generated an average drawdown ($\Delta T_{s,r/\infty}$) of -3.5K. However, due to sufficient recovery, no long term drawdown occurred. The heat pump delivered an average heat sink temperature (T_{sk}) of 49.1°C. Comprehensive results from this data have been published in Burke (2010) and are therefore not duplicated in this thesis.

Table 6-2: Summary of test results during 10 test periods between January 2007 and February 2010; adapted and supplemented from Burke (2010)

Test #	Days	Operational time per hour (Duty)	Total thermal extraction (Q_s) [kWh_{th}]	Coefficient Of Performance*, COP	Average collector area extract flux [W/m^2]
HC1	69	69%	10,193 kWh	2.8 (3.1)	18.1 W/m^2
HC2	55	34%	5,242 kWh	3.0 (3.3)	10.1 W/m^2
HC3	11	59%	1,342 kWh	3.1 (3.4)	15.0 W/m^2
HC4	68	33%	5,943 kWh	2.8 (3.1)	8.8 W/m^2
HC5	6	93%	1,239 kWh	2.8 (3.0)	23.6 W/m^2
HC6	16	93%	2,811 kWh	2.7 (2.9)	22.4 W/m^2
HC7	1	35%	107 kWh	3.3 (3.6)	10.4 W/m^2
HC8	1	48%	105 kWh	3.4 (3.7)	16.2 W/m^2
HC9	66	89%	14,164 kWh	2.7 (2.9)	21.1 W/m^2
HC10	13	91%	1,939 kWh	2.53 (2.69)	15.88 W/m^2

Note: *The bracketed value is calculated using EN14511 the others are calculated using Equation 3-2 and account for power consumed by collector circulating pumps

6.1.2 $GSHP_{HC}$ Operational Characteristics

Figures 6-2, 6-3, 6-4 and 6-5 display a series of four data-sets, each lasting three days, from HC2, HC3, HC9 and HC10 respectively. These datasets demonstrate four different kinds of $GSHP_{HC}$ operation. In each case, the 3 day period shown comes from close to the start of the test period during the thermal drawdown process. COPs, identified as 'HP-IRL/H', were

calculated using Equation 3-2 which includes collector circulating pump power and the drawdown ($\Delta T_{s,r/\infty}$) [K] is calculated using Equation 6-3. The temperature lift (ΔT_{hp}) [K] is the temperature difference between the sink flow temperature ($T_{sk,f}$) and the source return temperature ($T_{s,r}$) is calculated using Equation 6-4. Finally, a new concept called ΔT_{true} [K], defined in Equation 6-5, is introduced which quantifies the temperature difference that exists between the true heat sink (T_{room}) and the true heat source ($T_{g,\infty}$).

$$\Delta T_{hp} = T_{sk,f} - T_{s,r} \tag{6-4}$$

$$\Delta T_{true} = T_{room} - T_{g,\infty} = T_{IiBC} - T_{P1,-0.9m} \tag{6-5}$$

Figures 6-2 through 6-4 represent the first transient plots of *GSHP$_{HC}$* COP in this thesis.

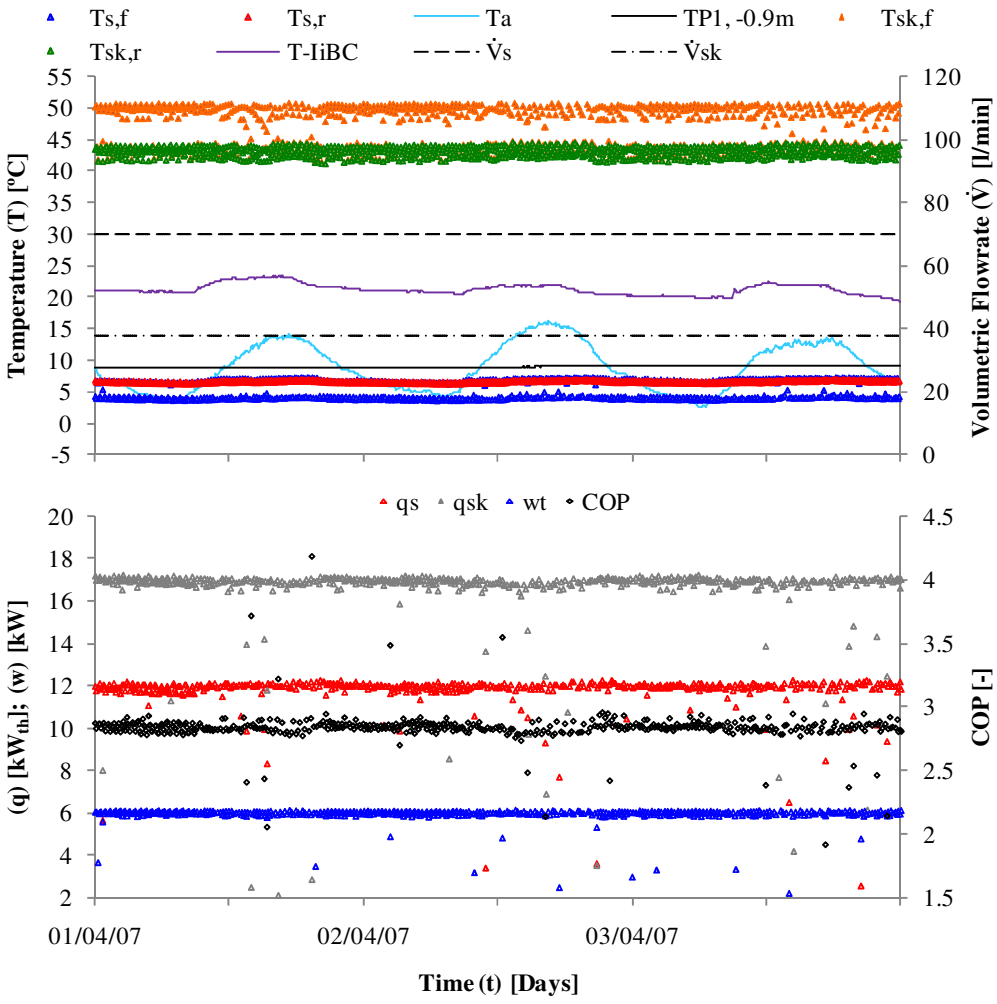

Figure 6-2: HP-IRL/H performance data measured between the 01/04/07 and 03/04/07 during HC2

The heat extraction cycle for test period HC2 began on 31/03/2007. The following observations were drawn from Figure 6-2 spanning from 01/04/2007 to 03/04/2007:

- April, mild weather with periodic fluctuation in air temperature between 4 and 14ºC with an average of 9ºC
- 24 hour 'continuous' heat pump operation
- Building demand was less than $GSHP_{HC}$ capacity (34% duty) resulting in cycling
- $\dot{V}_s$ was 70l/min
- $\dot{V}_{sk}$ was 38l/min
- T_{sk} was stable at 50ºC
- T_{liBC} varied periodically between 21 and 23.5ºC
- $T_{P1,\ -0.9m}$ was stable at 9ºC
- $T_{s,r}$ varied between 6.7 and 7ºC
- $\Delta T_{s,r/\infty}$ varied between 2 and 2.3K (not shown in Figure 6-2)
- ΔT_{hp} was 44K on average
- ΔT_{true} varied between 12 and 14.5K (The ground temperature was in the warm range but the room temperature was high. During the day T_a approached 15ºC and T_{liBC} approached 24ºC, at these temperatures limited heat is required by the building)
- Heat pump capacity (q_{sk}) was 17kWth, with q_s of 11.9 kWth and w_t of 6.0kW
- The COP was 2.8; this low COP reflects the fact that heat demand was extremely low and hence the heat storage tank was maintained at a high temperature
- Cycling was less frequent at night (off for 5 minutes in every 25 minute period) than day (off for 10 minutes in every 20 minute period), frequency of cycling reflects the periodic fluctuation in air temperature

The heat extraction cycle for test period HC3 began on 08/11/2007. The following conclusions can be drawn specifically from Figure 6-3 spanning from the 11/11/2007 to 13/11/2007:

- November, mild weather with daytime air temperature of 10 to 12ºC with a cool morning on November 12th
- 14 hour 'scheduled' heat pump operation
- Building demand was less than $GSHP_{HC}$ capacity (59% duty) resulting in cycling
- $\dot{V}_s$ was 70l/min
- $\dot{V}_{sk}$ was 38l/min
- T_{sk} varied from 25 to 50ºC during daily operation

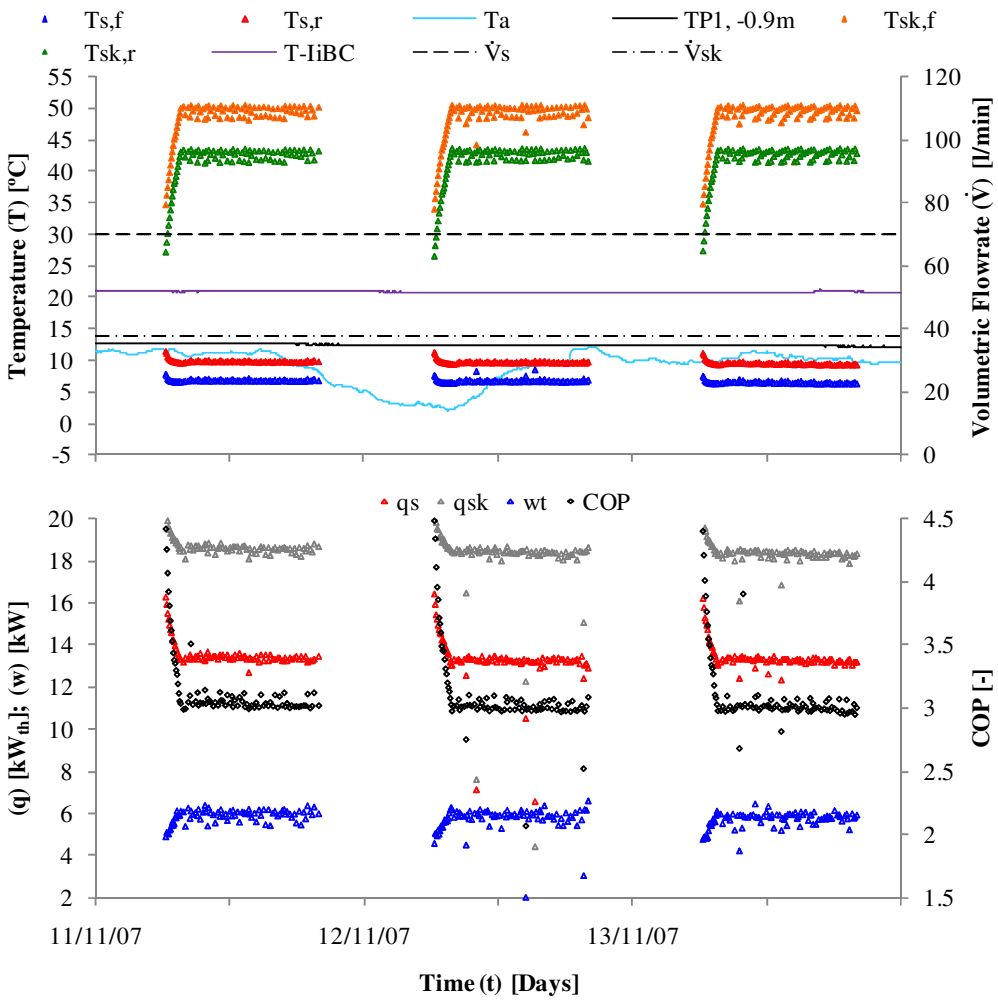

Figure 6-3: HP-IRL/H performance data measured between 11/11/07 and 13/11/07 from HC3

- T_{IiBC} varied between 20 and 21ºC
- $T_{P1,\ -0.9m}$ was 12.5ºC
- $T_{s,r}$ varied between 10 and 9.8ºC
- $\Delta T_{s,r/\infty}$ varied between 2.5 and 2.7K
- ΔT_{hp} varied between 15 and 40K
- ΔT_{true} was 7.5 to 8.5K (the ground temperature is in the warm range but the room temperature is also warm, during the day T_a remains at 12ºC, at this T_a some heat was required in the building)
- Steady-state heat pump capacity (q_{sk}) was 18.4kWth, with q_s of 13.3kW$_{th}$ and w_t of 6.0kW
- The COP was 3.0 at steady-state; however, COP was as high as 4.5 at the start of daily operation when T_{sk} was 25ºC

- Once steady-state was reached the system cycles off for 10 minutes in every 30 minute period

The heat extraction cycle for test period HC9 began on 05/01/2009. The following conclusions can be drawn specifically from Figure 6-4 spanning from 07/01/2009 to 09/01/2009:

- January, cold weather with approximate periodic fluctuation in air temperature between -2.5 and 6ºC with an average of 2ºC
- The heat pump was in 24 hour 'continuous' operation, although the heat distribution system was turned off for 30 minutes at the end of each day, during this time the buffer tank temperature increases

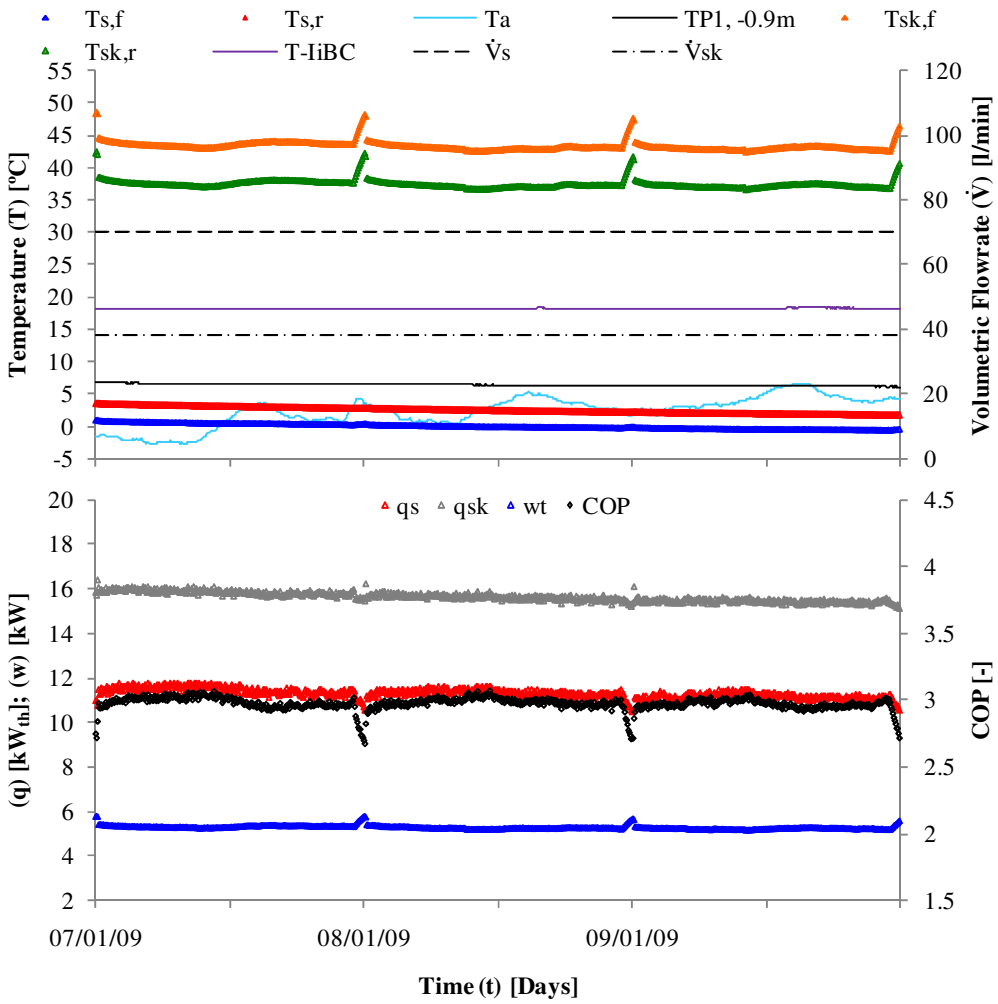

Figure 6-4: HP-IRL/H performance data measured between 07/01/09 and 09/01/09 during HC9

- Building demand was greater than heat pump capacity resulting in no cycling, average duty over 66 days of HC9 was 89%
- $\dot{V}_s$ was 70l/min
- $\dot{V}_{sk}$ was 38l/min
- T_{sk} was 43.5ºC, however it increases to 47ºC when the heat distribution system is off
- T_{liBC} was 18ºC
- $T_{P1,\ -0.9m}$ drops from 6.7 to 6ºC
- $T_{s,r}$ dropped from 3.5 to 1.5ºC over the course of the three day test period
- $\Delta T_{s,r/\infty}$ increased from 3.2 to 4.5K over the course of the three day test period
- ΔT_{hp} increased from 39.5 to 41.5K over the course of the three day test period, with a peak of 45.5K when the heat distribution system is switched off
- ΔT_{true} was 11.3K (the ground temperature is in the cool range but the room temperature is also cool, during the day T_a only approaches 5ºC, at this T_a a lot of heat was required by the building)
- The heat pump capacity (q_{sk}) dropped from 15.7 to 15.4kWth, with q_s of 11.5kW_{th} and w_t of only 5.1 to 5.8kW due to the cool storage tank temperature
- COP was 3.0 during steady-state, however it drops to 2.5 when the heat distribution system was turned off

The heat extraction cycle for test period HC10 began on 05/02/2010. The following conclusions can be drawn specifically from Figure 6-5 spanning from 06/02/2010 to 08/02/2010:

- February, cool weather with approximate periodic fluctuation in air temperature between 3 and 8ºC with an average of 4ºC
- The heat pump was in 24 hour 'continuous' operation
- Building demand was greater than heat pump capacity resulting in no cycling, average duty over 13 days of HC9 was 91%
- $\dot{V}_s$ was 32l/min which is just under half the recommended evaporator flow rate
- $\dot{V}_{sk}$ was 38l/min
- T_{sk} was 49ºC, however it drops to 45ºC during off cycles
- T_{liBC} varied between 19 and 20ºC
- $T_{P1,\ -0.9m}$ increases from 5.5 to 5.7ºC
- $T_{s,r}$ dropped from 5.8 to 4.2ºC over the course of the three day test period

- $\Delta T_{s,r/\infty}$ increased from 0 to 1.5K over the course of the three day test period

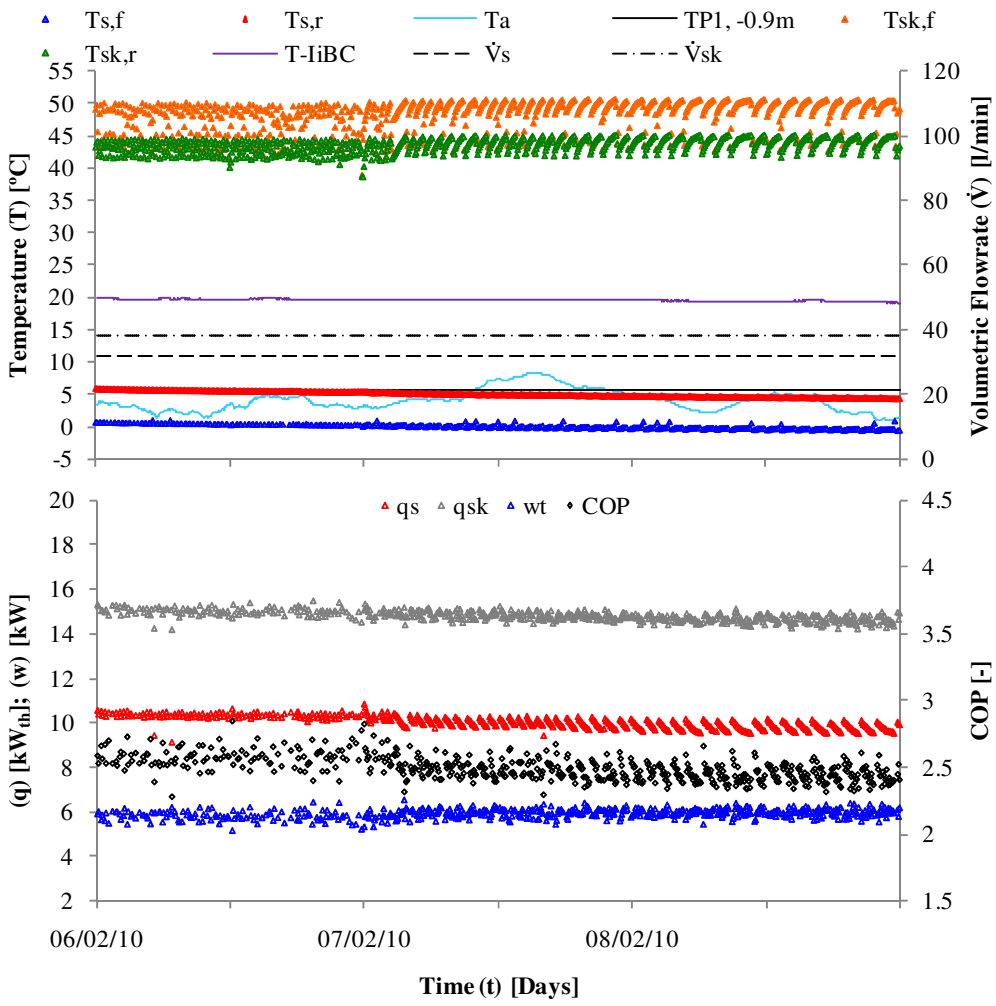

Figure 6-5: HP-IRL/H performance data measured between 06/02/10 and 08/02/10 during HC10

- ΔT_{hp} increased from 43.2 to 44.8K over the course of the three day test period
- ΔT_{true} was 13.5K (the ground temperature is in the cool range but the room temperature is also cool, during the day T_a only approaches 7ºC, at this T_a a lot of heat was required by the building)
- Heat pump capacity (q_{sk}) dropped from 15.2 to 14.9kWth, with q_s dropping from 10.2 to 9.7kWth w_t of 6 to 6.1kW
- COP dropped from 2.53 to 2.44

A summary of the findings from Figure 6-2 through 6-5 are presented in Table 6-3.

Table 6-3: Summary of quasi-steady-state findings from the final day of Figures 6-2 through 6-5

Period	Dates displayed	$T_{g,\infty}$ [ºC]	$T_{s,r}$ [ºC]	$T_{sk,f}$ [ºC]	ΔT_{hp} [K]	$\dot{V}_s$ [l/min]	$\dot{V}_{sk}$ [l/min]	q_s [kW_{th}]	q_{sk} [kW_{th}]	w_t [kW]	COP [-]
HC2	01/04/07 to 03/04/07	9	6.7	50	43.3	70	38	11.9	17	6	2.8
HC3	11/11/07 to 13/11/07	12.5	9.8	50	40.2	70	38	13.3	18.4	6	3
HC9	07/01/09 to 09/01/09	6	1.5	43.5	42	70	38	11.5	15.7	5.1	3
HC10	06/02/10 to 08/02/10	5.7	4.2	49	44.8	32	38	9.7	14.9	6	2.53

The overall conclusions from the analysis of Figures 6-2 through 6-5 relevant to simulation of *$GSHP_{HC}$* are:

- As expected, both $T_{s,r}$ and $T_{sk,f}$ are affected by q_s and q_{sk} respectively, overtime
- All the operating parameters of the heat pump, q_s, q_{sk} and COP, are influenced by $T_{s,r}$ and $T_{sk,f}$
- Therefore, a number of feedback loops identified as *coupled collector and heat pump performance transience* co-exist
- For accuracy and to mimic real life, changes in both $T_{s,r}$ and $T_{sk,f}$, due to heat extraction and delivery, must be tracked and the influence of these on q_s, q_{sk} and COP accounted for
- Due to the limited size of the heat storage tank, changes in the heat distribution system have immediate impact on the storage tank temperature leading to a short term influence on COP
- Due to the large semi-infinite nature of the ground, changes in the source temperature happen slowly compared to changes in the building and lead to long term influence on SPF
- The source flow rate $\dot{V}_s$ has a significant influence on the heat pump
    - Reduced flow rates yield warmer source return temperatures ($T_{s,r}$)
    - However, the extraction rate (q_s) is reduced (reasons for this are discussed in Sub-section 6.5.2)
    - By comparing HC2 with HC10, where ΔT_{hp} is approximately equal in both, it appears that reducing flow rate yields no net gain in COP

6.1.3 Test Program Conclusions

The *HP-IRL/H* test program included 10 test periods, identified as HC1 through HC10; the test periods included heat pump duty of 10 to 100% and test durations of 1 to 69 days. The demand for heat in the *IiBC* was driven by external air temperature, solar intensity and wind

speed along with heating schedules for the building. Drawdown in the source temperature was proportional to the extraction rate which was driven by *IiBC* heat demand.

It was shown that, as expected, *GSHP$_{HC}$* operation influences temperatures in the source and the sink which in turn influence the performance of the *GSHP$_{HC}$*. COP decreases with increase in the sink temperature, which can change substantially in the time scale of minutes. COP decreases with decrease in source temperature, which changes more slowly in the timescale of hours to days. Reduced source flow rate can increase the source return temperature but also reduces evaporator capacity and yields no net gain in COP. The influence of source and sink conditions on COP will be investigated further in the subsequent sections.

6.2 SOLTERRA 500 THERMODYNAMIC CHARACTERISATION

The *Solterra 500* heat pump manufactured by *Geostar Engineering Ltd.* operated on a standard *vapour-compression cycle*. The thermodynamic processes of the *ideal vapour-compression cycle* are described in Sub-section 2.1.3. Detailed performance data on the *Solterra 500* was published in a 2004 report by *Arsenal Research* (Zottl, 2003) and this is summarised in Table 3-4.

The measured values for q_{sk}, q_s, w_c and COPs, identified as 'Sol 500', are plotted against temperature lift (ΔT_{hp}) in Figure 6-6 (Zottl, 2003).

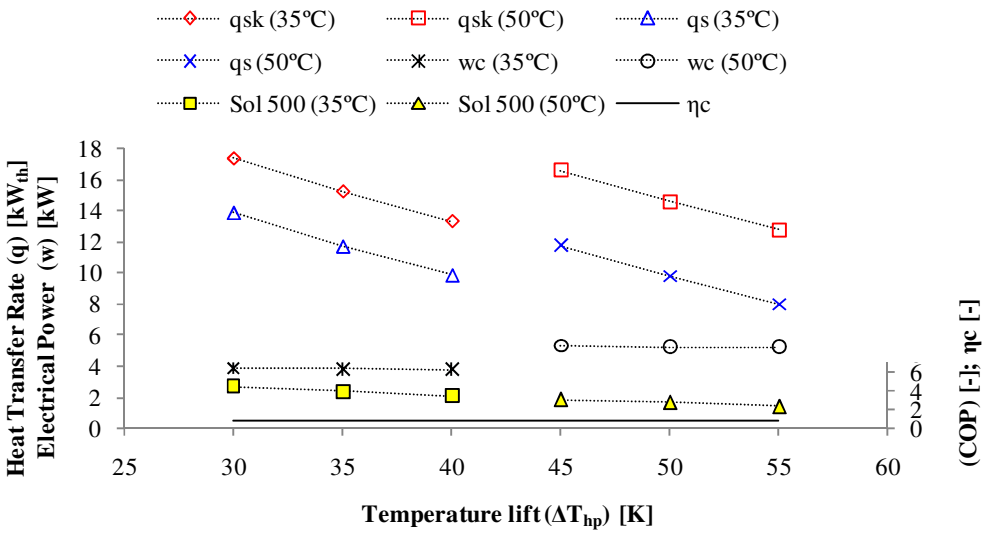

Figure 6-6: Summary of the Solterra 500 heat pump performance measured by Arsenal Research (Zottl, 2003)

The following observations are made:

- The COP is inversely proportional to the temperature lift (ΔT_{hp})
- The COP drops from 4.5 at ΔT_{hp} of 30K to 2.4 at ΔT_{hp} of 55K
- The influence of ΔT_{hp} on COP is approximately linear regardless of sink flow temperature ($T_{sk,f}$) [ºC].
- However, the influence of ΔT_{hp} on q_{sk}, q_s and w_c is divided into two bands for T_{sk} of 35 and 50ºC respectively
- Within these bands q_{sk} and q_s decrease linearly with ΔT_{hp}
- The compressor efficiency (η_c) is constant at approximately 0.9 for all ΔT_{hp} and regardless of T_{sk}

6.2.1 Characterising the Solterra 500 using Carnot Efficiency

One straightforward way of characterising the *Solterra 500*, is by comparing it with a Carnot heat pump operating between the same source and sink. The Carnot heat pump involves a highly idealised reversible cycle consisting of isentropic compression and expansion with isothermal heat absorption and rejection, shown in Figure 6-7.

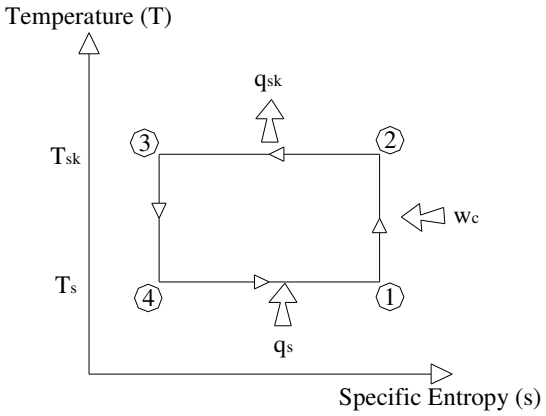

Figure 6-7: Carnot heat pump cycle

The variation in the COP of a real heat pump with T_s [K] and T_{sk} [K] can be compared to that of a Carnot heat pump with the ratio being the Carnot efficiency (η). Based on this, the COP of a real heat pump can be written using Equation 6-6. The calculated variation of COP, identified as 'η = 0.45', with ΔT_{hp} is compared with the *Solterra 500* data from *Arsenal Research* in Figure 6-8.

$$COP_{real} = \eta COP_{Carnot} = \frac{\eta T_{sk}}{T_{sk} - T_s} = \frac{\eta T_{sk}}{\Delta T_{hp}} \quad (6\text{-}6)$$

It can be seen in Figure 6-8 that:

- The COP is slightly higher across the range of ΔT_{hp} for T_{sk} of 50ºC than 30ºC, this is due to the nature of Equation 6-6
- The Carnot efficiency η for the *Solterra 500* is approximately 0.45 at T_{sk} of 35ºC, η is slightly less, approximately 0.425 (not shown in Figure 6-8) at T_{sk} of 50ºC.

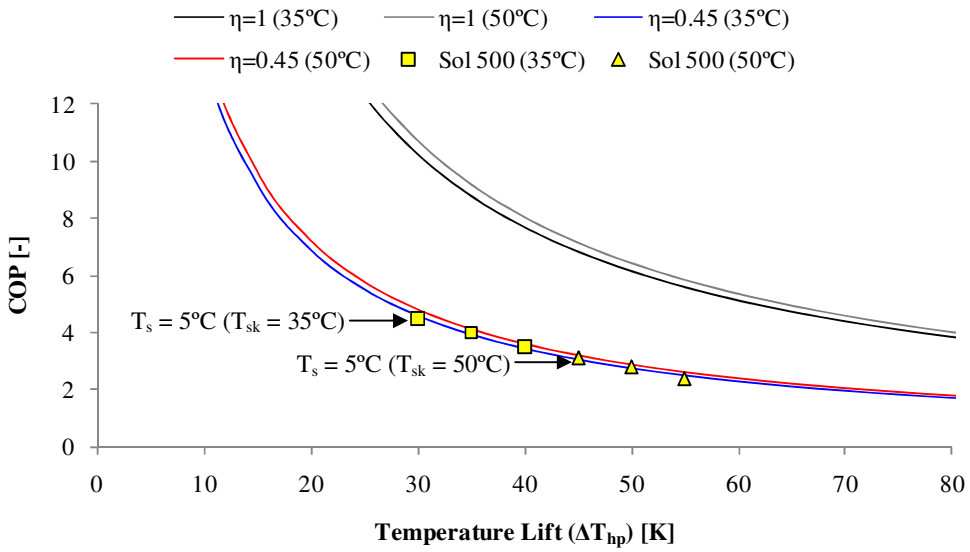

Figure 6-8: Carnot heat pump compared with the Solterra 500 COPs measured by Arsenal Research

Figure 6-9 compares both calculated and measured COP values plotted against source return temperature ($T_{s,r}$) [ºC] for two distinct sink temperatures ($T_{sk,f}$) of 35 and 50ºC

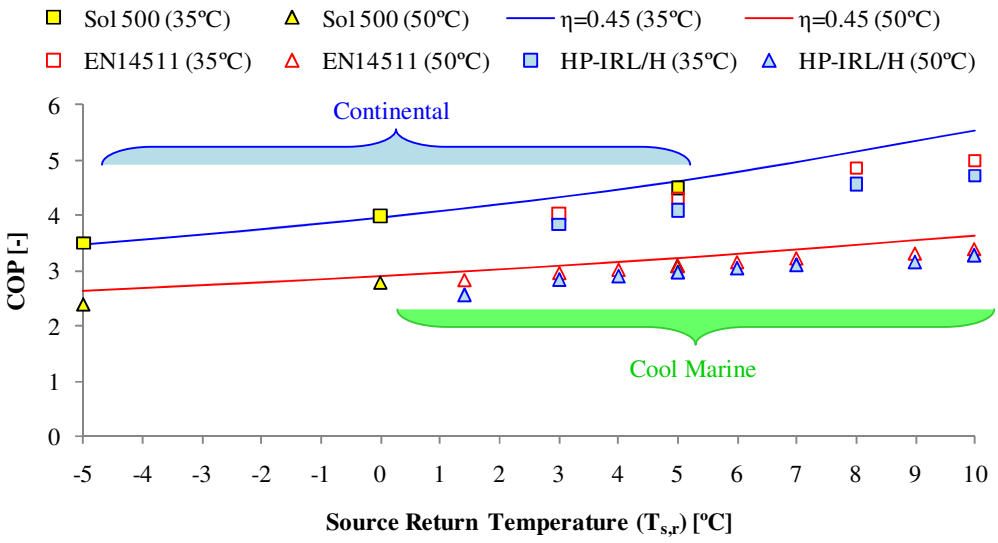

Figure 6-9: Influence of source return temperature on Solterra 500 COP

COPs identified as 'EN14511' were taken from *HP-IRL/H* measurements where only the compressor's power consumption plus the pumping power through the evaporator (≈100W) was included in the COP calculations, as per BSI – EN14511 standard.

The following conclusions can be drawn from Figure 6-9:

- All COPs measured at $T_{sk,f}$ of 35ºC are 45% higher than COPs at the same $T_{s,r}$ measured at $T_{sk,f}$ of 50ºC
- The 'EN14511' COPs measured at 50ºC were consistent with the 'Sol 500' COPs
- The 'EN14511' COPs measured at 35ºC were 4% lower than the 'Sol 500' COPs
    - This may be due to the heat distribution inefficiency in the IiBC at low temperatures, outlined in Chapter 3
- The 'HP-IRL/H' COPs are between 5 and 10% lower than the 'Sol 500' COPs due to the inclusion of collector circulation power in Equation 3-2
- The difference between the 'HP-IRL/H' and 'Sol 500' COP values is less pronounced at T_{sk} of 50ºC than at 35ºC, see Figure 6-6, since more power is consumed by the compressor at a T_{sk} of 50ºC meaning the additional pumping power represents a smaller fraction of total power
- Over the 3.5 year *HP-IRL/H* study the return temperature $T_{s,r}$ was never brought below 1.4ºC and at times was as high as 10ºC; this is indicative of the *Cool Marine* climate under which the system was operated
- The test range of -5ºC to 5ºC under which standardised European testing is conducted is more indicative of a *Continental* climate
- A Carnot efficiency of 0.425 (not graphed) is more representative of the *Solterra 500* operating at 50ºC, the 0.45 value which works at 30ºC is too high at 50ºC
- The 'EN15411' COP recorded at $T_{s,r}$ of 8 to 10ºC for both T_{sk} of 35 and 50ºC are lower than the Carnot theory predicts, this may indicate that the *Solterra 500* is operating outside its design range of -5ºC to 5ºC

6.2.2 Model AL-7: Source and Sink Dependent Heat Pump Component Model

$GSHP_{HC}$ performance-feedback loops, identified in Sub-section 6.1.2, demonstrate that in order to accurately simulate a $GSHP_{HC}$ system over time it is necessary to:

- Calculate the decrease in source return temperature $T_{s,r}$ due to heat extraction q_s (measured during *HP-IRL/H*, estimated in Chapter 6 and simulated in Chapter 7)

- Calculate the increase in sink flow temperature $T_{sk,f}$ due to heat delivery q_{sk} (measured during *HP-IRL/H*)

While simultaneously:

- Accounting for the influence of changes in both $T_{s,r}$ and $T_{sk,f}$ on the heat pump's operational parameters q_s, q_{sk} and COP

Step-wise simulation (introduced in Section 5.4.2) allows for coupled problems to be solved either in turn or iteratively within the time-step with limited error. Therefore, parameters q_s and q_{sk} can be updated at the start of each time-step based on both $T_{s,r}$ and $T_{sk,f}$ values calculated in the previous time-step. The *Solterra 500* performance, as measured by *Arsenal Research* and within a limited range of T_s and T_{sk}, can be modelled using the linear equations shown in Figure 6-10 and summarised in Table 6-4. These represent the variation in q_s, q_{sk} and COP with $T_{s,r}$, for specific $T_{sk,f}$ of 35 and 50ºC and are based on Table 3-4 (Zottl, 2003).

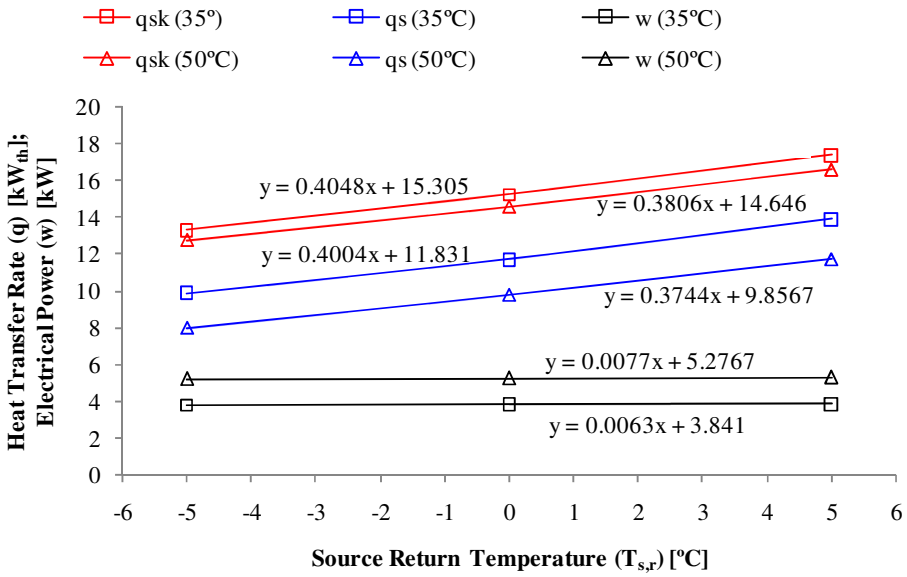

Figure 6-10: Variation in Solterra 500 q_{sk}, q_s and w with $T_{s,r}$ for specific T_{sk} of 35 and 50ºC

Table 6-4: Summary of linear equations describing q_s and q_{sk} variations with $T_{s,r}$ for specific $T_{sk,f}$ of 35 and 50ºC and variation in COP with temperature lift (ΔT_{hp})

No.	Dependent	Independent	Equation
Sample	q	$T_{s,r}$	$q = \Delta q/\Delta T_{s,r}(T_{s,r}) + q_0$
1.	q_s (T_{sk}=35ºC)	$T_{s,r}$	$q_s = 0.4004T_{s,r} + 11.831$
2.	q_{sk} (T_{sk}=35ºC)	$T_{s,r}$	$q_{sk} = 0.4048T_{s,r} + 15.305$
3.	q_s (T_{sk}=50ºC)	$T_{s,r}$	$q_s = 0.3744T_{s,r} + 9.8567$
4.	q_{sk} (T_{sk}=50ºC)	$T_{s,r}$	$q_{sk} = 0.3806T_{s,r} + 14.646$
5.	COP	ΔT_{hp}	$COP = -0.0829\Delta T_{hp} + 6.9048$

As previously displayed in Figure 6-6, the COP variation across the range of ΔT_{hp} can be represented with a single expression, No. 5 in Table 6-4. However as shown in Figure 6-10, expressions for q_s and q_{sk} are divided into two bands depending on $T_{sk,f}$ and hence require four equations, No. 1 & 2 at 35ºC and No. 3 & 4 at 50ºC. Additionally, while these equations are suitable for a range of $T_{s,r}$ (-5 to 5ºC), they are unsuitable for modelling the *Solterra 500* at $T_{sk,f}$ other than 35 and 50ºC. A novel solution to this problem, identified as model AL-7, is to write an equation of q_s or q_{sk} in terms of both $T_{s,r}$ and $T_{sk,f}$ such as Equation 6-7.

$$q(T_{sk,f}, T_{s,r}) = \frac{\Delta q}{\Delta T_{s,r}}(T_{sk,f})(T_{s,r}) + q_0(T_{sk,f}) \quad (6\text{-}7)$$

Where the slope ($\Delta q/\Delta T_{s,r}$) and heat transfer rate at 0ºC (q_0) are both a function of $T_{sk,f}$ and can be found by plotting lines that intersect the $\Delta q/\Delta T_{s,r}$ and q_0 values at 35 and 50ºC for both q_s and q_{sk}. This process is shown in Figure 6-11. A summary of the linear equations describing the variation of $\Delta q/\Delta T_{s,r}$ and q_0 to be used for calculating q_s or q_{sk} using Equation 6-7 are presented in Table 6-5.

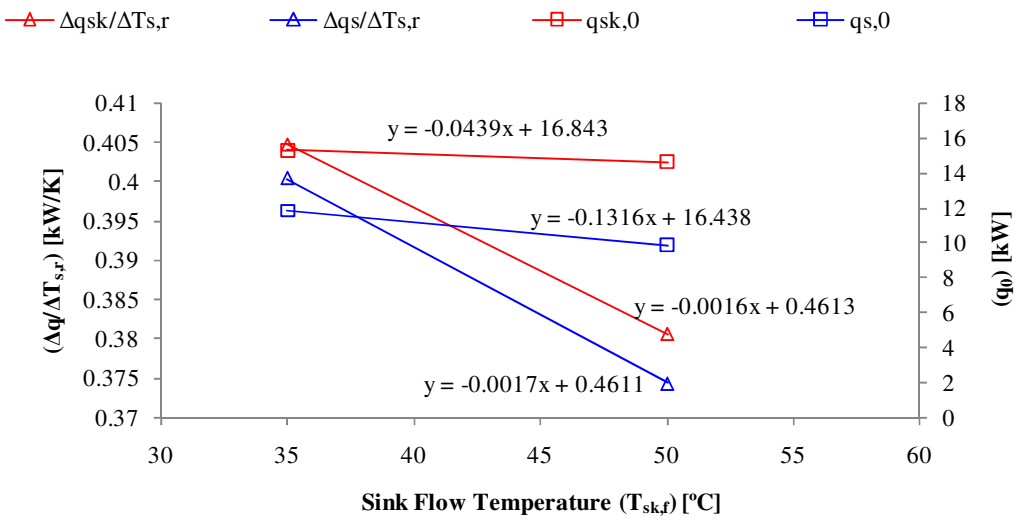

Figure 6-11: Variation in the m and c values for the linear relationships presented in Table 6-3 with sink flow temperature

Table 6-5: Summary of the linear equations describing the m and c variations with $T_{sk,f}$

No.	Dependent	Independent	Equation
1.	$\Delta q_s/\Delta T_{s,r}$	$T_{sk,f}$	$\Delta q_s/\Delta T_{s,r} = -0.0017T_{sk,f} + 0.4611$
2.	$\Delta q_{sk}/\Delta T_{s,r}$	$T_{sk,f}$	$\Delta q_{sk}/\Delta T_{s,r} = -0.0016T_{sk,f} + 0.4613$
3.	$q_{s,0}$	$T_{sk,f}$	$q_{s,0} = -0.1316T_{sk,f} + 16.438$
4.	$q_{sk,0}$	$T_{sk,f}$	$q_{sk,0} = -0.0439T_{sk,f} + 16.843$

By substituting the linear equations from Table 6-5 into Equation 6-7, an expression for q_s and q_{sk} in terms of both $T_{s,r}$ and $T_{sk,f}$ can be created, as shown in Equation 6-8 and 6-9 respectively.

$$q_s(T_{sk,f}, T_{s,r}) = (-0.0017T_{sk,f} + 0.4611)T_{s,r} + (-0.1316T_{sk,f} + 16.438) \quad (6\text{-}8)$$

$$q_{sk}(T_{sk,f}, T_{s,r}) = (-0.0016T_{sk,f} + 0.4613)T_{s,r} + (-0.0439T_{sk,f} + 16.843) \quad (6\text{-}9)$$

Since the focus of *HP-IRL/H* was on the heat source, Equation 6-8 was then compared with measured q_s data from HC9, as shown in Figure 6-12. HC9 was used since the *GSHP$_{HC}$* operated at 100% duty during the majority of this test period.

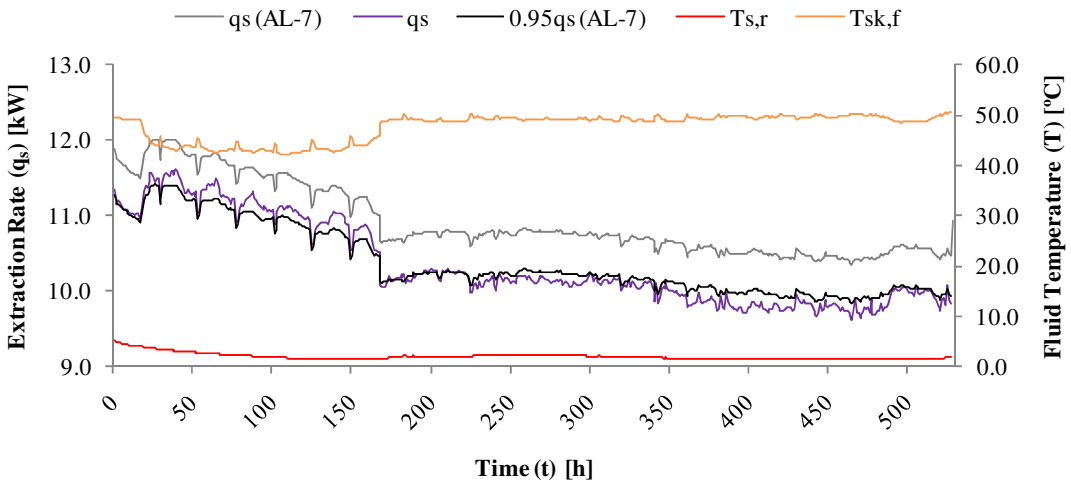

Figure 6-12: Comparison of calculated, modified calculation and measured q_s from HC9

It was observed that the measured q_s values differed from Equation 6-8 by about 0.4kW$_{th}$ equivalent to a factor of 0.95. This error was most likely caused by: marginal error of ±0.138kWth in the *Arsenal Research* data (Zottl, 2003) used to derive Equation 6-8, equivalent error in the *HP-IRL/H* data used to test Equation 6-8, a small difference in the source flow rate between *Arsenal* and *HP-IRL/H* tests and finally, error introduced by the assumption of linear variation with both $T_{s,r}$ and $T_{sk,f}$. Therefore, for the purpose of simulation in Chapter 7, the final q_s [kW$_{th}$] expression which was calibrated with *HP-IRL/H* data is Equation 6-10. These findings apply for a source flowrate of 58 to 70l/min only. As shown in Table 6-3, the evaporator capacity drops at lower flowrates. These equations are derived from heat pump performance data measured at a mass flowrate of 1.021kg/s (≈58l/min) (Zottl, 2003).

$$q_s(T_{sk,f}, T_{s,r}) = 0.95[(-0.0017T_{sk,f} + 0.4611)T_{s,r} + (-0.1316T_{sk,f} + 16.438)] \quad (6\text{-}10)$$

6.2.3 Source-side Efficiency Considerations

As expressed in Equation 6-5, ΔT_{true} defines the temperature lift that exists between the true source and sink ($\Delta T_{true} = T_{room} - T_{g,\infty}$), however in reality the heat pump's compressor achieves a temperature lift of $\Delta T_{comp} = T_{cond} - T_{evap}$ and gets credit for $\Delta T_{hp} = T_{sk,f} - T_{s,r}$ in heat pump documentation. As shown in Figure 6-13, temperature differences exist on the source side between $T_{g,\infty}$, $T_{s,r}$ and T_{evap} and similarly temperature differences exist on the sink side between T_{cond}, $T_{sk,f}$ and T_{room}. Of course, a temperature difference (ΔT) [K] is essential for heat transfer (q) [W] to take place, however the temperature difference is proportional to the resistance (R) [K/W] as shown in Equation 6-11. A reduction in resistance may be possible though improved design of the collector (*split-level collector*), evaporator, condenser and heat distribution system.

$$\Delta T = qR \tag{6-11}$$

Figure 6-13 is a novel diagram created to identify thermal resistances in a *$GSHP_{HC}$* heating system and highlight areas for improvement. Figure 6-13 utilises the same colour coding used for describing the *$GSHP_{HC}$* operating principle in Figures 3-8, 3-9 and 3-12.

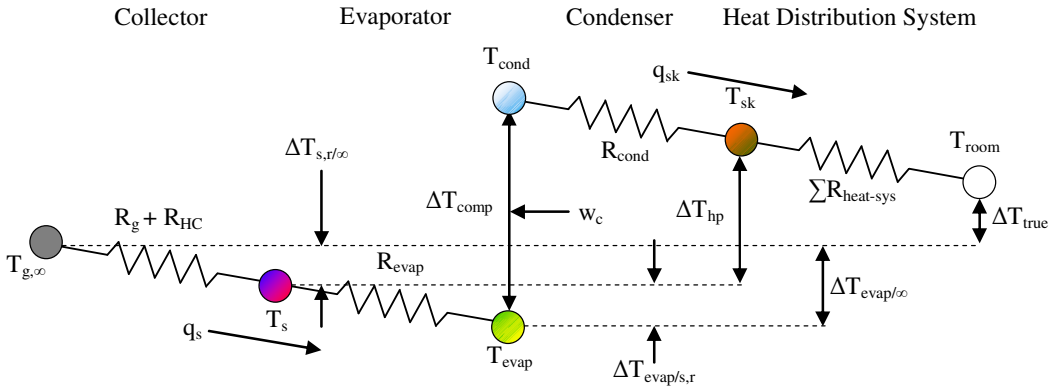

Figure 6-13: Thermal resistances between source and sink, highlighting areas for improvement in $GSHP_{HC}$ design

Similar discussions have been presented in Belgium (Dumont & Frere, 2005) and Sweden (Karlsson, 2007). The temperature differences $\Delta T_{evap/s,r} = T_{evap} - T_{s,r}$ and $\Delta T_{evap/\infty} = T_{evap} - T_{\infty}$, as shown in Figure 6-13, were studied by Karlsson (2007) and Dumont & Frere (2005) respectively. The measured values of $\Delta T_{evap/\infty}$ shown in Figure 6-14 are equivalent to the sum of $\Delta T_{evap/s,r}$ and source drawdown $\Delta T_{s,r/\infty}$ as defined in Equation 6-3 which is a function of collector design and operational duty. *HP-IRL/H* focuses on source drawdown $\Delta T_{s,r/\infty}$ and developing methods to predict and minimise or offset source drawdown.

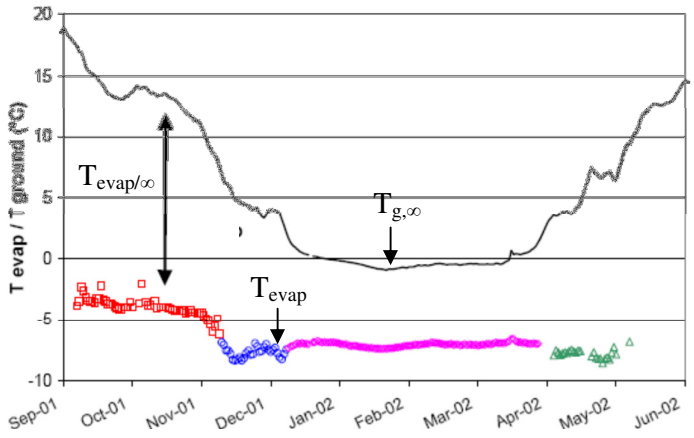

Figure 6-14: Comparison of measured ground temperature and evaporating temperature for a GSHP$_{HC}$ in Belgium (Dumont & Frere, 2005)

Figure 6-15 was created using experimental data from test periods HC2, HC3 and HC9, presented in Figure 6-1. Figure 6-15 displays the effect of temperature lift (ΔT_{hp}) on *Solterra 500* COP interpreted in 7 different ways. To summarise, the COP's identified in previous discussions are:

- HP-IRL/H: defined in Sub-section 6.1.2 is calculated from *HP-IRL/H* measured data using Equation 3-2 which includes $w_c + w_{P1} + w_{P2} + w_{stb}$
- Sol 500: defined in Section 6.2 is calculated by *Arsenal Research* and includes $w_c + w_{evap}$, where w_{evap} [W] is the power consumed in overcoming the pressure drop of 32.5kPa in the evaporator
- $\eta = 0.45$: defined in Sub-section 6.2.1 is calculated using Equation 6-6 with a Carnot efficiency of 0.45
- EN14511: defined in Sub-section 6.2.1 is calculated from *HP-IRL/H* measured data but only includes $w_c + w_{evap}$

COP's not previously identified are:

- Compressor: calculated from *HP-IRL/H* measured data but includes only w_c
- Total: calculated from *HP-IRL/H* measured data including $w_c + w_{P1} + w_{P2} + w_{P3} + w_{stb}$
- ΔT_{true}: calculated from *HP-IRL/H* measured data using Equation 3-2 which includes $w_c + w_{P1} + w_{P2} + w_{stb}$ but plotted at ΔT_{true} as defined in Sub-section 6.1.2

In Figure 6-15, data for the HP-IRL/H, EN14511, Compressor and Total COPs is taken from measurements during HC3, taken at 5 minute intervals when ΔT_{hp} ranged from 20 to 38K as shown in Figure 6-3, combined with hourly averaged measurements from HC9 when ΔT_{hp}

ranged from 38K to 48K as shown in Figure 6-4; ΔT_{true} data combines steady-state values from HC2, HC3 and HC9 as shown in Figures 6-2, 6-3 and 6-4.

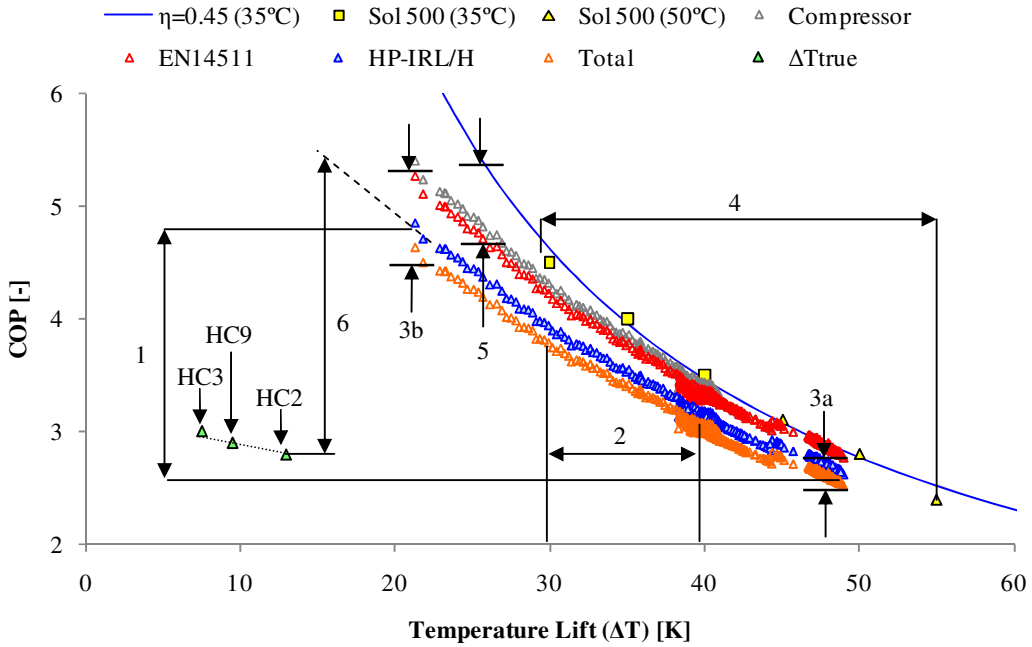

Figure 6-15: Solterra 500 COP, expressed in 7 different ways, using data taken from Arsenal Research (Zottl, 2003), HC2, HC3 and HC9

The following observations are made, using the points 1 to 6 identified in Figure 6-15:

- (1) HP-IRL/H COP drops from 4.7 at a temperature lift of 22K to 2.7 at a temperature lift of 48K:
  - This equates to a total decrease of 42% or 1.63% per Kelvin
  - The EN14511 and Sol 500 measured COPs show similar trends
- (2) The heat sink delivery temperature (T_{sk}) at steady-state in the *HP-IRL/H* test facility is too high (≈ 50ºC):
  - This leads to steady-state ΔT_{hp} of between 40 and 50K and causes the COP to be between 15 and 30% lower than it would be at ΔT_{hp} of 30K
  - ΔT_{hp} could be as low as 25 to 33.6K for a T_{sk} of 35ºC given the mild nature of the maritime ground source ($T_{s,r}$ of 1.4 to 10ºC) shown in Figure 6-9.
  - This problem is due to the retrofit nature of the *GSHP$_{HC}$* and does not occur in new-builds where a low T_{sk} has been incorporated into the design through under-floor heating, Fan Coil Units (FCUs) or a combined heating and ventilation system as discussed in Sub-section 2.1.3

- (3) The difference between the highest and lowest COP, namely the 'Compressor' COP and the 'Total' COP respectively, is due to the electrical power consumed by the source-side circulating pumps, the sink-side pump and standby ($w_{P1} + w_{P2} + w_{P3} + w_{stb}$):
  - The pumping power ($w_{P1} + w_{P2} + w_{P3}$) is power lost to pipe friction
  - (3a) The inclusion of $w_{P1} + w_{P2} + w_{P3} + w_{stb}$ leads to a 8% reduction in COP from 2.85 to 2.6 at ΔT_{hp} of 48K
  - (3b) The inclusion of $w_{P1} + w_{P2} + w_{P3} + w_{stb}$ leads to a 13% reduction in COP from 5.2 to 4.5 at a ΔT_{hp} of 22K
  - The difference is explained by Figure 3-14(e), where the 0.62kW used by components other than the compressor ($w_{P1} + w_{P2} + w_{P3} + w_{stb}$) comprises 14% of the total 4.32kW consumed at a T_{sk} of 32ºC but only makes up 10% of the 6.02kW used at a T_{sk} of 50ºC
  - By conducting a '1st Law' analysis, it has been shown that some or all of this power lost to friction is recovered by the collector in the form of heat (Burke, 2010)
  - However, a '2nd Law' analysis suggests that while the energy is recovered as heat, exergy is destroyed and money is wasted since costly, high quality electrical power returns from the ground as low-grade heat in the place of plentiful and free ground-heat
  - Therefore, careful consideration of friction head loss and reduction in hydraulic resistance when designing collectors and heat distribution systems can improve the cost effectiveness of the *$GSHP_{HC}$* system
- (4) It can be seen that the range of ΔT_{hp} at which the real heat pump (*Solterra 500*) mimics a Carnot heat pump of 45% efficiency is limited to a 25K interval between ΔT_{hp} of 30 and 55K; this is an unavoidable feature of all heat pumps which are designed to operate in a certain range
- (5) It can be seen that in the *Cool Marine* climate the *Solterra 500* operates for some time in the 'low lift' end of the range defined in Point 4:
  - However it fails to achieve the 45% Carnot efficiency at ΔT_{hp} of 27K for example
  - The question then arises: could a heat pump for *Cool Marine* climates be designed to operate between the mild ground source (1.4 to 10ºC) and a low temperature heat distribution system (such as under-floor heating or FCU at 30 to 35ºC) so that the maritime ΔT_{hp} range (20 to 35K) would be better catered for and better fractions of theoretical COPs achieved?

- (6) Due to the 'thermal resistances' to heat flow described in Figure 6-13 the COP achieved for the true temperature lift (ΔT_{true}) is well below a decent Carnot efficiency of 0.45:
  - A large part of this is due to the high T_{sk} needed for the conventional radiators in IiBC which has already been discussed in points 1 and 4
  - However, another significant aspect is also the ground resistance and collector resistance causing 'source drawdown'; much of the remainder of this thesis focuses on predicting and minimising or offsetting drawdown in the heat source

6.2.4 Thermodynamic Conclusions

This section characterised *HP-IRL/H* measurements of *Solterra 500* COP, calculated using Equation 3-2, by comparing them with COP's from *Arsenal Research*, COP's from a Carnot Heat Pump with a Carnot efficiency of 45% and COP's taken from the *HP-IRL/H* data calculated using EN14511. Using *Arsenal Research* data and *HP-IRL/H* data, novel equations for q_s, q_{sk} and COP were derived as a function of both T_s and T_{sk} for use in simulation of a holistic $GSHP_{HC}$ system in Chapter 7. Finally, this section highlighted areas for potential thermodynamic, thermal and hydraulic improvements to $GSHP_{HC}$ which may enhance the performance and cost effectiveness of $GSHP_{HC}$. Thermal and hydraulic aspects of $GSHP_{HC}$ are further assessed in the next two sections along with Chapters 7 and 8, while changes to the heat pump unit are beyond the scope and remit of this project.

6.3 $GSHP_{HC}$ HYDRAULIC AND THERMAL CHARACTERISATION

In this section the operation of the $GSHP_{HC}$ designed and built by *Dunstar Ltd.* is characterised using hydraulic and thermal analytical methods. An idealised schematic of a generic $GSHP_{HC}$ is presented in Figure 6-16. This includes the heat source, the heat pump and the heat storage tank which supplies thermal energy to the heat sink. Thermal energy is transferred from the heat source to the heat pump's evaporator via the horizontal *parallel, inline* collector which consists of flow and return manifolds connected together by underground pipes and connected to the heat pump by run-out pipes. For clarity the following two $GSHP_{HC}$ definitions have been adopted:

- Collector pipe-network: refers to the flow and return manifold, the N underground pipes which connect these manifolds and the fluid within
- Source pipe-network: refers to the collector (as described above) plus the two run-out pipes, the source-side of the evaporator and the fluid within

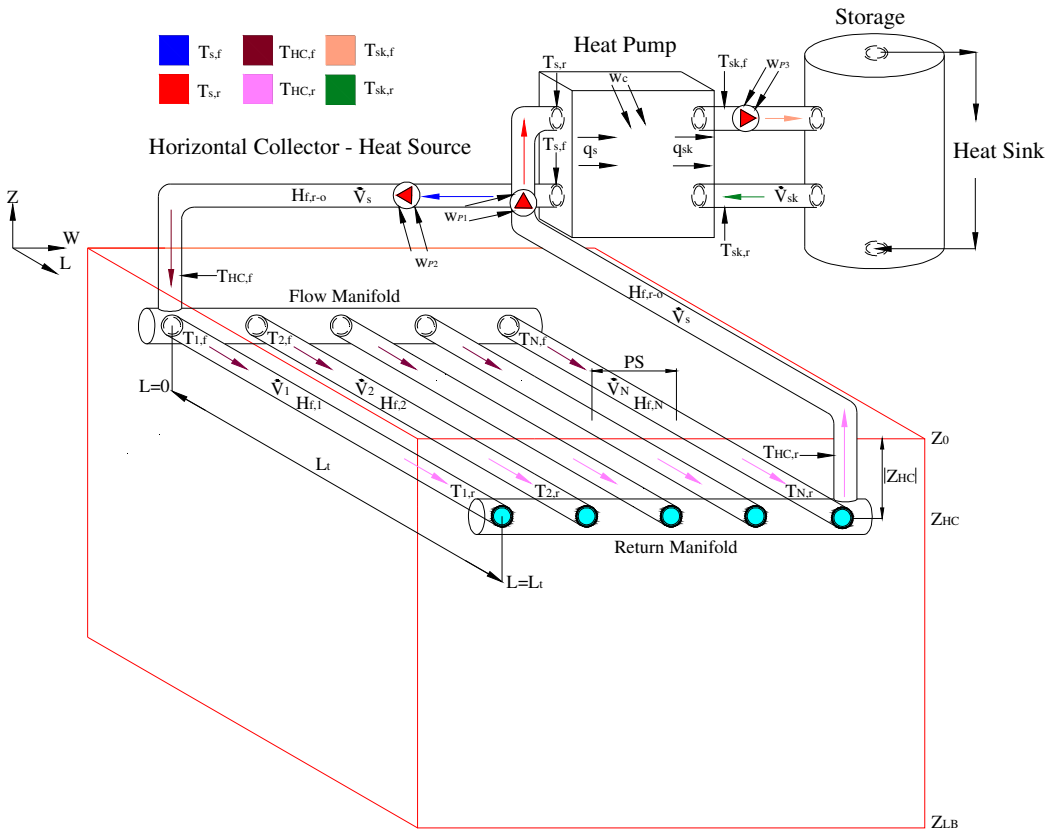

Figure 6-16: Idealised GSHP$_{HC}$ schematic showing the heat pump and heat source pipe-network which consists of a typical parallel horizontal collector plus run-out pipes

6.3.1 Model AL-8: Collector Head Loss Curve, Flowrate and Pumping Power

The heat transfer fluid which circulates through the source pipe network consists of a water and ethylene-glycol mixture; the properties of both the constituents and the mixture are summarised in Table 3-6. This is referred to as the 'source fluid', or simply 'fluid'. An electrical water pump or pumps in series circulate this fluid. Therefore a hydraulic analysis of the source fluid flow, identified as analytical method AL-8 in Figure 3-28, Section 3.8, was conducted as part of *HP-IRL/H*. The *HP-IRL/H* collector is built in the *parallel configuration*; the hydraulic parameters of this *parallel* collector are now developed.

The total flow rate through the source pipe-network $\dot{V}_s$ [m^3/s] is divided among the N *parallel array* collector-pipes as follows:

$$\dot{V}_s = \dot{V}_1 + \dot{V}_2 \ldots + \dot{V}_N \tag{6-12}$$

For N identical pipes of equal length, such as the *HP-IRL/H* collector, then $\dot{V}_s$ is divided equally with $\dot{V}_p$ flowing through each pipe as shown in Equation 6-13.

$$\dot{V}_s = N\dot{V}_p \tag{6-13}$$

The major head loss due to friction in the N pipes of a *parallel array* collector ($H_{f,HC}$) [m] with negligible manifold loss is defined using Equation 6-14.

$$H_{f,HC} = H_{f,1} = H_{f,2} \ldots = H_{f,N} \tag{6-14}$$

The *HP-IRL/H* heat source, like many others, includes run-out pipes which route the fluid between the heat pump and the collector and back to the heat pump; these pipes contribute a head loss referred to as $H_{f,r\text{-}o}$ [m]. The collector and the run-out pipes contain fittings which contribute minor losses referred to as $H_{m,HC}$ [m] and $H_{m,r\text{-}o}$ [m] respectively. Finally, the source side of the evaporator heat exchanger often contributes the most significant head loss ($H_{f,evap}$) [m]. For *Solterra 500*, Zottl (2003) quotes an evaporator pressure drop of 32.45kPa (equivalent to $H_{f,evap}$ of 3.13m) at a mass flowrate of 1.021kg/s (58l/min). Therefore, the total head loss for the heat source pipe-network ($H_{f,s}$) [m] is defined using Equation 6-15.

$$H_{f,s} = H_{f,HC} + H_{f,r-o} + H_{m,HC} + H_{m,r-o} + H_{f,evap} \tag{6-15}$$

Head loss due to friction is calculated using the *Darcy-Weisbach method* presented in Equation 6-16 using the friction factor (f).

$$H_f = \frac{u^2}{2g} f \frac{L}{D_{in}} \tag{6-16}$$

Where, u [m/s] is the velocity, g [m/s^2] is acceleration due to gravity, f [-] is the friction factor, L [m] is the pipe length and D_{in} [m] is the internal pipe diameter. The minor head loss is represented by Equation 6-17 using the sum of the minor loss coefficients (*K*) [-].

$$H_m = \frac{u^2}{2g} \sum K \tag{6-17}$$

Making the assumption that polyethylene pipes can be represented as smooth wall ducts, the following correlations can be used, where the transition from laminar to turbulent flow in ducts is assumed to be at $Re_D \approx 2300$.

$$f_{lam} = \frac{64}{Re_D} \tag{6-18}$$

$$f_{turb} = 0.316 Re_D^{-0.25} \tag{6-19}$$

Where the Reynolds number is defined using Equation 6-20, where u [m/s] is velocity, D_{in} [m] is the pipe's internal diameter and *v* [m^2/s] is the kinematic viscosity of the water-glycol mixture, defined in Table 3-6.

$$Re_D = uD_{in}/\nu \tag{6-20}$$

The head loss in the source-side of the *Solterra 500* evaporator ($H_{f,evap}$) [m] is a function of the source flow rate ($\dot{V}_s$) [m^3/s] and can be approximated using an empirical correlation as $H_{f,evap} = 602912(\dot{V}_s)^{1.744}$. The total head loss in the source pipe-network is overcome by head developed in a pump or pumps in series. Pump head (H_P) is a function of pump flow rate as described by the pump curve. For two identical water pumps in series, as is the case for the *HP-IRL/H* system, the series pump curve is found by doubling the pump head (H_P), developed by one of these *Grundfos UPS-25-80* pumps, at each flow rate value. Since the total head loss in the heat source pipe network ($H_{f,s}$) and the total pump head (H_P) developed are both a function of flow rate, the source operating point is found to be the intersection of the $H_{f,s}$ and H_P curves. The source flow rate predicted using this method was 84l/min, as shown in Figure 6-17.

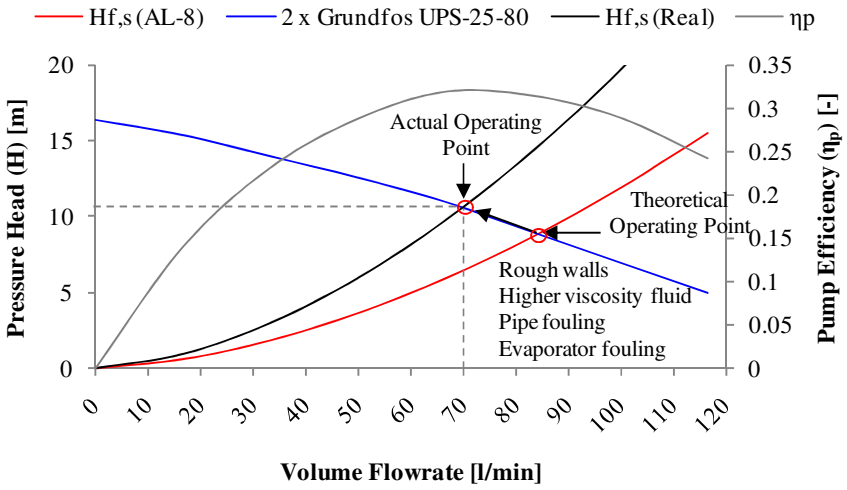

Figure 6-17: Hydraulic analysis of the heat source pipe-network using model AL-8

The flowrate predicted by the *Pipe Flow Expert* software, identified as NL-3 in Section 3.8 and shown in Figure 6-18, was 83l/min. However, using both the *Burkett* paddle wheel flow meter and the *Endress and Hauser* ultrasonic flow meter described in Section 3.4, the measured flow rate was found to be 70l/min ±1.4l/min. The difference is attributed to: the assumption of smooth duct flow in Equations 6-18 and 6-19, deviation from the published *Grundfos UPS-25-80* water pump curve when the pump is used to circulate the water-glycol mixture, fouling in the pipe-network and fouling in the evaporator in particular. The electrical power consumed in pumping fluid around the heat source pipe-network is found as follows:

$$w_P = \rho g \dot{V}_s H_{f,s} / \eta \qquad (6\text{-}21)$$

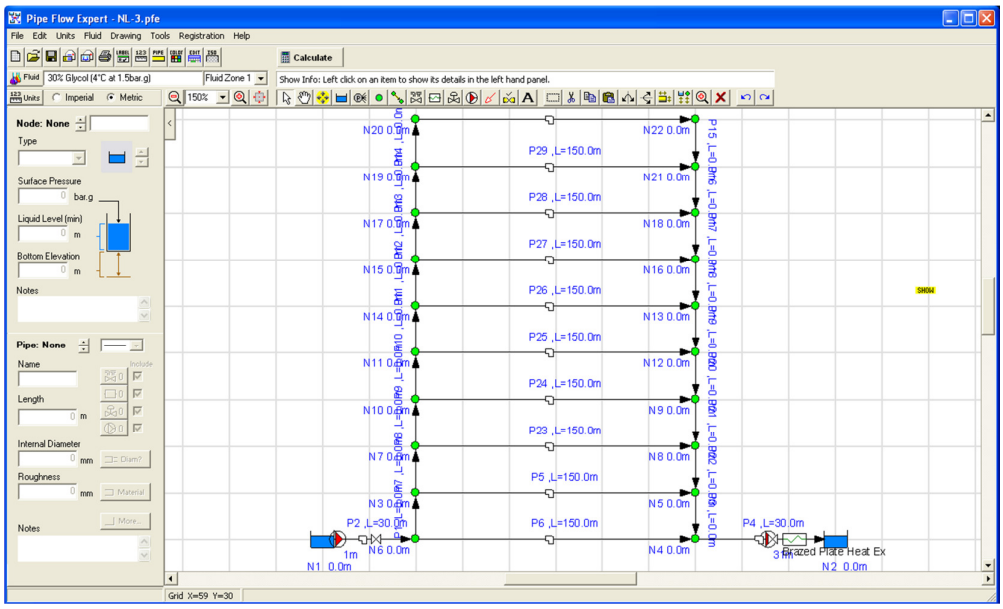

Figure 6-18: Hydraulic analysis of the heat source pipe-network using Pipe Flow Expert Software

This equates to $w_{P1} + w_{P2}$ of 416W at the actual operating point or 387.8W at the theoretical operating point predicted by AL-8 and the *Pipe Flow Expert* for ideal conditions. According to the manufacturer's information, *Grundfos UPS-25-80* pumps have a power consumption of between 180 and 200W. Power consumed in components other than the compressor ($w_{P1} + w_{P2} + w_{P3} + w_{stb}$) was measured using the *Vydas* power meter (accuracy of ±5%) and summed to 620W ± 30W. Measured standby power (w_{stb}) was approximately 50W and the power consumed by the sink-side *Grundfos UPS-25-80* (w_{P3}) was between 180 and 200W. This equates to measured pumping power $w_{P1} + w_{P2}$ of between 370 and 390W ± 5%. As discussed in Sub-section 6.2.3, the inclusion of $w_{P1} + w_{P2} + w_{P3} + w_{stb}$ can reduce COP by between 8 and 13%; therefore, pumping power consumption should be considered in collector design using the described method.

6.3.2 Basic Thermal Characterisation

It can be seen in Figure 6-16 that two return temperatures, collector return ($T_{HC,r}$) [ºC] and source return ($T_{s,r}$) [ºC], have been defined. In cases where the *run-out* pipes are long (>10m), in direct contact with the building or ground and un-insulated, these return temperatures must be considered as distinctly different. However, in the case of the *GSHP$_{HC}$* used in *HP-IRL/H*, the *run-out* pipes were insulated (10mm of lagging) and routed to the collector through ducting without direct contact with the building or ground. Measured temperatures, shown in Figure 6-19, indicate that the difference ($\Delta T_{HC,r/s,r} = T_{HC,r} - T_{s,r}$) is negligible.

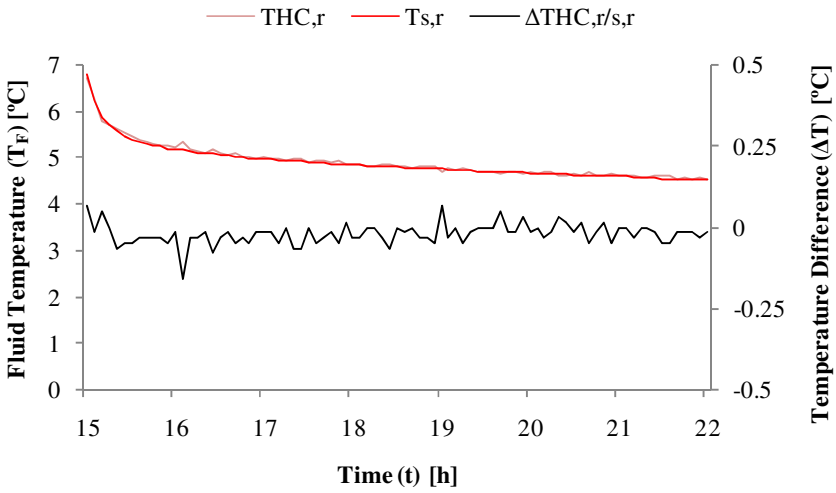

Figure 6-19: Comparison of collector and source return temperature measured on 05/01/2009 during HC9 at the return manifold and the heat pump entrance respectively

The return temperature of the *parallel array* is as defined as follows for the general *GSHP$_{HC}$* situation.

$$T_{s,r} \approx T_{HC,r} = (\dot{V}_1 T_{1,r} + \dot{V}_2 T_{2,r} + \ \ldots \ \dot{V}_N T_{N,r})/\dot{V}_s \tag{6-22}$$

For a properly balanced *parallel array*, as discussed in Sub-section 6.3.1, and with negligible heat transfer in the return run-in, then it is assumed that the source return temperature is equal to the return temperature of any pipe.

$$T_{s,r} = T_{HC,r} = T_{1,r} = T_{2,r} \ldots = T_{N,r} \tag{6-23}$$

In winter mode, the heat pump removes heat q_s [kW] from the fluid as it circulates through the evaporator. This lowers the fluid temperature by an amount ΔT_{evap} [K] proportional to q_s and inversely proportional to the mass flow rate ($\dot{m}_s$) [kg/s]. As the cooled fluid flows through the under-ground collector pipes its temperature increases by an amount ΔT_{HC} [K]. The *GSHP$_{HC}$* problem can be defined as a simple fluid temperature increase in a pipe. However, it is the boundary condition at the outer surface of the pipe which causes difficulty. Firstly, typical boundary conditions which are not appropriate are:

- Constant heat flux at the pipe boundary (for example a pipe heated electrically on the external surface)
- Constant temperature at the pipe boundary (for example a pipe submerged in a large body of fluid at a constant temperature)

However, one boundary condition which can approximate the situation is:

- Predictable temperature at the farfield boundary (a pipe surrounded with a very thick cylinder of ground)

The farfield boundary, depicted in Figure 6-20, is the outer boundary of the cylinder of ground surrounding the pipe that has been affected by operation of the *GSHP$_{HC}$*. The diameter of this imaginary cylinder (D_∞) [m] grows with time (t) while the *GSHP$_{HC}$* is operated; as D_∞ grows the ΔT_{HC} which the pipe achieves is diminished. The temperature at this farfield boundary ($T_{g,\infty}$) [ºC] is typically not constant, but can be predicted with reasonable accuracy using analytical or numerical methods as shown in Chapters 4 and 5.

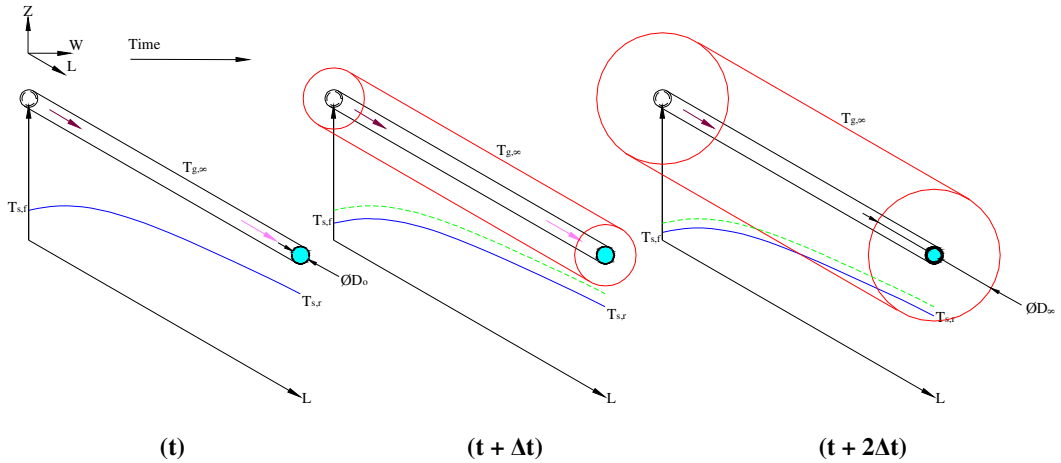

Figure 6-20: Schematic representation of growth in the farfield boundary which is the outer boundary of the cylinder of ground surrounding the pipe that has been affected by operation of the GSHP$_{HC}$

6.3.3 Comparing Parallel and Series Collector Flow Configuration

Based on the *GSHP$_{HC}$ design groups* and associated literature presented in Table 2-13, Sub-section 2.5.5, it was seen that the question of *collector flow configuration* has received limited attention to date. Figures 6-21(a) and (b) contrast the *in-line, parallel* array commonly used in Ireland with the *serpentine, series* array commonly tested in the literature (Metz, 1981; Inalli & Esen, 2004; Pulat *et al.*, 2009). Table 6-6 summarises the thermo-hydraulic differences between the *parallel* and *series* collector. In this authors opinion the following are significant benefits of the *parallel configuration*:

- Enables use of the recommended flowrate in the evaporator while using a low flowrate in the individual parallel pipes, simultaneously
  - Low flowrate reduces head loss while improving temperature increase
- More fluid can be sent underground with less head loss
- More pipe length can be buried in the ground with less head loss

- When area is restricted, parallel slinky pipes can be used

➢ Pipes with smaller cross section can be used with less head loss

- Smaller cross-section aids heat transfer

➢ More heat exchange surface area buried underground with less head loss

A proposed method for advancing *parallel collector* design is presented in Appendix K.

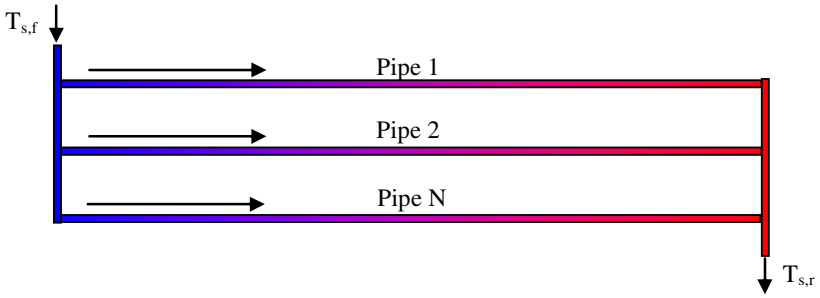

(a) Parallel flow configuration, in-line array with straight pipe routing

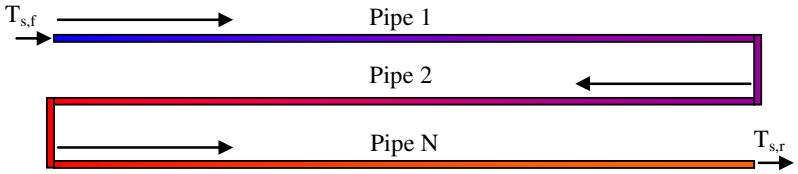

(b) Series flow configuration, in-line array with serpentine pipe routing

Figure 6-21: Comparison of parallel and series collector pipe networks

Table 6-6: Thermo-hydraulic comparison of parallel and series collector pipe networks

	Parallel array	**Series array**
Flowrate	$\dot{V}_s = \dot{V}_1 + \dot{V}_2 \ldots + \dot{V}_N$	$\dot{V}_s = \dot{V}_1 = \dot{V}_2 \ldots = \dot{V}_N$
Head loss	$H_{f,s} = H_{f,1} = H_{f,2} \ldots = H_{f,N}$	$H_{f,s} = H_{f,1} + H_{f,2} \ldots + H_{f,N}$
Fluid warming distance	$L_t = L_1 = L_2 \ldots = L_N$	$L_t = L_1 + L_2 \ldots + L_N$
Return temperature	$T_{s,r} = (\dot{V}_1 T_{1,r} + \dot{V}_2 T_{2,r} + \ \ldots \ \dot{V}_N T_{N,r})/\dot{V}_s$	$T_{s,r} = T_{N,r}$
Balanced collector	$T_{s,r} = T_{N,r}$	$T_{s,r} = T_{N,r}$

The benefit of parallel piping can be further increased by burying two parallel collectors within the same area of ground in a split-level fashion at $Z_{HC,A}$ and $Z_{HC,B}$. Fluid is then circulated in parallel through both collector levels or through one collector level based on an intelligent control strategy. As well as having the positive thermo-hydraulic influences listed above, it is shown in Section 8.2 that this collector design spreads the heat extraction across two partially independent ground layers. This also adds the advantages of reducing the volumetric ground heat extraction (q_s/V_{HC}) [W/m^3] which reduces thermal drawdown at the *collector-ground interface.*

6.4 MODEL AL-9: ESTIMATING SOURCE RETURN TEMPERATURE

The group of simple equations described in this section for estimating source return temperature ($T_{s,r}$) have been identified as AL-9 as introduced in Figure 3-28, Section 3.8. As established in the previous section, the temperature of the fluid returning from the *HP-IRL/H* source ($T_{s,r}$) [ºC] can be considered equal to the temperature of the fluid returning from the collector ($T_{HC,r}$) [ºC] which is equal to the return temperature from any of the N collector pipes ($T_{N,r}$) [ºC]. As summarised in Equation 6-24, $T_{N,r}$ is equal to the source fluid temperature at the pipe exit ($T_{F,Lt}$) [ºC] which depends on pipe length (L_t) and *$GSHP_{HC}$* operating time (t), along with the pipe size and material, and both the fluid and ground thermal properties.

$$T_{s,r} \approx T_{HC,r} = T_{N,r} = T_{F,L_t}(L_t, t) \tag{6-24}$$

Figure 6-22 shows a schematic of pipe N, of variable length (L) [m], where the fluid temperature ($T_{F,L}$) can be described in terms of $T_{g,\infty}$ and $T_{s,f}$ using Equation 6-25 (Incorpera & DeWitt, 2002).

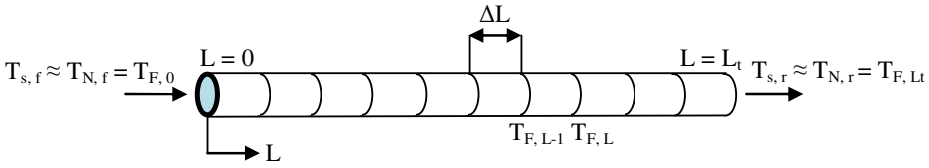

Figure 6-22: Nomenclature for collector pipe analytical model, wider context shown in Figure 6.16

$$T_{F,L}(L, t) = T_{g,\infty} + \left[\left(T_{s,f} - T_{g,\infty}\right) \exp\left(\frac{-1}{\dot{m}_p c_{p,f} R(L,t)}\right)\right] \tag{6-25}$$

In Equations 6-25, $\dot{m}_p$ [kg/s] is the mass flow rate in a single collector pipe, $c_{p,F}$ [J/kgK] is the constant pressure specific heat capacity of the fluid, R(L,t) [K/W] is the total thermal resistance that exists between the fluid and the point of the farfield temperature ($T_{g,\infty}$) for a pipe L meters long. The resistance R reduces with pipe length (L) and increases with time (t). Figure 6-23 displays the increase in fluid temperature at the start of a heat extraction cycle (t_0) and after 10 days for a $T_{s,f}$ of 2ºC and a $T_{g,\infty}$ of 10ºC. It can be seen that as expected from Equation 6-25, the temperature increase is non-linear with a ΔT_{HC} of 4.46K for a 75m pipe but a ΔT_{HC} of only 6.29K for a 150m pipe, at t_0. Figure 6-23 also shows the influence had by time and the growth in the farfield cyclinder around the pipe, the ΔT_{HC} of 6.29K is reduced to a ΔT_{HC} of 3.46K after 10 days of continuous heat extraction.

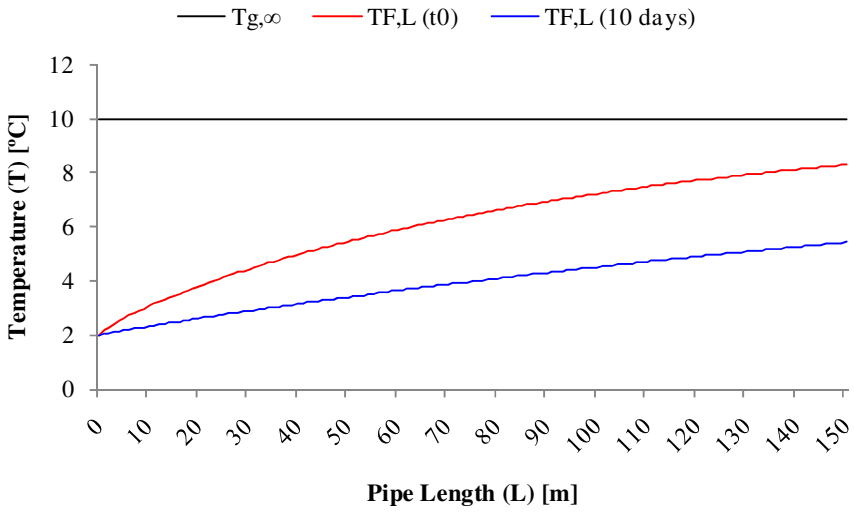

Figure 6-23: Predicted fluid temperature increase with collector pipe length using Equation 6-25

The grouping of terms on the right side of Equation 6-25 will be used subsequently and are identified as the pipe fluid calculation factor $\varphi(\dot{m}_p, R(L,t))$, as shown in Equation 6-26.

$$\exp\left(\frac{-1}{\dot{m}_p c_{p,F} R(L,t)}\right) = \varphi(\dot{m}_p, R(L,t)) \quad (6\text{-}26)$$

The total resistance R(L,t) includes fluid convection resistance R_F (L) [K/W], pipe conduction resistance R_p(L) [K/W], thermal contact resistance at the pipe ground interface $R_{p\text{-}g}(L,\theta_{wg})$ [K/W] and ground conduction resistance R_g(L,t) [K/W], which are summed as follows:

$$R(L,t) = R_F(L) + R_p(L) + R_{p-g}(L,\theta_{wg}) + R_g(L,t) \quad (6\text{-}27)$$

As discussed in Chapter 5, the ground moisture content θ_{wg} [m^3/m^3] is relatively high (>0.25 m^3/m^3) at a depth of 1m in the *HP-IRL/H* site during winter. When this is the case, then the pipe-ground thermal contact resistance ($R_{p\text{-}g}$) can be ignored for winter heating mode (O'Connell & Cassidy, 2004). However, the ground thermal resistance (R_g) cannot be ignored and depends on the farfield diameter (D_∞) which grows with operation time (t).

6.4.1 Farfield Distance

The farfield diameter (D_∞) [m] or radius (r_∞) [m] is a function of time (t) [s] and ground diffusivity (α_g) [m^2/s] and can be defined by Equation 6-28 (Hart & Couvillion, 1986).

$$D_\infty(t) = 2r_\infty(t) = 2(4\sqrt{\alpha_g t}) \quad (6\text{-}28)$$

This relationship, which is independent of heat extraction rate (q_s), has been examined and verified during this *HP-IRL/H* project. This novel verification process involved comparing Equation 6-28 with the results of numerical model NL-4, which is described and experimentally validated in Chapter 7, at two different q_s values of 5 and 10kW. It was seen that propagation (r_∞) [m] of the cooling influence was equal at q_s of 5 and 10kW, as shown in Figure 6-24. However as expected, the magnitude of the cooling influence ($\Delta T_{s,r/\infty}$) was approximately double at 10kW compared to 5kW.

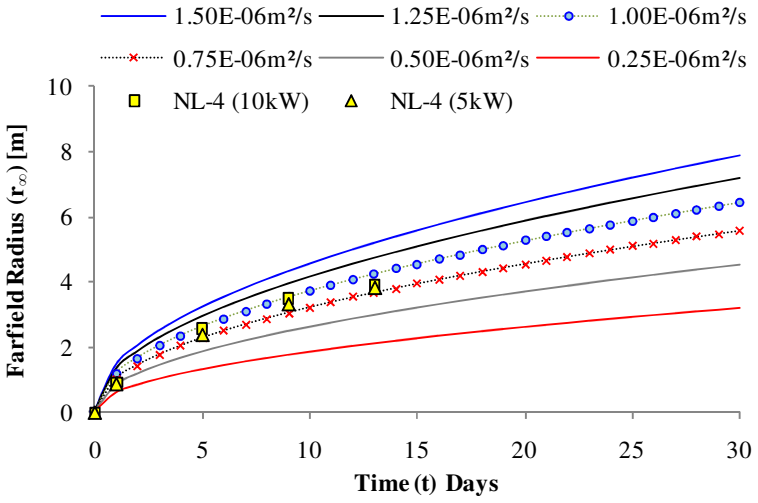

Figure 6-24: Predicted (Equation 6-28) and simulated (NL-4) change in farfield radius with thermal diffusivity and time

6.4.2 Convection Coefficient

The convection coefficient (h) [W/m^{2}K] for heat transfer between the inner collector pipe wall and the source fluid is defined in Equation 6-29, where NuD [-] is the Nusselt number while D_{in} [m] and k_F [W/mK], the internal pipe diameter and fluid conductivity, are defined in Tables 3-5 and 3-6 respectively.

$$h = \frac{Nu_D k_F}{D_{in}} \tag{6-29}$$

The Nusselt number (Nu_D) is defined using the correlation in Equation 6-30 (Incorpera & DeWitt, 2002), where Re_D is the Reynolds number, defined in Equation 6-20, and Pr [-] is the Prandtl number, defined in Table 3-6.

$$Nu_D(L) = 3.66 + \frac{0.0668(\frac{D_{in}}{L})Re_D Pr}{1+0.04[(\frac{D_{in}}{L})Re_D Pr]^{(2/3)}} \tag{6-30}$$

The convection coefficient (h) calculated for a *HP-IRL/H* collector pipe operating at a flowrate of 7l/min is displayed in Figure 6-25. This indicates a thermal entrance length (L_{th}) [m] of between 50 and 70m which corresponds with a value of 55m found using the common correlation of $0.05D_{in}Re_DPr$ (Incorpera & DeWitt, 2002).

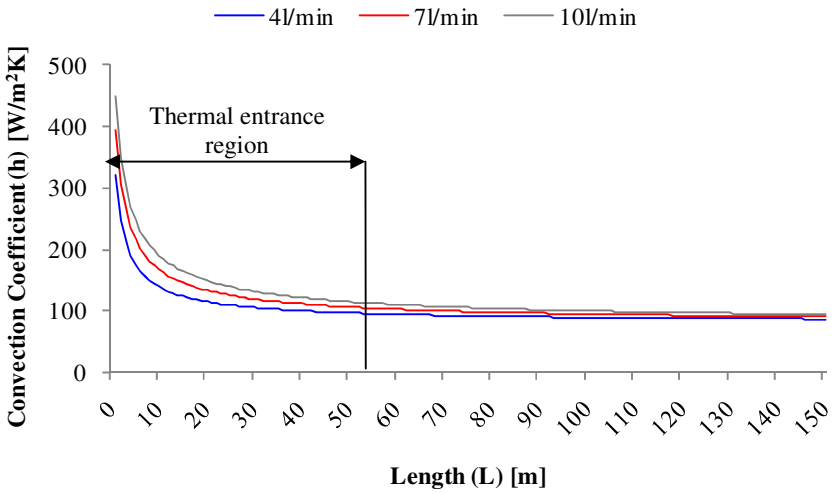

Figure 6-25: Variation of the convection coefficient (h) with HP-IRL/H collector pipe length and flowrate

6.4.3 Radial and Linear Ground Resistance

There are two common methods for estimating thermal resistance. These are radial and linear resistance, shown in Figures 6-26(a) and (b) respectively. However, neither of these methods fully describes the horizontal collector behaviour at all times.

The radial method (R_{rad}), shown in Figure 6-26(a), assumes axis-symmetric heat transfer conditions and would be suited to an isolated pipe in an infinite medium unbounded in any direction. While this is appropriate for the early portion of any *GSHP$_{HC}$* operation period, this model fails when thermal interaction between neighbouring collector pipes takes place or when the farfield radius reaches the surface.

The linear method (R_{lin}), presented in Figure 6-26(b) assumes heat transfer along linear, vertically aligned temperature gradients and would be suited where: the pipe could be treated as a horizontal plate, the adiabatic boundaries extend above and below the collector pipe in a parallel fashion and the collector 'edge effects' can be ignored. Figure 6-26(c) introduces an alternative numerical method used in Chapter 7, which overcomes the limitations of both the radial and linear method by splitting the ground around the pipe into small squares.

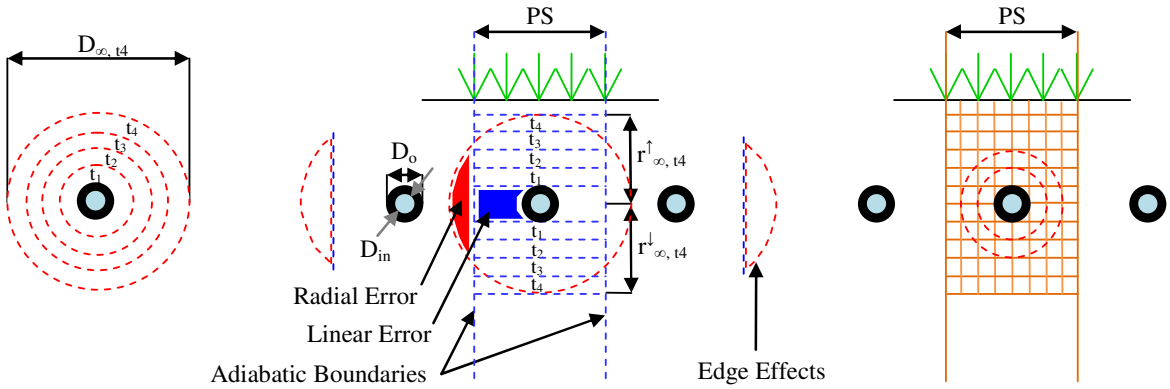

(a) Radial resistance **(b) Linear resistance** **(c) Chapter 7 numerical method**

Figure 6-26: Models for estimating the increase in ground resistance due to growth in the farfield diameter with time during ground heat extraction

The total thermal resistance between the fluid and the farfield, assuming the axis-symmetric heat transfer of Figure 6-26(a), can be defined using the radial resistance expression in Equation 6-31. Where, h [W/m^{2}K] is the convection coefficient for fluid flow in the pipe, Figure 6-25, k_p [W/mK] is the pipes thermal conductivity, Table 3-6, and k_g [W/mK] is the grounds thermal conductivity Table 5-5 and 5-7.

$$R_{rad}(L,t) = \frac{1}{\pi D_i h L} + \frac{\ln(D_o/D_{in})}{2\pi k_p L} + \frac{\ln(D_\infty(t)/D_o)}{2\pi k_g L} \quad (6\text{-}31)$$

The total thermal resistance between the fluid and the farfield, assuming heat transfer along linear temperature gradients of Figure 6-26(b) for a pipe spacing (PS) [m], can be defined using the novel combined radial pipe and linear ground resistance expression in Equation 6-32. Thermal resistance above ($R^{\uparrow}$) and below ($R^{\downarrow}$) the pipe are summed in parallel and the growth of the farfield radius upward ($r^{\uparrow}_{\infty}$) is limited by the ground surface.

$$R_{lin}(L,t) = \frac{1}{\pi D_i h L} + \frac{\ln(D_o/D_i)}{2\pi k_p L} + \frac{1}{[PSk_gL/r^{\uparrow}_{\infty}(t)]+[PSk_gL/r^{\downarrow}_{\infty}(t)]} \quad (6\text{-}32)$$

Figure 6-27 displays the total resistance for a 150m pipe with a flow rate of 7l/min calculated using both the radial (R_{rad}) and the combined radial and linear (R_{lin}) method over a 30 day *GSHP$_{HC}$* operational period. Figure 6-27 also displays the calculation factor ($\varphi(R)$) from Equation 6-26 as it varies over 30 days with both methods. The growth in the farfield radius over the 30 day operational period, which causes the change in R and φ is shown in Figure 6-24. By comparison of Figures 6-24 and 6-27, it is observed that while the farfield distance continues to the grow, the influence of this growth on R_{rad} or R_{lin} then φ_{rad} or φ_{lin} and ultimately $T_{s,r}$ reaches a steady-state value after 5 to 7 days. This equates to the medium-term steady-state of the horizontal collector.

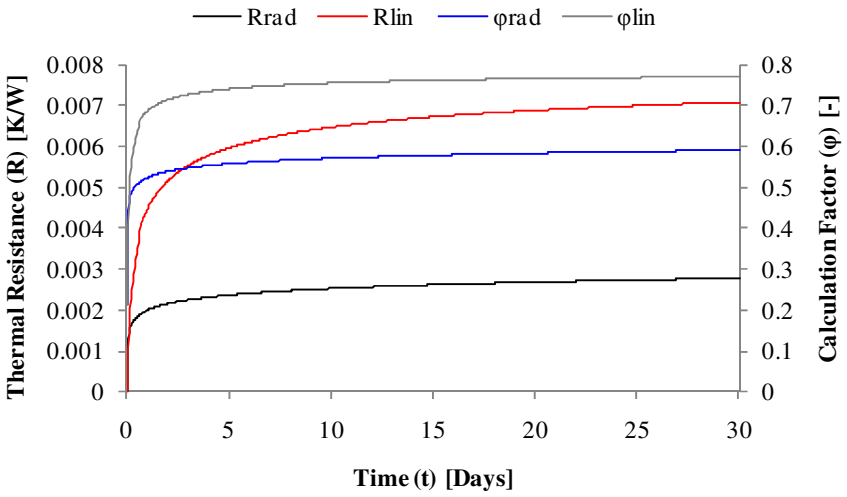

Figure 6-27: Variation in total thermal resistance and the calculation factor with time for radial (Figure 6-26(a)) and linear (Figure 6-26(b)) approximations of the 150m long horizontal collector pipes

6.4.4 AL-9 Comparison with Experimental Data

The suitability of the radial and linear methods was then established by comparing $T_{s,r}$ values found with both estimates with measured data. By substituting the calculation factor ($\varphi(L,t)$) [-] from Equation 6-26 into Equation 6-25, the source return temperature $T_{s,r}$ was defined using Equation 6-33.

$$T_{s,r} = T_{g,\infty} + \varphi\left(T_{s,f} - T_{g,\infty}\right) \tag{6-33}$$

The source flow temperature ($T_{s,f}$) was defined using Equation 6-34, where ΔT_{evap} is the temperature drop in the evaporator for the extraction rate q_s [W] at a source mass flow of $\dot{m}_s$ [kg/s].

$$T_{s,f} = T_{s,r} - \Delta T_{evap} = T_{s,r} - \frac{q_s(T_{sk,f}, T_{s,r})}{\dot{m}_s c_{p,F}} \tag{6-34}$$

As demonstrated in Sub-section 6.2.2, the extraction rate is a function of the source and the sink temperature. Based on the *Solterra 500* data (Zottl, 2003), Equation 6-35 was used to represent the heat pump at a fixed $T_{sk,f}$ of 50ºC.

$$q_s\left(T_{sk,f} = 50°C\right)[W] = 1000(0.3744T_{s,r} + 9.8567) \tag{6-35}$$

By substituting Equation 6-34 and 6-35 into Equation 6-33 and solving for the return temperature ($T_{s,r}$), then the expression in Equation 6-36 was derived, where $T_{g,\infty}$ (Z,t) [ºC] is the farfield temperature, $\varphi(L,t)$ [-] is the calculation factor, $\dot{m}_p$ [kg/s] is the mass flow rate in one pipe and $c_{p,F}$ [J/kgK] is the fluid's specific heat capacity.

$$T_{s,r} = \frac{T_{g,\infty} - \varphi T_{g,\infty} - \varphi \frac{9856.7}{\dot{m}_s c_{p,F}}}{1 - \varphi + \varphi \frac{374.4}{\dot{m}_s c_{p,F}}} \quad (6\text{-}36)$$

As discussed in Chapters 4 and 5, there are numerous methods for calculating the farfield temperature or alternatively the ground temperature data can be used when available:

$$T_{g,\infty}(Z,t) = T_{g,Z_{HC}} = T_{P1,-0.9m} \approx T_{AL-4,-1.0m} \approx T_{NL-1,-1.0m} \approx T_{NL-2,-1.0m} \quad (6\text{-}37)$$

The *HP-IRL/H* horizontal collector described in Chapter 3 can be summarised as follows:

- Collector area (A_{HC}) of 430m^2
- 10 collector pipes, each 150m long, N=10 meaning 9 pipe spaces (N-1)
- Flow rate of 70l/min in the source, results in 7l/min for each of the 10 pipes

Equation 6-38 is an approximate relationship between the collector area (A_{HC}) [m^2], the pipe length (L_t) [m], the number of pipes (N) and the average pipe spacing (PS) [m], which results in an average pipe spacing of 0.32m for the *HP-IRL/H* collector. Observations of pipe spacing in Table 3-5 varied between 0.25 and 0.4m which results in an average of 0.325m.

$$A_{HC} \approx L_t(N-1)PS \quad (6\text{-}38)$$

Figure 6-28 displays four temperature time series. These are the measured farfield temperature used in Equation 6-36 ($T_{P1,\ -0.9m}$), the measured return temperature ($T_{s,r}$), the return temperature estimated using the radial method, $T_{s,r}$(AL-9-R_{rad}), the return temperature estimated with the linear method, $T_{s,r}$(AL-9-R_{lin}), and finally the average of the latter two, $T_{s,r}$ (AL-9-R_{ave}). HC9, defined in Figure 6-1, was chosen for comparison because of the 25 day long, steady-state, non-stop operation during this period.

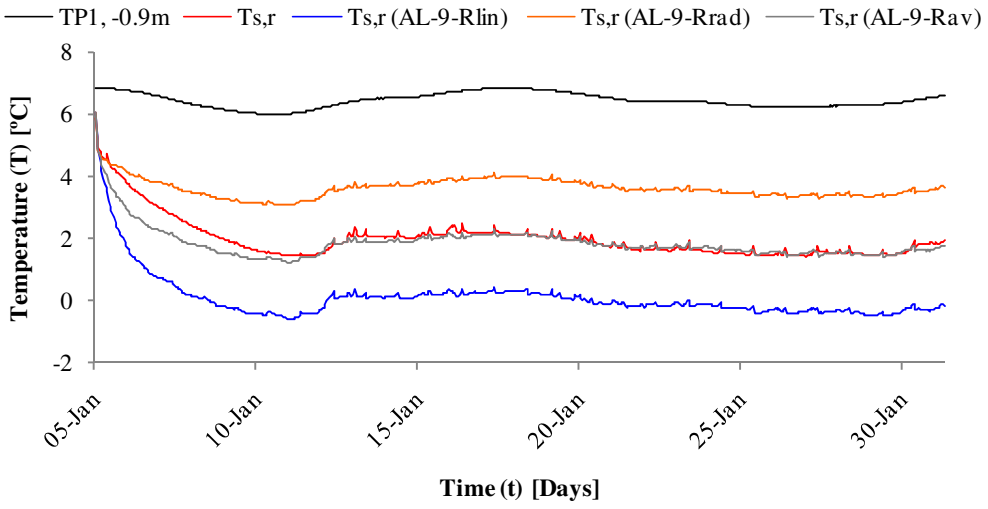

Figure 6-28: Comparison of estimated and measured return temperatures ($T_{s,r}$) during HC9

It can be seen that, as expected, neither the radial or linear method accurately describes the horizontal collector with accuracy better than ±2K. The radial method over-estimates the return temperature while the linear method under-estimates the return temperature. The average of the two methods however, conveniently produces estimations within ±0.2K of the actual return temperature, particularly during the steady-state condition achieved after 5 to 7 days.

Both the advantages and disadvantages of this method lie in its simplicity. The method requires only basic collector dimensions, farfield temperature and the length of the operation cycle in order to estimate the variation in source return temperature with time. However, it is only suitable for estimates in steady-state or long term type analysis. It is shown in the next section that this method can be applied to cyclic operation by using an average extraction rate ($q_{s,h}$) which is equivalent to the actual extraction rate (q_s) multiplied by the percentage duty (D_{hp}) as shown in Equation 6-2.

6.5 THERMAL DRAWDOWN

Burke (2010) defined a 4 stage cycle, shown in Figure 6-29, to describe typical variation in medium-term *GSHP$_{HC}$* operation with time.

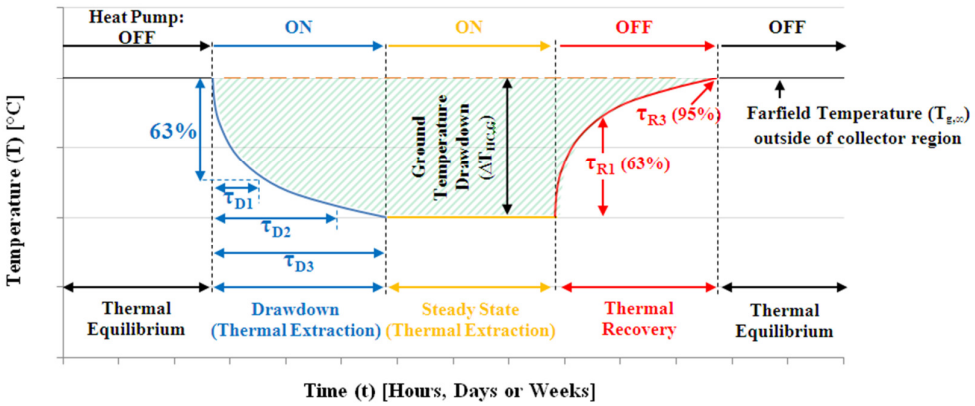

Figure 6-29: Characterisation of thermal equilibrium, thermal drawdown, steady-state extraction and thermal recovery stages associated with medium-term thermal extraction cycles (Burke, 2010)

The schematic is divided as follows:

- Thermal equilibrium: the GTD within the collector area (such as P5) is identical to the GTD in the reference profile (P1)

- Drawdown thermal extraction: the source return temperature drops with time as the *GSHP$_{HC}$* operates
- Steady-state thermal extraction: the farfield radius will continue to grow but the total resistance (R) and the calculation factor (φ) reach steady-state and the source return temperature stabilises
- Thermal recovery: the *GSHP$_{HC}$* is switched off and the ground temperature begins to return to equilibrium

The extent of the drawdown ($\Delta T_{s,r/\infty}$) [K], as defined in Equation 6-3, is the difference between the source return temperature ($T_{s,r}$) [ºC] and ground farfield temperature ($T_{g,\infty}$) [ºC]. Burke (2010) studied thermal drawdown using the 9 sets of experimental data (HC1 through HC9). The results of this characterisation for 4 periods (HC3, HC4, HC6 and HC9) are shown in Figure 6-30, where the steady-state drawdown (identified as $\Delta T_{HC,G}$ [K]) is shown to be proportional to the '*collector thermal extraction rate* [flux]' (identified as q''_{HC} [W/m^2]). Within this analysis the assumption was made that a cycling *GSHP$_{HC}$* (with off periods within each hour or each day) was equivalent to a *GSHP$_{HC}$* extracting heat constantly at this percentage of the nominal extraction rate (q_s) (as discussed in Sub-section 6.1.1).

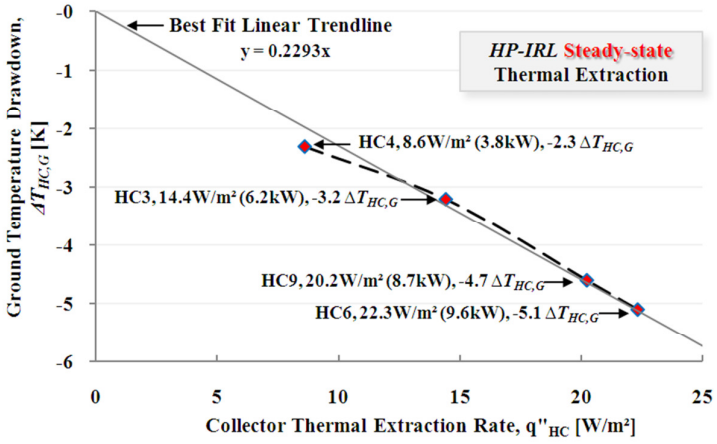

Figure 6-30: Temperature drawdown compared with thermal extraction rate [flux] (Burke, 2010)

6.5.1 Model AL-10: Estimating Steady-State Thermal Drawdown

While Burke (2010) established a clear relationship between drawdown and extraction flux for the *HP-IRL/H* collector, this study sought to develop a method of estimating drawdown for conceptual *GSHP$_{HC}$* designs. This method, identified as AL-10 in Section 3.8, is based on basic *GSHP$_{HC}$ design variables* and uses a novel derivation from the basic collector heat transfer principles discussed in Section 6.4. Substituting Equation 6-34 into Equation 6-33

gives Equation 6-39 which includes only the temperature terms $T_{s,r}$ and $T_{g,\infty}$ which define source drawdown ($T_{s,r/\infty}$) in Equation 6-3.

$$T_{s,r} = T_{g,\infty} + \varphi T_{s,r} - \varphi \frac{q_s}{\dot{m}_s c_{p,F}} - \varphi T_{g,\infty} \tag{6-39}$$

Rearranging the terms in Equation 6-39 yields the following:

$$(T_{s,r} - T_\infty) - \varphi(T_{s,r} - T_\infty) = -\varphi \frac{q_s}{\dot{m}_s c_{p,F}} \tag{6-40}$$

From this, Equation 6-41 can be written which defines the drawdown ($\Delta T_{s,r/\infty}$) [K] in terms of extraction (q_s) [W], source flow rate ($\dot{m}_s$) [kg/s] and calculation factor ($\varphi_{Lt}(\dot{m}_p, R)$) [-] which in combination incorporate 11 *GSHP$_{HC}$* parameters defined and discussed in Section 6.4.

$$\Delta T_{s,r/\infty}(q_s, \dot{m}_s, c_{p,F}, N, L_t, D_{in}, D_o, Nu_D, k_F, k_p, k_g, PS) = \frac{-q_s \varphi_{L_t}}{\dot{m}_s c_{p,F}(1-\varphi_{L_t})} \tag{6-41}$$

As shown in Sub-section 6.4.3, the calculation factor at the pipe exit (φ_{Lt}) [-] can be evaluated using either radial or linear ground resistance, with neither method fully describing collector operation at all times. Figure 6-31 displays four extraction-drawdown trends. These are the measured trend, $\Delta T_{s,r/\infty}$ (Burke, 2010), the estimated trend using radial resistance, $\Delta T_{s,r/\infty}$ (AL-10-R_{rad}) in red, the estimated trend using linear resistance, $\Delta T_{s,r/\infty}$ (AL-10-R_{lin}) in blue, and finally the average of the latter two, $\Delta T_{s,r/\infty}$ (AL-10-R_{av}) in grey.

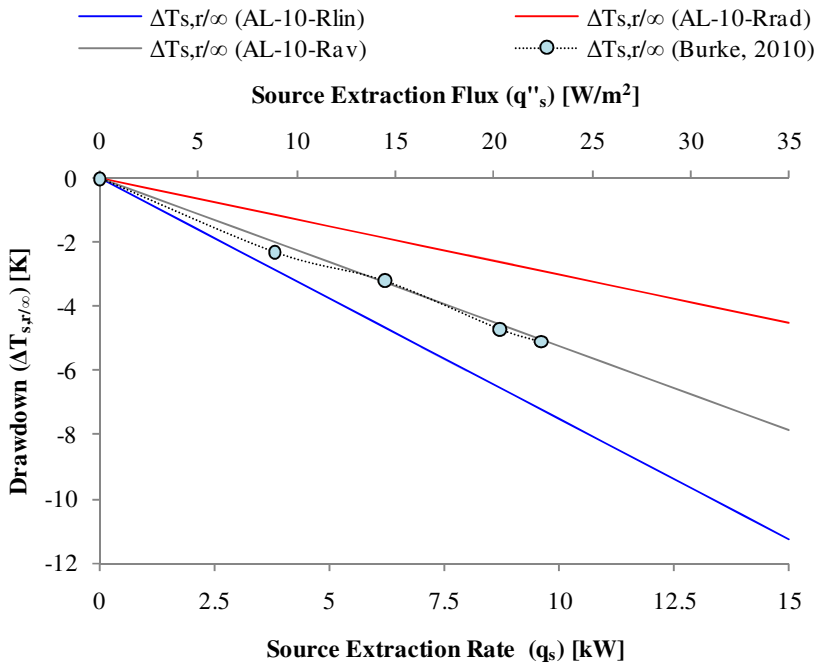

Figure 6-31: The variation in collector drawdown with source extraction rate and source extraction flux

As expected, Figure 6-31 shows that neither the radial or linear method accurately describes the horizontal collector drawdown. The radial method under-estimates the drawdown while the linear method over-estimates the drawdown. However, the average of the two methods conveniently produces an accurate estimation of the actual drawdown, with deviations less than 0.2K for each of the four tests shown.

6.5.2 Influence of Flowrate

It can be seen in Equation 6-41 that a number of variables influence the thermal drawdown. One variable which can be controlled during *$GSHP_{HC}$* operation is the source mass flow rate ($\dot{m}_s$). The source mass flow rate ($\dot{m}_s$) [kg/s] is a component of Equation 6-41 and therefore has a direct influence on source drawdown. Additionally, the associated pipe mass flowrate ($\dot{m}_p$) [kg/s] influences the calculation factor (φ), defined in Equation 6-26, which is another component of Equation 6-41. Finally, the associated pipe flowrate ($\dot{V}_p$) [m^3/s] influences convection coefficient (h), defined in Equation 6-29, which is a component of Equation 6-26.

Combining these influences, it was shown that by reducing the source flow rate the source return drawdown ($\Delta T_{s,r/\infty}$) was reduced, meaning warmer return fluid ($T_{s,r}$). However, by reducing the source flowrate, the flow rate through the evaporator is also reduced and this will cause a larger temperature drop across the evaporator (ΔT_{evap}), reduced source extraction rate, or both. Equation 6-42 defines the flow temperature drawdown ($\Delta T_{s,f/\infty}$) [K] in terms of extraction (q_s) [W], source flow rate ($\dot{m}_s$) [kg/s] and calculation factor ($\varphi(\dot{m}_s, R)$) [-].

$$\Delta T_{s,f/\infty} = T_{s,f} - T_{\infty} = \frac{-q_s \varphi_{L_t}}{\dot{m}_s c_{p,F}(1-\varphi_{L_t})} - \frac{q_s}{\dot{m}_s c_{p,F}} \tag{6-42}$$

Figure 6-32 displays 5 minute (non-steady) flow and return drawdown values, at 70l/min from HC9 (in blue and red respectively) and also at 32l/min from HC10 (in green and orange respectively). Figure 6-32 also displays 5 minute source extraction rates during HC9 and HC10 in black and grey respectively. As expected, non-steady return drawdown ($\Delta T_{s,r/\infty}$) after 10 days was -4.5K at 70l/min compared to only -2.7K at 32l/min, a difference of 1.8K. Non-steady flow drawdown ($\Delta T_{s,f/\infty}$) after 10 days was -6.76K at 70l/min compared to -7.3K at 32l/min, a difference of 0.54K. The increase in flow drawdown at 32l/min (from -6.76 to -7.3K) appears minimal compared to the beneficial decrease in return drawdown (from -4.5K to -2.7K). However, Figure 6-32 also shows that non-steady source extraction (q_s) after 10 days was only 8.76kW at 32l/min compared to 10.25kW at 70l/min.

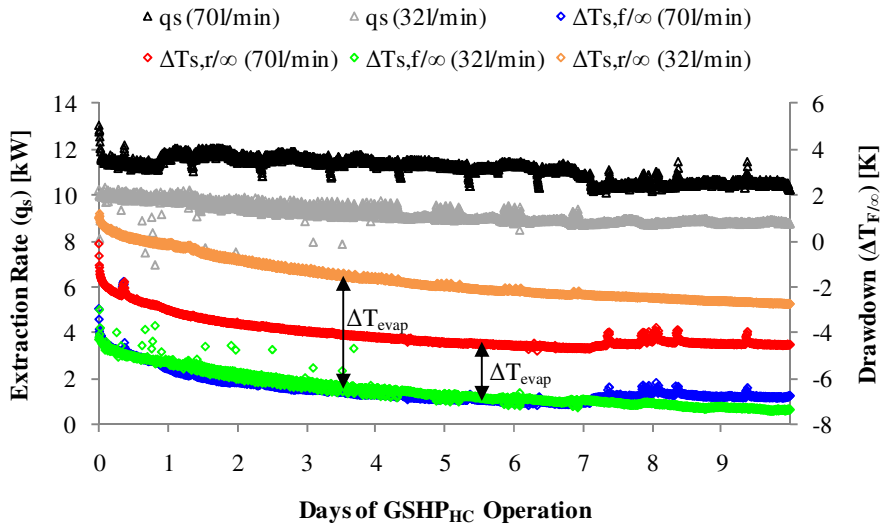

Figure 6-32: Measured source flow and return thermal drawdown and source extraction rate for two flowrates of 70 and 32l/min during HC9 and HC10 respectively

This reduction in heat extraction (q_s) when flowrate was reduced to 32l/min resulted in lower capacity (q_{sk}) and lower COP. Average HP-IRL/H COP, quoted in Table 6-2, was only 2.53 during HC10, even though in theory the reduction in source return drawdown ($\Delta T_{s,r/\infty}$) should yield higher COP. The low COP was caused by reduced extraction (q_s) and this reduction in q_s at low flowrates is most likely due to:

- The evaporator heat transfer coefficient (h_{evap}) [W/m^{2}K] is a function of flowrate ($\dot{V}$)
  - For a constant LMTD in a heat exchanger it has been shown that heat transfer (q) [W] drops with flowrate ($\dot{V}$) [m^3/s] (IIT, 2011)
- The compressors limited range of ΔP and hence ΔT_{evap} leads to a $\dot{V}\Delta T_{evap}$ imbalance
  - Over limited ranges, reduction in $\dot{V}$ is countered by an increase in ΔT_{evap}
  - However, at some point while $\dot{V}$ continues to drop ΔT_{evap} has reached a limit

This is something that could be overlooked in a numerical-only study. For a numerical study where optimum collector flowrates are sought it is essential that the heat pump component model is sensitive to source and sink flowrates as well as source and sink temperatures and this is a recommendation in Section 9.3.

Figure 6-33 shows the steady-state flow and return drawdown plotted against extraction rate, calculated from Equations 6-42 and 6-41 respectively, using R_{av} [K/W], at source flow rates of 32 and 70l/min.

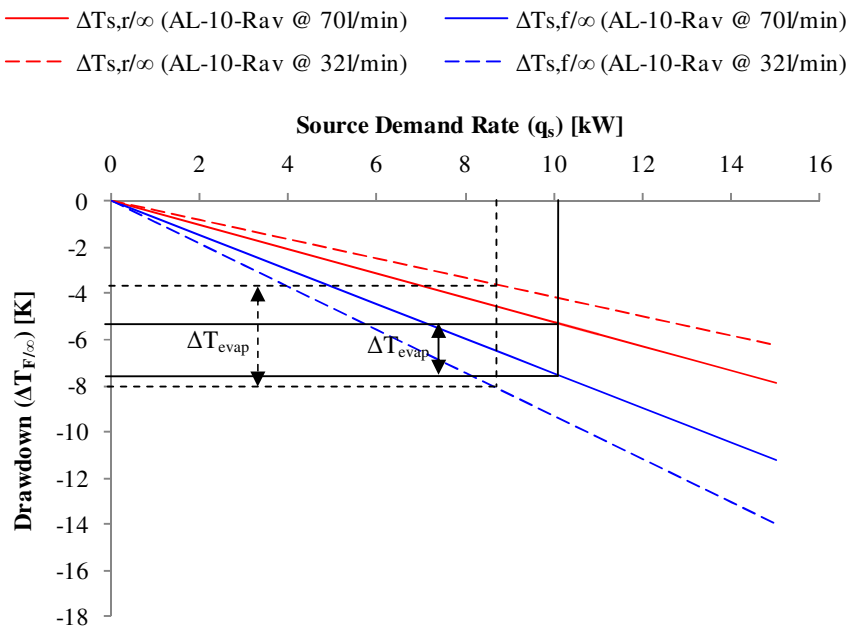

Figure 6-33: Estimated influence of flow rate on flow and return drawdown using resistance R_{av}

Figure 6-33 serves to explain the measured results displayed in Figure 6-32. It can be seen that predicted $\Delta T_{s,r}$ at 32l/min and 8.76kW is considerably less than $\Delta T_{s,r}$ at 70l/min and 10.25kW, while predicted $\Delta T_{s,f}$ at 20l/min and 8.76kW is similar to $\Delta T_{s,f}$ at 70l/min and 10.2kW.

Finally, since Figures 6-32 and 6-33 display the increased ΔT_{evap} at low flowrate, Figures 6-34(a) and (b) display photographs of the flow *run-out* and flow manifold during HC10 respectively. It can be seen that increased ΔT_{evap} during February 2010, the coolest month at Z= -1m during a colder than average winter, results in sub-0ºC flow temperatures and frost on pipes, even with extraction (q_s) below normal.

(a) Flow and return run-out pipes **(b) Flow and return manifolds**

Figure 6-34: Flow run-out and flow manifold sub-zero temperatures during HC10 at low flow rate operation (flow rate was reduced from 70 to 32l/min)

6.5.3 Influence of Pipe Spacing

Source return drawdown, expressed in Equation 6-41, and evaluated at either $R_{lin}(PS)$ or $R_{av}(PS)$ is also a function of pipe spacing (PS). Typically, increased pipe spacing means reduced ground resistance in both the R_{lin} and R_{av} model and hence reduced drawdown. Figure 6-35 displays measured *collector-ground interface* temperatures in test profiles P3, P5 and P6 ($T_{P3,\ -1.15m}$, $T_{P5,\ -1.0m}$ and $T_{P6,\ -1.2m}$ respectively) along with source flow and return temperatures ($T_{s,f}$ and $T_{s,r}$) and farfield temperature ($T_{P1,\ -0.9m}$), recorded during HC9. As discussed in Sub-section 3.5.1, P3, P5 and P6 are located a distance (L) along the collector of 43, 100 and 138m respectively, with a pipe spacing (PS) of 0.4, 0.25 and 0.4m respectively.

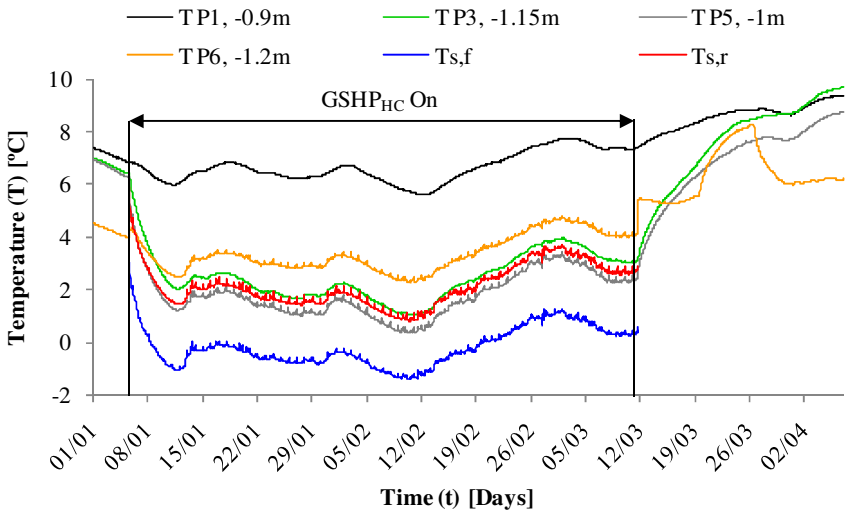

Figure 6-35: Effect of pipe spacing on localised drawdown caused by the collector in the underground heat source during HC9 (January to March 2009)

It can be seen that $T_{P5,\ -1.0m}$ displays the coldest temperature, since the pipe spacing is constricted in P5 as discussed in Sub-section 3.5.1. $T_{P6,\ -1.2m}$ displays the warmest temperatures, since collector pipes are parallel and well spaced in P6. P6 is also warmer because it is located towards the end of the collector, as discussed in the next section. After 12/03/2009, when $GSHP_{HC}$ is switched off, P6 also shows influence from the *run-out* pipes of the vertical collector located nearby, when $GSHP_{VC}$ is switched on. While the end of the collector is warmest as expected, P3 is located towards the start of the collector and $T_{P3,\ -1.15m}$ is cooler than $T_{P6,\ -1.2m}$, as expected. However, $T_{P3,\ -1.15m}$ is warmer than $T_{P5,\ -1.0m}$ which is located at the middle of the collector; this is due to the constricted pipes in P5. Based on this, it is good installation practice to avoid constrictions in the layout of the in-line pipes, since the increased drawdown at P5 has a negative influence on the source return temperature. Simulations of alternative pipe spacings are presented in Section 8.3.

6.6 MODEL AL-11: SPATIAL AND TEMPORAL VARIATION IN COLLECTOR HEAT EXTRACTION RATE

In the past, many *$GSHP_{HC}$* sizing software tools were based on the assumption that the collector pipe's heat extraction rate (q') [W/m] was constant along the pipe length (L). However, this assumption has since been questioned (Wibbels & Den Braven, 1994) and the temperature difference between $T_{P6,\ -1.2m}$ and $T_{P3,\ -1.15m}$ in Figure 6-35, both with PS of 0.4m but located some 95m apart, provides evidence that the extraction rate varies significantly with pipe length. Therefore, the data measured in *HP-IRL/H* can now be used to test this assumption.

The experimental set-up is displayed in Figure 6-36, where the heat flux sensors in P8 and P9 are located on one end of the collector pipe, 25 and 5m from the pipe exit respectively. Ideally, heat flux sensors placed at the entrance and exit of the collector pipe could be used to measure heat flux variation with length simultaneously. However, due to the surface covers present, as discussed in Sub-section 3.5.1, access to the collector pipes was limited to one end only. Therefore, the flow reversal capabilities of the collector, presented in Sub-section 3.3.3, were used with $H_{P8,\ -1.11m}$ and $H_{P9,\ -1.35m}$ to establish the effect of distance (L) from the flow manifold on the local heat flux ($q''_{\Delta L}$) at the *collector-ground interface*. Table 6-7 describes Test No. 1 and 2, conducted to measure *collector-ground interface* heat flux at the pipe inlet and pipe exit respectively.

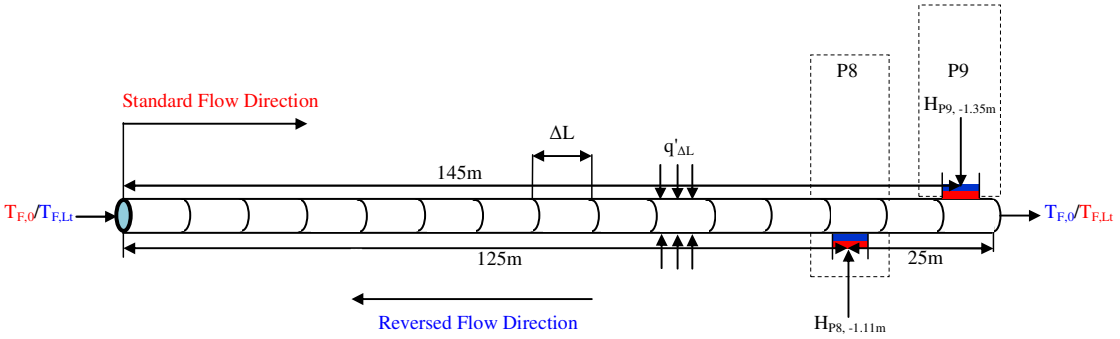

Figure 6-36: Schematic of heat flux sensor placement in P8 and P9 for flow reversal experiment

Table 6-7: Flow reversal tests conducted to establish the effect of distance from flow manifold on local heat flux at the collector-ground interface

Test No.	Dates	Flow Direction	L_{P8}	L_{P9}	$q_{s,av}$
1.	25th October to 5th November 2010	Reversed	25m	5m	≈ 10kW
2.	5th to 18th November 2010	Standard	125m	145m	≈ 10kW

Figures 6-37(a) and (b) display the heat flux (q") [W/m^2] at the *collector-ground interface* in P8 and P9 measured every 10 minutes during a 9 day period of reversed flow followed by an 11 day period of standard flow. Since the tests took place in October and early November when IiBC heat demand was relatively low, the heat pump cycled frequently resulting in a scattering of measured heat flux values; maximum values recorded each day correspond to on-cycles.

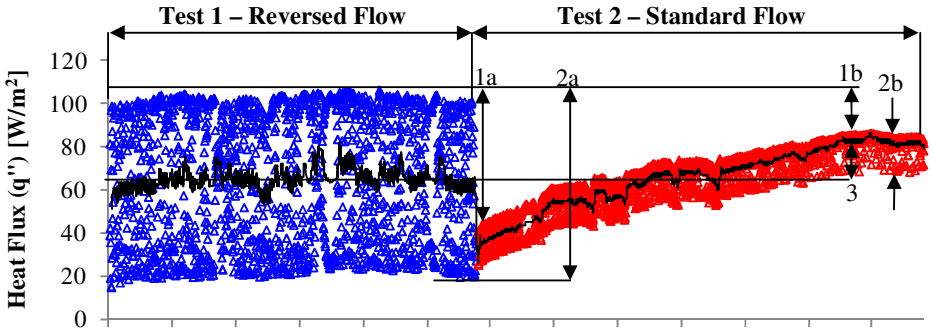

(a) Data from $H_{P8,\ -1.11m}$, located 125 and 25m from inlet for standard and reversed flow respectively

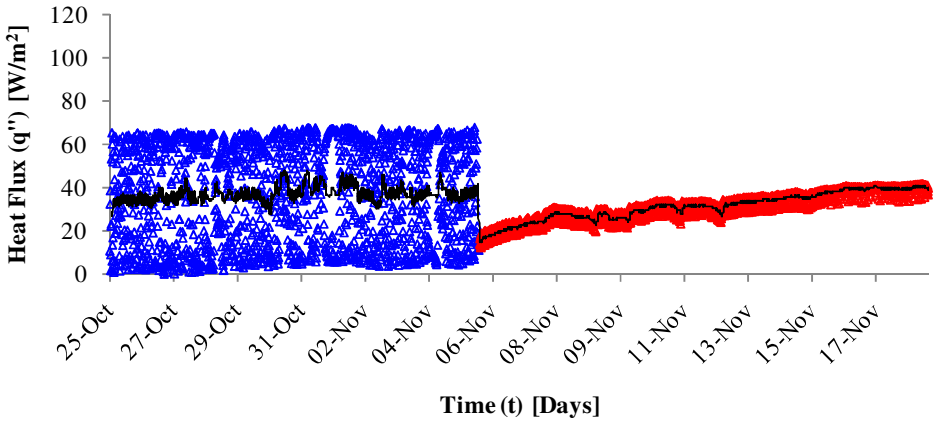

(b) Data from $H_{P9,\ -1.35m}$, located 145 and 5m from inlet for standard and reversed flow respectively

Figure 6-37: Collector-ground interface heat flux tests conducted between 25th of October and 18th of November 2010

The following observations are made, using the points 1 to 3 identified in Figure 6-37:

- (1) A transient period follows the switch-over from reversed to standard flow:
  - (a) $H_{P8,\ -1.11m}$ located 25m from the pipe exit during Test 2 - Standard flow initially displays an on-cycle heat flux of 50W/m^2 compared with an on cycle-heat flux over 100W/m^2 during reversed flow
  - This is due to the thermal depletion of this region which was the pipe inlet during Test 1 – Reversed flow

- (b) However, following a 4 day recovery period $H_{P8,\ -1.11m}$ located 25m from the pipe exit displays an on-cycle heat flux of 84W/m^2
- This steady-state, on-cycle value, recorded 25m from the pipe exit during Test 2 – Standard Flow, is still 16% lower than the equivalent steady-state, on-cycle value recorded 25m from the pipe inlet in Test 1 – Reversed flow
- $H_{P9,\ -1.35m}$, located 5m from the pipe's inlet and exit during Tests 1 and 2 respectively, displays similar trends but with a 30% reduction in steady-state, on-cycle, heat extraction
- As expected, these results in combination with $T_{P6,\ -1.2m}$ and $T_{P3,\ -1.15m}$ in Figure 6-35 display the impact of distance from the collector inlet on local heat extraction rates

- (2) Cyclic heat pump operation leads to a scattering in heat flux records fluctuating between the on-cycle maximums and minimums at the end of each off-cycle
  - (a) During Test 1, $H_{P8,\ -1.11m}$ located 25m from the pipe's inlet records fluctuations of approximately 80W/m^2 between the on-cycle maximums of 100W/m^2 and minimums of 20W/m^2 at the end of each off-cycle
  - (b) During Test 2, $H_{P8,\ -1.11m}$ located 25m from the pipe's exit records fluctuations of only 18W/m^2 between the on-cycle maximums of 84W/m^2 and minimums of 26W/m^2 at the end of each off-cycle
  - This equates to over 75% reduction in the amplitude of the fluctuations
  - $H_{P9,\ -1.35m}$, located 5m from the pipe's inlet and exit during Tests 1 and 2 respectively, displays similar trends but with an 80% reduction in fluctuations
  - These results possibly indicate that the collector exit recovers more quickly than the inlet however further investigation is required
- (3) Due to the reduction in the cyclic operation amplitude discussed in Point 2, the running average heat flux at the *collector-ground interface* measured by $H_{P8,\ -1.11m}$ is higher in Test 2 than Test 1
  - For $H_{P9,\ -1.35m}$ the running average heat flux in Test 1 and 2 are approximately equal

In order to characterise the findings of Figure 6-37 an equation relating the variation in local heat extraction with length was derived. The heat extraction rate (q) for a pipe can be written in terms of the entering and exiting fluid temperatures ($T_{F,0}$) and ($T_{F,Lt}$) respectively using Equation 6-43. These temperatures can be considered equivalent to $T_{s,f}$ and $T_{s,r}$ for a properly balanced *parallel array* collector or a *series collector*, as defined in Section 6.4.

$$q = \dot{m}c_{p,F}(T_{F,L_t} - T_{F,0}) \quad (6\text{-}43)$$

The average heat transfer rate per meter of piping is as follows:

$$q'_{av} = q/L_t \quad (6\text{-}44)$$

The local heat transfer rate for a segment (ΔL) can be written in terms of the temperature difference between fluid exiting consecutive sections:

$$q'_{\Delta L} = \dot{m}c_{p,F}(T_{F,L} - T_{F,L-1})/\Delta L \quad (6\text{-}45)$$

The local and average heat transfer rate per meter can be related using the local heat transfer ratio ($\beta_{\Delta L}$) [-] as follows:

$$q'_{\Delta L} = \beta_{\Delta L} q'_{av} \quad (6\text{-}46)$$

Where the ratio $\beta_{\Delta L}$ can be calculated using the calculation factor φ from Equation 6-26

$$\beta_{\Delta L}(L, \dot{V}_S, t) = [(\varphi_{L-1} - \varphi_L)/\Delta L]/[\left(1 - \varphi_{L_t}\right)/L_t] \quad (6\text{-}47)$$

The heat extraction per meter can be converted into a local heat flux as follows:

$$q''_{\Delta L} = q'_{\Delta L}/\pi D_o \quad (6\text{-}48)$$

Figure 6-38 compares the measured and calculated heat flux decay with length, measured points are taken from Figure 6-37 and the local heat transfer ratio ($\beta_{\Delta L}$) is also displayed. Due to the idealised nature of the calculated heat flux decay ($q''_{\Delta L}$) there is very little correspondence in magnitude with measured values however the predicted decay trends are similar.

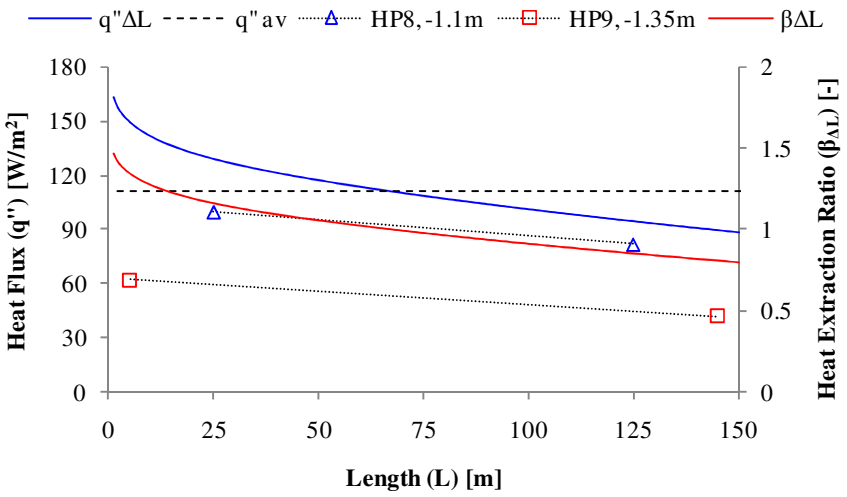

Figure 6-38: Comparison of measured (at steady-state) and calculated heat flux variation with length and the heat flux ratio; the modelled heat flux and the ratio are calculated after 10 days of collector operation

Based on calculated values it can be seen that local heat transfer ratio ($\beta_{\Delta L}$) varies with length (L), time (t) and pipe flow rate ($\dot{V}_p$). Figure 6-39(a) displays the variation in $\beta_{\Delta L}$ with time for 4 different positions along the collector.

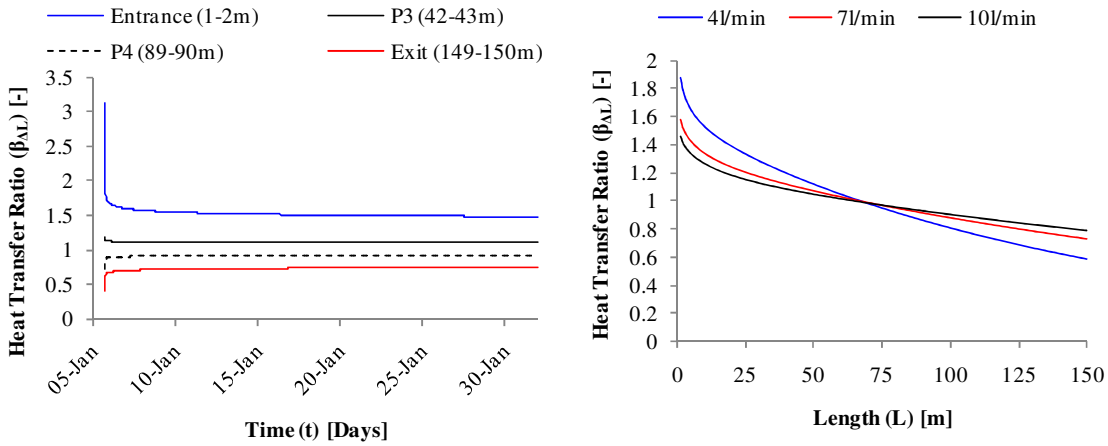

(a) Influence of time on $\beta_{\Delta L}$ at 4 collector points (b) Variation in $\beta_{\Delta L}$ with L after 10 days at 3 flow rates

Figure 6-39: Calculated trends examining factors that influence the local heat transfer ratio ($\beta_{\Delta L}$)

It can be seen that $\beta_{\Delta L}$ changes rapidly over the 1 to 2 days of operation but reaches a steady-state value after about 5 to 7 days. Figure 6-39(b) displays the variation in $\beta_{\Delta L}$ with length for 3 different pipe flow rates calculated after 10 days of collector operation. It can be seen that, as expected, for lower flow rates more heat is extracted near the collector inlet and less at the exit; increasing flow rate flattens the $\beta_{\Delta L}$ curve. This heat transfer ratio ($\beta_{\Delta L}$) will be used as a sub-model for NL-4 in Chapter 7; NL-4 aims to simulate cooling of the ground for individual points in the collector area.

6.7 SUMMARY

This chapter described analytical characterisation of *GSHP$_{HC}$* operation and made the following contributions to the *HP-IRL/H* project:

- Over the course of the 1328 day test program, the *GSHP$_{HC}$* operated for 303 days, delivering 72,514 kWh$_{th}$ of energy (261 GJ) to the IiBC building
- 7 key *GSHP$_{HC}$* system parameters; building demand, heat pump capacity, delivery and duty, source capacity and extraction and source drawdown were identified in Section 6.1

- 10 individual test periods, labelled HC1 through HC10, were identified between January 2007 and February 2010 which included a wide range of test durations (1 to 69 days) and duty levels (10 to 100%)
- The average source extraction rate, which is duty multiplied by nominal extraction, was defined in Sub-section 6.1.1
- *$GSHP_{HC}$* characterisation was divided into 3 parts
    - Thermodynamic characterisation
    - Hydraulic characterisation
    - Thermal characterisation

Thermodynamic characterisation

- This section characterised *HP-IRL/H* measurements of *Solterra 500* COP, calculated using Equation 3-2, by comparing them with COP's from *Arsenal Research* for the *Solterra 500*, COP's from an idealised Carnot Heat Pump with a Carnot efficiency of 45% and COP's taken from the *HP-IRL/H* data calculated using EN14511
- Using Arsenal Research data and *HP-IRL/H* data, novel equations for q_s, q_{sk} and COP were derived as a function of both T_s and T_{sk} for use in simulation of a holistic *$GSHP_{HC}$* system in Chapter 7
- *Solterra 500* COP was interpreted in 7 different ways and comparisons were made between the following
    - 'HP-IRL/H' Sub-section 6.1.2
    - 'Sol 500' Section 6.2
    - '$\eta = 0.45$' Sub-section 6.2.1
    - 'EN 14511' Sub-section 6.2.1
    - 'Compressor' Sub-section 6.2.3
    - 'Total' Sub-section 6.2.3
    - 'ΔT_{true}' Sub-section 6.2.3
- Findings from these comparisons are summarised in Sub-section 6.2.3
- Areas for potential thermodynamic, thermal and hydraulic improvements to *$GSHP_{HC}$* which may improve the cost effectiveness of *$GSHP_{HC}$* were highlighted

Hydraulic Characterisation

- Distinct definitions of the collector piping network and the source piping network were established in Section 6.3

- Simple formulae for estimating total source head loss, source flow rate and pumping power consumption were grouped together in Sub-section 6.3.1 and identified as Model AL-8
- For a parallel collector of N HDPE-pipes with equal length (L) and internal diameter (D_i), identified as a 'balanced collector' the following assumptions are held:
  - Equal flow rate ($\dot{V}_p$) in each pipe
  - Total flow rate ($\dot{V}_s$) is the sum of flows in each pipe
  - Total head loss (H_f) is equal to head loss in any one of the pipes
- Total head loss in the source piping network was attributed to the following sources in order of magnitude:
  - Evaporator (closely packed plates on source-side of heat exchanger)
  - Collector pipes (major losses due to friction)
  - Run-out pipes (major losses due to friction)
  - Fittings (minor losses due to friction)
- AL-8 and the *Pipeflow Expert* software predicted a source flow rate of 84 and 83l/min respectively, while the *Burkett* and *Endress & Hauser* flow-meters measured 70l/min ± 5%; reasons for the discrepancy are assumed to be:
  - Assumption of smooth wall ducts in calculations (HDPE pipes are not totally smooth)
  - Use of a pump curve for water in calculations (system is filled with higher viscosity water-ethylene glycol mixture)
  - Fouling of collector and run-out pipes over time
  - Fouling of brazed-plate heat exchanger (a considerable source of resistance)
- Periodic cleaning of the evaporator or filters by trained installers during servicing may be advisable
- Velocities of $2 < v < 5$m/s are recommended for efficient piping networks
- Predicted pumping power consumption was 387.8W while measured power consumption was between 370 and 390W ± 5%

Thermal Characterisation

- For a balanced collector with negligible heat loss/gain in the run-out piping the following assumptions are held:
  - Source return ($T_{s,r}$) equals collector return ($T_{HC,r}$)
  - Collector return ($T_{HC,r}$) equals return from any pipe in the array ($T_{N,r}$)

- The *$GSHP_{HC}$* involves a cycle of source fluid temperature ($T_{F,L}$) increasing with length in the underground pipes and decreasing in the heat pump's evaporator
- The boundary condition at the outer face of these underground pipes is identified as the *collector-ground interface*
    - Constant heat flux and constant temperature boundary conditions do not accurately represent the *collector-ground interface*
    - Predictable temperatures at a farfield distance is the most realistic boundary condition for collector pipes
    - Farfield distance increases with *$GSHP_{HC}$* operation time

Estimating Source Return Temperature

- Simple formulae for estimating farfield diameter (D_∞), pipe-fluid convection coefficients (h), total ground resistance (R) and fluid temperature increase (ΔT_{HC}) were grouped together in Section 6.4 and identified as Model AL-9
- Models and simulations for farfield temperature ($T_{g,\infty}$) are presented in Chapters 4 and 5
- Radial and linear ground resistance formula (R_{rad} and R_{lin}) led to over-estimated and under-estimated source return temperature respectively, however the average of the two conveniently gives a good estimation

Estimating Thermal Drawdown

- Based on Burke (2010) the following four stages in a long-term heat extraction cycle were indentified:
    - Equilibrium
    - Drawdown
    - Steady-state extraction
    - Recovery
- Formulae taken from Model AL-9 were solved simultaneously and identified as AL-10, in order to estimate source return drawdown ($\Delta T_{s,r/\infty}$) as a function of extraction rate (q_s) and based on 11 *$GSHP_{HC}$ design variables*
- Radial and linear ground resistance formula (R_{rad} and R_{lin}) led to under-estimated and over-estimated source return drawdown respectively, however the average of the two conveniently gives a good estimation
- Reducing flow rate will reduce source return drawdown ($\Delta T_{s,r/\infty}$) which is beneficial to COP

- However the evaporator heat transfer coefficient (h_{evap}) is also reduced
- No net gain in COP is achieved

- As expected, increasing pipe spacing (PS) will reduce return drawdown ($\Delta T_{s,r/\infty}$), however pipe spacing is limited by the area of land available
  - The maximum PS possible should always be used

Spatial and Temporal Variation in Local Heat Extraction

- The local heat extraction by the collector pipes is influenced by:
  - Distance from collector inlet (L)
  - $GSHP_{HC}$ operation time (t)
  - Source flow rate ($\dot{V}_s$)
- Experimental data was used to characterise the influence of L
- By simultaneously solving a group of formulae, identified as AL-11, an expression relating local heat extraction ($q'_{\Delta L}$) to average heat extraction (q'_{av}) using the local heat extraction ratio ($\beta_{\Delta L}$) was derived
  - This ratio will be used as a boundary condition in model NL-4 in Chapter 7

Based on the extensive characterisation of $GSHP_{HC}$ in this chapter and the extraction of sub-models for the heat pump (AL-7) and the collector (AL-11), Chapter 7 now presents methods for transient simulation of the ground, collector and heat pump.

CHAPTER 7

$GSHP_{HC}$ NUMERICAL SIMULATION

GMIT
GALWAY-MAYO INSTITUTE OF TECHNOLOGY
INSTITIÚID TEICNEOLAÍOCHTA NA GAILLIMHE-MAIGH EO

7. $GSHP_{HC}$ NUMERICAL SIMULATION

This chapter describes the methods developed for the transient simulation of the $GSHP_{HC}$ and the surrounding ground region during periods of heat pump operation. According to CLEFS – Research and Simulation, the threefold purposes of simulation are understanding, design and action (Klein, 2002). Building on Chapter 6, the goal of this chapter is to create a robust simulation tool that provides insight and understanding of $GSHP_{HC}$ operation and offers the potential to conduct parametric design studies of the type presented in Chapter 8 for new collector designs with fixed and active control strategies.

Two separate were created: NL-4 simulates the influence of horizontal collector heat extraction on the GTD only, while NL-5 simulates both the temperature increase in the source fluid as it circulates underground and the cooling influence of this fluid on the GTD, simultaneously.

This chapter is divided into five sections as follows:

- Literature review
- Model NL-4 development
- Model NL-5 development
- Model NL-1, NL-4 and NL-5 validation
- Discussion

7.1 LITERATURE REVIEW

A review was conducted of the 11 numerical studies listed in Table 7-1. These studies were conducted in 5 countries and involve a variety of methods such as FDM, FEM and ANN. Notably, prior to Wu *et al.* (2010) in England, there had been no reported simulation of $GSHP_{HC}$ from a *Cool Marine* region other than Idaho which is a *Semiarid Continental* state with *Cool Marine* counties on the western border (Wibbels & Den Braven, 1994). Additionally, there is only one report of horizontal, parallel, inline pipe simulation but in the *Semiarid Continental/Dry Summer Subtropical* climate of Turkey (Demir *et al.*, 2009). Based on the literature review the proposed simulation methods can be grouped as follows:

- Analytical solutions
- Energy balance solutions – typically solved using numerical methods

These simulation methods and results are discussed in greater detail in the subsequent text.

Table 7-1: Simulation methods developed for predicting $GSHP_{HC}$ and HGHE performance

No.	Author (Year)	Location	GHE Type	Model Type	Coordinates or Elements	Boundaries	Model Details
1.	Ingersoll (1950)	-	Vertical	Line Source	Radial	-	-
2.	Eskilson (1987)	Lund, Sweden	Vertical	Numerical-analytical	-	-	Lund type, *g-functions*
3.	Mei (1986)	Tennessee, USA	Horizontal, serpentine	Numerical FD	Radial	Analytical	Transient, conduction, quasi-freezing
4.	Wibbels & Den Braven (1994)	Idaho, USA	Horizontal, Series	-	Radial	Farfield ground temperature	-
5.	Tarnawski and Leong (1993)	Halifax, Canada	Horizontal, 9 Types	Numerical FE	Triangular Elements	6 weather parameters	Transient, heat & mass, freezing
6.	Giardina (1995)	Wisconsin, USA	Horizontal, straight Pipe	Numerical FD	Radial	-	-
7.	Piechowski (1996)	Melbourne, Australia	Horizontal, straight Pipe	Numerical FD	Radial and Cartesian	Surface Convection	Transient, heat & mass
8.	Chiasson (1999)	Oklahoma, USA	Bridge deck heat rejecter	Numerical FD	Cartesian	-	Transient, conduction
9.	Esen *et. al* (2007)	Elazig, Turkey	Horizontal, series	Numerical FD	Cartesian	Surface Convection	Transient, conduction
10.	Esen *et. al* (2008)	Elazig, Turkey	Horizontal, series	Numerical ANN	Neurons	Weather parameters	N/A
11.	Demir *et. al.* (2009)	Istanbul, Turkey	Horizontal, parallel	Numerical FD	Cartesian	7 weather parameters	Transient, conduction
12.	Wu *et. al.* (2010)	Nottingham, England	Horizontal, parallel, slinky	Numerical CFD-FLUENT	Mixed	-	Transient conduction - convection

7.1.1 Analytical Solutions

One of the earliest analytical approaches to GSHP simulation is the 'line source theory' used by Ingersoll & Plass (1948) to model borehole heat exchangers. The method assumes constant heat extraction or rejection per meter of a small diameter 'line source' in an infinite medium. At the BNL, discussed in Section 3.1, the ground was divided into blocks and modified line source theory was used (Metz, 1983). Another method pioneered by the Swedish research group at the University of Lund for $GSHP_{VC}$ involves a numerical-analytical hybrid method; a numerical solution for a single pipe is completed and then superimposed for multiple pipes using *g – functions* (Eskilson, 1987). A detailed mathematical analysis of horizontal pipes, using the superposition technique, was also published by the Swedish Council for Building

Research (Claesson & Dunand, 1983). The model AL-9, presented in Chapter 6, is an analytical method that can be used to estimate the source fluid return temperature ($T_{s,r}$) [ºC] given knowledge of how long the *GSHP$_{HC}$* has been operational during that season.

7.1.2 Energy Balance Solutions

Adapted from Giardina (1995), Figure 7-1 displays a representation of a single pipe utilised in the first significant attempt at transient modelling of both the fluid and the GTD, conducted at the Oakridge National Laboratory (ORNL) (Mei, 1986).

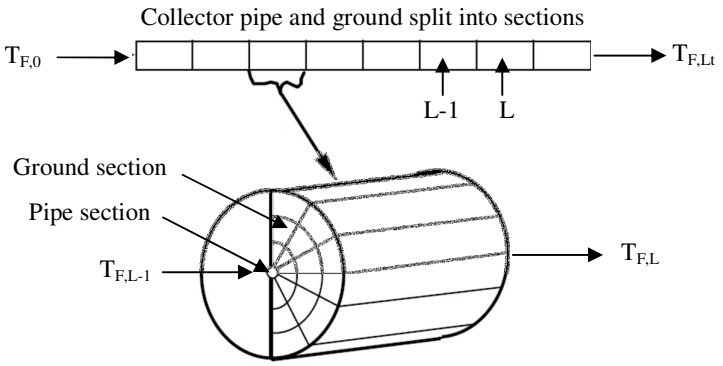

Figure 7-1: Representation of the Mei (1986) isolated collector pipe simulation method (Giardina, 1995)

The ORNL method is based on a more realistic representation of an actual collector by concentrating on the temperature of the fluid as it flows through the pipe and simultaneously tracking changes in the GTD. The method, shown in Figure 7-1, can be summarised as follows:

- A single pipe and the surrounding cylinder of ground is simulated
- The combined pipe-ground domain is divided into sections in the flow direction
- Equations for each section's exiting fluid temperature and the *collector-ground interface* temperature are written and then solved numerically
- The consecutive sections are linked by the fluid temperature; the exit of section L-1 becomes the entrance to section L and so on over the length of the buried pipe

Due to the realistic way in which this method mimics *GSHP$_{HC}$* geometry and heat transfer, it was hailed as a significant improvement for the horizontal type GHE (Piechowski, 1996).

7.1.3 Radial Geometry

The ORNL method was used to simulate experimental results from the BNL test facility which is reviewed as facility No. 1, Table 3-1. A summary of BNL *$GSHP_{HC}$* details relevant to the ORNL simulation are presented in Table 7-2 (Metz, 1979; Mei, 1986).

Table 7-2: BNL experimental and ORNL numerical details (Metz, 1979; Mei, 1986)

$GSHP_{HC}$ design variable (Model Parameter)	**Value**
Collector Configuration	Series (2 x 76m pipes)
Pipe Routing	Serpentine
Pipe Layout	Inline
Pipe Length (L_t) [m]	152.5m
Burial Depth (Z_{HC}) [m]	-1.2m
Pipe Spacing (PS)	1 to 2m
Inner Pipe Diameter (D_{in}) [m]	0.04
Outer Pipe Diameter (D_o) [m]	0.046
Pipe Conductivity (k_p) [W/mK]	0.46
Pipe Specific Heat Capacity ($c_{p,p}$) [J/kgK]	2174
Heat Transfer Fluid	Water/Ethylene Glycol (80/20)
Soil Texture	Sandy (moisture $0.1m^3/m^3$)
Ground Conductivity (k_g) [W/mK]	1.731
Ground Diffusivity (α_g) [m^2/s]	1×10^{-6}
Source Flow Rate ($\dot{V}_s$) [m^3/h]	0.927 (15.45 l/min)
Mean Annual Ground Temperature ($T_{g,y}$) [°C]	10.23
Mean to Peak Surface Temperature Amplitude ($A_{sur,y}$) [K]	12.759
Annual Phase Shift Angle (λ_0) [rad]	0.352 (20 days)

Mei (1986) describes the simulation as a '*ground coil model with radially symmetrical temperature profile*'. The radial geometry used in the simulation is displayed in Figure 7-2(a). Mei (1986) plotted simulated and experimental results against time (t) [days] for comparison in Figure 7-2(b). It can be seen that the simulation over-estimates the return temperature $T_{s,r}$ with $\Delta T_{sim/exp}$ ranging between 0.2 and 1.6K. This over-estimation begins 1.5 days into the simulation process. Using the farfield radius approximation in Equation 7-1 (Hart & Couvillion, 1986), it can be seen that r_∞ exceeds the Z_{HC} distance of 1.2m to the surface after only 1.1 days of operation. This coincides with the onset of the over-estimation in $T_{s,r}$ by the simulation.

$$R_\infty = 4\sqrt{1 \times 10^{-6}(60 * 60 * 24 * 1.1)} = 1.233\text{m} > |Z_{HC}| \qquad (7\text{-}1)$$

It is also seen in Section 6-4 that model AL-9 with radial ground resistance (R_{rad}) [K/W] produces a return temperature over-estimation ($\Delta T_{sim/exp}$) of approximately 1.9K at steady-state. There are two sources of the over-estimation when using radial geometry to simulate either the *HP-IRL/H* or the BNL horizontal collector and these are as follows:

- Extension of the farfield radius beyond half the pipe spacing (r_∞>PS/2), as shown in Figure 6-24(b)
- Extension of the farfield radius beyond the burial depth (r_∞>|Z_{HC}|), as shown in Figure 7-2(a)

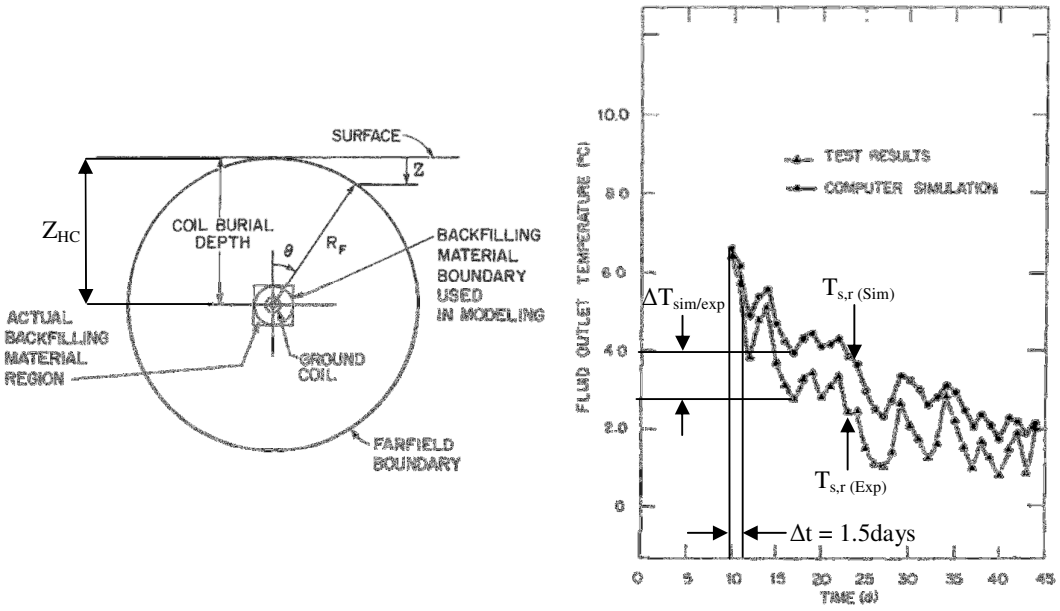

(a) Model geometry **(b) Comparison with experimental data**

Figure 7-2: Aspects of the transient numerical model developed at ORNL (Mei, 1986)

In the case of the BNL *series* horizontal collector, |Z_{HC}| is 1.2m and PS is 1 to 2m, while at *HP-IRL/H*, |Z_{HC}| is 0.85 to 1.3m and PS is 0.25 to 0.4m. Since the collector depth and more significantly the pipe spacing of the *HP-IRL/H* collector are smaller that deployed in the Metz (1979) and Mei (1986), this implies that the prediction accuracy of this radial method is likely to be lower for the *HP-IRL/H* collector.

7.1.4 Cartesian Geometry

The radial sections method, pioneered at ORNL has also been used for *GSHP$_{HC}$* collector simulations in Idaho, USA(Wibbels & Den Braven, 1994) and Wisconsin, USA(Giardina, 1995), for HGHE heat rejection simulations in Melbourne Australia (Piechowski, 1996) and worldwide for both heating and cooling by users of the TRNSYS software, listed in Table 2-12 and discussed in Sub-section 7.1.8. However, there has recently been a shift away from the radial geometry of the ORNL model and towards a Cartesian geometry for the simulation of pavement HGHE heat rejection systems in Oklahoma, USA (Chiasson, 1999) and *GSHP$_{HC}$*

collectors in Turkey (Esen *et al.*, 2007; Demir *et al.*, 2009). The recent model geometry developed by Demir *et. al.* (2009) at Yildiz Technical University is shown in Figure 7-3.

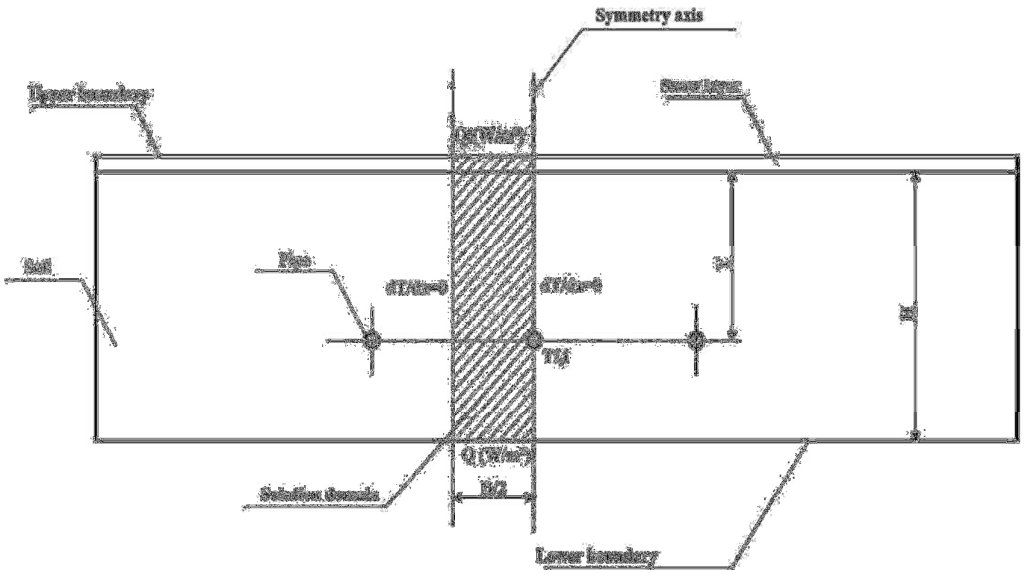

Figure 7-3: Model geometry developed at Yildiz Technical University (Demir *et al.*, 2009)

The details of the Yildiz experimental facility (reviewed as Facility No. 12, Table 3-1) and the model geometry shown in Figure 7-3, are presented in Table 7-3.

Table 7-3: Yildiz Technical University experimental and numerical details (Demir *et al.*, 2009)

GSHP$_{HC}$ design variable (Parameter)	**Value**
Collector configuration	Parallel (3 x 40m pipes)
Pipe Layout	In-line
Pipe length (L_t) [m]	40m
Pipe spacing (PS) [m]	3m
Burial Depth (Z_{HC}) [m]	-1.8m
Inner Pipe Diameter (D_{in}) [m]	0.0146
Outer Pipe Diameter (D_o) [m]	0.02
Pipe Conductivity (k_p) [W/mK]	0.899
Heat Transfer Fluid	Water
Source Flow Rate ($\dot{V}_s$) [m^3/h]	0.4277 (7.128 l/min)
Mesh step in x and y direction (dx = dy) [m]	0.1
Mesh step along pipe axis (dz) [m]	1
Time step (dt) [s]	1800

From the *HP-IRL/H* perspective, the positive aspects of the Yildiz approach shown in Figure 7-3, that were previously included or since utilised in the NL-4 and NL-5 models, are:

- The positioning of adiabatic planes, labelled 'symmetry axis', allow for parallel, in-line pipes with small pipe spacing to be simulated
- The positioning of the 'upper and lower boundaries' with distinct boundary conditions allows for inclusion of transient weather conditions or diurnal resource and a seasonal resource or possibly a geothermal heat flux above and below respectively
- Use of the bulk ground surface as the reference position (Z_0) on the vertical dimension
- Inclusion of a surface cover layer, in this case 'snow layer', above the bulk ground surface

However, from the *HP-IRL/H* perspective, the negative aspects of the Yildiz modelling approach and areas for improvement in NL-4 and NL-5 are:

- Lower boundary condition, labelled 'Q [W/m^2]', is a heat flux condition located a short distance beneath the collector, this doesn't mimic reality and calculation of a transient heat flux value for this boundary is a difficult task
- A mesh step (section length) along the pipe axis of 1m is used for the 40m Yildiz collector, however this increment is excessively small for simulating the 150m long pipes used in the *HP-IRL/H* collector

A comparison between the measured and simulated source return temperature ($T_{s,r}$) from Yildiz University along with the $T_{s,r}$ obtained from using the Mei (1986) and the Metz (1983) models are shown in Figure 7-4 (Demir *et al.*, 2009).

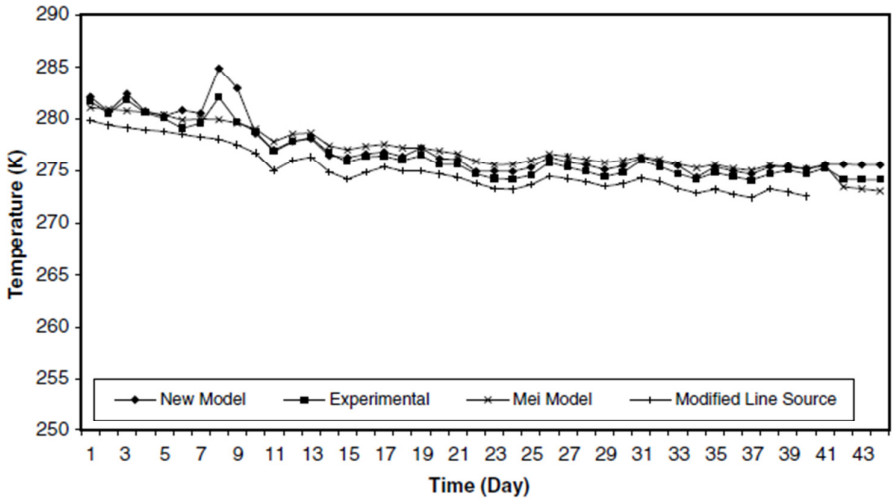

Figure 7-4: Experimental and simulated source return temperatures from the Yildiz Technical Institute (Demir *et al.*, 2009)

The excessive 40K y-axis scale, used in Figure 7-4, makes it difficult to assess the predictive accuracy. However, it can be seen that the Metz model (labelled 'modified line source') under-estimates $T_{s,r}$, the Mei model over-estimates $T_{s,r}$ and the Demir *et. al.* model (labelled 'new model') achieves the best fit with experimental $T_{s,r}$ results. Demir *et al.* (2009) quotes a maximum difference between numerical results and experimental data of 10%.

The Demir *et al.* (2009) model is the most recent simulation of $GSHP_{HC}$ and one of the only models to include parallel pipes and weather influence by employing a Cartesian geometry. However, Demir *et al.* (2009) states that while transient return temperatures ($T_{s,r}(t)$) at the model pipe exit were simulated, the transient flow temperatures ($T_{s,f}(t)$) at the model pipe entrance were taken from experimental data. Correspondingly, there is no mention of a complimentary heat pump model (such as AL-7) which simulates heat extraction (q_s) [W] from the return fluid and responds to the collector-heat pump performance transience ($q_s(T_{s,r}, T_{sk,f})$) as identified in Sub-sections 6.1.2 and 6.2.2. Finally, there is no reference to methods for simulating feedback control within a heat pump-collector simulation; Burke (2010) highlighted potential performance benefits from feedback control of *split-level collectors*.

Therefore, this study sought to expand on the successful Demir *et al.* (2009) method by including a high level of climate and inter-pipe sensitivity along with a complimentary heat pump model (AL-7) and the potential for active control for split-level collectors.

7.1.5 Choosing a Model Geometry

There are advantages and disadvantages to both the radial and Cartesian geometries.

For pipes that are configured in *parallel*, buried *in-line*, with a *pipe spacing* PS of 0.3 to 0.8m (industry standard, Table 2-11) and a *burial depth* $|Z_{HC}|$ of 1.5 to 2m (industry standard, Table 2-10) then the assumption of *radially symmetrical heat transfer* is invalid for $GSHP_{HC}$ operational time-scale of days, weeks or months, as described in Sub-section 7.1.3.

However, on the $GSHP_{HC}$ operational time-scale of minutes or hours, primarily at the start of $GSHP_{HC}$ operation and before any inter-pipe thermal interference can occur, the radial geometry is the more realistic and the more suitable geometry of the two. This is because at the start of a $GSHP_{HC}$ operational cycle, the heat transfer is confined to the cylindrical collector pipe and the cylindrical *collector-ground interface*. Therefore at the start of a cycle, a cylindrical or radial geometry mimics real operation more accurately as demonstrated in Figure 7-5 (Piechowski, 1996).

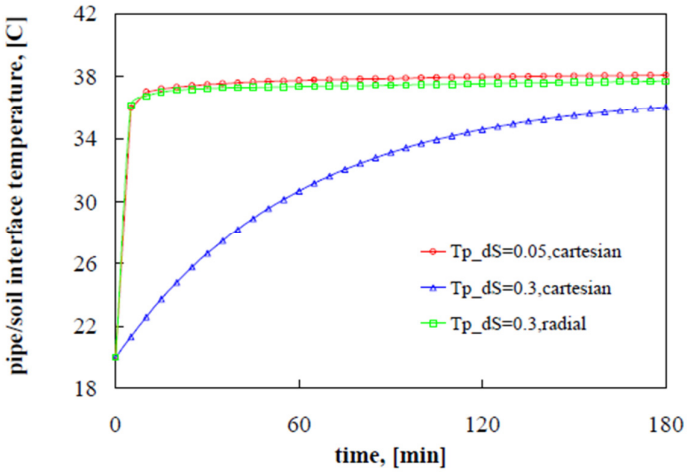

Figure 7-5: Comparison of Cartesian and radial geometry at pipe-ground interface (Piechowski, 1996)

Over the course of 180 minutes Piechowski (1996) compared simulated results from Cartesian models with coarse mesh (dS = 0.3m) and fine mesh (dS = 0.05m) with simulated results from a radial model with coarse mesh (dS = 0.3m). Findings, presented in Figure 7-5, show that the coarse mesh Cartesian model reacts more slowly to heating at the *collector-ground interface* (due to the disproportionately larger volume of the mesh elements). However this error can be accounted for using the finer mesh (0.05m) and the error also decays with time and disappears at time greater than 3 hours.

Therefore, one of the following three methods can be used to insure simulation accuracy:

- Combining the short-term accuracy of the radial geometry at the start of *GSHP$_{HC}$* operation with the long-term accuracy of the Cartesian geometry (after thermal interference) by using radial geometry at the *collector-ground interface* and Cartesian geometry for the remainder of the ground simulation domain.
- Use all Cartesian geometry but with small space increments (mesh size) as demonstrated in Figure 7-5 (Piechowski, 1996)
    - This will lead to inefficient simulation
- Use an all Cartesian geometry but with a variation in mesh size, small mesh at the *collector-ground interface* and at the *ground-atmosphere interface* but larger mesh size for the remainder of the simulation domain where thermal gradients are less pronounced

The latter method has been adopted for *HP-IRL/H* simulations and the approach along with plans for future refinements are discussed in Sub-section 7.3.5.

7.1.6 Coupled Heat and Mass Transfer

The influence of coupled heat and mass transfer, discussed in Sub-section 5.2.4, has been included in simulations of $GSHP_{HC}$ collectors in Halifax, Canada (Tarnawski & Leong, 1993; Healy & Ugursal, 1997) and HGHE used to reject heat to the ground in Melbourne, Australia (Piechowski, 1996). However, Gauthier *et al.* (1997) concluded that moisture gradients accounted for less than 0.1% of the total heat transfer in soil, a finding supported by the work of Puri (1986). Simulations of $GSHP_{HC}$ at ORNL, USA (Mei, 1986), Quebec, Canada (Gauthier *et al.*, 1997) and Turkey (Esen *et al.*, 2007; Demir *et al.*, 2009) were conducted using pure conduction with good predictive accuracy reported. Given the lack of agreement among authors on the importance of heat and mass transfer, a review was conducted of the most detailed study, Piechowski (1996).

Piechowski (1996) used Equation 7-2 and 7-3 to simulate 3-D coupled heat and mass transfer around a heat rejecting HGHE, where DC_e is the latent heat diffusion coefficient, DC_{T} and DC_{θ} are the thermal and isothermal moisture diffusivity and e is vaporisation in pores. All other terms C, k_g, T, θ_{wg}, θ_{liq}, L_v, ρ_{liq} and K are defined in Section 5.2. The isothermal water diffusion component ($\nabla DC_{\theta}\nabla\theta_{\mathrm{liq}}$) replaces the conventional form ($\nabla \mathrm{K}\nabla\Phi$), discussed in Sub-section 5.2.3, using a common chain rule substitution discussed in Marshall *et al.* (1996).

$$\mathrm{C}\frac{\partial \mathrm{T}}{\partial \mathrm{t}} = \nabla\left(\mathrm{k_g}\nabla \mathrm{T}\right) + \nabla\left(DC_e\nabla\theta_{\mathrm{liq}}\right) + L_v e\rho_{\mathrm{liq}}\frac{\partial \mathrm{K}}{\partial \mathrm{Z}} \tag{7-2}$$

$$\frac{\partial \theta_{\mathrm{wg}}}{\partial \mathrm{t}} = \nabla(DC_{\mathrm{T}}\nabla \mathrm{T}) + \nabla\left(DC_{\theta}\nabla\theta_{\mathrm{liq}}\right) + \frac{\partial \mathrm{K}}{\partial \mathrm{Z}} \tag{7-3}$$

In this situation moisture movement is driven by moisture gradients, identified as isothermal moisture diffusion, and also by temperature gradients, identified as thermal moisture diffusion. Heat is transported by conduction and also by liquid advection and vapour diffusion. However, DC_e, DC_{T} and DC_{θ} are phenomenological coefficients which are site-specific and these are not readily available or easily measured.

Piechowski (1996) made the following observations:

- Coupled heat and mass transfer can predict the drying around heat rejecting HGHE in summer mode
- The isothermal moisture transfer exceeds and cancels out the thermal moisture transfer for moisture contents above $0.15 m^3/m^3$
- Below $0.15 m^3/m^3$, some drying takes place around the HGHE however it is very slow; a fluid at T_F of 40ºC circulated in ground at T_g of 20ºC does not produce a sufficient temperature gradient to induce significant thermal moisture transfer

Based on this latter observation by Piechowski (1996) for HGHE in summer mode, this author concludes that:

- For winter mode, the thermal moisture transfer towards the collector would therefore be extremely small with a fluid temperature T_F of 0 to 5ºC circulated in almost saturated ground at T_g of approximately 10ºC

In discussing the influence of heat and mass transfer on HGHE performance, Piechowski's following conclusions appear to be contradictive:

- Piechowski (1996), Sub-section 5.3.4: "There is very little difference in results from the two options. The only significant difference is noticeable at low moisture contents less than $0.15m^3/m^3$"
- Piechowski (1996), Section 8.2: "Heat and mass transfer has a major influence on the performance of a GHE"

However Figure 7-6, extracted from Piechowski (1996) clearly describes the minimal influence had by heat and mass transfer in simulations of HGHE operation. This figure corroborates the conclusions made by Piechowski in Sub-section 5.3.4.

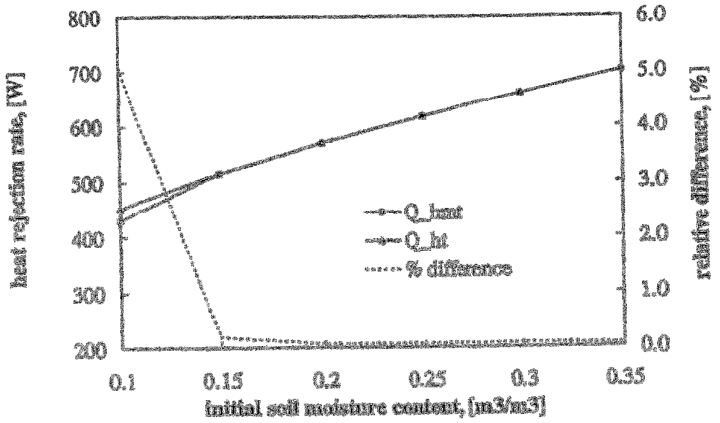

Figure 7-6: Comparison of the ground heat rejection rate simulated using a combined heat and mass transfer simulation (Q_hmt) with a pure conduction simulation (Q_ht) (Piechowski, 1996)

Heat and mass transfer can therefore be ignored, provided the ground moisture content around the collector pipes is in excess of $0.15m^3/m^3$. It is shown in Section 5.2.3.1 that ground moisture content at collector level in the *HP-IRL/H* site is between 0.275 and $0.3m^3/m^3$ during winter. Figure 7-7 displays measurements of *collector-ground interface* temperature ($T_{P8,\ -1.1m}$) during $GSHP_{HC}$ operation in February 2010 (test period HC10) along with measured precipitation levels (Z_{prec}) (all liquid rainfall) and moisture content at both the *collector-*

ground interface ($M_{P8,\ -1.1m}$), the *ground-atmosphere interface* ($M_{P8,\ -0.0m}$) and one intermediate level at -0.55m ($M_{P8,\ -0.55m}$). Figure 7-8(a) displays simultaneous measurements of ground temperature and moisture content gradients extending from the bulk ground surface to collector level in P8 on 3 days (5th, 10th and 15th) during *GSHP$_{HC}$* operation in February 2010 (test period HC10).

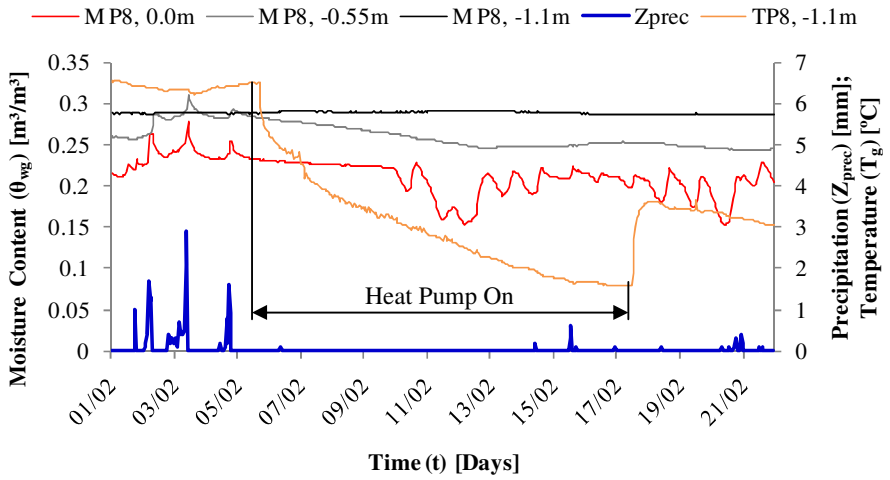

Figure 7-7: Variation in moisture content at the ground surface (0.0m), the collector depth (-1.1m) and one intermediate level (-0.55m) with precipitation levels during GSHP$_{HC}$ operation in February 2010

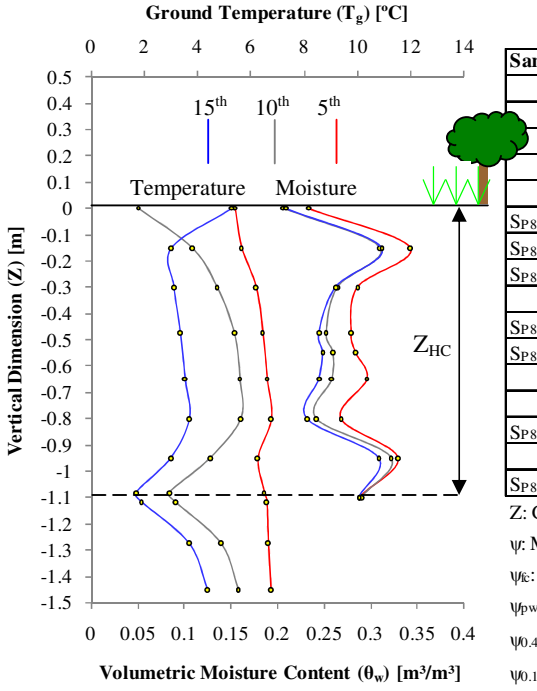

Sample	Layer	Z [m]	ψ [m]	
	Atmosphere	-	-10,000	
	-	-	ψ_{fc} [m]	ψ_{pw} [m]
	Shrub Leaves	-	-102	-306
	Shrub Stem/Xylem	+0.15	-71	-255
	Grass and Roots	+0.05	-3	-173
$S_{P8,\ -0.05m}$	Sod with Roots	-0.05	-3	-153
$S_{P8,\ -0.15m}$	Peat/ Top Soil	-0.15	$\psi_{0.4}$[m]	$\psi_{0.1}$ [m]
$S_{P8,\ -0.25m}$	Sandy clay loam with gravel	-0.25	-0.14	-88
-	-	-	-	-
$S_{P8,\ -0.45m}$	Sandy loam with cement traces	-0.45	-0.1	-14
$S_{P8,\ -0.55m}$	Sandy loam with gravel	-0.55	-0.1	-14
-	-	-	-	-
-	-	-	-	-
$S_{P8,\ -0.85m}$	Sandy clay loam with gravel	-0.85	-0.14	-88
-	-	-	-	-
$S_{P8,\ -1.05m}$	Sandy loam	-1.05	-0.1	-14

Z: Gravimetric potential

ψ: Matric potential

ψ_{fc}: Plant matric potential at field capacity

ψ_{pw}: Plant matric potential at permanent wilt

$\psi_{0.4}$: Soil matric potential at 0.4m^3/m^3

$\psi_{0.1}$: Soil matric potential at 0.1m^3/m^3

(a) Temperature and moisture gradients **(b) Layered matric potential analysis**

Figure 7-8: Simultaneous temperature and moisture content gradients measured around the collector in P8 during GSHP$_{HC}$ operation in February 2010

As discussed in Sub-section 5.2.3.2, ground water flux ($J"_{wg}$) is analogous to ground heat flux ($q"_G$) and occurs along water potential gradients ($d\Phi/dZ$) which are analogous to temperature gradients (dT/dZ). Therefore, Figure 7-8(b) displays a matric (ψ) and gravimetric (Z) water potential analysis of the ground layers and the surface cover. For plant life, two values for matric potential are quoted. These are for field capacity and permanent wilt, defined in Campbell & Norman (1998). Similarly for soil/ground, two values for matric potential are quoted at moisture contents of $0.4m^3/m^3$ and $0.1m^3/m^3$. Based on Piechowski (1996) and Figures 7-7 and 7-8, the following observations are made:

- Coupled heat and mass theory suggests that thermal moisture diffusion should occur along temperature gradients towards the cooled collector layer (Z = -1.1m)
- Figure 7-7 indicates that collector depth moisture content ($M_{P8,\ -1.1m}$) did not change while the temperature ($T_{P8,\ -1.1m}$) decreased by 4.9K during heat pump operation
- Figure 7-8(a), indicates that moisture content above the collector ($M_{P8,\ -0.95m}$) reduces during $GSHP_{HC}$ operation, indicating no moisture migration towards the collector
- This corresponds with conclusions made by Piechowski (1996), that a thermal gradient of 6.67K/m is insufficient to drive significant moisture movement
- Additionally, the moisture content at collector depth ($M_{P8,\ -1.1m}$) does not respond to significant rainfall between February 1st and 5th or the dry spell between February 5th and 15th indicating a degree of saturation
- The highest moisture contents are measured in layers Z= -0.15m and -0.95m which correspond approximately with highest attractive force (ψ = -3 to -153 and -0.14 to -88m respectively) due to the presence of absorptive organic material and clays
- Significant drying is evident between February 5th and 15th, particularly in layers between Z= -0.25 and -0.8m where the lowest attractive forces exist
- Moisture from these layers is lost to the sod/roots, then the shrub/grass cover and finally to the atmosphere, which each have increasingly higher attractive forces
- The periodic variation in ($M_{P8,\ 0.0m}$) at θ_{wg} less than $0.225m^3/m^3$ is caused by thermal vapour movement ($J"_{vap,T}$), a component of coupled heat and mass transfer, driven by periodic solar heating at the surface, as discussed in Sub-section 5.2.4.2

Therefore, based on this data, the simulations of Piechowski (1996) and as concluded by Mei (1986); Gauthier *et al.* (1997); Esen *et al.* (2007) and Demir *et al.* (2009) a conduction only heat transfer simulation is sufficiently accurate for winter mode GHE. However, it is still important to account for the substantial influence of site-specific moisture content on the ground's thermal conductivity, shown in Figure 5-10.

7.1.7 Ground Water Freezing

Prolonged periods (weeks or months) of sub-0ºC conditions at the *ground-atmosphere interface* (discussed in Sub-section 5.5.1.2) and/or prolonged extreme heat extraction at the *collector-ground interface* can cause freezing of the ground moisture. For this reason, simulations conducted in cold climates include ground freezing algorithms such as those presented in Sub-section 5.2.4 (Engelmark & Svensson, 1993; Endrizzi *et al.*, 2008). Tarnawski & Leong (1993) presented an example of such a simulation created for the *Moderate Sub-polar* climate in Halifax, Canada.

It was shown in Sub-section 5.5.1.2 that temperatures below 0.3ºC were not common at the *HP-IRL/H* site. Over the 3.64 years of the *HP-IRL/H* project, the air temperature (T_a), surface cover temperature (T_{cov}), bulk surface temperature (T_{sur}) and bulk ground temperature (T_g) were less than 0.3ºC for 1.68%, 1.63%, 0.7% and 0% of that time. More importantly, the temperature at the *collector-ground interface* was below 0.3ºC for 0% of the *HP-IRL/H* test program. It was shown in Figure 6.1 that a prolonged (69 day) extreme heat extraction test (18.1 W/m^2) during HC9 (January 5th to March 11th) resulted in a sub-0ºC flow temperature ($T_{s,f}$), but failed to freeze the *collector-ground interface* in any collector profile, P3 through P7. Therefore, it was concluded that ground freezing could be avoided with good collector design in the *Cool Marine* climate. As a result, this effect was not simulated; Esen *et al.* (2007) and Demir *et al.* (2009) reached a similar conclusion.

7.1.8 Holistic Simulation

The importance of holistic analysis and simulation of SET was introduced in Section 2.1. Additionally, the measured influence of *$GSHP_{HC}$* operation on source and sink temperatures (T_s and T_{sk}) and the resulting influence of T_s and T_{sk} on COP were highlighted in Sub-section 6.1.2.

The TRNSYS simulation environment, shown in Figure 7-9(a), is well suited to holistic simulations. Components such as buildings, heat pumps, solar panels and wind turbines can be interconnected and simulated based on site specific weather conditions. However, Figure 7-9(b) displays the TRNSYS collector component which is based on the ORNL '*radially symmetrical*' geometry. It was shown in Sub-section 7.1.3 that this geometry is unsuitable for the *HP-IRL/H* collector and is also unsuitable for shallow, *parallel*, *in-line*, horizontal collectors in general. However, method NL-5 described in this chapter can be used to create a holistic simulation for this collector type.

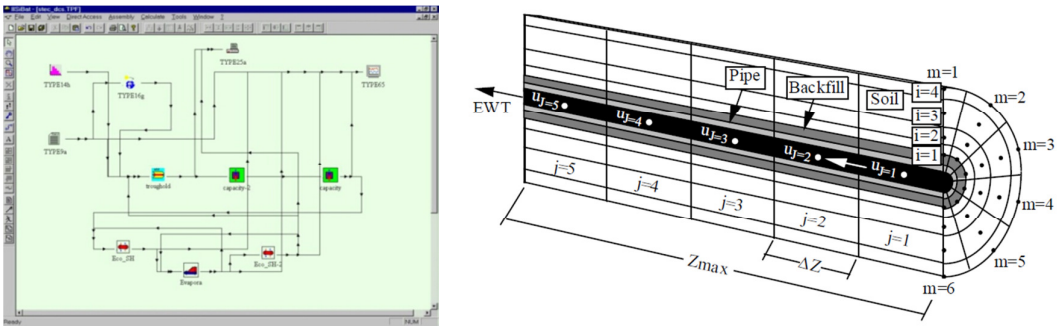

(a) TRNSYS holistic simulation environment (b) TRNSYS collector component based on ORNL model

Figure 7-9: Creating a holistic TRNSYS model

7.2 MODEL NL-4: TWO-DIMENSIONAL GTD RESPONSE TO GSHP$_{HC}$

Model NL-4, first introduced in Figure 3-28, uses the FDM to simulate transient 2-D (W, Z, t) ground temperature response to collector heat extraction.

7.2.1 Assumptions

In order to simulate heat extraction within the collector volume, without simulating the entire collector volume, a *pipe-ground simulation domain* is chosen as follows:

- For the purpose of efficient simulation, the parallel collector may be seen as an *infinite array of pipes* (this assumes 'edge effects' are ignored)
  - Therefore the simulation can be carried out for one collector pipe subject to symmetrical boundary conditions (Gauthier *et al.*, 1997)
- Furthermore, this pipe and the associated ground domain can be split in half along a line of symmetry which bisects the pipe (Esen *et al.*, 2007; Demir *et al.*, 2009)
- It is assumed that heat transfer in the ground along the L dimension is negligible in comparison to ground heat transfer along the Z and W dimensions (Piechowski, 1996; Demir *et al.*, 2009)
  - Therefore the influence of heat extraction on individual sections (ΔL) of ground can be simulated independently

Therefore, as shown in Figure 7-10, the *pipe-ground simulation domain* measures: PS/2 [m] in the W dimension, $|Z_{LB}|$ [m] in the Z dimension and one unit ΔL [m] in the L dimension, with the collector located at Z_{HC}. It is now possible to apply an appropriate heat extraction rate to this *pipe-ground simulation domain* at the depth of the collector Z_{HC} and simulate the resulting drop in temperature throughout the entire *pipe-ground simulation domain* selected. However, based on the variation in local heat extraction ($q'_{\Delta L}$) [W/m] with both length (L) and

time (t), as seen in Section 6.6, simulating 'real-life' collector operation is not straightforward using NL-4. By incorporating the local heat extraction ratio ($\beta_{\Delta L}$), described in AL-11, with small pipe space-increments ($\Delta L \leq 10m$) the accuracy of NL-4 is greatly improved.

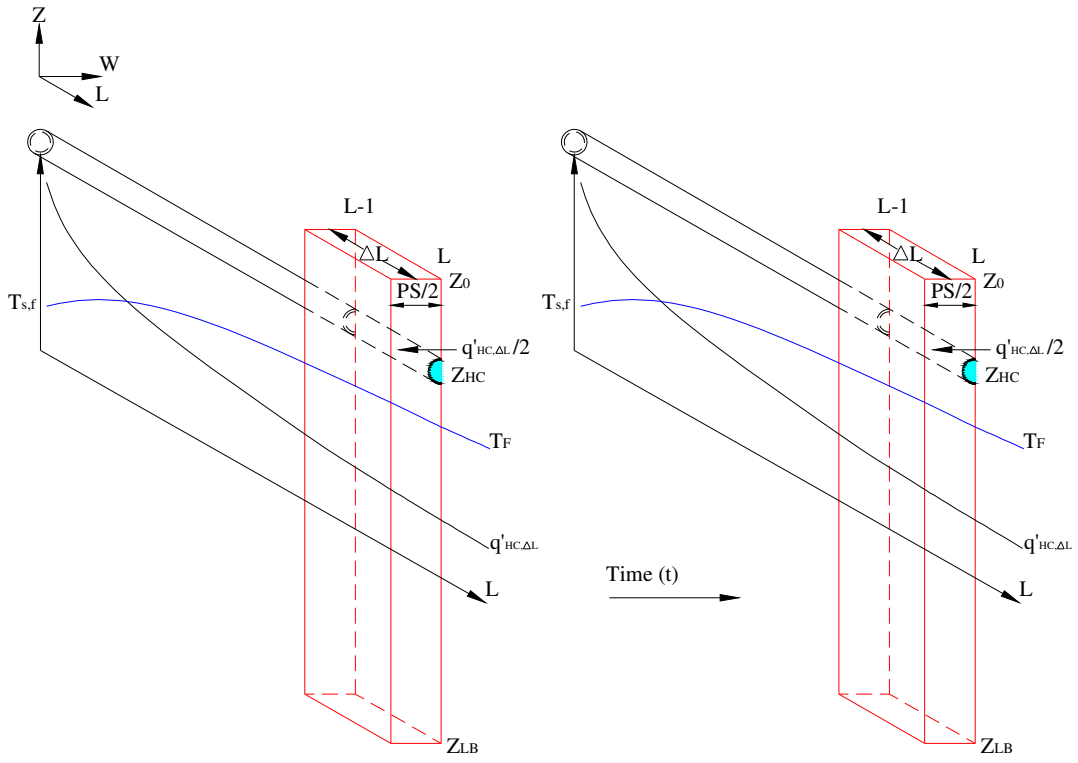

(a) Previous time-step (p = t - Δt) **(b) Current time-step (t)**

Figure 7-10: NL-4 model geometry displaying the pipe-ground simulation domain in brown line colour

After the *HP-IRL/H* horizontal collector was sub-divided into the *pipe-ground simulation domain* identified in Figure 7-10. The W-Z plane of this *pipe-ground simulation domain* is then discretised into a matrix of nodes shown in Figure 7-11. Each node has an associated temperature $T_{W,Z}$ and Fourier number $Fo_{W,Z}$. $T_{W,Z}$ changes in time (t) while $Fo_{W,Z}$ can change with moisture content ($\theta_{wg}(t)$) or remain constant. Nodes are spaced ΔW [m] apart on the horizontal dimension and ΔZ [m] apart on the vertical dimension. For convenience ΔW and ΔZ are often equal, the selection of ΔZ and ΔW is discussed in Sub-section 7.3.5. The resulting grid, shown in Figure 7-11, is referred to as the simulation mesh and greater accuracy is achieved with a finer mesh. A ΔZ of PS/4 was used in AL-4 simulations. Methods to improve mesh efficiency for the *pipe-ground simulation domain* are discussed in Sub-section 7.3.5.

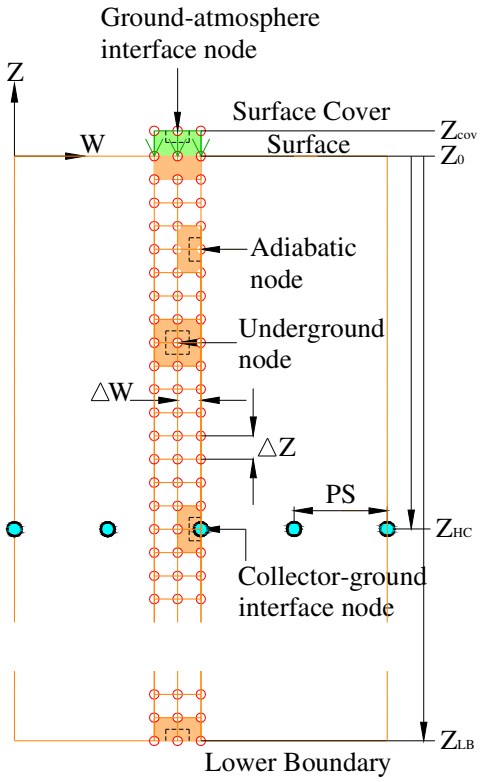

Figure 7-11: Assigning nodes to the W-Z plane of the NL-4 pipe-ground simulation domain

7.2.2 Applying the Finite Difference Method

Based on the *simulation domain* shown in Figure 7-10 and the mesh applied to the W-Z plane in Figure 7-11, EFD equations were written for each node of the mesh. While the alternative IFD equations offer more flexibility in Δt selection and typically more efficient solutions when programmed in a *Fortran* or *C++* environment, for the purpose of developing and validating the *simulation domain* and trialling *MS-Excel* simulations with built-in feedback control, EFD equations were used. Future development of the equations and an upgrade to IFD are discussed in Section 9.3.

As shown in Figure 7-11, the following distinct node types were defined:

- *Ground-atmosphere interface* node
- Underground node
- Adiabatic node
- *Collector-ground interface node* (heat extraction condition)
- Lower boundary node

Equations for each of these nodes in the current time-step ($T_{W,Z}$) [ºC] were developed in the explicit form as described in the subsequent text.

7.2.2.1 Ground-atmosphere Interface Node

The *ground-atmosphere interface node* shown in Figure 7-12 is similar to that in the 1-D ground simulation NL-1, Section 5.4, except that NL-4 is a 2-D model. The equations are therefore written in the 2-D format for compatibility with the underground nodes.

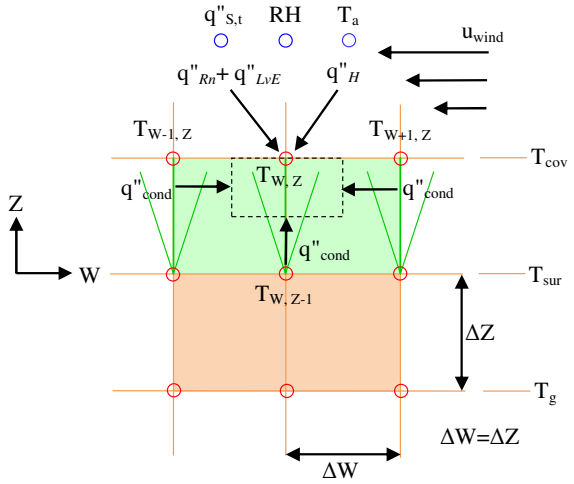

Figure 7-12: NL-4 geometry for the ground-atmosphere interface node, for bare ground $T_{cov} \rightarrow T_{sur}$

Using the energy balance method to formulate FD equations described in Incorpera & DeWitt (2002), the surface can be described using Equation 7-4. Where, q_{Rn} [W], q_H [W], q_{LvE} [W] and q_G[W] are the net radiation, sensible, latent and ground heat transfer rates respectively and q_{st} [W] is the rate of change in stored energy.

$$q_{R_n} + q_H + q_{L_vE} + q_G = q_{st} \tag{7-4}$$

The heat transfer rates and the rate of change in stored energy for the half volume surface node ($\Delta W*\Delta Z/2*\Delta L$ m^3) are equated as follows:

$$q^{(R_n+L_vE)\rightarrow(W,Z)} + q^{(H)\rightarrow(W,Z)} + q^{(W-1,Z)\rightarrow(W,Z)} + q^{(W+1,Z)\rightarrow(W,Z)} + q^{(W,Z-1)\rightarrow(W,Z)} = q_{st} \tag{7-5}$$

Each term of Equation 7-5 is defined in terms of the 2-D geometry shown in Figure 7-12 as follows, where the superscript p indicates a value from the previous time-step:

$$q^{(R_n+L_vE)\rightarrow(W,Z)} = (q"_{R_n} + q"_{L_vE})(\Delta W.\Delta L) \tag{7-6}$$

$$q^{(H)\rightarrow(W,Z)} = h(\Delta W.\Delta L)\left(T_a - T^p_{W,Z}\right) \tag{7-7}$$

$$q^{(W-1,Z)\rightarrow(W,Z)} = k\left(\frac{\Delta Z}{2}.\Delta L\right)\frac{T^p_{W-1,Z} - T^p_{W,Z}}{\Delta W} \tag{7-8}$$

$$q^{(W+1,Z)\rightarrow(W,Z)} = k\left(\frac{\Delta Z}{2}.\Delta L\right)\frac{T^{p}_{W+1,Z}-T^{p}_{W,Z}}{\Delta W} \quad (7\text{-}9)$$

$$q^{(W,Z-1)\rightarrow(W,Z)} = k(\Delta W.\Delta L)\frac{T^{p}_{W,Z-1}-T^{p}_{W,Z}}{\Delta Z} \quad (7\text{-}10)$$

$$q_{st} = \rho c\left(\frac{\Delta Z}{2}.\Delta W.\Delta L\right)\frac{T_{W,Z}-T^{p}_{W,Z}}{\Delta t} \quad (7\text{-}11)$$

For simplicity, the ΔW and ΔZ space increments can be set equal and only ΔZ is used from here on:

$$(\Delta Z = \Delta W) = \Delta Z \quad (7\text{-}12)$$

Finally, the individual definitions are substituted back into Equation 7-5 and the ΔL increments cancel out, therefore the 2-D equation is written as Equation 7-13.

$$T_{W,Z} = Fo\left(2T^{p}_{W,Z-1} + T^{p}_{W-1,Z} + T^{p}_{W+1,Z} + 2BiT_a\right) + (1 - 4Fo - 2BiFo)T^{p}_{W,Z} + 2Fo\frac{(q''_{Rn}+q''_{LvE})\Delta Z}{k} \quad (7\text{-}13)$$

The Fourier number (Fo) and Biot number (Bi) are defined using Equations 5-33 and 5-37. The Fourier number is subject to the following stability criteria:

$$Fo(2 + Bi) \leq \frac{1}{2} \quad (7\text{-}14)$$

The net radiation flux (q''_{Rn}) [W/m^{2}K] can be defined using Equation 5-3 where outgoing long-wave radiation is a function of $T^{p}_{W,Z}$ and atmospheric emissivity (ε_a) [-] can be defined using Equations 5-40, 5-41 and 5-42. The latent heat flux can be defined using Equation 5-45 where coefficients are evaluated at $T^{p}_{W,Z}$ and T_a. The convection coefficient (h) [W/mK] can be defined as a function of wind speed (u_{wind}) [m/s] using Equations 5-43 and 5-44. For the nodes situated on the adiabatic lines (lines of symmetry) that were used to define the *pipe-ground simulation domain* in Figure 7-12, Equation 7-13 is modified. For an adiabatic line on the left, missing node $T_{W-1,Z}$, the following expression was used:

$$T_{W,Z} = Fo\left(2T^{p}_{W,Z-1} + 2T^{p}_{W+1,Z} + 2BiT_a\right) + (1 - 4Fo - 2BiFo)T^{p}_{W,Z} + 2Fo\frac{(q''_{Rn}+q''_{LvE})\Delta Z}{k} \quad (7\text{-}15)$$

For an adiabatic line on the right, missing node $T_{W+1,Z}$, the following was used:

$$T_{W,Z} = Fo\left(2T^{p}_{W,Z-1} + 2T^{p}_{W-1,Z} + 2BiT_a\right) + (1 - 4Fo - 2BiFo)T^{p}_{W,Z} + 2Fo\frac{(q''_{Rn}+q''_{LvE})\Delta Z}{k} \quad (7\text{-}16)$$

7.2.2.2 Underground Nodes

For the nodes located within the ground, such as those depicted in Figure 7-13, the standard 2-D conduction EFD equations are described in Incorpera & DeWitt (2002).

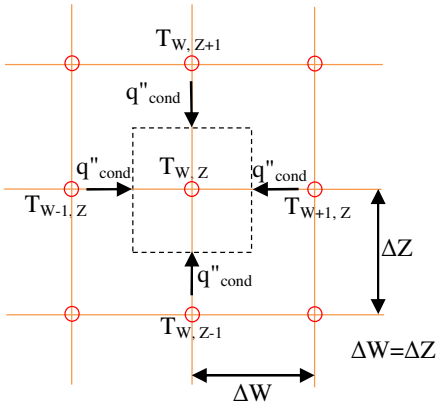

Figure 7-13: NL-4 geometry for the underground node

For a standard underground node the EFD equation is:

$$T_{W,Z} = Fo\left(T^{p}_{W-1,Z} + T^{p}_{W+1,Z} + T^{p}_{W,Z-1} + T^{p}_{W,Z+1}\right) + (1 - 4Fo)T^{p}_{W,Z} \qquad (7\text{-}17)$$

For an adiabatic line on the left, missing node $T_{W-1,Z}$, the following was used:

$$T_{W,Z} = Fo\left(2T^{p}_{W+1,Z} + T^{p}_{W,Z-1} + T^{p}_{W,Z+1}\right) + (1 - 4Fo)T^{p}_{W,Z} \qquad (7\text{-}18)$$

For an adiabatic line on the right, missing node $T_{W+1,Z}$, the following was used:

$$T_{W,Z} = Fo\left(2T^{p}_{W-1,Z} + T^{p}_{W,Z-1} + T^{p}_{W,Z+1}\right) + (1 - 4Fo)T^{p}_{W,Z} \qquad (7\text{-}19)$$

7.2.2.3 Collector-ground Interface Node (Heat Extraction Condition)

The energy balance at the *collector-ground interface node* is shown in Equation 7-20. Where, q_G [W] and q_{HC} [W] are the ground and horizontal collector heat transfer rates respectively and q_{st} [W] is the rate of change in stored thermal energy.

$$q_G + q_{HC} = q_{st} \qquad (7\text{-}20)$$

Based on Figure 7-14 it can be seen that the ground heat transfer q_G for the half volume node consists of three separate terms as shown in Equation 7-21.

$$q^{(W-1,Z)\rightarrow(W,Z)} + q^{(W,Z-1)\rightarrow(W,Z)} + q^{(W,Z+1)\rightarrow(W,Z)} + q^{(HC)\rightarrow(W,Z)} = q_{st} \qquad (7\text{-}21)$$

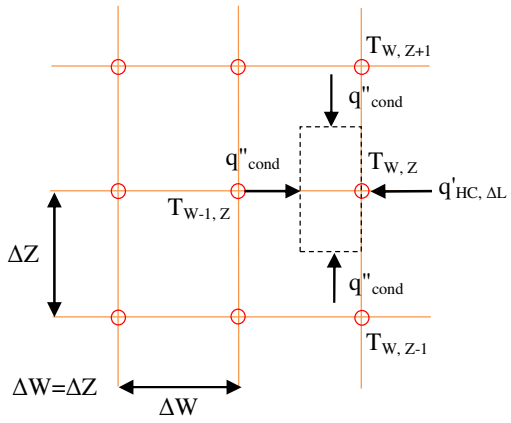

Figure 7-14: NL-4 geometry for the collector-ground interface node

The terms in Equation 7-21 are then individually defined using the geometry in Figure 7-14 as follows:

$$q^{(W-1,Z)\rightarrow(W,Z)} = k(\Delta Z.\,\Delta L)\frac{T^{p}_{W-1,Z}-T^{p}_{W,Z}}{\Delta W} \tag{7-22}$$

$$q^{(W,Z-1)\rightarrow(W,Z)} = k(\frac{\Delta W}{2}.\,\Delta L)\frac{T^{p}_{W,Z-1}-T^{p}_{W,Z}}{\Delta Z} \tag{7-23}$$

$$q^{(W,Z+1)\rightarrow(W,Z)} = k(\frac{\Delta W}{2}.\,\Delta L)\frac{T^{p}_{W,Z+1}-T^{p}_{W,Z}}{\Delta Z} \tag{7-24}$$

$$q^{(HC)\rightarrow(W,Z)} = q'_{HC,\Delta L}(\Delta L) \tag{7-25}$$

$$q_{st} = \rho c(\frac{\Delta W}{2}.\,\Delta Z.\,\Delta L)\frac{T_{W,Z}-T^{p}_{W,Z}}{\Delta t} \tag{7-26}$$

Substituting Equations 7-22 through 7-26 into Equation 7-21 and solving for $T_{W,Z}$ results in Equation 7-27.

$$T_{W,Z} = Fo\left(2T^{p}_{W-1,Z} + T^{p}_{W,Z-1} + T^{p}_{W,Z+1}\right) + (1-4Fo)T^{p}_{W,Z} + 2Fo\frac{q'_{HC,\Delta L}}{k} \tag{7-27}$$

In winter mode, the heat extraction rate per meter ($q'_{HC,\Delta L}$) [W/m] for a bisected pipe section is found using Equation 7-28, where $\left[\frac{1}{0}\right]$ represents the on/off status of the heat pump during the current time-step, $\beta_{\Delta L}$ [-] is the local heat extraction ratio, q_s [W] is the source extraction rate, N [-] is the number of pipes in the parallel collector and L_t [m] is the total length of each pipe.

$$q'_{HC,\Delta L} = -1\left[\frac{1}{0}\right]\frac{\beta_{\Delta L}q_s(T_{sk,f},T_{s,r})}{2NL_t} \tag{7-28}$$

The source extraction q_s ($T_{sk,f}$, $T_{s,r}$) [W] and the local heat flux ratio $\beta_{\Delta L}$ (L, $\dot{V}$, t) [-] were defined with Equations 6-10 and 6-47 from models AL-7 and AL-11 respectively.

7.2.2.4 Lower Boundary Node and Initial Conditions

As shown in Section 4-1 ground temperature at depths greater than 1 to 2m varies only with the seasons, therefore Equation 4-14 from model AL-4 can be used to calculate the variation in ground temperature with time (t) at the lower boundary nodes of the model (T_{LB}). It is important that the lower boundary (Z_{LB}) is established at a sufficient distance from the collector level (Z_{HC}). The greater the distance ($Z_{LB} - Z_{HC}$) the greater the accuracy of the model, however increased nodes increases the solution time. Since all nodal equations at time (t) are written in terms of the previous time-step (p), an initial temperature is required for every node of the *pipe-ground simulation domain* at the beginning of a simulated *$GSHP_{HC}$* operation. Equation 4-14 (AL-4) or 4-18 (AL-5) can be used to approximate the temperatures of all the nodes, from T_{cov}/T_{sur} to T_{LB} including T_{HC}, at the beginning of the heat extraction season.

7.2.3 NL-4 Implementation

Model NL-4 was implemented in *MS-Excel*; a simplified sample is shown in Figure 7-15 which is based on the following conditions:

- As discussed in Sub-section 7.2.1 the dimensions of the W-Z plane are PS/2 x $\left|Z_{LB}\right|$ [m]
- As discussed in Sub-section 3.5.1, pipe spacing (PS) at the *HP-IRL/H* site varies between 0.25m in P4 and P5 and 0.4m in P3 and P6
- $\left|Z_{LB}\right|$ was assigned a value of 5, 7.5 and 10m in validations and a value of 5m was deemed sufficiently accurate
- With $\Delta W=\Delta Z=PS/4$ [m], the ΔZ dimension therefore varied between 0.0625m for P4 and P5 and 0.1m for P3 and P6
- With these ΔZ values the matrix of nodes (W, Z) needed for simulations were (3, 80) for P4 and P5 and (3, 50) for P3 and P6
- These matrices were transposed to (80, 3) and (50, 3), as shown in Figure 7-15, for convenient implementation as a series of *MS-Excel* rows
- The collector is located at Z_{HC} = -1m, therefore this is 16 and 10 nodes from the surface in P4/P5 and P3/P6 models respectively
- With a ground thermal diffusivity of 1.05 x 10^{-6} m^2/s, defined in Section 4.5.4, and a minimum ΔZ of 0.0625m, a Δt of 720s was required to insure the Fourier number satisfies the stability criteria in Equation7-14

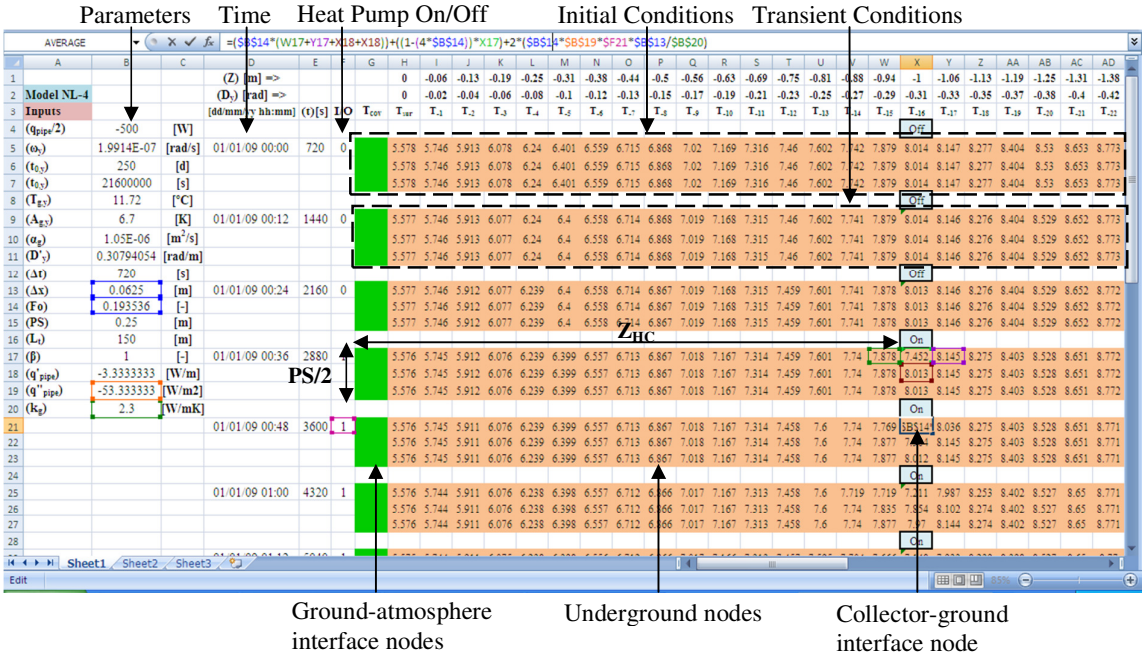

Figure 7-15: Model NL-4 implemented in MS-Excel for PS of 0.25m, $|Z_{LB}|$ of 5m and Z_{HC} of -1m with ΔZ of 0.0625m and Δt of 720s

For input of equations, *Excel* is switched to '*show formula*' mode; this pauses the calculation of equations temporarily, while:

- The initial conditions (Equation 4-14) are input for all nodes at time t_0; thereafter the transient conditions (Equations 7-13, 7-17 and 7-27 or their adiabatic equivalents) are used while Equation 4-14 is used for T_{LB}
- In the simplified sample shown in Figure 7-15, Equation 4-14 is also used for T_{sur}
- Nodes using Equation 4-14 are linked with time (dd/mm/yyyy hh:mm) counted in column E, Figure 7-15
- *Collector-ground interface* equations are linked to the heat pump on/off signal, monitored in column F, Figure 7-15
- *Ground-atmosphere interface* equations (not used in this sample) are linked to site and time dependent, measured weather data stored in columns
- All nodes which depend on the conditions in the previous time-step are linked accordingly, an example is shown for the *collector-ground interface* node in cell 'X21'
- The equations in this format and appropriate input columns are then propagated downward over the time-span of the required simulation, for large simulations (3 months) *Excel* requires as much as 12 hours to complete this process

For solution of equations, '*show formula*' mode is then switched off

- Results for nodes of interest, at times of interest, can then be extracted by filtering through results with built-in *Excel* functionality
- Model parameters assigned to Column B, Figure 7-15, can be changed and the *Excel* program then recalculates all equations requiring 5 to 10 minutes

NL-4 validation using *HP-IRL/H* data is presented in Sub-section 7.4.2 while Section 8.2 demonstrates the potential of this straightforward model to simulate novel *split-level collectors* with *collector temperature feedback control* yielding $GSHP_{HC}$ performance improvements.

7.3 MODEL NL-5: UNDERGROUND FLUID WARMING AND GROUND COOLING

Model NL-5, first introduced in Figure 3-28, uses the FDM to simulate transient 1-D (L, t) warming of the source fluid as it circulates underground and the simultaneous 'quasi 3-D' [(W, Z), L, t] ground temperature response to the cold fluid.

7.3.1 Assumptions

In order to simulate the heat transfer within the collector volume, without simulating the entire collector volume, a *pipe-ground simulation domain* is again chosen. Similarly to NL-4 the following assumptions can be used:

- An array of balanced *parallel* pipes can be simulated using a single pipe with symmetry (Gauthier *et al.*, 1997)
- An additional line of symmetry bisects this single pipe (Esen *et al.*, 2007; Demir *et al.*, 2009)

Therefore, as shown in Figure 7-16, the bisected *pipe-ground simulation domain* measures: L_t [m] in the L dimension, PS/2 [m] in the W dimension and $|Z_{LB}|$ [m] in the Z dimension, with the *collector-ground interface* located at Z_{HC}. Additionally, it was seen from AL-9, Section 6.4, that the fluid temperature increase along the L dimension is non-linear. Hence, the pipe needs to be sub-divided into sections of length ΔL [m] thereby allowing series of linear fluid temperature increases to approximate the non-linear curve. A further assumption, discussed in NL-4, is as follows:

- Heat transfer in the L dimension is negligible (Piechowski, 1996; Demir *et al.*, 2009)

Based on this, the ground sections described need only be linked in time and not in the L dimension, while the fluid sections are linked in both time and the L dimension. This results in a quasi 3-D or 2½-D geometry (Loomans *et al.*, 2003).

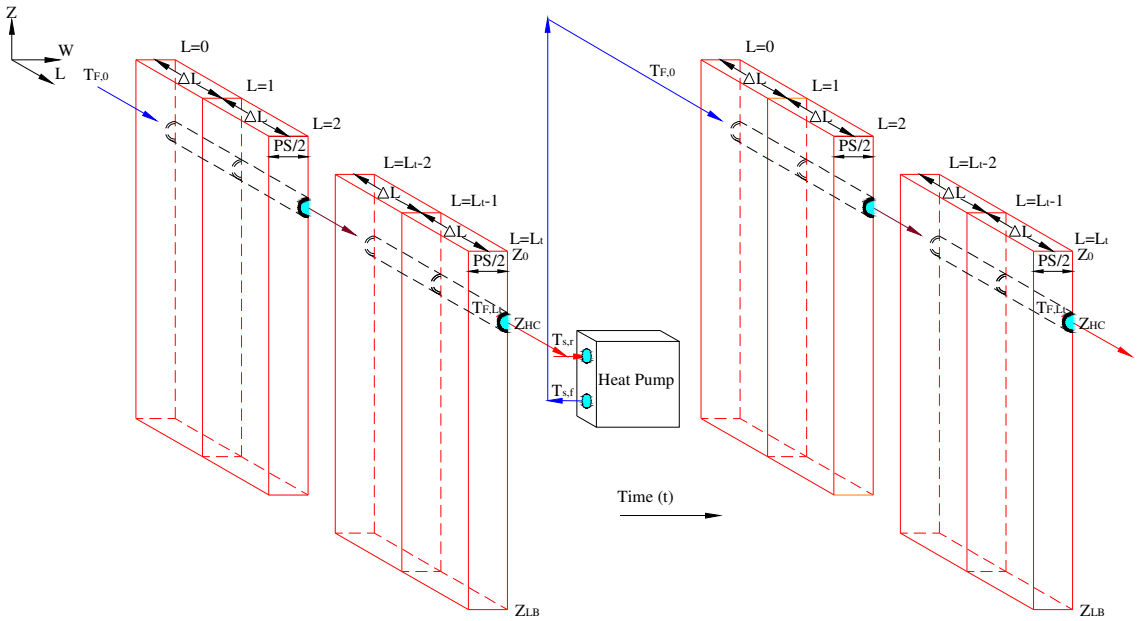

(a) Previous time-step (p = t - Δt) **(b) Current time-step (t)**

Figure 7-16: Model geometry for NL-5 displaying the ground-pipe simulation domain, the sectioning in the L dimension and the heat extraction by the heat pump

The assumptions described allow for a bisected pipe of the collector to be chosen for simulation and this half pipe is then divided into pipe sections of equal length ΔL as follows:

- Each pipe section has a fluid temperature node at the section entrance ($T_{F,L-1}$) and exit ($T_{F,L}$)
- The fluid exiting a section L-1 enters the next section L and therefore the exit node of pipe section L-1 is also the entrance node for the next section L
- At the end of the collector pipe ($L=L_t$) the exit node ($T_{F,Lt}$) is equivalent to the source return temperature ($T_{s,r}$), as discussed in Section 6-3, and is therefore the entrance node of the heat pump
- The source flow temperature ($T_{s,f}$) at the heat pump exit node then becomes the entrance node to the collector pipe ($T_{F,0}$) in the next time-step.
- The nodes at the entrance and exit of the heat pump are the last collector node and the first collector node respectively.

7.3.2 Applying the Finite Difference Method

EFD equations that represent the following nodes are documented for model NL-4 in Sub-section 7.2.2:

- *Ground-atmosphere interface* node (including adiabatic equivalents)
- Underground node (including adiabatic equivalents)
- *Collector-ground interface* node (heat extraction condition)
- Lower boundary node (using AL-4)
- Initial conditions for all nodes (using AL-4 or AL-5)

Therefore, this sub-section describes the following additional nodes needed for NL-5:

- Pipe section exiting fluid node
- *Collector-ground interface* node (heat transfer condition)
- Heat pump's evaporator exiting fluid node

Equations for each of these nodes in the current time-step ($T_{W,Z}$) [ºC] were developed in the explicit form as described in the subsequent sections.

7.3.2.1 Pipe Section Exiting Fluid Node

The geometry used to derive an equation for the fluid exit node is presented in Figure 7-17.

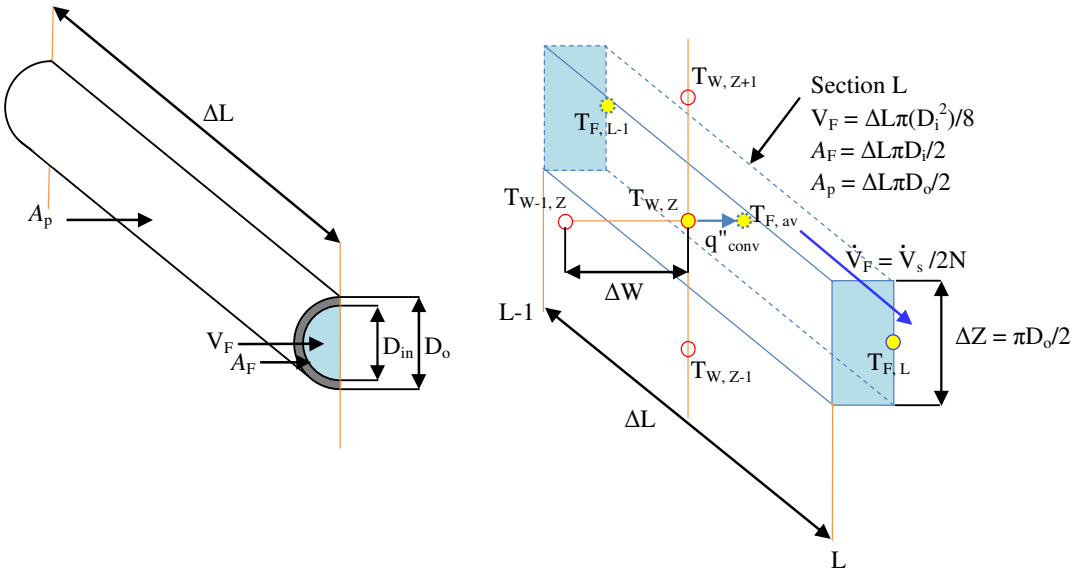

(a) Section L of bisected collector pipe N **(b) Section L model geometry**

Figure 7-17: NL-5 geometry for the exiting fluid node of any pipe section identified as 'Section L'

Unlike the FD equations for the ground nodes $T_{W,Z}$ in NL-4 where the EFD convention is to sum energy flows into the node, the equation for the fluid exit node ($T_{F,L}$) is derived based on an energy balance for the steady-flow 'control volume' of fluid ($\Delta L\pi(D_{in}^2)/8$) which lies between the entrance node ($T_{F,L-1}$) and exit node ($T_{F,L}$) of the bisected pipe section. The rate that energy enters this volume (q_{ent}) [W] minus the rate that energy exits this volume (q_{exit}) [W] is equal to the rate of change in stored energy in the volume (q_{st}) [W], as follows:

$$q_{ent} - q_{exit} = q_{st} \tag{7-29}$$

Energy enters the volume within the fluid ($q_{F,ent}$) [W] and energy exits within the fluid ($q_{F,exit}$) [W]. Energy also enters the volume primarily through convection (q_{conv}) [W] from the *collector-ground interface* (the pipe wall) as follows:

$$q_{F,ent} - q_{F,exit} + q_{conv} = q_{st} \tag{7-30}$$

Equation 7-30 is rearranged to the form shown in Equation 7-31.

$$q_{F,exit} - q_{F,ent} = q_{conv} - q_{st} \tag{7-31}$$

Expanding each term in Equation 7-31 using the geometry shown in Figure 7-17, yields Equation 7-32.

$$\rho_F c_{p,F} \dot{V}_F \left(T_{F,L} - T_{F,L-1}\right) = U A_p \left(T_{W,Z} - T_{F,av}\right) - \rho_F c_{p,F} V_F \frac{dT_{F,av}}{dt} \tag{7-32}$$

In Equation 7-32, ρ_F [kg/m^3] and $c_{p,F}$ [J/kgK] are the fluid density and constant pressure specific heat capacity, $\dot{V}_F$ [m^3/s] is the flow rate in a bisected pipe, A_p [m^2] is the surface area of the bisected pipe exterior and $T_{W,Z}$ [ºC] is the ground temperature at the *collector-ground interface*. The heat transfer coefficient (U) [W/m^{2}K] is used rather than the typical convection coefficient (h) [W/m^{2}K] as it represents a combination of fluid convection and pipe wall conduction. The average fluid volume temperature ($T_{F,av} = (T_{F,L-1} + T_{F,L})/2$) [ºC] is used to calculate the convection heat transfer rate (q_{conv}) as it gives a better representation of the heat transfer rate along the entire pipe section length (ΔL), particularly for longer pipe sections. Evaluating all heat transfer at $T_{F,av}$ in this thesis, is a novel development on the pipe section method used by Piechowski (1996) and Demir (2009) which is shown to improve accuracy in Sub-section 7.4.3.2. Equation 7-32 is further expanded to the form shown in Equation 7-33, where the superscript p indicates a value from the previous time-step.

$$\dot{V}_F \left(T_{F,L} - T_{F,L-1}\right) = \frac{U A_p}{2\rho_F c_{p,F}} \left(2T_{W,Z} - T_{F,L} - T_{F,L-1}\right) - \frac{V_F}{2\Delta t} \left(T_{F,L} + T_{F,L-1} - T_{F,L}^p - T_{F,L-1}^p\right) \tag{7-33}$$

Equation 7-33 is then rearranged into the form shown in Equation 7-34.

$$\dot{V}_F T_{F,L} + \frac{U A_p}{2\rho_F c_{p,F}} T_{F,L} + \frac{V_F}{2\Delta t} T_{F,L} = \dot{V}_F T_{F,L-1} + \frac{U A_p}{2\rho_F c_{p,F}} \left(2T_{W,Z} - T_{F,L-1}\right) + \frac{V_F}{2\Delta t} \left(T^p_{F,L} + T^p_{F,L-1} - T_{F,L-1}\right) \tag{7-34}$$

Finally, some terms are grouped and replaced with a_1, a_2 and a_3 to simplify the equation as follows:

$$a_1 = \frac{U A_p}{2\rho_F c_{p,F}} \tag{7-35}$$

$$U = \frac{1}{R A_p} \tag{7-36}$$

$$R = \frac{1}{h_L A_f} + \frac{Ln(D_o/D_{in})}{2\pi k_p \Delta L} \tag{7-37}$$

$$A_p = \frac{\Delta L \pi D_o}{2} \tag{7-38}$$

$$A_F = \frac{\Delta L \pi D_{in}}{2} \tag{7-39}$$

$$a_2 = \frac{V_F}{2\Delta t} \tag{7-40}$$

$$V_F = \frac{\Delta L \pi \left(D_{in}{}^2\right)}{8} \tag{7-41}$$

$$a_3 = \dot{V}_F + a_1 + a_2 \tag{7-42}$$

Where the volumetric flow rate in the bisected pipe section is defined as:

$$\dot{V}_F = \frac{\dot{V}_p}{2} = \frac{\dot{V}_s}{2N} \tag{7-43}$$

The pipe section exit node temperature ($T_{F,L}$) can now be written as Equation 7-44.

$$T_{F,L} = \frac{\dot{V}_F T_{F,L-1} + a_1\left(2T_{W,Z} - T_{F,L-1}\right) + a_2\left(T^p_{F,L} + T^p_{F,L-1} - T_{F,L-1}\right)}{a_3} \tag{7-44}$$

7.3.2.2 Collector-Ground Interface Node (Heat Transfer Condition)

The geometry used to derive an equation for the horizontal *collector-ground interface* node is shown in Figure 7-18. A 2-D mesh is used since heat transfer in the L dimension of sections is negligible and, as shown in Sub-section 7.2.2, the ΔL dimension cancels in all equation derivations. Unlike the heat extraction condition in NL-4, heat transfer to the collector in NL-5 takes place in the form of convection/conduction heat transfer to the fluid volume of the pipe section.

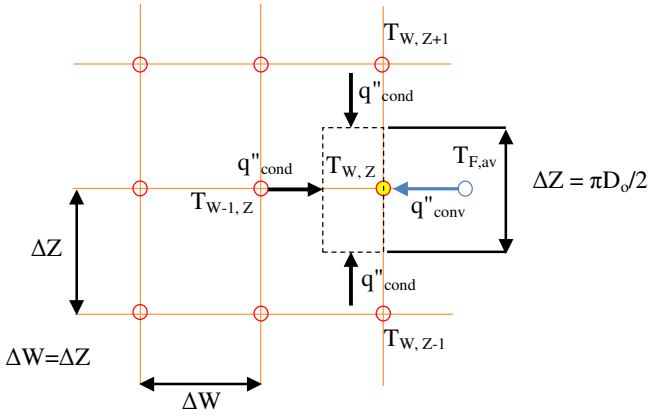

Figure 7-18: NL-5 geometry for the collector-ground interface node

The FD equation for a 2-D transient node with a convection boundary is presented by Incorpera & DeWitt (2002) as:

$$T_{W,Z} = Fo\left(2T^{p}_{W-1,Z} + T^{p}_{W,Z+1} + T^{p}_{W,Z-1} + 2BiT_{F,av}\right) + (1 - 4Fo - 2BiFo)T^{p}_{W,Z} \quad (7\text{-}45)$$

Some terms are grouped and replaced with a_4 and a_5 to simplify the equation as follows:

$$Fo = \frac{\alpha_g \Delta t}{(\Delta Z)^2} \quad (7\text{-}46)$$

$$Bi = \frac{U\Delta Z}{k_g} \quad (7\text{-}47)$$

$$\Delta Z = \pi D_0/2 \quad (7\text{-}48)$$

$$a_4 = BiFo \quad (7\text{-}49)$$

$$a_5 = 1 - 4Fo - 2a_4 \quad (7\text{-}50)$$

Equation 7-45 is modified to the following form:

$$T_{W,Z} - 2a_4 T_{F,av} = Fo\left(2T^{p}_{W-1,Z} + T^{p}_{W,Z+1} + T^{p}_{W,Z-1}\right) + a_5 T^{p}_{W,Z} \quad (7\text{-}51)$$

In order to solve for the fluid exit node ($T_{F,L}$) and the *collector-ground interface* node ($T_{W,Z}$) simultaneously, $T_{F,av}$ must be substituted into Equation 7-52. $T_{F,av}$ is the average of $T_{F,L-1}$ and $T_{F,L}$ as shown in Equation 7-52.

$$T_{F,av} = 0.5T_{F,L-1} + 0.5\frac{\dot{V}_F T_{F,L-1} + a_1(2T_{W,Z} - T_{F,L-1}) + a_2(T^{p}_{F,L} + T^{p}_{F,L-1} - T_{F,L-1})}{a_3} \quad (7\text{-}52)$$

Equation 7-52 is multiplied by $2a_4$ and some terms are grouped and replaced with a_6 to simplify the equation as follows:

$$a_6 = \frac{a_4}{a_3} \quad (7\text{-}53)$$

$$2a_4T_{F,av} = a_4T_{F,L-1} + a_6\{\dot{V}_F T_{F,L-1} + a_1\left(2T_{W,Z} - T_{F,L-1}\right) + a_2(T^p_{F,L} + T^p_{F,L-1} - T_{F,L-1})\}$$

(7-54)

Then $2a_4T_{F,av}$ is subtracted from $T_{W,Z}$ to replicate the left hand side of Equation 7-51 as follows:

$$T_{W,Z} - 2a_4T_{F,av} = [T_{W,Z} - a_6a_1 2T_{W,Z}] - [a_4T_{F,L-1} + a_6\{\dot{V}_F T_{F,L-1} - a_1T_{F,L-1} + a_2(T^p_{F,L} + T^p_{F,L-1} - T_{F,L-1})\}]$$

(7-55)

Inserting Equation 7-55 into Equation 7-51 and then replacing some terms with a_7, to simplify the equation, yields Equation 7-57.

$$a_7 = 1 - 2a_6a_1 \tag{7-56}$$

$$T_{W,Z} = \frac{Fo\left(2T^p_{W-1,Z} + T^p_{W,Z+1} + T^p_{W,Z-1}\right) + a_5T^p_{W,Z} + a_4T_{F,L-1} + a_6(\dot{V}_F T_{F,L-1} - a_1T_{F,L-1} + a_2(T^p_{F,L} + T^p_{F,L-1} - T_{F,L-1}))}{a_7}$$

(7-57)

Replacing some terms with a_8 reduces Equation 7-57 to Equation 7-59.

$$a_8 = \dot{V}_F - a_1 - a_2 \tag{7-58}$$

The horizontal *collector-ground interface* node temperature $T_{W,Z}$ can now be written as:

$$T_{W,Z} = \frac{Fo\left(2T^p_{W-1,Z} + T^p_{W,Z+1} + T^p_{W,Z-1}\right) + a_5T^p_{W,Z} + a_4T_{F,L-1} + a_6(a_8T_{F,L-1} + a_2(T^p_{F,L} + T^p_{F,L-1}))}{a_7} \tag{7-59}$$

Due to the $T^p_{W,Z}$ coefficient in Equation 7-45 (1-4Fo-2BiFo), the stability criteria for this *collector-ground interface* node is the same as that for the *ground-atmosphere interface* node (SC described in Equation 7-14), however the Biot number is that of the collector fluid flow rather than the atmospheric air flow.

Due to the derivation based on $T_{F,av}$ evaluations of heat transfer rates, this pipe section exit node ($T_{F,L}$) is more robust than those previously published and suitable for use with longer pipe sections ($\Delta L \approx 10m$); ΔL sensitivity analysis is presented in Sub-section 7.4.3.2.

7.3.2.3 Heat Pump's Evaporator Exiting Fluid Node

The NL-5 nodal geometry for the evaporator source-side entrance and exit node is shown in Figures 7-19. For a balanced *parallel* collector with pipes of equal length (L_t) and diameters (D_{in} and D_o), the flow is divided equally among the N pipes and therefore the return temperature of each pipe is equivalent to the source return temperature ($T_{N,r} = T_{s,r}$), as discussed in Section 6.3. Additionally, as temperature is an intensive property of a fluid

(Cengel & Boles, 2002) the exit temperature of the bisected pipe simulation ($T_{F,Lt}$) is equivalent to $T_{N,r}$ and $T_{s,r}$. Similarly, the source flow temperature ($T_{s,f}$) at the heat pump exit is equivalent to $T_{N,f}$ and $T_{F,0}$.

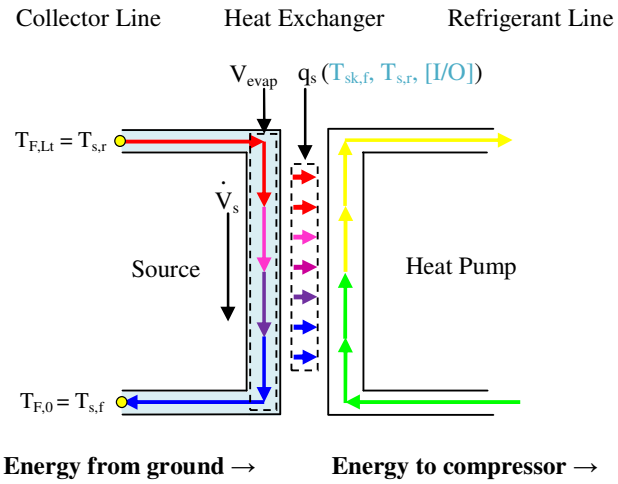

Figure 7-19: NL-5 geometry for heat pump's evaporator exiting fluid node

Like the pipe section exit node, the heat pump exit node derivation begins with the simple energy balance for a steady-flow control volume (V_{evap}) shown in Equation 7-60.

$$q_{ent} - q_{exit} = q_{st} \tag{7-60}$$

Energy enters the volume in the fluid ($q_{F,ent}$) [W] and energy exits in the fluid ($q_{F,exit}$) [W], energy also leaves the volume through heat extraction (q_s) [W] at the *ground source-heat pump interface* (the evaporator wall) as follows:

$$q_{F,ent} - q_{F,exit} - q_s = q_{st} \tag{7-61}$$

Equation 7-61 is expanded to the form shown in Equation 7-62, where $\dot{V}_s$ [m^3/s] is the total source flow rate, q_s [W] is the source extraction by the heat pump, V_{evap} [m^3] is the volume of the evaporator's source side plate network and the superscript p refers to the previous time-step.

$$\dot{V}_s\left(T_{F,L_t} - T_{F,0}\right) - \frac{q_s}{\rho_F c_{p,F}} = \frac{V_{evap}}{\Delta t}\left(T_{F,0} - T_{F,0}^{p}\right) \tag{7-62}$$

When the volume of the evaporator's source side (V_{evap}) [m^3] is small and only a small amount of heat can be stored in it, Equation 7-62 reduces to:

$$T_{F,0} = T_{F,L_t} - \frac{q_s}{\rho_F c_{p,F} \dot{V}_s} \tag{7-63}$$

Including V_{evap}, then Equation 7-62 can be re-written as Equation 7-64 with a_9 defined in Equation 7-65.

$$T_{F,0} = \frac{\dot{V}_s T_{F,L_t} + a_9 T_{F,0}^p - (q_s / \rho_F c_{p,F})}{(\dot{V}_s + a_9)} \tag{7-64}$$

$$a_9 = \frac{V_{evap}}{2\Delta t} \tag{7-65}$$

The linear heat pump model Equation 6-10, from AL-7 in Sub-section 6.2.2, has been modified to suit Equation 7-64 as follows:

$$q_s\left(T_{sk,f}, T_{F,L_t}, \begin{bmatrix}1\\0\end{bmatrix}\right)[W] = \begin{bmatrix}1\\0\end{bmatrix} 950[(-0.0017T_{sk,f} + 0.4611)T_{F,L_t} + (-0.1316T_{sk,f} + 16.438)] \tag{7-66}$$

There is no need to solve Equations 7-66 and 7-64 simultaneously as q_s is evaluated at $T_{F,Lt}$ which is known from Equation 7-44 and the purpose of Equation 7-64 is to find $T_{F,0}$.

Figure 7-20 shows a comparison between simulated ΔT_{evap} for an evaporator with zero heat storage (Equation 7-63) and an evaporator containing 0.5l of water-glycol fluid (Equation 7-64). Where ΔT_{evap} is the temperature difference across the evaporator's source side as follows:

$$\Delta T_{evap} = T_{F,L_t} - T_{F,0} \tag{7-67}$$

It can be seen that the stored energy is significant only at the start of a cycle; accounting for this stored energy in simulations is important for a heat pump system that cycles frequently.

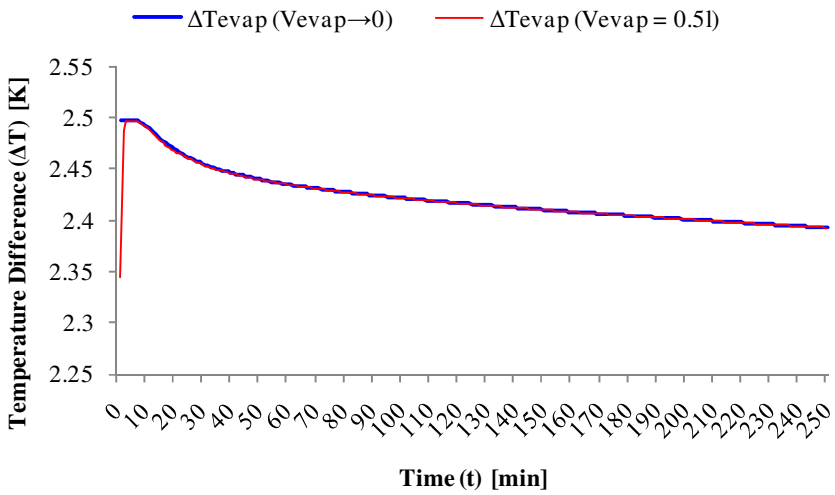

Figure 7-20: Variation in simulated evaporator temperature drop (ΔT_{evap}) with time using NL-5

Coupling the collector elements of NL-5 with a heat pump component which includes $T_{s,r}$ feed-back such as AL-7, is a novel element of this method and represents a significant development on the Demir *et al.* 2009 method.

7.3.2.4 Other Nodes in the Pipe-ground Simulation Domain

The other nodes required to complete the NL-5 *pipe-ground simulation domain* can be catered for using previously defined nodes and sub-models as follows:

- For the *ground-atmosphere interface,* the nodes described in model NL-4, Sub-section 7.2.2.1 and validated in NL-1, Section 5.4 can be used
- In the absence of high resolution weather data the ground surface temperature (T_{sur}) variation with time can be expressed using model AL-4 or AL-5 for hourly resolution, Section 4.2
- For standard or adiabatic underground nodes the equations described in Sub-section 7.2.2.2 can be used
- Model AL-4 can be used to calculate the variation in ground temperature (T_{LB}) with time (t) at the lower boundary nodes of the model
- Model AL-4 or AL-5 for hourly resolution can also be used to approximate the initial conditions for all the nodes, from T_{cov}/T_{sur} to T_{LB} and including $T_{F,L}$ for all pipe sections, at the beginning of the heat pump cycle simulation

7.3.3 NL-5 Implementation

As shown in Figure 7-21, model NL-5 was implemented in *MS-Excel* in a manner similar to NL-4 described in Sub-section 7.2.3, but based on the following conditions:

- As discussed in Sub-section 7.3.1, the dimensions of the W-Z-L plane are PS/2 x $\left|Z_{LB}\right|$ x L_t [m].
- As discussed in Sub-section 3.5.1, pipe spacing (PS) at the *HP-IRL/H* site varies between 0.25m in P4 and P5 and 0.4m in P3 and P6.
- With model NL-5 the option exists to either vary PS with length (L) or use the average PS of 0.32m derived using Equation 6-38, Section 6.4.3.1.
- A value of 5m was deemed sufficiently accurate for $\left|Z_{LB}\right|$ in Sub-section 7.2.3
- L_t is fixed at 150m, as shown in Table 3-5
- With $\Delta W=\Delta Z=(\pi D_o/2)$ [m], the ΔZ dimension for a 32mm pipe was approximated at 0.05m.

- Section length (ΔL) was assigned a value of 1, 5 and 10m in validations
  - While a ΔL of 1m was deemed necessary by Piechowski (1996) and Demir *et al.* (2009),
  - A value of 10m was deemed sufficiently accurate for NL-5 due to the novel $T_{F,av}$ concept introduced in Equation 7-32
- With these ΔZ and ΔL values the matrix of nodes (W, Z, L) needed for long-term simulation were (4, 100, 15)

Figure 7-21 shows a sample short-term simulation test with reduced matrices of (3, 16, 15):

- This simulation was used to test NL-5 accuracy over short time periods
- The accuracy of the *simulation domain* over long periods was tested using NL-4
- Unlike model NL-4, the matrices were not transposed
  - On a macro-level, pipe length (L) increases from left to right while time (t) increases from top to bottom
  - On a micro level, ground section width (W) increases from left to right while ground section depth (-Z) increases from top to bottom
- With a ground thermal diffusivity of 1.05 x 10^{-6} m^2/s, a ΔZ of 0.05m and a maximum collector Biot number of 3, a Δt of 60s was chosen to insure the Fourier number satisfies the stability criteria in Equation 7-14

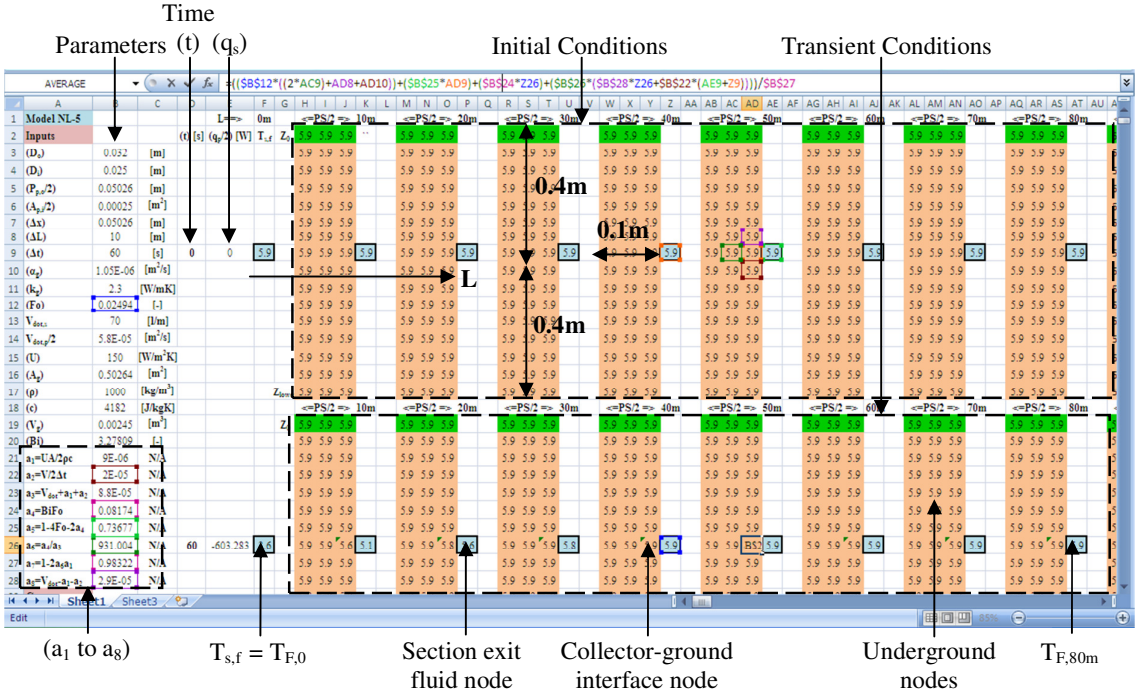

Figure 7-21: Model NL-5 implemented in MS-Excel with ΔZ = ΔW of 0.05m, ΔL of 10m and Δt of 60s

For input of equations, *Excel* is switched to '*show formula*' mode; this pauses the calculation of equations temporarily, while:

- The initial conditions are input for all nodes at t_0; thereafter the transient conditions are used
- The $T_{F,0}$ nodes (column F) are linked to the q_s values (column E) which are a function of the return node from the previous time-step (T^{p}_{F,L_t})
- The quasi-3-D model, NL-5, requires fluid nodes to be linked in length (L) along with ground nodes linked in W, Z and t, as was the case in NL-4
- The equations in this format and appropriate input columns are then propagated downward over the time-span of the required simulation, for large simulations (3 months) *Excel* requires as much as 12 hours to complete this process

For solution of equations, '*show formula*' mode is switched off

- Results for nodes of interest, at times of interest, can then be extracted by filtering through results with built-in *Excel* functionality
- Model parameters stored in Column B, Figure 7-15, can be changed and *Excel* then recalculates all equations within 10 minutes

7.3.4 NL-5 Sample Results

Figures 7-22(a) and (b) display quasi 3-D ((W, Z), L), colour coded, temperature maps of simulated ground and fluid temperatures over 3 time-steps. Figure 7-22(c) displays a comparison between the simulated, underground fluid temperature increase (ΔT_{HC}) after 1 and 700 minutes respectively. These figures are based on results from numerical simulations using model NL-5 in *MS-Excel* as described in Sub-section 7.3.3.

These sample results display the influence of both time (t) and pipe length (L) on the collector fluid temperature and the temperature of the surrounding ground. After 1 minute of operation, ground cooling is localised about the collector pipe while after 700 minutes the farfield radius has expanded to the limits of the sample model domain.

Cooling of the source can be seen particularly at the collector pipe inlet. Growth in the farfield (r_∞) [m] is equal at all lengths (L), however as expected, the magnitude of the ground cooling is more extreme at the pipe inlet. Figure 7-22(c) demonstrates how the collector becomes less effective as a heat source with operation time and COP decreases as a result. Detailed validations of NL-5 using *HP-IRL/H* data are presented in Sub-section 7.4.3.

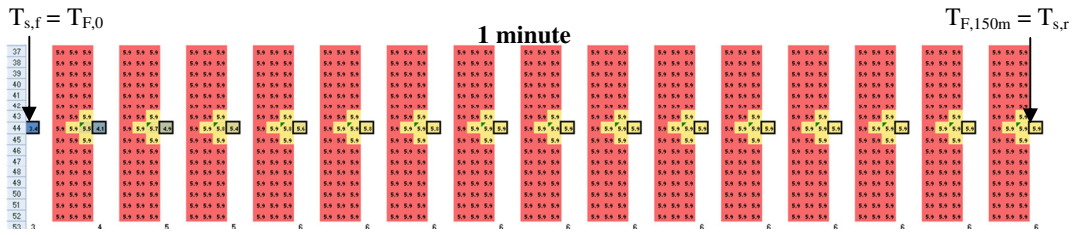

(a) $T_{F,0}$, $T_{F,10m}$.....$T_{F,150m}$ with surrounding ground temperature matrices after 1 minute of heat pump operation

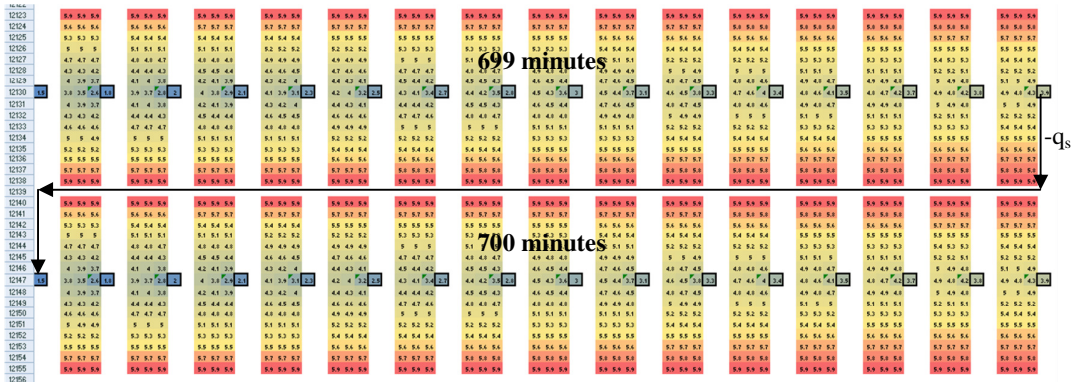

(b) $T_{F,0}$, $T_{F,10m}$.....$T_{F,150m}$ with surrounding ground temperature matrices after 699 and 700 minutes of operation

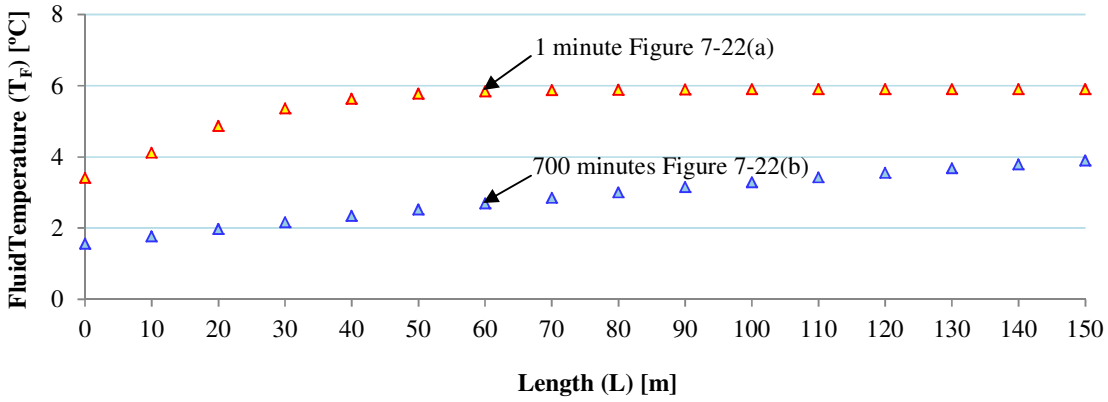

(c) Increase in $T_{F,L}$ with pipe length between $T_{F,0}$ and $T_{F,150m}$ after 1 and 700 minutes of operation

Figure 7-22: Typical output from model NL-5 sample simulation

7.3.5 Efficient Meshing of the Pipe-ground Simulation Domain

The *pipe-ground simulation domain*, defined as (PS/2, Z_{LB}, L_t) [m] in Sub-section 7.3.1, measures (0.15, 5, 150) [m] for the *HP-IRL/H* collector. Figure 7-23(a) displays the W-Z plane of the *pipe-ground simulation domain* including the collector pipe drawn exactly to scale. As discussed in Sub-section 7.1.5 and shown in Figures 7-23(b) and (c), efficient meshing of the W-Z plane can be achieved by concentrating the finer mesh at the *ground-atmosphere interface* and the *collector-ground interface*, while using a coarser mesh, as shown in Figures 7-23(d) and (e), where temperature gradients are less pronounced.

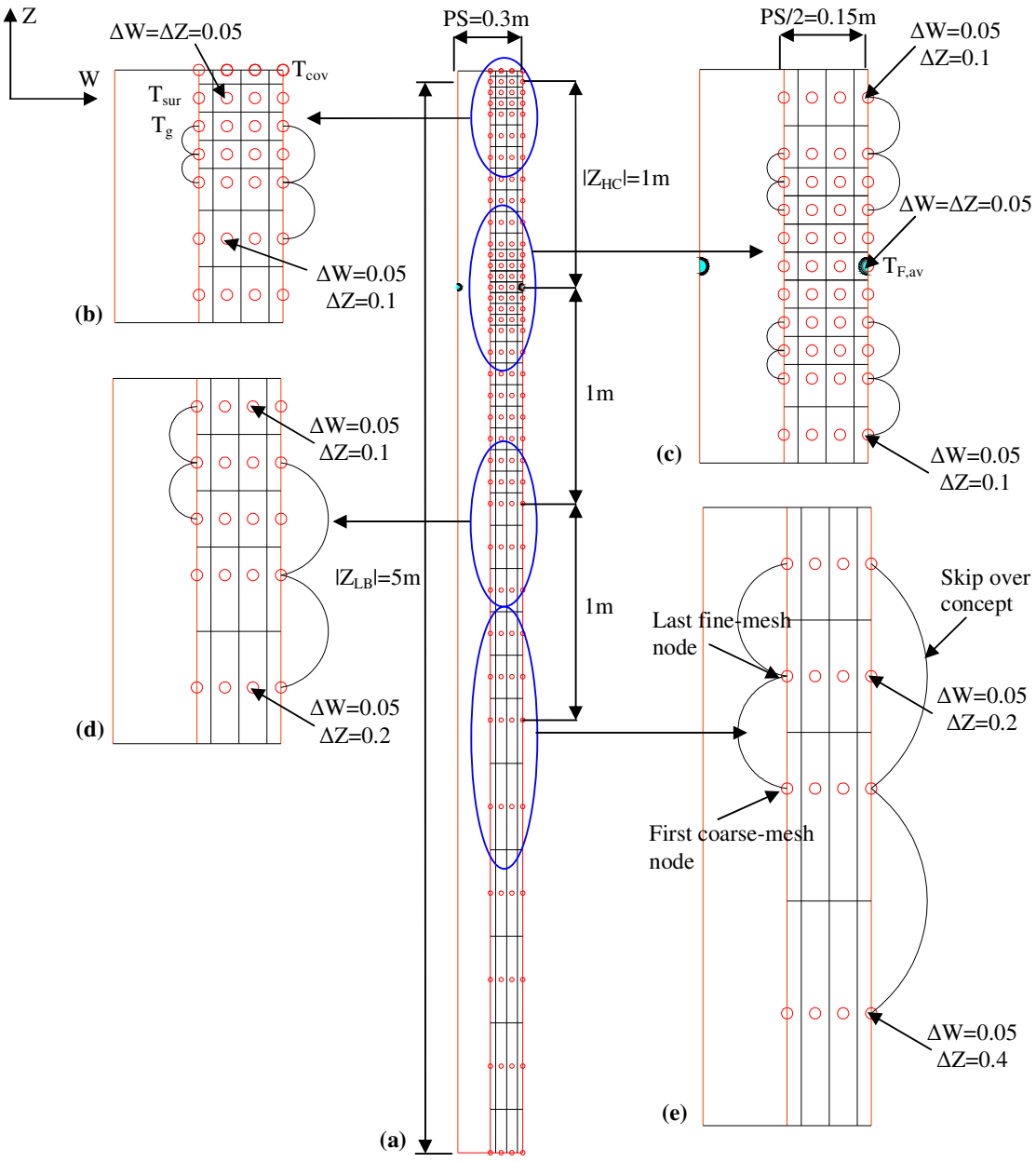

Figure 7-23: Efficient meshing the W-Z plane of the pipe-ground simulation domain, the W-Z plane and mesh sizes are drawn to scale using the HP-IRL/H dimensions

Figure 7-23(b) displays the *ground-atmosphere interface* and the *mesh-interface* between the (0.05, 0.05) [m] and the (0.05, 0.1) [m] meshes. Figure 7-23(c) displays the *collector-ground interface* and the *mesh-interfaces* between the (0.05, 0.05) [m] and the (0.05, 0.1) [m] meshes. Figures 7-23(d) and (e) display the *mesh-interfaces* at Z= -2m and Z= -3m respectively, where mesh size is increased to (0.05, 0.2) [m] and then (0.05, 0.4m). By implementing these changes to the mesh, the following two problems arise:

- Interface nodes cannot be linked in the normal fashion

- The underground nodes become non-uniform ($\Delta W \neq \Delta Z$)

Solutions to these two problems are now discussed.

7.3.5.1 Skip Over Concept

Since solutions for the 'last fine-mesh node' and the 'first coarse-mesh node' both require an equidistant node on their left and right, the 'skip over concept' shown in Figures 7-23(b), (c) and (d) and labelled in Figure 7-23(e) is used. Figure 7-24 displays one-dimensional testing of the interface between surface fine-mesh and underground coarse-mesh using the 'skip over'. This meshing of alternative FDM grids can be achieved with no loss in accuracy.

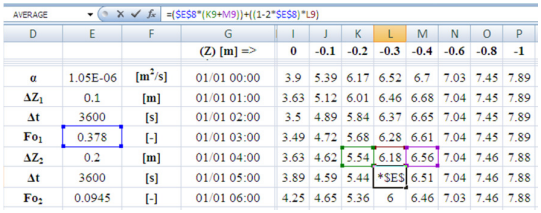

			(Z) [m] =>	0	-0.1	-0.2	-0.3	-0.4	-0.6	-0.8	-1
α	1.05E-06	[m^2/s]	01/01 00:00	3.9	5.39	6.17	6.52	6.7	7.03	7.45	7.89
ΔZ_1	0.1	[m]	01/01 01:00	3.63	5.12	6.01	6.46	6.68	7.04	7.45	7.89
Δt	3600	[s]	01/01 02:00	3.5	4.89	5.84	6.37	6.65	7.04	7.45	7.89
Fo_1	0.378	[-]	01/01 03:00	3.49	4.72	5.68	6.28	6.61	7.04	7.45	7.89
ΔZ_2	0.2	[m]	01/01 04:00	3.63	4.62	5.54	6.18	6.56	7.04	7.46	7.88
Δt	3600	[s]	01/01 05:00	3.89	4.59	5.44	*$ES	6.51	7.04	7.46	7.88
Fo_2	0.0945	[-]	01/01 06:00	4.25	4.65	5.36	6	6.46	7.03	7.46	7.88

(a) Last fine-mesh node solution uses Fo_1

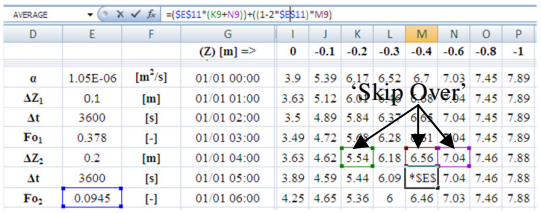

			(Z) [m] =>	0	-0.1	-0.2	-0.3	-0.4	-0.6	-0.8	-1
α	1.05E-06	[m^2/s]	01/01 00:00	3.9	5.39	6.17	6.52	6.7	7.03	7.45	7.89
ΔZ_1	0.1	[m]	01/01 01:00	3.63	5.12	6.01	6.46	6.68	7.04	7.45	7.89
Δt	3600	[s]	01/01 02:00	3.5	4.89	5.84	6.37	6.65	7.04	7.45	7.89
Fo_1	0.378	[-]	01/01 03:00	3.49	4.72	5.68	6.28	6.61	7.04	7.45	7.89
ΔZ_2	0.2	[m]	01/01 04:00	3.63	4.62	5.54	6.18	6.56	7.04	7.46	7.88
Δt	3600	[s]	01/01 05:00	3.89	4.59	5.44	6.09	*$ES	7.04	7.46	7.88
Fo_2	0.0945	[-]	01/01 06:00	4.25	4.65	5.36	6	6.46	7.03	7.46	7.88

(b) First coarse-mesh node solution uses Fo_2

Figure 7-24: 1-D testing of the mesh-interface between surface fine-mesh and underground coarse-mesh

7.3.5.2 Two Dimensional Non-uniform Underground Node

As expected, Figure 7-23 also shows that by increasing the ΔZ dimension while maintaining a constant ΔW dimension the underground nodes become non-uniform ($\Delta W \neq \Delta Z$) as shown in Figure 7-25.

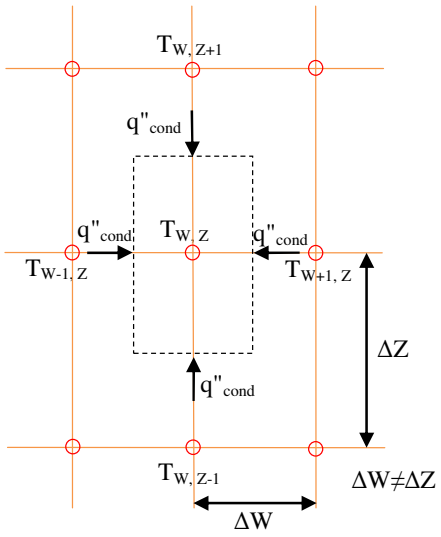

Figure 7-25: Model geometry for the non-uniform underground node

The solution for the non-uniform node differs from the standard 2-D node described in Sub-section 7.2.2.2 and in numerous text books (Incorpera & DeWitt, 2002). Therefore, a solution was derived based on the energy balance in Equation 7-68.

$$q^{(W-1,Z)\rightarrow(W,Z)} + q^{(W+1,Z)\rightarrow(W,Z)} + q^{(W,Z-1)\rightarrow(W,Z)} + q^{(W,Z+1)\rightarrow(W,Z)} = q_{st} \quad (7\text{-}68)$$

The terms in Equation 7-68 are then individually defined, using the geometry in Figure 7-25, as follows:

$$q^{(W-1,Z)\rightarrow(W,Z)} = k(\Delta Z.\Delta L)\frac{T^{p}_{W-1,Z} - T^{p}_{W,Z}}{\Delta W} \quad (7\text{-}69)$$

$$q^{(W+1,Z)\rightarrow(W,Z)} = k(\Delta Z.\Delta L)\frac{T^{p}_{W+1,Z} - T^{p}_{W,Z}}{\Delta W} \quad (7\text{-}70)$$

$$q^{(W,Z-1)\rightarrow(W,Z)} = k(\Delta W.\Delta L)\frac{T^{p}_{W,Z-1} - T^{p}_{W,Z}}{\Delta Z} \quad (7\text{-}71)$$

$$q^{(W,Z+1)\rightarrow(W,Z)} = k(\Delta W.\Delta L)\frac{T^{p}_{W,Z+1} - T^{p}_{W,Z}}{\Delta Z} \quad (7\text{-}72)$$

$$q_{st} = \rho c(\Delta W.\Delta Z.\Delta L)\frac{T_{W,Z} - T^{p}_{W,Z}}{\Delta t} \quad (7\text{-}73)$$

Substituting Equations 7-69 through 7-73 into Equation 7-68 and simplifying using the twin Fourier numbers Fo_W and Fo_Z results in Equations 7-74, where Fo_W and Fo_Z are defined in Equations 7-75 and 7-76 respectively.

$$T_{W,Z} = Fo_W(T^{p}_{W-1,Z} + T^{p}_{W+1,Z}) + Fo_Z(T^{p}_{W,Z-1} + T^{p}_{W,Z+1}) + (1 - 2Fo_W - 2Fo_Z)T^{p}_{W,Z} \quad (7\text{-}74)$$

$$Fo_W = \frac{\alpha\Delta t}{\Delta W^2} \quad (7\text{-}75)$$

$$Fo_Z = \frac{\alpha\Delta t}{\Delta Z^2} \quad (7\text{-}76)$$

The developments described here and in the previous sub-section mean that a variety of Fourier numbers (Fo_1, Fo_2...Fo_n) are required at different layers and for non-uniform layers twin Fourier numbers ($Fo_{n,W}$ and $Fo_{n,Z}$) are required. Alternatively, 1-D (Z only) solutions can be sufficient in layers other than the *collector-ground interface* region and these 1-D solutions can then be interfaced with the 2-D *collector-ground interface* mesh at a sufficient distance from Z_{HC}.

7.3.5.3 Spatial, Temporal and Solution Intensity-Comparison

It was shown in Sub-section 7.3.2.1 that ΔL could be increased from 1 to 10m using the novel $T_{F,av}$ concept. Additionally, it was shown in the previous sub-section that ΔZ can be increased

from 0.05 to 0.4m in regions where thermal gradients are less pronounced. Using the *HP-IRL/H* collector dimensions to evaluate the number of equation solutions required per time-step and per hour of $GSHP_{HC}$ operation, Table 7-4 compares the spatial and temporal solution intensity of the NL-5 method, outlined in this section, with the most recent $GSHP_{HC}$ simulation method presented by Demir *et al*. (2009).

Table 7-4: Spatial and temporal solution intensity comparison

Comparison		**Demir *et al.* (2009)**	***HP-IRL/H* NL-5**
	ΔW [m]	0.1	0.05
	ΔZ [m]	0.1	0.05, 0.1, 0.2, 0.4
	ΔL [m]	1	10
# of Spatial Increments	(W, Z, L)	(≈2, 50, 150)	(3, 37, 15)
	Equations/time-step	15,000	1665
FDM	Equation format	IFD	EFD
Temporal	Δt [min]	30	1
	Equations/hour of heat pump operation	30,000	99,900
Solution	Equation Solution method	Thomas Algorithm	*MS-Excel*

Table 7-4 demonstrates that while NL-5 requires only 1665 equations per time-step, approximately 10 times less than Demir *et al.* (2009), the short EFD time-step of 1 minute means over 3 times as many equations must be solved per hour of heat pump operation. However, the *Solterra 500* and many other heat pumps cycle on and off every 5 to 10 minutes meaning a time-step of 5 minutes or less must be catered for; this puts the NL-5 solution intensity on a par with Demir *et al.* (2009).

7.3.6 Distinctive Elements of the NL-5 Method

Model NL-5 is a distinctly versatile method for simulating horizontal collectors, as it accommodates the following variations:

- Below the collector the lower boundary (Z_{LB}) condition can be either: fixed temperature, periodic temperature (Equation 4-14, AL-4) or a geothermal heat flux
  - This flexibility is not possible with existing axis-symmetric models
- The ground thermal properties can be varied with depth allowing for a surface cover layer such as grass, a variety of soil texture layers, sand around the collector pipes, and bedrock beneath the collector to be incorporated into the model (this is the case at *HP-IRL/H* site)
  - This is not possible with existing axis-symmetric models

- Additionally the thermal properties of these layers can be varied based on moisture content at the site (AL-6)

- Heat exchanger pipe spacing (PS) and the depth of the pipe (Z_{HC}) can be varied along the length of the collector pipe (L) (this is the case at *HP-IRL/H* site)
  - This is not possible with existing axis-symmetric models
- The collector pipe convection coefficient (h) can be varied along the length (L), according to Equation 6-30
  - This allows NL-5 to mimic real-life more accurately
- Surface cover can be varied with length (this is the case at *HP-IRL/H* site)
  - This is typically not possible with existing models
- The intensity of solar radiation incident on the *ground-atmosphere interface* can be varied depending on surface slope and orientation using Equation 5-39 and model AL-1, described in Sub-section 4.2.1, to calculate hourly cosΘ values
  - This is the first time such a boundary condition has been included in $GSHP_{HC}$ simulation
  - This is the first study to highlight the potential significance of surface slope, mainly because this depends on mild conditions during *Cool Marine* winters
- Source extraction (q_s) for the heat pump varies with both $T_{s,r}$ and $T_{sk,f}$ according to model AL-7, described in Sub-section 6.2.2
  - This allows NL-5 to mimic real-life $GSHP_{HC}$ operation more accurately
- Flow rate through the collector can be varied
- Concepts for low resistance pipe designs can be tested by changing the combined heat transfer coefficient (U) [W/m^2K]:
  - Convection resistance can be lowered to mimic internal fins
  - Conduction resistance can be lowered to mimic external fins

7.4 VALIDATION

This section presents testing and validation of the transient numerical simulation methods developed during the *HP-IRL/H* project. The numerical methods NL-1 (Sub-section 5.4.1), NL-4 (Section 7.2) and NL-5 (Section 7.3) are used in Chapter 8 to test changes to the surface cover, the collector design and the collector control respectively. Therefore, it is important to assess model functionality and prediction accuracy. Given the extensive experimental facility, described in Chapter 3, and the considerable data gathered between 2007 and 2010, the methods of '*historical* [experimental] *data validation*', '*extreme condition testing*' and

'*comparison to other models*' were used (Sargent, 1996). Table 7-5 presents an overview of the validation methodology. Key simulation components were tested individually in order to quantify individual sources of error in isolation.

Table 7-5: Overview of the validation methodology

Model	Purpose of test	Period of test
NL-1	Long-term testing of the *ground-atmosphere interface* node at hourly intervals	01/01/2008 to 31/12/2008 and 05/01/2009 to 06/04/2009 (HC9)
NL-4	Long-term testing of the *pipe-ground simulation domain* and the *collector-ground interface* node (heat flux condition) at 12 minute intervals	05/01/2009 to 06/04/2009 (HC9) and 05/02/2010 to 26/02/2010 (HC10)
NL-5	Short-term testing of the pipe section exiting fluid node and the *collector-ground interface* node (convection condition) at 1 minute intervals during steady and cyclic operation patterns	11/11/2007 (HC3) and 05/01/2009 (HC9)

7.4.1 NL-1 Validation

As shown in Table 7-5, NL-1 was tested primarily between January and December 2008 at 1 hour intervals; 2008 was the most complete climate and ground dataset gathered during *HP-IRL/H*. The goal of the validation process was to trial the 1-D *ground-atmosphere interface* node in isolation. This node is used in the 2-D form in both NL-4 and NL-5 where the influence of a horizontal collector is also included; therefore it is tested here without any collector influence using the reference profile, P1.

7.4.1.1 Historical Data Validation

Comparison of simulated and measured undisturbed ground temperatures was previously described in Sub-section 5.4.3. The comparison in this section aims to establish short-term maximum and average error along with possible sources of error. Figures 7-26(a), (b), (c) and (d) display an hourly comparison of measured (P1) and simulated (NL-1) ground temperature at the ground surface (Z = 0.0m) and beneath the surface (Z = -0.15m), over one week in spring, summer, autumn and winter respectively. Predictive accuracy improves with depth due to dampening of short-term fluctuations. However, validation is conducted at 0.0m and -0.15m, where error is likely to be greatest, in accordance with the *extreme condition testing* methodology of Sargent (1996). Measured values of air temperature (T_a) [ºC], wind speed (u_{wind}) [kph] and solar radiation intensity ($q''_{S,t}$) [W/m^2] are overlaid. Values for September 21st are not presented due to a gap in data.

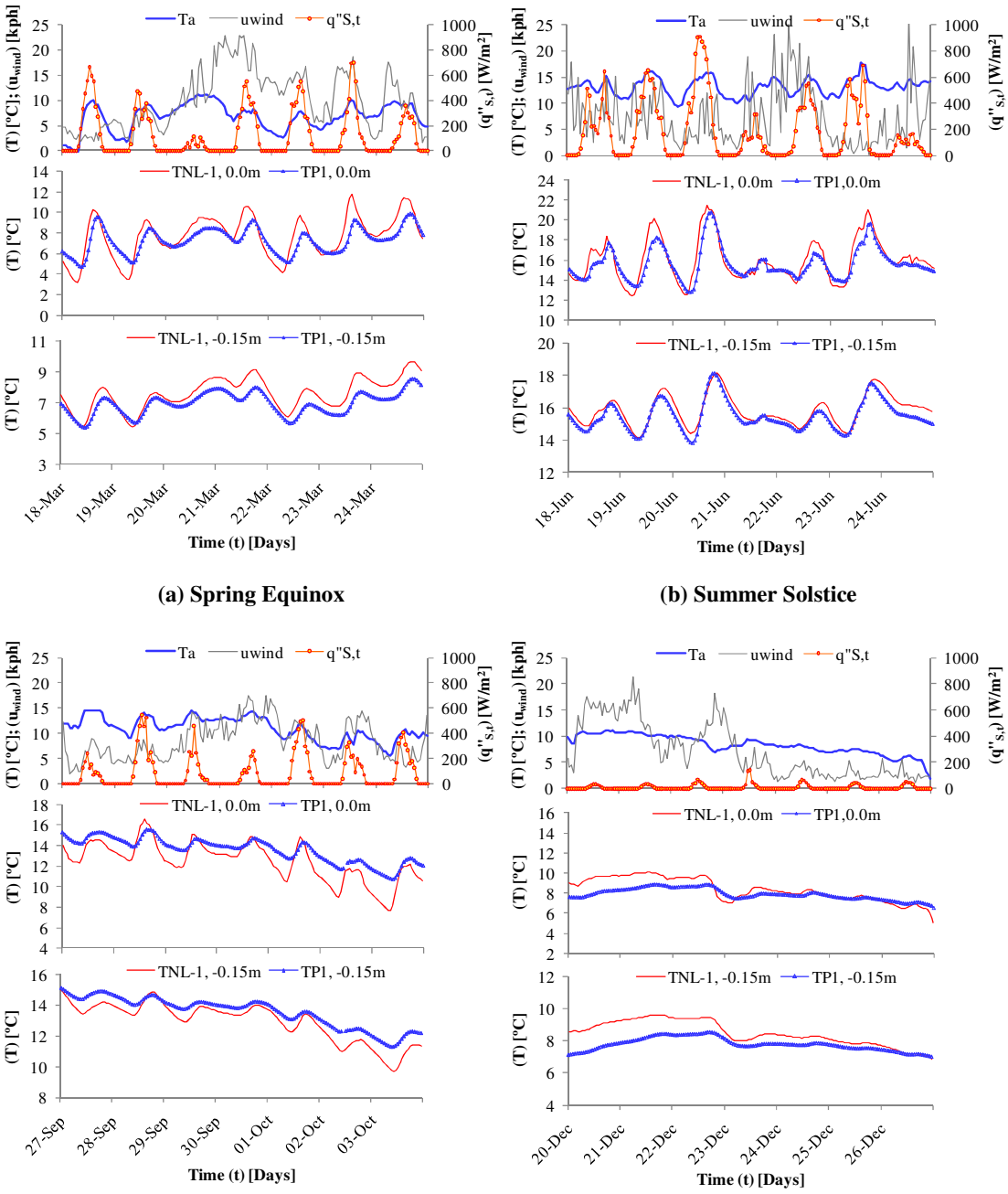

(a) Spring Equinox **(b) Summer Solstice**

(c) Autumn (DAQ error on 21st) **(d) Winter Solstice**

Figure 7-26: Comparison of measured and simulated (NL-1) temperatures at 0.0 and -0.15m during 2008

Based on the data displayed in Figure 7-26, the mean and maximum simulation error in each season is displayed in Table 7-6. The average error at the ground surface (0.0m) is highest in autumn, at -1.1K, and approximately equal during all other seasons, at +0.3 to 0.4K. During winter, the season that *GSHP$_{HC}$* simulation is most likely conducted, the average and maximum error at the surface are +0.4K and +1.6K respectively. The simulation appears to operate best during the daylight hours and particularly during periods of increased solar

intensity. Surface cooling at night is often over-estimated, particularly during periods of high winds suggesting error in the convection coefficient correlation. Additionally, *HP-IRL/H* wind speed data was measured at 10m above ground, which may over-estimate wind speed at ground level.

Table 7-6: Prediction accuracy of model NL-1 at the ground surface and subsurface for 2008

	Z	Spring	Summer	Autumn	Winter
NL-1 Mean error	0.0m	+0.4K	+0.3K	-1.1K	+0.4K
NL-1 Mean error	-0.15m	+0.6K	+0.4K	-0.6K	+0.7K
NL-1 Maximum error	0.0m	+3.6K	+3.1K	-3.1K	+1.6K
NL-1 Maximum error	-0.15m	+1.5K	+0.8K	-1.6K	+1.4K

7.4.1.2 Comparison to Other Models

Figure 7-27 displays measured ground temperatures and those simulated using both NL-1 and NL-2 which was created using the *SHAW23* software, described in Sub-section 5.4.2.

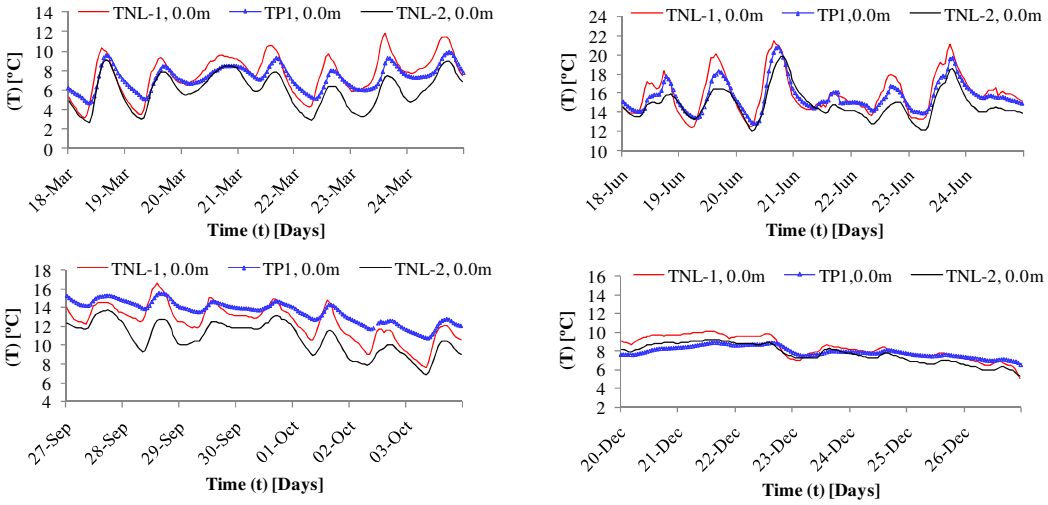

Figure 7-27: Comparison of measured ground temperatures, over the 4 seasons of 2008, with temperatures simulated using the HP-IRL/H model (NL-1) and the SHAW23 model (NL-2)

In Sub-section 5.4.3 models NL-1 and NL-2 were shown to have annual R^2 values at Z= 0.0m of 0.9026 and 0.9375 with average annual error at all depths of -0.2K and -0.5K respectively. Figure 7-27 shows that model NL-1 simulates ground surface temperature more accurately than *SHAW23* in all seasons except winter. This is due to the freedom which a custom model, developed in *HP-IRL/H*, gives to create a more accurate replica of site specific ground conditions and thermal properties of layers. Additionally, a custom model can then be

modified to include a horizontal collector while the *SHAW23* software is not designed for such a purpose.

7.4.1.3 Vertical Space Increment ΔZ and Stability Criteria

As discussed in Sub-section 5.4.1, the stability of an EFD numerical simulation is sensitive to the ratio between the vertical space increment (ΔZ) and the time-step (Δt). In the underground layers this does not present a problem since larger increments ($\Delta Z \geq 0.2$m) can be used to satisfy the stability criteria. However, at the *ground-atmosphere interface* a problem occurs when including thin surface cover layers ($Z_{cov} \leq 0.1$m). One solution to this problem, as shown in Figure 7-28, is to combine the surface cover layer with the bulk surface layer and then simulate this combined layer with average or weighted-average thermal properties. The surface temperature (T_{sur}) which corresponds to $T_{P1,\ 0.0m}$ can then be calculated by interpolating between the T_{cov} and T_g solutions.

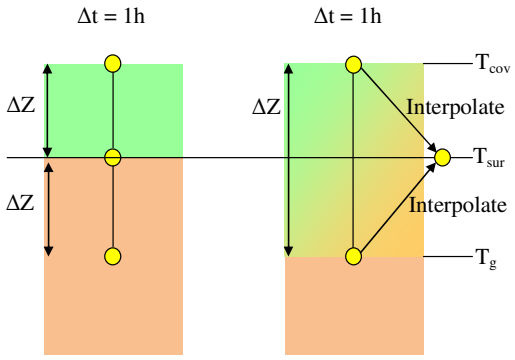

(a) Small ΔZ unstable **(b) Larger ΔZ stable**

Figure 7-28: Solution to calculating a stable surface temperature under a thin surface cover layer

Figure 7-29 displays a comparison between NL-1 simulations using the methods shown in Figures 7-28(a) and (b) evaluated at ΔZ of 0.1 and 0.25m respectively. It can be seen that the instability in $T_{NL\text{-}1,\ 0.0m}$ which occurs at ΔZ of 0.1m can be avoided using a ΔZ of 0.25m and interpolating between $T_{NL\text{-}1,\ +0.1m}$ and $T_{NL\text{-}1,\ -0.15m}$. As discussed in Sub-section 5.4.1, instability in the numerical solution occurs when Fo(1 + Bi) exceeds 0.5, where Fo is the Fourier number (Equation 5-33) and Bi is the Biot number (Equation 5-37). High wind speeds (u_{wind}) result in an increased convection coefficient (h) and hence increased Biot number (Bi). For ΔZ = 0.1 the Fo number is also high and as a result Fo(1 + Bi) exceeds 0.5. However, for ΔZ = 0.25m the reduced Fo number compensates for the increased Bi and instability is avoided. Therefore, this concept has been used in NL-1 simulations of undisturbed GTD in this study.

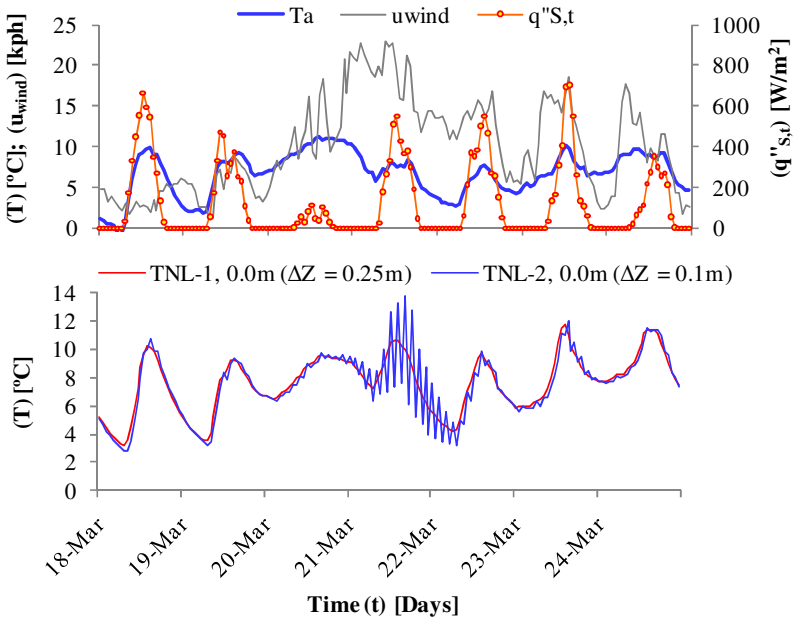

Figure 7-29: Comparison of simulated ground temperatures, created using model NL-1 with ΔZ of 0.25m and 0.1m; at ΔZ of 0.25m $T_{NL-1,\ 0.0m}$ are interpolated from $T_{NL-1,\ +0.1m}$ and $T_{NL-1,-0.15m}$

7.4.1.4 Net Longwave Radiation Model

Figure 7-30 presents a comparison between NL-1 simulations of ground temperatures using modelled net longwave radiation ($q_{Rn,LW}$) included in Equation 5-3 and measured net longwave radiation ($q_{Rn,LW}$) using sensors No. 3 and 4, Table 3-10. It can be seen that use of the $q_{Rn,LW}$ model results in only slight difference between simulated results with a maximum difference of 2.2K during December 25th, 2008.

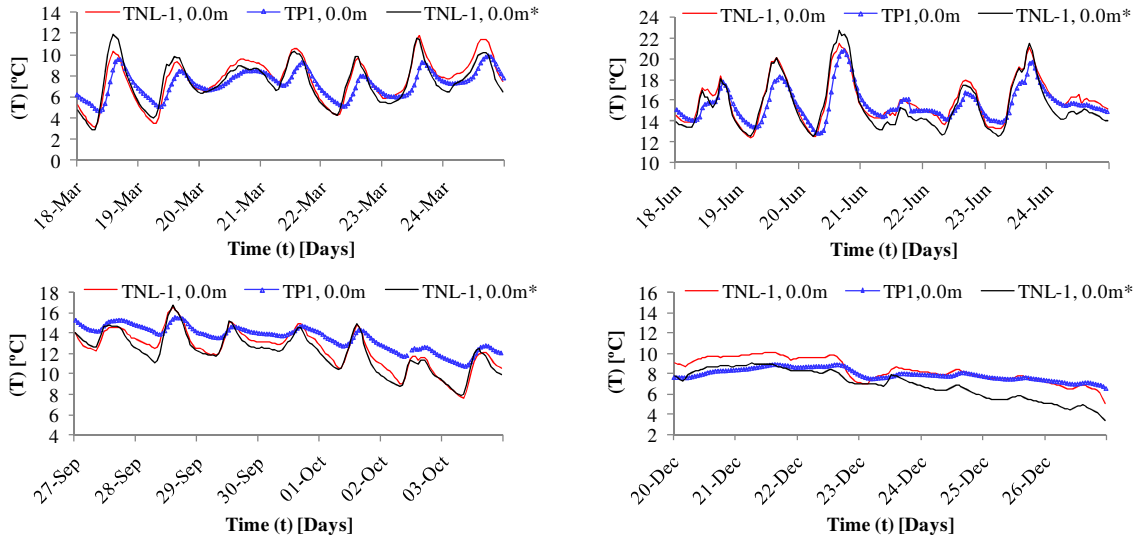

Figure 7-30: Comparison of measured ground temperatures with simulated values identified as $T_{NL-1,\ 0.0m}$ and $T_{NL-1,\ 0.0m}$* created using measured and calculated longwave radiation respectively

7.4.2 NL-4 Validation

As shown in Table 7-5, NL-4 was tested primarily between January and April 2009 (HC9) at 12 minute intervals. HC9, as defined in Table 6-2, combined extreme (21.1W/m^2) and prolonged (66 days) steady heat extraction. The goal of the validation process was to test the *pipe-ground simulation domain* and the *collector-ground interface* (heat flux condition) node in isolation. Therefore, the *ground-atmosphere interface node* was replaced with measured ground surface temperatures (T_{sur}), to remove average error of -1.1 to +0.3K introduced by the *ground-atmosphere interface node*, as defined in Sub-section 7.4.1.1. The *pipe-ground simulation domain* is used in the quasi 3-D form for NL-5, where the section exiting fluid node and the *collector-ground interface* (convection coefficient) are also included; therefore it is tested here in its simplest form using P3 and P4.

7.4.2.1 Historical Data Validation

As the goal of NL-4 testing was to validate the long-term validity of the *pipe-ground simulation domain*, testing involved an *extreme condition test* (Sargent, 1996). As shown in Equation 7-27, NL-4 involves applying a heat extraction load (q'_{HC}) to a pipe-ground section (ΔL). Additionally, as shown in Section 6.5, local heat extraction per meter ($q'_{HC,\,\Delta L}$) varies along collector length (L) and with time (t). Therefore, as shown in Equation 7-28, it is necessary to multiply the source extraction rate per meter of bisected pipe by the local heat extraction ratio ($\beta_{\Delta L}$). Figure 7-31 displays the variation in local heat extraction ratio ($\beta_{\Delta L}$) with operating time, this was calculated at the pipe inlet, P3, P4 and the pipe exit using model AL-11, described in Section 6.5.

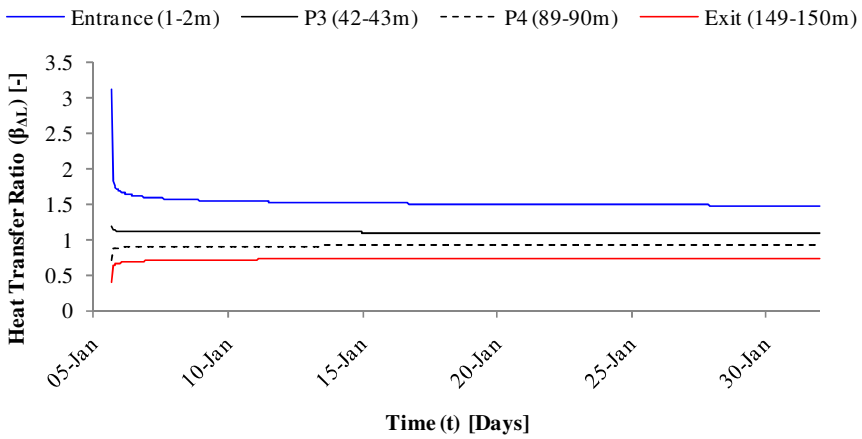

Figure 7-31: The variation in local heat extraction ratio ($\beta_{\Delta L}$) with time for four positions along the collector pipe length (L), calculated using AL-11

NL-4 simulations of P3, P4 and the pipe exit were then created using the steady-state $\beta_{\Delta L}$ values from Figure 7-31, measured q_s data from HC9 and the same Δt of 720s. The three models also require the parameters, PS, ΔZ, T_{sur} and q_s listed in Table 7-7.

Table 7-7: The values used for modelling four positions along the collector pipes

Location	L-1 to L	($\beta_{\Delta L}$) [-]	PS [m]	ΔZ [m]	Δt [s]	q_s [kW]	T_{sur} [ºC]	Z_{HC} [m]
Pipe Inlet	1 to 2m	1.43	0.3 (mean)	0.075	720	q_s (HP-IRL/H)	$T_{P1,\ 0.0m}$	-1m (mean)
Profile 3	42 to 43m	1.09	0.4	0.1	720	q_s (HP-IRL/H)	$T_{P3,\ -0.15m}$	-1.1m
Profile 4	89 to 90m	0.93	0.25	0.0625	720	q_s (HP-IRL/H)	$T_{P1,\ 0.0m}$	-1.0m
Pipe Exit	149 to 150m	0.76	0.3 (mean)	0.075	720	q_s (HP-IRL/H)	$T_{P1,\ 0.0m}$	-1m (mean)

Figure 7-32(a) compares measured and simulated *collector-ground interface* temperatures, $T_{P3,\ -1.15m}$ and $T_{NL-4,\ -1.1m}$ respectively, between January 1st and April 6th 2009. Based on the data presented in Figure 7-32(a), a maximum error for $T_{NL-4,\ -1.1m}$ of -0.96K was measured, with an average error of -0.25K and R^2 of 0.9832. Figure 7-32(b) compares measured and simulated temperature gradients for P3, in blue and red respectively. As discussed in Sub-section 7.4.2, $T_{P3,\ -0.15m}$ was used as the upper boundary condition in the NL-4 simulation and measured q_s data was also used in order to test the heat extraction component of NL-4 in isolation. Figure 7-32(b) shows that the simulated temperature gradients correspond to within 0.5K of the measured gradients, validating the choice of *pipe-ground simulation domain* selected in Sub-section 7.2.1. Figure 7-33 shows similar accuracy is achieved for P4. Figures 7-32(b) and 7-33(b) present novel thermal gradients extending 2m beneath the collector to Z= -3.0m which are not typically shown in the literature.

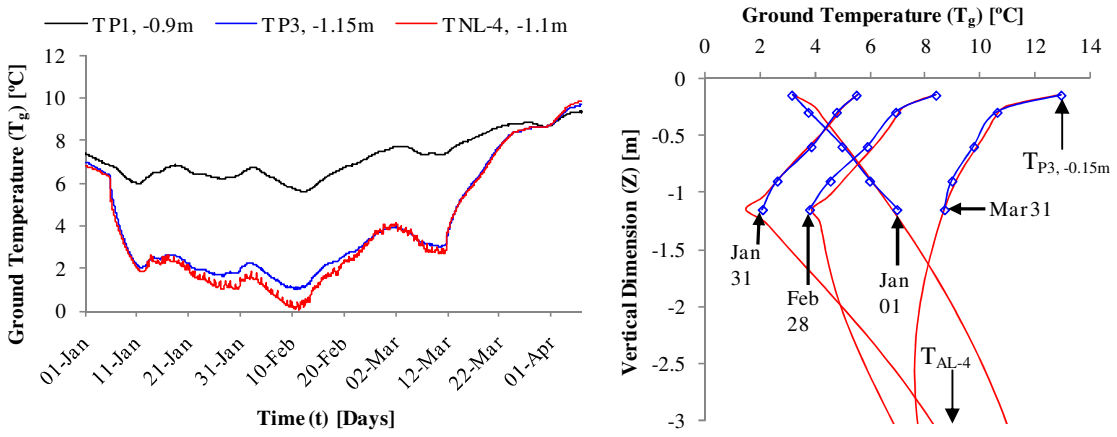

(a) Collector-ground interface and reference temperature **(b) P3 vertical temperature gradients**

Figure 7-32: Comparison of measured and simulated ground temperatures for P3 during HC9

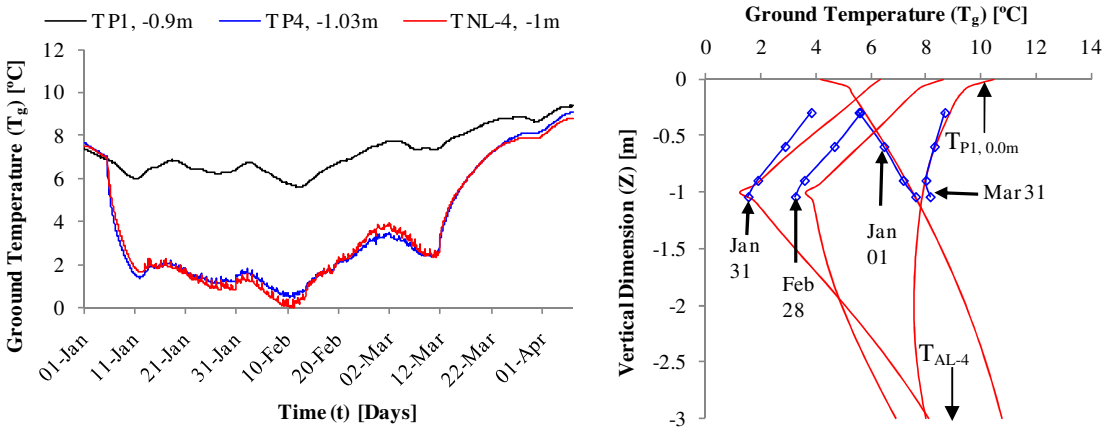

(a) Collector-ground interface and reference temperature **(b) P4 vertical temperature gradients**

Figure 7-33: Comparison of measured and simulated ground temperatures for P4 during HC9

7.4.2.2 Comparison to Other Models

The *collector-ground interface* node at the pipe exit section ($T_{p\text{-}g,\ 150m}$) was compared to $T_{s,r}$ and also $T_{s,r}$ (AL-9) which was evaluated using R_{rad} which assumes axis-symmetric heat transfer. Figure 7-34 shows a maximum error of +1K for NL-4 compared to a maximum error of +1.7K for AL-9, also an average error of +0.5K for NL-4 compared to an average error of +1.3K for AL-9. This comparison shows that while simulating the *collector-ground interface* at the pipe exit using a combination of NL-4 and $\beta_{\Delta L}$ from AL-11 is a simplified method, it gives a better approximation of $T_{s,r}$ than an axis-symmetric approach to a *parallel, inline* collector which form the basis of the Mei (1986) model and the TRNSYS software.

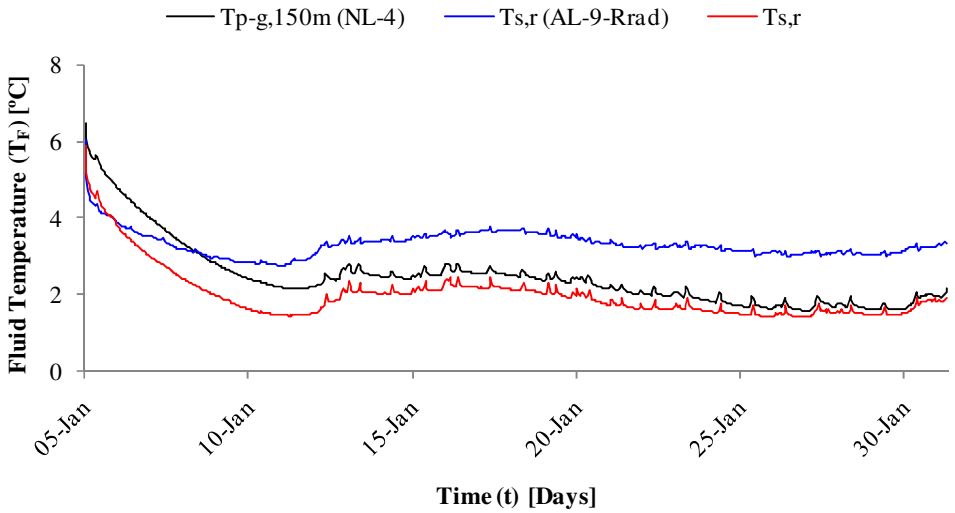

Figure 7-34: Comparison of measured source return temperature with simulated collector-ground interface temperature at the pipe exit section

7.4.3 NL-5 Validation

As shown in Table 7-5, NL-5 was tested primarily in November 2007 (HC3) and January 2009 (HC9) at 1 minute intervals. HC3, as defined in Table 6-2 and characterised in Figure 6-3, consisted of cyclic *GSHP$_{HC}$* operation with 59% duty due to low heat demand. HC9, as defined in Table 6-2 and characterised in Figure 6-4, consisted primarily of continuous *GSHP$_{HC}$* operation during the first month, with average duty for the 66 day period of 89%. The goal of the validation process was to test the pipe section exiting fluid node, the *collector-ground interface* node (heat transfer condition) and the heat pump's evaporator exiting fluid node which includes the linear heat pump model (AL-7) in isolation. Therefore, in order to remove error introduced by the *ground atmosphere interface node* and initial conditions, measured ground temperatures are used as the boundary and initial conditions in tests of NL-5.

7.4.3.1 Historical Data Validation

Figures 7-35(a) and (b) compare measured and simulated (NL-5) source flow ($T_{s,f}$) and return ($T_{s,r}$) temperatures, during HC3 and HC9 respectively.

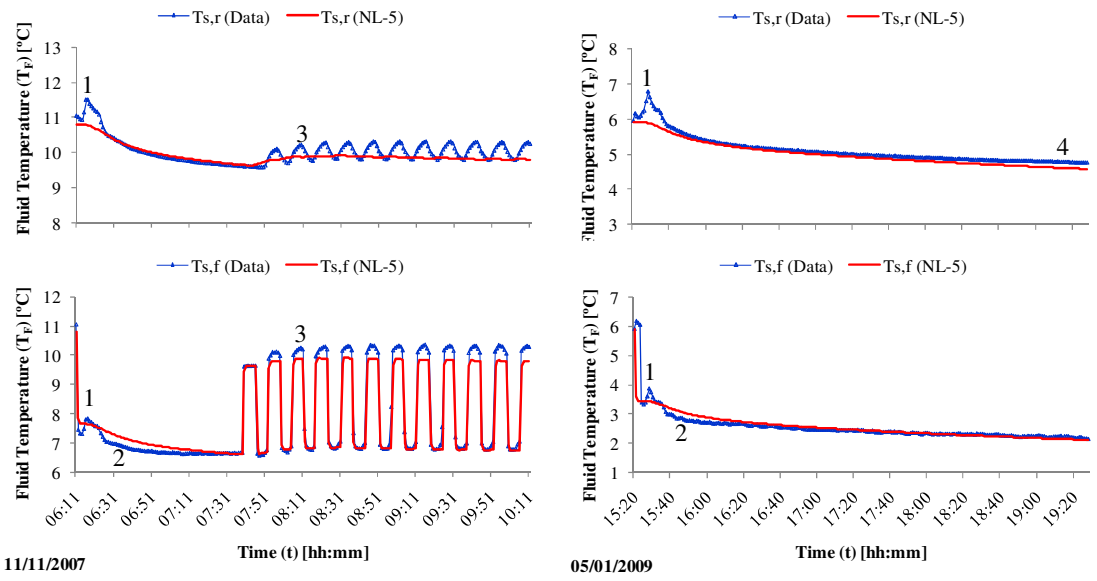

(a) HC3 cyclic operation during 11/11/2007 **(b) HC9 continuous operation during 05/01/2009**

Figure 7-35: Comparison of measured and simulated (NL-5) source flow and return temperatures during HC3 and HC9

During the cyclic operation of HC3, $T_{s,r}$ is simulated with a maximum error of -0.71K and an average error of -0.13K, $T_{s,f}$ is simulated with a maximum error of -1.39K and an average error -0.07K.

During the continuous operation of HC9, $T_{s,r}$ is simulated with a maximum error of -0.89K and an average error -0.12K, $T_{s,f}$ is simulated with a maximum error of -2.67K and an average error of -0.0079.

The simulated values correspond closely with measured values with the exception of 4 points identified. Possible reasons for these deviations are:

- (1) The source flow ($T_{s,f}$) and return ($T_{s,r}$) display a spike in temperature at the start of both heat extraction cycles
  - This may be caused by residual heat in the *$GSHP_{HC}$* run-out pipes or within the *Solterra 500* heat pump refrigerant
  - Neither of these components are included in NL-5 and as a result measured and simulated results differ at these times
- (2) Model NL-1 over estimates the source flow temperature ($T_{s,f}$) at the start of both heat extraction cycles
  - This is caused by a low extraction rate q_s [W] calculated by the heat pump model AL-7 which was used as a component of the NL-5 simulation
  - AL-7 was configured for a fixed $T_{sk,f}$ of 50ºC in simulations, whereas in reality the $T_{sk,f}$ heats up slowly from storage tank morning temperature (≈ 25ºC)
  - At lower $T_{sk,f}$ more heat is extracted from the source fluid as discussed in Sub-section 6.2.2
  - Coupling the model with storage tank data or a building-storage tank model would rectify this error
- (3) During the off period of cyclic operation the measured fluid temperatures exceed the predicted values
  - Some increase in temperature during these times is expected as the collector-ground interface undergoes short-term recovery
  - However, this is predicted by the simulation and the additional temperature increase in the measured results may be due to residual heat in the run-out pipes or heat pump
- (4) After 4 hours the predicted temperature for continuous operation begins to deviate slightly from the measured values
  - Like point 2, this may be linked to sink side temperatures and incorrect conditions used for AL-7

7.4.3.2 Length Increment (ΔL) and Accuracy

While Piechowski (1996) and Demir *et al.* (2009) used pipe length increments (ΔL) of 1m, the collector pipes they simulated were 24 and 40m long respectively. The *HP-IRL/H* collector pipes are 150m long and therefore an alternative ΔL of 10m was sought to reduce the number of sections required. Hence, novel equations for the pipe section exits ($T_{F,L}$) were derived in Sub-section 7.3.2.1, based on heat transfer rates at the average section temperature ($T_{F,av}$) rather than the exit temperature ($T_{F,L}$) as was used by Piechowski (1996).

Figure 7-36 shows a comparison between source return temperature simulated using exit nodes from the ($T_{F,L}$) derivation and the new ($T_{F,av}$) derivation. It can be seen that by changing from ΔL of 1m to ΔL of 10m using the ($T_{F,L}$) derivation an error is introduced. However with a ΔL of 10m using the ($T_{F,av}$) derivation this error is eliminated. This novel development means future simulations of this kind for any buried pipe systems can be conducted with larger sections lengths (ΔL) with no loss of accuracy.

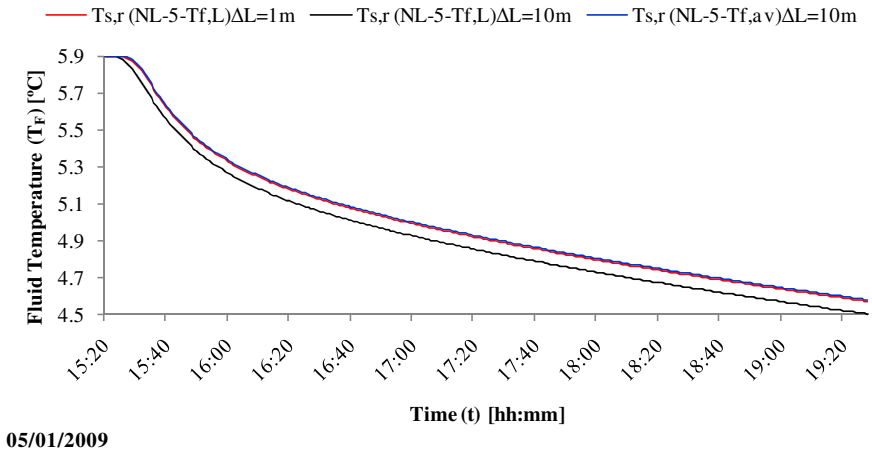

Figure 7-36: Comparison of NL-5 simulations using $T_{F,L}$ nodes derived at $T_{F,L}$ and $T_{F,av}$ for ΔL of 1m and 10m

7.5 DISCUSSION

The transient numerical models NL-1, NL-4 and NL-5 developed during the *HP-IRL/H* project have many practical advantages and also limitations when compared to existing methods/software. Along with this there are many benefits to developing custom models and immense insight is gained. These are now discussed.

7.5.1 Advantages of NL-1, NL-4 and NL-5

Advantages and distinctive elements of the modelling methods developed during *HP-IRL/H* are as follows:

- Improvements in the solution intensity per time-step using the $T_{F,av}$, non-uniform node and skip-over concepts are discussed in Sub-section 7.3.5
- Distinctive elements including weather influence, PS, Z_{HC} and h variability with L, *in-line, parallel* pipe interference and coupling to a responsive heat pump model are discussed in Sub-section 7.3.6
- Additionally, equations are written in EFD form, this means the mathematical solution is straight forward and does not require a complex solution algorithm,
    - Significantly, this enables straightforward inclusion of built-in *collector temperature feedback control*, a distinctive element of the *CSDC* approach

7.5.2 Limitations of Models

Limitations of the models are as follows:

- Unlike IFD equations, the EFD equations are only conditionally stable meaning an appropriate time-step needs to be used:
    - This is 1 hour for NL-1, 12 minutes for NL-4 and 1 minute for NL-5
    - However, since the *Solterra 500* undergoes cyclic operation on the time-scale of 5 to 10 minutes, these time-steps are required regardless
    - Upgrading to IFD is envisaged provided *collector temperature feedback control* can be accommodated in the code
- When compared with an analytical radial solution, the Cartesian coordinates produce a slight error (<0.5K) in the simulated results over the first 2 hours of simulation due the fact that a cylindrical pipe is represented by rectangular nodes
    - However, by concentrating a fine mesh at the *collector-ground interface* this error is greatly reduced
    - Coupling radial and Cartesian coordinates at the *collector-ground interface* is also envisaged
- Some real life processes such as soil freezing and combined heat and moisture transfer have been excluded
    - It has been shown in Sub-sections 7.1.6 and 7.1.7 that these processes are not needed for the mild and moist *Cool Marine* winter-mode operation under investigation in *HP-IRL/H*

- However, the mathematics of these processes has been researched in detail in Section 5.2 and future versions of the models can be altered to include these

- The model is implemented in *MS-Excel* for testing/validation and for the purposes of this *HP-IRL/H* project
  - However, it is envisaged that implementation in a more suitable programming environment, such as *Fortran* or *C++*, will make these modelling methods more useful for future C*i*SET research aims

7.5.3 Benefits to HP-IRL/H, CiSET and GSHP Research

Several detailed GSHP modelling procedures and design software tools already exist, as listed in Table 7-1 and Table 2-11 respectively, the most complete of these appears to be G-HEADS (Tarnawski & Leong, 1993; Healy & Ugursal, 1997). The author of this thesis accepts that the modelling methods described here were informed by components of the many other models referenced and in some aspects are less complete (incorporating fewer variables). However, the models have been developed to answer specific collector design and control questions relevant to the *Cool Marine* climate and achieve this requiring only the relevant inputs.

Therefore, these custom models have the following benefits to *HP-IRL/H*, C*i*SET and GSHP research.

- Less inputs are required, the models can survive on multiyear average inputs ($T_{g,y}$, $A_{sur,y}$ and $d_{sur,max}$); transient weather values ($q''_{s,t}$, T_a, RH, P_a and u_{wind}); heat pump datasheet values (q_s, q_{sk} and COP) and heat pump operational schedules [I/O]
- Good accuracy is achieved as presented in Section 7.4
- More experimental knowledge and empirical trends relevant to an actual $GSHP_{HC}$ application and the *Cool Marine* situation are incorporated
- First reported example of successful transient simulation of $GSHP_{HC}$ in the *Cool Marine geo-cluster*
- First reported example of a Cartesian horizontal collector model (NL-5) coupled to a responsive heat pump model (AL-7) with *collector-temperature feedback control*
- Validated with a substantial amount of experimental data (a range of experimental test periods taken from 3.6 years worth of data)
- Development of these models facilitated immense insight into the heat transfer processes and feedback loops involved in the operation of a complete $GSHP_{HC}$ system
- Facilitated learning in numerical methods for the C*i*SET team and formed the basis for continued numerical research into other SET and Hybrid SET

7.6 SUMMARY

This chapter presented a summary of transient numerical simulation methods developed during *HP-IRL/H* and contributed the following to the *HP-IRL/H* project:

Literature Review

- A review was conducted of 12 previous simulation methods, published in 5 countries using FDM, FEM and ANN numerical approaches
    - Other than Wibbels and Den Braven (1994) from Idaho, USA which is partially *Cool Marine* state and Wu *et al.* (2010), no simulation method was reported from a *Cool Marine* region
    - Demir *et al*. (2009) published the only simulation method for *parallel, inline* pipes but did not couple this with a responsive heat pump model
    - Previous methods are divided into 'analytical methods' and 'energy balance methods'
- The two most common analytical methods are:
    - The line-source method which treats the collector as a long thin line of constant heat flux
    - The *g*-functions method which involves superimposing a numerical solution for one pipe to simulate many pipes using an numerical/analytical approach
- The energy balance method was pioneered at the ORNL by Mei (1986) and involves splitting the collector into pipe-ground sections for simulation
    - The energy balance method can be used with radial or Cartesian geometries
    - Radial geometry introduces long-term error for *parallel, in-line* and shallow collectors
    - Cartesian geometry introduces short term error for cylindrical pipes
    - A combination of the two methods is proposed by Piechowski (1996)
    - A Cartesian geometry only with fine mesh elements at the *collector-ground interface* is also suitable
- Coupled heat and mass transfer and ground freezing are included in models by Piechowski (1996) and Tarnawski & Leong (1993) respectively
    - However, experimental results indicate that these processes can be ignored in mild and moist soil under the *Cool Marine* climate

Model NL-4: Transient 2-D GTD response to heat extraction by $GSHP_{HC}$

- Based on assumptions from the literature, a *pipe-ground simulation domain* is defined in Sub-section 7.2.1
- 2-D EFD equations for the following nodes are developed in Sub-section 7.2.2
  - *Ground-atmosphere interface* node
  - Underground nodes
  - Adiabatic nodes
  - Collector-ground interface node (Heat extraction condition)
  - Lower boundary nodes
  - Initial conditions
- Model NL-4 is implemented in *MS-Excel* as described in Sub-section 7.2.3 with the following conditions:
  - $\Delta Z = \Delta W = PS/4$ [m]
  - $\Delta t = 12$ minutes

Model NL-5: Transient underground fluid warming and simultaneous 3-D ground cooling

- Based on assumptions from the literature, a *pipe-ground simulation domain* is defined in Sub-section 7.3.1
- EFD equations for the following nodes are developed in Sub-section 7.3.2
  - Pipe section exiting fluid node
  - *Collector-ground interface* node (heat transfer condition)
  - Heat pump's evaporator exiting fluid node
- A sample model based on NL-5 was implemented in *MS-Excel* as described in Sub-section 7.3.3 with the following conditions:
  - $\Delta L = 10$m
  - $\Delta Z = \Delta W = 0.05$m
  - $\Delta t = 1$ minute
- Results from this sample model, showing 1-D fluid warming and quasi 3-D ground cooling are presented in Sub-section 7.3.4; these results show:
  - The influence of time on $GSHP_{HC}$ operation
  - The influence of distance from inlet (L) on fluid warming and ground cooling
  - Thermal interference between pipes
- A study on efficient meshing of the quasi 3-D pipe-ground simulation domain is presented in Sub-section 7.3.5

- It is shown that a fine mesh can be concentrated around the *collector-ground interface* and the *ground-atmosphere interface*
- Non-uniform nodes can be used in regions where temperature gradients are less pronounced
- The skip-over method is required to interface nodes of different sizes
- Multiple and twin-multiple Fourier numbers are required for multi-dimensional and non-uniform meshes

- Finally, model NL-5 has many distinctive elements which are discussed in Sub-section 7.3.6; these include:
  - Weather influence and thermal interference between pipes can be accounted for
  - PS, Z_{HC}, h, a, ε and other parameters can be varied along the collector length (L)

Validation

- Validations were presented for models NL-1, NL-4 and NL-5
- The validation method involved:
  - Historical data validation
  - Comparison with other models
  - Extreme condition testing
  - Parametric studies
- NL-1 is validated in Sub-section 7.4.1
  - The goal of these validations was to test the *ground-atmosphere interface* node in isolation therefore NL-1 was compared with P1 where no collector influence was present
  - Average annual error at all depths of -0.2K
  - Annual R^2 value at the bulk ground surface of 0.9026
  - The maximum average error at the bulk ground surface was -1.1K measured in autumn with average error of between +0.3 and +0.4K in the other three months
  - During winter when $GSHP_{HC}$ is used average error is +0.4K and maximum error is +1.6K
  - For hourly simulations ($\Delta t = 3600s$) ΔZ of 0.25m are required, temperatures at smaller Z intervals can be found by interpolating
- NL-4 is validated in Sub-section 7.4.2

- The goal of these validations was to test the *pipe-ground simulation domain* and the *collector-ground interface* node (heat extraction condition) in isolation, therefore NL-4 was compared to P3 and P4
- Measured boundary conditions were used in order to remove any error
- Comparing NL-4 with P3 produced an average error of -0.25K, a maximum error of -0.96K and an R^2 value of 0.9832
- Similar accuracy was measured when comparing NL-4 with P4
- NL-4 can be used to estimate return temperature ($T_{s,r}$) by simulating the exit of the collector pipe
- Comparing NL-4 with $T_{s,r}$ produced an average error of +0.5K with a maximum error of +1K

➢ NL-5 is validated in Sub-section 7.4.3

- The goal of these validations was to test the pipe section exiting fluid node, the collector-ground interface node (heat transfer condition) and the evaporator exiting fluid node in isolation, therefore NL-5 was compared to $T_{s,r}$ and $T_{s,f}$
- Measured boundary and initial conditions were used in order to remove error
- Simulations predicted flow and return temperatures with great accuracy
- During the cyclic operation of HC3, $T_{s,r}$ is simulated with a maximum error of -0.71K and an average error of -0.13K, $T_{s,f}$ is simulated with a maximum error of -1.39K and an average error -0.07K.
- During the continuous operation of HC9, $T_{s,r}$ is simulated with a maximum error of -0.89K and an average error -0.12K, $T_{s,f}$ is simulated with a maximum error of -2.67K and an average error of -0.0079.
- 2 sources of error were identified during continuous operation
- 4 sources of error were indentified during cyclic operation
- A parametric study showed that the $T_{F,av}$ validations used in Section 7.3 enabled a ΔL of 10m to be used instead of 1m with no error

The *HP-IRL/H* models have many advantages due to the realistic boundary conditions used and the influence of weather and pipe interference which are replicated. The models also have limitations due to the EFD formulation. The development of custom models has provided immense insight into *$GSHP_{HC}$* and these models can now be used to demonstrate the *CSDC* performance potential in Chapter 8.

CHAPTER 8

CLIMATE SENSITIVE DESIGN AND CONTROL

GMIT
GALWAY-MAYO INSTITUTE OF TECHNOLOGY
INSTITIÚID TEICNEOLAÍOCHTA NA GAILLIMHE-MAIGH EO

8. CLIMATE SENSITIVE DESIGN AND CONTROL

This chapter brings together the suite of numerical models, identified in Figure 3-28 and developed in Chapters 5, 6 and 7, to demonstrate the potential performance improvements that can accrue from undertaking a *CSDC* approach. Due to the flexibility of the numerical tools and the number of variables that can be investigated, this chapter (i) demonstrates how the numerical tools could be used to deliver a *CSDC* methodology (ii) presents the results of a simple demonstration exercise undertaken to establish the potential impact of *CSDC* on heat pump performance (iii) indentifies areas for future work.

Based on the $GSHP_{HC}$ *design groups* and associated literature presented in Table 2-13, 5 *design groups* were seen to have received limited attention to date. Of those 5, the following 3 remain to be explored in this chapter:

- *Surface cover*
- *Pipe layout and burial*
- *Operational control*

Therefore, this chapter describes the findings of numerical investigations on the $GSHP_{HC}$ performance sensitivity to: new *surface covers* such as a southerly-incline; new *pipe layout and burial methods* such as *split-level collectors* and non-uniform pipe spacing; as well as *collector temperature feedback control*. Results are divided into the following four sections:

- Ground temperature simulations – NL-1 and NL-2
- Heat extraction and control simulations – NL-4
- Collector design simulations – NL-5
- Summary and future work

8.1 GROUND TEMPERATURE SIMULATIONS – NL-1 and NL-2

This section describes the application of simulation tools NL-1 and NL-2, introduced in Figure 3-28, and described in Section 5.4, to simulate the undisturbed GTD under modified ground surfaces. It was assumed that any increase in undisturbed ground temperature at collector depth, due to modifications, yields an equivalent increase in source return temperature relative to a standard ground design. It was also assumed that an increase of 1K in source return temperature yields an average COP improvement of 2% (Cengel & Boles, 2002; Warnelof & Kronstrom, 2005; Burke *et al.*, 2008).

Inclined Ground Surface

As described in Sub-section 5.5.1.4, the occurrence of warmer ground surface temperatures on southerly slopes has been well established (Safanda, 1999; Kang *et al.*, 2000; Bennie *et al.*, 2008), however these investigations are outside of the $GSHP_{HC}$ literature. As defined in Figure 8-1, the Sun's angle of incidence ($\Theta = 90 - \acute{\alpha}$) [°] is much greater for a horizontal surface (β=0°, γ=N/A) than a surface with a southerly incline (β=40°, γ=180°) during winter.

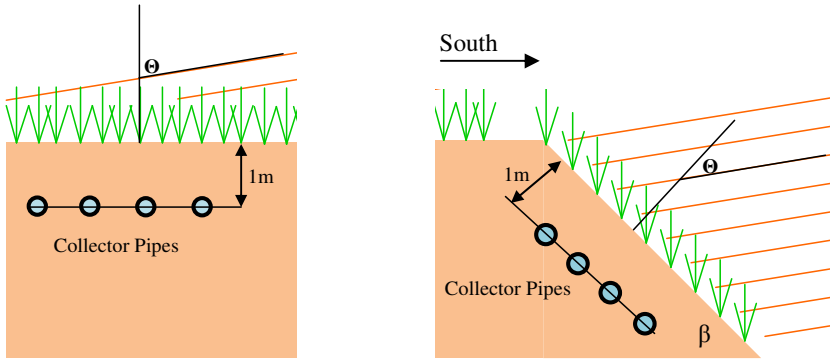

(a) Horizontal surface (β=0°, γ=N/A) **(b) Southerly incline (β=40°, γ=180°)**

Figure 8-1: Collector surface cover slope and orientation

The intensity of the Sun's rays is proportional to cosΘ (Sproul, 2007) and is therefore much stronger on southerly inclines relative to horizontal surfaces (Allen *et al.*, 2006). However, since the winter day is short and the path of the Sun's rays through the Earth's atmosphere is extended, coupled with the likelihood of cloudy skies and cold ambient temperatures, the surface temperatures on a southerly incline may not reflect the full positive impact of the increase in cosΘ. Winters in Ireland are typically quite mild and snow free, therefore this investigation sought to simulate the potential temperature increase in the ground between Z=0 and -1m for a 40° southerly incline under measured Irish *Cool Marine* climate conditions and therefore establish the temperature increase around the collector pipes at Z= -1m.

The following methods were used in order to calculate the influence of surface slope and orientation on incident solar radiation intensity and then simulate the GTD under an inclined surface:

- The influence of surface slope on the hourly angle of incidence (Θ) was found using Equation 4-7, AL-1, Sub-section 4.2.1
- The influence of angle of incidence (Θ) on measured solar radiation values ($q''_{s,t}$) was found using Equation 5-39, NL-1, Sub-section 5.4.1.2

- The GTD between 0 and -5m and also between 0 and -1.8m was simulated using NL-1 and NL-2 respectively, Section 5.4

The simulated findings of NL-1 and NL-2 were similar. Figures 8-2(a) and (b) display the daily average and daily maximum temperature differences between the southerly incline (β=40º, γ=180º) and the horizontal surface during 2008 using measured Irish *Cool Marine* climate conditions and the NL-2 model of the *HP-IRL/H* site created in *SHAW23* software.

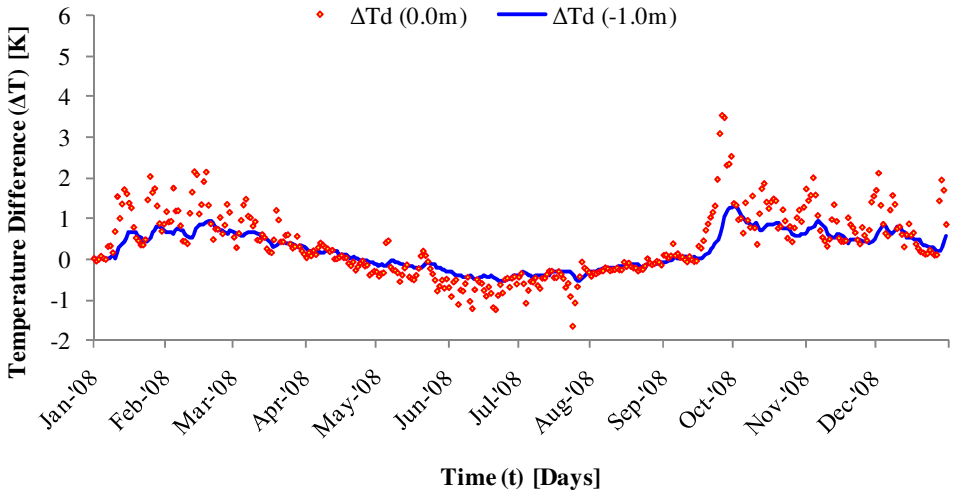

(a) Daily average temperature differences based on hourly NL-2 simulations

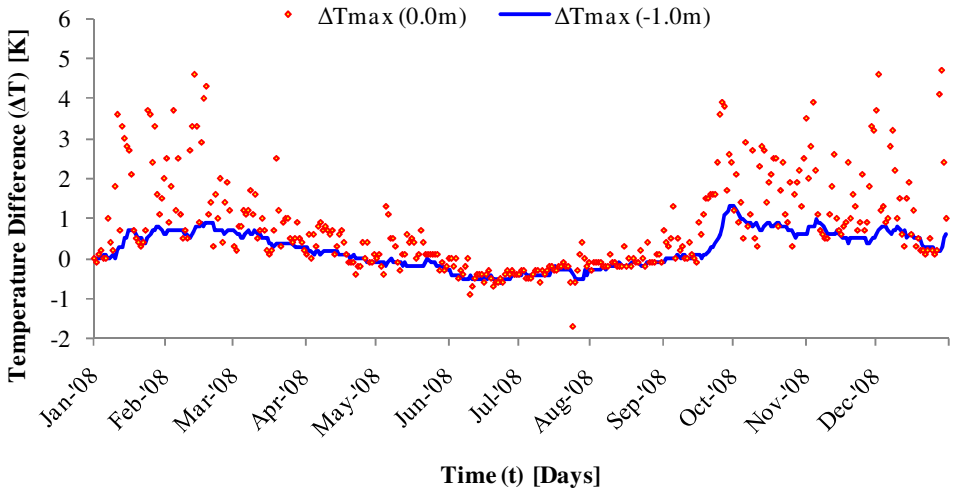

(b) Daily maximum temperature differences based on hourly NL-2 simulations

Figure 8-2: Simulated temperature difference between a southerly incline (β=40º, γ=180º) and flat surface at 0.0m and collector depth of -1.0m under measured Irish Cool Marine conditions

Firstly, it is noticeable from Figures 8-2(a) and (b) that the maximum advantage from an inclined surface occurs during the heating season of October to March, the southerly incline has an inferior angle of incidence and is a little cooler during summer.

At typical Irish collector depth (-1.0m) and the bulk surface (0.0m) the daily average results indicate an average temperature increases of 0.55K and 0.96K respectively during peak heating months of December, January and February. These daily average findings translate to only 1.1 and 1.92% improvement in COP from collectors at -1.0m and 0.0m respectively. However, long-term use of a surface collector (0.0m) alone is not recommended due to the depletion of the surface layer's limited heat capacity which will occur.

At the bulk surface (0.0m), the daily maximum results indicate maximum and average increases of 4.65K (ΔCOP of 9.3%) and 1.65K (ΔCOP of 3.3%) during the peak heating months of December, January and February. The daily maximums typically lag the solar radiation cycle and occur in the afternoon in accordance with model AL-5, Sub-section 4.2.5. These findings at 0.0m indicate a potential 3.3% increase in COP between 14:00 and 16:00 during December, January and February. This suggests that in order to gain SPF advantage from the southerly incline, a shallow collector operating as part of a *split-level collector* system should be operated primarily at these times before this energy is lost to the environment. This demands *temperature feedback control* described in Sub-section 8.2.4.

8.2 HEAT EXTRACTION AND CONTROL SIMULATIONS – NL-4

This section describes the application of the simulation tool NL-4, defined in Figure 3-28 and developed in Section 7.2, to simulate the influence of heat extraction by modified collector designs, with a variety of control strategies, on the GTD/source temperature. It is assumed that in many cases the area available to the collector (A_{HC}) is limited by available ground area or budget; therefore for comparison, the collectors analysed here occupy the same 430m^2 used by the *HP-IRL/H* collector, described in Sub-section 3.3.2.

8.2.1 Split-Level Collectors

Claesson and Dunand (1983) recognised that approximately 50% of the heat extracted by collector pipes is drawn from within 5 pipe diameters of the collector pipe. This equates to a 0.17m radius for the *HP-IRL/H* collector which emphasises the importance of the *immediate backfill*, and its thermal properties as discussed in Section 2.3.5. However, this also implies that the most extreme temperature gradients occur in this layer, measuring 0.17m above and

below the collector. Therefore, the layers above and below this range are at a higher temperature which could potentially be exploited by deploying *split-level collectors*; Burke (2010) reported a potential 8% increase in COP using *split-level collectors* in two separate ground areas. In addition, Figure 8-3 displays the measured ambient air temperature (T_a), solar radiation ($q''_{s,t}$), surface temperature ($T_{P1,\ 0.0m}$) along with the reference temperature ($T_{P1,\ -0.9m}$) and *collector-ground interface* temperature ($T_{P5,\ -1.0m}$) during HC9 between the 1st of January and the 4th of April, 2009.

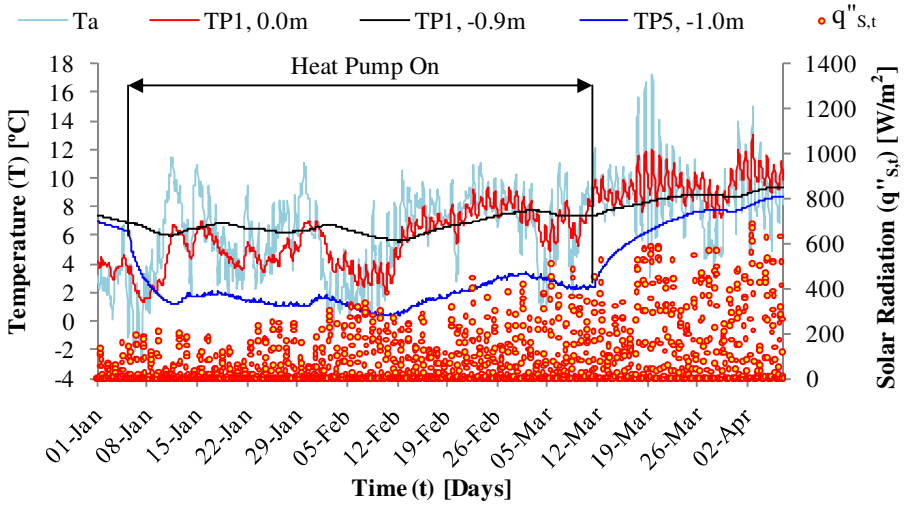

Figure 8-3: Measured weather variables and ground temperatures during the HC9 test period

This period was chosen as January is the coldest month at the ground surface (0.0m) and February is the coldest month at -1.0m. It can be seen that while $T_{P1,\ -0.9m}$ records temperatures in excess of $T_{P1,\ 0.0m}$ during much of January and early February the influence of heat pump operation draws $T_{P5,\ -1.0m}$ below $T_{P1,\ 0.0m}$ for much of this period. From late February onward the surface heating phase begins and $T_{P1,\ 0.0m}$ exceeds $T_{P1,\ -0.9m}$. Additionally, when ground temperature drawdown is considered, the air temperature (T_a) exceeds $T_{P1,\ -0.9m}$ on most occasions, indicating that the ambient air may offer a superior heat source at these times. Given the experimental data in Figure 8-3, the following questions then arise:

- Can the inclusion of two, *split-level collectors*, operating in two distinctive ground layers as shown in Figures 8-4(b) and (c) reduce the volumetric heat extraction q_s/V_{HC} [W/m^3] around each collector and produce higher source temperatures?
- Can the inclusion of both deep and shallow collectors take advantage of a wider variety of ground heat resources?

- A deep collector positioned below the *diurnal stability depth* will avoid all of the night cooling from diurnal cycles, characterised in Section 4.6, and the worst of the winter cooling from seasonal cycles, characterised in Section 4.5
- A shallow collector can then work in combination with the deep collector, positioned to capture the peaks in diurnal cycles, characterised in Section 4.6

➢ Can control strategies be implemented to further improve collector performance?

Therefore, as shown in Figure 8-4(b) and (c), the concept of two collectors A and B occupying the same collector area (A_{HC}) as the *HP-IRL/H* collector but located in two distinct ground layers at $Z_{HC,A}$ and $Z_{HC,B}$ respectively is proposed. Two generations of the split-level concept were tested; the first shown in Figure 8-5(b), involved equal spacing of 0.75m between Z_0, $Z_{HC,A}$ and $Z_{HC,B}$; the second shown in Figure 8-5(c), saw $Z_{HC,A}$ and $Z_{HC,B}$ moved 0.25m upward and downward respectively.

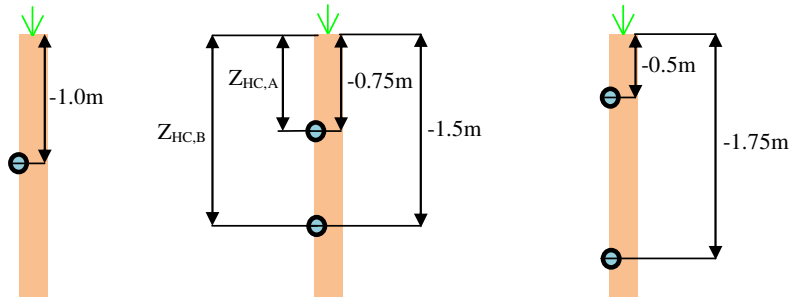

(a) Standard Collector **(b) Split-level -0.75 and -1.5m** **(c) Split-level -0.5 and -1.75m**

Figure 8-4: Full-size collectors occupying A_{HC} equivalent to HP-IRL/H collector

In combination with the split-level collector concept, the following pre-defined control strategies, shown in Figure 8-5, were tested:

- Full-load cyclic extraction, as defined in Figure 8-5(a), involves extracting 100% of q_s from collector A for 24 hours before switching to collector B for 24 hours
  - This allows each collector volume a 24 hour rest period
- Half-load continuous extraction, as defined in Figure 8-5(b), involves extracting 50% of q_s from both collector A and B simultaneously
  - This reduces the volumetric extraction rate q_s/V_{HC} [W/m^3]

A responsive control strategy, identified as full-load *collector temperature feedback control* is defined in Sub-section 8.2.4.

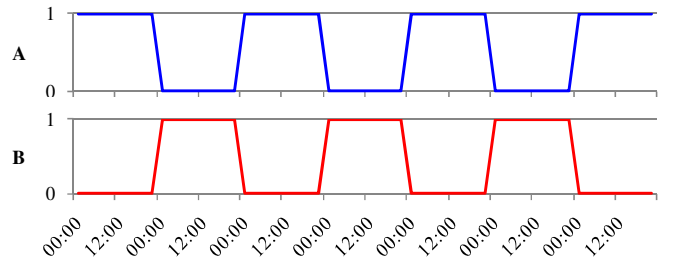

(a) Full-load cyclic extraction

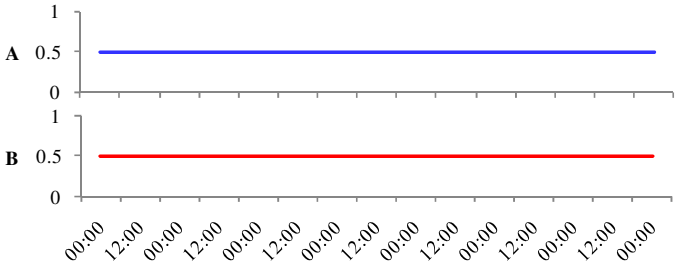

(b) Half-load continuous extraction

Figure 8-5: Pre-defined control strategies

8.2.2 Pre-defined Control – Full-Load Cyclic Extraction

Using the 'full-load cyclic extraction' strategy defined in Figure 8-5(a), for the split-level collectors at $Z_{HC,A}$ = -0.75 and $Z_{HC,B}$ = -1.5m defined in Figure 8-4(b), a step-wise simulation was conducted using NL-4, Section 7.2 with measured heat extraction data (q_s) and surface temperature data ($T_{P1,\ 0.0m}$). Figures 8-6(a) and (b) compare the simulated *collector-ground interface* temperature (T_{p-g}) for collectors A and B respectively with simulated T_{p-g} for a standard collector at -1.0m a simulated reference temperature at -1.0m.

Figure 8-6(a) shows the simulated *collector-ground interface* temperature for split-level collector A, located at Z = -0.75m. It can be seen that collector A out-performs the standard collector by cooling the *collector-ground interface* at A only every-second day, as a result the *collector-ground interface* at A is on average 1.03K warmer. The greatest difference occurs in February and March when the ground's surface undergoes the spring normalising phase of its periodic cycle, described in Figure 4-16, and surface heat begins penetrating to Z= -0.75m. For relatively mild ambient/surface conditions in February and March, it is conceivable that a collector even closer to the surface at Z= -0.5 to -0.25m may yield even further gains. Air temperatures and surface temperatures of 5ºC or more could be classed as relatively mild conditions considering the deeper ground has been cooled to between 0 and 2ºC and heat demand for a building would still be high at these ambient temperatures.

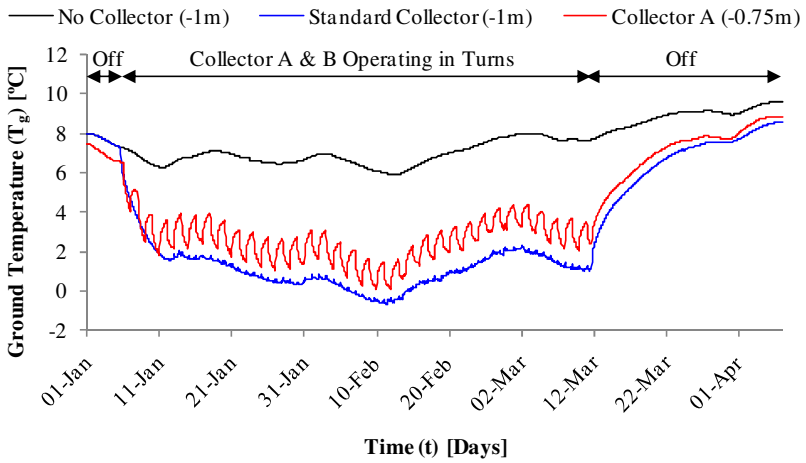

(a) Collector A at Z = -0.75m, operating every second day yields average T_{p-g} gain of +1.03K

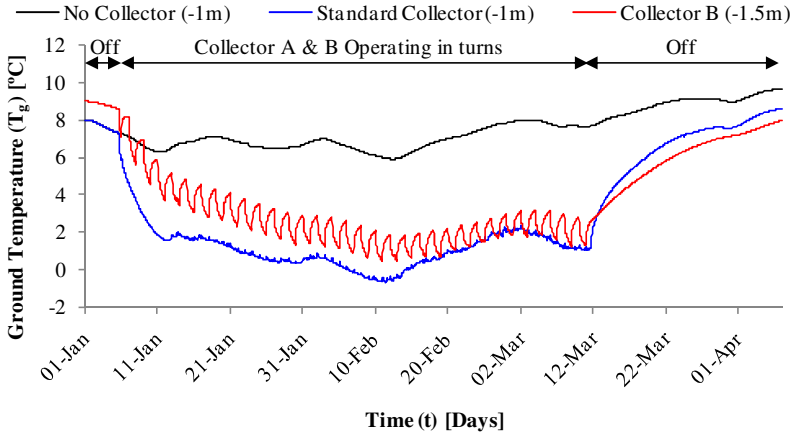

(b) Collector B at Z = -1.5m, operating every second day yields average T_{p-g} gain of +1.12K

Figure 8-6: Simulated results of split level, full-size collectors activated under full-load cyclic control shown in Figure 8-5(a)

Figure 8-6(b) shows that collector B yields a significant advantage over the standard collector during January and early February, however in late February and March the two begin to converge. The *collector-ground interface* at B is on average 1.12K warmer than the *collector-ground interface* of the standard collector. Not surprisingly, collector B out-performs collector A during January when the ground surface is still in cooling phase (Figure 4-16), while collector A out-performs collector B in March when the ground surface is in spring normalising phase (Figure 4-16).

Figure 8-7 allows further insight into these transient ground conditions with plots of vertical ground temperature gradients in January and March.

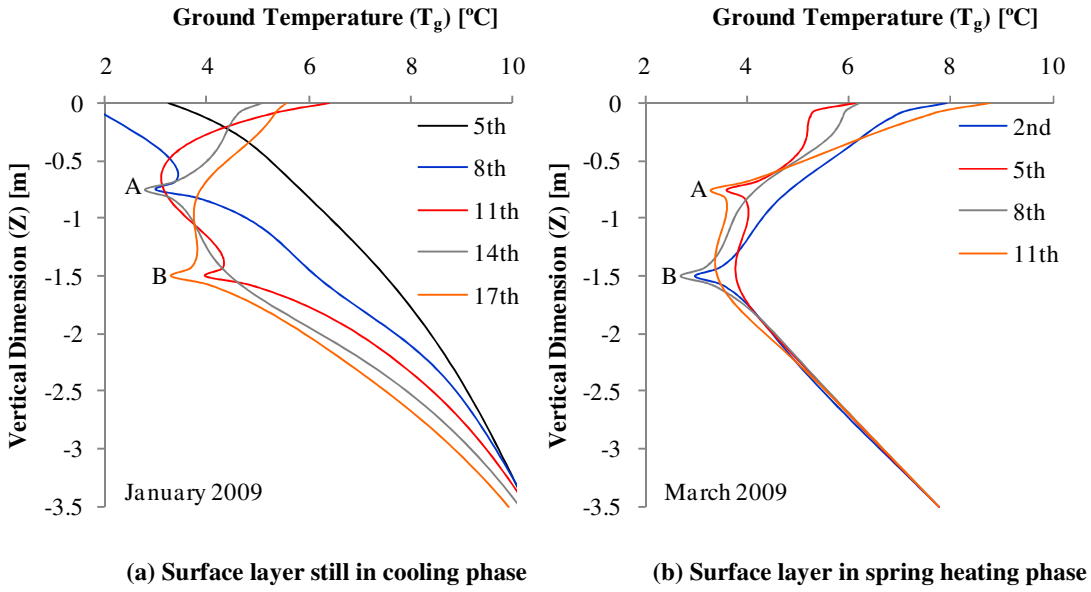

(a) Surface layer still in cooling phase **(b) Surface layer in spring heating phase**

Figure 8-7: A series of simulated vertical ground temperature gradients from within the collector area in January and March 2009

As shown in Figures 8-6 and 8-7, the split-level collector extracts heat from the ground with the following positive aspects:

- Extracting heat from two levels $Z_{HC,A}$ and $Z_{HC,B}$ allows:
  - Extraction of heat from two localised volumes of ground which if sufficiently spaced are partially independent
  - The volumetric heat extraction (q_s/V_{HC}) [W/m^3] in close proximity to collector A or B is reduced compared to a single collector
- Full-load cyclic extraction from these two volumes allows short term recovery in each volume for 24 hours in every 48 hour period
- As the two collectors are located at different depths they can offer a choice of heat source which may be superior to a single level heat source at different times of the year, particularly in spring and summer (shallow collector A) or in winter (deep collector B)

Based on the above discussion it can be concluded that shallower and deeper locations for collectors A and B respectively could potentially increase T_{p-g} gains as follows:

- As the spacing increases, the impact of A on B and vice-versa is reduced and heat can be extracted from the ground volumes surrounding the pipes with greater independence
- The impact of the recovery cycle is improved with this independence

- This independence is also advantageous for half-load continuous operation

- By moving A closer to the surface and moving B deeper the variety of thermal resource is increased:
  - A (the *diurnal resource*) offers a potentially superior source on spring days for *Cool Marine* climates particularly during peaks in diurnal cycles
    - Provided collector A is not too close to the surface whereby the ground heat capacity between the pipes and the surface is reduced below a critical level
  - B (the *seasonal resource*) offers an ideal source for colder winter days

8.2.3 Full-Load Cyclic vs. Half-Load Continuous

To quantify the impact of increasing $\Delta Z_{A/B}$ and reducing $|Z_{HC,A}|$, the split level collector simulation was repeated with $Z_{HC,A}$ = -0.5m and $Z_{HC,B}$ = -1.75m. Therefore, as shown in Figure 8-4(c), both collector depths have been altered by 0.25m. Additional simulations were also conducted with the 'half-load continuous' strategy defined in Figure 8-5(b). Figure 8-8 displays the results of these simulations.

On average both full-load cyclic extraction and half-load continuous extraction produce identical gains in *collector-ground interface* temperature. This indicates that 24 hour drawdown and recovery progress at the same rate.

For this simulated *split-level collector* example with either full-load cyclic or half-load continuous operation, the *collector-ground interface* temperature at collectors A (-0.5m) and B (-1.75m) are maintained 1.9 and 1.99K higher than the standard collector (-1.0m). The gains for collector A are best in late February and March while gains for collector B are best in January and early February.

By again assuming an increase of 1 Kelvin in source return temperature yields an average COP improvement of 2% (Cengel & Boles, 2002; Warnelof & Kronstrom, 2005; Burke *et al.*, 2008) and assuming warmer temperatures at the *collector-ground interface* (T_{p-g}) lead to equivalent gains in source return temperature ($T_{s,r}$), Figure 8-9 displays the calculated percentage gain in COP when the *split-level collectors* A and B activated with full-load cyclic control are compared to a standard single-level collector. Since the heat pump utilises collector A or B only on the discharge cycle, the COP values are calculated for these times only.

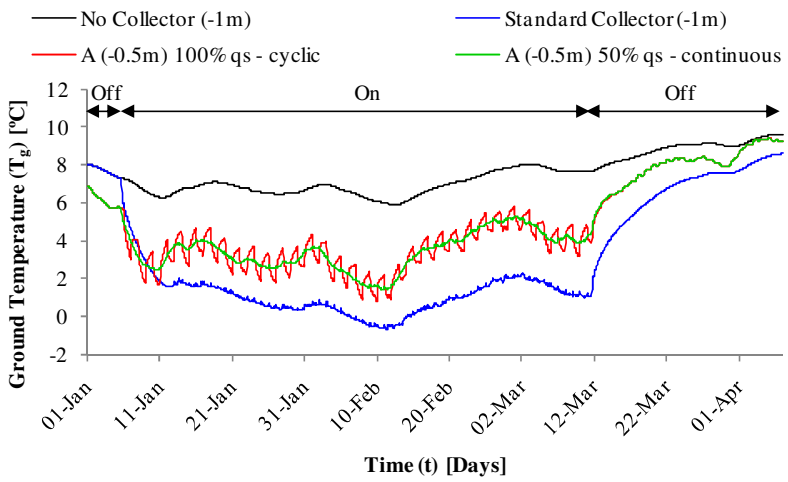

(a) Collector A at Z = -0.5m, with both cyclic and continuous extraction yields average gain of +1.9K

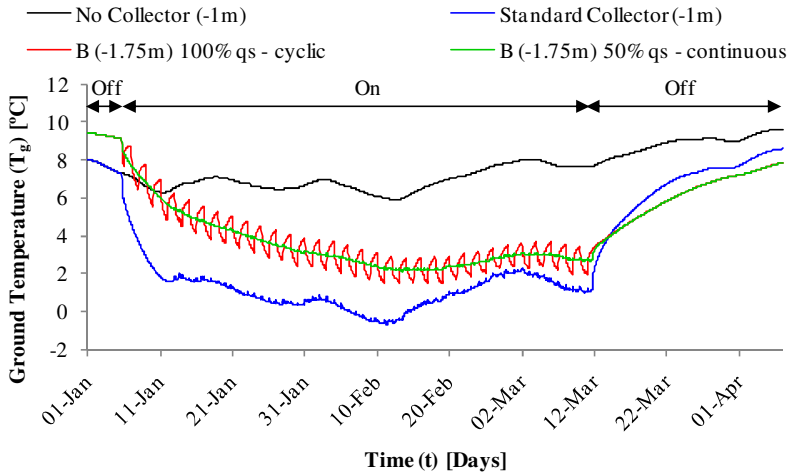

(b) Collector B at Z = -1.75m, with both cyclic and continuous extraction yields average gain of +1.99K

Figure 8-8: Simulations of split-level, full-size collectors undergoing both cyclic and continuous extraction

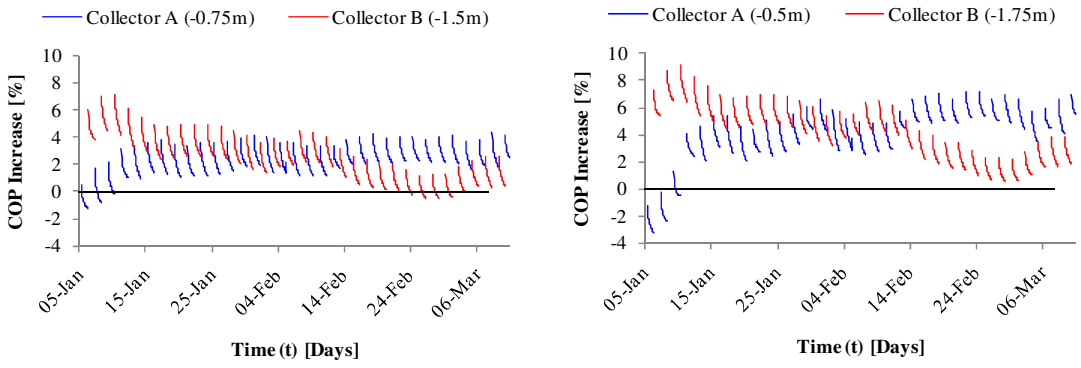

(a) A & B at Z = -0.75 and -1.5m respectively **(b) A & B at Z = -0.5 and -1.75m respectively**

Figure 8-9: Percentage increase in heat pump COP for split-level, cyclic collectors A and B over the standard single collector

As expected the gain from collector A is best in March, while the gain from collector B is best in January. Accounting for the fact that both collectors A and B are only utilised on the discharge cycle, the average COP gains for A at -0.75m and B at -1.5m are 2.05% and 2.23% respectively with an average COP gain of 2.14%. The average COP gains for A at -0.5m and B at -1.75m are 3.8% and 4% respectively with an average COP gain of 3.9%. Spreading the collectors apart in the second simulation has a significant positive influence by reducing the volumetric heat extraction (q_s/V_{HC}) [W/m^3] in each of the partially-independent ground volumes. Moving collector A closer to the surface also has a significant positive influence on COP, however only during mild weather at the surface, as shown in Figure 8-3. Collector A has a negative influence on COP during early January (5^{th} to 10^{th}) due to the cold surface conditions; interestingly this pattern is not repeated during the next cold period (1^{st} to 10^{th} of February) and this is because the standard collector has undergone significant drawdown at this point while drawdown at collector A, a component of a *split-level collector*, is noticeably reduced. It can be seen as expected that the cross-over between superior COP gain for collector B in January and superior COP gain for collector A in March occurs in mid-February.

Based on these findings and the transient temperature gradients displayed in Figure 8-7, it is proposed that the *split-level collectors* and hence the $GSHP_{HC}$ could benefit from more intelligent control. Therefore in place of the pre-defined control strategies trialled thus far, a new responsive control strategy based on *collector temperature feedback* is now described.

8.2.4 Responsive Control – Full-load Collector Temperature Feedback

Based on the identical COP gains of 3.9% from full-load cyclic and half-load continuous control, a responsive control strategy is tested. Figure 8-10 shows a schematic of a *split-level collector* to be simulated with either NL-4 or NL-5, while Table 8-1 summarises the full-load *collector temperature feedback* control logic to be used with either NL-4 or NL-5. Both control strategies are designed so that full-load heat is extracted using the collector which offers the highest source temperature. For step-wise simulation these strategies are implemented by comparing temperatures from the previous time-step, as shown in Table 8-1.

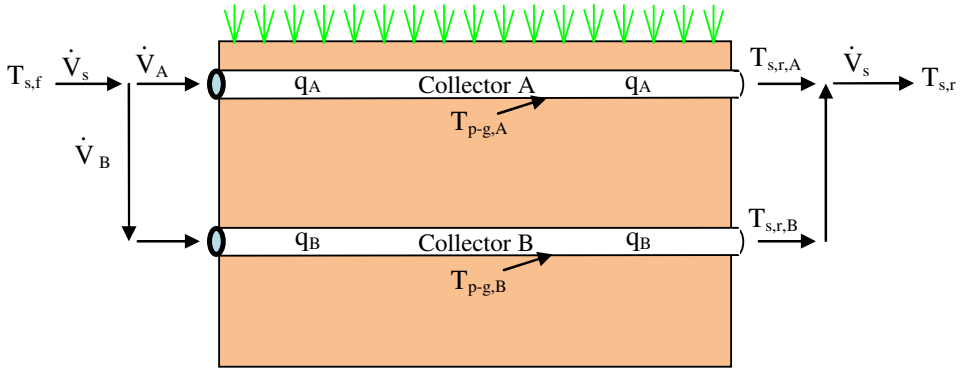

Figure 8-10: Schematic of proposed split level collector with responsive control using NL-4 or NL-5

Table 8-1: Collector temperature feedback logic for split level collector simulation with NL-4 or NL-5

NL-4	NL-4	NL-5	NL-5
Condition	**Extraction Control**	**Condition**	**Flow Control**
$T_{p\text{-}g,A}{}^{p} > T_{p\text{-}g,B}{}^{p}$	$q_A = q_s$ and $q_B = 0$	$T_{s,r,A}{}^{p} > T_{s,r,B}{}^{p}$	$\dot{V}_A = \dot{V}_s$ and $\dot{V}_B = 0$
$T_{p\text{-}g,B}{}^{p} > T_{p\text{-}g,A}{}^{p}$	$q_B = q_s$ and $q_B = 0$	$T_{s,r,B}{}^{p} > T_{s,r,A}{}^{p}$	$\dot{V}_B = \dot{V}_s$ and $\dot{V}_A = 0$

Figure 8-11 displays the daily thermal energy extracted ($Q_{s,d}$) [kWh] from collectors A and B based on simulated *collector temperature feedback control* in a simulation driven by measured extraction rate data (q_s) [kW]. Figure 8-11 demonstrates how this type of intelligent control selects the collector which offers the highest temperature. This dictates collector B is to be used between the 5th and the 10th of January. Between the 11th of January and the 14th of February collectors A and B take turns resulting in approximately equivalent daily totals being extracted from each layer. Finally, from the 14th of February until the 1st of March collector A dominates, however collector B is again chosen after the 6th of March.

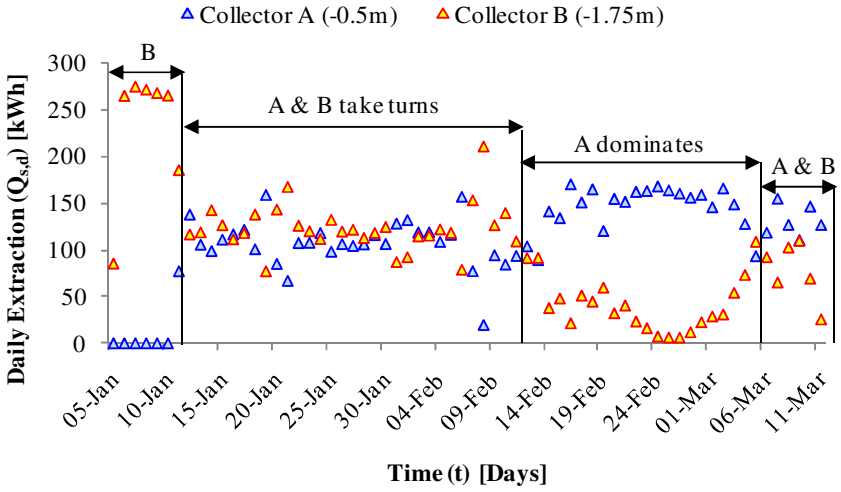

Figure 8-11: Heat extraction from collectors A and B based on active control

Figure 8-12 displays the simulated *collector-ground interface* temperature for collectors A and B at -0.5 and -1.75m respectively with the *collector temperature feedback control* strategy. Due to the responsive control strategy, the *collector-ground interface* temperatures of both collectors converge at a value which is 2.3K in excess of the standard collector and this equates to a 4.6% increase in COP.

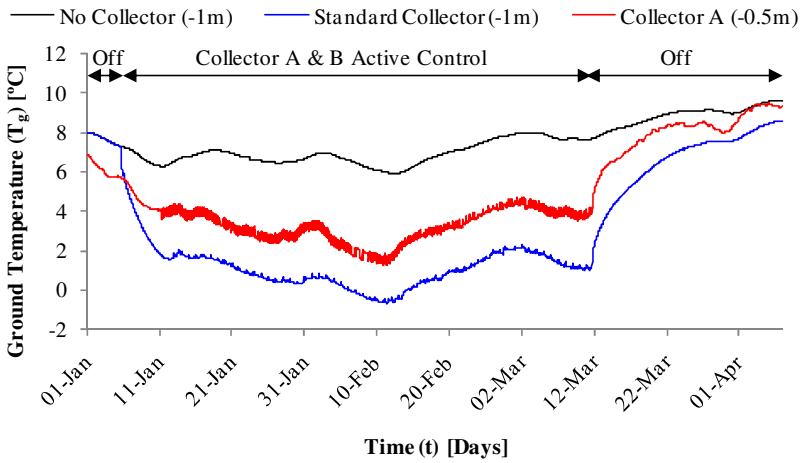

(a) Collector A at Z= -0.5m, operating with responsive control, yields an average gain of 2.3K

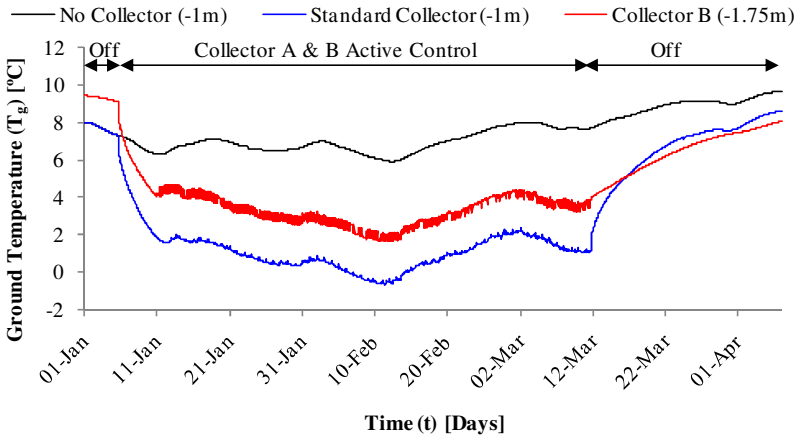

(a) Collector B at Z= -1.75m, operating with responsive control, yields an average gain of 2.3K

Figure 8-12: Simulated results for split-level, full-size, full-load collectors operating with responsive control

This scoping exercise has demonstrated that deployment of *split-level collectors* at -0.5 and -1.75m utilising *collector temperature feedback control*, produced a 4.6% COP advantage over the high performing collector tested during *HP-IRL/H*, by taking advantage of reduced q_s/V_{HC} [W/m^3] as well as utilizing the positive elements of both the *diurnal* and *seasonal* ground thermal energy resources (defined in Section 4.1) through intelligent control. Additionally this

split-level combination produces source drawdown ($\Delta T_{s,r/\infty}$) of only -3.5K under continuous 24hr operation. As summarised in Table 2-11, VDI-4640 (2001) recommends a maximum allowable source drawdown ($\Delta T_{s,r/\infty}$) of -12K at base load and -18K a peak load. Therefore the deployment of *split-level collectors* at -0.5 and -1.75m utilising *collector temperature feedback control*, produced a source temperature 14.5K above the recommended lower limit at peak load. This benchmarks the significant performance potential from *CSDC* against a commonly referenced design guide.

8.3 COLLECTOR DESIGN – NL-5

This section describes the application of the simulation tool NL-5, defined in Figure 3-28 and developed in Section 7.3, to simulate the influence of modified collector designs on the source return temperature. Again it is assumed that the area available to the collector (A_{HC}) is limited, therefore area occupied by proposed collector designs is equivalent to the *HP-IRL/H* collector and is maintained constant in comparative simulations.

As shown in Figure 7-22, the ground cooling caused by a horizontal collector is most extreme at the collector pipe inlet (L≈0m). Additionally, it was shown in Figure 6-35 that increased pipe spacing (PS) reduces ground cooling caused by the collector. Therefore, it was proposed to counteract extreme cooling at the pipe inlet by increasing pipe spacing at this point. However, in order to maintain constant collector area it is necessary to balance this pipe spacing increase at the inlet with pipe spacing decrease at the pipe exit, resulting in non-uniform pipe spacing as shown in Figure 8-13(b).

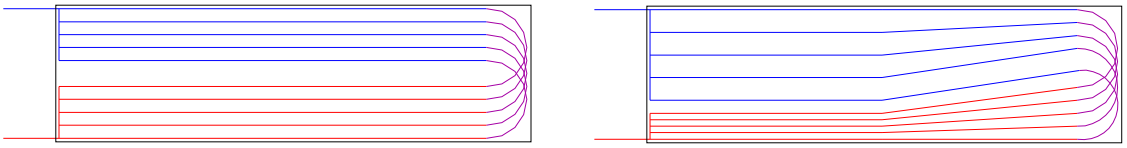

(a) Uniform pipe spacing **(b) Non-uniform pipe spacing**

Figure 8-13: Alternative collector designs, occupying equivalent area and simulated using NL-5

Figures 8-14(a) and (b) display screen-shots from simulations of collectors with both uniform and non-uniform pipe spacing as shown in Figures 8-13(a) and (b). These simulations were conducted using the NL-5 method described in Section 7.3. In the first simulation PS was maintained constant at 0.2m while in the second simulation PS was set at 0.3m over the first 50m, 0.2m between 51 and 100m and 0.1m from 101m to 150m. A 12 hour heat extraction

cycle was simulated for both collector types and the underground fluid temperature increase during the final time-step is compared in Figure 8-14(c). Simulated results indicate that while the first 50m of the non-uniform collector expectedly outperform those of the uniform collector, the final 50m underperform and the net influence on collector performance is a negative one with a source return temperature ($T_{s,r}$) reduction of -0.2K after 12 hours of operation.

However, in completing this exercise, model NL-5 has proven itself an extremely useful tool and future investigations of this type may potentially deliver gains in ($T_{s,r}$).

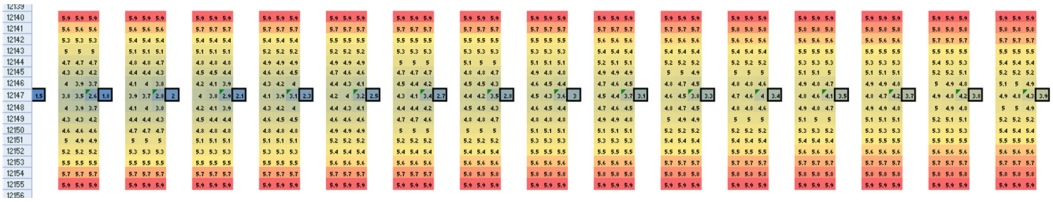

(a) Simulation results: uniform pipe spacing of PS = 0.2m, after 12 hours of continuous heat extraction

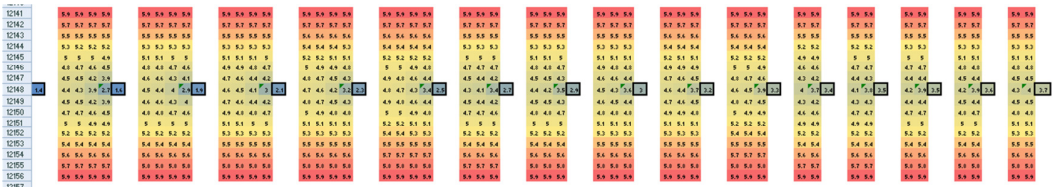

(b) Simulation results: non-uniform pipe spacing of PS = 0.3m from L=0 to 50m, PS = 0.2m from L=51 to 100m and PS= 0.1m from L=101 to 150m, after 12 hours of continuous heat extraction

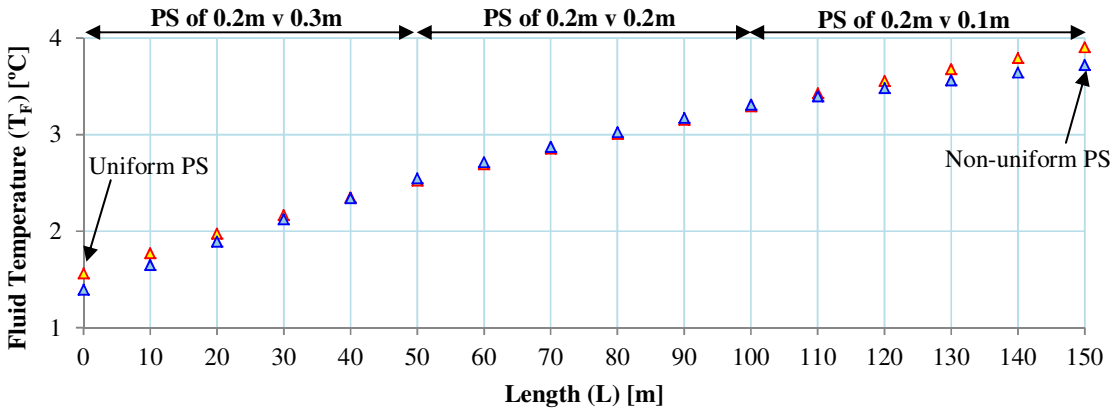

(c) Comparison of fluid temperature (T_F) increase with length (L) for uniform (orange-marker) and non-uniform (blue-marker) pipe spacing after 12 hours of continuous heat extraction

Figure 8-14: Simulated results for both uniform and non-uniform pipe spacing after 12hours of operation

8.4 SUMMARY AND FUTURE WORK

This chapter has demonstrated the capacity of models developed during *HP-IRL/H* to simulate a variety of physical and control alterations to $GSHP_{HC}$ which were previously not attempted. Additionally, the preliminary performance gains from *CSDC* have been established and additional gains are possible through further *thermo-environmental analysis*. Table 8-2 presents a summary of the preliminary investigations conducted and described within this chapter. Three month average COP gain from *split-level collectors* with *feedback control* was 4.6% and the option to deploy this collector under an inclined surface can yield increases of 6.5 to 7.9% and potentially more.

Table 8-2: Summary of investigations completed and future investigations

No.	Investigations completed	Models used	Increase in COP and timescale
1	Southerly incline collector depth (-1.0m)	NL-1/ NL-2	1.1% all day (3 month average)
2	Southerly incline bulk surface (0.0m)	NL-1/ NL-2	1.9% all day (3 month average)
3	Southerly incline bulk surface (0.0m)	NL-1/ NL-2	3.3% afternoon (3 month average)
4	Southerly incline bulk surface (0.0m)	NL-1/ NL-2	9.3% afternoon (3 month maximum)
5	Split-level (-0.75 and -1.5m) Full-load Cyclic	NL-4	2.1% all day (3 month average)
6	Split-level (-0.5 and -1.75m) Full-load Cyclic	NL-4	3.9% all day (3 month average)
7	Split-level (-0.5 and -1.75m) Half-load Continuous	NL-4	3.9% all day (3 month average)
8	Split-level (-0.5 and -1.75m) Full-load Collector Temperature Feedback ($T_{p\text{-}g}{}^{p}$)	NL-4	4.6% all day (3 month average)
9	Non-uniform pipe spacing	NL-5	0% 12 hour extraction cycle
(i)	Certain coupling of No.s 1 and 9 (-0.5 and -1.75m)		1.1 + 4.6 = 5.7% all day (3 months)
(ii)	Potential coupling of No.s 2 and 9 (-0.1 and -1.75m)		1.9 + 4.6 = 6.5% all day (3 months)
(iii)	Potential coupling of No.s 3 and 9 (-0.1 and -1.75m)		3.3 + 4.6 = 7.9% afternoon (3 months)
(iv)	Potential coupling of No.s 4 and 9 (-0.1 and -1.75m)		9.3 + 4.6 = 13.9% afternoon (maximum)

The scope for future work in *CSDC* for $GSHP_{HC}$ in winter mode is significant. The next level of a *CSDC* approach would be to examine a *split-level*, inclined source and numerically compare this with the building heat demand profile to match the best source temperatures with demand using heat storage mechanisms and control. Investigations of this kind using component models, ANN and genetic algorithms are underway at C*i*SET. Additionally, the potential for surface level collectors in asphalt (large, cheap, quasi-solar collectors) coupled to new 70ºC heat pumps for hot water in summer, may increase the full year SPF significantly.

CHAPTER 9

CONCLUSIONS AND RECOMMENDATIONS

9. CONCLUSIONS AND RECOMMENDATIONS

This *HP-IRL/H* study delivered on its stated aim to develop and experimentally validate numerical methods and demonstrate the potential of a *Climate Sensitive Design and Control* (*CSDC*) approach in a *Cool Marine* climate. This study demonstrates a potential 7.9% improvement in COP over 3 months is possible by combining: a *split-level collector* (with both diurnal and seasonal arrays); a southerly incline; and crucially, *collector temperature feedback control*. Significant scope for future work also exists. Additionally, the combined experimental and numerical, *thermo-environmental* analysis of $GSHP_{HC}$ enabled the interactions between the local *Cool-Marine* climate, the ground, the collector and the heat pump to be completely understood. The following three sections document the project summary from which conclusions and recommendations for future work are drawn.

9.1 SUMMARY

This study delivered the following objectives, summarised in order of Chapters 1 through 8:

Chapter 1 identified the current status of $GSHP_{HC}$ within the available SET, including:

- Current and projected growth in the use of SET to provide thermal energy
- Economic and environmental advantages of $GSHP_{HC}$
- Recent research, knowledge deficits and future research direction
- Need for climate sensitive designs and active control strategies for all SETs

Chapter 2 presented a thorough review of the $GSHP_{HC}$ technology, including:

- Overview of $GSHP_{HC}$ operating within a broad 'system' that includes the ground, the building, the climate and the energy supply
- Identification of 23 $GSHP_{HC}$ *design variables* based on over 15 publications
- A summary of 12 basic design guides and 12 software design tools
- A review of 14 recent publications on 7 different analysis methods aimed at improving cost effectiveness
- Definitions provided for both *Climate Sensitive Design and Control* (*CSDC*) ethos and a multi-disciplinary *thermo-environmental analysis* methodology required to execute *CSDC*

Chapter 3 described the construction of the *HP-IRL/H* experimental testing facility based around a 1,125m^2 commercial building and a 15kW heat pump with a 430m^2 horizontal collector, including:

- A review of 13 other experimental studies on $GSHP_{HC}$ that influenced the facility design, sensor installation and test program at the *HP-IRL/H* site
- Instrumentation of a 15kW$_{th}$ heat pump and 10 x 150m long parallel pipe array with 15 sensors to measure the heat pump's instantaneous and seasonal thermal performance
- Burial of over 100 sensors to continuously measure the ground temperature, moisture content and heat flux within and adjacent to the 430m^2 horizontal collector area
- Installation of 11 weather sensors to continuously monitor fluctuations in local climate
- Installation of 2 types of DAQ and programming of 2 software packages that recorded over 50 million data points between 2007 and 2010
- A road map for analytical and numerical methods presented in subsequent chapters

Chapter 4 delivered an extensive analysis of ground temperature variation with both depth and time in a variety of geographical locations and climate types, including:

- Definition of 3 ground thermal energy resources; *geothermal*, *seasonal* and *diurnal*
- Grouping of 5 analytical models AL-1 through AL-5 which define periodic variation in surface and ground temperature conditions
- Reviewing of 11 publications on GTDs measured internationally
- Establishing the sensitivity of GTD to latitude, *climate classification* and air temperature extremes
- Undertaking Fourier analysis of temperature fluctuations in the *HP-IRL/H geothermal*, *seasonal* and *diurnal resources* using the geothermal gradient, AL-4 and AL-5

Chapter 5 details a theoretical investigation of transient ground heat transfer processes at the *HP-IRL/H* site, including:

- A review of 8 studies on the *ground-atmosphere interface*
  - Measurement of temperatures and heat fluxes at the *HP-IRL/H* site's *ground-atmosphere interface*
- A review of 5 studies on underground heat transfer
  - Description of pure conduction and combined heat and mass transfer in the ground
- A review of 8 studies on ground thermal and hydraulic properties
  - Measurement of properties at the *HP-IRL/H* site
  - Calculation of thermal properties using AL-6

- Ground temperature simulation using two methods NL-1 and NL-2 and comparison with measured ground temperatures
- Experimental investigation of the surface cover influence on GTD

Chapter 6 summarises the salient features of the experimental testing and characterisation of $GSHP_{HC}$ system performance, including:

- Definition of 10 experimental test periods HC1 through HC10 that delivered 303 test days between 2007 and 2010
- Thermodynamic characterisation of the *Solterra 500* and development of heat pump component model AL-7
- Basic hydraulic characterisation of collector and development of pumping power calculator AL-8
- Development of AL-9 used for estimating source return temperature
- Development of AL-10 used to predict thermal drawdown in the source
- Investigation of spatial and temporal variation in collector heat flux and development of AL-11 to characterise these variations
- Comparative study and discussion on collector dimensioning methods

Chapter 7 documents the transient numerical simulation that resulted from combining the relevant, validated sub-models from Chapters 4, 5 and 6 in an FDM tool, including:

- A review of 12 studies on numerical simulation of horizontal collectors
- Definition and discretisation of the *pipe-ground simulation domain*
- Development of NL-4 for simulating the long-term influence of horizontal collectors on GTD
- Development of NL-5 for simulating both the fluid temperature increase in collector pipes, decrease in the evaporator and the associated cooling of the collector area simultaneously
- Experimental validation of models NL-1, NL-4 and NL-5

Chapter 8 overviews the deployment of the novel *HP-IRL/H* simulation tools to test climate sensitive collector designs and operational control including:

- Ground temperature simulations – NL-1 and NL-2
    - Aimed at raising ground temperature within the collector area using passive low cost changes to the *ground-atmosphere interface*
- Heat extraction and control simulations – NL-4

  - Aimed at raising *collector-ground interface* temperature through *split-level collector* designs and both fixed and responsive control strategies
- Collector pipe spacing and design simulations – NL-5

The main conclusions and recommendations resulting from this research are summarised in the subsequent sections.

9.2 CONCLUSIONS

The conclusions resulting from this *HP-IRL/H* research project are discussed in the following subsections. Conclusions are grouped under headings based around specific aspects of the combined experimental and numerical *thermo-environmental* analysis of $GSHP_{HC}$ and the key findings pertaining to the performance potential of the *CSDC* approach.

9.2.1 Experimental Testing

The *HP-IRL/H* experimental facility constructed at GMIT facilitated the most comprehensive experimental study on $GSHP_{HC}$ to date. The facility successfully captured the response of standard $GSHP_{HC}$ performance indicators to a range of system dynamics including: transient source and sink temperatures and energy content; collector and heat distribution system thermo-hydraulic design; climate influences; as well as operational control and duty cycles. In addition, the facility also captured the influence of climate on collector and reference ground temperatures as well as generating thermal property values and investigating combined heat and mass transfer around the collector.

The following are a sample of the key findings from the experimental portion of the *thermo-environmental* analysis:

Measured seasonal and diurnal thermal energy resources:

- Average annual ground and air temperatures ($T_{g,y}$ and $T_{a,y}$) were 11.72ºC ±0.3ºC and was 9.8ºC ±0.3ºC respectively between 2007 and 2010
- Annual mean-to-peak surface and air amplitudes ($A_{sur,y}$ and $A_{a,y}$) were 6.7 and 5.2K respectively between 2007 and 2010 with maximums around the 23rd of July
- On average, the daily mean-to-peak amplitude ($A_{g,d}$) at the surface was 1.97K between 2007 and 2010 with maximums 3 to 4 hours after solar noon
- Using AL-4 and AL-5, the *seasonal stability and diurnal depths* were estimated at Z= -16.0 and -1.0m respectively

These findings were used as boundary conditions in simulations and can also be used to inform collector burial and control

Measured ground moisture content at the HP-IRL/H site:

- The moisture content in the horizontal collector area is typically in excess of $0.25m^3/m^3$ during winter heat pump operation, this is well above the critical moisture content of $0.15m^3/m^3$ considered important for heat extraction
- Surface moisture content was $0.35m^3/m^3$ in November 2009 after a 2 week wet period
- Surface moisture content was $0.15m^3/m^3$ in mid-June 2010 after a 2 week dry period
- Moisture content at -1.1m remained constant at $0.3m^3/m^3$ over the 10 month period
- The periodic variation in moisture content at 0.0m over 24hr periods can be attributed to combined heat and mass transfer driven by incident solar radiation
- The peaks in moisture content seen on vertical gradients correspond to ground layers of high matric potential which is a suction force

These findings confirm the suitability of the moist *Cool Marine* climate to $GSHP_{HC}$

Measured thermo-physical properties of HP-IRL/H site:

- Soil texture in the collector area is dominated by sand which aids heat and water flow
- The average properties of the collector area are as follows:
  - Thermal diffusivity – 1.05×10^{-6} m^2/s
  - Thermal conductivity – 2.6 W/mK
  - Volumetric heat capacity – 2.48×10^{-6} J/m^3K
  - Density – 1586.5 kg/m^3
  - Specific heat capacity – 1563.2 J/kgK

These findings indicate that *HP-IRL/H* heat transfer properties exceed the literature average, highlighting the importance of sand to heat flow; these properties were also used in models.

Measured surface influences at the HP-IRL/H site:

- Over 3.64 years, air temperatures were below +0.3ºC for just 1.68% of this time; surface cover and bulk ground surface temperatures were below +0.3ºC for 1.63 and 0.70% of this time respectively; while underground temperatures including *collector-ground interface* temperatures were below +0.3ºC for 0% of this time

- Bare surfaces containing brick were +7.5K warmer in summer and -1.5K colder in winter when compared to grass/sod cover

These findings confirm that soil freezing can be ignored in Irish models and indicate that grass and brick surfaces have advantages for collectors in winter and summer respectively.

Measured heat and mass transfer at HP-IRL/H collector-ground interface:

- Since there is continually a high level of moisture ($0.3m^3/m^3$) at the *collector-ground interface*, no moisture migration due to a temperature gradient induced by collector heat extraction was detected
- During dry surface conditions, neither the influence of gravity nor the ground moisture transfer associated with temperature gradients (which both act downward towards the collector) can equal the moisture transfer due to matric suction which acts upward toward the drying root/sod surface

These findings confirm that coupled heat and mass transfer processes can be ignored in *HP-IRL/H* simulations however thermal properties are influenced by site dependent moisture content.

Measured COP sensitivities:

- $GSHP_{HC}$ system COPs, identified as 'HP-IRL/H', drops from 4.7 to 2.7 with ΔT_{hp} increase from 22 to 48K; this equates to a 1.63% reduction in COP per Kelvin
- $GSHP_{HC}$ – *IiBC* COPs, identified as 'Total', which include all power consumption ($w_{p1} + w_{p2} + w_{p3} + w_s + w_c$), are between 8 and 13% lower than heat pump unit COPs which are identified as 'Sol 500' and measured to the EN-14511 standard
- The collector and heat pump system undergoes coupled performance transience during operation
- COP, q_s and q_{sk} reduce with reduction in flow rates $\dot{V}_s$ and $\dot{V}_{sk}$

These findings have delivered greater insight into the dynamics of a commercial heat pump in an actual application and have provided input data and sub-models for simulations.

Collector dimensions

- The most frequently referenced rules of thumb are as follows (the *HP-IRL/H* equivalents are shown in brackets):

- Mass flow rate per unit capacity: 0.162 to 0.192 $m^3/h/kW_{th}$ (0.28)
- Total buried pipe per unit capacity: 35 to 60 m/kW_{th} (100)
- Capacity per unit area of collector: 8 to 40 W/m^2 (35)
- Collector pipe spacing: 0.3 to 0.8m (0.25 to 0.4)
- Collector depth: 1.2 to 1.5m (0.8 to 1.35)

- COPs measured during *HP-IRL/H* between ΔT_{hp} of 48 and 22K range between:
  - 2.85 and 5.2 for the *Solterra 500* unit only, identified as 'EN-14511'
  - 2.6 and 4.5 for the total $GSHP_{HC}$ system, identified as 'Total'
- COP drops by 8 to 13% when all electrical power consumption is included

However, comparing these to results from other experimental systems, these findings indicate that splitting a flow rate of $0.28m^3/h/kW_{th}$ and a pipe length of $100m/kW_{th}$ across 10 parallel pipes has resulted in a highly efficient collector system

This experimental portion of the *thermo-environmental* analysis has led to a comprehensive understanding of the climate→ground→collector→heat pump system.

9.2.2 Numerical Simulation

The numerical portion of the *thermo-environmental* analysis yielded 11 analytical equations and 5 numerical models. The simple, yet effective numerical approaches in EFD maintained high accuracy while uniquely catering for all the *HP-IRL/H* collector dynamics including: closely positioned *parallel, in-line* pipes with thermal interference; hourly weather influence at the surface; multiple surface covers and ground layers; thermally coupled collector and heat pump performance transience; as well as new *CSDC split-level collector* designs and novel control strategies.

The following are a sample of the key findings from the numerical *thermo-environmental* analysis:

Simulating undisturbed ground temperatures

- Model NL-1, developed and validated in Sections 5.4 and 7.4 respectively, simulates ground heat transfer using a surface energy balance and ground conduction
  - Comparison with measured values at $T_{P1,\ 0.0m}$ and $T_{P1,\ -0.15m}$ indicated R^2 values of 0.902 and 0.972 respectively, annual error at all depths was ±0.2K

- Model NL-2, created using the software *SHAW23*, simulates ground heat transfer using both surface energy and mass balance and combined heat and mass transfer in the ground
    - Comparison with measured values at $T_{P1,\ 0.0m}$ and $T_{P1,\ -0.15m}$ indicate R^2 values of 0.937 and 0.968 respectively, annual error at all depths was ±0.5K

These findings indicate that the NL-1 surface equations are suitable for use in $GSHP_{HC}$ modelling under *Cool Marine* conditions.

Simulating cooling at the collector-ground interface

- Model NL-4, developed and validated in Sections 7.2 and 7.4 respectively, predicted *collector-ground interface* temperatures in P3 and P4 over a 3 month period with:
    - Maximum error was -0.96K
    - Average error was -0.25K
    - An R^2 value of 0.9832
- When comparing simulations of the *collector-ground interface* in the pipe exit section (L= 150m) with measured source return temperature ($T_{s,r}$) over a one month period:
    - The maximum error was +1.0K
    - The average error was +0.5K

This model is therefore suitable for investigating the effect of heat extraction by collector pipes in a variety of depths including *split-level collectors* with *feedback control*.

Predicting source flow and return temperatures

Model NL-5, developed and validated in Sections 7.3 and 7.4 respectively, predicted the following:

- Cyclic operation during HC3
    - $T_{s,r}$ is simulated with a maximum error of -0.71K and an average error of -0.13K
    - $T_{s,f}$ is simulated with a maximum error of -1.39K and an average error -0.07K
- Continuous operation during HC9
    - $T_{s,r}$ is simulated with a maximum error of -0.89K and an average error -0.12K
    - $T_{s,f}$ is simulated with a maximum error of -2.67K and an average error of -0.0079

- The main sources of error were:
  - Assumptions made in heat pump component model NL-7
  - Assumptions made with boundary conditions and the *collector-pipe interface*
  - Sources of heat or residual heat within the heat pump or building which are not accounted for by the NL-5 model

This accuracy compares well with values quoted by Mei (1986) and Demir *et al.* (2009) of ±10%. Importantly, this method caters for $GSHP_{HC}$ dynamics such as coupled performance transience which was absent from previous models; however upgrades to NL-5 discussed in future work are also desirable.

9.2.3 Climate Sensitive Design and Control

The combined experimental and numerical *thermo-environmental analyses* described thus far provided the models, boundary conditions and input data that allowed for the performance potential of the *CSDC* approach to be demonstrated.

The following are some of the key findings from simulations testing the *CSDC* approach:

Comparison of simulated collector designs occupying an identical collector area

- A collector ground surface with a southerly incline of 40º yielded:
  - An average 1.92% COP increase for a surface collector (0.0m) between December and February
  - An average 1.1% COP increase for standard collector (-1.0m) between December and February
  - With a potential 3.3% COP increase during the afternoon at 0.0m which can be captured using intelligent control
- *Split-level collectors* with either full-load cyclic or half-load continuous control yielded:
  - An average 2.14% increase in COP for split-level collectors A and B positioned at -0.75 and -1.5m between January and March
  - An average 3.9% increase in COP for split-level collectors A and B positioned at -0.5 and -1.75m between January and March
- *Split-level collectors* using *collector temperature feedback control* yielded:
  - An average 4.6% increase in COP for *split-level collectors* positioned at -0.5 and -1.75m between January and March

In combination, these modifications to the ground surface and the collector design with feedback control can yield potential COP gains of 6.5 to 7.9% over 3 months.

In conclusion, these preliminary simulations have demonstrated the performance potential of *CSDC* using the experimentally validated numerical methods developed in this project which was the stated aim of the study.

There is also significant scope to further *CSDC* in larger upgraded simulations and to include the building demand profile in control algorithms for inclined, *split-level collectors* with thermal storage.

9.2.4 Limitations

The following limitations or constraints to this study have been identified:

Experimental

- The *heat distribution system* in the *IiBC* consisted of radiators which require a flow temperature of at least 50ºC, this constrained the magnitude of measured COPs achieved by the *Solterra 500*
- Additional temperature sensors on the copper refrigerant lines of the *Solterra 500* to measure approximate T_{evap} and T_{cond} were not included
- Testing the *Solterra 500* at a wide range of source and sink flow rates was not achieved
- Additional temperature and heat flux sensoring of the *IiBC's heat distribution system* to deliver further insight into the dynamics of the heat sink could not be afforded
- With the exception of P6 and P8, it was not possible to construct vertical temperature profiles extending below the horizontal collector
- In order to capture as many collector phenomenon as possible, 9 vertical profiles were created, however as a result some profiles lack sufficient numbers of sensors

Numerical

- The EFD form of heat transfer equations were used which limit the choice of spatial and temporal increments
- Cartesian coordinates were used at the *pipe-ground interface* to replicate the cylindrical pipe, this introduces a small error at the start of a heat pump cycle
- Heat and mass transfer and soil freezing algorithms were not necessary for the mild and moist *Cool Marine* climate but would be needed in cold and dry regions

9.3 RECOMMENDATIONS FOR FUTURE WORK

The experimental facility, the database of measurements, the numerical models and the numerical results developed during this *HP-IRL/H* project creates the opportunity for further research in the following areas:

Upgrading model NL-5 to NL-6 or NL-7

- Expanding the heat pump component model AL-7 to include sensitivity to source and sink flow rates $\dot{V}_s$ and $\dot{V}_{sk}$ as well as the sensitivity to source and sink temperatures T_s and T_{sk} which is already included:
  - This requires further experimental testing at a variety of flow rates
  - This type of testing is typically not done by test institutes but can be achieved using the *HP-IRL/H* facility
- Expanding the *ground-atmosphere interface* to include automatic sensitivity to slope and orientation
- Coupling of radial and Cartesian geometries at the *collector-ground interface*:
  - This reduces the need for small nodes at the *collector-ground interface*
  - This mimics the real-life heat transfer process more closely and improves accuracy
- Further use of either non-uniform 2-D nodes or 1-D nodes which are then coupled with uniform 2-D nodes to increase mesh efficiency in ground locations where thermal gradients are less pronounced
- Inclusion of moisture movement and freezing, described in Chapter 5, in the NL-5 ground temperature modelling
  - While moisture movement and freezing can be neglected in the mild and moist *Cool Marine* conditions, it is necessary to include these for simulations in some *Continental* regions and all *Moderate Subpolar* regions
- Conversion of FDM equations from EFD to IFD form to achieve unconditional stability
  - Implicit equations require a solution method such as the Thomas Algorithm
  - Unconditional stability allows more freedom in selecting space and time increments
- Coding of the FDM solution in a more versatile language such as *Fortran* or *C++*

Optimisation simulations

- Future optimisation simulations can be conducted using the existing EFD models NL-4 and NL-5 or upgraded IFD versions NL-6 or NL-7
- ANNs can be trained using large datasets created with the FDM simulations
- These ANNs can be coupled with *genetic algorithms* and the task of finding optimum collector designs can be assigned to a computer

New collector testing

- Based on existing and further simulations of modified collector designs and control strategies which show substantial gains in COP, experimental tests should be conducted to confirm these gains over one or more heating seasons and benchmark these collector designs against standard/existing designs
- Tests should be conducted with *split-level collectors* using *collector temperature feedback control*, installed on a south facing slopes with the option of night-time insulation or a surface cover designed for this purpose
- During the *HP-IRL/H* project the $GSHP_{HC}$ test facility was equipped to combine solar collectors with the horizontal collector in the future by:
    - Using solar collectors to add additional heat to the ground source return fluid, possibly during cool but clear-sky conditions in winter
    - Using solar collectors to add heat to the ground, possibly during mild clear-sky conditions in spring for use at night or in the coming cooler days

REFERENCES


GMIT
GALWAY-MAYO INSTITUTE OF TECHNOLOGY
INSTITIÚID TEICNEOLAÍOCHTA NA GAILLIMHE-MAIGH EO

REFERENCES

Aittomaki, A. & Toivanen, O., 1999. Criteria for Dimensioning of Horizontal Ground Heat Exchangers in Cold Climates. In 6th International IEA Heat Pump Conference. Berlin, 1999.

Akpinar, E.K. & Hepbasli, A., 2007. A Comparative Study on Exergetic Assessment of two Ground-Source (Geothermal) Heat Pump Systems for Residential Applications. Building and Environment, 42, pp.2004-13.

Alhuthaili, S., 2004. Theoretical, Experimental and Field Testing of Ground Source Heat Pump Systems. PhD Thesis. Nottingham, UK: University of Nottingham.

Alistair B., S., 2007. Derivation of the Solar Geometric Relationships Using Vector Analysis. Renewable Energy, 32, pp.1187-205.

Allen, A., Milenic, D. & Sikora, P., 2003. Utilisation of the Urban 'Heat Island' Effect on Shallow Gravel Aquifers as a Source of Low Enthalpy Hydrogeothermal Energy. Geothermics, 32(4-6), pp.569-78.

Allen, R.G., Trezza, R. & Tasumi, M., 2006. Analytical Integrated Functions for Daily Solar Radiation on Slopes. Agricultural and Forest Meteorology, 139, pp.55-73.

Asaeda, T. & Thanh Ca, V., 2000. Characteristics of Permeable Pavement During Hot Summer Weather and the Impact on the Thermal Environment. Building and Environment, 35, pp.363-75.

Badesku, V., 2007. Simple and Accurate Model for the Ground Heat Exchanger of a Passive House. Renewable Energy, 32, pp.845-55.

Beltrami, H., 2001. On the Relationship Between Ground Temperature Histories and Meteorological Records: A Report on the Pomquet Station. Global and Planetary Change, 29, pp.327-48.

Bennie, J., Huntley, B., Wiltshire, A., Hill, M.O. & Baxter, R., 2008. Slope, aspect and climate: Spatially explicit and implicit models of topographic microclimate in chalk grassland. Ecological Modelling, 216, pp.47-59.

Berg, L., 1980. Building heat conservation and the feasilibility of solar hot water heating in long island shellfish hatcheries. Technical Document. OSTI.

Bi, Y., Chen, L. & Wu, C., 2002. Ground Heat Exchanger Temperature Distribution Analysis and Experimental Verification. Applied Thermal Engineering, 22, pp.183-89.

Bose, J.E., Smith, M.D. & Spitler, J.D., 2002. Advances in Ground Source Heat Pump Systems an International Overview. In 7th International Energy Agency Heat Pump Conference. Beijing, China, 2002.

Bryden, H.L. & Imawaki, S., 2001. Ocean Heat Transport. Ocean Circulation and Climate, pp.455-74.

Burke, N., 2010. An Experimental Characterisation of Ground and Air Source Heat Pump Technologies in the Irish Maritime Climate. PhD Thesis. Galway, Ireland: Galway-Mayo Institute of Technology.

Burke, N., Greene, M., Lohan, J. & Clarke, R., 2008. Heat Pump Performance Sensitivity to Horizontal and Vertical Designs in a Maritime Climate Region. In IEA, 9th International Heat Pump Conference. Zurich, Switzerland, 2008. International Energy Agency.

Cahill, A.T. & Parlange, M.B., 1998. On water vapor transport in field soils. Water Resources Research, 34(4), pp.731-39.

Campbell, G.S. & Norman, J.M., 1998. An Introduction to Environmental Biophysics. 2nd ed. New York: Springer Science and Business Media Inc.

Caneta-Research, 2003. Global Warming Impacts of Ground-Source Heat Pumps Compared to Other Heating and Cooling Systems. An Update for the Canadian Geoexchange Coalition. Mississauga, Ontario.

Cengel, Y.A., 2000. Fundamentals of Thermal-Fluid Sciences. McGraw Hill.

Cengel, Y.A. & Boles, M.A., 2002. Thermodynamics An Engineering Approach. 4th ed. New York: McGraw-Hill.

Chiasson, A., 1999. Advances in Modelling of Ground Source Heat Pump Systems. Masters Thesis. Oklahoma: Oklahoma State University.

CIBSE, 1981. Building Energy Code - Part 2: Calculation of Energy Demands and Targets for the Design of New Buildings and Services. Technical Document. London: The Chartered Institution of Building Services Engineers.

CIBSE-TM38, 2010. CIBSE Engineering and Sustainable Built Environment. [Online] Available at: http://www.cibse.org/index.cfm?go=page.view&item=638 [Accessed 12 November 2010].

Claesson, J. & Dunand, A., 1983. Heat Extraction from the Ground by Horizontal Pipes. Swedish Council for Building Research.

Clarke, R., 2009. Development of a Data Acquisition System to Characterise Sustainable Energy Technologies and to Support Web-Based Learning (DAQ-WBL). MSc Thesis. Galway, Ireland: GMIT Galway-Mayo Institute of Technology.

Davis, C.P. & Carrington, C.G., 2005. Energy Use in Controlled Temperature Marine Aquaculture. International Journal of Energy Research, 29(3), pp.265-82.

DCENR, 2010. Draft National Renewable Energy Action Plan. Dublin: Government of Ireland.

DCMNR, 2007. Delivering a Sustainable Energy Future for Ireland 'The Energy Policy Framework 2007-2020'. Government White Paper. Dublin.

De Vries, D.A., 1958. Simultaneous Transfer of Heat and Moisture in Porous Media. Transactions American Geophysical Union, 39(5), pp.909-16.

Deffeyes, K.S., 2002. Hubbert's Peak: The Impending World Oil Shortage. Princeton University Press.

DEHLG, 2007. Irish National Climate Change Strategy 2007-2012. Policy Document. Dublin: Irish Government.

DEHLG, 2007. S.I. No. 83 Ammendment to Planning and Development Regulations. Dublin: Government of Ireland.

DEHLG, 2007. Technical Guidance Document, Part L, Conservation of Fuel and Energy. Dublin: Government of Ireland.

DEHLG, 2008. S.I. No. 235 Planning and Development Regulations. Dublin: Government of Ireland.

DEHLG, 2008. S.I. No. 259 Building Regulations Part L Ammendment. Dublin: Government of Ireland.

DEHLG, 2010. Building Regulations Part L Ammendment. Dublin: Government of Ireland.

Demir, H., Koyun, A. & Temir, G., 2009. Heat Transfer of Horizontal Parallel Pipe Ground Heat Exchanger and Experimental Verification. Applied Thermal Engineering, 29, pp.224-23.

Dennehy, E., Howley, M., Ó Gallachóir, B. & Barriscale, A., 2010. Renewable Energy in Ireland 2010 Update. Dublin: Sustainable Energy Authority of Ireland.

Deru, M.P. & Kirkpatrick, A.T., 2001. Ground-Coupled Heat and Moisture Transfer from Buildings Part 1: Analysis and Modelling. In National Solar Conferences Forum. Washington D.C., 2001. American Solar Energy Society.

Diao, N., Li, Q. & Fang, Z., 2004. Heat Transfer in Ground Heat Exchangers with Ground Water Advection. International Journal of Thermal Sciences, 4, pp.1203-11.

Dimplex, 2010. Installation and Operating Instructions SI 5ME through SI 14ME - Brine to Water Heat Pump for Indoor Installation. Users Manual. Dimplex.

Doherty, P.S., Al-Huthaili, S., Riffat, S.B. & Abodahab, N., 2004. Ground Source Heat Pump- Description and Preliminary Results of the Eco-House System. Applied Thermal Engineering, 24, pp.2627-41.

Drown, D.C. & Den Braven, K.R., 1992. The Effect of Soil Conditions on Heat Transfer in Ground Source Heat Pumps. Solar Engineering, 1, pp.411-16.

Dumont, E. & Frere, M., 2005. Performance of Ground Source Residential Heat Pumps. In 8th International Energy Agency Heat Pump Conference. Las Vegas, Nevada, 2005.

Dunstar, 2003. Solterrra Geoenergy Heating Systems-Owners Manual. Cork: Dunstar Ltd.

Duprez, M.E., Dumont, E. & Frere, M., 2007. Modelling of reciprocating and scroll compressors. International Journal of Refrigeration, 30, pp.873-86.

Elias, E.A., Cichota, R., Torriani, H.H. & De Jong Van Lier, Q., 2004. Analytical Soil-Temperature Model: Correction for Temporal Variation of Daily Amplitude. Soil Science Society of America Journal, 68, pp.784-88.

Elias, E., Cichota, R., Torriani, H.H. & De Jong Van Lier, Q., 2004. Analytical Soil-Temperature Model: Correction for Temporal Variation of Daily Amplitude. Soil Sci. Soc. Am.J., 68, pp.784-88.

Endrizzi, S., Rigon, R. & DallAmico, M., 2008. A Soil Freeze/Thaw Model through the Soil Water Characteristic Curve. In Ninth International Conference on Permafrost. Fairbanks, Alaska, 2008.

Engelmark, H. & Svensson, U., 1993. Numerical Modelling of Phase Change in Freezing and Thawing Unsaturated Soil. Nordic Hydrology, 24, pp.95-110.

Esen, H., Inalli, M. & Esen, M., 2006. Technoeconomic Appraisal of a Ground Source Heat Pump System for a heating Season in Eastern Turkey. Energy Conservation and Managment, 47, pp.1281-97.

Esen, H., Inalli, M. & Esen, M., 2006. Technoeconomic Appraisal of a Ground Source Heat Pump System for a Heating Season in Eastern Turkey. Energy Conversion and Managment, 47, pp.1281-97.

Esen, H., Inalli, M. & Esen, M., 2007. Numerical and Experimental Analysis of a Horizontal Ground-Coupled Heat Pump System. Building and Environment, 42, pp.1126-34.

Esen, H., Inalli, M., Esen, M. & Pihtili, K., 2007. Energy and exergy analysis of a ground-coupled heat pump system with two horizontal ground heat exchangers. Building and Environment, 42, pp.3606-15.

Esen, H., Inalli, M., Sengur, A. & Esen, M., 2008. Performance Prediciton of a Ground-Coupled Heat Pump System Using Artificial Neural Networks. Expert Systems with Applications, 35, pp.1940-48.

Esen, H., Inalli, M., Sengur, A. & Esen, M., 2008. Performance Prediction of a Ground-Coupled Heat Pump System using Artificial Neural Networks. Expert Systems with Applications, 35, pp.1940-48.

Eskilson, P., 1987. Thermal analysis of heat extraction boreholes. Lund, Sweden: Department of Mathematical Physics, University of Lund.

Eskilson, P. & Claesson, J., 1988. Simulation Model for Thermally Interacting Boreholes. Numerical Heat Transfer, 13, pp.149-65.

EST, 2007. CE82 Domestic Ground Source Heat Pumps: Design and installation of closed-loop systems – A guide for specifiers, their advisors and potential users. Technical Guidance Document. London.

Feist, W., 2004. First Steps: What can be a Passive House in Your Region with Your Climate. Darmstadt: Passive House Institute.

Fernando, P., Palm, B., Lundqvist, P. & Granryd, E., 2004. Propance heat pump with low refrigerant charge: design and laboratory tests. International Journal of Refrigeration, 27, pp.761-73.

Flerchinger, G.N., 2000. The Simultaneous Heat and Water (SHAW) Model: Technical Documentation. Boise, Idaho: Northwest Watershed Research Center USDA Agricultural Research Service.

Florides, G. & Kalogirou, S., 2007. Ground Heat Exchangers-A Review of Systems, Models and Applications. Renewable Energy, 32, pp.2461-78.

Gan, G., Riffat, S.B. & Chong, C., 2007. A Novel Rainwater-Ground Source Heat Pump - Measurement and Simulation. Applied Thermal Engineering, 27, pp.430-41.

Garimella, S., 2003. Innovations in Energy Efficient and Environmentally Friendly. Energy, 28, pp.1593-614.

Gauthier, C., Lacroix, M. & Bernier, H., 1997. Numerical Simulation of Soil Heat Exchanger-Storage System for Greenhouses. Solar Energy, 60(6), pp.333-46.

Genchi, Y., Kikegawa, Y. & Inaba, A., 2002. CO2 payback–time assessment of a regional-scale heating and cooling system using a ground source heat–pump in a high energy–consumption area in Tokyo. Applied Energy, 71, pp.417-160.

Giardina, J., 1995. Evaluation of Ground Coupled Heat Pumps for the State of Wisconsin. Masters Thesis. University of Wisconsin.

Giardina, J.J., 1995. Evaluation of Ground Coupled Heat Pumps for the State of Wisconsin. Masters Thesis. Madison, Wisconsin: University of Wisconsin-Madison.

GLD2010, 2010. Ground Loop Design Software Technical Documentation. Maple Plain, MN, USA: Thermal Dynamics Inc.

Golaka, A.R.T. & Exell, R.H.B., 2004. The Downward Atmospheric Longwave Radiation at Night in Northern Thailand. Technical. Bangkok, Thailand: King Mongkut's University of Technology Thonburi.

Goodman, R., Jones, G., Kelly, J., Slowey, E. & O'Neill, N., 2004. Geothermal Energy Resource Map of Ireland-Final Report. Dublin: Sustainable Energy Authority of Ireland CSA Group.

Grandall, A.C., 1946. House Heating with an Earth Heat Pump. Electrical World, 126, pp.94-95.

Groppe, H., 2005. Peak Oil: Myth vs Reality. In Denver World Oil Conference. Denver, 2005.

Gunerhan, A. & Hepbasli, A., 2007. Determination of the Optimum Tilt Angle of Solar Collectors for Building Applications. Building and the Environment, 42, pp.779-83.

Gupta, R. & Irving, R., 2008. Assessing the Potential of Ground Source Heat Pumps to Provide Low-Carbon Heating and Cooling in UK Dwellings in a Changing Climate. In Air Conditioning and the Low Carbon Cooling Challenge. Windsor, 2008.

Haider-Khan, M., 2004. Modeling, Simulation and Optimization of Ground Source Heat Pump Systems. Masters Thesis. Oklahoma State University.

Hamada, Y., Nakamura, M., Saitoh, H., Kubota, H. & Ochifuji, K., 2007. Improved underground heat exchanger by using no-dig method for space heating and cooling. Renewable Energy, 32, pp.480-95.

Hart, D.P. & Couvillion, R., 1986. Earth-Coupled Heat Transfer. Technical. Dublin, OH, USA: National Water Well Association.

Healy, P.F. & Ugursal, V.I., 1997. Performance and Economic Feasibility of Ground Source heat Pumps in Cold Climate. International Journal of Energy Research, 221, pp.857-70.

Hellstrom, G. & Sanner, B., 1994. Software for Dimensioning Deep Boreholes for Heat Extraction. In 6th International Conference on Energy Storage., 1994.

Hepbasli, A., Akdemir, O. & Hancioglu, E., 2003. Experimental Study of a Closed Loop Vertical Ground Source Heat Pump System. Energy Conversion and Management, 44, pp.527-48.

Hermansson, A., 2004. Mathematical Model for Paved Surface Summer and Winter Temperature: Comparison of Calculated and Measured Temperatures. Cold Regions Science and Technology, 40, pp.1-17.

Hern, S.D., 2004. Design of an Experimental Facility for Hybrid Ground Source Heat Pump Systems. Masters Thesis. Oklahoma State University.

HLGGE, 2009. Developing the Green Economy in Ireland. Dublin: High Level Group on Green Enterprise, Government of Ireland.

Howley, M., O'Gallachoir, B. & Dennehy, E., 2009. Energy in Ireland 1990-2008. Dublin: Sustainable Energy Ireland.

IEA-HPC, 2010. Heat Pump Centre. [Online] Available at: http://www.heatpumpcentre.org [Accessed 9 November 2010].

IIT, 2011. Analysis of Complete Vapour Compression Refrigeration Systems. Indian Institute of Technology.

Inalli, M. & Esen, H., 2004. Experimental Thermal Performance Evaluation of a Horizontal Ground-Source Heat Pump. Applied Thermal Engineering, 24, pp.2219-32.

Incorpera, F.P. & DeWitt, D.P., 2002. Heat and Mass Transfer. John Wiley and Sons.

Ingersoll, L.R. & Plass, H.J., 1948. Theory of the Ground Pipe Heat Source for the Heat Pump. Heating Piping Air Conditioning Journal, 20, pp.119-22.

IPCC, 2007. Climate Change 2007: Synthesis Report. Contribution of Working Groups I, II and III to the Fourth Assessment Report of the Intergovernmental Panel on Climate Change. Geneva, Switzerland: IPCC.

Izquierdo, M. & Carrillo, M., 1997. Optimization of Aquaculture Systems in Spain. Energy Conservation and Managment, 38(9), pp.879-88.

Jayatissa, W., Davis, C., Carrington, G. & Chen, G., 2002. Energy Use in Controlled Temperature Marine Aquaculture. International Journal of Energy Research, 26(15), pp.1333-43.

Kammen, D.M., Kapadia, K. & Fripp, M., 2004. Putting Renewables to Work: How Many Jobs Can the Clean Energy Industry Generate? RAEL Report. University of California, Berkeley.

Kang, S., Kim, S., Oh, S. & Lee, D., 2000. Predicting spatial and temporal patterns of soil temperature based on topography, surface cover and air temperature. Forest Ecology and Management, 136, pp.173-84.

Karlsson, F., 2007. Capacity Control of Residential Heat Pump Heating Systems. PhD Thesis. Goteburg, Sweden: Chalmers University of Technology.

Karlsson, F. & Fahlen, P., 2007. Capacity-controlled ground source heat pumps in hydronic heating systems. International Journal of Refrigeration, 30, pp.221-29.

Kavanaugh, S.P., 1984. Simulation and Experimental Verification of Vertical Ground-Coupled Heat Pump Systems. PhD Thesis. Oklahoma, USA: Oklahoma State University.

Kavanaugh, S.P. & Rafferty, K., 1997. Ground-source heat pumps: design of geothermal systems for commercial and institutional buildings. ASHRAE, 167.

Kim, D.H., Jenkins, B.M., Rumsey, T.R., Yore, M.W. & Kim, N.J., 2007. Simulation and Model Validation of a Horizontal Shallow Basin Solar Concentrator. Solar Energy, 81, pp.463-75.

Klein, E., 2002. Understanding, Design, Action: The Threefold Purpose of Simulation. Research and Simulation, 47(Winter 2002-2003), pp.6-8.

Koeppe, C.E. & De Long, C.G., 1958. Weather and Climate. McGraw-Hill Book Company Inc.

Koppelaar, R., 2005. World Oil Production & Peaking Outlook. In Stitching Peak Oil-Nederland., 2005.

Kottek, M., Grieser, J., Beck, C., Rudolf, B. & Rubel, F., 2006. World Map of the Köppen-Geiger Climate Classification Updated. Meteorologische Zeitschrift, 15(3), pp.259-63.

Koyun, A., Demir, H. & Torun, Z., 2009. Experimental Study of Heat Transfer of Buried Finned Pipe for Ground Source Heat Pump Applications. International Communications in Heat and Mass Transfer, 36, pp.739-43.

Kumar, R., Ramesh, S. & Kaushik, S.C., 2003. Performance Evaluation and Energy Conservation Potential of Earth-Air-Tunnel System Coupled with Non-Air-Conditioned Building. Building and Environment, 38, pp.807-13.

Lazzarin, R.M., 2007. Technological Innovations in Heat Pump Systems. International Journal of Low Carbon Technologies, 2(3), pp.262-88.

Leong, W.H., Tarnawski, V.R. & Aittomaki, A., 1998. Effect of Soil Type and Moisture Content on Ground Heat Pump Performance. International Journal of Refrigeration, 21(8), pp.595-606.

Lim, K., Lee, S. & Lee, C., 2007. An Experimental Study on the Thermal Performance of Ground Heat Exchanger. Experimental Thermal and Fluid Science, 31, pp.985-90.

Ling, F. & Zhang, T., 2004. A Numerical Model for Surface Energy Balance and Thermal Regime of the Active Layer and Permafrost Containing Unfrozen Water. Cold Regions Science and Technology, 38, pp.1-15.

Liu, J.Y., 1991. Solutions of Luikov Equations of Heat and Mass Transfer in Capillary-Porous Bodies. International Journal of Heat and Mass Transfer, 34(7), pp.1747-54.

Lohan, J., Burke, N. & Greene, M., 2006. Climate Variables that Influence the Thermal Performance of Horizontal Collector Ground Source Heat Pumps. In 8th Biennial ASME Conference on Engineering Systems Design and Analysis. Torino, Italy, 2006. ASME.

Loomans, M., Oversloot, H., de Bondt, A., Jansen, R. & van Rij, H., 2003. Design tool for the thermal energy potential of Asphalt Pavements. In Eighth International IBPSA Conference. Eindhoven, Netherlands, 2003.

Lorentzen, G., 1995. The Use of Natural Refrigerants: A Complete Solution to the CFC/HCFC Predicament. International Journal of Refrigeration, 18(3), pp.190-97.

Lund, H., 2007. Renewable Energy Strategies for Sustainable Development. Energy, 32(6), pp.912-19.

Lund, H., 2010. Renewable Energy Systems - The Choice and Modeling of 100% Renewable Solutions. Burlington, MA: Academic Press - Elsevier Inc.

Lundqvist, P., 2011. Research Needs for Efficient Heat Pumps in the EU. Presentation. Brussels: Hybrid Renewable Energy Systems and Heat Pumps - Workshop.

Lund, J.W., Sanner, B., Rybach, L., Curtis, R. & Hellstrom, G., 2003. Geothermal Heat Pumps-A World Review. Renewable Energy World, 6(4), pp.218-27.

Marshall, T.J., Holmes, J.W. & Rose, C.W., 1996. Soil Physics. Cambridge University Press.

Martin, C.L. & Goswami, D.Y., 2005. Solar Energy Pocket Reference. ISES.

McDonald, A. & Schrattenholzer, L., 2001. Learning Rates for Energy Technologies. Energy Policy, 29, pp.255-61.

Mei, V.C., 1986. Theoretical Heat Pump Ground Coil Analysis with Variable Ground Farfield Boundary Conditions. AIChE Journal, 32(7), pp.1211-15.

Mei, V.C., 1987. Effect of Backfilling Material on Ground Coil Performance. Transactions of the ASME, 93(2), pp.1845-57.

Mendes, N., Philippi, P.C. & Lamberts, R., 2002. A New Mathematical Method to Solve Highly Coupled Equations of Heat and Mass Transfer in Porous Media. International Journal of Heat and Mass Transfer, 45, pp.509-18.

Met, 2010. The Irish Meteorological Service Online. [Online] Available at: http://www.met.ie [Accessed 23 July 2010].

Metz, P.D., 1979. Experimental Results from the First Year of Operation of the Solar Ground Coupling Research Facility at Brookhaven National Laboratory. In 2nd International Conference on Alternative Energy Sources. Miami Beach, FL, 1979.

Metz, P.D., 1981. Design, Operation and Performance of a Ground Coupled Heat Pump System in a Cold Climate. In 16th Intersoc. Energy Conversion Eng. Conf. Atlanta, Georgia, 1981.

Metz, P.D., 1983. A Simple Computer Program to Model 3-Dimensional Underground Heat Flow with Realistic Boundary Conditions. Transactions ASME, 105, pp.42-49.

Michopoulos, N. & Kyriakis, N., 2009. Predicting the Fluid Temperature at the Exit of the Vertical Ground Heat Exchangers. Applied Energy, 86, pp.2065-70.

Mihalakakou, G., 2002. On Estimating Soil Surface Temperature Profiles. Energy and Buildings, 34, pp.251-59.

Mihalakakou, G. & Lewis, J.O., 1996. The Influence of Different Ground Covers on the Heating Potential of Earth to Air Heat Exchangers. Renewable Energy, 7(1), pp.33-46.

Mihalakakou, G., Santamouris, M., Lewis, J.O. & Asimakopoulos, D.N., 1997. On the application of the energy balance equation to predict ground temperature profiles. Solar Energy, 60(3/4), pp.181-90.

Neksa, P., 2002. CO2 Heat Pump Systems. International Journal of Refrigeration, 25, pp.421-27.

Neymark, J., Judkoff, R., Knabe, G., Le, H.T., Durig, M., Glass, A. & Zweifel, G., 2002. Applying the Building Energy Simulation Test (BESTEST) diagnostic method to verification of space conditioning equipment models used in whole-building energy simulation programs. Energy and Buildings, 34(9), pp.917-31.

Ochsner, T.E., Horton, R. & Ren, T., 2001. A New Perspective on Soil Thermal Properties. Soil Science Society of America Journal, 65, pp.1641-47.

Ochsner, T.E., Horton, R. & Ren, T., 2001. A New Perspective on Soil Thermal Properties. Soil Science Society of America Journal, 65, pp.1641-47.

O'Connell, S. & Cassidy, S., 2003. Recent Large Scale Ground-Source Heat Pump Installations in Ireland. In International Geothermal Conference. Reykjavík, Iceland, 2003.

O'Connell, S. & Cassidy, S.F., 2004. Experimental and Theoretical Determination of Soil-Collector Thermal Contact Resistance for a Ground-Source Heat Pump. In 3rd International Heat Powered Cycles Conference. Larnaca, Cyprus, 2004.

Paepe, M.D. & Janssens, A., 2003. Thermo-hydraulic Design of Earth-Air Heat Exchangers. Energy and Buildings, 35, pp.389-97.

Pahud, D., 2002. Geothermal Energy and Heat Storage. Technical Document. Universitaria Professionale della Svizzera Italiana.

Palm, B., 2007. Refrigeration Systems with Minimum Charge of refrigerant. Applied Thermal Engineering, 27, pp.1693-701.

Palyvos, J.A., 2008. A Survey of Wind Convection Coefficient Correlations for Building Envelope Energy Systems Modelling. Applied Thermal Engineering, 28, pp.801-08.

Peel, M.C., Finlayson, B.L. & McMahon, T.A., 2007. Updated World Map of the Koppen-Geiger Climate Classification. Hydrology and Earth System Sciences, 4, pp.439-73.

Piechowski, M., 1996. A Ground-Coupled Heat Pump System with Thermal Storage. PhD Thesis. Melbourne: The University of Melbourne.

Poireau, M., 2010. NMP 2011 Work Program Draft. European Union.

Pollack, H.N., Smerdon, J.E. & Van Keken, P.E., 2005. Variable Seasonal Coupling Between Air and Ground Temperatures: A Simple Representation in Terms of Subsurface Thermal Diffusivity. Geophysical Research Letters, 32.

Popiel, C.O., Wojtkowiak, J. & Biernacka, B., 2001. Measurement of Temperature Distribution in Ground. Experimental Thermal and Fluid Science, Int. Journal, 25, pp.301-09.

Poulek, V. & Libra, M., 1998. New Solar Tracker. Solar Energy Materials and Solar Cells , 51, pp.113-20.

Pulat, E., Coskun, S., Unlu, k. & Yamankaradeniz, N., 2009. Experimental Study of Horizontal Ground Source Heat Pump Performance for Mild Climate in Turkey. Energy, (xx), pp.1-12.

Puri, V.M., 1986. Feasibility and Performance Curves for Intermittent Earth Tube Heat Exchangers. American Society of Agricultural Engineering, 29, pp.526-32.

Qin, Z., Berliner, P. & Karnieli, A., 2002. Numerical Solution of a Complete Surface Energy Balance Model for Simulation of Heat Fluxes and Surface Temperature Under Bare Soil Environment. Applied Mathematics and Computation, 130, pp.171-200.

Ramamoorthy, M., 2001. Applications of Hybrid Ground Source Heat Pump Systems to Buildings and Bridge Decks. Masters Thesis. Oklahoma State University.

Remund, C.P., 1994. Thermal Performance Evaluation of Common Soils for Horizontal Ground Source Heat Pump Application. Heat Pump and Refrigeration Systems Design, 32, pp.45-62.

REN21, 2009. Renewables Global Status Report 2009 Update. Deutsche Gesellschaft für Technische Zusammenarbeit (GTZ) GmbH.

Retscreen, 2005. Ground Source Heat Pump Project Analysis. Minister of Natural Resources.

Rybach, L. & Sanner, B., 2000. Ground-Source Heat Pump Systems the European Experience. GHC Bulletin.

Safanda, J., 1999. Ground Surface Temperature as a Function of Slope Angle and Slope Orientation and its Effect on the Subsurface Temperature Field. Tectonophysics, 306, pp.367-75.

Saito, H. & Simunek, J., 2009. Effects of Meteorological Models on the Solution of the Surface Energy Balance and Soil Temperature Variations in Bare Soils. Journal of Hydrology, 373, pp.545-61.

Salomone, L.A. & Marlowe, J.I., 1989. Soil and Rock Classification for the Design of Ground-Coupled Heat Pump Systems - Field Manual. Stillwater, Oklahoma: International Ground Source Heat Pump Association.

Salomone, A. & Wechsler, H., 1984. Influence of Soil Type and Gradation on the Thermal Resistivity of Soils. Underground Space, 8(5-6), pp.363-71.

Sand, J.R., Fischer, S.K. & Baxter, V.D., 1997. Energy and Global Warming Impacts of HFC Refrigerants and Emerging Technologies. Technical Document. Oakridge, Tennessee: U.S. Department of Energy Oakridge National Laboratory.

Sanner, B., 2008. Guidelines, Standards, Certification and Legal Permits for Ground Source Heat Pumps in the European Union. In 9th International IEA Heat Pump Conference. Zurich, Switzerland, 2008.

Sanner, B., Karytsas, C., Mendrinos, D. & Rybach, L., 2003. Current Status of Ground Source Heat Pumps and Underground Thermal Energy Storage in Europe. Geothermics, 32, pp.579-88.

Santamouris, M., Mihalakakou, G., Balaras, C.A., Argiriou, A., Asimakopoulos, D. & Vallindras, M., 1995. Use of Buried Pipes for Energy Conservation in Cooling of Agricultural Greenhouses. Solar Energy, 55(2), pp.111-24.

Sargent, R.G., 1996. Verifying and Validating Simulation Models. In 1996 Winter Simulation Conference. Coronado, California, 1996.

Saxton, K.E. & Rawls, W.J., 2006. Soil Water Characteristic Estimates by Texture and Organic Matter for Hydrologic Solutions. Soil Science Society of America Journal, 70, pp.1569-78.

Schmidt, W.L., Gosnold, W.D. & Enz, J.W., 2001. A Decade of Air–ground Temperature Exchange from Fargo, North Dakota. Global and Planetary Change, 29, pp.311-25.

SEAI, 2006. Renewable Heat Pumps. Dublin: Sustainable Energy Authority of Ireland.

SEAI, 2008. Dwelling Energy Assessment Procedure (Version 3.1). User's Manual. Dublin: Sustainable Energy Authority of Ireland.

SEAI, 2008. Heating and Domestic Hot Water Systems for dwellings – Achieving compliance with Part L 2008. Dublin: Department of the Environment Heritage and Local Government.

SEAI, 2010. Commercial/Industrial Fuels Comparison of Energy Costs. Guidance. Dublin: Sustainable Energy Authority of Ireland.

SEAI, 2010. Domestic Fuels - Comparison of Energy Costs. Technical Guidance. Dublin, Ireland: Sustainable Energy Authority of Ireland.

SEAI, 2010. Strategic Plan 2010-2015. Dublin: Sustainable Energy Authority of Ireland.

Singh, S. & Marsh, L., 1996. Modelling Thermal Environment of a Recirculating Aquaculture Facility. Aquaculture, 139(1-2), pp.11-18.

Smerdon, J.E., Pollack, H.N..C.V., Enz, J.W., Kresl, M., Safanda, J. & Wehmiller, J.F., 2004. Air-ground Temperature Coupling and Subsurface Propogation of Annual Temperature Signals. Journal of Geophysical Research, 109.

Spitler, J.D. & Cullen, J., 2008. Misconceptions Regarding Design of Ground-source Heat Pump Systems. In World Renewable Energy Congress. Glasgow, Scotland, 2008.

Stephens, P., 2003. Innovation in Business Centre Design Study. Building Energy Rating.

Stevens, J.W., 2004. Optimal Placement Depth for Air-Ground Heat Transfer Systems. Applied Thermal Engineering, 24, pp.149-57.

Stevens, J.W., 2004. Optimal Placement Depth for Air-Ground Heat Transfer Systems. Applied Thermal Engineering, (24), pp.149-57.

Svec, O.J., 1987. Potential of Ground Heat Source Systems. International Journal of Energy Research, 11, pp.573-81.

Svec, O.J., 1991. Design Evaluation of the Ground Source Heat Pump with Horizontal Spiral Heat Exchangers. In 5th International Congress on Thermal Energy Storage. Scheveningen, 1991.

Takasugi, S., Akazawa, T., Okumura, T. & Hanano, M., 2001. Feasibility Study on the Utilisation of Geothermal Heat Pump (GHP) Systems in Japan. Geo-Heat Centre Quarterly Bulletin, 22(1), pp.3-8.

Takebayashi, H. & Moriyama, M., 2009. Study on the urban heat island mitigation effect achieved by converting to grass-covered parking. Solar Energy, 83, pp.1211-23.

Tarnawski, V.R. & Leong, W.H., 1993. Computer Analysis, Design and Simulation of Horizontal Ground Heat Exchangers. International Journal of Energy Research, 17, pp.467-77.

Tarnawski, V.R., Leong, W.H., Momose, T. & Hamada, Y., 2009. Analysis of ground source heat pumps with horizontal ground heat exchangers for northern Japan. Renewable Energy, 34, pp.127-34.

Tessy Chacko, P. & Renuka, G., 2002. Temperature mapping, thermal diffusivity and subsoil heat flux at Kariavattom of Kerala. Proc. Indian Acad. Sci. (Earth Planet. Sci.), 111(1), pp.79-85.

Thomas, H.R. & Li, C.L.W., 1995. Modelling Transient Heat and Moissture Transfer in Unsaturated Soil Using Parallel Computing Approach. International Journal for Numerical and Analytical Methods in Geomechanics, 19, pp.345-66.

Timmons, M.B., Ebeling, J.M., Wheaton, F.W., Summerfelt, S.T. & Vinci, B.J., 2002. Recirculating Aquaculture Systems. 2nd ed. Ithaca, New York: Cayuga Aqua Ventures.

Van Buren, M.A., Watt, W.E., Marsalek, J. & Anderson, B.C., 2000. Thermal Enhancement of Stormwater Runoff by Paved Surfaces. Water Resources, 34(4), pp.1359-71.

Van Wijk, W.R. & De Vries, D.A., 1963. Periodic Temperature variations in a Homogenous Soil. In W.R. Van Wijk, ed. Physics of Plant Environment. Amsterdam: North Holland Publ. Co.

VDI-4640, 2004. Thermal Use of the Underground-Direct Uses. Standard. Dusseldorf: Verien Deutscher Ingenieure.

Vision-Learning, 2010. Vision Learning - The Hydrological Cycle. [Online] Available at: http://www.visionlearning.com/library/module_viewer.php?mid=99&l= [Accessed 10 December 2010].

Walker, N., Scheer, J., Clancy, M. & Ó Gallachóir, B., 2009. Energy Forecasts for Ireland to 2020. Dublin: Sustainable Energy Authority of Ireland.

Wang, H., Qi, C., Wang, E. & Zhao, J., 2009. A Case Study of Underground Thermal Storage in a Solar-Ground Coupled Heat Pump System for Residential Buildings. Renewable Energy, 34, pp.307-14.

Warnelof, J. & Kronstrom, U., 2005. Ground Source Heat Pump with a New Compact Collector. In IEA 8th International Heat Pump Conference. Las Vegas, Nevada, 2005. International Energy Agency.

White, F.M., 1999. Fluid Mechanics. 4th ed. Singapore: WCB/McGraw-Hill.

Wibbels, M. & Den Braven, K., 1994. The Effect of Cyclic Operation of a Horizontal Ground Loop on Ground Coupled Heat Pump Performance. AES-Heat Pump and Refrigeration Systems Design, Analysis and Applications, 32, pp.33-44.

WMO, 2010. World Weather Information Service - Official Observation. Official Forecasts. [Online] Available at: http://worldweather.wmo.int/ [Accessed 28 June 2010].

Wu, Y., Gan, G., Verhouf, A., Vidale, P.L. & Gonzalez, R.G., 2010. Experimental Measurement and Numerical Simulation of Horizontal-Coupled Slinky Ground Source Heat Exchangers. Applied Thermal Engineering, 30, pp.2574-83.

Yeung, K.-w.D., 1996. Enhancements to a Ground Loop Heat Exchanger Design Program. Masters Thesis. Oklahoma State University.

Zhiqiang, L., Xiaolin, L., Hanqing, W. & Wangming, P., 2008. Performance comparison of air source heat pump with R407C and R22 under frosting and defrosting. Energy Conservation and Management, 49, pp.232-39.

Zogou, O. & Stamatelos, A., 1998. Effect of Climatic Conditions on the Design of Heat Pump Systems for Space Heating and Cooling. Energy Convers. Mgmt, 39(7), pp.609-22.

Zottl, A., 2003. Type test of the heat pump Solterra 500 as prescribed by the D-A-C-H testing regulation for the testing of brine/water heat pumps. Vienna: Arsenal Research.

APPENDICES


GMIT
GALWAY-MAYO INSTITUTE OF TECHNOLOGY
INSTITIÚID TEICNEOLAÍOCHTA NA GAILLIMHE-MAIGH EO

A. HEAT PUMP STANDARDS

The following are standards which are relevant to the design and installation of heat pumps, ground heat exchangers and related systems:

EN 1861:2008	Refrigeration systems and heat pumps. Flexible pipe elements, vibration isolators, expansion joints and non-metallic tubes. Requirements, design and installation.
EN 12693:2008	Refrigeration systems and heat pumps. Safety and environmental requirements.
EN 15450:2007	Heating systems in buildings – Design of heat pump heating systems
EN 14276:2006/2007	Pressure equipment for refrigerating systems and heat pumps - Vessels & Piping – General requirements
CEN/TS 14825:2006	Air conditioners, liquid chilling packages and heat pumps with electrically driven compressors for space heating and cooling – Testing and rating at part load conditions
EN 15316-4-2:2005	Heating systems in buildings – Method for calculation of system energy requirements and system efficiencies – Part 4-2: Space heating generation systems, heat pump systems
EN 14511:2004	Air conditioners, liquid chilling packages and heat pumps with electrically driven compressors for space heating and cooling – requirements and testing
EN 12178:2003	Refrigerating systems and heat pumps – Liquid level indicating devices – Requirements, testing and marking
EN 255-2:2001	Air conditioners, liquid chilling packages and heat pumps with electrically driven compressors – Heating mode – Part 2: Testing and requirements for marking for space heating units (superseded by EN 14511)
EN 13136:2001/A1:2005	Refrigerating systems and heat pumps – Pressure relief devices and their associated piping – Method for calculation
EN 13313:2001	Refrigerating systems and heat pumps – Competence of personnel
EN 378:2000/2003/2008	Refrigerating systems and heat pumps – Safety and environmental requirements
EN 1736:2000	Refrigerating systems and heat pumps – Flexible pipe elements, vibration isolators and expansion joints – Requirements, design and installation
EN 12309:1999/2000	Gas-fired absorption and adsorption air-conditioning and/or heat pump appliances with a net heat input not exceeding 70 kW – Safety and rational use of energy
EN 12263:1998	Refrigerating systems and heat pumps – Safety switching devices for limiting the pressure – Requirements and tests

EN 1861:1998	Refrigerating systems and heat pumps – System flow diagrams and piping and instrument diagrams – Layout and symbols
ISO 13256-1:1998	Water-source heat pumps – Testing and rating for performance – Part 1: Water-to-air and brine-to-air heat pumps
ISO 13261:1998	Sound power rating of air-conditioning and air-source heat pump equipment
ISO 13253:1995	Ducted air-conditioners and air-to-air heat pumps – Testing and rating for performance
ISO 5151:1994	Non-ducted air conditioners and heat pumps – Testing and rating for performance
ISO 5149:1993	Mechanical refrigerating systems used for cooling and heating - Safety requirements

B. CLIMATE CLASSIFICATIONS

Figure B-1 displays the World climate classification map Koeppe & De Long (1958)

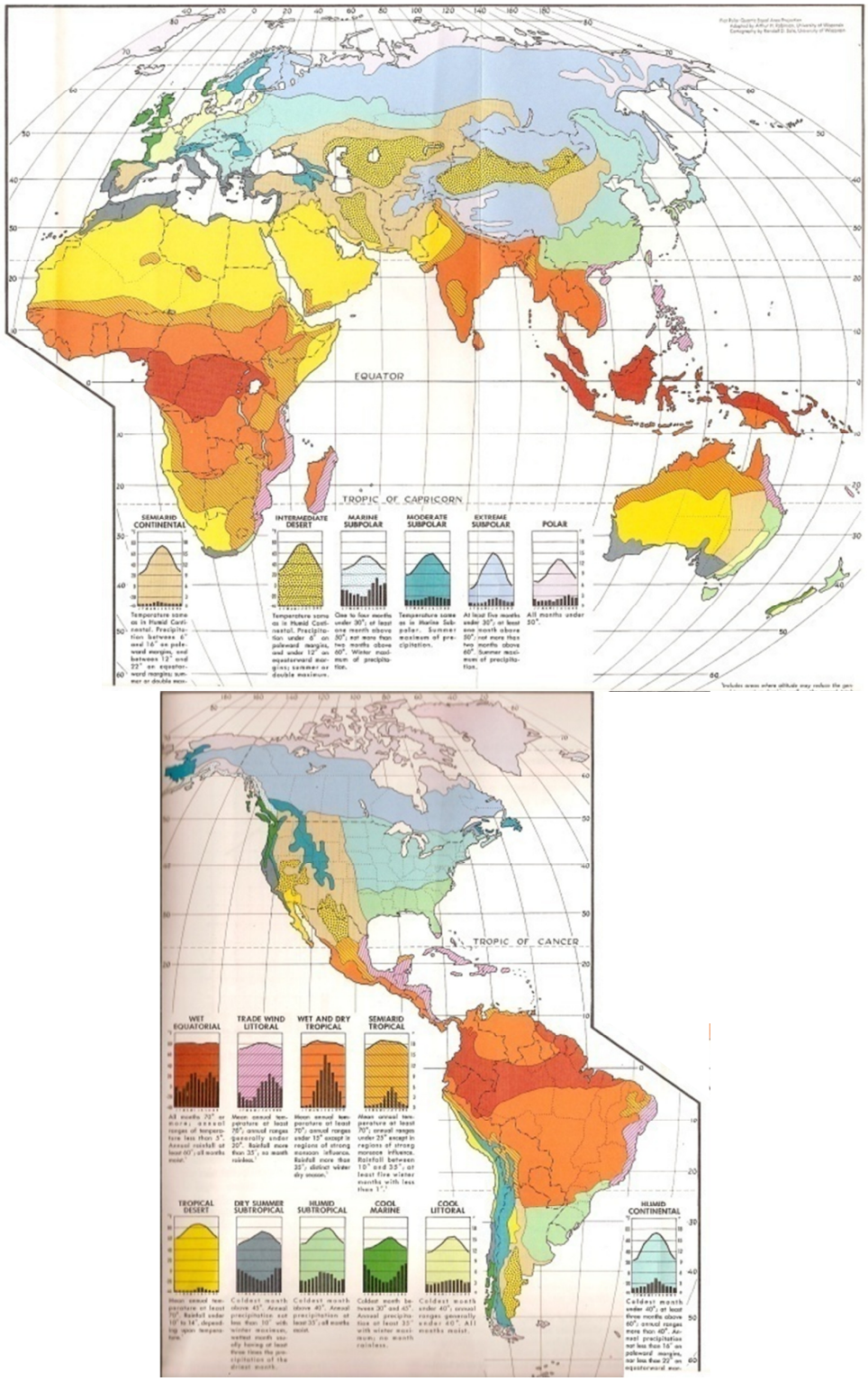

Figure B-1: World Climate Classification Map (Koeppe & De Long, 1958)

Wet Equatorial

All months 70°F (+21°C) or more, annual range of temperature less than 5°F (2.7°C). Annual rainfall at least 60" (1500mm), all months moist.

Trade Wind Littoral

Mean annual temperature at least 70°F (+21°C), annual ranges generally under 20°F (10.8°C). Rainfall more than 35" (890mm), no month rainless.

Wet and Dry Tropical

Mean annual temperature at least 70°F (+21°C), annual ranges generally under 15°F (7.1°C), except in strong monsoon influence. Rainfall more than 35" (890mm), distinct winter dry season.

Semiarid Tropical

Mean annual temperature at least 70°F (+21°C), annual ranges generally under 25°F (13.5°C), except in strong monsoon influence. Rainfall between 10" (250mm) and 35" (890mm), at least 5 winter months with less than 1" (25mm).

Tropical Desert

Mean annual temperature at least 70°F (+21°C). Rainfall under 10" (250mm) to 14" (350mm), depending upon temperature.

Dry Summer Subtropical

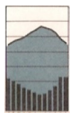

Coldest month above 45°F (+7.2°C). Annual precipitation not less than 10" (250mm) with winter maximum, wettest month usually having at least three times the precipitation of the driest month.

Humid Subtropical

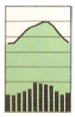

Coldest month above 40°F (+4.4°C). Annual rainfall at least 35" (890mm), all months moist.

Cool Marine

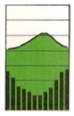

Coldest month between 30°F (-1.1°C) and 45°F (+7.2°C). Annual precipitation at least 35" (890mm) with winter maximum, no month rainless.

Cool Littoral

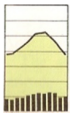

Coldest month under 40°F (+4.4°C), annual ranges generally under 40°F (21.6°C). All months moist.

Humid Continental

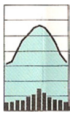

Coldest month under 40°F (+4.4°C), at least three months above 60°F (+15.5°C), annual ranges more than 40°F (21.6°C). Annual precipitation not less than 16" (400mm) on poleward margins, nor less than 22" (560mm) on equatorial margins.

Semiarid Continental

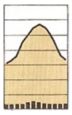

Temperature same as *Humid Continental*. Precipitation between 6" (150mm) and 16" (400mm) on poleward margins, and between 12" (300mm) and 22" (560mm) on equatorial margins; summer or double maximum.

Intermediate Desert

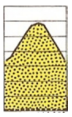

Temperature same as *Humid Continental*. Precipitation under 6" (150mm) on poleward margins, and under 12" (300mm) on equatorial margins; summer or double maximum.

Marine Subpolar

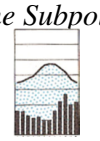

One to four months under 30°F (-1.1°C), at least one month above 50°F (+10°C); not more than two months above 60°F (+15.5°C). Winter maximum of precipitation.

Moderate Subpolar

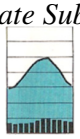

Temperature same as *marine subpolar*. Summer maximum of precipitation.

Extreme Subpolar

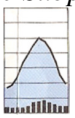

One to five months under 30°F (-1.1°C), at least one month above 50°F (+10°C); not more than two months above 60°F (+15.5°C). Summer maximum of precipitation.

Polar

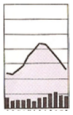

All months under 50°F (+10°C).

C. R407C Thermo-physical Properties

R-407C is a zeotropic hydrofluorocarbon blend of R-32, R-125, and R-134a. The R-32 serves to provide the heat capacity, R-125 decreases flammability, R-134a reduces pressure.

Figures C-1 and C-2 display the thermo-physical properties: specific volume (v) [m^3/kg], specific enthalpy (*h*) [kJ/kg] and specific entropy (s) [kJ/kgK] of R407C saturated liquid and vapour at saturation temperature (T_{sat}) [ºC] and saturation pressure (P_{sat}) [kPa].

(temp.)	(press.)	(specific volume)		(specific enthalpy)		(spec. entropy)	
°C	kPa	m3/kg		kJ/kg		kJ/(kgK)	
相(phase)		液(liq.)	汽(vap.)	液(liq.)	汽(vap.)	液(liq.)	汽(vap.)
-80	11.9	0.0007	2.7694	94.5	364.5	0.64	2.07
-78	13.8	0.0007	2.3866	97.0	365.7	0.66	2.06
-76	15.8	0.0007	2.0645	99.6	366.9	0.67	2.05
-74	18.1	0.0007	1.7924	102.2	368.1	0.68	2.04
-72	20.7	0.0007	1.5616	104.7	369.3	0.69	2.04
-70	23.5	0.0007	1.3651	107.3	370.6	0.71	2.03
-68	26.7	0.0007	1.1972	109.9	371.8	0.72	2.02
-66	30.2	0.0007	1.0532	112.4	373.0	0.73	2.01
-64	34.0	0.0007	0.9294	115.0	374.2	0.75	2.01
-62	38.3	0.0007	0.8225	117.6	375.4	0.76	2.00
-60	43.0	0.0007	0.7299	120.2	376.7	0.77	1.99
-58	48.1	0.0007	0.6495	122.8	377.9	0.78	1.99
-56	53.7	0.0007	0.5795	125.4	379.1	0.79	1.98
-54	59.9	0.0007	0.5183	128.0	380.3	0.81	1.98
-52	66.6	0.0007	0.4648	130.6	381.5	0.82	1.97
-50	73.8	0.0007	0.4177	133.2	382.7	0.83	1.97
-48	81.7	0.0007	0.3762	135.8	383.9	0.84	1.96
-46	90.3	0.0007	0.3396	138.4	385.1	0.85	1.96
-44	99.5	0.0007	0.3072	141.0	386.3	0.86	1.95
-42	109.5	0.0007	0.2785	143.7	387.4	0.87	1.95
-40	120.3	0.0007	0.2529	146.3	388.6	0.89	1.94
-38	131.8	0.0007	0.2301	148.9	389.8	0.90	1.94
-36	144.3	0.0007	0.2098	151.6	391.0	0.91	1.93
-34	157.6	0.0007	0.1916	154.2	392.1	0.92	1.93
-32	171.9	0.0007	0.1753	156.9	393.3	0.93	1.93
-30	187.1	0.0007	0.1606	159.6	394.4	0.94	1.92
-28	203.4	0.0008	0.1474	162.3	395.5	0.95	1.92
-26	220.8	0.0008	0.1354	165.0	396.7	0.96	1.91
-24	239.3	0.0008	0.1247	167.7	397.8	0.97	1.91
-22	259.0	0.0008	0.1149	170.4	398.9	0.99	1.91
-20	279.9	0.0008	0.1061	173.1	400.0	1.00	1.90
-18	302.1	0.0008	0.0980	175.8	401.1	1.01	1.90
-16	325.6	0.0008	0.0907	178.5	402.2	1.02	1.90
-14	350.5	0.0008	0.0840	181.3	403.2	1.03	1.90
-12	376.9	0.0008	0.0780	184.0	404.3	1.04	1.89
-10	404.7	0.0008	0.0724	186.8	405.3	1.05	1.89
-8	434.0	0.0008	0.0673	189.6	406.4	1.06	1.89
-6	465.0	0.0008	0.0626	192.4	407.4	1.07	1.88
-4	497.5	0.0008	0.0584	195.2	408.4	1.08	1.88
-2	531.8	0.0008	0.0544	198.0	409.4	1.09	1.88

Figure C-1: R407C thermo-physical properties for -80 to -2ºC (11.9 to 531.8kPa)

(temp.)	(press.)	(specific volume)		(specific enthalpy)		(spec. entropy)	
°C	kPa	m3/kg		kJ/kg		kJ/(kgK)	
相(phase)		液(liq.)	汽(vap.)	液(liq.)	汽(vap.)	液(liq.)	汽(vap.)
0	567.9	0.0008	0.0508	200.8	410.3	1.10	1.88
2	605.7	0.0008	0.0474	203.7	411.3	1.11	1.87
4	645.4	0.0008	0.0444	206.5	412.3	1.12	1.87
6	687.1	0.0008	0.0415	209.4	413.2	1.13	1.87
8	730.7	0.0008	0.0389	212.3	414.1	1.14	1.87
10	776.4	0.0008	0.0364	215.2	415.0	1.15	1.87
12	824.2	0.0008	0.0342	218.1	415.9	1.16	1.86
14	874.1	0.0008	0.0321	221.1	416.7	1.17	1.86
16	926.3	0.0009	0.0301	224.0	417.5	1.18	1.86
18	980.8	0.0009	0.0283	227.0	418.3	1.19	1.86
20	1037.6	0.0009	0.0266	230.0	419.1	1.20	1.85
22	1096.8	0.0009	0.0250	233.0	419.9	1.21	1.85
24	1158.5	0.0009	0.0235	236.1	420.6	1.22	1.85
26	1222.8	0.0009	0.0222	239.1	421.3	1.23	1.85
28	1289.6	0.0009	0.0209	242.2	422.0	1.24	1.85
30	1359.1	0.0009	0.0197	245.3	422.6	1.25	1.84
32	1431.4	0.0009	0.0185	248.4	423.3	1.26	1.84
34	1506.4	0.0009	0.0175	251.6	423.8	1.27	1.84
36	1584.3	0.0009	0.0165	254.8	424.4	1.28	1.84
38	1665.2	0.0009	0.0156	258.0	424.9	1.29	1.83
40	1749.0	0.0009	0.0147	261.2	425.3	1.30	1.83
42	1836.0	0.0009	0.0138	264.5	425.8	1.31	1.83
44	1926.1	0.0010	0.0131	267.8	426.1	1.32	1.83
46	2019.4	0.0010	0.0123	271.2	426.4	1.33	1.82
48	2116.0	0.0010	0.0116	274.6	426.7	1.34	1.82
50	2216.0	0.0010	0.0110	278.0	426.9	1.35	1.82
52	2319.4	0.0010	0.0103	281.5	427.1	1.36	1.82
54	2426.4	0.0010	0.0098	285.0	427.1	1.38	1.81
56	2537.0	0.0010	0.0092	288.6	427.1	1.39	1.81
58	2651.2	0.0010	0.0087	292.3	427.0	1.40	1.81
60	2769.2	0.0011	0.0081	296.0	426.8	1.41	1.80
62	2891.1	0.0011	0.0077	299.8	426.6	1.42	1.80
64	3017.0	0.0011	0.0072	303.7	426.2	1.43	1.80
66	3146.8	0.0011	0.0068	307.7	425.6	1.44	1.79
68	3280.8	0.0011	0.0063	311.7	424.9	1.45	1.79
70	3418.9	0.0011	0.0059	316.0	424.0	1.46	1.78
72	3561.3	0.0012	0.0055	320.3	422.9	1.48	1.78
74	3708.0	0.0012	0.0051	324.9	421.5	1.49	1.77
76	3859.1	0.0012	0.0048	329.8	419.8	1.50	1.76
78	4014.4	0.0013	0.0044	335.0	417.7	1.52	1.75

Figure C-2: R407C thermo-physical properties for 0 to 78ºC (567.9 to 4014.4kPa)

Figure C-3 displays the saturation curve for R407C.

Figure C-4 displays the evaporating and condensing pressure for the *Solterra 500* heat pump.

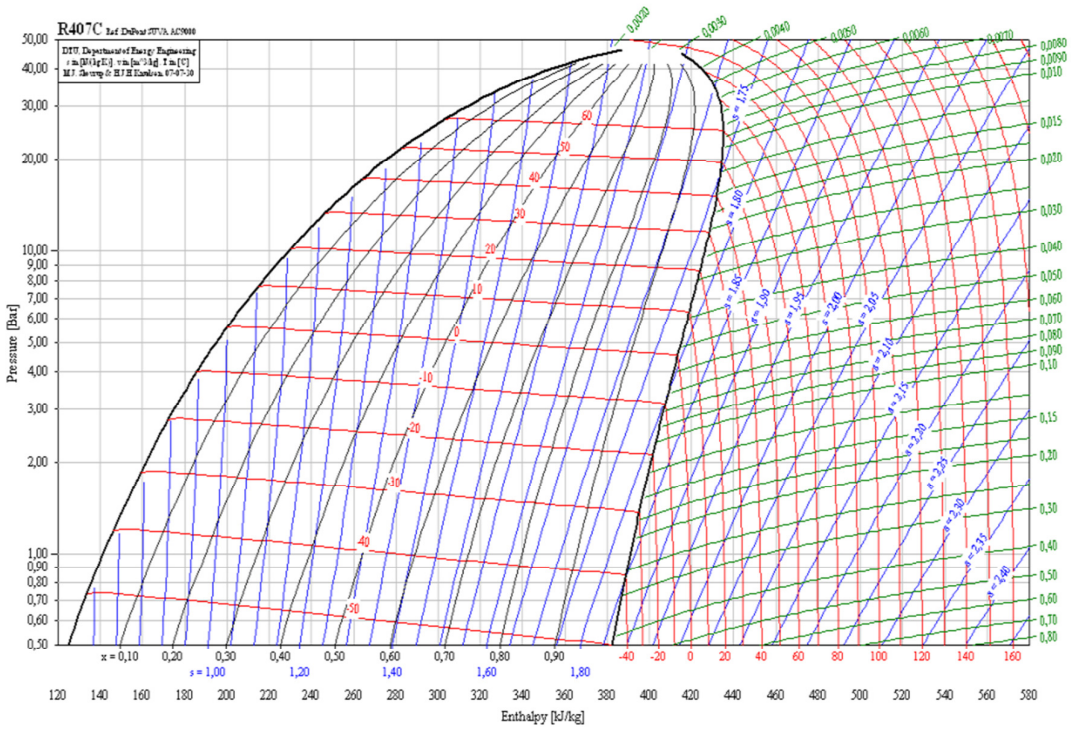

Figure C-3: Pressure - Specific Enthalpy (P-h) diagram for R407C showing saturation curve

Evaporating Pressure Condensing Pressure

Figure C-4: Evaporating and condensing pressure for *Solterra 500* heat pump

D. TEMPERATURE SENSOR CALIBRATION

The temperature sensors tested, sensor purpose and measured accuracies are as follows:

- *Omega 4-Wire PT100 Class B 1/10 DIN* RTD Fluid Sensors
  - Used to measure source and sink fluid temperatures ($T_{s,f}$, $T_{s,r}$, $T_{sk,f}$ and $T_{sk,r}$)
  - The factory accuracy of ±(1/10)(0.3+0.005(T))ºC was confirmed for all 4 sensors from 0 to 60ºC which are the expected temperature ranges
  - Accuracies as good as ±0.015ºC @ 0ºC were observed during the ice-water test
- *Omega 4-Wire PT100 Class A* RTD Fluid Sensors
  - Used to measure horizontal collector fluid temperatures ($T_{HC,f}$ and $T_{HC,r}$)
  - The factory accuracy of ±(0.3+0.005T)ºC was confirmed for both sensors at 0, 10 and 20ºC which are the expected temperature ranges
- *Sontay 4-Wire PT100 Class A* RTD Ground Sensors
  - Used to measure ground temperatures in P1 through P7
  - The factory accuracy of ±(0.3+0.005T)ºC was confirmed for all sensors at 0, 10 and 20ºC which are the expected temperature ranges
- *Sontay 3-Wire PT100 Class A* RTD Ground Sensors
  - Used to measure ground temperatures in P8 and P9
  - The factory accuracy of ±(0.3+0.005T)ºC was confirmed for all sensors at 0, 10 and 20ºC which are the expected temperature ranges

The following four methods were used to establish temperature sensor accuracy:

- Deionised ice-water test to establish accuracy at 0ºC
- Jofra (D55SE) temperature calibrator test to establish accuracy between 0 and 60ºC
- Comparison with *Omega 4-Wire PT100 Class B 1/10 DIN* RTD which have an accuracy of ±(1/10)(0.3+0.005(T))ºC to establish accuracy between 0 and 20ºC
- Comparison to one another to establish uniformity of all measurements

All calibration tests were conducted with coupling to the same DAQ system and software which was then used in the *HP-IRL/H* project. Figures D-1(a), (b), (c) and (d) display the ice-water test, *Jofra* calibrator test, *DIN 1/10* comparative test and coupling with the DAQ system, respectively.

(a) Deionised ice-water test

(b) *Jofra (D55SE)* temperature calibrator

(c) Comparative testing with DIN 1/10 sensors and each other

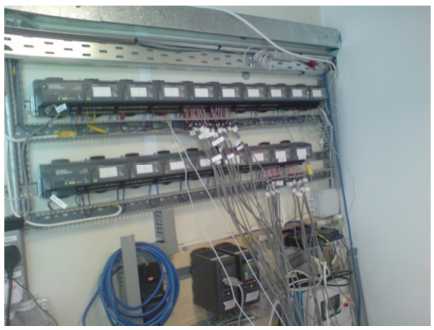

(d) Coupled testing with DAQ system

Figure D-1: Ground and fluid temperature sensor tests and calibration

E. ULTRASONIC FLOW METER CALIBRATION

Flow rate measurements $\dot{V}_s$ and $\dot{V}_{sk}$ were conducted at points on the copper piping used to couple HDPE *run-out* pipes to the evaporator heat exchanger and couple the storage tank to the condenser heat exchanger. To use the ultrasonic flow meter with pipes of varied size and material a specific coefficients are required. Tests were conducted to establish the appropriate coefficients for a range of copper pipes used in C*i*SET projects. This involved measuring the mass flow rate from a large rooftop reservoir using digital scales and DAQ as shown in Figures E-1. Tests established accuracy of ±3.5% at the $GSHP_{HC}$ sink flowrate.

(a) Continuous water flow from rooftop reservoir

(b) Ultrasonic flow meter probe on copper pipe

(c) Ultrasonic flow meter DAQ

(d) Mass flow measurement using digital scales and DAQ

Figure E-1: Flow meter calibration method

F. COP UNCERTAINTY CALCULATION

The COP was calculated using Equation F-1

$$\mathrm{COP} = \frac{q_{sk}}{w} = \frac{\rho_W c_{p,W} \dot{V}_s (T_{sk,f} - T_{sk,r})}{w} \quad \text{(F-1)}$$

Where the fluid density (ρ_W) [kg/m^3] and specific heat capacity ($c_{p,W}$) [J/kgK] were established using published empirical data for water, while the volumetric flow rate ($\dot{V}_s$) [m^3/s], sink temperatures ($T_{sk,f}$ and $T_{sk,r}$) [ºC] and power consumptions (w) [W] were measured using sensors described in Section 3.4.

The error in these measurements, summarised in Table 3-7, was as follows:

- Volumetric flow rate ($\dot{V}_s$) measured with Burkett Paddle Wheel Flow Meters has an accuracy of ±2% @ u=1m/s
  - The 2" copper pipes were fitted with a 1" bridging piece onto which the flow meters were attached to achieve this velocity and accuracy
  - This equates to lower and upper values of 98% and 102% respectively
- Sink temperatures ($T_{sk,f}$ and $T_{sk,r}$) accuracy of ±(1/10)(0.3+0.005(T))ºC
  - With a typical temperature difference across the heat sink (ΔT_{sk}) of 7K at an average temperature of 46ºC total uncertainty is ±0.106ºC
  - The total uncertainty of ±0.106ºC equates to (ΔT_{sk}) percentage uncertainty of ±1.5%
  - This equates to lower and upper values of 98.5% and 101.5% respectively
- Power consumption (w) accuracy of ±0.5%
  - This equates to lower and upper values of 99.5% and 100.5% respectively

The lower COP uncertainty was calculated as follows

$$\Delta \mathrm{COP}_{\mathrm{lower}}\ (\%) = \left[1 - \left(\frac{0.98 * 0.985}{1.005}\right)\right] * 100 = -4\% \quad \text{(F-2)}$$

The upper COP uncertainty was calculated as follows

$$\Delta \mathrm{COP}_{\mathrm{upper}}\ (\%) = \left[\left(\frac{1.02 * 1.015}{0.995}\right) - 1\right] * 100 = +4\% \quad \text{(F-3)}$$

Therefore the total COP uncertainty was found to be ±4%

G. HEAT FLUX AND MOISTURE SENSORS

Prior to underground installation in the vertical ground profiles, the heat flux (HFP01) and moisture (CS-616L) sensors were tested in a laboratory using the compacted sand bed shown in Figure G-1. Sensors were installed in horizontal profiles and connected to the CR1000 DAQ system via the AM16/32B multiplexer.

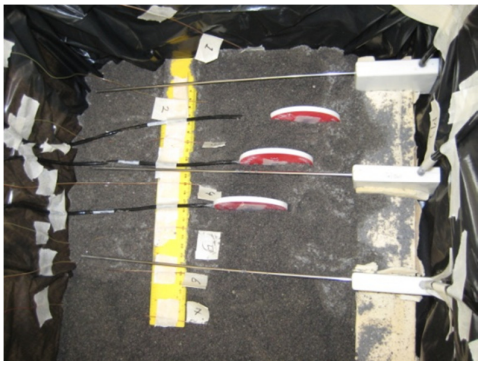

(a) Burying type K thermocouples, HFP01 and CS616L sensors in compacted sand

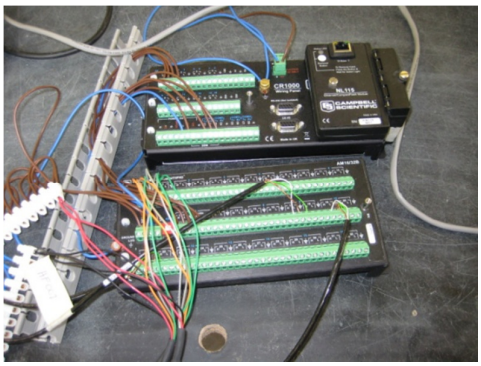

(b) CR1000, AM16/32B and NL115

Figure G-1: Construction of laboratory based heat flux and moisture senor testing rig

In order to test the moisture sensor response, measured volumes of water were added to the compacted sand bed at measured intervals. The change in volumetric moisture content was then calculated and compared with the sensor measurements. Figure G-2 displays a comparison between the two measurement methods along with the cumulative water added to the compacted sand bed.

Additionally, the influence of moisture content on thermal conductivity was established by attaching a 90W heater to the side of the compacted sand bed and insulating it on one side.

By measuring temperature gradients, heat flux values and moisture content, the trends displayed in Figured G-3(a) and (b) were established.

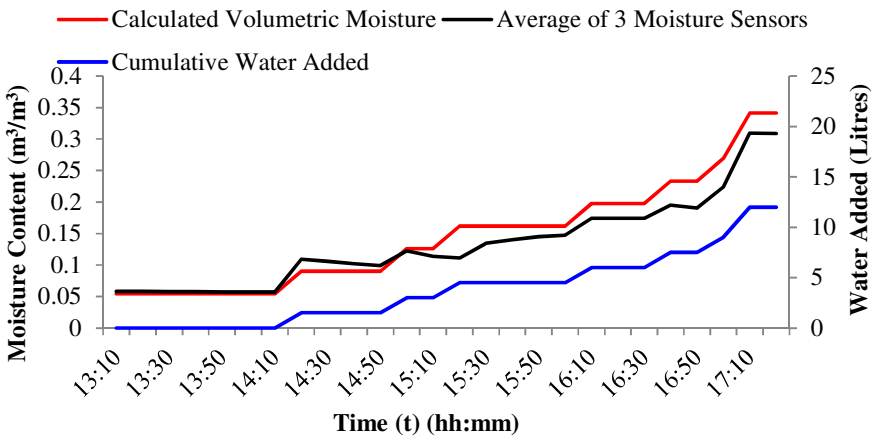

Figure G-2: Moisture sensor calibration results

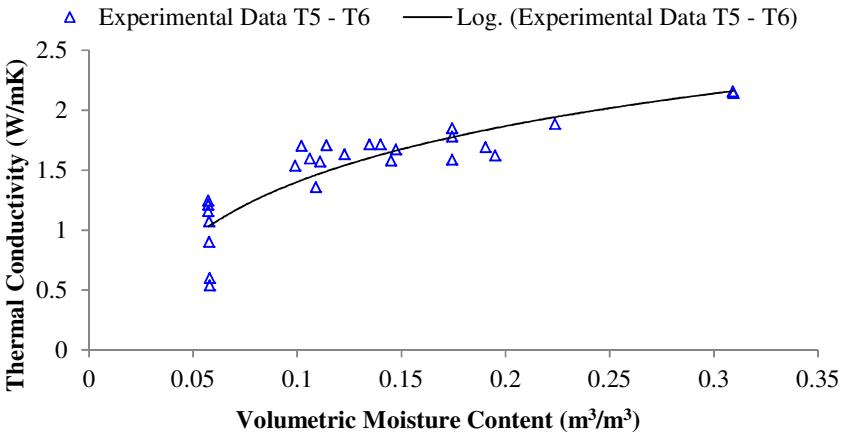

(a) Thermal conductivity established between T5 and T6

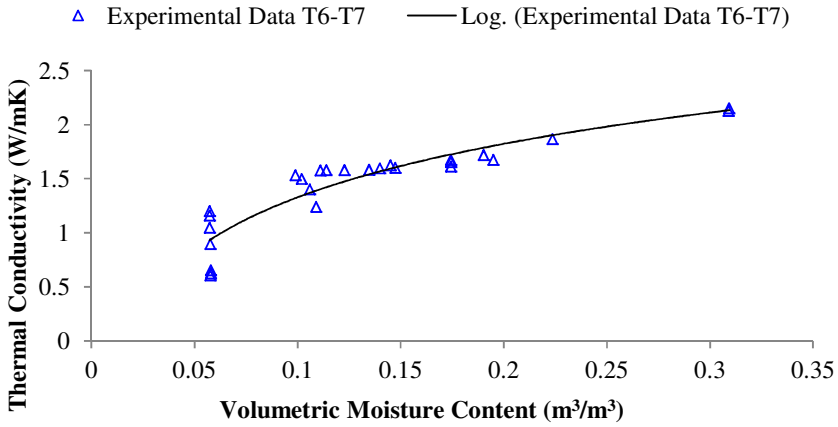

(b) Thermal conductivity established between T6 and T7

Figure G-3: Laboratory based thermal conductivity tests

H. WEATHER STATION COMPONENT CERTIFICATES

Calibration certificates for weather station components are presented in this appendix. Figure H-1 presents the calibration certificate for CMP 3 pyranometer

MEASUREMENT EXCELLENCE SINCE 1830 Kipp & Zonen 175 YEARS

Kipp & Zonen B.V.
Röntgenweg 1 2624 BD Delft
P.O. Box 507 2600 AM Delft
The Netherlands
T +31 (0)15 269 8000
F +31 (0)15 262 0351
E info@kippzonen.com
www.kippzonen.com

CALIBRATION CERTIFICATE

PYRANOMETER

PYRANOMETER MODEL	:	CMP 3
SERIAL NUMBER	:	050093
SENSITIVITY at normal incidence on horizontal pyranometer	:	13.46 µV/W/m^2
IMPEDANCE	:	33 Ohm
CALIBRATION PROCEDURE	:	The indoor calibration procedure is based on a side-by-side comparison with a reference pyranometer under an artificial sun fed by an AC voltage stabiliser. It embodies a 150 W Metal-Halide high-pressure gas discharge lamp. Behind the lamp is a reflector with a diameter of 16.2 cm. The reflector is 110 cm above the pyranometers producing a vertical beam. The reference and test pyranometers are mounted horizontally on a table, which can rotate. The irradiance at the pyranometers is approximately 500 W/m². During the calibration procedure the reference and test pyranometer are interchanged to correct for any non-homogeneity of the beam. The dark offsets of both pyranometers are measured before and after the interchange and taken into account.
REFERENCE PYRANOMETER	:	Kipp & Zonen CM 3 sn950512 active from 01/01/2005.
hierarchy of traceability	:	This pyranometer was compared with the sun and sky radiation as source under mainly clear sky conditions using the "continuous sun-and-shade method". The readings are referred to the World Radiometric Reference (WRR) as stated in the WMO Technical Regulations. The measurements were performed in Davos (latitude: 46.8143°, longitude: -9.8458°, altitude: 1588m above sea level). The inclination of the receiver surfaces versus their horizontal position were set to 0.0 degrees, the instrument signal wire to the north. During the comparisons, the instrument received global radiation intensities from 653 to 1005 with a mean of 820 W/m^2. The angle between the solar beam and the normal of the receiver surface varied from 24 to 50 with a mean of 39 degrees. The instrument temperature ranged from +11.7 to +20.7 with a mean of +17.7°C. The sensitivity calculation and the single measurements deviation (σ) are based on 1001 individual measurements. The obtained sensitivity value is valid for similar conditions and is: 16.04 ± 0.11 µV/W/m^2 (but is corrected by Kipp & Zonen to 16.33 µV/W/m². See "correction applied" below.) The testing was done June 7, July 28, 29, September 2, 5, 6, 7 and 9, 2004. Global radiation data were calculated from the direct solar radiation as measured with the absolute cavity pyrheliometer HF18748 (member of the WSG, WRR-Factor: 0.99568, based on the last International Pyrheliometer Comparison IPC-2000) and from the diffuse radiation as measured with a continuous disk shaded pyranometer Kipp & Zonen CM 22 sn020059 with sensitivity 8.91 (ventilated with heated air, instrument-wire to the north).
correction applied	:	+1.8 % This correction was necessary to correct for the mean directicnal errors of the reference CM 3 in Davos. This error is estimated at Kipp & Zonen measuring the cosine error for the mean angle of incidence at azimuth S-30° and S+30°. The reference CM 3 now measures the vertical directed beam of the indoor calibration facility more correctly.
IN CHARGE OF TEST	:	F. de Wit Date:August 29, 2005 Kipp & Zonen, Delft, Holland

Figure H-1: Calibration certificate for Kipp and Zonen CMP3 Pyranometer for total solar radiation measurement

Figure H-2 presents the calibration certificate for the CGR3 pyrgeometer

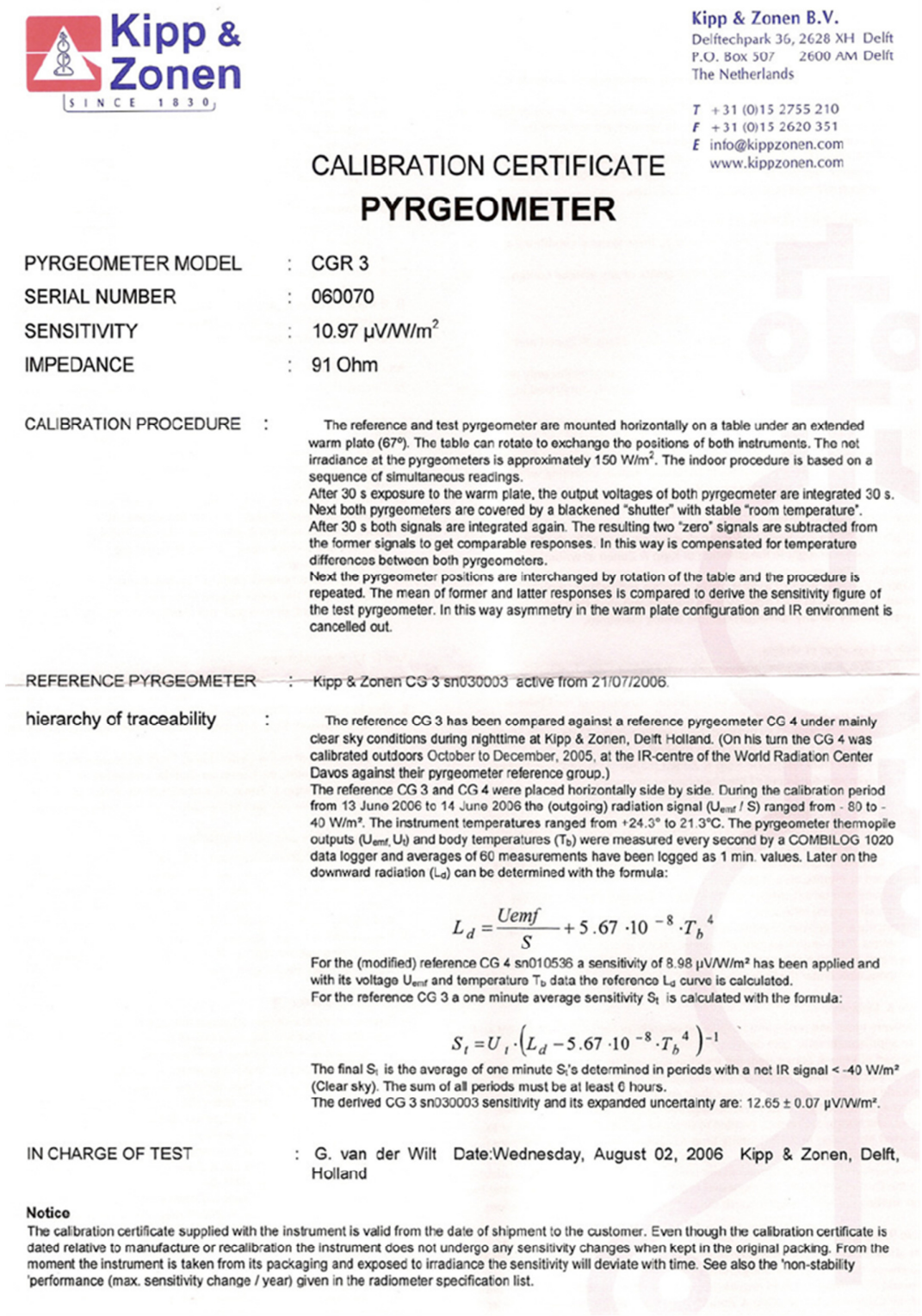

Kipp & Zonen B.V.
Delftechpark 36, 2628 XH Delft
P.O. Box 507 2600 AM Delft
The Netherlands

T +31 (0)15 2755 210
F +31 (0)15 2620 351
E info@kippzonen.com
www.kippzonen.com

CALIBRATION CERTIFICATE

PYRGEOMETER

PYRGEOMETER MODEL	:	CGR 3
SERIAL NUMBER	:	060070
SENSITIVITY	:	10.97 µV/W/m^2
IMPEDANCE	:	91 Ohm

CALIBRATION PROCEDURE :

The reference and test pyrgeometer are mounted horizontally on a table under an extended warm plate (67°). The table can rotate to exchange the positions of both instruments. The net irradiance at the pyrgeometers is approximately 150 W/m^2. The indoor procedure is based on a sequence of simultaneous readings.
After 30 s exposure to the warm plate, the output voltages of both pyrgeometer are integrated 30 s. Next both pyrgeometers are covered by a blackened "shutter" with stable "room temperature". After 30 s both signals are integrated again. The resulting two "zero" signals are subtracted from the former signals to get comparable responses. In this way is compensated for temperature differences between both pyrgeometers.
Next the pyrgeometer positions are interchanged by rotation of the table and the procedure is repeated. The mean of former and latter responses is compared to derive the sensitivity figure of the test pyrgeometer. In this way asymmetry in the warm plate configuration and IR environment is cancelled out.

REFERENCE PYRGEOMETER : Kipp & Zonen CG 3 sn030003 active from 21/07/2006.

hierarchy of traceability :

The reference CG 3 has been compared against a reference pyrgeometer CG 4 under mainly clear sky conditions during nighttime at Kipp & Zonen, Delft Holland. (On his turn the CG 4 was calibrated outdoors October to December, 2005, at the IR-centre of the World Radiation Center Davos against their pyrgeometer reference group.)
The reference CG 3 and CG 4 were placed horizontally side by side. During the calibration period from 13 June 2006 to 14 June 2006 the (outgoing) radiation signal (U_{emf} / S) ranged from - 80 to - 40 W/m². The instrument temperatures ranged from +24.3° to 21.3°C. The pyrgeometer thermopile outputs (U_{emf}, U_t) and body temperatures (T_b) were measured every second by a COMBILOG 1020 data logger and averages of 60 measurements have been logged as 1 min. values. Later on the downward radiation (L_d) can be determined with the formula:

$$L_d = \frac{Uemf}{S} + 5.67 \cdot 10^{-8} \cdot T_b^{\,4}$$

For the (modified) reference CG 4 sn010536 a sensitivity of 8.98 µV/W/m² has been applied and with its voltage U_{emf} and temperature T_b data the reference L_d curve is calculated.
For the reference CG 3 a one minute average sensitivity S_t is calculated with the formula:

$$S_t = U_t \cdot \left(L_d - 5.67 \cdot 10^{-8} \cdot T_b^{\,4}\right)^{-1}$$

The final S_t is the average of one minute S_t's determined in periods with a net IR signal < -40 W/m² (Clear sky). The sum of all periods must be at least 6 hours.
The derived CG 3 sn030003 sensitivity and its expanded uncertainty are: 12.65 ± 0.07 µV/W/m².

IN CHARGE OF TEST : G. van der Wilt Date:Wednesday, August 02, 2006 Kipp & Zonen, Delft, Holland

Notice
The calibration certificate supplied with the instrument is valid from the date of shipment to the customer. Even though the calibration certificate is dated relative to manufacture or recalibration the instrument does not undergo any sensitivity changes when kept in the original packing. From the moment the instrument is taken from its packaging and exposed to irradiance the sensitivity will deviate with time. See also the 'non-stability 'performance (max. sensitivity change / year) given in the radiometer specification list.

Figure H-2: Calibration certificate for Kipp and Zonen CMP3 Pyrgeometer for longwave radiation measurement

Figure H-3 presents the calibration certificate for the RM Young 05103 wind speed and direction sensor from which Vector Instruments anemometer and potentiometer were calibrated.

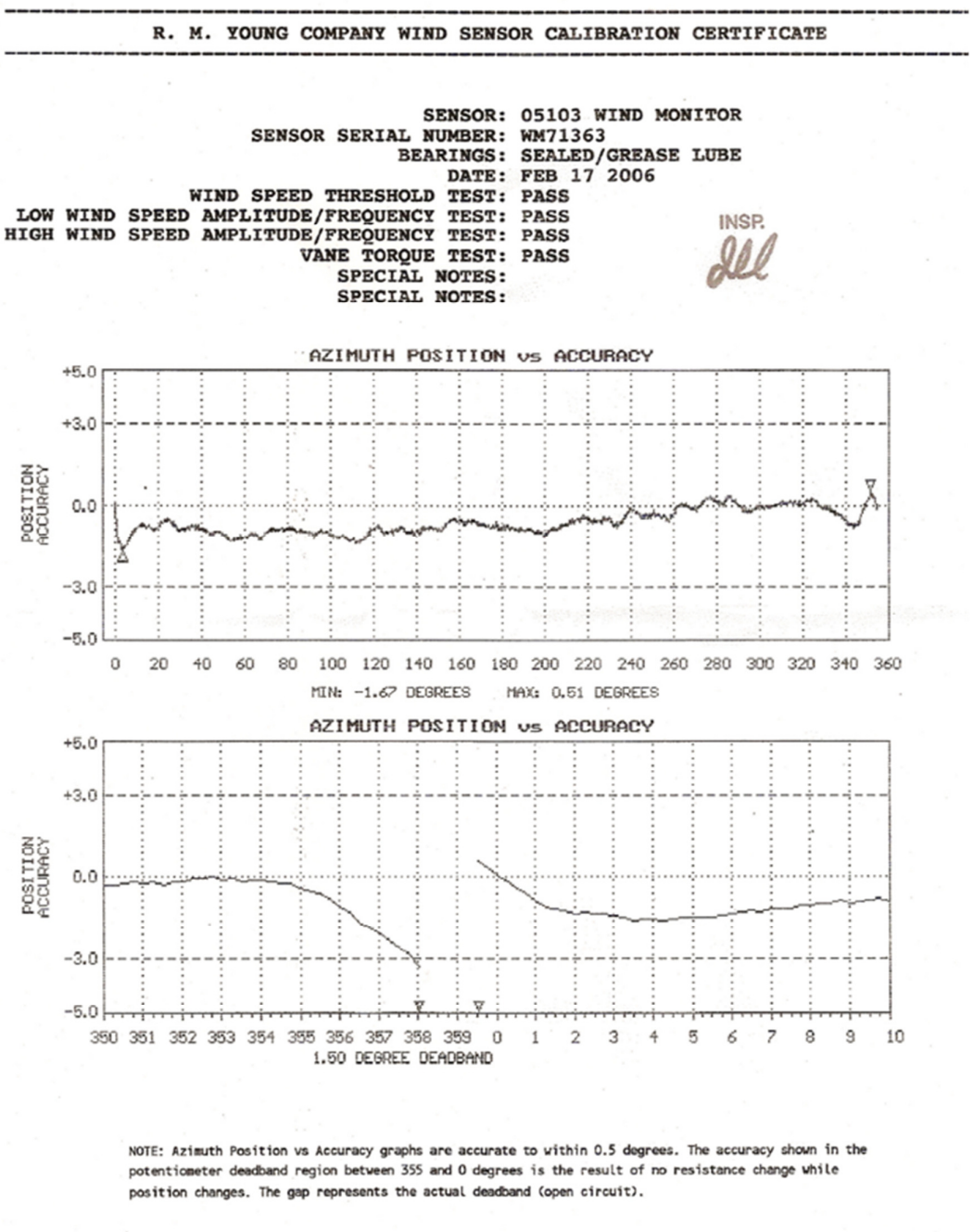

Figure H-3: Calibration certificate for RM Young 05103 wind speed and direction

Figure H-4 presents the calibration certificate for the Vaisala HMP45C humidity and temperature sensor

VAISALA

Certificate report nr. H06-06040012

CALIBRATION CERTIFICATE

Instrument	HMP45AC Humidity and temperature probe
Serial number	B0410012
Manufacturer	Vaisala Oyj, Finland
Calibration date	23rd January 2006
Test procedure	Doc210426-A

The above instrument was calibrated by comparing the relative humidity and temperature readings to two HMP233 factory working standards. At the time of shipment, the instrument described above met its operating specifications.

The relative humidity readings of the two HMP233 factory working standards have been calibrated at the Vaisala factory by using Hygro M-3 dewpoint meter. Hygro M-3 dewpoint meter has been calibrated at Vaisala Measurement Standards Laboratory (MSL) by using the MSL primary standard traceable to the NIST. The temperature readings of the two HMP233 factory working standards have been calibrated at MSL by using the MSL working standard traceable to the NIST. The temperature calibration at MSL has been accredited by the FINAS according to the ISO/IEC 17025.

Calibration results

Reference humidity* % RH	Observed humidity % RH	Difference %RH	Permissible difference %RH
0.5	1.5	+ 1.0	±2.0
46.0	46.4	+ 0.4	±2.0
73.7	74.3	+ 0.6	± 2.0
Reference temperature* °C	**Observed temperature** °C	**Difference** °C	**Permissible difference** °C
+ 23.02	+22.90	- 0.12	± 0.2

*Average of two references.

Equipment used in calibration

Type	Serial number	Calibration date	Certificate number
HMP233 / RH	P1740018	2006-01-13	H06-06020091
HMP233 / RH	623114	2006-01-13	H06-06020092
Vaisala HMP233 / T	P1740018	2005-05-03	K008-N00671
Vaisala HMP233 / T	623114	2005-05-03	K008-N00670
HYGRO M-3	361095	2005-01-26	N00160
HP 34401A	3146A68712	2005-11-03	K004-05S719

Uncertainties (95 % confidence level, k=2)
Humidity ±1.0%RH @ 0..15%RH, ±1.5%RH @ 15..78%RH
Temperature ± 0.13 °C
Ambient conditions / Humidity 34 ± 5%RH, Temperature 23 ± 1 °C, Pressure 1040 ± 1 hPa.

For Vaisala Oyj

Kirsi Juuska

Vaisala Oyj
Vanha Nurmijärventie 21
FIN-01670 Vantaa, Finland

Tel. (+ 358 9) 8949 2658
Fax (+ 358 9) 8949 2295
http://www.vaisala.com

Domicile Vantaa, Finland
Trade Reg. No. 96.607

Figure H-4: Calibration certificate for Vaisala HMP45C combined temperature and relative humidity sensor

Wind Speed Gauge Calibration

The R. M. Young 05103 Wind Monitor was calibrated using a wind tunnel was used. A variable speed drive allows control over the fan motor's frequency, which has been calibrated to control wind speeds. The wind speed detected by the gauge was measured at varying motor frequencies to ensure accurate measurements. The wind gauge in the wind tunnel is presented in Figures H-5(a) and (b).

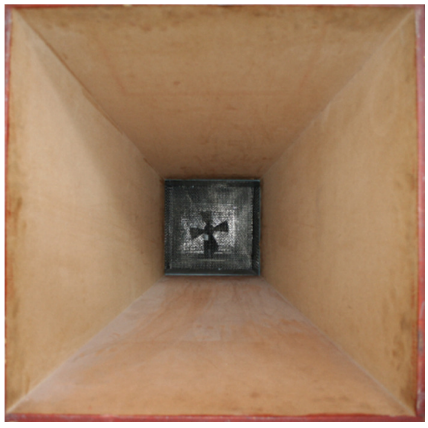

(a) Elevation view of wind tunnel tests

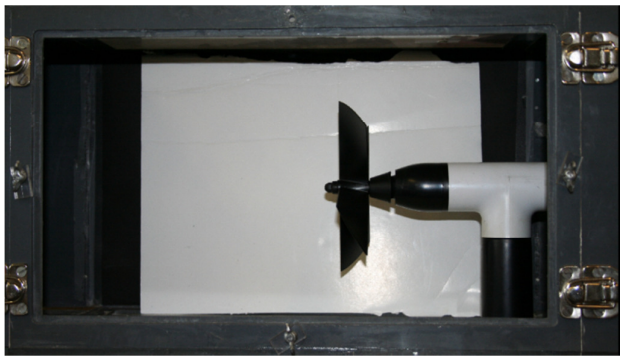

(b) End view of wind tunnel tests

Figure H-5: Wind gauge calibration tests

Rain Gauge Calibration

The RM Young rain gauge was calibrated by controlling the flow of water using a pipette and comparing the actual flow to the measured flow by the gauge. The calibration rig is shown in Figure H-6.

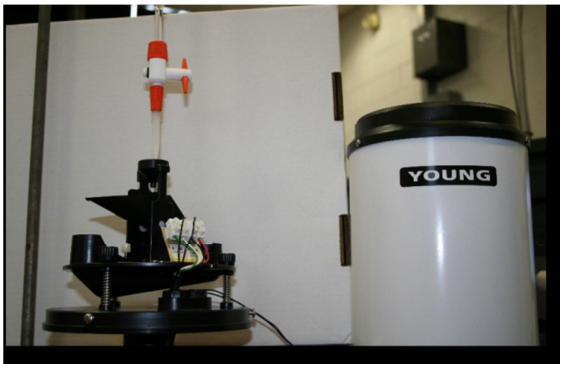

Figure H-6: Rain gauge calibration tests

I. SOLAR SEASONS

Figure I-1 depicts the seasonal change in declination and the angle of incidence.

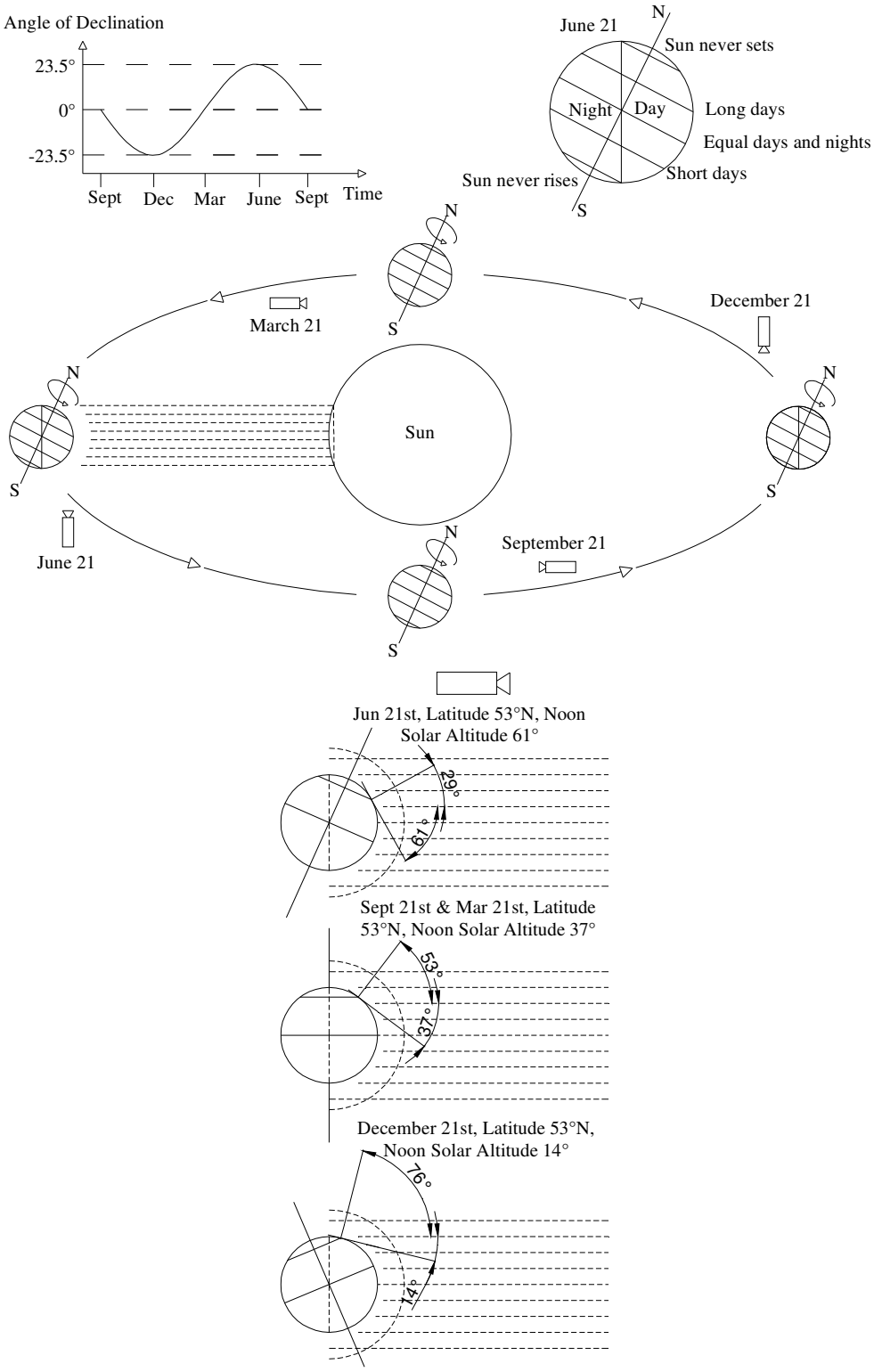

Figure I-1: Variation in declination with seasons and the influence on angle of incidence

J. SOIL THERMAL PROPERTIES FORMULAE

Volumetric heat capacity is found as follows

$$C_g = \rho_{bulk} c_{p,s} + \rho_w c_{p,w} \theta_{wg} \quad \text{(J-1)}$$

Thermal conductivity requires the conductivity, fraction and weighting factor for each constituent

$$k_g = \frac{\sum_{i=0}^{n} k_i x_i \delta_i}{\sum_{i=0}^{n} x_i \delta_i} \quad \text{(J-2)}$$

Weighting factors depend on the particle shape factors. Water is typically taken as a continuous fluid with a weighting factor of 1.

$$\delta_i = \frac{1}{3} \sum_{j=1}^{3} \left[1 + \left(\frac{k_i}{k_0} - 1\right) g_j\right]^{-1} \quad \text{(J-3)}$$

Where $g_1+g_2+g_3=1$ and $g_1=g_2$ then only g_1 must be determined for each constituent.

Above the critical water content the shape factor g_1 for air is found as follows

$$g_{1,a} = 0.333 - 0.298 \frac{\eta_a}{(1-v_s)} \quad \text{(J-4)}$$

Below the critical water content a linear interpolation is used

$$g_{1,a} = 0.013 + \frac{\theta_{wg}}{\theta_{w,c}} (g_{1,a,c} - 0.013) \quad \text{(J-5)}$$

For solids the shape factor g1 depends on the shape of solids, typical values are shown in Table J-1.

Table J-1: Solid shape factors (Piechowski, 1996)

	Quartz	Feldspar	Calcite	Clay Minerals	Mica	Organics
(n)	3	9	2	100	10	0
(g_1)	0.182	0.0947	0.236	0.00775	0.0696	0.5

The thermal diffusivity is defined as the ratio of the thermal conductivity (heat transport property) to the volumetric heat capacity (heat storage property) of the ground.

$$\alpha_g = \frac{k_g}{C_g} \quad \text{(J-6)}$$

K. COLLECTOR DIMENSIONS

Table K-1 presents the most frequently referenced 'rules of thumb' used to dimension a collectors with dimensions from *HP-IRL/H*, Hepbasli *et al.* (2003), Pulat *et al.* (2009) and Demir *et al.* (2009) listed beneath. COP values for the heat pump unit only (COP_{hp}) and the system (COP_{sys}), which includes non-compressor power, are quoted for *HP-IRL/H*, Hepbasli *et al.* (2003) and Pulat *et al.* (2009). It is noticeable that the *HP-IRL/H* COP_{hp} and COP_{sys} are the highest reported while the reported reduction in COP with the inclusion of non-compressor power is lowest for the *HP-IRL/H* collector.

Table K-1: Comparison of 4 ground collectors with frequently referenced 'rules of thumb'

Collector Design	**($\dot{V}_s$ / q_{sk}) [$m^3/h/kW_{th}$]**	**(L_t / q_{sk}) [m/kW_{th}]**	**(D_i) [m]**	**(q_{sk} /A_{HC}) [W/m^2]**	**(PS) [m]**	**($\|Z_{HC}\|$) [m]**	**COP_{hp} [-]**	**COP_{sys} [-]**
Frequently referenced 'rules of thumb'	0.162 to 0.192 (Kavanaugh & Rafferty 1997)	35 to 60 (Retscreen, 2005)	-	8 to 40 (VDI – 4640, 2004)	0.3 to 0.8 (VDI – 4640, 2004)	1.2 to 1.5 (VDI – 4640, 2004)	-	-
HP-IRL/H $GSHP_{HC}$ by Dunstar Ltd.	0.28 Parallel flow	100	0.026	35	0.25 to 0.4	0.8 to 1.35	2.85 to 5.2	2.6 to 4.5 (8 to 13% less)
$GSHP_{VC}$ Hepbalsi *et al.* (2003)	0.47 Series flow	14.686	0.031	N/A	N/A	N/A	1.656	1.339 (19% less)
$GSHP_{HC}$ Pulat *et al.* (2009)	0.167 Series flow	30	0.016	161	0.3	2	4.03 to 4.18	2.46 to 2.58 (39% less)
$GSHP_{HC}$ Demir *et al.* (2009)	0.106 Parallel flow	30	0.0125	15	2.5 to 3	1.8	-	-

A method for thermo-hydraulic dimensioning using the analytical methods developed in this *HP-IRL/H* study is now proposed.

Thermo-hydraulic Collector Dimensioning Process

This design process is concerned with the *collector dimensions* of N, L_t, $\dot{m}_s$, D_o and D_i alone and the following assumptions were made:

- Thermo-hydraulic design is independent of climate and soil conditions (Paepe & Janssens, 2003)
- The theoretical collector for optimisation is located in an infinite water source with no thermal interference between pipes
- Pipe-water interface temperature is constant along the pipe length (L)
- Pipes are approximated as smooth wall ducts

The following models and methods were used as building blocks for this analysis:

- Source return temperature was calculated using the collector thermal model, AL-9, described in Section 6.4
    - The ground resistance term (R_g) in Equation 6-31 was dropped based on the assumptions detailed
    - T_∞ has a constant value of 5ºC given the infinite water source assumption
- Heat pump extraction from the source (q_s) was found using model AL-7, described in Sub-section 6.2.2
    - This model is sensitive to $T_{s,r}$ and $T_{sk,f}$ however necessary data was not available to include the influence of $\dot{V}_s$ and $\dot{V}_{sk}$
    - For this reason the evaporator flow rate recommended by heat pump manufacturer should be used
- Heat pump COP was also found using model AL-7, Sub-section 6.2.2
    - This COP is based on 'Sol 500' COP from Arsenal Research
- Pumping power for the collector and run-out piping was calculated using the collector hydraulic model, AL-8, described in Sub-section 6.3.1
    - The evaporator head loss term $H_{f,evap}$ in Equation 6-15 was not included as this is already included in the *Solterra 500* COP evaluated by *Arsenal Research*
- COP was then modified to include pumping power for the collector
- The heat pump, collector materials and collector installation prices come from the techno-economic analysis database established by Burke (2010)
- Fuel prices were based on data from SEAI (SEAI, 2010)
- Payback is calculated for dwellings of variable annual heat demand, heat demand is input as kWh_{th}/annum

The following three feedback loops exist:

- $T_{s,f}$ is a function of q_s and $T_{s,r}$ (Equation 6-34)
- q_s is a function of $T_{s,r}$ and $T_{sk,f}$ (Equation 6-10)
- $T_{s,r}$ is calculated based on $T_{s,f}$ and T_∞ (Equation 6-25)

Therefore, as shown in Figure K-1, models AL-7 and AL-9 are set-up for simultaneous solution, similar to Equation 6-36, for variable inputs of $\dot{m}_s$, N, L_t and D_{in}. Model AL-8 calculates the pumping power for the collector and run-outs. Then the 'Sol 500' COP calculated from $T_{s,r}$ with AL-7 is then updated to a 'HP-IRL/H' COP by including the collector and run-out pumping power from AL-8.

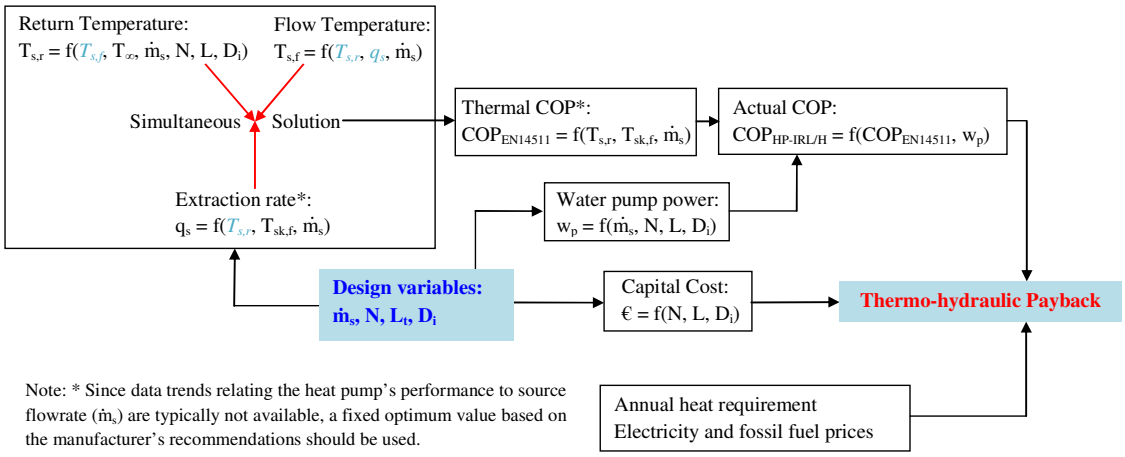

Figure K-1: Flowchart displaying the process used to solve AL-7 and AL-9 simultaneously while calculating pump power using AL-8

As shown in Figure K-2, the *MS-Excel Solver tool*, an add-on for *MS-Excel* was then included in the spreadsheet. The *solver tool* can achieve user-defined conditions (maximum, minimum or fixed value) for a dependent variable which is a function of a number of independent variables and conditions.

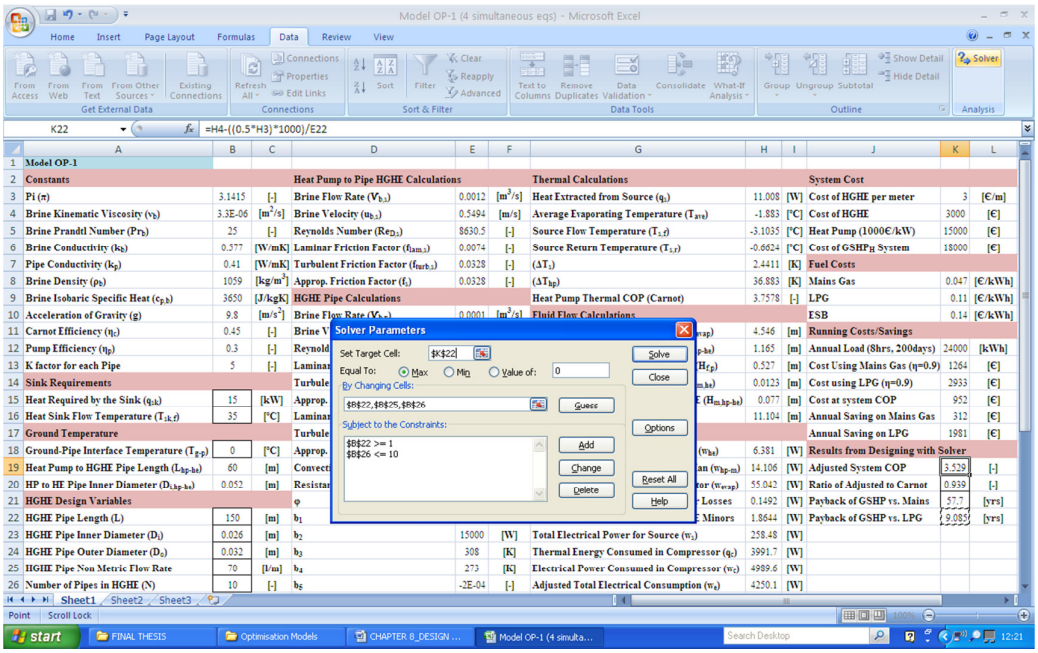

Figure K-2: Spreadsheet incorporating the simultaneous solution method shown in Figure K-1